

# **TOWARDS SELECTIVE POLY-ADP- RIBOSE POLYMERASE INHIBITORS**

By

Ilsa Talaya Okonogi Kirby

A DISSERTATION

Presented to the Department of Physiology & Pharmacology  
and the Oregon Health & Science University

School of Medicine

in partial fulfillment of the requirements for the degree of

Doctor of Philosophy

January 2019

School of Medicine

Oregon Health & Science University

CERTIFICATE OF APPROVAL

This is to certify that the PhD dissertation of  
Ilsa Talaya Okonogi Kirby  
has been approved

---

Michael Cohen, Ph.D. (Mentor)

---

Thomas Scanlan, Ph.D. (Committee Chair)

---

Carsten Schultz, Ph.D. (Member)

---

Michael Riscoe, Ph.D. (Member)

---

Kimberly Beatty, Ph.D (Member)

Copyright © 2019 Ilsa Talaya Kirby

# Table of Contents

<b>TOWARDS SELECTIVE POLY-ADP-RIBOSE POLYMERASE</b>	
<b>INHIBITORS .....</b>	<b>I</b>
<b>TABLE OF CONTENTS .....</b>	<b>IV</b>
<b>ACKNOWLEDGMENTS .....</b>	<b>XIV</b>
<b>ABSTRACT .....</b>	<b>XV</b>
<b>CHAPTER 1: INTRODUCTION.....</b>	<b>1</b>
<b>ABSTRACT .....</b>	<b>2</b>
<b>THE PARP FAMILY.....</b>	<b>4</b>
<b>COMMON AND DISTINCT FEATURES IN THE CATALYTIC</b>	
<b>DOMAIN OF PARPS .....</b>	<b>7</b>
<b>THE NAD<sup>+</sup> BINDING DOMAIN .....</b>	<b>7</b>
<b>HYE vs. HYΦ-PARPs .....</b>	<b>9</b>
<b>NON-CONSERVED LOOPS .....</b>	<b>9</b>
<b>EARLY DEVELOPMENTS IN THE FIELD: INITIAL FOCUS ON</b>	
<b>SMALL MOLECULE INHIBITORS OF PARP1 .....</b>	<b>11</b>
<b>THE FOUNDING PARP INHIBITORS .....</b>	<b>11</b>
<b>PARP1/2 IDENTIFIED AS THERAPEUTIC TARGETS IN CANCER .....</b>	<b>13</b>
<b>MOVING BEYOND PARP1/2.....</b>	<b>16</b>
<b>FORWARD CHEMICAL GENETIC SCREEN IDENTIFIES A SMALL MOLECULE</b>	
<b>INHIBITOR OF PARP5A/B.....</b>	<b>16</b>



A DEARTH OF SELECTIVE AND POTENT INHIBITORS FOR THE HYΦ-PARP SUBFAMILY.....	17
<b>STRUCTURAL STUDIES OF PARP INHIBITORS: INSIGHTS INTO INHIBITOR POTENCY AND SELECTIVITY .....</b>	<b>21</b>
STRUCTURAL STUDIES OF HYE-PARP INHIBITORS .....	21
STRUCTURAL STUDIES OF HYΦ-PARP INHIBITORS .....	22
PHARMACOPHORE FOR PARP INHIBITORS .....	23
<b>CHEMICAL AND BIOLOGICAL REAGENTS FOR MEASURING PARP ACTIVITY .....</b>	<b>24</b>
NAD <sup>+</sup> ANALOGUES FOR <i>IN VITRO</i> ANALYSIS .....	24
DETECTION METHODS WITH ENDOGENOUS NAD <sup>+</sup> .....	25
<b>ASSESSING PARP INHIBITOR SELECTIVITY ACROSS THE PARP FAMILY .....</b>	<b>28</b>
PROFILING USING PROTEIN STABILIZATION REVEAL LACK OF SELECTIVITY OF MANY PARP INHIBITORS .....	28
POLYPHARMACOLOGY AMONG PARP INHIBITORS .....	29
<b>FUTURE DIRECTIONS FOR THE FIELD .....</b>	<b>31</b>
<b>DISSERTATION OVERVIEW .....</b>	<b>34</b>
<b>CHAPTER 2: DEVELOPMENT OF A SENSITIVE, FAMILY-WIDE PARP INHIBITOR SCREENING ASSAY.....</b>	<b>36</b>
<b>ABSTRACT .....</b>	<b>37</b>
<b>INTRODUCTION .....</b>	<b>38</b>
<b>RESULTS .....</b>	<b>39</b>

ASSAY METHODOLOGY.....	39
ASSAY VALIDATION WITH LITERATURE COMPOUNDS .....	43
<b>DISCUSSION.....</b>	<b>45</b>
FUTURE DIRECTIONS .....	45
<b>CONCLUSIONS .....</b>	<b>49</b>
<b>METHODS .....</b>	<b>50</b>
<b>CHAPTER 3: A SELECTIVE PARP11 INHIBITOR SUGGESTS COUPLING BETWEEN CELLULAR LOCALIZATION AND CATALYTIC ACTIVITY .....</b>	<b>64</b>
<b>ABSTRACT .....</b>	<b>65</b>
<b>INTRODUCTION .....</b>	<b>66</b>
<b>RESULTS .....</b>	<b>68</b>
STRUCTURE-GUIDED DESIGN LEADS TO SMALL MOLECULE INHIBITORS SELECTIVE FOR HYΦ-PARPs .....	68
STRUCTURAL STUDIES OF ITK1 REVEAL A UNIQUE HYDROPHOBIC SUB- POCKET IN AN HYΦ-PARP .....	74
EXPLOITING DIFFERENCES IN THE D-LOOP FOR GENERATING SELECTIVITY AMONG HYΦ-PARP FAMILY MEMBERS.....	77
FURTHER MODIFICATION OF THE C-7 POSITION OF THE QDR SCAFFOLD LEADS TO IMPROVED POTENCY .....	78
DESIGN OF A POTENT AND SELECTIVE PARP11 INHIBITOR .....	81
ITK7 INHIBITS PARP11 AUTO-MARYLATION ACTIVITY IN CELLS AND CAUSES PARP11 TO DISSOCIATE FROM THE NUCLEAR ENVELOPE.....	83
<b>DISCUSSION.....</b>	<b>90</b>

<b>METHODS .....</b>	<b>92</b>
<b>CHAPTER 4: STRUCTURE GUIDED DESIGN OF A SELECTIVE PARP4 INHIBITOR .....</b>	<b>158</b>
<b>ABSTRACT .....</b>	<b>159</b>
<b>INTRODUCTION .....</b>	<b>160</b>
<b>RESULTS AND DISCUSSION.....</b>	<b>162</b>
SEQUENCE GUIDED DESIGN .....	162
STRUCTURAL EXTRAPOLATION SUGGESTS SPACE FOR A UNIQUE INHIBITOR INTERACTION WITH PARP4 .....	164
<i>IN VITRO</i> TESTING CONFIRMS PARP4 SPECIFICITY .....	166
<b>METHODS .....</b>	<b>171</b>
<b>CHAPTER 5: COVALENT INHIBITION OF PARP16 .....</b>	<b>190</b>
<b>ABSTRACT .....</b>	<b>191</b>
<b>INTRODUCTION .....</b>	<b>192</b>
<b>RESULTS .....</b>	<b>196</b>
STRUCTURE-GUIDED DESIGN LEADS TO A COVALENT PARP16 INHIBITOR .....	196
<i>IN VITRO</i> VALIDATION OF PARP16 COVALENT INHIBITOR MUTANT VALIDATION OF TARGET .....	199
HJ-52 BINDS TO PARP16 IN CELLS .....	201
PRELIMINARY WORK SUGGESTING CATALYTIC ACTIVITY MAY NOT BE REQUIRED FOR PARP16 INVOLVEMENT IN ER STRESS RESPONSE.....	205
<b>DISCUSSION.....</b>	<b>211</b>

METHODS .....	213
CHAPTER 6: ELABORATIONS ON THE OLAPARIB SCAFFOLD .....	222
ABSTRACT .....	223
INTRODUCTION .....	224
RESULTS .....	226
A SERIES OF ELABORATED OLAPARIB ANALOGUES LEAD TO A POTENT PARP7 INHIBITOR .....	228
A BRIEF EXPLORATION OF AZ0108 ANALOGUES .....	234
DISCUSSION.....	236
METHODS .....	237
CHAPTER 7: CONCLUDING REMARKS .....	262
APPENDIX A: FULL IC <sub>50</sub> DATA FOR COMPOUNDS IN CHAPTER 3 .....	269
APPENDIX B: FULL IC <sub>50</sub> DATA FOR COMPOUNDS IN CHAPTER 4 .....	280
APPENDIX C: MASS SPECTROMETRY ANALYSIS OF PARP16 AND HJ-52.....	286
APPENDIX D: FULL IC <sub>50</sub> DATA FOR COMPOUNDS IN CHAPTER 6 .....	288
APPENDIX E: H1 NMR SPECTRA.....	302
CHAPTER 3 .....	303
CHAPTER 4 .....	372

CHAPTER 5.....	387
CHAPTER 6 .....	389
<b>APPENDIX F: REPORTED COMPOUND LITERATURE</b>	
<b>REFERENCES .....</b>	<b>411</b>
<b>REFERENCES .....</b>	<b>0</b>

## List of Figures and Schemes

<b>Figure 1-1</b> MArYlation and PARylation .....	<b>5</b>
<b>Figure 1-2</b> Structural features of the NAD <sup>+</sup> binding site .....	<b>8</b>
<b>Figure 1-3</b> Timeline of PARP inhibitor development.....	<b>12</b>
<b>Figure 1-4</b> Structures of common PARP inhibitors and their classifications .....	<b>15</b>
<b>Figure 1-5</b> Different small molecules access different regions of the NAD <sup>+</sup> binding pocket: .....	<b>19</b>
<b>Figure 1-6</b> Major structural interactions of known PARP inhibitors with the NAD <sup>+</sup> binding pocket.....	<b>24</b>
<b>Figure 1-7</b> NAD <sup>+</sup> analogues and probes used to monitor PARP activity .....	<b>27</b>
<b>Figure 1-8</b> Heat map showing the known IC <sub>50</sub> values of PARP inhibitors shown in Figure 1-4.. .....	<b>30</b>
<b>Figure 2-1</b> Schematic showing the PARP inhibitor screening assay (PISA) workflow .....	<b>42</b>
<b>Figure 2-2</b> Results of PISA match reported values for published inhibitors.....	<b>44</b>
<b>Figure 3-1</b> Structure-Guided Design of Selective HYE PARP Inhibitors .....	<b>70</b>
<b>Scheme 3-1</b> Synthesis of ITK1-4 .....	<b>71</b>
<b>Figure 3-2</b> ITK inhibitor series screened across the PARP Family.....	<b>74</b>
<b>Figure 3-3</b> Exploiting a Hydrophobic Sub-pocket in HYE PARPs with C-7-Substituted QDR Analogs .....	<b>76</b>
<b>Scheme 3-2</b> Synthesis of ITK5-7 .....	<b>80</b>

<b>Figure 3-4</b> Dose response curves for ITK7 inhibiting PARP11 mediated MARylation of SRPK2 and NXF1 using either 6-a-NAD <sup>+</sup> or native NAD <sup>+</sup> .....	<b>82</b>
<b>Figure 3-5</b> ITK7 selectively inhibits PARP11 in cells. ....	<b>84</b>
<b>Figure 3-6</b> GFP-PARP11 and mRuby2-Nup50 co-localize at the nuclear envelope.....	<b>86</b>
<b>Figure 3-7</b> PARP11 Catalytic activity is required for nuclear envelope localization.....	<b>88</b>
<b>Figure 3-8</b> ITK7 causes GFP-PARP11 to dissociate from the nuclear envelope.....	<b>89</b>
<b>Figure 4-1</b> A unique threonine in the PARP4 active site may leave space for an inhibitor .....	<b>163</b>
<b>Figure 4-2</b> Comparison of a PARP1 crystal structure (PDB: 5DS3) with a model of the PARP4 active site .....	<b>164</b>
<b>Figure 4-3</b> A non-selective PARP inhibitor provides a starting point for PARP4 inhibitor design.....	<b>165</b>
<b>Scheme 4-1</b> Synthesis of C8 substituted QDR analogues.....	<b>167</b>
<b>Figure 4-4</b> Inhibitor series exploring modifications at the C8 position of the QDR scaffold.....	<b>169</b>
<b>Figure 5-1</b> Olaparib accesses a cysteine residue in the active site of PARP16 .....	<b>197</b>
<b>Scheme 5-1</b> Synthesis of HJ-52. <i>Synthesis performed by Dr. Haihong Jin.</i> .....	<b>198</b>
<b>Figure 5-3</b> Competition with a PARP16 occupancy probe show covalent labeling of GFP-PARP16 in cells by HJ-52 .....	<b>204</b>

<b>Figure 5-4</b> HJ-52 robustly labels wild-type GFP-PARP16 in cells but does not label C169S GFP-PARP16 mutant at statistically significant levels.....	<b>205</b>
<b>Figure 5-5</b> .....	<b>209</b>
<b>Figure 5-6</b> Preliminary cellular studies of PARP16 in the UPR. <i>Panels A and B provided by Dr. Rory Morgan</i> .....	<b>210</b>
<b>Figure 6-1</b> Olaparib and AZ0108 occupy the same steric space as a non-hydrolyzable NAD <sup>+</sup> analogue (BAD) within the PARP1 active site ...	<b>228</b>
<b>Figure 6-2</b> Olaparib analogues reveal minimalist compound necessary for PARP1 inhibition, clues to PARP3 inhibition, and a highly potent PARP7 inhibitor .....	<b>229</b>
<b>Scheme 6-1</b> Synthesis of olaparib analogues.....	<b>230</b>
<b>Figure 6-3</b> A structure-based approach to improve ITOK-03 selectivity for PARP7.....	<b>231</b>
<b>Scheme 6-2</b> Synthesis of C7 substituted ITOK-05 analogues .....	<b>233</b>
<b>Scheme 6-3</b> Synthesis of AZ0108 analogues.....	<b>235</b>
<b>Figure 6-4</b> AZ0108 series reveals structural features to target PARP6 .....	<b>235</b>
<b>Figure A-1</b> Dose response curves for QDR2 and ITK1-7, olaparib, and rucaparib against the active PARP family.....	<b>270</b>
<b>Figure A-2</b> <i>In vitro</i> testing of ITK7 against PARP6, PARP8, PARP12, and PARP16 .....	<b>271</b>
<b>Figure B-1</b> Dose response curves for AEP series against active PARP family .....	<b>281</b>
<b>Figure D-1</b> <i>In vitro</i> dose response curves for (A) olaparib and ITOK-01 - 11, and (B) AZ0108 and ITOK-12 - 17.....	<b>281</b>



## List of Tables

Table 2-1 Optimized protein concentrations for PISA.....	43
Table 2-2 In vitro IC <sub>50</sub> values for Olaparib, Rucaparib, and OUL35 ..	44
Table A-1 Approximate IC <sub>50</sub> values of compounds not appearing in Chapter 3 .....	277
Table A-2 In vitro IC <sub>50</sub> (μM) values for ITK1-7, olaparib and rucaparib .....	272
Table B-1 <i>In vitro</i> IC <sub>50</sub> (μM) values for full AEP series; SEM from a minimum of three dose-response experiments.....	282
Table D-1 In vitro IC <sub>50</sub> (μM) values for (A) ITOK-01 - 11, and (B) ITOK-12 - 17 .....	292
Table F-1 First reported literature source and CAS numbers for synthesized compounds. Novel compounds, and compounds reported as commercially available but without literature reports, are indicated.. .....	0

# Acknowledgments

Thank you to the Cohen lab members and collaborators for their guidance and support in my graduate work.

Thank you to Ian, Rory, Sky, Meredith, Lisa, Scotty, and Ana for their humor and fortitude during long days and late nights at the bench.

Thank you to my friends and family who are everything to me.

## Abstract

Poly-ADP-ribose-polymerases (PARPs) are a family of 17 post translationally modifying enzymes in humans that catalyze the transfer of ADP-ribose from nicotinamide adenine dinucleotide (NAD<sup>+</sup>) onto target amino acids and nucleotides. PARPs can append long dendritic chains of ADP-ribose (poly-ADP-ribosylation, or PARylation) or monomers of ADP-ribose targets (mono-ADP-ribosylation, or MARylation) to their). While the majority of the PARPs catalyze MARylation, there has been surprisingly little attention given to these enzymes or modification the last ten years. Even now, as evidence of the MARylating PARPs' importance in basic biology and human diseases masses, very little is known about the function, targets, or biological mechanisms of these PARPs. Conversely, the PARylating PARPs are well understood.

The majority of PARP inhibitors have been designed to target PARP1/2 and the taynkerases, PARP5a/b, and with few exceptions these inhibitors are non-selective. Only in the past five years has work begun to emerge on developing selective inhibitors for MARylating PARPs, and it has remained common practice in the field to only screen inhibitors against a small fraction of the PARP family members due to a lack of family wide activity assays, reliable reagents for detecting

ADP-ribosylation, and challenges in expressing and working with the PARP enzymes (Chapter 1).

In my dissertation work I sought to address the lack of selective inhibitors for MARYlating PARPs. To do this, I first designed a semi-high throughput family-wide activity assay for PARPs. Previous studies have used similar methods to screen compounds against a small number of PARP family members, but my work established to the first family-wide PARP inhibitor screening assay (Chapter 2). This assay was instrumental in structure-activity based inhibitor design of the first potent broad-spectrum MARYlating PARP inhibitor and the first selective PARP11 inhibitor. Application of my PARP11 inhibitor (ITK7) lead to the discovery of a possible link between PARP catalytic activity and localization (Chapter 3). I leveraged similar strategies to design the first selective PARP4 inhibitor (Chapter 4) and work to design the first selective PARP7 inhibitor (Chapter 6). Building on work done by former lab members Dr. Haihong Jin and Dr. Rory Morgan, I also investigated the cellular utility of a first in class covalent PARP16 inhibitor (Chapter 5). Overall, these inhibitors will be useful in studying the biological mechanisms and pathological relevance of MARYlating PARPs, and the methods used to design and validate them will provide a platform for future PARP inhibitor design.

# Chapter 1: Introduction

Ilsa T. Kirby and Michael S. Cohen

Portions of this chapter were originally published as part of the *Current Topics in Microbiology and Immunology* book series on September 22nd 2018 (© Springer Nature Switzerland AG 2018) (Kirby & Cohen 2018). It has been adapted for this dissertation and reprinted with permission.

## Abstract

Over the last 60 years poly-ADP-ribose polymerases (PARPs, 17 family members in humans) have emerged as important regulators of physiology and disease. Small molecule inhibitors have been essential tools for unraveling PARP function, and recently the first PARP inhibitors have been approved for the treatment of various human cancers. Despite the rapid expansion of the PARP field in recent decades, most of the PARP family remains poorly understood. This is due, in large part, to the dearth of small molecule inhibitors that selectively inhibit many PARP family members, in particular those that catalyze mono-ADP-ribosylation (MARylation). In contrast, there are numerous selective inhibitors for PARPs that catalyze poly-ADP-ribosylation (PARylation) and these have become useful not only as tools to reveal the functions of PARylation in the cell, but also to validate PARPs as therapeutic targets. There are currently three FDA approved PARP inhibitors (olaparib, rucaparib, and niraparib) that exhibit good selectivity for PARP1/2.

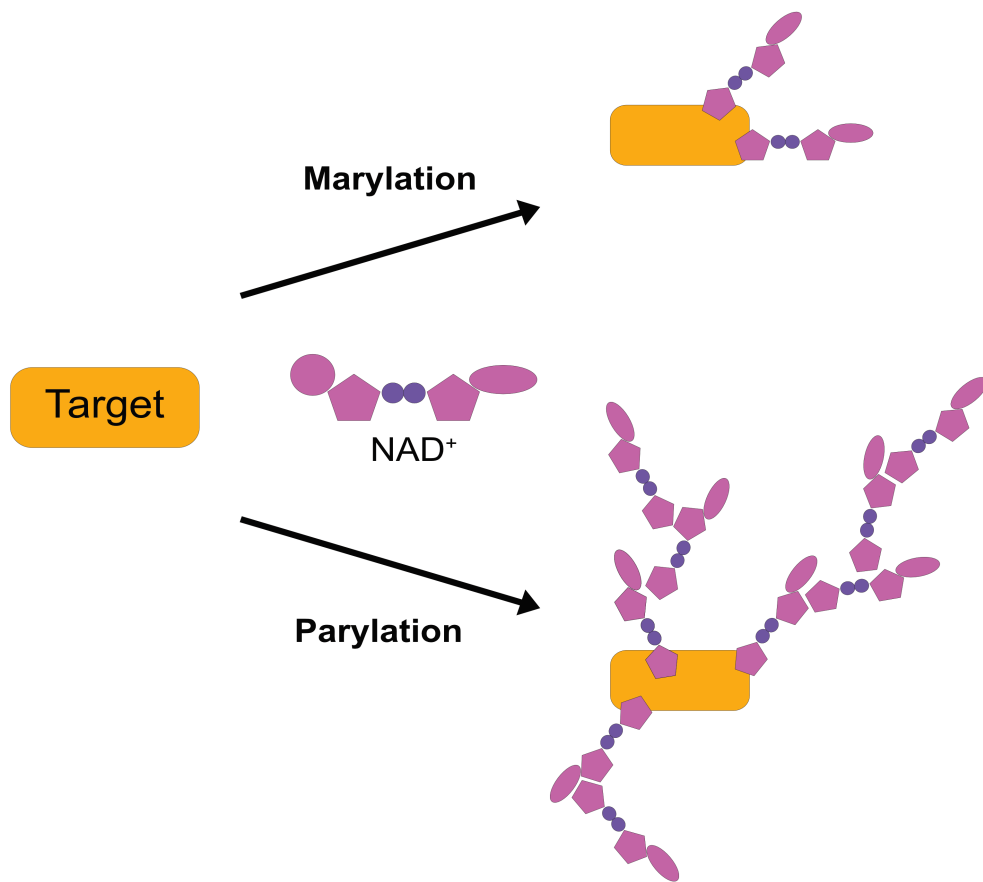
In the remaining sections of this chapter I will discuss the history of PARP inhibitor development, structural features of PARP inhibitors, PARP inhibitor screening assays, and the current challenges and opportunities for PARP inhibitor development. This discussion will set

the scene for my dissertation work developing PARP inhibitors and tools for assessing their efficacy.

# The PARP Family

Poly-ADP-ribose polymerases (PARPs1-16; also known as ADP-ribosyltransferases or ARTDs) catalyze the transfer of ADP-ribose (ADPr) from nicotinamide adenine dinucleotide (NAD<sup>+</sup>) to their target. Most PARPs (PARP3, 4, 6-8, 10-12, 14-16) transfer a single unit of ADPr onto targets, a process known as mono-ADP-ribosylation (MARylation) (Figure 1-1). Only four PARPs (PARP1, 2, 5a, 5b) have been shown to transfer multiple units of ADPr onto targets, a process known as poly-ADP-ribosylation (PARylation) (Figure 1-1). In most cases, ADPr is transferred onto amino acids in proteins; however, recent studies demonstrate that PARP-mediated ADPr transfer can occur on DNA (Munnur & Ahel 2017; Belousova et al. 2018). Similar to phosphorylation and other more well-characterized post-translational modifications (PTMs), both MARylation and PARylation are reversible suggesting that these PTMs are dynamic.





**Figure 1-1** MARYlation and PARYlation

PARPs catalyze the transfer either single units or dendritic chains of ADP-ribose from  $\text{NAD}^+$  to their targets in processes known as MARYlation and PARYlation, respectively.

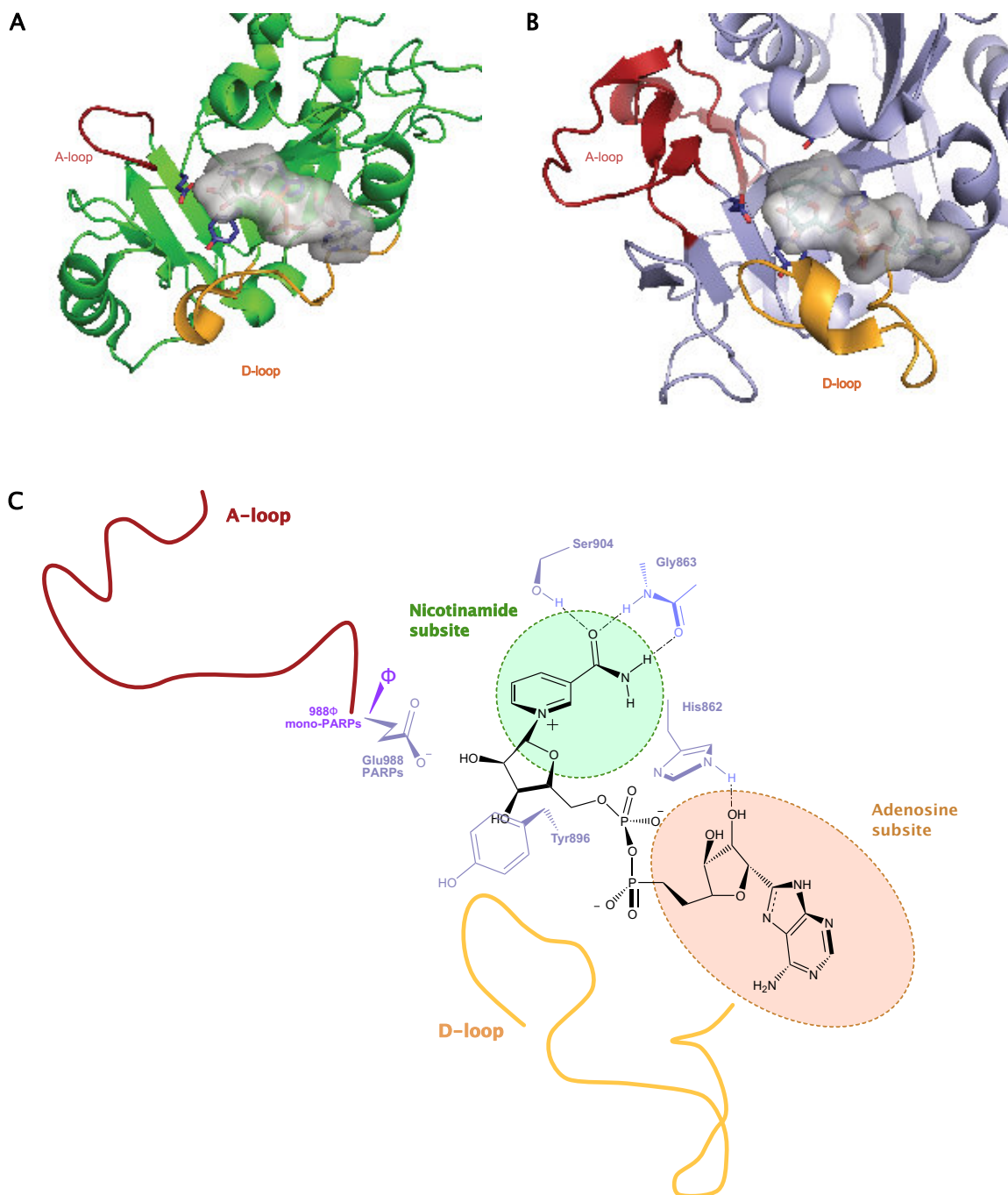
Though best known for their role in DNA damage repair, recent studies have revealed that PARPs play much wider roles in cells: from transcriptional regulation, miRNA processing, mRNA stability, and nuclear core complex biology to the unfolded protein response (Bock et al. 2015). Regarding the physiological role of PARPs, there is a wealth

of evidence demonstrating the involvement of PARPs in the immune system and T-cell regulation, which has been well reviewed (Rosado et al. 2013; Krishnakumar & Kraus 2010; Giansanti et al. 2010). PARP1, 2, and 14 have been shown to mediate pro-inflammatory responses (Mehrotra et al. 2013; Zingarelli et al. 1998; Andreone et al. 2003; Bai & Virág 2012). A recent study demonstrates a role of PARP6 in neurodevelopment (J. Y. Huang et al. 2016). Lastly, several PARPs are implicated in human diseases; for example, PARP14 mediates allergic responses in asthma (Mehrotra et al. 2013), and is a survival factor in multiple myeloma (Barbarulo et al. 2013), and hepatocellular carcinoma (Iansante et al. 2015).

# Common and distinct features in the catalytic domain of PARPs

## The NAD<sup>+</sup> binding domain

While the PARP family is diverse in regards to their domain architecture, they all share a highly conserved catalytic domain known as the ADP-ribosyltransferase (ART) fold, which binds NAD<sup>+</sup> in a conformation optimal for ADPr transfer. Nearly all PARP inhibitors target the ART fold and are competitive with NAD<sup>+</sup>. The key interaction between NAD<sup>+</sup> and PARPs has been gleaned from crystal structures of related ART bacterial toxins (diphtheria, pertussis, cholera, and certain clostridial toxins) (Hottiger et al. 2010) bound to NAD<sup>+</sup> (Tsurumura et al. 2013) (Figure 1-2A), and a recent structure of PARP1 bound to benzamide adenine dinucleotide (BAD) (Langelier et al. 2018), a non-hydrolyzable NAD<sup>+</sup> analog (Figure 1-2B). Two key interactions between NAD<sup>+</sup> and PARPs is the hydrogen bonding between the exocyclic amide of the nicotinamide moiety with the main chain of a conserved glycine (Gly863, human PARP1 numbering) and the side chain of a conserved serine (Ser 904, human PARP1 numbering) (Figure 1-2C). These interactions are commonly exploited by PARP inhibitors, as will be illustrated below.



**Figure 1-2** Structural features of the NAD<sup>+</sup> binding site

(A) The bacterial toxin ExoA (PDB 2ZIT) bound to endogenous NAD<sup>+</sup> shows how the HYE catalytic triad, A-loop, and D-loop hold NAD<sup>+</sup> in the binding site of an ADP-ribosylating protein

(B) PARP1 in complex with a non-hydrolyzable NAD<sup>+</sup> analogue (PDB 6BHV) closely mirrors the structural interactions of endogenous NAD<sup>+</sup> with ExoA  
(C) based on these crystal structures a simplified model of key interactions between NAD<sup>+</sup> and the PARP catalytic domain reveals two important regions: the nicotinamide subsite (green) and the adenosine subsite (orange).

### **HYE vs. HYΦ-PARPs**

Active PARPs can be divided into two subfamilies based on the sequence of an active site triad motif in the ART fold (Figure 1-2C). The histidine-tyrosine-glutamate (HYE) PARPs (PARP1, 2, 3, 4, 5a and 5b) and the histidine-tyrosine-hydrophobic amino acid (HYΦ) PARPs (PARP 6-8, 10-12, 14-16) (Hottiger et al. 2010). In both the HYE and HYΦ, the conserved histidine forms a hydrogen bond with the 2'-OH of the adenosine ribose and the conserved tyrosine  $\pi$ -stacks with the nicotinamide moiety (Figure 1-2C). The glutamate in the HYE-PARPs is necessary but not sufficient for the PARylation activity of several HYE-PARPs (Marsischky et al. 1995; Rolli et al. 1997). HYΦ-PARPs were recently shown to exclusively catalyze MARylation (Vyas et al. 2014).

### **Non-conserved loops**

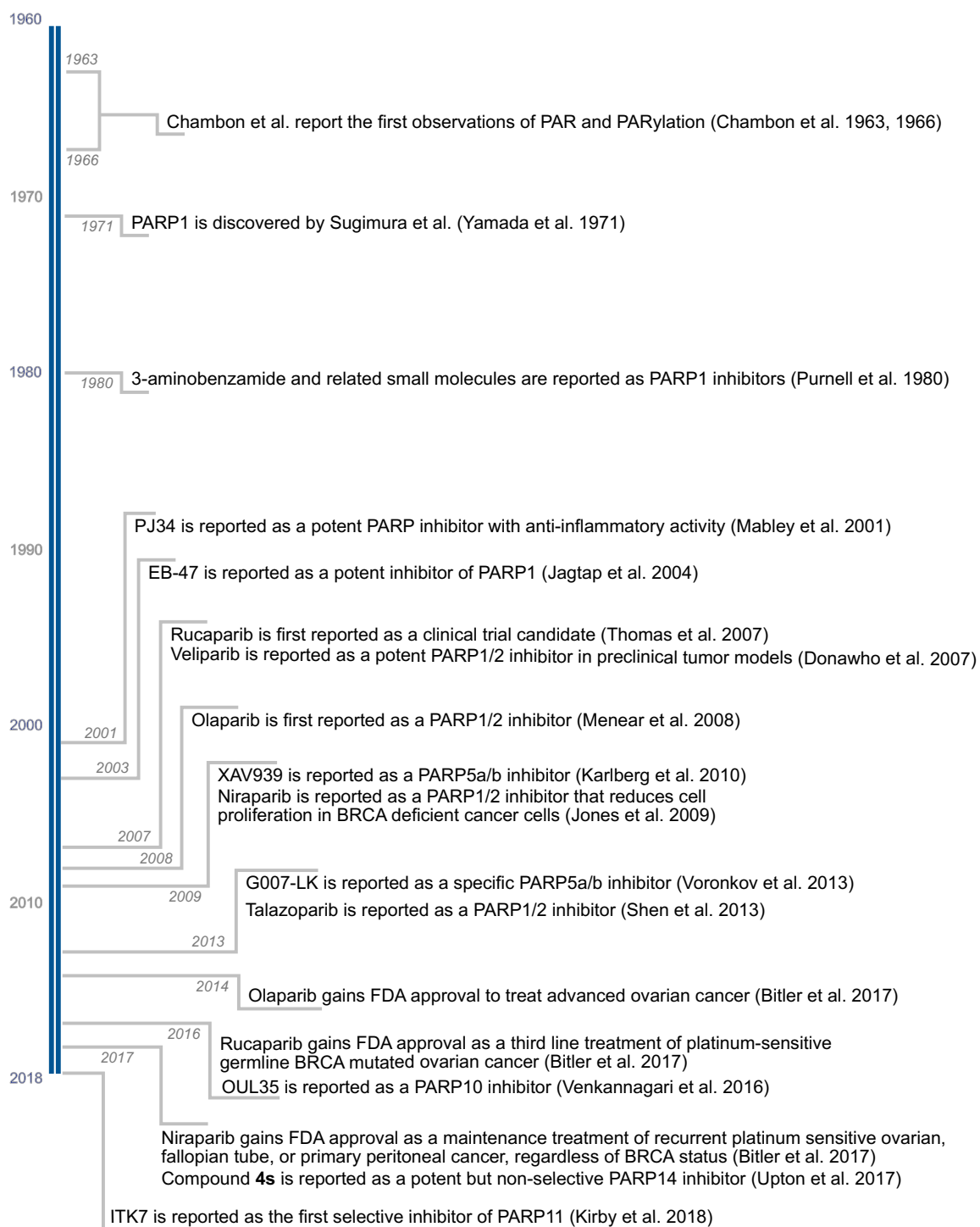
In addition to these conserved amino acids, there are two loop regions in the ART fold that are less well conserved yet thought to be critical for catalysis and NAD<sup>+</sup> binding: the acceptor loop (A-loop) and the

donor-loop (D-loop) (Figure 1-2A-C). The A-loop varies widely in terms of length and amino acid composition across the PARP family and is thought to interact with PARP substrates (Figure 1-2C). The D-loop is a variable region that interacts with the ADPr moiety of NAD<sup>+</sup> (Figure 1-2A-C). Based on mutagenesis studies of the related bacterial ARTs, the D-loop in PARPs is thought to be necessary for NAD<sup>+</sup> binding and ADPr transfer (Pinto & Schöler 2015). The high variability of the A-loop and D-loop of PARPs could be exploited for the design of isoform-selective inhibitors.

## Early developments in the field: initial focus on small molecule inhibitors of PARP1

### The founding PARP inhibitors

Interest in PARP inhibitors emerged in the early 1980s following the discovery of PARP1, the most ubiquitous and abundant PARP family member (Figure 1-3). The first described PARP1 inhibitors focused on targeting the nicotinamide subsite, and were simple biomimetics of nicotinamide such as 3-aminobenzamide (3-AB) (Purnell & Whish 1980) (Figure 1-4), which inhibits PARP1 with a half-maximal inhibitory concentration ( $IC_{50}$ ) around 10  $\mu$ M. These inhibitors played a crucial role in elucidating the role of PARP1 in DNA damage repair. Consistent with their role in DNA damage repair, these first generation PARP inhibitors were shown to potentiate the cytotoxicity induced by DNA damaging agents in cancer cells (Purnell & Whish 1980; NDUKA et al. 1980; Durrant & Boyle 1982). During the next two decades significant advances were made in PARP inhibitor development, and by the mid-2000s inhibitors with nanomolar  $IC_{50}$  values against PARP1, and the closely related PARP2, were identified.



**Figure 1-3** Timeline of PARP inhibitor development

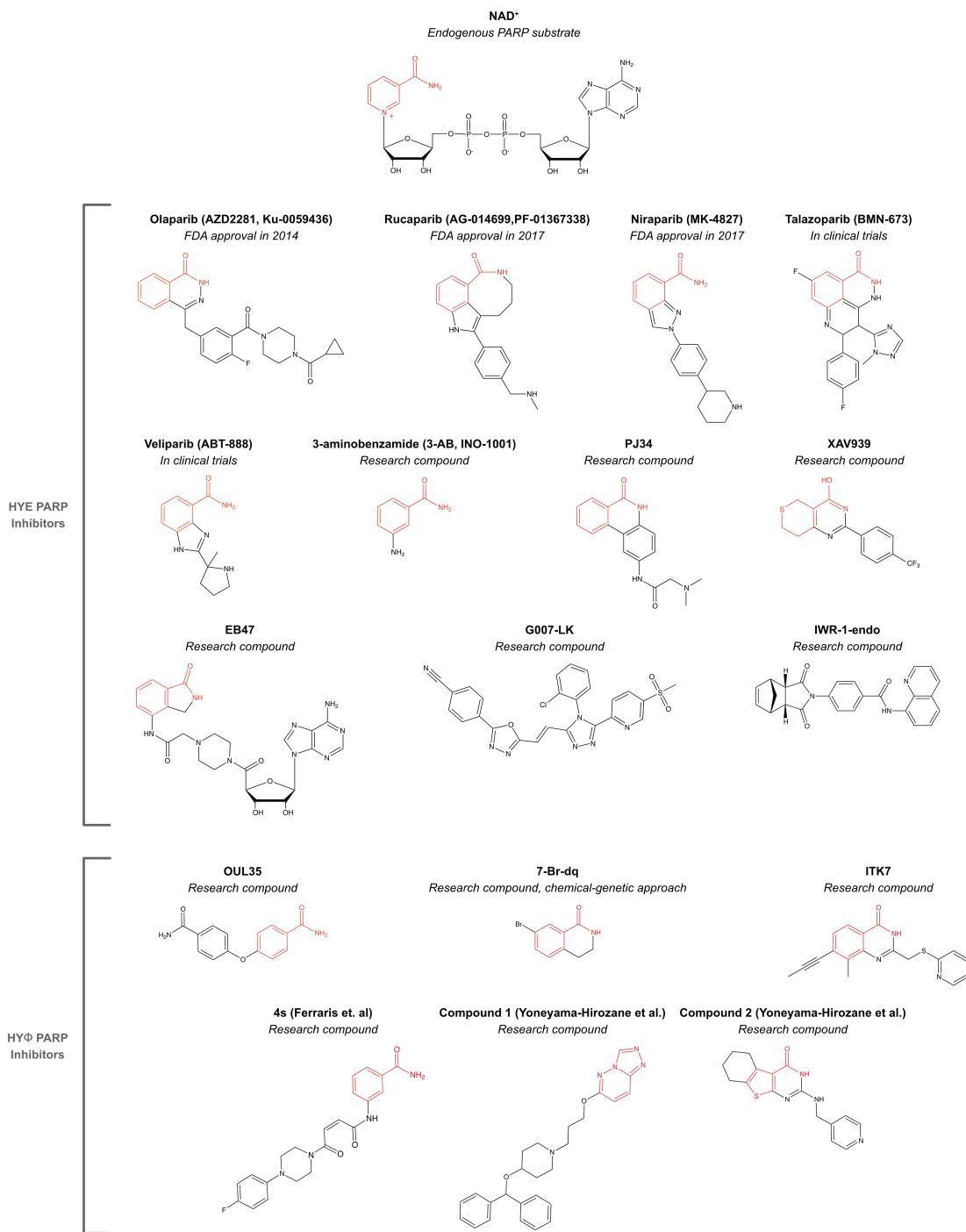


## **PARP1/2 identified as therapeutic targets in cancer**

In 2005, two seminal papers demonstrated that potent PARP1/2 inhibitors induce synthetic lethality in BRCA-deficient cancers by blocking PARP1 mediated DNA repair pathways (Farmer et al. 2005; Bryant et al. 2005). These studies motivated the development of PARP1/2 inhibitors as adjuvants with DNA damaging reagents or as single agents in cancers that have defects in the DNA repair machinery. First disclosed in 2008, the potent PARP1/2 inhibitor olaparib (Figure 1-4) effectively killed BRCA deficient cancer cells at low nanomolar concentrations (Menear et al. 2008). In 2009, Fong et al. published the first Phase 1 trial of olaparib reporting its antitumor effects in BRCA1/2 mutated cancer (Fong et al. 2009), and in 2014 olaparib became the first FDA approved PARP inhibitor. Since then off label and approved uses of olaparib have expanded beyond its original approval as a monotherapy for BRCA deficient ovarian cancers to include prostate cancer and germline mutated metastatic breast cancer. Following the FDA approval of olaparib, two more potent PARP1/2 inhibitors have entered the clinic: rucaparib in 2016, and niraparib in 2017 (Figure 1-4).

These FDA-approved PARP inhibitors have shifted the paradigm for cancer treatment. Because they exploit synthetic lethality, they are relatively non-toxic to normal cells, thus avoiding

many of the side effects of frontline chemotherapeutics. For a thorough review of PARP1 history, biology, and inhibitors see the following references (Ferraris 2010; Feng et al. 2015). For a recent review of the clinical applications of PARP1/2 inhibitors including olaparib, rucaparib, and niraparib, see the following references (Ohmoto & Yachida 2017; Mariappan et al. 2017)



**Figure 1-4** Structures of common PARP inhibitors and their classifications

## Moving beyond PARP1/2

### Forward chemical genetic screen identifies a small molecule inhibitor of PARP5a/b

The first inhibitor of the other PAR-generating PARPs, PARP5a/b (also known as tankyrase 1/2), was identified in a forward chemical genetic screen focused on identifying inhibitors of Wnt/ $\beta$ -catenin signaling (S.-M. A. Huang et al. 2009). A small molecule, XAV939 (Figure 1-4), was found to induce degradation of  $\beta$ -catenin by stabilizing axin, thereby blocking  $\beta$ -catenin-mediated transcription (S.-M. A. Huang et al. 2009). Using an immobilized, active analog of XAV939, it was shown that the target of XAV939 is PARP5a/b (S.-M. A. Huang et al. 2009). XAV939 potently inhibits the activity of PARP5a/b-mediated PARylation, and later structural studies demonstrate that XAV939 binds to the nicotinamide subsite in PARP5a (Figure 1-5F) (Karlberg et al. 2010). Knockdown of PARP5a/b phenocopied the effects of XAV939 on axin stabilization, providing evidence that PARP5a/b are the targets of XAV939 (S.-M. A. Huang et al. 2009). In this same study the authors showed that a previously described axin-stabilizing compound, IWR-1-endo, also potently inhibited PARP5a/b-mediated PARylation, suggesting that this compound stabilizes axin by inhibiting PARP5a/b catalytic activity (S.-M. A. Huang et al. 2009). Intriguingly, structural studies show IWR-1-endo binds exclusively to the adenosine subsite,

which at the time, was the first example of this type of binding mode to a PARP (Narwal et al. 2012).

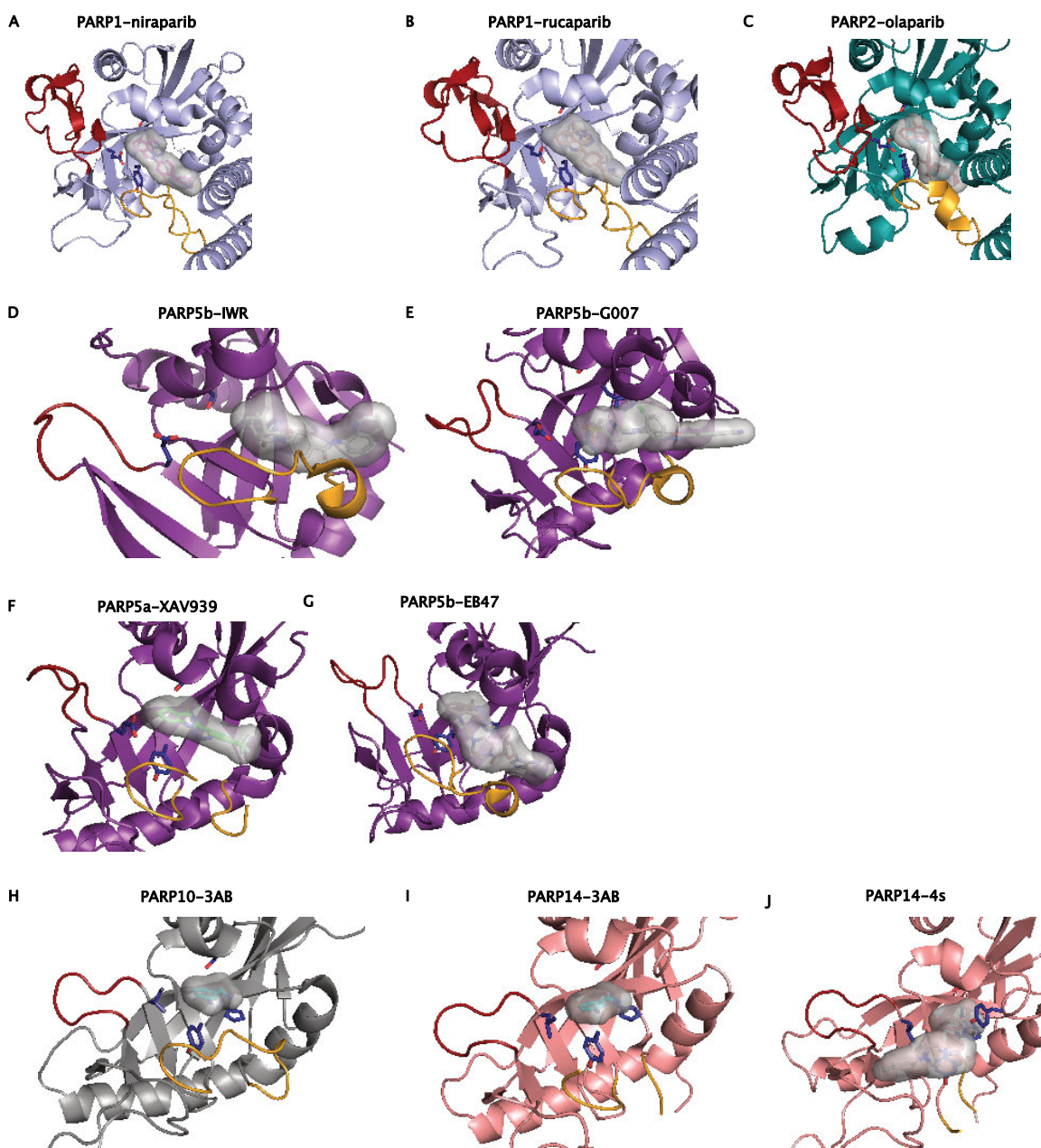
Since this study, several academic and industry efforts have led to the development of more potent and selective PARP5a/b inhibitors, including G007-LK (Figure 1-4) (Menear et al. 2008), which targets the adenosine subsite of the NAD<sup>+</sup> binding pocket (Figure 1-5). This compound as well as structurally unrelated PARP5a/b inhibitors have been invaluable tools for uncovering the roles of PARP5a/b-mediated PARylation in cells, and show promise as anticancer drugs (Zhan et al. 2014; Kamal et al. 2014; Vyas et al. 2014).

#### **A dearth of selective and potent inhibitors for the HYΦ-PARP subfamily**

Historically, PARP inhibitor design has focused on PARP1/2 and PARP5a/b with comparatively little attention given to the rest of the family. Recent years have seen a growing interest in the HYΦ-PARP subfamily, and a subsequent increase in HYΦ-PARP inhibitor development.

Of particular interest to many in drug discovery research has been PARP14 because of its role in several pathologies including asthma (Mehrotra et al. 2013), multiple myeloma (Barbarulo et al. 2013), and hepatocellular carcinoma (13). Promising inhibitors of PARP14 have been published by Upton et al. (e.g. 4s, Figure 1-4) (Upton et al. 2017)

and Yoneyama-Hirozane et al. at Takeda Pharmaceuticals (Compound 1 and 2, Figure 1-4) (Yoneyama-Hirozane et al. 2017). Upton et al. expanded on a previously identified small molecule inhibitor of PARP14 (Andersson et al. 2012; Ekblad et al. 2015) based on 3-AB to develop potent but non-selective PARP14 inhibitors containing cis-maleic amide substituents emanating from the 3-amino group of the 3-AB scaffold (Upton et al. 2017). Though originally designed to interact with the D-loop and adenosine subsite, crystal structure analysis of 4s shows that the cis-maleic amide substituent accesses an induced pocket adjacent to the NAD<sup>+</sup> binding site (further discussion below). Yoneyama-Hirozane et al. screened a small-molecule library to identify two compounds (Compound 1 and 2, Figure 1-4) based on divergent scaffolds that showed potent PARP14 inhibition and no activity against PARP1 up to 25  $\mu$ M (Yoneyama-Hirozane et al. 2017). Though untested against the majority of the PARP family, these scaffolds are promising starting points for further development of PARP14 inhibitors.



**Figure 1-5** Different small molecules access different regions of the NAD<sup>+</sup> binding pocket:

- A) PARP1 in complex with niraparib (PDB 4R6E)
- B) PARP1 in complex with rucaparib (PDB 4RV6)
- C) PARP2 in complex with olaparib (PDB 4TVJ)
- D) PARP5b in complex with EB-47 (PDB 4TK5)
- E) PARP5b in complex with IWR-1-endo (PDB 3UA9)

- F) PARP5b in complex with G007-LK
- G) PARP10 in complex with 3-aminobenzamide (PDB 3HKV)
- H) PARP14 in complex with 3-aminobenzamide (PDB 3GOY)
- I) PARP14 in complex with compound 4s (PDB 5NQE).

There have been some efforts to generate selective inhibitors for other HY $\Phi$ -PARPs. For example, a mono-selective inhibitor of PARP10 was developed using a chemical genetic strategy (Figure 1-4). A screen of a small-molecule library from the National Cancer Institute led to the discovery of a PARP10 inhibitor (OUL35, Figure 1-4) (Venkannagari et al. 2016). OUL35, an ether linked dimer of benzamide, appears to exhibit good selectivity for PARP10 when tested against several other PARP family members. Recently, a PARP11 inhibitor (ITK7, Figure 1-4) with low nanomolar potency and greater than 200-fold selectivity over the entire PARP family was reported. This inhibitor was used to elucidate the connection between PARP11 catalytic activity and localization to the nuclear pore (Kirby, Kojic, et al. 2018) (Chapter 3).

A number of non-selective PARP inhibitors and promising scaffolds have been described, but broadly speaking these compounds lack the selectivity or potency necessary for use as probes for exploring the individual role of HY $\Phi$ -PARPs in cells (Wahlberg et al. 2012; Thorsell et al. 2017).



# Structural studies of PARP inhibitors: insights into inhibitor potency and selectivity

## Structural studies of HYE-PARP inhibitors

Structural studies of PARPs bound to various inhibitors have provided insight into inhibitor potency and selectivity, and have been useful for structure-based design efforts. Here we discuss a few of these structures. The majority of structural studies have focused on HYE-PARPs, such as PARP1 and PARP5a/b (Figure 1-5).

The three FDA approved inhibitors olaparib, rucaparib, and niraparib all share similar binding modes to PARP1/2 despite their divergent scaffolds (Figure 1-4, 5A-C). A common, and seemingly essential, feature among these inhibitors is the interaction of an amide moiety (nicotinamide mimic) with the backbone glycine and side chain of an active site serine, which mimics the hydrogen bonding interaction observed with the nicotinamide of NAD<sup>+</sup> (Figure 1-2C, 5A-C). Additionally, these inhibitors contain various substituents that engage with, to varying degrees, the D-loop and adenosine subsite (Figure 1-5A-C).

Another potent PARP inhibitor, EB47, which is designed to mimic the full NAD<sup>+</sup> structure, occupies both the nicotinamide and adenosine subsites of PARP5b (Figure 1-5D). Unsurprisingly, this molecule is not specific for PARP5b, and has been shown to bind to

several PARPs (further discussion below). By contrast, two PARP5a/b inhibitors, IWR-1-endo and G007-LK, which do not contain nicotinamide mimics, occupy exclusively the adenosine subsite (Figure 1-5E,F). PARP inhibitors that target the adenosine subsite but not the nicotinamide subsite are still fairly uncommon, and their efficacy against HY $\Phi$ -PARPs has not been explored.

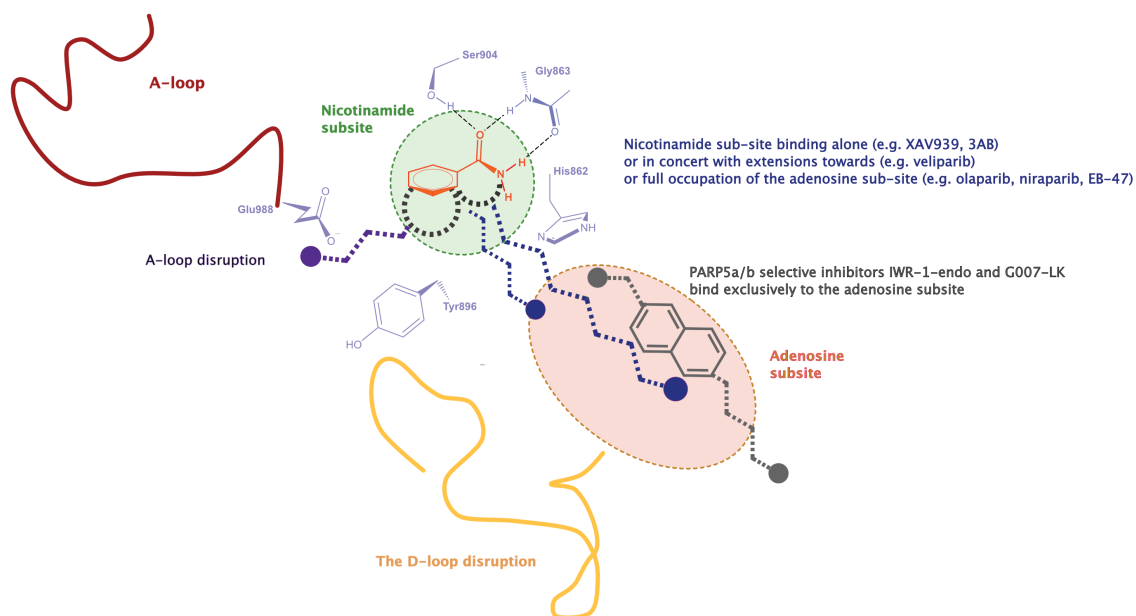
### **Structural studies of HY $\Phi$ -PARP inhibitors**

In recent years greater attention has been given to the HY $\Phi$ -PARPs, though inhibitors and crystal structures remain relatively rare by comparison to the better characterized HYE-PARP family members. Some of the first reported crystal structures of HY $\Phi$ -PARPs were PARP10 and PARP14 bound to 3-aminobenzamide (3-AB). As expected, 3-AB binds in the nicotinamide subsite in PARP10 and PARP14 and makes the same interactions with the conserved glycine backbone as the benzamide moiety of BAD bound to PARP1 (Figure 1-5G,H). The PARP14 inhibitors mentioned above, which extend substituents from the 3-amino position of the 3-AB scaffold, occupy a unique, induced pocket in PARP14. The crystal structure of one of these compounds (4s) shows that 3-AB binds in the nicotinamide subsite as expected, but that the cis-maleic amide substituent emanating from 3-amino position reaches into a nascent pocket (near the A-loop) that likely results from

a compound-induced movement of the D-loop (Figure 1-5I). This finding reveals a new pocket in PARP14, and perhaps other HYΦ-PARPs that could be targeted by other inhibitors.

### **Pharmacophore for PARP inhibitors**

From these structures we can construct a model to summarize known inhibitor interactions with the NAD<sup>+</sup> binding pocket, which can guide future PARP inhibitor development (Figure 1-6). A crucial feature of many PARP inhibitors is mimicking the interaction between the nicotinamide moiety of NAD<sup>+</sup> and the backbone glycine and side chain of an active site serine. Indeed, a wide range of scaffolds exploiting this interaction have been developed into successful PARP inhibitors. Targeting the nicotinamide site in concert with the adenosine subsite and D-loop appears optimal for potent PARP inhibition; however, many of these inhibitors are not selective (more on this below). Exclusively targeting the adenosine subsite, as has been shown for PARP5a/b, may result in more selective PARP inhibitors. Lastly, D-loop disrupting compounds (e.g. 4s) that can induce unique pockets outside the nicotinamide and adenosine subsites may turn out to be a generalizable approach for generating potent and selective PARP inhibitors.



**Figure 1-6** Major structural interactions of known PARP inhibitors with the NAD<sup>+</sup> binding pocket

Crystal structures of known PARP inhibitors demonstrate how various small molecules can exploit different features in the nicotinamide and adenosine subsites in the NAD<sup>+</sup> binding pocket.

## Chemical and Biological reagents for measuring PARP activity

### NAD<sup>+</sup> analogues for *in vitro* analysis

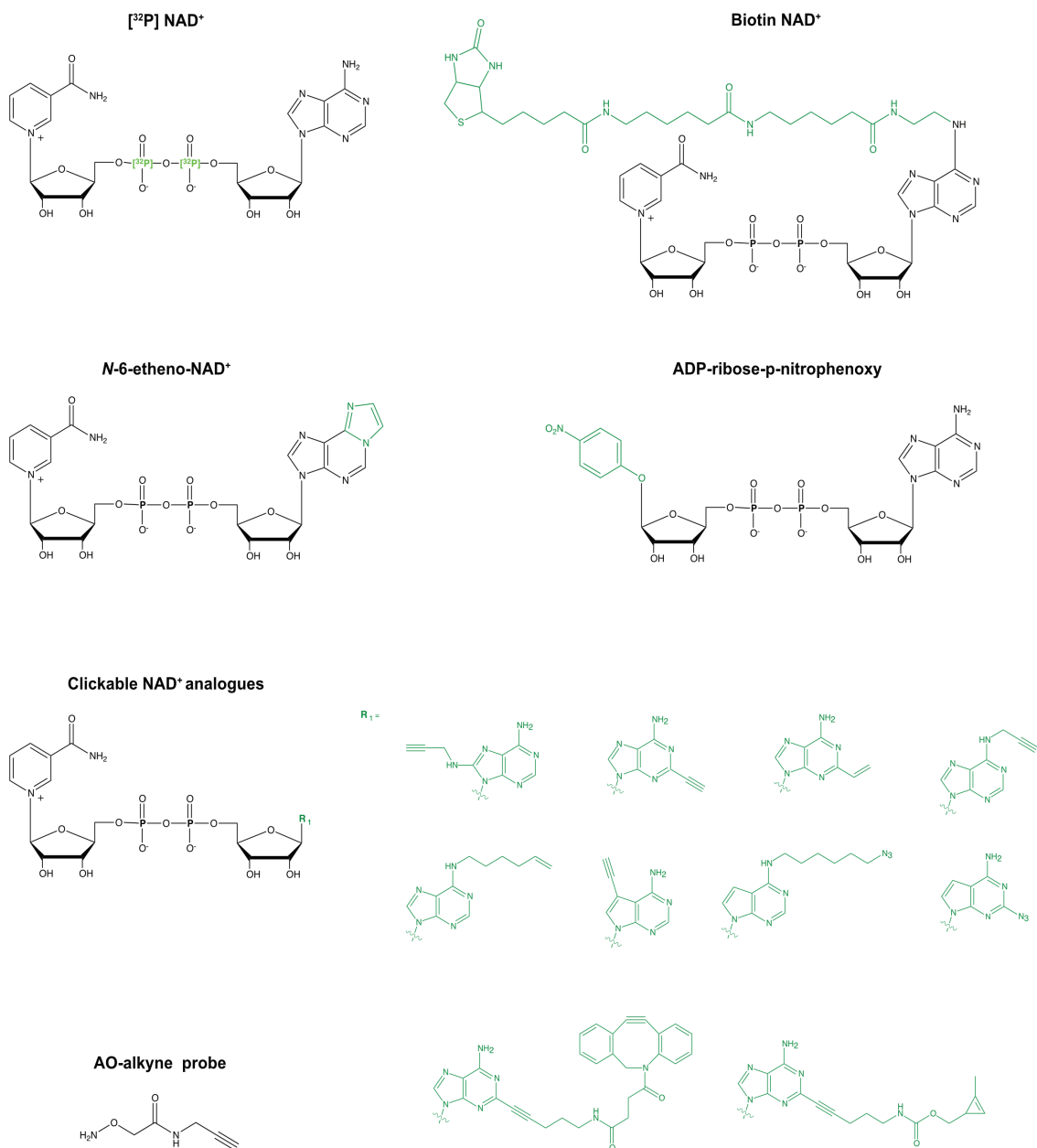
As described above, PARPs use NAD<sup>+</sup> as a substrate to mediate PARylation or MARylation. Historically, PARP activity was measured using radioactive NAD<sup>+</sup> (e.g. adenylate phosphate-32P NAD<sup>+</sup>) (Surowy

& Berger 1985) or using biotin-NAD<sup>+</sup> (Zhang & Snyder 1992) (Figure 1-7). Other NAD<sup>+</sup> analogs include N-6-etheno-NAD<sup>+</sup> (Barrio et al. 1972), a fluorescent NAD<sup>+</sup> analog, and ADP-ribose-p-nitrophenoxy (Oei et al. 1999), an analog in which the nicotinamide is replaced with a p-nitrophenol for use in colorimetric assays (Figure 1-7). Additionally, various “clickable” NAD<sup>+</sup> analogs have recently been developed, which contain an alkyne at various positions on the adenosine ring of NAD<sup>+</sup> (Figure 1-7) (Wallrodt et al. 2016; Wang et al. 2014; Carter-OConnell et al. 2014). These clickable NAD<sup>+</sup> analogs can be coupled to a fluorescent-azide (visualize) or biotin-azide (visualize and identify) via the Huisgen 1,3-dipolar cycloaddition (“click reaction”).

### **Detection methods with endogenous NAD<sup>+</sup>**

In addition to using NAD<sup>+</sup> analogs, several other strategies for detecting PARylation or MARYlation have been described. For PARylation detection, one of the most commonly used reagents are antibodies that specifically recognize PARylated substrates (e.g. 10H) (Kawamitsu et al. 1984; Meyer & Hilz 1986; Küpper et al. 1996). Recently, protein-based reagents for detecting both PARylated and MARYlated proteins have been described. These reagents consist of domains that recognize either ADPr (e.g. macro domain) or poly-ADPr (e.g. WWE domain) fused to Fc (Karras et al. 2005; Dani et al. 2009). These reagents have

been used in Western blot experiments, as well as plate-based assays and pulldown experiments (Wang et al. 2014). Lastly, an aminooxy-alkyne probe (AO-alkyne, Figure 1-7) was described. This probe reacts with the open form of the ribose ring to form a stable oxime, resulting in the clickable probe being covalently linked to the ADP-ribose modification and available for detection via click-chemistry (Morgan & Cohen 2015) . This reaction proceeds under acidic pH or in the presence of the oxime catalyst PDA under neutral conditions. The AO-alkyne probe can readily detect proteins that are ADP-ribosylated on acidic amino acids., and can also be used in cells for detecting cellular PARylation and MARylation (Morgan & Cohen 2015).



**Figure 1-7 NAD<sup>+</sup> analogues and probes used to monitor PARP activity.** Salient modifications to NAD<sup>+</sup> are highlighted in green.

# Assessing PARP inhibitor selectivity across the PARP family

## Profiling using protein stabilization reveal lack of selectivity of many PARP inhibitors

Arguably the most important aspect of inhibitor development is assessing its target selectivity. Among other things, this is essential for understanding any cell-based or in vivo studies conducted with an inhibitor. Unfortunately, there are few studies that assess PARP inhibitor selectivity across multiple PARP family members. One of the first examples of profiling inhibitor selectivity across multiple PARP family members was described in 2012. In this study, known and potential PARP inhibitors were screened against 13 PARPs using differential scanning fluorimetry (DSF), which assesses whether a compound can stabilize proteins (Wahlberg et al. 2012). One of the main findings of this study was that compounds previously described as selective PARP1/2 inhibitors, such as veliparib, rucaparib and olaparib, stabilize several other HYE-PARPs, suggesting that these compounds may not be as selective as previously thought. In general, most of the known PARP inhibitors did not stabilize HYΦ-PARPs, suggesting that they would not inhibit these PARPs. While this study provided the first insight into PARP inhibitor selectivity, DSF only assesses whether these PARP inhibitors can stabilize PARPs, which does

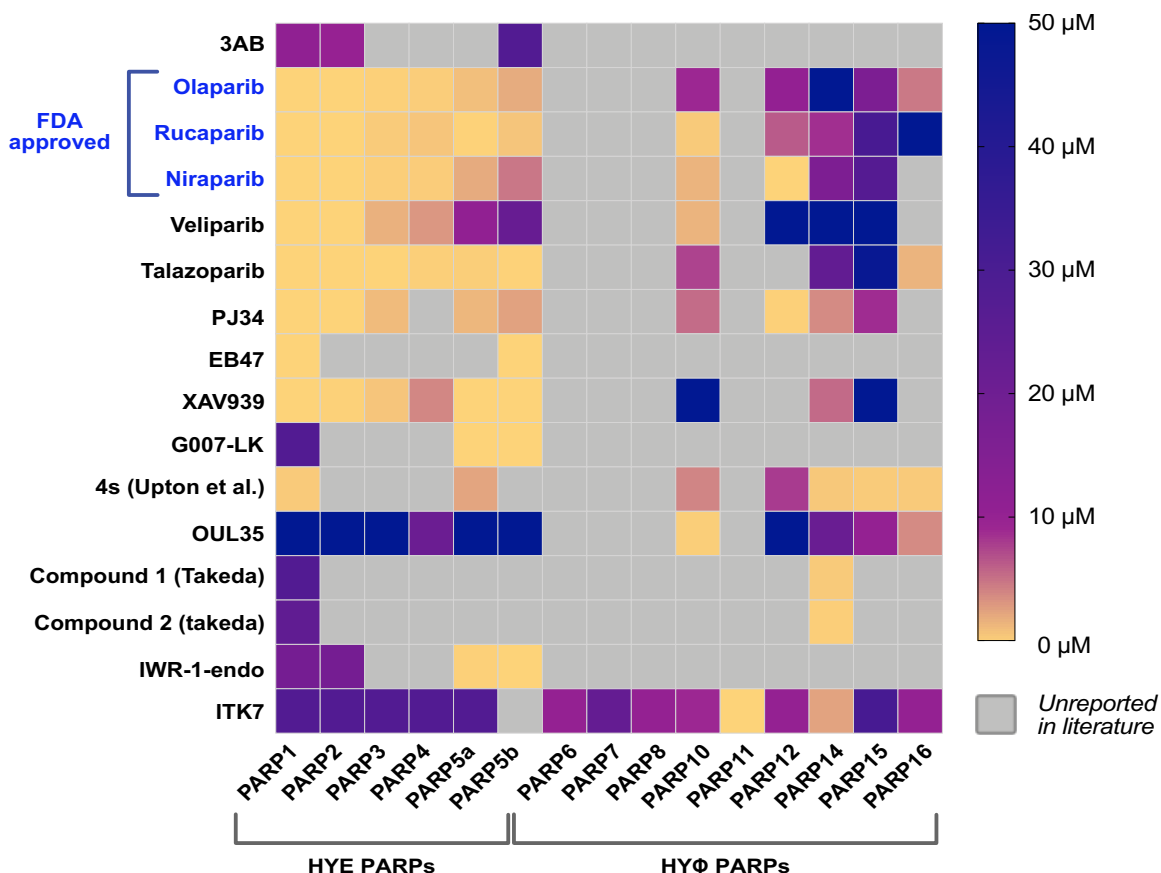


not necessarily correlate with inhibition of catalytic activity. Development of a plate based screening assay for the full PARP family will be discussed in Chapter 2 of this dissertation.

### **Polypharmacology among PARP inhibitors**

Recently, a high throughput 96 well plate-based ADP-ribosylation assay using biotin-NAD<sup>+</sup> was used for screening known PARP inhibitors against 11 PARP family members (Thorsell et al. 2017), most of which were the same PARPs used in the DSF study. In general, there was reasonable agreement between the ADP-ribosylation activity study and the DSF study, although the DSF study slightly overestimated PARP inhibitor selectivity. The selectivity profile of various PARP inhibitors are summarized in a heat map shown in Figure 1-8 (S.-M. A. Huang et al. 2009; Ishida et al. 2006; Papeo et al. 2014; Thorsell et al. 2017; Upton et al. 2017; Voronkov et al. 2013). There are several important findings worth noting: 1. veliparib appears to be the most potent and selective PARP1/2 inhibitor, exhibiting greater than 100-fold selectivity for PARP1/2 versus other PARPs; 2. XAV939, which was previously described as a selective inhibitor of PARP5a/b, potently inhibits PARP1 and PARP2, whereas IWR-1 is highly selective for PARP5a/b; 3. rucaparib and olaparib, while most selective for PARP1

and PARP2, inhibit several other PARP family members with sub-micromolar IC<sub>50</sub> values.



**Figure 1-8** Heat map showing the known IC<sub>50</sub> values of PARP inhibitors shown in Figure 1-4. Grey squares indicate values unreported in the literature.

The IC<sub>50</sub> values used to generate this heat map were taken from several sources, as referenced in the text. Gray: values unreported in the literature.

While a comprehensive assay for screening inhibitors across the entire PARP family is still needed to fully assess family-wide PARP

inhibitor selectivity, these findings have several important implications for interpreting results from cell-based assays. For example, a PubMed search reveals that many papers describe studies using XAV939 in cell-based assays at concentrations that also inhibit PARP1 and PARP2, making it difficult to conclude that the effects of the compound were in fact due to PARP5a/b inhibition. For selective inhibition of PARP5a/b in cells the adenosine pocket binders IWR-1 or G007-LK are better options in our opinion.

Lastly, these findings have important implications for evaluating PARP inhibitors in a clinical setting for cancer treatment. The different selectivity profiles of the three FDA-approved PARP inhibitors (Figure 1-8) could potentially contribute to efficacy and/or toxicity. Knowing the selectivity profiles will help assess the effectiveness of polypharmacology for certain cancers.

## **Future directions for the field**

The growing interest in PARPs should catalyze the development of selective PARP inhibitors to use as tools for uncovering the role of PARPs in cells and as potential therapeutics. The multifarious PARP-inhibitor structures available should guide the design of the next generation of more potent and selective inhibitors, especially for the

HYΦ-PARP subfamily for which there are a dearth of inhibitors. Exploiting differences in the variable A-loop or D-loop or targeting regions outside the NAD<sup>+</sup>-binding site may provide strategies for the ultimate goal of generating potent and selective inhibitors for every PARP family member. Covalent inhibitors that target non-conserved nucleophilic amino acids is another potential strategy for the design of potent and selective inhibitors. With the exception of some early work (Watson et al. 1998), this inhibition strategy has not been pursued.

As new PARP inhibitors continue to be developed, it will be important to standardize *in vitro* PARP inhibitor screening assays. This is essential for comparing IC<sub>50</sub> values, which depend on the concentration of NAD<sup>+</sup> or NAD<sup>+</sup> analog, obtained in different labs. Another consideration is the use of co-activators. PARP1, for example requires single stranded DNA for activation whereas PARP2 and PARP3 are optimally activated by 5'-phosphorylated double strand nicked DNA. Most assays assessing PARP activity have focused on auto-ADP-ribosylation. However, PARPs can also trans-P/MARylate targets in a cellular context (Carter-OConnell et al. 2016; Gibson et al. 2016). It will be important to incorporate this into *in vitro* assays as auto- versus trans-modification may yield different inhibition profiles. In some cases, co-activators may be required for optimal trans-P/MARylation.

For example, recently, it was shown that histone PARylation factor 1 (HPF1), which binds to PARP1, promotes PARP1 trans-PARylation of histones on serines (Gibbs-Seymour et al. 2016). Whether protein co-activators exist for other PARP family members is unclear, but as we learn more about PARP activation mechanisms these will need to be incorporated into *in vitro* PARP inhibitor screening assays.

Approaches to broadly assess PARP selectivity in a cellular context are desperately needed. Chemical proteomics approaches using resin bound PARP inhibitors is one potential strategy. This approach has the ability to identify potential non-PARP targets. Indeed, a recent study using resin bound olaparib, veliparib, rucaparib, and niraparib revealed that rucaparib and niraparib also target hexose-6-Phosphate Dehydrogenase (H6PD) and Deoxycytidine kinase (DCK), and inhibition of these targets may be clinically relevant (Knezevic et al. 2016). This chemical proteomics approach could also be used to profile PARP inhibitors in cell lysates, similar to the way Kinobeads have been used to profile kinase inhibitors (Golkowski et al 2014). However, this approach requires a potent pan-PARP inhibitor which unfortunately doesn't currently exist. Another approach could be to use activity-based protein profiling (ABPP), which exploits a conserved nucleophile in an enzyme active site for the development of a broad-

spectrum probe for screening inhibitors across an enzyme family in cell lysates or cells (Cravatt et al. 2008). Such an approach for PARPs could be quite useful for profiling PARP inhibitors in a cellular context.

## Dissertation Overview

In my dissertation research I have aimed to address some of the limitations in the PARP inhibitor field. In the early phases of my research I focused on developing a streamlined plate assay for testing inhibitors against the full PARP family *in vitro* to facilitate my overall goal of creating selective inhibitors of individual PARPs (Chapter 2). Using this assay I was able to perform iterative structure guided design of PARP inhibitors to target first the HYΦ-PARPs broadly, and then PARP11 specifically (Chapter 3). This inhibitor was then leveraged to uncover a heretofore unknown connection between the catalytic activity of PARP11 and its localization to the nuclear pore (Chapter 3). Using the same starting scaffold as the selective PARP11 inhibitor I then developed selective inhibitors for PARP2 and PARP4 that will benefit from further optimization (Chapter 4). From there I moved on to exploring modifications on the olaparib scaffold to target HYE-PARPs and found a surprisingly tight structure-activity-relationship (SAR) around an extremely potent PARP7 inhibitor (Chapter 5). Finally, I had

the opportunity to continue the work of Drs. Haihong Jin, Rory Morgan, and the Taunton lab (University of California, San Francisco) to use covalent inhibitors to explore the role of catalytic activity in PARP16 biological function (Chapter 6). Overall, the screening methods and SAR I have developed during my dissertation research will facilitate future work on selective PARP inhibitor design. The inhibitors that I designed will allow PARP biologists to study the functions and cellular mechanisms of PARP4, PARP11, and PARP16 in a cellular context.

## Chapter 2: Development of a Sensitive, Family-wide PARP Inhibitor Screening Assay

Ilsa T. Kirby, Rory K. Morgan, and Michael S. Cohen

Portions of this chapter were originally published as part of volume 1813 the *Methods in Molecular Biology* book series on August 11th 2018 (© Springer Science+Business Media, LLC, part of Springer Nature 2018) (Kirby, Morgan, et al. 2018). It has been adapted for this dissertation and reprinted with permission. This work was in collaboration with Dr. Rory K. Morgan who expressed and purified PARP10<sub>cat</sub> and PARP15<sub>cat</sub>, and optimized the native NAD<sup>+</sup> protocol.



## Abstract

Poly-ADP-ribose polymerases (also known as ADP-ribosyltransferases or ARTDs) are a family of 17 enzymes in humans that catalyze the reversible post-translational, modification known as ADP-ribosylation. PARPs are implicated in diverse cellular processes, from DNA repair to the unfolded protein response. Small molecule inhibitors of PARPs have improved our understanding of PARP-mediated biology, and in some cases, have emerged as promising treatments for cancers and other human diseases. However, these advancements are hindered, in part, by a poor understanding of inhibitor selectivity across the PARP family. Here, we describe a sensitive, semi-high throughput plate assay to test the potency and selectivity of small molecules against all active PARP enzymes *in vitro* using either native NAD<sup>+</sup> or a clickable NAD<sup>+</sup> analogue.

## Introduction

Poly-ADP-ribose polymerases (PARPs1-16; also known as ADP-ribosyltransferases or ARTDs) catalyze the reversible post-translational modification known as ADP-ribosylation, which involves the transfer of ADP-ribose from nicotinamide adenine dinucleotide (NAD<sup>+</sup>) to amino acids in target proteins. PARPs have emerged as key regulators of diverse cellular processes and their dysregulation has been linked to a wide range of pathologies, such as allergic asthma (Mehrotra et al. 2013) and cancer (Barbarulo et al. 2013). As such, there has been increasing interest in the development of PARP inhibitors as potential therapeutics as well as tools to further explore PARP biology. While potent small molecule inhibitors exist for some PARPs (e.g. PARP1, 2, 3, 5a, and 5b), potent and selective inhibitors for the majority of PARP family members are scarce (Wahlberg et al. 2012). Moreover, there are few studies that explore the selectivity of existing PARP inhibitors (Venkannagari et al. 2016; Thorsell et al. 2017). An understanding of inhibitor selectivity across the PARP family is critical for their use as tool compounds and as potential clinical treatments. To facilitate the development of selective PARP inhibitors we devised a plate assay for screening PARP inhibitors against several recombinant PARPs in parallel.

Our lab has explored several methods for measuring PARP activity, including clickable NAD<sup>+</sup> analogues (Carter-OConnell et al. 2014) and a clickable aminooxy alkyne (AO-alkyne) probe with in-gel readouts (Morgan & Cohen 2015). These methods are useful for cellular and biochemical analysis of PARP-mediated ADP-ribosylation, but are not practical for high-throughput inhibitor screening. To address this challenge, we adapted our PARP activity assay to a 96-well plate format.

## Results

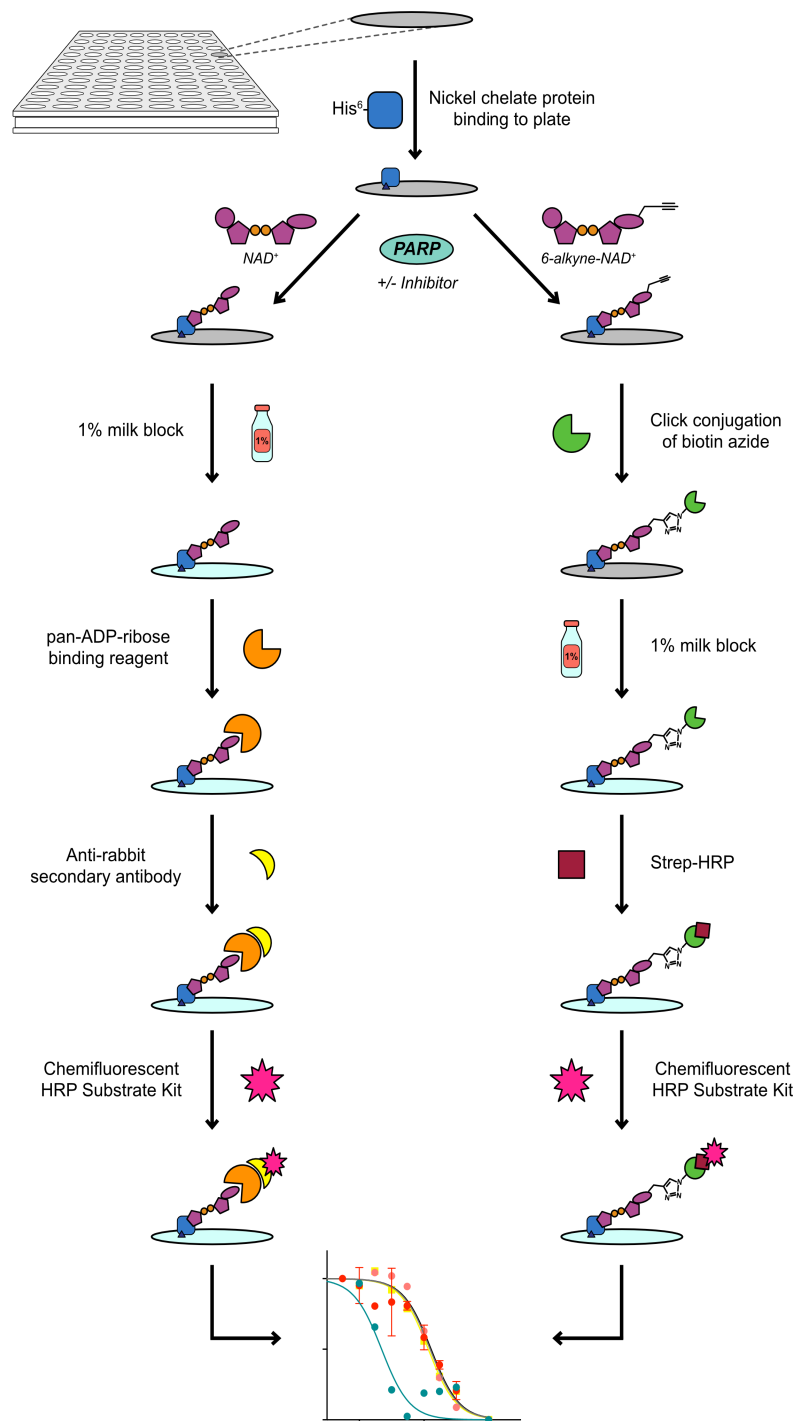
### Assay Methodology

In this method proteins are bound to Ni-NTA plates (Pierce) via His-tags. Depending on the PARP being tested SRSF protein kinase 2 (SRPK2), a known PARP substrate (Venkannagari et al. 2013), or the PARP itself can be bound to a plate to measure trans- or cis- ADP-ribosylation. This assay has also been validated using a GST- tagged version of PARP7 chelated to a glutathione coated 96 well plate (Pierce). Following protein binding to the plate one of the 15 active PARP enzymes is added to the plate (PARP specific concentrations in Table 2-1) in combination with physiologically relevant concentrations (Cambronne et al. 2016) of a *either* native NAD<sup>+</sup> *or* a clickable NAD<sup>+</sup>

analogue, 6-alkyne-NAD<sup>+</sup> (6-a-NAD<sup>+</sup>) (Carter-OConnell et al. 2014). Following the enzymatic reaction with NAD<sup>+</sup> *or* 6-a-NAD<sup>+</sup> the assay diverges:

- *If NAD<sup>+</sup> is used* the plate is blocked in 1% milk in 1X PBST, then incubated with an pan-ADP-ribose antibody or binding reagent (Cell Signaling Technology or Millipore, respectively) followed by an anti-rabbit HRP-linked secondary antibody (Cell Signaling Technology) (Figure 2-1, left path). This method is ideal for testing covalent inhibitors that contain an alkyne tag and excludes any possibility of substrate specific changes to reaction kinetics.
- *If 6-a-NAD<sup>+</sup> is used* samples are subjected to click conjugation with biotin-azide, followed by a 5% milk block in 1X PBST, and then incubation with Streptavidin-HRP (Strep-HRP). The extent of ADP-ribosylation of SRPK2 is then detected with QuantaRed™ enhanced chemifluorescent HRP substrate kit (Thermo Scientific) and the signal read on a plate reader (Figure 2-1) (Figure 2-1, right path). This method tends to give a higher signal than using native NAD<sup>+</sup>, likely due to the lower sensitivity of the ADPr-binding reagent used in that method.

In either case, the extent of ADP-ribosylation is then quantified using a chemifluorescent HRP substrate kit (Thermo Scientific) and the signal read on a plate reader. For explicit details and instructions on performing this assay see the methods section of this chapter.



**Figure 2-1** Schematic showing the PARP inhibitor screening assay (PISA) workflow

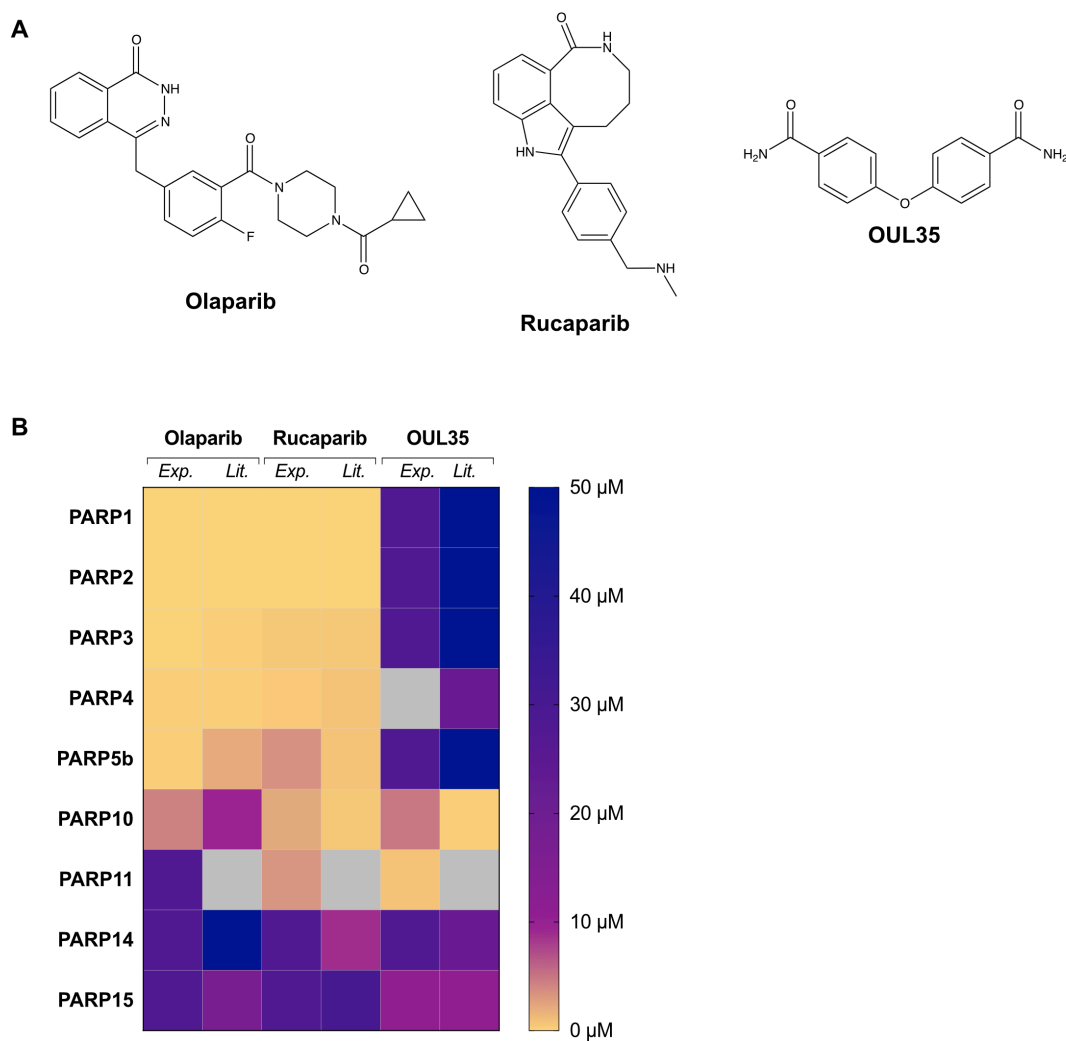
**Table 2-1** Optimized protein concentrations for PISA

PARP	Concentration ( $\mu$ M)	Reaction type
His <sub>6</sub> -PARP1 <sub>FL</sub>	0.01	Trans-ADPribosylation on SRPK2
His <sub>6</sub> -PARP2 <sub>FL</sub>	0.01	Trans-ADPribosylation on SRPK2
His <sub>6</sub> -PARP3 <sub>FL</sub>	0.3	Trans-ADPribosylation on SRPK2
Sumo-PARP4 <sub>brct-cat</sub>	10 $\mu$ M solution bound*	Auto-ADP-ribosylation
Sumo-PARP5 <sub>cat</sub>	0.3	Trans-ADPribosylation on SRPK2
Sumo-PARP6 <sub>FL</sub>	0.3	Trans-ADPribosylation on SRPK2
Sumo-PARP7 <sub>FL</sub>	0.25	Trans-ADPribosylation on SRPK2
Sumo-PARP8 <sub>FL</sub>	0.2	Trans-ADPribosylation on SRPK2
His <sub>6</sub> -PARP10 <sub>cat</sub>	0.005	Trans-ADPribosylation on SRPK2
Sumo-PARP10 <sub>FL</sub>	0.005	Trans-ADPribosylation on SRPK2
Sumo-PARP11 <sub>FL</sub>	0.005	Trans-ADPribosylation on SRPK2
His <sub>6</sub> -PARP14 <sub>wwe</sub>	0.005	Trans-ADPribosylation on SRPK2
His <sub>6</sub> -PARP15 <sub>cat</sub>	0.025	Trans-ADPribosylation on SRPK2
Sumo-PARP16 <sub>FL</sub>	1 $\mu$ M solution bound*	Auto-ADP-ribosylation

\* Reported binding capacity of ~9 pmol for 27 kDa His- tagged proteins on each well

### Assay Validation with Literature Compounds

As preliminary validation of this method we tested two FDA approved PARP inhibitors, olaparib (Menear et al. 2008) and rucaparib (Thomas et al. 2007), and a recently published PARP10 inhibitor, OUL35 (Venkannagari et al. 2016), against a representative panel of PARPs— PARP1<sub>FL</sub>, PARP2<sub>FL</sub>, PARP3<sub>FL</sub>, PARP4<sub>brct-cat</sub>, PARP5<sub>cat</sub>, PARP10<sub>cat</sub>, PARP11<sub>FL</sub>, PARP14<sub>wwe-cat</sub>, and PARP15<sub>cat</sub> (Figure 2-2, Table 2-2).



**Figure 2-2** Results of PISA match reported values for published inhibitors

(A) Structures of Olaparib and Rucaparib, two recently FDA approved PARP inhibitors, as well as OUL35, a recently described PARP10 inhibitor.

(B) Heat map showing  $IC_{50}$  values ( $\mu M$ ) obtained using our inhibitor screening plate assay.

**Table 2-2** In vitro  $IC_{50}$  values for Olaparib, Rucaparib, and OUL35; SEM from a minimum of three dose-response experiments.  $IC_{50}$  values for Olaparib and Rucaparib against several PARPs were consistent with previous studies,



whereas the IC<sub>50</sub> value for OUL35 against PARP10<sub>cat</sub> was higher than determined previously (Thorsell et al. 2017; Venkannagari et al. 2016).

	<b>Olaparib</b> (IC <sub>50</sub> , $\mu$ M)		<b>Rucaparib</b> (IC <sub>50</sub> , $\mu$ M)		<b>OUL35</b> (IC <sub>50</sub> , $\mu$ M)	
	<i>Experimental</i>	<i>Literature</i>	<i>Experimental</i>	<i>Literature</i>	<i>Experimental</i>	<i>Literature</i>
<b>PARP1<sub>FL</sub></b>	0.025 $\pm$ 0.002	0.0014, 0.005	0.0075 $\pm$ 0.002	0.0032	>10	>100
<b>PARP2<sub>FL</sub></b>	0.0066 $\pm$ 0.0003	0.0012	0.0049 $\pm$ 0.001	0.028	>10	>100
<b>PARP3<sub>FL</sub></b>	0.0831 $\pm$ 0.04	0.230	0.717 $\pm$ 0.3	0.512	>10	>100
<b>PAPR4<sub>bact-cat</sub></b>	0.241 $\pm$ 0.02	0.410	0.450 $\pm$ 0.1	0.839	<i>nt</i>	22.6
<b>PARP5<sub>cat</sub></b>	0.211 $\pm$ 0.08	2.34	3.61 $\pm$ 0.4	0.108	>10	>100
<b>PARP10<sub>cat</sub></b>	4.5 $\pm$ 0.3	1.3	2.5 $\pm$ 0.2	2.3	4.97 $\pm$ 0.9	0.329
<b>PARP11<sub>FL</sub></b>	>10	<i>nt</i>	3.4 $\pm$ 0.5	<i>nt</i>	0.933 $\pm$ 0.1	<i>nt</i>
<b>PARP14<sub>wws</sub></b>	>10	>100	>10	8.8	>10	23.4
<b>PARP15<sub>cat</sub></b>	>10	2.3417.6	>10	32.6	>10	>10

## Discussion

### Future Directions

In its current iteration this assay is a powerful tool for comparing inhibitor potency across the active PARPs. Through its development we have identified some important weaknesses of the assay and propose some avenues of potential improvement.

One major caveat of the assay is that some PARPs appear to have much lower catalytic activity in cells than *the* recombinant protein. For example, we have been unable to detect GFP-PAR\

P16 activity in cells (Chapter 5), but recombinant PARP16 has robust activity on the plate. Similar disparities in cellular and *in vitro* activity have been observed for several of the PARPs, suggesting that it may be possible to “force” PARP activity outside the cell in a non-biologically relevant manner. Conversely, we know that some PARPs require activators in the cell, such as damaged DNA for PARP1/2 and a specific 5’ phosphorylated and nicked dumbbell RNA to activate PARP3 (it should be noted that in my hands damaged DNA is not necessary for PARP1/2 activity in this assay, but the 5’ phosphorylated and nicked dumbbell RNA is requisition for PARP3 activity). These observations suggest that the activity we are able to observe from recombinant PARPs in this assay is not reflective of what is happening in an intact cell. There are likely numerous interactions that may activate, suppress, or modulate PARP activity that we are not currently recapitulating in this assay. As PARP modulators are discovered they can be readily incorporated into this assay, but until that time we are left to work with what information we have. In the end we must acknowledge that there is no substitute for testing inhibitors in cells

(and indeed even then there are many confounding factors and limitations even to those assays), and we must objectively view this assay as a tool with specific and bounded application.

This assay is best applied for inhibitor development, measuring the impact of structural changes on a scaffold on compound potency and selectivity within the parameters of the PARP activity we are able to capture on the plate. The modular and semi-high throughput format of this assay greatly facilitates medicinal chemistry efforts within the PARP family, allowing for thorough, comparative screening of compounds across the entire active family in the space of a few days. This allows for a much faster identification of a compound worthy of testing in cells, where it must then be fully validated before being used for mechanistic experiments.

One possible approach for improving this assay might be to look to the ever-growing body of evidence that PARPs may target nucleic acids in addition, or perhaps instead of, amino acids. Much of this work has been done by the Ahel lab, whom I have produced recombinant PARPs for to facilitate this work. It is possible that nucleic acids are the real, biologically relevant targets of some, or perhaps all, PARPs. If this theory is born out it would follow that a plate assay with DNA or even RNA bound to the plates for PARPs to modify could lead to a higher

signal, especially for PARPs that appear to be less active in this assay, such as full length PARP15.

Another important factor to keep in mind is that we have observed differences in inhibitor potency for different constructs of some PARPs. For instance, a truncated PARP7 construct consisting of only the catalytic and WWE domains was not inhibited by a compound that, in cells, potently inhibits the full length PARP7. When we obtained and tested a full length recombinant PARP7 and tested it on the plate the results were commiserate with the cellular data. Because of their comparative ease of production several truncated PARPs are currently used in this assay: PARP4<sub>cat-brct</sub>, PARP5<sub>bc</sub>, PARP12<sub>cat</sub>, PARP14<sub>wwe-cat</sub>, and PARP15<sub>cat</sub>. PARP10<sub>cat</sub> was used until recently being swapped for PARP10<sub>FL</sub> after Dr. Rory Morgan observed differences in potency for some of his compounds between the two constructs. Ideally, we will move towards using full length constructs of all of the PARPs in this assay, but practically that presents some serious practical issues in the cases of larger and harder to purify PARPs such as PARP4 and PARP14. A more reasonable goal for future assay development is to move towards full length, or at least more complete, PARP constructs wherever possible and in parallel validate results of lead compounds in

cells for all PARPs with particular priority given to those that are represented as truncated constructs in this assay.

## **Conclusions**

A growing appreciation for the importance of the biological role of PARPs has brought increased attention to PARP inhibitor development. Unfortunately, because the majority of work has focused on PARP1/2 there has been little effort put towards understanding the more recently described PARP family members (Figure 1-3). Even with our ever-growing recognition of the biological importance of all the PARP family members and their potential interactions, PARP inhibitors are rarely screened against even half of the PARP family. This has led to potentially misleading results in studies where conclusions about the effects of inhibition of a particular PARP are drawn without investigating potential intra-family off target effects of an inhibitor. As new assays have begun to emerge in the field to test some of the PARPs a scan of the literature will reveal broad spectrum PARP inhibition by the most commonly used PARP inhibitors, but moreover there are no published reports testing reported compounds against all of the PARPs (Figure 1-8).

To address this, we developed a modular 96-well plate assay to screen inhibitors against the full family of active PARP enzymes using native NAD<sup>+</sup> or a commercially available clickable NAD<sup>+</sup> analogue. We have validated this assay by reproducing literature IC<sub>50</sub> values for clinical PARP inhibitors, and revealed potentially important unreported targets of other published compounds (Figure 2-2, Table 2-2). This assay was an integral part of developing the first selective inhibitor of PARP11 (Chapter 3) and revealing precise molecular interactions between PARP7 and olaparib based inhibitors (Chapter 6). We hope this assay, and the strategies we have developed to express and purify all the active PARPs in bacteria, will be adopted and improved upon by others in the PARP field to standardize full family characterization of PARP inhibitors.

## Methods

### Cloning

cDNA encoding human PARP1<sub>FL</sub>, PARP2<sub>FL</sub>, PARP4<sub>cat-brct</sub>, PARP5<sub>bcat</sub>, PARP10<sub>cat</sub>, PARP11<sub>FL</sub>, PARP14<sub>wwe-cat</sub>, PARP15<sub>cat</sub>, and SRPK2 were obtained as previously described (Carter-OConnell et al. 2014) (Morgan & Cohen 2015) (Kirby, Kojic, et al. 2018).

Individual cDNA constructs encoding PARP6<sub>FL</sub>, PARP8<sub>FL</sub>, PARP7<sub>FL</sub>, PARP10<sub>FL</sub>, PARP15<sub>FL</sub>, and PARP16<sub>FL</sub> were obtained using

gBlock gene fragments containing the PARP11 gene as template (IDT) and the following primers (IDT) for subsequent Gibson assembly cloning:

PARP6<sub>FL</sub>:

- *Forward*: TACTTCCAATCCAATGCAGACATCAAAGGCC  
AGTTCTGGA
- *Reverse*: TTATCCACTTCCAATGTTATTAGTTTGT  
GTAAACCTGAGTTCCGATCA

PARP7<sub>FL</sub>:

- *Forward*: TACTTCCAATCCAATGCAGAAACCACCG  
CCGAACCTGAG
- *Reverse*: TTATCCACTTCCAATGTTATTAAATGGAAA  
CAGTGTTACTGACTTC

PARP8<sub>FL</sub>:

- *Forward*: TACTTCCAATCCAATGCAGGGATGTGTTCAA  
GGCAAGAGAG
- *Reverse*: TTATCCACTTCCAATGTTATTAACCAGTCGCA  
GTCTGATTACCAATC

PARP10<sub>FL</sub>:

- *Forward*: TACTTCCAATCCAATGCAGTTGCAAT  
GGCGGAG
- *Reverse*: TTATCCACTTCCAATGTTATTAAGTGTCT  
GGGGAGCG

PARP15<sub>FL</sub>:

- *Forward*: TACTTCCAATCCAATGCAGCGGCACCAGGGC  
CTT

- *Reverse:* TTATCCACTTCCAATGTTATTAAGCCGTGA  
AAGTTATGAGATATTCTGGGTAAG

PARP16<sub>FL</sub>:

- *Forward:* TACTTCCAATCCAATGCACAACCAAGCGG  
ATGGGC
- *Reverse:* TTATCCACTTCCAATGTTATTACGCTCT  
TGATTTTGGGGGTTT

The amplified fragments were gel purified and cloned into a pET-His-SUMO-TEV LIC cloning vector (1B), a gift from Scott Gradia (Addgene plasmid # 29653) by an isothermal assembly protocol using the Gibson assembly mix (NEB). cDNA encoding human PARP12 was obtained from a HeLa cell cDNA library. The catalytic domain (residues 489–684) of PARP12 was PCR-amplified from the cDNA library using primers with noncomplementary restriction enzyme sites located at the 5' (EcoRI) and 3' (XhoI) ends. The amplified product was cloned into pET-28b<sup>+</sup> (Novagen). The human PARP3 plasmid was obtained from DNAsu.

### **General expression and purification of human PARPs in *E. coli***

A plasmid in a pET-His6 or pET-His6-SUMO-TEV vector was transformed into *Escherichia coli* BL21 (DE3) competent cells (Millipore) and grown on an LB agar plate with kanamycin (50 mg/mL)



and chloramphenicol (34 mg/mL) overnight at 37°C. A swath of cells was inoculated into a 50 mL starter culture of LB media with kanamycin (50 mg/mL) and chloramphenicol (34 mg/mL) at 225 rpm, 37°C overnight. For each protein of interest 1-2 liters of terrific broth (TB) media (12 g bacto tryptone, 24 g yeast extract, 0.4% glycerol, 17 mM KH<sub>2</sub>PO<sub>4</sub>, 72 mM K<sub>2</sub>HPO<sub>4</sub>, 1% glucose, 50 µg/mL kanamycin, 34 µg/mL chloramphenicol) was inoculated with the starter culture and grown to an OD = 0.8-1.0 at 37°C, 225 rpm. Isopropyl-β-thiogalactoside, IPTG (Sigma-Aldrich) was added to 0.4 mM to induce protein expression for 18-24 hrs at 16°C, 225 rpm. Cells were harvested by centrifuging, resuspended in lysis buffer (20 mM HEPES, pH 7.5, 1 mM β-mercaptoethanol, 1 mM benzamidine, 0.2% NP-40, 0.2% TWEEN-20, 500 mM NaCl, 1 mM phenylmethylsulfonyl fluoride (PMSF), 8.3 mg/L DNase I (Roche)) and lysed by sonication at 0°C (Branson sonifier 450). Lysates were incubated with pre-washed Ni-NTA agarose resin (50% slurry, Qiagen) with end-over-end rotation at 4°C for 1 h. Following extensive washing with buffer B1+20 (20 mM HEPES, pH 7.5, 1 mM β-Me, 1 mM PMSF, 1 mM benzamidine, 500 mM NaCl, 20 mM imidazole).

- *For PARP1 and PARP2:* protein was eluted in 20 mL buffer B1+400 (20 mM HEPES, pH 7.5, 1 mM β-Me, 500 mM NaCl,

400 mM imidazole) and diluted with 30 mL of buffer 3AB<sup>+</sup>400 (100 mM Tris-HCl, pH 7.5, 0.5 mM EDTA, 14 mM  $\beta$ -Me, 0.4 M NaCl). Eluate was then loaded to a pre-washed 3-aminobenzamide-sepharose 4B chromatography column by gravity flow. The column was washed with buffer 3AB<sup>+</sup>400 followed by an equal volume of buffer 3AB<sup>+</sup>800 (100 mM Tris-HCl, pH 7.5, 0.5 mM EDTA, 14 mM  $\beta$ -Me, 0.8 M NaCl) and protein was eluted in buffer 3AB<sup>+</sup>MetB (100 mM Tris-HCl, pH 7.5, 0.5 mM EDTA, 14 mM  $\beta$ -Me, 0.4 M NaCl, 2 mM 3-methoxybenzamide).

- *For all other proteins:* protein was eluted in four fractions of B1 containing 100-400 mM imidazole.

Fractions were analyzed by SDS page gel stained with coomassie blue, or western blot visualized with ponceau stain. Fractions found to contain the desired protein as judged by molecular weight were dialyzed to 50 mM Tris-HCl, pH 7.5, 0.1 mM EDTA, 1 mM  $\beta$ -Me, 0.4 M NaCl at 4°C. Protein concentration was determined from a standard curve of His6-PARP1<sub>FL</sub> of a known concentration on western blot visualized with a monoclonal anti-His antibody (Proteintech). Proteins were obtained in >90% purity.

## **Chemical Compounds**

6-alkyne-NAD<sup>+</sup> was synthesized as previously described (Carter-OConnell et al. 2014).

OUL35 was synthesized as previously described (Venkannagari et al. 2016)

Olaparib and rucaparib were obtained commercially from Selleck Chemicals, catalogue numbers S1060 and S1098 respectively.

## **Detailed instructions for performing plate assay**

### **Materials**

1. Ni-NTA plates: Thermo Scientific Pierce nickel coated white 96-well plates, store at 4°C.
2. Human PARP buffer (hB): 50 mM HEPES pH 7.5, 100 mM NaCl, 4 mM MgCl<sub>2</sub>, 0.2 mM TCEP. (see Note 1)
3. Inhibitor stock solutions: stock solution in DMSO (800X), store at -20°C. (see Note 2)
4. 4X inhibitor solutions: 0.5% DMSO in hB, make fresh for each use. (see Note 3)
5. 4X 6-a-NAD<sup>+</sup> solution: 400 μM in hB, make fresh for each use (see Note 4). 6-a-NAD<sup>+</sup> used in assay development was synthesized in house by the Cohen lab. This reagent is also

available through Biology Life Science Institute (Cat No. N051-01).

6. Activated DNA: Sigma-Aldrich Deoxyribonucleic acid from calf thymus, type XV, activated, lyophilized powder. 0.1 mg/mL stock in DI H<sub>2</sub>O, store at -20°C.
7. Dumbbell nick-5'phosphorylated DNA hairpin (dNick-5'P): hairpin formed by slow annealing step in annealing buffer (Langelier et al. 2014), 100 µM stock stored at -20°C.
8. 2X inhibitor/2X 6-a-NAD<sup>+</sup> solution: equal volumes of 4X inhibitor solution and 4X 6-a-NAD<sup>+</sup> solution, 0.25% DMSO
9. 1X PBST: 0.02% Tween-20 in 1X PBS, store at room temperature.
10. ADPr binding reagent: 10 ng/mL in AbDil (1X PBS with 2% BSA and 1 mg/mL sodium azide), store at 4°C. This reagent was made in house by Dr. Carter O'Connell for use in the Cohen lab, it is also available through Millipore (Cat no. MABE1016).
11. Anti-Rabbit IgG HRP linked antibody (Cell Signaling Technology): 40 ng/mL in 5% milk in 1X PBST, make fresh for each use.

12. Click chemistry: Combine the following components in the following order for 1 mL click buffer (CB):
- 10  $\mu$ L Tris(1-benzyl-1H-1,2,3,-triazol-4-yl)methylamine (TBTA) (Click Chemistry Tools): 5 mM stock solution in DMSO (50X), stored at -20°C
  - 10  $\mu$ L Copper(II) sulfate ( $\text{CuSO}_4$ ): 50 mM stock solution in water (50X), stored at room temperature.
  - 20  $\mu$ L Biotin-PEG3-Azide (Click Chemistry Tools): 5 mM stock solution in DMSO (50X), stored at -20°C.
  - 20  $\mu$ L Tris(2-carboxyethyl)phosphine hydrochloride (TCEP): 50 mM stock solution in water (50X), made fresh in water (see Note 5)
  - 100  $\mu$ L 10X PBS (10X)
  - 820  $\mu$ L DI H<sub>2</sub>O
13. 1% milk solution: 1% w/v non-fat dry milk in 1X PBST.
14. Strep-HRP solution: 0.05 ng/ $\mu$ L in 1X PBS.
15. QuantaRed Detection Solution: Thermo Scientific QuantaRed Enhanced Chemifluorescent HRP Substrate.
16. QuantaRed Working Solution: 49.5% QuantaRed Enhancer solution, 49.5% QuantaRed Enhancer solution, 1% ADHP concentrate solution. (see Note 6)

17. Molecular Devices SpectraMax i3 multi-mode platform plate reader. Settings: Fluorescence Intensity Top mode, monochromator, endpoint reading; landscape height 14.6 mm; excitation wavelength 570 nm, bandwidth 9 nm; emission wavelength 600 nm, bandwidth 15 nm; 6 flashes per read; read height 1 mm.

## Method

This procedure provides a simple, sensitive, and generalizable assay for screening PARP inhibitors in parallel. The assay allows for head-to-head comparison of inhibitors across the PARP family with accurate and precise results over many independent trials. For optimal results all incubations should be performed at the specified temperature with gentle agitation. Recombinant proteins are stored in 10% glycerol at -80°C and undergo no more than two freeze thaw cycles.

1. Ni-NTA plate preparation with SRPK2: binding of His6-SRPK to the Ni-NTA plates provide immobilized targets for ADP-ribosylation by various PARPs in the enzymatic reaction
  - Thaw SRPK2 on ice and dilute into cold hB buffer to a concentration of 0.3  $\mu$ M.

- Add 50  $\mu$ L of SRPK2 solution *or* PARP solution if performing an automodification assay to each well of Ni-NTA plate and incubate for 1 hour.
  - Wash each well with 1X PBST (1x, 100  $\mu$ L), 1X PBS (1x, 100  $\mu$ L), and hB (1x, 100  $\mu$ L), incubate each wash for at least 1 minute.
  - From here proceed with either step 2 (native NAD<sup>+</sup> labeling) or 3 (6-a-NAD<sup>+</sup> labeling).
2. ADP-ribosylation reaction with native NAD<sup>+</sup>: PARP enzymes ribosylate SRPK or auto-ribosylate. This modification is then detected with an ADPribose binding reagent (Millipore, cat no. MABE1016) followed by an anti-rabbit HRP-linked secondary antibody (Cell Signaling Technology). Addition of PARP inhibitors will reduce ADP-ribosylation levels according to their potency.
- Add 25  $\mu$ L 2X enzyme to each well (see Table 2-1 for enzyme concentrations) followed by 25  $\mu$ L 2X inhibitor/2X NAD<sup>+</sup> to each well. Incubate at 30°C for 1 hour. In auto-ribosylation assays hB buffer is added instead of 2X enzyme solution.

- Remove reaction mixture and wash each well with 1X PBST (2x, 100  $\mu$ L), 1X PBS (1x, 100  $\mu$ L).
  - Add 50  $\mu$ L 1% milk solution and incubate for 30 min at RT.
  - Remove milk solution and wash each well with 1X PBST (2x, 100  $\mu$ L), 1X PBS (1x, 100  $\mu$ L).
  - Add 50  $\mu$ L pan-ADPr binding reagent and incubate for 60 min at RT.
  - Remove pan-ADPr binding reagent and wash each well with 1X PBST (2x, 100  $\mu$ L), 1X PBS (1x, 100  $\mu$ L).
  - Add 50  $\mu$ L anti-rabbit IgG HPR linked secondary antibody and incubate for 30 min at RT.
  - Remove secondary antibody and wash each well with 1X PBST (2x, 100  $\mu$ L), 1X PBS (1x, 100  $\mu$ L).
  - Add 100  $\mu$ L QuantaRed Working Solution to each well and incubate until sufficient signal is obtained.
  - Add 10  $\mu$ L QuantaRed stop solution to quench reaction. Image within five min of quenching.
  - Image plate
3. ADP-ribosylation reaction with 6-a-NAD<sup>+</sup>: PARP enzymes transfer 6-alkyne-ADP-ribose from 6-a-NAD<sup>+</sup> onto His6-



SRPK2 or auto-ribosylate. Addition of PARP inhibitors will reduce 6-alkyne-ADP-ribosylation levels according to their potency. The clickable 6-alkyne-ADP-ribose is conjugated with biotin-azide via click chemistry. Strep-HRP and a chemifluorescent HRP substrate provide a readout of ADP-ribosylation levels.

- Add 25  $\mu$ L 2X enzyme to each well (see Table 2-1 for enzyme concentrations) followed by 25  $\mu$ L 2X inhibitor/2X 6-a-NAD<sup>+</sup> to each well. Incubate at 30°C for 1 hour. In auto-ribosylation assays hB buffer is added instead of 2X enzyme solution.
- Remove reaction mixture and wash each well with 1X PBST (2x, 100  $\mu$ L), 1X PBS (1x, 100  $\mu$ L).
- Add 50  $\mu$ L 1X click buffer to each well and incubate for 30 min at RT.
- Remove click buffer and wash each well with 1X PBST (2x, 100  $\mu$ L), 1X PBS (1x, 100  $\mu$ L).
- Add 50  $\mu$ L 1% milk solution and incubate for 30 min at RT.
- Remove milk solution and wash each well with 1X PBST (2x, 100  $\mu$ L), 1X PBS (1x, 100  $\mu$ L).

- Add 50  $\mu$ L Strep-HRP solution to each well and incubate for 30 min at RT.
- Remove Strep-HRP solution and wash each well with 1X PBST (2x, 100  $\mu$ L), 1X PBS (1x, 100  $\mu$ L).
- Add 100  $\mu$ L QuantaRed Working Solution to each well and incubate until sufficient signal is obtained.
- Add 10  $\mu$ L QuantaRed stop solution to quench reaction. Image within five min of quenching.
- Image plate

**Notes:**

1. Make 100 mM TCEP stock solution in water fresh for every use.
2. Storage and shelf life depends on individual compound stability.
3. Some inhibitors may be insoluble at higher concentrations; this can be solved with agitation and gentle heating within the bounds of confirmed stability for each inhibitor on a case-by-case basis.
4. 6-a-NAD<sup>+</sup> should be stored at -80°C for up to one year, multiple freeze thaws should be avoided to maintain optimal activity.

5. Prepare fresh immediately before use, addition of TCEP should cause a color change from light blue to green. Once added to the plate the click solution should still be discernibly blue tinted.
6. Let components warm to room temperature before combining. Use solution within five minutes of making.

## **Chapter 3: A Selective PARP11 Inhibitor suggests Coupling between Cellular Localization and Catalytic Activity**

**Ilsa T. Kirby**, Ana Kojic, Moriah R. Arnold, Ann-Gerd Thorsell, Tobias Karlberg, Anke Vermehren-Schmaedick, Raashi Sreenivasan, Carsten Schultz, Herwig Schöler, and Michael S. Cohen

Portions of this chapter were originally published on December 20th 2018 in *Cell Chemical Biology* (© 2018 Elsevier Ltd) (Kirby, Kojic, et al. 2018). It has been adapted for this dissertation and reprinted with permission from the journal. This work was in collaboration with Ana Kojic who performed the live-cell imaging; Moriah R. Arnold who conducted cellular studies of ITK7; Drs. Ann-Gerd Thorsell, Tobias Karlberg, and Herwig Schöler who conducted the crystallography studies; Dr. Anke Vermehren-Schmaedick who conducted the immunoprecipitation assays; Dr. Raashi Sreenivasan who prepared the Sumo-PARP11 construct for bacterial expression

## Abstract

Poly-ADP-ribose polymerases (PARPs1-16) play pivotal roles in diverse cellular processes. PARPs (PARP1-5) that catalyze poly-ADP-ribosylation (PARylation) are the best characterized PARP family members because of the availability of potent and selective inhibitors for these PARPs. There has been comparatively little success in developing selective inhibitors of PARPs (PARP6-8, 10-12, 14-16) that catalyze mono-ADP-ribosylation (MARylation), limiting our understanding of the cellular role of these PARPs. We describe the structure-guided design of small molecule inhibitors of PARPs that catalyze MARylation. The most selective analog, ITK7, potently ( $IC_{50} = 14$  nM) inhibits the MARylation activity of PARP11, a nuclear envelope localized PARP. ITK7 is greater than 200-fold selective over other PARP family members. ITK7 inhibits PARP11 auto-MARylation in cells in a dose-dependent manner. Using live cell imaging, we show that ITK7 causes PARP11 to dissociate from the nuclear envelope. These results suggest that the cellular localization of PARP11 is regulated by its catalytic activity.

## Introduction

Poly-ADP-ribose polymerases (PARPs1-16; also known as ADP-ribosyltransferases or ARTDs) have emerged as key regulators of diverse cellular processes, including DNA repair, transcription, the unfolded protein response, and RNA processing (Gupte et al. 2017). PARPs catalyze the reversible post-translational modification known as ADP-ribosylation, which involves the transfer of ADP-ribose from nicotinamide adenine dinucleotide (NAD<sup>+</sup>) to amino acids in protein substrates. Active PARPs can be divided into two subfamilies based on the presence of a shared, active site triad motif: the HYE-PARPs (PARP1, 2, 3, 4, 5a and 5b) and the HYΦ-PARPs (PARP 6-8, 10-12, 14-16) (Hottiger et al. 2010). The glutamate in the HYE motif is necessary for the poly-ADP-ribosylation (PARylation) activity of several HYE-PARPs (Marsischky et al. 1995; Rolli et al. 1997). In contrast to the HYE-PARPs, the HYΦ-PARPs contain a hydrophobic (Φ) amino acid in the third position of the triad. Recently, all HYΦ-PARPs were shown to catalyze mono-ADP-ribosylation (MARylation) exclusively (Vyas et al. 2014). In contrast to HYE-PARPs, HYΦ-PARPs remain largely uncharacterized and we know very little about the role of MARylation in cells. Our laboratory has recently developed a chemical genetic strategy to identify the direct targets of HYΦ-PARPs, which serves as a starting

point to understand the cellular function of MARYlation (Carter-OConnell et al. 2016).

Selective inhibitors of PARP1,2 (e.g. veliparib) (Donawho et al., 2007) have validated the roles for these PARPs in the DNA damage response pathway. Likewise, selective inhibitors of PARP5a,b (AZ6102) (Johannes, Almeida, Barlaam, et al. 2015) demonstrated roles for PARP5a,b in Wnt signaling (S.-M. A. Huang et al. 2009), and revealed cross-talk between PARYlation and ubiquitylation. As selective inhibitors of HYE-PARPs have been used to better understand the function of PARYlation in cells, selective small molecule inhibitors of individual HYΦ-PARPs would be useful probes to further dissect the function of MARYlation in cells. Unfortunately, there is a dearth of inhibitors that potently and selectively inhibit the HYΦ-PARP subfamily. Consequently, we know very little about the roles for HYΦ-PARPs in cells (Wahlberg et al. 2012). Recent studies demonstrate that HYΦ-PARPs (e.g. PARP14) are therapeutic targets for several cancers (Iansante et al. 2015; Barbarulo et al. 2013) as well as allergic asthma (Mehrotra et al. 2013) highlighting the need to develop selective inhibitors of HYΦ-PARPs.

Thus far, the only published small molecule inhibitors targeting HYΦ-PARPs are against PARP10 (Venkannagari et al. 2016; Morgan et

al. 2018) and PARP14 (Peng et al. 2016; Yoneyama-Hirozane et al. 2017; Upton et al. 2017). While OUL35 was shown to be selective for PARP10 over several other PARP family members, the recently described inhibitors of PARP14 are either not selective over HYE-PARPs or their selectivity has not been fully determined. Ekblad et al. described a set of non-selective inhibitors that inhibited PARP1, PARP10, PARP14, and PARP15 with low micromolar potency, but were not screened beyond these enzymes (Ekblad et al. 2015). One major challenge in developing inhibitors of HY $\Phi$ -PARPs is identifying compounds that do not inhibit HYE-PARPs yet are potent enough to be used in cellular studies. Herein, we describe a structure-guided approach for developing small molecule inhibitors designed to exploit unique structural features found in HY $\Phi$ -PARPs. This strategy led to the first selective small molecule inhibitor of PARP11 (ITK7) that exhibits cellular activity.

## Results

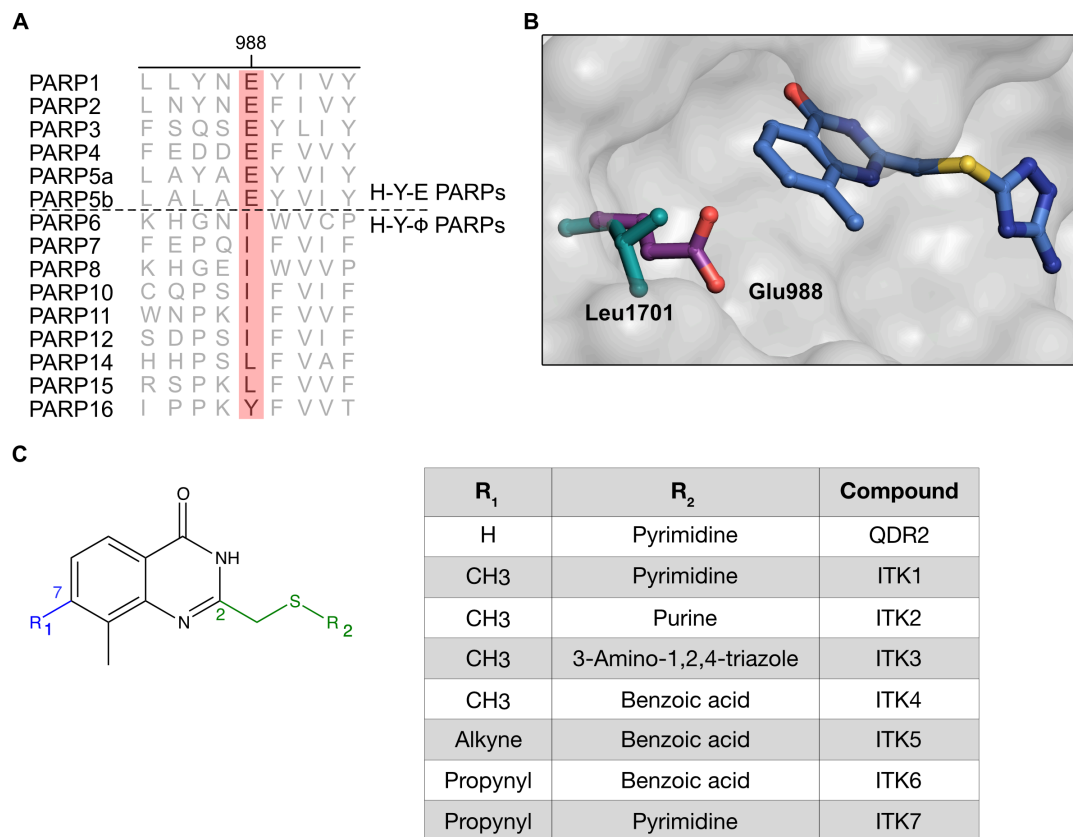
### **Structure-guided design leads to small molecule inhibitors selective for HY $\Phi$ -PARPs**

Initially, we sought to identify amino acid differences in the active site between HYE-PARPs and HY $\Phi$ -PARPs that we could exploit for



inhibitor design. As discussed above, one major difference between HYE-PARPs and HY $\Phi$ -PARPs is the identity of the amino acid at the third position in the triad motif (corresponding to position 988, human PARP1 numbering) (Figure 1A). This position sits at the base of the nicotinamide-binding pocket. We reasoned that the major difference (i.e. acidic versus hydrophobic) in the amino acid at the third position of the conserved triad could potentially be exploited for the development of selective inhibitors of HY $\Phi$ -PARPs.

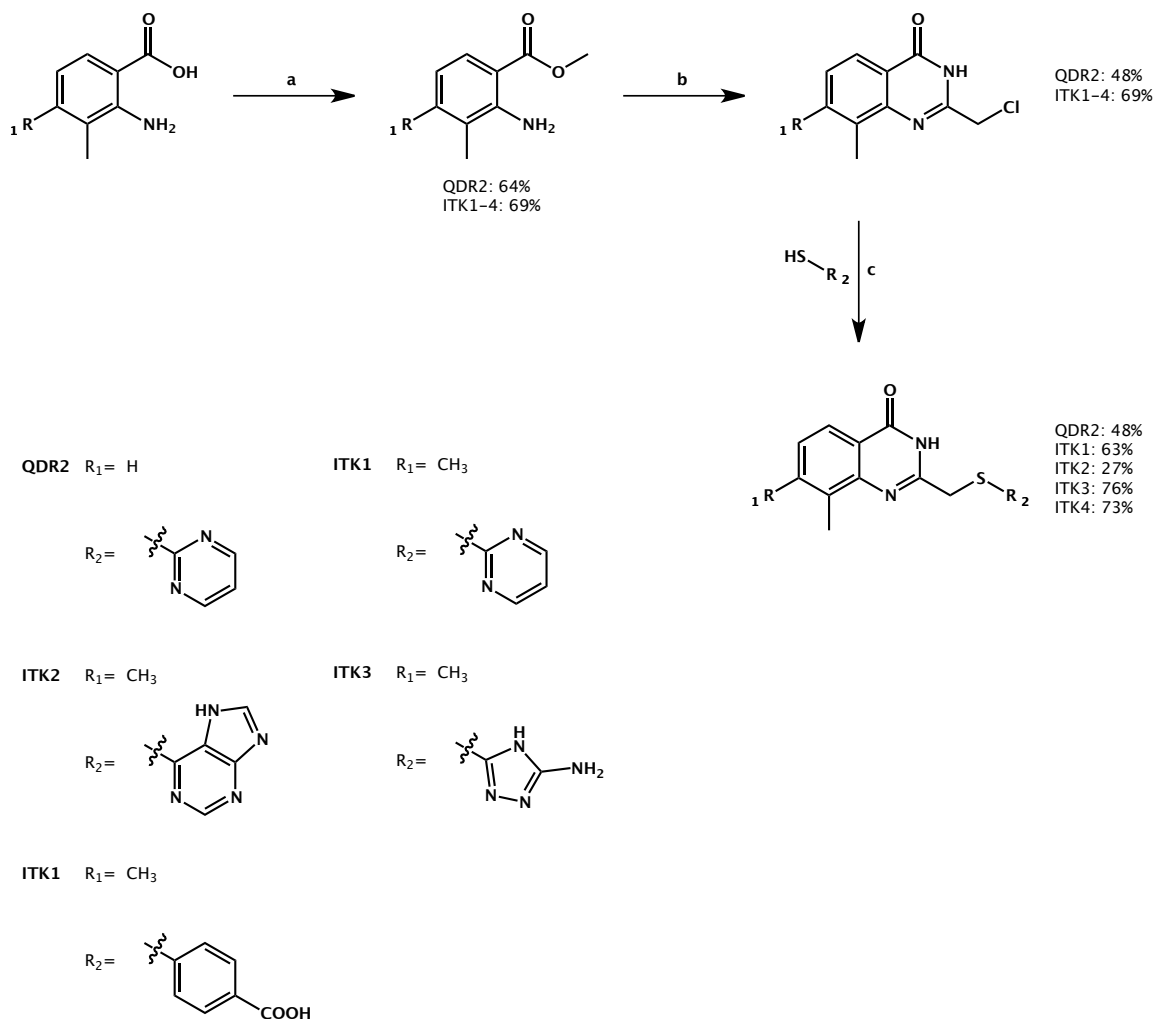
To this end, we needed an appropriate scaffold as a starting point for HY $\Phi$ -PARP-selective inhibitors. We scrutinized the structure of a pan-PARP inhibitor with a quinazolin-4(3H)-one (QDR) scaffold (referred to here as QDR1) bound to the nicotinamide binding-site of PARP14 (Wahlberg et al. 2012). By overlaying the PARP14-QDR1 structure with that of PARP1 we hypothesized that small, aliphatic substituents at the C-7 position of the QDR scaffold would interact favorably with hydrophobic amino acids ( $\Phi$ ) in the third position of HY $\Phi$ -PARPs, but would sterically clash with the charged glutamic acid in the third position of HYE-PARPs (Figure 1B,C).



**Figure 3-1** Structure-Guided Design of Selective HYE PARP Inhibitors

- (A) Structure-based sequence alignment of the PARPs. PARylating PARPs contain a glutamate (Glu988, human PARP1 numbering) in the third position of the HYE triad, while MARYlating PARPs contain a hydrophobic ( $\Phi$ ) amino acid at this position.
- (B) The crystal structure of QDR1 bound to the catalytic domain of PARP14 (PDB: 3SMI) shows that substituents at the C-7 position of the QDR scaffold would clash with the glutamate (purple) in the third position of the HYE triad but interact favorably with hydrophobic amino acids in the third position (Leu1701, teal) of the HY $\Phi$  triad.
- (C) Chemical structure of QDR-based inhibitors described in this study.

To test this hypothesis, we synthesized a QDR-based compound containing a methyl group at the C-7 position as well as the des-methyl version (ITK1 and QDR2, Figure 3-1C and Scheme 3-1).



**Scheme 3-1** Synthesis of ITK1-4

a) cat.  $H_2SO_4$ , MeOH,  $80^\circ C$ ; b) chloroacetonitrile, 4 M HCl (1,4-dioxane),  $110^\circ C$ ; c) NaH, DMF, RT.

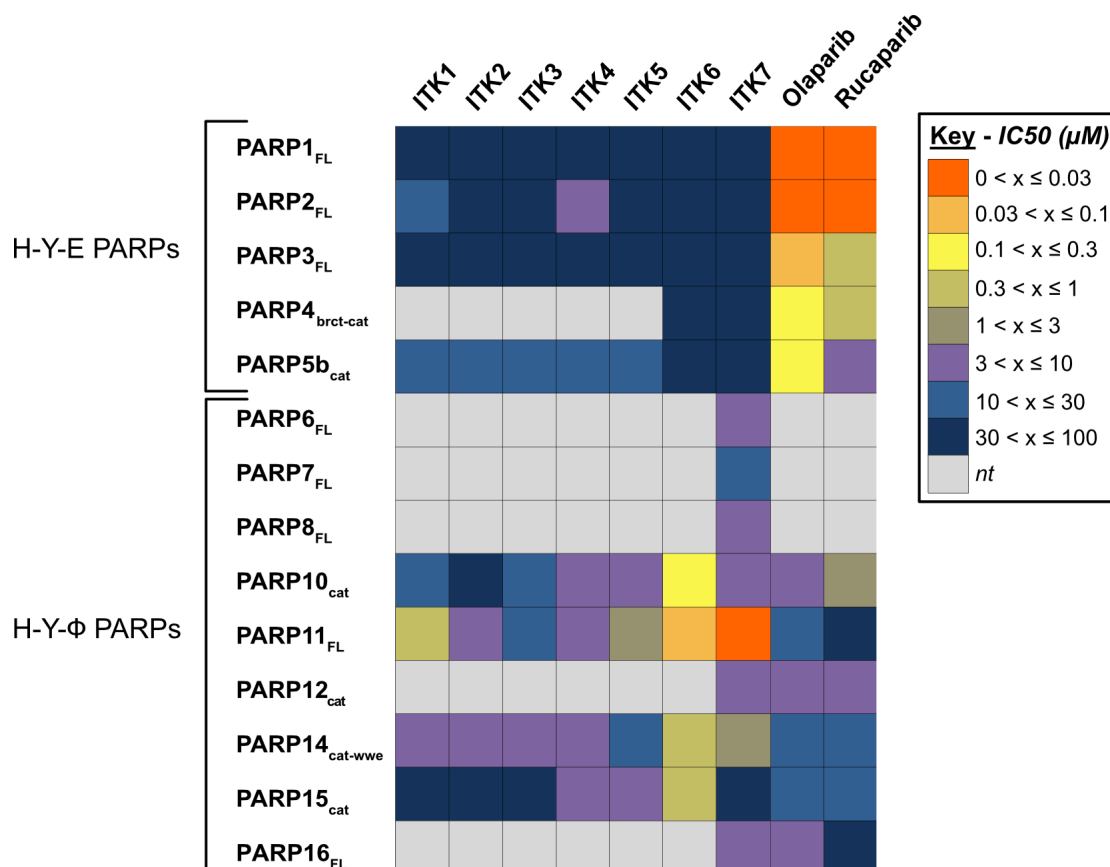
These analogs contain a 2-mercaptopyrimidine substituent at the C-2 position of the QDR scaffold. We initially tested ITK1 and

QDR2 against two well-characterized HYE-PARPs (PARP1 and PARP2) (Figure 3-2, Appendix A) using histones as protein substrates and a clickable NAD<sup>+</sup> analog (N-6 alkyne-NAD<sup>+</sup>) that is used to monitor ADP-ribosylation *in vitro* (Carter-OConnell et al. 2014). We found that QDR2 was moderately potent against PARP1 (IC<sub>50</sub> = 1.3 μM) and PARP2 (IC<sub>50</sub> = 0.8 μM). In contrast, ITK1 only weakly inhibited PARP2 (IC<sub>50</sub> = 17.4 μM) and did not inhibit PARP1 at concentrations up to 30 μM. Additionally, ITK1 did not inhibit PARP3 or the catalytic domain of PARP5b (PARP5<sub>cat</sub>) at concentrations up to 10 μM (Figure 3-2, Appendix A). The catalytic domain of PARP5b was used as described in previous studies (Thorsell et al. 2017). Thus, the replacement of a hydrogen atom for a methyl group at the C-7 position of the QDR scaffold decreases potency against HYE-PARPs. Other small substituents at the C-7 position including a methoxy and a CF<sub>3</sub> were not as promising, and our initial SAR suggests that the C-6 methyl is key for inhibitor potency (Appendix A).

We next determined if ITK1 inhibited HYΦ-PARPs, and if it was more potent than the des-methyl analog QDR2. It should be noted that for several of the PARPs used for these *in vitro* MARYlation assays, the catalytic domain alone or a combination of the catalytic domain and another domain were used because of our inability to generate in E.

coli sufficient quantity and purity of several of the full-length PARPs. Indeed, previous studies have used catalytic domain fragments of PARPs for inhibitor screens (Thorsell et al. 2017; Ekblad et al. 2015; Peng et al. 2016; Upton et al. 2017; Yoneyama-Hirozane et al. 2017). We focused initially on the HY $\Phi$ -PARP PARP14 because our structural analysis was based on the crystal structure of PARP14 bound to QDR1. We expressed and purified a truncated PARP14 containing the catalytic and WWE domains (PARP14<sub>cat-wwe</sub>) and tested its activity using the promiscuous HY $\Phi$ -PARP substrate SRSF protein kinase 2 (SRPK2) (Venkannagari et al. 2013). PARP14<sub>cat-wwe</sub> exhibits robust *in vitro* MArYlation activity against SRPK2. We found that ITK1 was 2-fold more potent than QDR2 against PARP14<sub>cat-wwe</sub> (IC<sub>50</sub> = 8.6  $\mu$ M versus 16  $\mu$ M) (Figure 3-2, Appendix A).

We next screened ITK1 against several other HY $\Phi$ -PARPs: PARP10<sub>cat</sub>, PARP11, and PARP15<sub>cat</sub> (Figure 3-2, Appendix A). ITK1 was less potent against PARP10<sub>cat</sub> (IC<sub>50</sub> = 19.7  $\mu$ M) and PARP15<sub>cat</sub> (IC<sub>50</sub> >30  $\mu$ M) compared to PARP14<sub>cat-wwe</sub>. By contrast, ITK1 inhibited PARP11 with sub-micromolar potency (IC<sub>50</sub> = 0.55  $\mu$ M). Taken together, these data suggest that modification at the C-7 position is a promising approach toward selectively inhibiting HY $\Phi$ -PARPs and not HYE-PARPs.



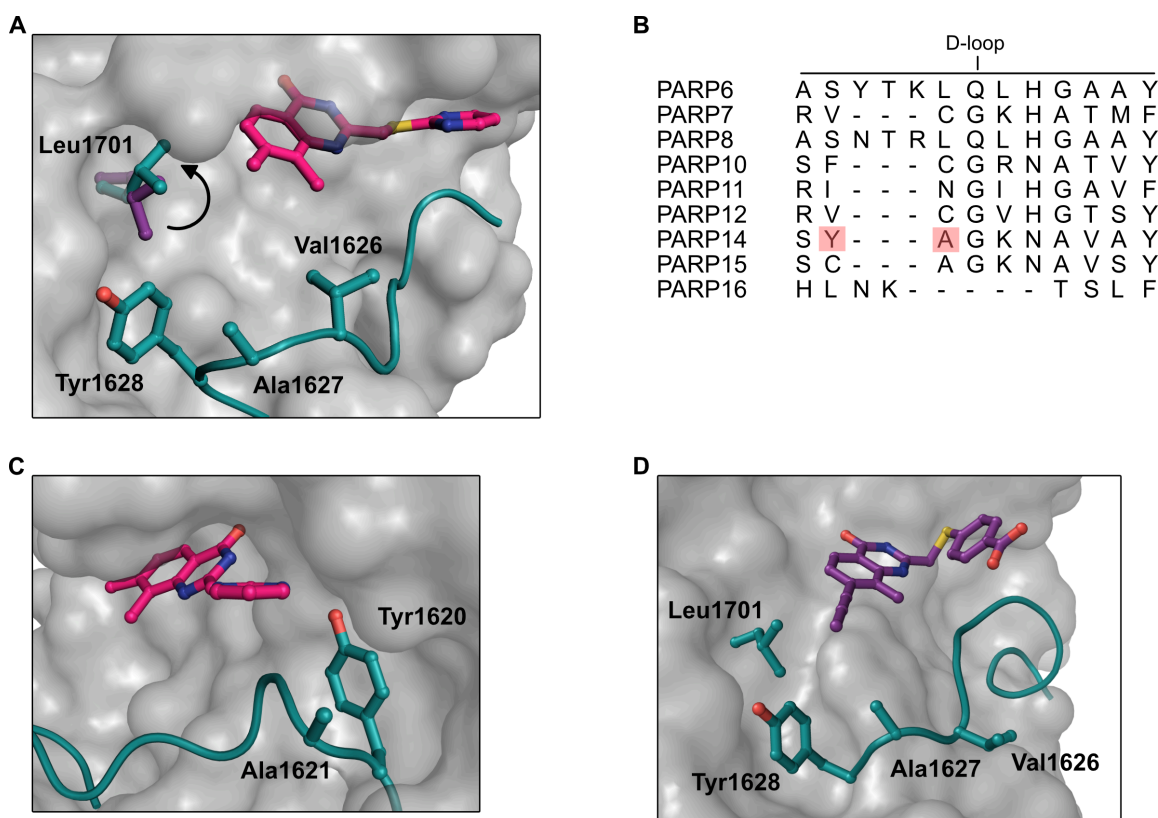
**Figure 3-2** ITK inhibitor series screened across the PARP Family

Heatmap depicting the IC<sub>50</sub> values determined for the ITK series, olaparib, and rucaparib against the PARPs. Values based on at least three replicates.

### Structural studies of ITK1 reveal a unique hydrophobic sub-pocket in an HYΦ-PARP

To gain more insight into the interaction of ITK1 with an HYΦ-PARP, we solved a crystal structure of ITK1 bound to the catalytic domain of PARP14. PARP14 was used for structural studies because it is easy to

crystallize compared to other PARP family members (unpublished results) and we could directly compare the PARP14-ITK1 structure to the previously determined PARP14-QDR1 structure. Comparing the PARP14-ITK1 structure to the PARP14-QDR1 structure revealed that Leu1701 rotates toward the methyl group at the C-7 position of QDR2 to form a potential hydrophobic interaction (Figure 3A). The C-7 methyl group also points toward a hydrophobic sub-pocket lined by Leu1701, Val1626, Ala1627, and Tyr1628, which are located at the C-terminus of the donor-loop (D-loop) (Figure 3-3A). The D-loop—a flexible loop that abuts the NAD<sup>+</sup> binding site—is one of the least conserved elements in the PARP catalytic domains (Figure 3-3B) (Pinto & Schüler 2015). While the exact function of the D-loop is unclear, structural and functional studies of related MARYlating bacterial toxins suggest its involvement in NAD<sup>+</sup> binding as well as substrate recognition (Jørgensen et al. 2005; Jørgensen et al. 2008). While structural comparison of various HYΦ-PARP-inhibitor complexes highlights D-loop flexibility, the hydrophobic sub-pocket appears to be a static feature of HYΦ-PARPs (Wahlberg et al. 2012). The hydrophobic sub-pocket is sterically occluded by the glutamate in HYE-PARPs and could potentially serve as a selectivity filter within the HYΦ-PARP active site.



**Figure 3-3** Exploiting a Hydrophobic Sub-pocket in HYE PARPs with C-7-Substituted QDR Analogs

- (A) Crystal structure of ITK1 (magenta) (PDB: 6FYM) bound to PARP14<sub>cat</sub>. Leu1701 rotates toward the C-7 methyl group of ITK1 to make hydrophobic contacts compared with its position bound to QDR1 (violet, Leu1701 in the QDR1 bound structure; teal, Leu1701 in ITK1 bound structure). The C-7 methyl group of ITK1 projects into a hydrophobic sub-pocket formed by Leu1701 and amino acids located at the C terminus of the D-loop.
- (B) Structure-based sequence alignment showing the amino acids in the D-loop. Tyr1620 and Ala1621 in PARP14 are highlighted in pink, Val1626, Ala1627, and Tyr1628 in PARP14 are highlighted in yellow.
- (C) Interactions between the amino acids (Ala1621 and Tyr1620, in particular) in the N terminus of the D-loop (teal) and the C-2 substituent of ITK1.



(D) Crystal structure of ITK6 (violet) (PDB: 6FZM) bound to PARP14<sub>cat</sub>. The propynyl substituent at the C-2 position of ITK6 occupies the hydrophobic sub-pocket.

### **Exploiting differences in the D-loop for generating selectivity among HYΦ-PARP family members**

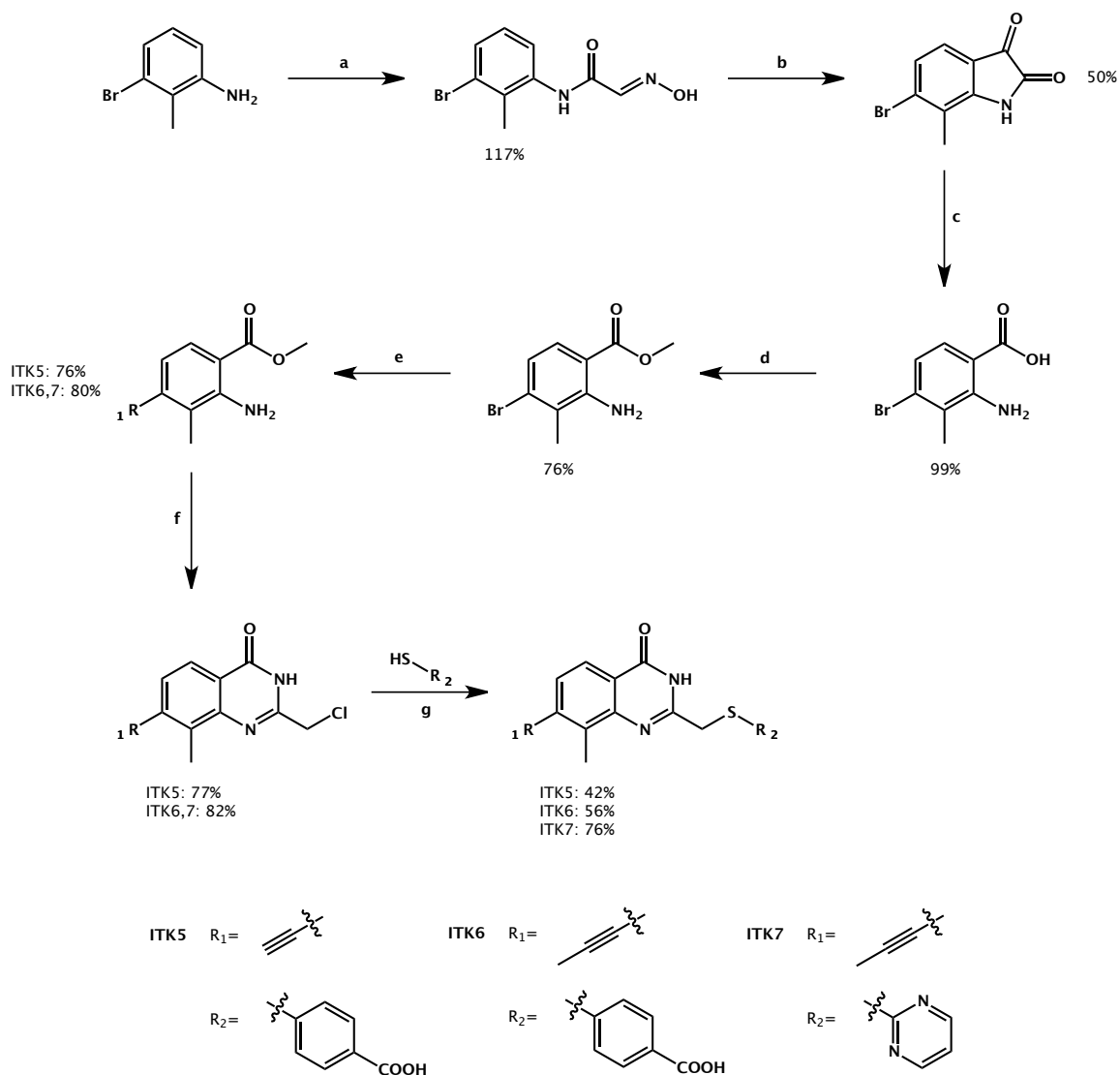
In the PARP14-ITK1 structure the N-terminus region of the PARP14 D-loop interacts with the pyrimidine substituent at the C-2 position of ITK1 (Figure 3-3C). Given the lack of sequence conservation within the D-loop of various HYΦ-PARPs we envisaged that modifications at this position could result in selective inhibition of individual HYΦ-PARP family members. We synthesized three C-7 methyl QDR analogs with diverse aromatic substituents attached via a thioether linkage at C-2 (ITK2: adenosine, ITK3: 3-amino-triazole, ITK4: p-benzoic acid) (Figure 3-1C and Scheme 3-1). We screened these compounds against the HYE-PARPs (PARP1-3 and PARP5<sub>bcat</sub>) and the HYΦ-PARPs (PARP10<sub>cat</sub>, PARP11, PARP14<sub>cat-wwe</sub>, and PARP15<sub>cat</sub>) (Figure 3-2, Appendix A). None of the C-7 methyl QDR analogs inhibited PARPs 1-3 (up to 30 μM) or PARP5<sub>bcat</sub> (up to 10 μM) except ITK4, which modestly inhibited PARP2 (IC<sub>50</sub> = 8.5 μM) but did not inhibit the other HYE-PARPs. Therefore, the methyl substituent at C-7 decreases binding of QDR analogs to HYE-PARPs. Among the HYΦ-PARPs, ITK2-4 did not exhibit improved potency or selectivity compared to

ITK1. Indeed, ITK1 remained most potent and selective against PARP11 (Figure 3-2, Appendix A). These data indicate that selectivity for PARP11 can be achieved with a pyrimidine at the C-2 position of the QDR scaffold. This selectivity is likely due, in part, to specific interactions between the pyrimidine and amino acids in the D-loop of PARP11; future structural studies will be useful for testing this hypothesis.

#### **Further modification of the C-7 position of the QDR scaffold leads to improved potency**

After exploring the C-2 position of the QDR scaffold we wondered if further modification at the C-7 position with a larger substituent would yield increases in HYΦ-PARP potency and selectivity by expanding into the hydrophobic sub-pocket. Initially we focused on the QDR analog that has a p-benzoic acid emanating from the C-2 position (ITK4) because this substituent yielded broad-spectrum HYΦ-PARP inhibition (Figure 3-2, T Figure 3-2, Appendix A). We synthesized two compounds containing either an alkynyl (ITK5) or a propynyl (ITK6) substituent at the C-7 position (Figure 1 and Scheme 3-2). ITK5 exhibited similar potency to ITK4 against the HYΦ-PARPs whereas ITK6 exhibited substantially improved potency against PARP10<sub>cat</sub> (60-fold) and PARP11 (55-fold), while modestly improving potency against

PARP14<sub>cat-wwe</sub> (10-fold) and PARP15<sub>cat</sub> (15-fold) (Figure 3-2, Appendix A). Importantly, ITK6 did not inhibit PARP1-4 and PAR5b up to 30  $\mu$ M. We obtained a crystal structure of ITK6 bound to the catalytic domain of PARP14, which confirmed our hypothesis that the propynyl substituent projects further into the unique hydrophobic sub-pocket (Figure 3-3D). These results show that targeting the unique hydrophobic sub-pocket found in the HY $\Phi$ -PARP sub-family is a viable strategy for the development for HY $\Phi$ -PARP-family selective inhibitors.



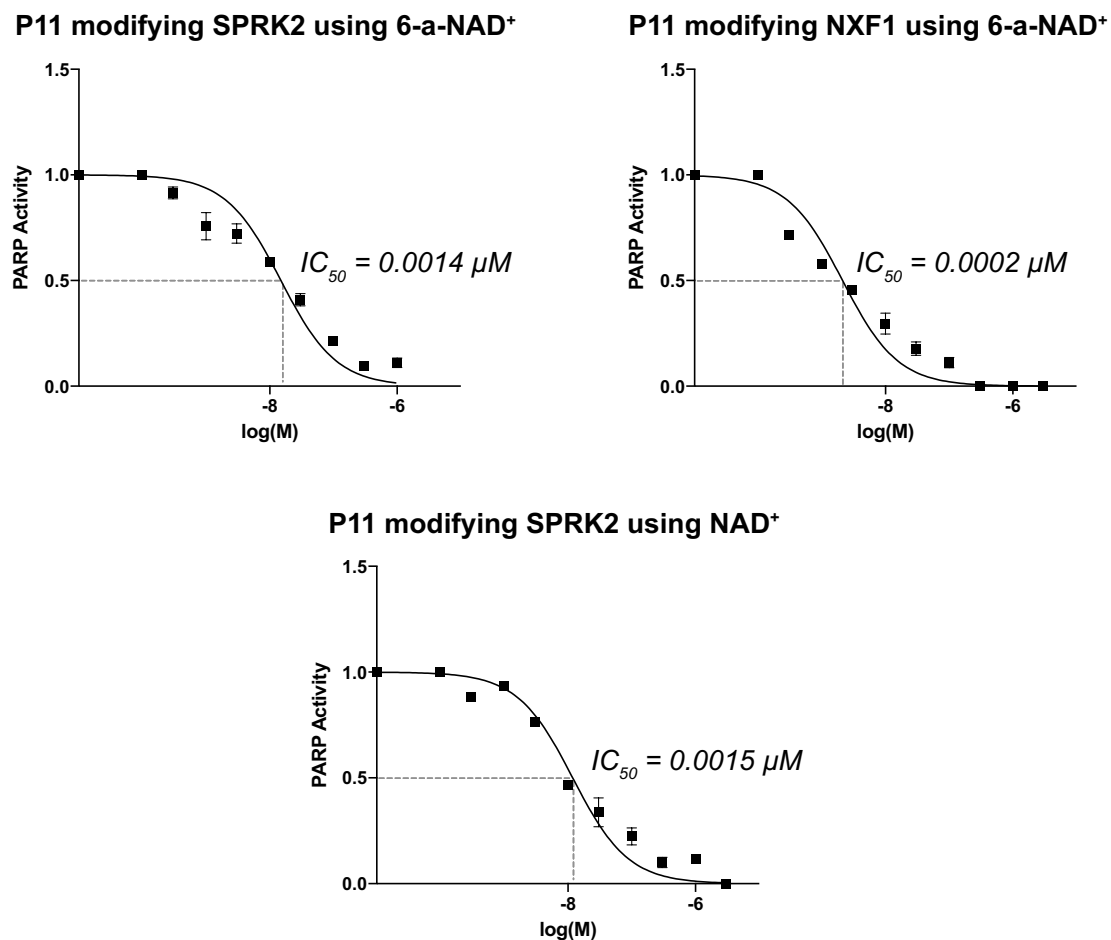
### Scheme 3-2 Synthesis of ITK5-7

a) chloral hydrate,  $(\text{NH}_2\text{OH})_2\cdot\text{H}_2\text{SO}_4$ , HCl,  $\text{NaSO}_4$ ,  $\text{H}_2\text{O}$ ,  $35\text{--}75^\circ\text{C}$ ; b)  $\text{H}_2\text{SO}_4$ ,  $80^\circ\text{C}$ ; c)  $\text{H}_2\text{O}_2$  (30%), 1 M NaOH, then HCl, RT; d) cat. )  $\text{H}_2\text{SO}_4$ , MeOH,  $80^\circ\text{C}$ ; e) ITK5: TMS-acetylene and  $\text{Pd}(\text{PPh}_3)_2\text{Cl}_2$  (10% molar), ITK6 and ITK7: Tributyl(1-propynyl)tin and palladium tetrakis (10% molar), toluene,  $115^\circ\text{C}$ ; f) chloroacetonitrile, 4 M HCl (1,4-dioxane),  $110^\circ\text{C}$ ; g) NaH, DMF, RT.

### **Design of a potent and selective PARP11 inhibitor**

The structure activity relationship study exploring the thioether linkage at the C-2 position of the QDR scaffold demonstrated that the pyrimidine at the C-2 position of ITK1 yielded the best selectivity for PARP11 (Figure 3-2, Appendix A). We reasoned that replacing the C-7 methyl in ITK1 with a propynyl group (ITK7) (Figure 3-1 and Scheme 3-2) would yield a more potent and selective PARP11 inhibitor. Indeed, we found that ITK7 potently inhibited PARP11 ( $IC_{50} = 0.014 \mu M$ ) and was at least 200-fold more selective for PARP11 compared to other HY $\Phi$ -PARPs while not inhibiting any of the HYE-PARPs up to 30  $\mu M$  (Figure 3-2, Appendix A). ITK7 exhibited similar potency against PARP11 when Nuclear Export Factor 1 (NXF1), a previously identified cellular target of PARP11 (Carter-OConnell et al. 2016), was used as a substrate instead of the pan-substrate SRPK2 demonstrating that inhibition was not dependent on the protein target (Figure 3-4). Furthermore, ITK7 exhibited similar potency against PARP11 when native  $NAD^+$  was used instead of 6-a- $NAD^+$  (Figure S2). Compared to two FDA-approved drugs olaparib and rucaparib (Menear et al. 2008; Thomas et al. 2007; Bitler et al. 2017), which potently inhibit several HYE-PARPs (Wahlberg et al. 2012; Thorsell et al. 2017), and only modestly inhibit a few HY $\Phi$ -

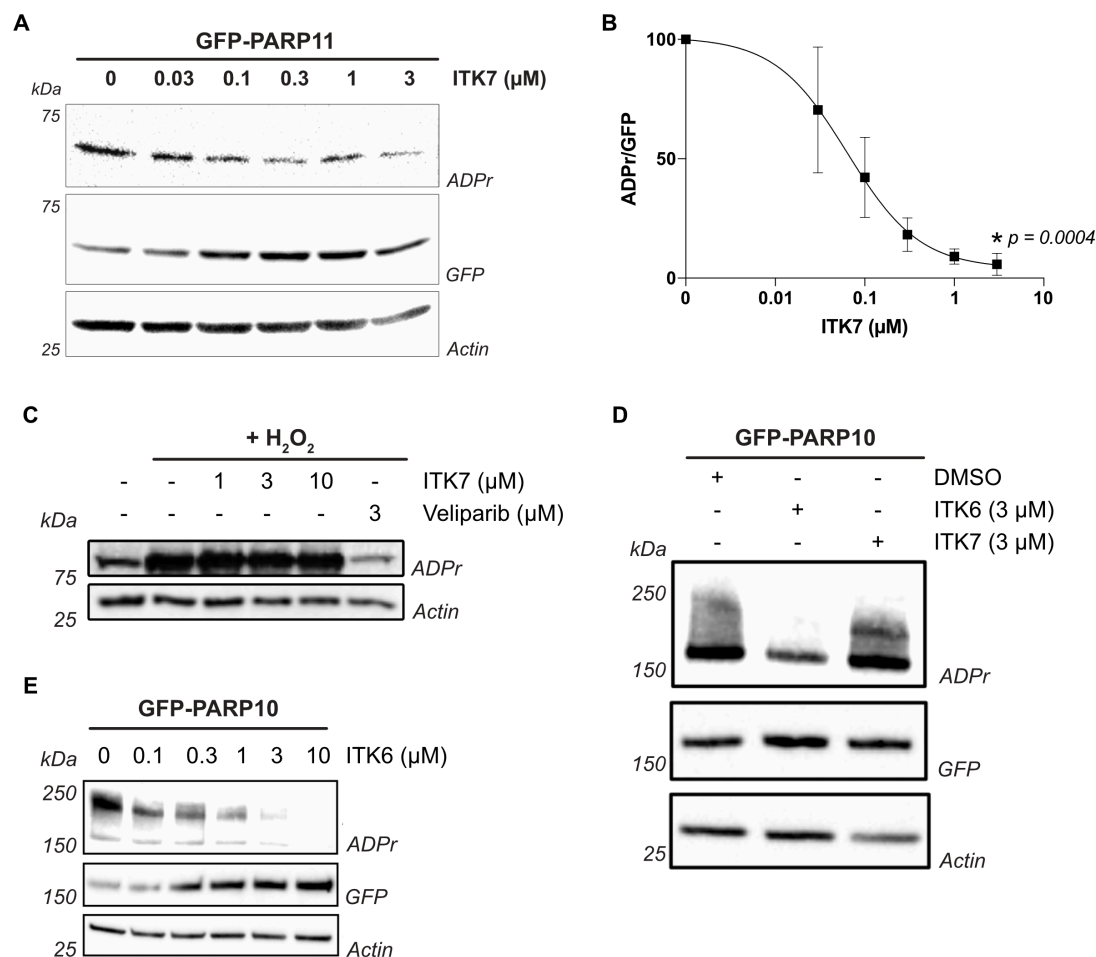
PARPs (Figure 3-2, Appendix A), ITK7 is one of the most potent and selective PARP inhibitors described to date.



**Figure 3-4** Dose response curves for ITK7 inhibiting PARP11 mediated MARYlation of SRPK2 and NXF1 using either 6-a-NAD<sup>+</sup> or native NAD<sup>+</sup> in *in vitro* plate assays. Curves generated using Prism 7 (Graph Pad); error bars indicate  $\pm$ SEM from at least two replicates.

**ITK7 inhibits PARP11 auto-MARylation activity in cells and causes PARP11 to dissociate from the nuclear envelope.**

We next examined the effects of ITK7 on PARP11 activity in cells. Similar to other PARPs, PARP11 undergoes auto-MARylation (Vyas et al. 2014; Carter-OConnell et al. 2016). Because there are no validated cell-based assays for examining endogenous PARP11 activity or function, we used HeLa cells expressing full-length GFP-PARP11 to test the efficacy of ITK7. These cells were treated with increasing concentrations of ITK7 for 3 h (Figure 3-5A). ITK7 exhibited a dose-dependent inhibition of PARP11-dependent auto-MARylation ( $EC_{50} = 0.013 \mu\text{M}$ ) (Figure 3-5A,B). Consistent with *in vitro* PARP activity assays, ITK7 did not inhibit H<sub>2</sub>O<sub>2</sub>-activated PARP1 auto-PARylation (Figure 3-5C). We further found that, unlike our pan-HYΦ-PARP inhibitor ITK6, ITK7 did not inhibit PARP10 auto-MARylation in cells (Figure 3-5 D,E) further demonstrating the specificity of ITK7 for PARP11.



**Figure 3-5** ITK7 selectively inhibits PARP11 in cells.

- (A) ITK7 inhibits GFP-PARP11 auto-MARylation activity in a dose-dependent manner in HeLa cells. The signal for PARP11 auto-MARylation does not disappear completely, which is likely due to incomplete removal of MAR on PARP11.
- (B) Quantification of results shown in (A). Error bars represent  $\pm$  SEM from three replicates (Prism 7).
- (C) ITK7 does not inhibit H<sub>2</sub>O<sub>2</sub>-stimulated PARP1/2 activity in cells. HEK 293T cells were stimulated with H<sub>2</sub>O<sub>2</sub> (500  $\mu$ M) for 15 min in the presence of DMSO, ITK7 or veliparib. As expected, veliparib, a PARP1/2-selective inhibitor, completely inhibits H<sub>2</sub>O<sub>2</sub>-mediated PARP1 PARylation while ITK7 has no effect. Lysates were prepared and PAR/MARylation

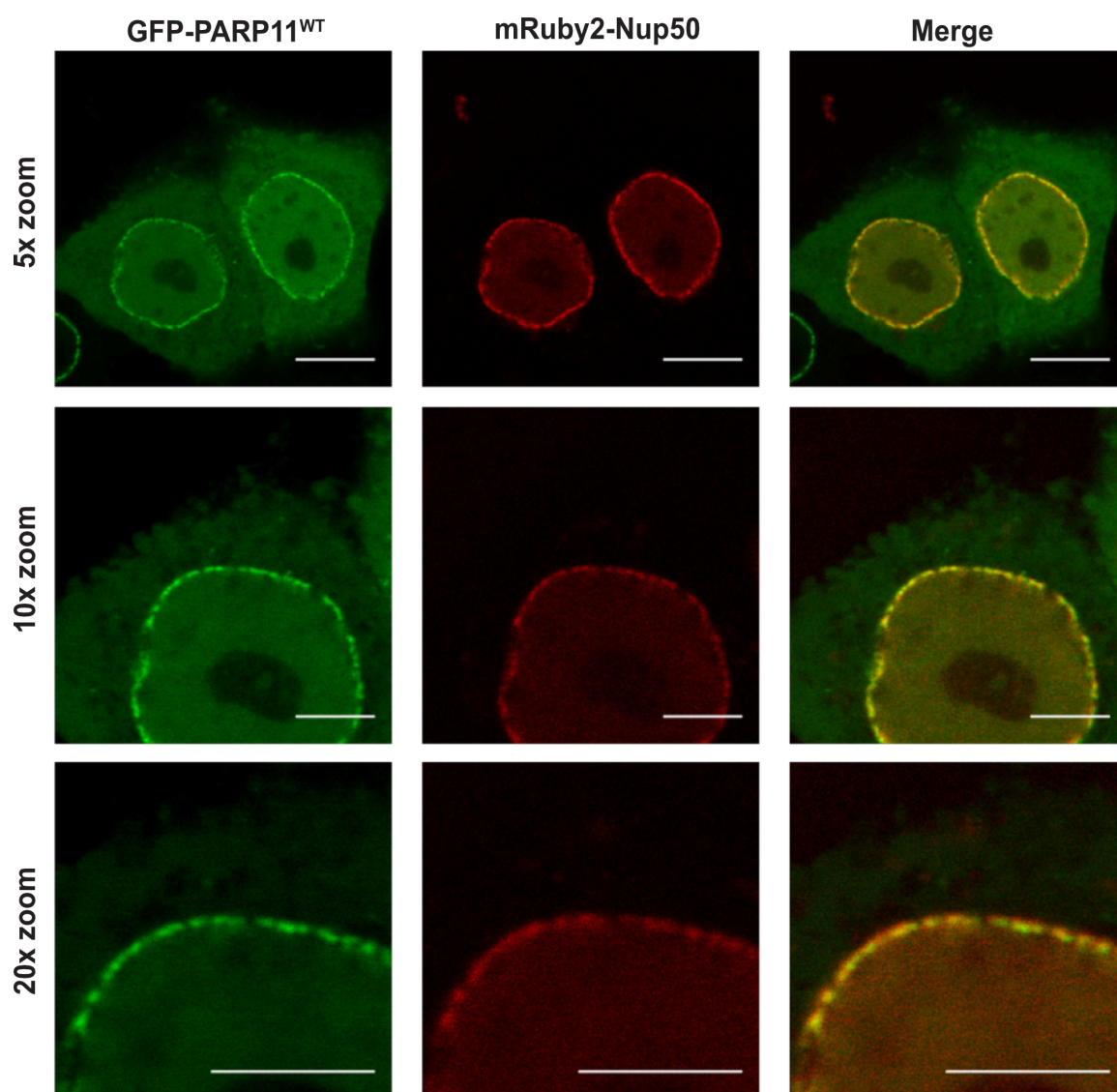


was analyzed by Western blot with an ADP-ribose (ADPr) binding reagent. Blot was also probed with antibodies for GFP and actin. The band of interest represents auto-PARylated GFP-PARP1.

(D) ITK6, a pan-HYΦ-PARP inhibitor, inhibits PARP10 auto-MARylation in cells in a dose dependent manner. HEK 293T cells were transfected with GFP-PARP10. Cells were then incubated with increasing concentrations of ITK6 for 90 min. Lysates were prepared and MARylation of PARP10 was analyzed by Western.

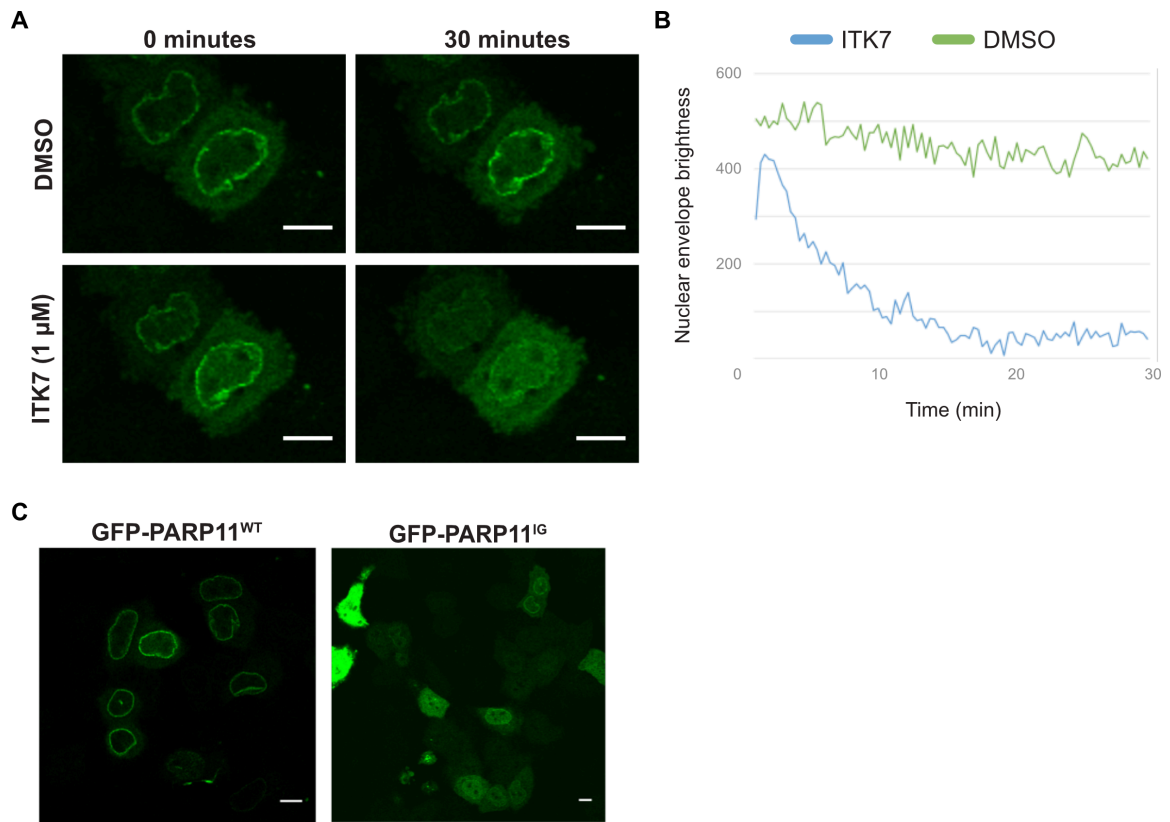
(E) ITK6 inhibits PARP10 auto-MARylation in cells whereas ITK7 does not inhibit PARP10. HEK 293T cells were transfected with GFP-PARP10. 24 h post-transfection cells were treated with either ITK6 (3 μM) or ITK7 (3 μM) for 3 h. Lysates were prepared and PAR/MARylation was analyzed by Western blot with an ADP-ribose (ADPr) binding reagent.

We and others have demonstrated that PARP11 localizes to the nuclear envelope (Carter-OConnell et al. 2016; Meyer-Ficca et al. 2015) and MARylates several nuclear pore complex (NPC) proteins in HEK 293T cells (Carter-OConnell et al. 2016). In this study, we confirmed that GFP-PARP11 localizes to the nuclear envelope and showed that it colocalizes with a mRuby2-tagged nuclear pore complex protein NUP50 in HeLa cells (Figure 3-6).



**Figure 3-6** GFP-PARP11 and mRuby2-Nup50 co-localize at the nuclear envelope  
 GFP-PARP11 and mRuby2-Nup50 were transfected in HeLa cells. Cells were grown in 8 well Lab-Tek with glass bottom. Images were taken sequentially to avoid any possible bleed through from GFP to the red channel. Images were acquired with 60x/NA 1.40 oil objective on Olympus FluoView 12000 microscope, with 5x, 10x or 20x zoom (Scale bar 10  $\mu$ m in 5x zoom, and 5 $\mu$ m in 10x and 20x zoom).

A previous study showed that PARP11 nuclear envelope localization requires the presence of the catalytic domain (Meyer-Ficca et al. 2015). Consistent with this result, we found that a GFP-tagged PARP11 mutant with severely compromised catalytic activity—I313G (IG) GFP-PARP11 (Carter-OConnell et al. 2016)—exhibited substantially reduced nuclear envelope localization compared to WT GFP-PARP11 (Figure 3-7A). Taken together, these results suggest that the catalytic activity of PARP11 is required for nuclear envelope localization. To further test this notion, we treated GFP-PARP11 transfected HeLa cells with ITK7 (1  $\mu$ M) and used live cell imaging to monitor GFP-PARP11 localization. We found that GFP-PARP11 dissociated within 30 minutes from the nuclear pore upon treatment with ITK7 (1  $\mu$ M), while treatment with DMSO had no effect (Figure 3-7B,C, Video 3-1, Video 3-2).

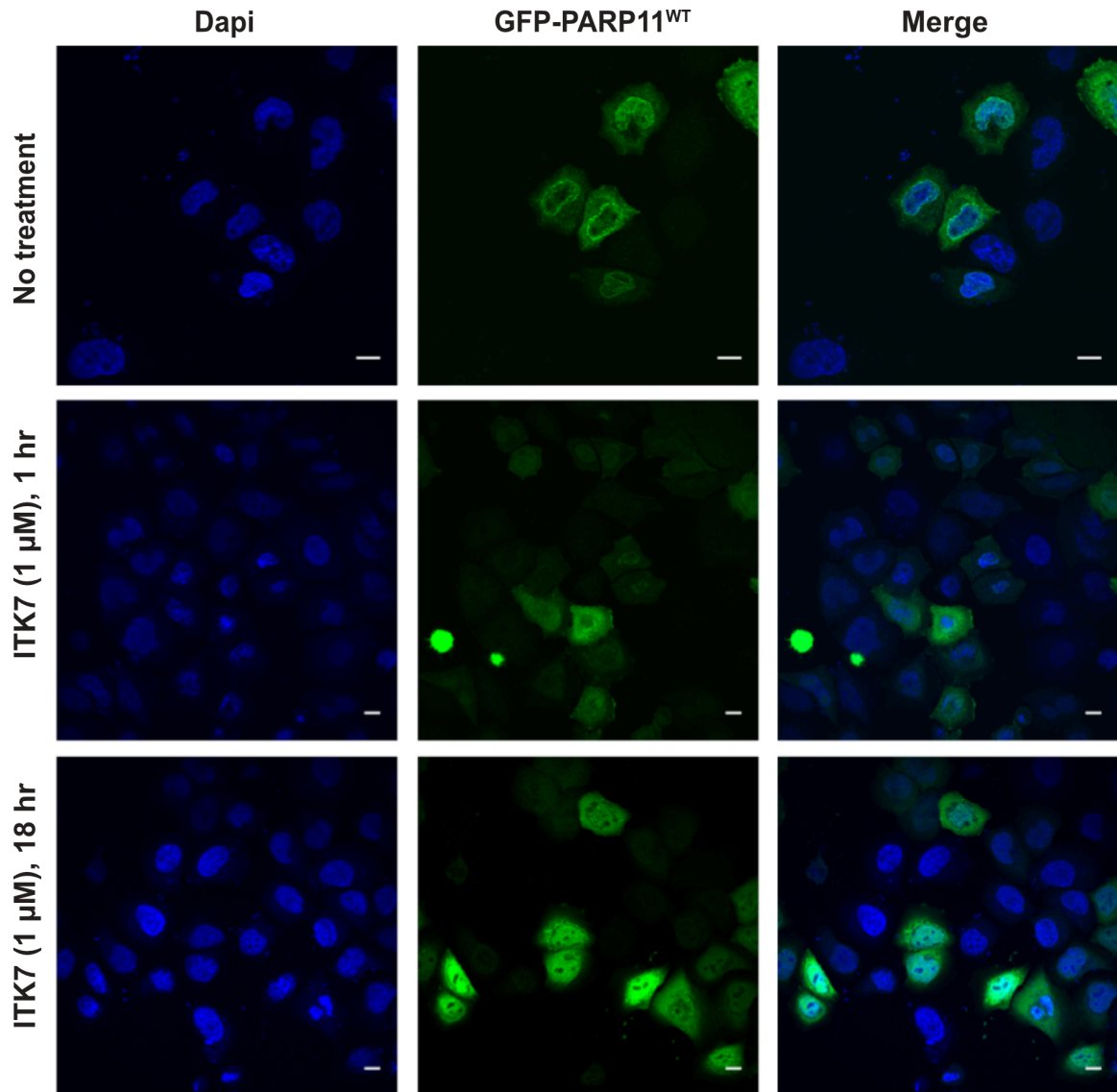


**Figure 3-7** PARP11 Catalytic activity is required for nuclear envelope localization

- (A) A catalytically compromised PARP11 mutant (I313G (IG) GFP-PARP11) does not localize to the nuclear envelope. HeLa cells were transfected with either wild-type or IG-GFP-PARP11 and imaged 20 hr post-transfection.
- (B) Treatment of HeLa cells with ITK7 caused PARP11 to dissociate from the nuclear envelope. HeLa cells transfected with GFP-PARP11 were treated with either ITK7 or DMSO, and images were acquired every 20 s. Scale bars, 10 μm.
- (C) Quantification of results shown in (B).

Upon longer term treatment (18 h), GFP-PARP11 could no longer be detected at the nuclear envelope and appeared to accumulate in the nucleus (Figure 3-8). These results strongly support the hypothesis that

the catalytic activity of PARP11 is required for localization to the nuclear envelope.



**Figure 3-8** ITK7 causes GFP-PARP11 to dissociate from the nuclear envelope  
HeLa cells were transfected with GFP-PARP11 grown on glass cover-slips. After ITK7 (1  $\mu$ M) treatment for 1 or 18 h cells were fixed and mounted using mounting medium containing DAPI. Images were taken on the Olympus Fluoview 2000 microscope using an 60x/NA 1.40 oil objective (scale bar 10  $\mu$ m).

## Discussion

Through structure-guided design we developed QDR-based inhibitors that selectively inhibit the HY $\Phi$ -PARP subfamily. Substitution of the C-7 position of the QDR scaffold is an effective strategy to improve potency against HY $\Phi$ -PARPs and decrease potency against the HYE-PARPs. Our structural studies reveal that inhibitor selectivity is due to the exploitation of a hydrophobic sub-pocket unique to the HY $\Phi$ -PARP family. Our most potent QDR analog, ITK7, exhibited selectivity for PARP11 over related HY $\Phi$ -PARPs but did not inhibit HYE-PARPs. Future studies will explore the hydrophobic sub-pocket in PARP11 and other HY $\Phi$ -PARPs to increase the potency and selectivity of our QDR analogs.

This study demonstrates that the selectivity within the HY $\Phi$ -PARP subfamily can be optimized by varying the substituent emanating from the C-2 position of the QDR scaffold. Indeed, we found that the pyrimidine at the C-2 position of ITK1 and ITK7 exhibited preference for PARP11 over other HY $\Phi$ -PARPs. This is presumably due to differences in the D-loop between HY $\Phi$ -PARPs as the amino acids in the active site that are oriented toward the C-2 substituent are not conserved across the HY $\Phi$ -PARP family. Indeed, two out of the three amino acids (Ala229 and Val230, human PARP11

numbering) that line the hydrophobic sub-pocket are not well conserved across the HYΦ-PARP family (Figure 3-3B). This lack of conservation within the D-loop will be exploited to improve selectivity for a given HYΦ-PARP family member in future studies.

We previously demonstrated that PARP11 is a nuclear envelope-localized PARP and modifies several NPC family members (Carter-OConnell et al. 2016). How PARP11 regulates NPC proteins is unclear. Our work reveals that ITK7 causes PARP11 to rapidly dissociate from the envelope within 30 min. Moreover, a catalytically compromised mutant does not localize to the nuclear envelope. This study links, for the first time, the catalytic activity of PARP11 to nuclear envelope localization. Future studies will focus on understanding how catalytic activity, and in particular auto-MARylation, regulates PARP11 nuclear envelope localization. Given that many PARPs exhibit distinct localization patterns in cells (Vyas et al. 2014) it will be interesting to determine if catalytic activity generally regulates PARP cellular localization. These studies will be greatly facilitated by selective and potent inhibitors of individual PARP family members.

# Methods

## Cloning

cDNA encoding full length human PARP1, full length human PARP2, human PARP10 catalytic domain, human PARP15 catalytic domain, GFP-PARP11<sup>WT</sup>, GFP-PARP11<sup>IG</sup>, NXF1, and SRPK2 were obtained as previously described (Carter-OConnell et al. 2014; Morgan & Cohen 2015; Meyer-Ficca et al. 2015). cDNA encoding full length human PARP11 and cDNA encoding the human PARP4 catalytic and BRCT domains (a1-572, PARP4<sub>brct-cat</sub>) were obtained using gBlock gene fragments containing the PARP11 gene as template (IDT) and the following primers (IDT) for subsequent Gibson assembly cloning:

PARP11:

- Forward: ATCGAGGAAAACCTGTACTTCCAATCCAA  
TTTTTCACAAAGCAGAAGAATTATTTTCT
- Reverse: CTCGAATTCGGATCCGTTATCCACTTC  
CAATTCAATGAAAGTCTATCAAGTACTCAGGAT

PARP4<sub>brct-cat</sub>

- Forward: TACTTCCAATCCAATGCAGTGATGGGAATCTTT  
GCAAATTG
- Reverse: TTATCCACTTCCAATGTTATTAGTCCTTTAT  
CTGATCTCCAGGCAT



The amplified fragments were gel purified and cloned into a pET-His-SUMO-TEV LIC cloning vector (1B), a gift from Scott Gradia (Addgene plasmid #29653) by an isothermal assembly protocol using the Gibson assembly mix (NEB). cDNA encoding the human PARP14 catalytic and WWE domains (aa1459-1801, PARP14<sub>cat-wwe</sub>) was cloned into the pNIC-Bsa4 vector using standard procedures. The human PARP3 plasmid was obtained from DNAsu.

#### **Expression and Purification of human PARP1-3, PARP10<sub>cat</sub>, PARP15<sub>cat</sub>, and SRPK2**

N-terminus hexahistidine (His6) human PARP1, PARP2, PARP5<sub>bcat</sub>, PARP10<sub>cat</sub>, PARP14<sub>wwe-cat</sub>, PARP15<sub>cat</sub>, and SRPK2 were expressed as previously described (Carter-OConnell et al. 2014; Morgan & Cohen 2015). Greater than or equal to 90% purity was achieved for human PARP1, PARP2, PARP10<sub>cat</sub>, and PARP15<sub>cat</sub>. PARP3<sub>FL</sub> Greater than or equal to 70% purity was achieved for SRPK2. Protein concentration and purity were determined by comparison to an in-gel standard curve of BSA (Bio-Rad).

## **Expression and Purification of human full length PARP11<sub>FL</sub> and PARP4<sub>brct-cat</sub>**

pET-His-SUMO-TEV-PARP11<sub>FL</sub> or -PARP4<sub>brct-cat</sub> plasmid was transformed into Escherichia coli BL21 (DE3) competent cells (Millipore) for His6-SUMO-PARP4/11 expression and grown on LB agar plates (with kanamycin and chloramphenicol) overnight at 37°C. A swath of cells was inoculated into a 10 mL starter culture of LB media (with 50 µg/mL kanamycin, 34 µg/mL chloramphenicol) at 225 rpm, 37°C overnight. One or more liters of terrific broth (TB) media (12 g bacto tryptone, 24 g yeast extract, 0.4% glycerol, 17 mM KH<sub>2</sub>PO<sub>4</sub>, 72 mM K<sub>2</sub>HPO<sub>4</sub>, 1% glucose, 50 µg/mL kanamycin, 34 µg/mL chloramphenicol) was inoculated with the starter culture and grown to an OD = 0.4-0.5 at 37°C, 225 rpm. Isopropyl-β-thiogalactoside, IPTG (Sigma-Aldrich) was added to 0.4 mM to induce protein expression for 2.5-3 hrs at 37°C, 225 rpm. Cells were harvested by centrifuging, resuspended in lysis buffer (20 mM HEPES, pH 7.5, 1 mM β-mercaptoethanol, 1 mM benzamidine, 0.2% NP-40, 0.2% TWEEN-20, 500 mM NaCl, 1 mM phenylmethylsulfonyl fluoride (PMSF), 8.3 mg/L DNase I (Roche)) and lysed by sonication at 0°C (Branson sonifier 450). The lysate containing the soluble protein was clarified by centrifugation (12,000g, 30 min at 4°C). PARP11 was purified in a single step using immobilized metal affinity chromatography (Ni-NTA resin,

Qiagen). >70% purity was achieved for PARP11 and >90% purity for PARP4.

### **Expression and Purification of human PARP7<sub>FL</sub>**

GST-PARP7<sub>FL</sub> was expressed in *Escherichia coli* BL21 (DE3) competent cells (Millipore). Cells were first cultured in LB media overnight at 225 rpm and 37°C in an Excella® E24 Incubator (New Brunswick Scientific). Two liters of TB media (12 g bacto tryptone, 24 g yeast extract, 0.4% glycerol, 17 mM KH<sub>2</sub>PO<sub>4</sub>, 72 mM K<sub>2</sub>HPO<sub>4</sub>, 1% glucose, 100 µg/mL ampicillin, µg/mL chloramphenicol) was inoculated with the starting culture and grown to OD<sub>600</sub> = 1.0 at 225 rpm and 37°C. The temperature was reduced to 16°C and expression was induced by adding isopropyl β-d-thiogalactoside (IPTG) to 0.4 mM. After incubation at 16°C for 24 h, cells were harvested by centrifugation, resuspended in lysis buffer (20 mM HEPES, pH 7.5, 1 mM β-mercaptoethanol, 1 mM benzamidine, 0.2% NP-40, 0.2% TWEEN-20, 500 mM NaCl, 1 mM phenylmethylsulfonyl fluoride (PMSF), 8.3 mg/L DNase I (Roche)) at 4°C, and lysed by sonication at 0°C, and the resulting lysate was clarified by centrifugation at 12,000 G for 30 min at 4°C. PARP7<sub>FL</sub> was purified in a single step using immobilized affinity chromatography (Glutathione Sepharose 4B, Fisher Scientific). Greater than or equal to 90% purity was achieved.

### **Expression and Purification of human PARP14<sub>cat-wwe</sub>**

N-terminus His6-PARP14<sub>cat-wwe</sub> was expressed in the Escherichia coli BL21 (DE3) competent cells (Millipore). Cells were first cultured in LB media overnight at 225 rpm and 37°C in an Excella® E24 Incubator (New Brunswick Scientific). Two liters of TB media (12 g bacto tryptone, 24 g yeast extract, 0.4% glycerol, 17 mM KH<sub>2</sub>PO<sub>4</sub>, 72 mM K<sub>2</sub>HPO<sub>4</sub>, 1% glucose, 50 µg/mL kanamycin, 34 µg/mL chloramphenicol) was inoculated with the starting culture and grown to OD<sub>600</sub> = 1.0 at 225 rpm and 37°C. The temperature was reduced to 16°C and expression was induced by adding isopropyl β-d-thiogalactoside (IPTG) to 0.4 mM. After incubation at 16°C for 24 h, cells were harvested by centrifugation, resuspended in lysis buffer (20 mM HEPES, pH 7.5, 1 mM β-mercaptoethanol, 1 mM benzamidine, 0.2% NP-40, 0.2% TWEEN-20, 500 mM NaCl, 1 mM phenylmethylsulfonyl fluoride (PMSF), 8.3 mg/L DNase I (Roche)) at 4°C, and lysed by sonication at 0°C, and the resulting lysate was clarified by centrifugation at 12,000 G for 30 min at 4°C. PARP14<sub>cat-wwe</sub> was purified in a single step using immobilized metal affinity chromatography (Ni-NTA resin, Qiagen). Greater than or equal to 90% purity was achieved.

### **Histone H1 Plate Assays**

52 nM PARP1 or 46 nM PARP2 in pB<sub>1-1-1</sub> (20 mM HEPES pH 7.5, 5 mM MgCl<sub>2</sub>, 5 mM CaCl<sub>2</sub>, 0.01% NP-40, 25 mM KCl, 0.5 mM TCEP, 0.1 mg/mL activated DNA (Sigma) were added to individual wells of an 96-well Histone H1 strip plate (Trevigen). Varying concentrations of each inhibitor (0-200  $\mu$ M) were pre-incubated with 200  $\mu$ M 6-a-NAD<sup>+</sup> in pB at RT for 5-10 min, then added to the histone plate. Final reaction concentrations: 26 nM PARP1, 23 nM PARP2, 0-100  $\mu$ M inhibitor, and 100  $\mu$ M 6-a-NAD<sup>+</sup>. This reaction proceeded for 30 min at 30°C, then the plate was washed three times with 1X PBS, three times with 1X PBST (1X PBS, 0.1% Triton X-100), once with 1X PBS, then click conjugation was performed in CB (100  $\mu$ M biotin-PEG3-azide, 100  $\mu$ M Tris[(1-benzyl-1H-1,2,3-triazol-4-yl)methyl]amine (TBTA, Sigma), 1 mM CuSO<sub>4</sub>, 1 mM TCEP, 1X PBS) for 30 min at RT. The plate was then washed three times with 1X PBS, three times with 1X PBST, once with 1X PBS, and then blocked with 1% milk (Carnation) in 1X PBST for 30 min at RT. The plate was then washed three times with 1X PBS, three times with 1X PBST, once with 1X PBS, and then incubated with Strep-HRP (300 ng/ $\mu$ L BSA, 0.05 ng/ $\mu$ L

Strep-HRP, 1X PBS) for 30 min at RT. The plate was then washed three times with 1X PBS, three times with 1X PBST, once with 1X PBS, and then developed with QuantaRed™ Enhanced Chemifluorescent HRP Substrate (Thermo) for 30-45 s before quenching with Quanta Red Stop Solution. Fluorescence for each sample and control was read at excitation 570 nM and emission 600 nM with a Spectra Max i3 (Molecular Devices) within five min of development. Inhibitor dose response curves were fit using linear regression in Prism 7 (GraphPad™ Software). The mean IC<sub>50</sub> for each compound was calculated from at least three independent assays.

### **SRPK2 Plate Assays**

96-well nickel coated plate (Pierce) was incubated with 350 ng His6-tagged SRPK2 in hB (50 mM HEPES pH 7.5, 100 mM NaCl, 4 mM MgCl<sub>2</sub>, 0.2 mM TCEP) for 60 min at RT. After extensively washing the plate, 2-600 ng (2x) of HYΦ-PARPs (PARP10, 11, 14, and 15) and HYE-PARPs (PARP3<sub>FL</sub> and PARP5<sub>bcat</sub>) in hB were added to individual wells of the 96-well plate. PARP3<sub>FL</sub> was activated by Dnick 5'P as described previously (Langelier et al. 2014). Varying concentrations of each inhibitor (0-200 μM) were pre-incubated with 200 μM 6-a-NAD<sup>+</sup> (2x) in hB at room

temperature for 5-10 min, then added to the plate. This reaction proceeded for 60 min at 30°C, the plate was then washed three times with 1X PBST (1X PBS, 0.01% Tween-20), once with 1X PBS, then click conjugation was performed in CB (100  $\mu$ M biotin-PEG3-azide, 100  $\mu$ M Tris[(1-benzyl-1H-1,2,3-triazol-4-yl)methyl]amine (TBTA, Sigma), 1 mM CuSO<sub>4</sub>, 1 mM TCEP, 1X PBS) for 30 min at RT. The plate was then washed three times with 1X PBST, once with 1X PBS, and then blocked with 1% milk (Carnation) in 1X PBST for 30 min at RT. The plate was then washed three times with 1X PBST, once with 1X PBS, and then incubated with Strep-HRP (300 ng/ $\mu$ L BSA, 0.05 ng/ $\mu$ L Strep-HRP, 1X PBS) for 30 min at RT. The plate was then washed three times with 1X PBST, once with 1X PBS, and then developed with QuantaRed™ Enhanced Chemifluorescent HRP Substrate (Thermo) for 30-45 s before quenching with Quanta Red Stop Solution. Fluorescence for each sample and control was read at excitation 570 nM and emission 600 nM with a Spectra Max i3 (Molecular Devices) within five min of development. Inhibitor dose response curves were fit using linear regression in Prism 7 (GraphPad™ Software). The mean IC<sub>50</sub> for each compound was calculated from at least three independent assays.

### **NXF1 Plate Assay**

96-well nickel coated plate (Pierce) was incubated with 350 ng His6 tagged NXF1 in hB (50 mM HEPES pH 7.5, 100 mM NaCl, 4 mM MgCl<sub>2</sub>, 0.2 mM TCEP) for 60 min at RT. The rest of this assay was carried out according to the above procedure for SRPK2 plate assays for HYΦ-PARPs.

### **Auto-modification Plate Assay for PARP4<sub>brct-cat</sub>**

96-well nickel coated plate (Pierce) was incubated with 500 ng His6-SUMO tagged PARP4<sub>brct-cat</sub> in hB (50 mM HEPES pH 7.5, 100 mM NaCl, 4 mM MgCl<sub>2</sub>, 0.2 mM TCEP) for 60 min at RT. After extensively washing the plate, 660 ng of PARP4CB in hB was added to individual wells of the 96-well plate. Varying concentrations of each inhibitor (0-200 μM) were pre-incubated with 200 μM 6-a-NAD<sup>+</sup> in hB at room temperature for 5-10 min, then added to the plate. The rest of this assay is carried according to the above procedure for SRPK2 Plate Assays for HYΦ-PARPs.

### **Auto-modification Plate Assay for PARP7<sub>FL</sub>**

96-well glutathione coated plate (Pierce) was incubated with 250 ng GST tagged PARP7<sub>FL</sub> in hB (50 mM HEPES pH 7.5, 100 mM NaCl, 4 mM MgCl<sub>2</sub>, 0.2 mM TCEP) for 60 min at RT. After extensively washing the plate, 100 ng of PARP7<sub>FL</sub> in hB was added to individual wells of the



96-well plate. Varying concentrations of each inhibitor (0-200  $\mu$ M) were pre-incubated with 200  $\mu$ M 6-a-NAD<sup>+</sup> in hB at room temperature for 5-10 min, then added to the plate. The rest of this assay is carried according to the above procedure for SRPK2 Plate Assays for HY $\Phi$ -PARPs.

### **Native NAD<sup>+</sup> Plate Assay**

96-well nickel coated plate (Pierce) was incubated with 350 ng His6-tagged SRPK2 in hB (50 mM HEPES pH 7.5, 100 mM NaCl, 4 mM MgCl<sub>2</sub>, 0.2 mM TCEP) for 60 min at RT. After extensively washing the plate, 2-660 ng (2x) of HY $\Phi$ -PARPs (PARP10, 11, 14, and 15) and HYE-PARPs (PARP3<sub>FL</sub> and PARP5<sub>bcat</sub>) in hB  $\rightarrow$  were added to individual wells of the 96-well plate. PARP3<sub>FL</sub> was activated by Dnick 5'P as described previously ((Langelier et al. 2014). Varying concentrations of each inhibitor (0-200  $\mu$ M) were pre-incubated with 200  $\mu$ M NAD<sup>+</sup> (2x) in hB at room temperature for 5-10 min, then added to the plate. This reaction proceeded for 60 min at 30°C, the plate was then washed three times with 1X PBST (1X PBS, 0.01% Tween-20), then blocked with 1% milk (Carnation) in 1X PBST for 30 min at RT. The plate was then washed three times with 1X PBST, once with 1X PBS, and then incubated with a pan-ADP-ribose binding reagent (MABE1016, Millipore) (Gibson et al. 2017) for 30 h at RT The plate was then washed

three times with 1X PBST, once with 1X PBS, and then incubated with HRP-conjugated secondary antibodies. The plate was then washed three times with 1X PBST, once with 1X PBS, and then developed with QuantaRed™ Enhanced Chemifluorescent HRP Substrate (Thermo) for 30-45 s before quenching with Quanta Red Stop Solution. Fluorescence for each sample and control was read at excitation 570 nM and emission 600 nM with a Spectra Max i3 (Molecular Devices) within five min of development. Inhibitor dose response curves were fit using linear regression in Prism 7 (GraphPad™ Software).

#### **PARP immunoprecipitation auto-MARylation activity assay**

PARP immunoprecipitation auto-MARylation activity assays were performed as previously described (J. Y. Huang et al. 2016), with some modifications. HEK 293T cells were transfected with GFP-tagged PARP6, PARP7, PARP8, PARP12 and PARP16 expression plasmids (generated in house) containing an N-terminus GFP epitope. HEK 293T cells plated on 6-well plates (Greiner Bio-One) were transfected with 3.5 µg plasmid per well using CalPhos mammalian transfection kit (Clontech). Cells were collected 24 h post-transfection and lysed in 250 µL per well with cytosolic lysis buffer (CLB: 50mM HEPES (pH 7.4), 150 mM NaCl, 1 mM MgCl<sub>2</sub>, 1 mM TCEP, 1% Triton X-100; complemented with complete protease inhibitors (Roche), phosphatase inhibitor

cocktails 2 and 3 (Sigma), and 1  $\mu$ M veliparib, a PARP1/2-selective inhibitor). Lysates were centrifuged at 10,000 rpm for 10 min at 4°C and supernatants were transferred to new sample tubes. 40  $\mu$ L of suspended GFP-Trap magnetic bead slurry (Chromotek) were added to 1 mg protein lysates for 1 h at 4°C with constant rotation to immunoprecipitate GFP-PARPs. Following removal of supernatant, beads were washed three times with CLB, and once with PARP reaction buffer (PRB: 50 mM Tris-HCl (pH 7.5), 50 mM NaCl, 0.5 mM TCEP, 0.1% Triton X-100; complemented with complete TM protease inhibitors phosphatase inhibitor cocktails 2 and 3, and 1  $\mu$ M veliparib), for 5 min per wash, and splitting the samples into two during the last PRB wash. For the ADPr labeling, 100  $\mu$ M 6-alkyne-nicotinamide adenine dinucleotide (6-a-NAD<sup>+</sup>) ((Carter-OConnell et al. 2014)) in 50  $\mu$ L PRB was added to beads and incubated for 1.5 h at 25°C/650 rpm (400  $\mu$ M of 6-a-NAD<sup>+</sup> for GFP-PARP16), in the presence or absence of 30  $\mu$ M ITK7 inhibitor. Following removal of 6-a-NAD<sup>+</sup>, beads were washed twice with PRB and once with PBS for 5 min per wash. Click reaction mixture (1 mM CuSO<sub>4</sub>, 1 mM TCEP, 100  $\mu$ M TBTA, 100  $\mu$ M biotin-azide; 25  $\mu$ L volume) was added to beads and incubated for 1 h at 25°C/650 rpm. Following removal of click reaction mixture, 40  $\mu$ L of 1.5X Laemmli sample buffer with 5%  $\beta$ -mercaptoethanol was added

to beads. Samples were heated at 95°C for 5 min and supernatants were resolved by SDS-PAGE and transferred onto 0.45 µm nitrocellulose membranes (GE healthcare bio-sciences). Membrane blots were blocked with 5% milk-TBST for 1 h at room temperature. Blots were probed for PARP6 expression with anti-GFP primary antibody (chicken polyclonal, Abcam clone ab13970, 1:5000) for 2 h at room temperature and HRP-conjugated goat anti-chicken IgG secondary antibody for 1 h at room temperature. To detect PARP6 auto-MARylation activity, blots were probed for biotinylated proteins with HRP-conjugated streptavidin antibody (Jackson ImmunoResearch, 0.4 µg/mL) for 60 min at room temperature. ECL HRP substrate (SuperSignal<sup>TM</sup> West Pico, ThermoFisher) was added to detect protein targets by chemiluminescence. Blots were imaged for chemiluminescent signal on a ChemiDoc MP system (Bio-Rad).

### **GFP-PARP10 MARylation in cells**

HEK 293T cells were transfected with GFP-PARP10 using the calcium phosphate method (Clontech). 24 h post transfection, cells were treated with increasing concentrations of ITK6 (90 min) in serum-free media at 37°C. Cells were washed with PBS, and lysed (CLB: 50 mM HEPES (pH 7.4), 150 mM NaCl, 1 mM MgCl<sub>2</sub>, 1 mM TCEP, 1% Triton X-100) with protease inhibitors (Roche). Lysates were centrifuged at 14,000

rpm for 10 min at 4°C and supernatants were transferred to a new tube with 2x Laemmli sample buffer with 5%  $\beta$ -mercaptoethanol. Samples were resolved by SDS-PAGE and transferred onto nitrocellulose membranes. Membrane blots were blocked with 5% milk-TBST for 60 min at RT, followed by incubation with a pan-ADP-ribose binding reagent (MABE1016, Millipore) or a chicken GFP antibody (ab13970, Abcam) for 60 min at RT, followed by incubation with HRP-conjugated secondary antibodies. Proteins were detected by chemiluminescence and imaged on a ChemiDoc MP system (Bio-Rad).

#### **H<sub>2</sub>O<sub>2</sub>-stimulated HYE-PARP activation**

HEK 293T cells were pre-treated with the indicated concentrations of ITK7 or veliparib for 15 min at 37°C, followed by incubation with H<sub>2</sub>O<sub>2</sub> (500  $\mu$ M) for an additional 15 min. Cells were washed with PBS, lysed in CLB (50 mM HEPES (pH 7.4), 150 mM NaCl, 1 mM MgCl<sub>2</sub>, 1 mM TCEP, 1% Triton X-100), and prepared for Western blot analysis as described above.

#### **GFP-PARP11 auto-MARylation in cells**

HeLa cells were transfected with 3  $\mu$ g of WT GFP-PARP11 using Lipofectamine 3000 (Thermo Fisher). 24 h post transfection, cells were treated with increasing concentrations of ITK7 in serum-free media at 37°C for 3 h. Cells were lysed in cytosolic lysis buffer (CLB: 50 mM

HEPES (pH 7.4), 150 mM NaCl, 1 mM MgCl<sub>2</sub>, 1% Triton X-100) in the presence of protease inhibitors (Roche), phosphatase inhibitor cocktails 2 and 3 (Sigma), 3  $\mu$ M veliparib, 1.2 mM phenylmethylsulfonyl fluoride (Thermo Fisher), and 1mM Tris(2-carboxyethyl)phosphine hydrochloride (Thermo Scientific). Lysates were centrifuged at 10,000 rpm for 10 min at 4°C and supernatants were transferred to a new tube. Protein concentrations were determined via the Bradford Assay (Bio-Rad). Each sample was added to 4X Laemmli sample buffer with 5%  $\beta$ -mercaptoethanol and brought to a final volume of 20  $\mu$ L. Samples were heated at 95°C for 5 min and supernatants were resolved by SDS-PAGE before being transferred onto nitrocellulose membranes (Bio-Rad). Membrane blots were blocked with 5% milk-TBST for 1 h at RT, followed by probing with a pan-ADP-ribose antibody (Cell Signaling mAb 83732, 1:1000), GFP primary antibody (ChromoTek, PABG1, 1:1000), or  $\beta$ -actin primary antibody (Santa Cruz Biotechnology 47778, 1:1000) for 2 h at RT. Blots were then incubated with HRP-conjugated secondary antibodies for 1 h at RT. Blots were exposed to ECL HRP substrate (SuperSignal<sup>TM</sup> West Pico PLUS, ThermoFisher) to detect protein targets by chemiluminescence and imaged on a ChemiDoc MP system (Bio-Rad).

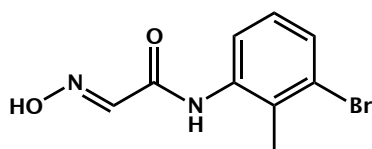
### **Imaging experiments in HeLa cells**

All images were acquired on an Olympus FV1200 microscope with a PLAPON 60x/1.4NA oil objective. Live cell imaging was performed in DMEM on 37C with 5% CO<sub>2</sub>. Cells were grown in NUNC glass bottom 8-well Lab-Tek dishes (Fisher). 25,000 cells were seeded per well, transfected using Lipofectamine2000 (Invitrogen) and imaged the next day. An image was acquired every 20 s in the GFP channel, and cells were treated with DMSO or ITK7 directly in the Lab-Tek after the acquisition of the 1st frame. For fixed samples, cells were seeded on glass coverslips (Fisher) and transfected using Lipofectamine2000 (Invitrogen). After treatments with ITK7 cells were fixed with 5% PFA for 5 min. The fixation was stopped by washing the cells with 30 mM glycine (Fisher). After PBS wash coverslips were mounted on slides with ProLong Diamond Antifade Mountant with DAPI (Invitrogen).

### **Chemistry**

**General:** <sup>1</sup>H NMR spectra were recorded on a Bruker DPX spectrometer at 400 MHz. Chemical shifts are reported as parts per million (ppm) downfield from an internal tetramethylsilane standard or solvent references. For air- and water-sensitive reactions, glassware was flame- or oven-dried prior to use and reactions were performed under argon. Dimethylformamide was dried using the solvent

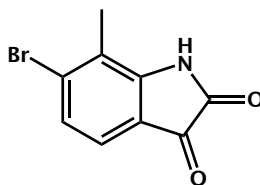
purification system manufactured by Glass Contour, Inc. (Laguna Beach, CA). All other solvents were of ACS chemical grade (Fisher Scientific) and used without further purification unless otherwise indicated. Commercially available starting reagents were used without further purification. Analytical thin-layer chromatography was performed with silica gel 60 F254 glass plates (SiliCycle). Flash column chromatography was conducted self-packed columns containing 200-400 mesh silica gel (SiliCycle) on a Combiflash Companion purification system (Teledyne ISCO). High performance liquid chromatography (HPLC) was performed on a Varian Prostar 210 (Agilent) using Polaris 5 C18-A columns (Analytical: 150 x 4.6 mm, 3  $\mu$ m; Preparative: 150 x 21.2 mm, 5  $\mu$ m) (Agilent). All final products in the main text were  $\geq 95\%$  pure as assessed by analytical HPLC (mobile phase A: 0.1% formic acid (aq), mobile phase B: 0.1% formic acid in acetonitrile; flow rate = 1.0 mL/min; conditions: pre-run A = 70 % B = 30%, 10 min A = 5% B = 95%, 12 min A = 5% B = 95%, 13 min A = 70% B = 30%; UV-Vis detection:  $\lambda_1$  = 254 nm,  $\lambda_2$  = 220 nm. Retention times (Rt) refer to UV = 254 nm. Novel compounds indicated, for literature reports of synthesized compounds see Appendix F.



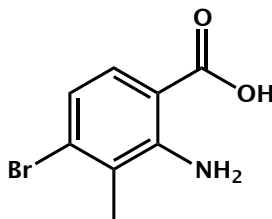


*2-Hydroxyimino-N-(2-methyl-3-bromo-phenyl)-acetamide:*

Trichloroacetylaldehyde hydrate (976 mg, 5.92 mmol) and anhydrous sodium sulfate (4.5 mg, 32 mmol) were dissolved in water (15 mL), and a suspension of 3-bromo-2-methylaniline (0.67 mL, 5.38 mmol) and hydroxylamine sulfate (4.4 g, 27 mmol) in 1 N HCl (6 mL) was added. The resultant suspension of white solids in clear solution was stirred at 35°C for 1 h, then 52°C for 1.5 h, and finally 75°C for 1 h. The reaction mixture was cooled to RT and the product isolated as pale tan solids by vacuum filtration: 1.61 g (117% crude); <sup>1</sup>H NMR (400 MHz, Chloroform-d)  $\delta$  8.23 (s, 1H), 7.88 (d, J = 8.1 Hz, 1H), 7.83 (s, 1H), 7.61 (s, 1H), 7.41 (d, J = 8.0 Hz, 1H), 7.10 (t, J = 8.1 Hz, 1H), 2.39 (s, 3H).

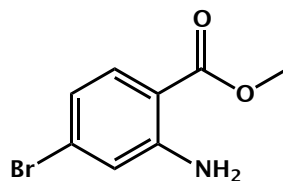


*6-Bromo-7-methylindoline-2,3-dione:* 2-hydroxyimino-N-(2-methyl-3-bromo-phenyl)-acetamide (1.61 g, 6.24 mmol) was added in small portions to 60°C sulfuric acid and stirred at 80°C for 1 h. The reaction mixture was cooled to RT and the product isolated as bright orange solids by vacuum filtration: 649 mg (50% crude); <sup>1</sup>H NMR (400 MHz, DMSO-d<sub>6</sub>)  $\delta$  11.28 (s, 1H), 7.34 (d, J = 8.0 Hz, 1H), 7.28 (d, J = 8.0 Hz, 1H), 2.24 (s, 3H).

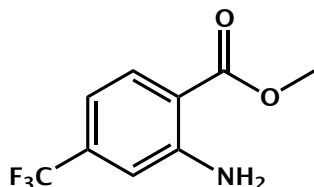


*2-Amino-4-bromo-3-methylbenzoic acid*: 6-bromo-7-methylindoline-2,3-dione (649 mg, 2.70 mmol) dissolved in 1.3 N NaOH (135 mL) was combined with 30% H<sub>2</sub>O<sub>2</sub> (7.0 mL) and water (70 mL) and stirred RT for 1 h. The reaction mixture was acidulated with 1 N HCl and the product precipitated as a white solid: 620 mg (99% crude, 45% over three steps); <sup>1</sup>H NMR (400 MHz, DMSO-d<sub>6</sub>) δ 7.52 (d, J = 8.6 Hz, 1H), 6.78 (d, J = 8.7 Hz, 1H), 2.22 (s, 2H).

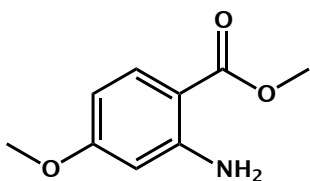
**General procedure for synthesis of benzoates:** To a solution of the appropriate benzoic acid in methanol was added concentrated sulfuric acid (1% v/v) at RT. The reaction mixture was refluxed at 90°C for 18 h, monitored by TLC analysis (20% EtOAc in hexanes). Once complete the reaction mixture was poured over saturated aqueous sodium bicarbonate and separated with EtOAc. The aqueous layer was extracted with EtOAc (3x). The combined organic layers were washed with sat. aqueous sodium bicarbonate (1x), water (1x), and brine (1x), then dried over sodium sulfate and concentrated in vacuo to yield desired benzoate.



*Methyl 2-amino-4-bromobenzoate*: from 2-amino-4-bromobenzoic acid (100 mg, 0.46 mmol); yield 80 mg (76%) white solids;  $^1\text{H}$  NMR (400 MHz, Chloroform- $d$ )  $\delta$  7.70 (d,  $J$  = 8.6 Hz, 1H), 7.26 (d,  $J$  = 2.6 Hz, 1H), 6.84 (d,  $J$  = 1.9 Hz, 1H), 6.76 (dd,  $J$  = 8.6, 1.9 Hz, 1H), 5.78 (s, 1H), 3.86 (s, 2H).

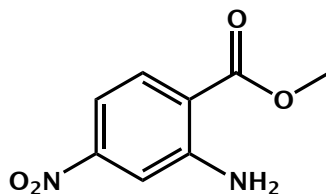


*Methyl 2-amino-4-(trifluoromethyl)benzoate*: from 2-amino-4-(trifluoromethyl)benzoic acid (50 mg, 0.24 mmol) white solids; yield 50 mg (95%);  $^1\text{H}$  NMR (400 MHz, Chloroform- $d$ )  $\delta$  8.02 – 7.92 (m, 1H), 6.93 – 6.76 (m, 2H), 5.91 (s, 2H), 3.90 (s, 3H).

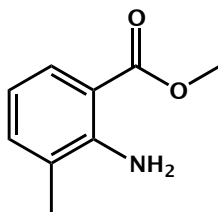


*Methyl 2-amino-4-methoxybenzoate*: from 2-amino-4-methoxybenzoic acid (250 mg, 1.5 mmol); yield 207 mg (76%) cream solids;  $^1\text{H}$  NMR

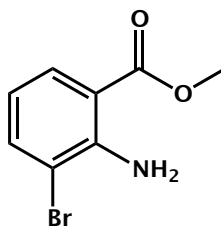
(400 MHz, Chloroform-d)  $\delta$  7.78 (d,  $J$  = 8.9 Hz, 1H), 6.23 (dd,  $J$  = 9.0, 2.5 Hz, 1H), 6.10 (d,  $J$  = 2.4 Hz, 1H), 5.80 (s, 2H), 3.81 (d,  $J$  = 20.8 Hz, 6H).



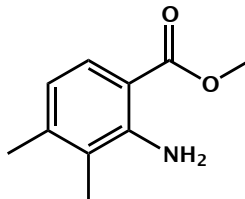
*Methyl 2-amino-4-nitrobenzoate*: from 2-amino-4-nitrobenzoate (500 mg, 2.74 mmol); yield: 94.7 mg (18%) tan solids;  $^1\text{H}$  NMR (400 MHz, DMSO-d<sub>6</sub>)  $\delta$  7.89 (d,  $J$  = 8.5 Hz, 1H), 7.39 (d,  $J$  = 2.4 Hz, 1H), 7.14 (dd,  $J$  = 8.5, 2.5 Hz, 1H), 1.61 (s, 3H).



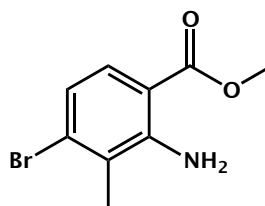
*Methyl 2-amino-3-methylbenzoate*: from 2-amino-3-methylbenzoic acid (500 mg, 3.3 mmol); yield 348 mg (64%) white solids;  $^1\text{H}$  NMR (400 MHz, Chloroform-d)  $\delta$  7.77 (ddd,  $J$  = 8.1, 1.6, 0.6 Hz, 1H), 7.19 (ddq,  $J$  = 7.2, 1.7, 0.8 Hz, 1H), 6.59 (dd,  $J$  = 8.1, 7.2 Hz, 1H), 5.83 (s, 2H), 3.87 (s, 3H), 2.17 (d,  $J$  = 0.7 Hz, 3H).



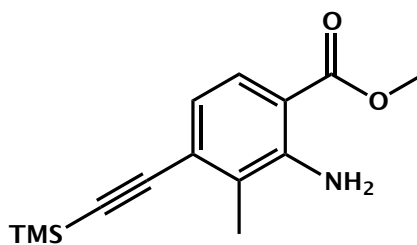
*Methyl 2-amino-3-bromobenzoate*: from 2-amino-3-bromobenzoic acid (1.0 g, 4.7 mmol); yield 680 mg (68%) white solids; Taken on crude.



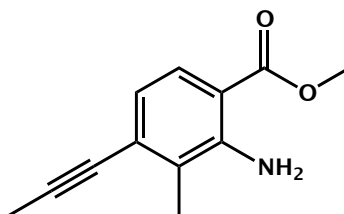
*Methyl 2-amino-3,4-dimethylbenzoate*: from 2-amino-3,4-dimethylbenzoic acid (500 mg, 3.0 mmol) white solids; yield 400 mg (75%); <sup>1</sup>H NMR (400 MHz, Chloroform-d)  $\delta$  7.67 (d,  $J$  = 8.2 Hz, 1H), 6.52 (d,  $J$  = 8.3 Hz, 1H), 5.86 (s, 2H), 3.86 (s, 3H), 2.29 (s, 3H), 2.07 (s, 3H).



*Methyl 2-amino-4-bromo-3-methylbenzoate*: from 2-amino-4-bromo-3-methylbenzoic acid (620 mg, 2.69 mmol) tan solids; yield 454 mg (69%); <sup>1</sup>H NMR (400 MHz, DMSO-*d*<sub>6</sub>)  $\delta$  7.53 (d,  $J$  = 8.7 Hz, 1H), 6.85 (s, 2H), 6.81 (d,  $J$  = 8.7 Hz, 1H), 3.79 (s, 3H), 2.23 (s, 3H).

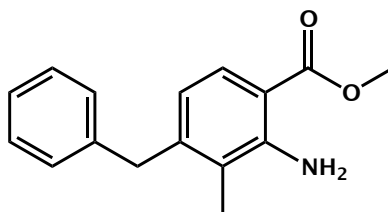


*Methyl 2-amino-3-methyl-4-((trimethylsilyl)ethynyl)benzoate (novel compound)*: TMS-acetylene (0.85 mL, 6.15 mmol) and CuI (78 mg, 0.41 mmol) were dissolved in anhydrous DMF (2 mL) in an oven dried bomb flask (15 mL capacity) and stirred under argon at RT for 30 min; solution went from clear to orange. Pd(PPh<sub>3</sub>)<sub>2</sub>Cl<sub>2</sub> (144 mg, 0.205 mmol), TEA (0.36 mL, 4.10 mmol), and Methyl 2-amino-4-bromo-3-methylbenzoate (500 mg, 2.05 mmol), and additional anhydrous DMF (10 mL) were quickly added and the flask sealed under argon. The reaction proceeded at 110°C for 18 h, solution turned black over several h. The flask was cooled to RT and the reaction mixture was diluted in EtOAc (20 mL) and filtered through celite. Organics were washed with water (100 mL, 3x), and brine (100 mL, 3x). The reaction was concentrated in vacuo and the residue purified on a Combiflash Companion system (4 g Redisep silica column; 0-10% EtOAc in hexanes). A mixture of the product (70%) and starting material (30%) was obtained as a yellow oil and taken on as a mixture: 328 mg (86%). <sup>1</sup>H NMR (400 MHz, DMSO-d<sub>6</sub>) δ 7.53 (d, J = 8.6 Hz, 1H), 6.85 (s, 2H), 6.81 (dd, J = 8.7, 1.5 Hz, 1H), 3.79 (d, J = 1.5 Hz, 3H), 2.23 (d, J = 1.4 Hz, 3H).



*Methyl 2-amino-3-methyl-4-(prop-1-yn-1-yl)benzoate (novel compound):*

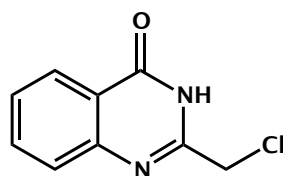
methyl 2-amino-3-methyl-4-bromobenzoate (200 mg, 0.99 mmol) was dissolved in anhydrous toluene and concentrated (3x 4 mL) then dried under vacuum for 1 h. The flask was evacuated and refilled with argon gas (3x), then anhydrous toluene (8 mL) was added via syringe and the solution degassed with argon 10 min. Tributyl(1-propynyl)tin (0.36 mL, 1.20 mmol) was added via syringe and the solution degassed 5 min. Palladium tetrakis (124 mg, 0.11 mmol) was added quickly and the solution degassed with argon for 3 min. The reaction mixture was refluxed at 115°C for 2.5 h. TLC analysis (10% EtOAc in hexanes) showed consumption of starting benzoate. The reaction was cooled to RT and concentrated in vacuo. The crude residue was purified via a Combiflash Companion system (4 g Redisep silica column; 0-20% EtOAc in hexanes). Product was isolated as white solids: 130 mg (80%); <sup>1</sup>H NMR (400 MHz, Chloroform-d) δ 7.68 (d, J = 8.3 Hz, 1H), 6.71 (d, J = 8.4 Hz, 1H), 5.88 (s, 2H), 3.86 (s, 3H), 2.28 (s, 3H), 2.11 (s, 3H).



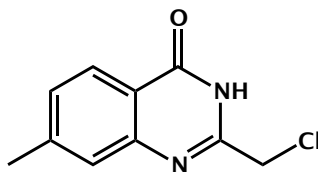
*Methyl 2-amino-4-benzyl-3-methylbenzoate (novel compound):* methyl 2-amino-3-methyl-4-bromobenzoate (100 mg, 0.41 mmol), potassium benzyltrifluoroborate (0.82, 162 mg), 2-Dicyclohexylphosphino-2',6'-diisopropoxy-1,1'-biphenyl (38 mg, 0.082 mmol), cesium bicarbonate (400 mg, 1.23 mmol), and 47.5% palladium(III) acetate (9 mg, 0.041 mmol) were added to a flame dried RBF, dried under vacuum for 30 minutes, and evacuated then refilled with argon gas (3x). A mixture of toluene and water (3:1) was degassed with argon for 15 minutes then added via syringe to the flask. The reaction was refluxed under argon at 110°C for 2 hrs. TLC analysis (10% EtOAc in hexanes) showed consumption of starting benzoate. The reaction was cooled to RT and concentrated in vacuo. The crude residue was purified on a Combiflash Companion system (4 g Redisep silica column; 0-30% EtOAc in hexanes). Product was isolated as a pale yellow solid: 53 mg (51%); <sup>1</sup>H NMR (400 MHz, Chloroform-d) δ 7.73 (d, J = 8.2 Hz, 1H), 7.28 – 7.24 (m, 2H), 7.19 (d, J = 7.3 Hz, 1H), 7.13 – 7.06 (m, 2H), 6.53 (d, J = 8.3 Hz, 1H), 5.89 (s, 2H), 4.01 (s, 2H), 3.86 (s, 3H), 2.17 (s, 3H).



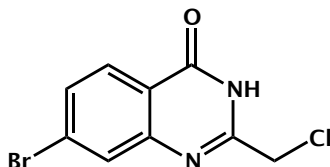
**General procedure for synthesis of quinazolin-4(3H)-ones:** The appropriate benzoate was added to a flame-dried flask and dissolved in 4 M HCl (1,4-dioxane) under argon. To this solution was added chloroacetonitrile (3 eqv.), and the reaction mixture was refluxed under argon at 125°C overnight. Once TLC analysis revealed consumption of the starting benzoate the reaction was cooled to RT and poured over cold sat. Aqueous sodium bicarbonate and left to stand at 4°C. The desired quinazolin-4(3H)-one readily precipitated and was collected by vacuum filtration.



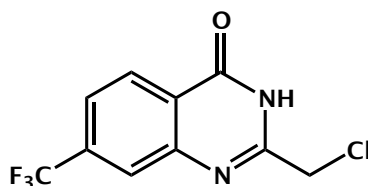
*2-(Chloromethyl)quinazolin-4(3H)-one:* from methyl 2-aminobenzoate (0.86 mL, 6.62 mmol); yield 1.35 g (100%) tan solids; <sup>1</sup>H NMR (400 MHz, DMSO-d<sub>6</sub>) δ 12.60 (s, 1H), 8.13 (dd, J = 7.9, 1.5 Hz, 1H), 7.84 (ddd, J = 8.6, 7.1, 1.6 Hz, 1H), 7.68 (d, J = 8.0 Hz, 1H), 7.60 – 7.51 (m, 1H), 4.55 (s, 2H).



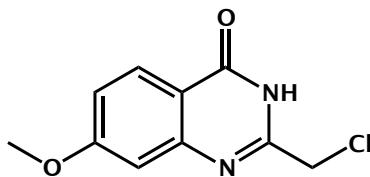
*2-(Chloromethyl)-7-methlyquinaxolin-4(3H)-one*: from methyl 2-amino-4-methlybenzoate (160 mg, 0.97 mmol); yield 125 mg (62%) tan solids; <sup>1</sup>H NMR (400 MHz, Chloroform-d)  $\delta$  9.44 (s, 1H), 8.17 (d, J = 8.1 Hz, 1H), 7.48 (s, 1H), 7.35 (d, J = 8.0 Hz, 1H), 4.57 (s, 2H), 2.52 (s, 3H).



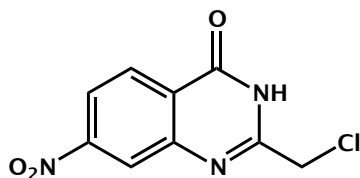
*7-Bromo-2-(chloromethyl)quinazolin-4(3H)-one*: from methyl 2-amino-4-bromobenzoate (40 mg, 0.15 mmol); yield 31 mg (76%) brown solids; <sup>1</sup>H NMR (400 MHz, DMSO-d<sub>6</sub>)  $\delta$  12.75 (s, 1H), 8.02 (d, J = 8.4 Hz, 1H), 7.90 (d, J = 1.9 Hz, 1H), 7.71 (dd, J = 8.4, 2.0 Hz, 1H), 4.54 (s, 2H).



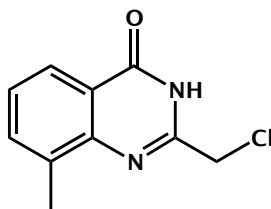
*2-(Chloromethyl)-7-(trifluoromethyl)quinazolin-4(3H)-one*: from methyl 2-amino-4-trifluorobenzoate (50 mg, 0.22 mmol); yield 60 mg (103%) tan solids; <sup>1</sup>H NMR (400 MHz, Chloroform-d)  $\delta$  10.35 (s, 1H), 8.43 (dt, J = 8.4, 0.8 Hz, 1H), 8.00 (dd, J = 1.7, 0.9 Hz, 1H), 7.75 (dd, J = 8.3, 1.7 Hz, 1H), 4.61 (s, 2H).



*2-(chloromethyl)-7-methoxyquinazolin-4(3H)-one*: from methyl 2-amino-4-methoxybenzoate (100 mg, 0.55 mmol); yield 124.5 mg (100%) tan solids; <sup>1</sup>H NMR (400 MHz, DMSO-*d*<sub>6</sub>) δ 12.45 (s, 1H), 8.01 (d, *J* = 8.4 Hz, 1H), 7.12 (d, *J* = 8.3 Hz, 2H), 4.52 (s, 2H), 3.89 (s, 3H).

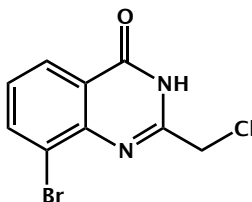


*2-(Chloromethyl)-7-nitroquinazolin-4(3H)-one*: from methyl 2-amino-4-nitrobenzoate (90 mg, 0.46 mmol); yield 125 mg (113%) burnt sienna solids; <sup>1</sup>H NMR (400 MHz, DMSO-*d*<sub>6</sub>) δ 13.02 (s, 1H), 8.39 (d, *J* = 2.2 Hz, 1H), 8.33 (s, 1H), 8.27 (d, *J* = 2.3 Hz, 1H), 4.59 (s, 2H).

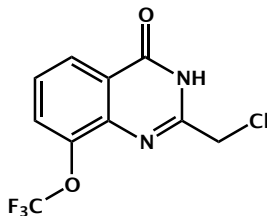


*2-(Chloromethyl)-8-methylquinazolin-4(3H)-one*: from methyl 2-amino-3-methylbenzoate (250 mg, 1.52 mmol); yield 210 mg (48%) tan solids; <sup>1</sup>H NMR (400 MHz, DMSO-*d*<sub>6</sub>) δ 12.57 (s, 1H), 7.97 (d, *J* = 7.9 Hz, 1H),

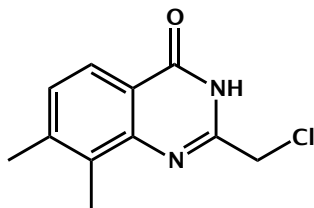
7.70 (d,  $J = 7.5$  Hz, 1H), 7.44 (t,  $J = 7.6$  Hz, 1H), 4.56 (d,  $J = 1.3$  Hz, 2H), 2.53 (d,  $J = 9.2$  Hz, 3H).



*8-Bromo-2-(chloromethyl)quinazolin-4(3H)-one*: from methyl 2-amino-3-bromobenzoate (100 mg, 0.43 mmol); yield 30 mg (30%) brown solids, carried on crude;  $^1\text{H}$  NMR (400 MHz, DMSO- $d_6$ )  $\delta$  12.86 (s, 1H), 8.15 (ddd,  $J = 16.2, 7.9, 1.4$  Hz, 2H), 7.79 (dd,  $J = 8.0, 1.5$  Hz, 1H), 7.68 (dd,  $J = 7.7, 1.6$  Hz, 1H), 7.46 (t,  $J = 7.8$  Hz, 1H), 6.71 (s, 2H), 6.56 (t,  $J = 7.9$  Hz, 1H), 4.57 (s, 2H), 3.82 (s, 3H).

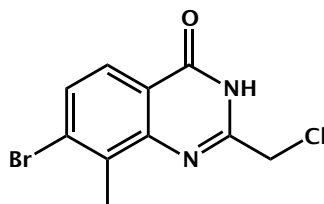


*2-(Chloromethyl)-8-(trifluoromethoxy)quinazolin-4(3H)-one (novel compound)*: from methyl 2-amino-3(methoxy)benzoate (400 mg, 1.7 mmol); yield 30 mg (6%) tan solids;  $^1\text{H}$  NMR (400 MHz, DMSO- $d_6$ )  $\delta$  12.90 (s, 1H), 8.15 (dd,  $J = 8.1, 1.4$  Hz, 1H), 7.90 (dt,  $J = 8.0, 1.4$  Hz, 1H), 7.63 (t,  $J = 8.0$  Hz, 1H), 4.58 (s, 2H).

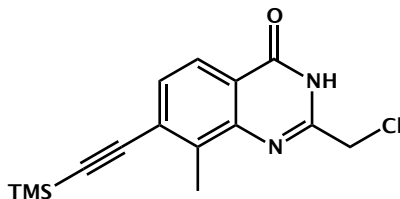


*2-(Chloromethyl)-7,8-dimethylquinazolin-4(3H)-one (novel compound):*

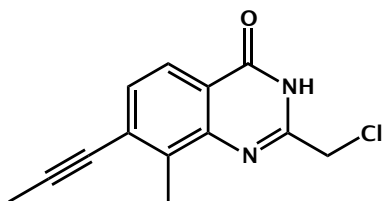
from methyl 2-amino-3,4-dimethylbenzoate (400 mg, 2.23 mmol);  
yield 343 mg (69%) tan solids; <sup>1</sup>H NMR (400 MHz, Chloroform-d)  $\delta$  9.53 (s, 1H), 8.05 (d,  $J$  = 8.1 Hz, 1H), 7.33 (d,  $J$  = 8.1 Hz, 1H), 4.60 (s, 2H), 2.54 (s, 3H), 2.44 (s, 3H).



*7-Bromo-2-(chloromethyl)-8-methylquinazolin-4(3H)-one:* from methyl 2-amino-4-bromo-3-methylbenzoate (100 mg, 0.41 mmol) tan solids;  
yield 75 mg (64%); <sup>1</sup>H NMR (400 MHz, DMSO-d<sub>6</sub>)  $\delta$  12.76 (s, 1H), 7.88 (d,  $J$  = 8.5 Hz, 1H), 7.75 (d,  $J$  = 8.6 Hz, 1H), 4.57 (s, 2H), 2.64 (s, 3H).



*2-(Chloromethyl)-7-ethynyl-8-methylquinazolin-4(3H)-one (novel compound)*: from methyl 2-amino-4-ethynyl-3-methylbenzoate (117 mg, 0.45 mmol); yield 80 mg (77%) tan solids; <sup>1</sup>H NMR (400 MHz, Chloroform-d) δ 10.48 (s, 1H), 8.10 – 8.05 (m, 1H), 7.55 (d, J = 8.3 Hz, 1H), 4.61 (s, 2H), 2.71 (s, 3H), 0.30 (s, 9H).



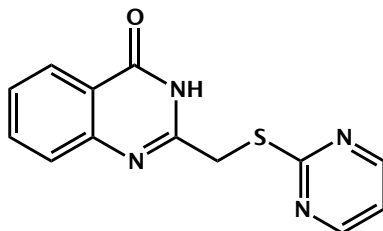
*2-(Chloromethyl)-8-methyl-7-(prop-1-yn-1-yl)quinazolin-4(3H)-one (novel compound)*: from methyl 2-amino-3-methyl-4-(prop-1-yn-1-yl)benzoate (125 mg, 0.62 mmol); yield 115 mg (82%) tan solids. <sup>1</sup>H NMR (400 MHz, DMSO-d<sub>6</sub>) δ 12.64 (s, 1H), 7.90 (d, J = 8.2 Hz, 1H), 7.47 (d, J = 8.2 Hz, 1H), 4.56 (s, 2H), 2.62 (s, 3H), 2.16 (s, 3H).

### General procedure for synthesis of

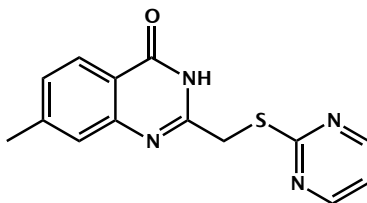
#### ((pyrimidin-2-ylthio)methyl)quinazolin-4(3H)-ones:

The appropriate thiol (2 eqv.) and sodium hydride (2 eqv.) were dissolved in anhydrous DMF and stirred at RT for 20 min. The appropriate quinazolin-4(3H)-one was added as a solid and the reaction mixture stirred at RT for 20 min. Once complete by TLC

analysis (100% EtOAc) the reaction was poured over water, isolated, and purified as indicated.

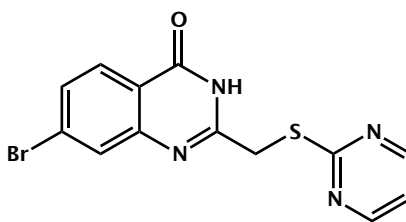


*2-((Pyrimidin-2-ylthio)methyl)quinazolin-4(3H)-one, ITK-A1*: from 2-(chloromethyl)quinazolin-4(3H)-one (50 mg, 0.26 mmol) and 2-mercapto pyrimidine; products precipitated as white solids in water; yield 41 mg (57%); <sup>1</sup>H NMR (400 MHz, Chloroform-d) δ 11.13 (s, 1H), 8.69 (d, J = 4.9 Hz, 2H), 8.26 (ddd, J = 8.0, 1.6, 0.6 Hz, 1H), 7.80 – 7.66 (m, 2H), 7.48 (ddd, J = 8.1, 7.0, 1.3 Hz, 1H), 7.17 (t, J = 4.9 Hz, 1H), 4.31 (s, 2H). MS m/z [M+H]<sup>+</sup> for C<sub>13</sub>H<sub>10</sub>N<sub>4</sub>OS: 271.06, found 270.7.



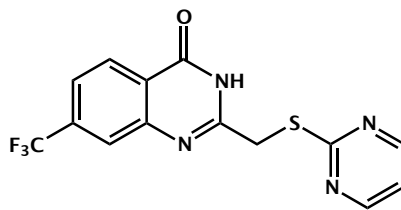
*7-Methyl-2-((pyrimidin-2-ylthio)methyl)quinazolin-4(3H)-one (novel compound), ITK-A2*: from 2-(chloromethyl)-7-methylquinazolin-4(3H)-one (25 mg, 0.11 mmol) and 2-mercaptopyrimidine; reaction poured over water and extracted with EtOAc (3x), combined organic

layers were washed with 1 N HCl (3x), and brine (3x), then dried over sodium sulfate and concentrated in vacuo to give white solids; yield 10 mg (32%); <sup>1</sup>H NMR (400 MHz, Chloroform-d) δ 10.98 (s, 1H), 8.68 (d, J = 4.9 Hz, 2H), 8.14 (d, J = 8.1 Hz, 1H), 7.48 (s, 1H), 7.29 (d, J = 11.8 Hz, 1H), 7.17 (t, J = 4.9 Hz, 1H), 4.29 (s, 2H), 2.50 (s, 3H). MS m/z [M+H]<sup>+</sup> for C<sub>14</sub>H<sub>12</sub>N<sub>4</sub>OS: 285.07, found 285.0.

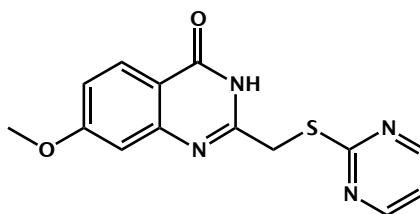


*7-Bromo-2-((pyrimidin-2-ylthio)methyl)quinazolin-4(3H)-one (novel compound), ITK-A3*: from 7-bromo-2-(chloromethyl)quinazolin-4(3H)-one (75 mg, 0.27 mmol) and 2-mercaptopyrimidine; reaction poured over water and extracted with EtOAc (3x), combined organic layers were washed with 1 N HCl (3x), and brine (3x), then dried over sodium sulfate and concentrated in vacuo to give white solids; yield 11.8 mg (13%); <sup>1</sup>H NMR (400 MHz, Chloroform-d) δ 11.17 (s, 1H), 8.69 (dd, J = 4.9, 1.7 Hz, 2H), 8.10 (dd, J = 8.4, 1.7 Hz, 1H), 7.86 (s, 1H), 7.57 (d, J = 8.6 Hz, 1H), 7.21 – 7.16 (m, 1H), 4.27 (d, J = 1.7 Hz, 2H). MS m/z [M+H]<sup>+</sup> for C<sub>13</sub>H<sub>9</sub>BrN<sub>4</sub>OS: 348.97, 350.97, found 348.9, 350.8.



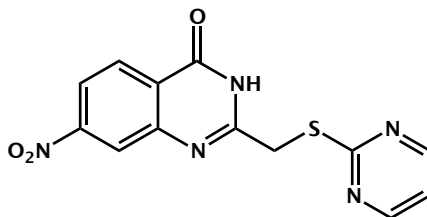


*2-((Pyrimidin-2-ylthio)methyl)-7-(trifluoromethyl)quinazolin-4(3H)-one* (*novel compound*), **ITK-A4**: from 2-(chloromethyl)-7-(trifluoromethyl)quinazolin-4(3H)-one (50 mg, 0.19 mmol) and 2-mercaptopyrimidine; product precipitated as tan solids in water; yield 52 mg (82%); <sup>1</sup>H NMR (400 MHz, Chloroform-d)  $\delta$  11.35 (s, 1H), 8.72 (d,  $J$  = 4.9 Hz, 2H), 8.39 (d,  $J$  = 8.3 Hz, 1H), 7.99 (t,  $J$  = 1.1 Hz, 1H), 7.72 – 7.67 (m, 1H), 7.22 (t,  $J$  = 4.9 Hz, 1H), 4.32 (s, 2H). MS  $m/z$  [M+H]<sup>+</sup> for C<sub>14</sub>H<sub>9</sub>F<sub>3</sub>N<sub>4</sub>OS: 339.04, found 338.9.

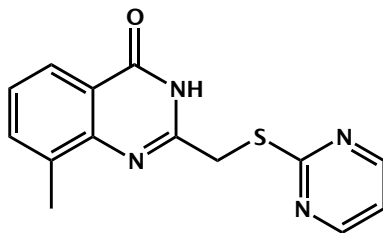


*7-Methoxy-2-((pyrimidin-2-ylthio)methyl)quinazolin-4(3H)-one* (*novel compound*), **ITK-A5**: 2-(chloromethyl)-7-methoxyquinazolin-4(3H)-one (124 mg, 0.55 mmol) and 2-mercaptopyrimidine; product precipitated as white solids in water; yield 50 mg (30%); <sup>1</sup>H NMR (400 MHz, Chloroform-d)  $\delta$  11.61 (s, 1H), 8.71 (d,  $J$  = 4.9 Hz, 2H), 8.15 (d,  $J$  = 8.9 Hz, 1H), 7.37 (s, 1H), 7.23 (t,  $J$  = 4.9 Hz, 1H), 7.12 (dd,  $J$  = 8.9, 2.4 Hz,

1H), 4.56 (s, 2H), 3.96 (s, 3H). MS m/z [M+H]<sup>+</sup> for C<sub>14</sub>H<sub>12</sub>N<sub>4</sub>O<sub>2</sub>S: 301.07, found 301.0.

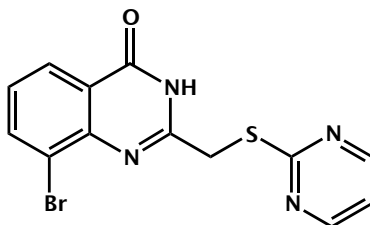


*7-Nitro-2-((pyrimidin-2-ylthio)methyl)quinazolin-4(3H)-one (novel compound), ITK-A6:* from 2-(chloromethyl)-7-nitroquinazolin-4(3H)-one (125 mg, 0.53 mmol) and 2-mercaptopyrimidine; product precipitated as yellow solids in water; yield 103 mg (62%); <sup>1</sup>H NMR (400 MHz, DMSO-d<sub>6</sub>) δ 12.89 (s, 1H), 8.66 (d, J = 4.9 Hz, 2H), 8.35 – 8.26 (m, 2H), 8.21 (dd, J = 8.7, 2.3 Hz, 1H), 7.25 (t, J = 4.9 Hz, 1H), 4.47 (s, 2H). MS m/z [M-H]<sup>-</sup> for C<sub>13</sub>H<sub>9</sub>N<sub>5</sub>O<sub>3</sub>S: 314.04, found 313.7.

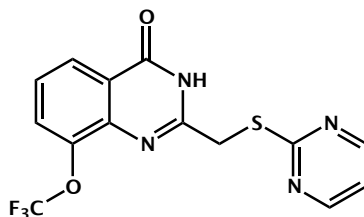


*8-Methyl-2-((pyrimidin-2-ylthio)methyl)quinazolin-4(3H)-one, QDR2:* From 2-(chloromethyl)-8-methylquinazolin-4(3H)-one (112 mg, 0.54 mmol); reaction was concentrated in vacuo and product recovered as a white solid; yield 55.3 mg (36%); <sup>1</sup>H NMR (400 MHz,

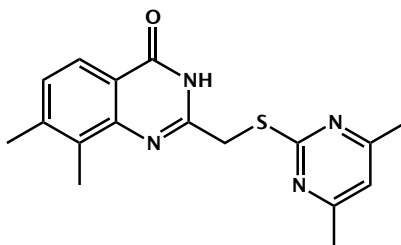
DMSO-d<sub>6</sub>)  $\delta$  12.46 (s, 1H), 8.70 (d,  $J$  = 4.9 Hz, 2H), 7.98 – 7.94 (m, 1H), 7.70 – 7.64 (m, 1H), 7.40 (t,  $J$  = 7.6 Hz, 1H), 7.29 (t,  $J$  = 4.9 Hz, 1H), 4.48 (s, 2H), 2.48 (s, 3H); Rt: 5.81 min. HRMS  $m/z$  [M+H]<sup>+</sup> for C<sub>14</sub>H<sub>13</sub>N<sub>4</sub>OS: 285.08046, found 285.08128.



*8-Bromo-2-((pyrimidin-2-ylthio)methyl)quinazolin-4(3H)-one (novel compound), ITK-A7*: from 8-bromo-2-(chloromethyl)quinazolin-4(3H)-one (30 mg, 0.11 mmol) and 2-mercaptopyrimidine; reaction poured over water and extracted with EtOAc (3x), combined organic layers were washed with water (3x), and brine (3x), then dried over sodium sulfate and concentrated in vacuo to yield light yellow solids. Solids were washed with MeOH to yield desired product; yield 15.6 mg (50%); <sup>1</sup>H NMR (400 MHz, Chloroform-d)  $\delta$  11.39 (s, 1H), 8.70 (d,  $J$  = 4.9 Hz, 2H), 8.22 (dd,  $J$  = 7.9, 1.5 Hz, 1H), 8.03 (dd,  $J$  = 7.7, 1.5 Hz, 1H), 7.32 (t,  $J$  = 7.8 Hz, 1H), 7.20 (t,  $J$  = 4.9 Hz, 1H), 4.37 (s, 2H). MS  $m/z$  [M+H]<sup>+</sup> for C<sub>14</sub>H<sub>12</sub>N<sub>4</sub>OS: 285.07, 286.08, found 313.7.

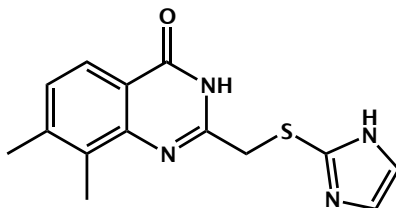


*2-((Pyrimidin-2-ylthio)methyl)-8-(trifluoromethoxy)quinazolin-4(3H)-one (novel compound), ITK-A8:* from 2-(chloromethyl)-8-(trifluoromethoxy)quinazolin-4(3H)-one (100 mg, 0.35 mmol) and 2-mercaptopyrimidine product precipitated as fine white solids in water; yield 100 mg (79%); <sup>1</sup>H NMR (400 MHz, Chloroform-d)  $\delta$  11.39 (s, 1H), 8.70 (d,  $J$  = 4.9 Hz, 2H), 8.22 (dd,  $J$  = 7.9, 1.5 Hz, 1H), 8.03 (dd,  $J$  = 7.7, 1.5 Hz, 1H), 7.32 (t,  $J$  = 7.8 Hz, 1H), 7.20 (t,  $J$  = 4.9 Hz, 1H), 4.37 (s, 2H). MS  $m/z$  [M+H]<sup>+</sup> for C<sub>14</sub>H<sub>9</sub>F<sub>3</sub>N<sub>4</sub>O<sub>2</sub>S: 355.04, found 354.9.

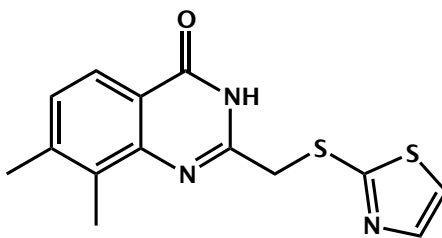


*2-(((4,6-Dimethylpyrimidin-2-yl)thio)methyl)-7,8-dimethylquinazolin-4(3H)-one (novel compound), ITK-A9:* from 2-(chloromethyl)-7,8-dimethylquinazolin-4(3H)-one (25 mg, 0.11 mmol) and 2-Mercapto-4,6-dimethyl-pyrimidine; product precipitated as white solids in water; yield 3 mg (8%); <sup>1</sup>H NMR (400 MHz, Chloroform-d)  $\delta$  11.82 (s,

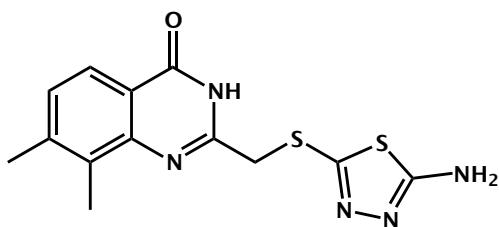
1H), 8.00 (d, J = 8.1 Hz, 1H), 7.27 (s, 1H), 6.87 (s, 1H), 4.28 (s, 2H), 2.57 – 2.54 (m, 9H), 2.43 (s, 3H). MS m/z [M+H]<sup>+</sup> for C<sub>17</sub>H<sub>18</sub>N<sub>4</sub>OS: 327.12, found 327.0.



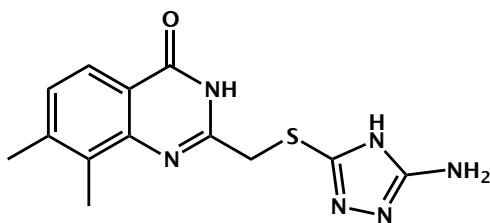
*2-(((1H-Imidazol-2-yl)thio)methyl)-7,8-dimethylquinazolin-4(3H)-one (novel compound), ITK-A10*: from 2-(chloromethyl)-7,8-dimethylquinazolin-4(3H)-one (25 mg, 0.11 mmol) and 2-mercaptoimidazole; reaction poured over water and extracted with EtOAc (3x), combined organic layers were washed with sat. aqueous sodium bicarbonate (3x), and brine (3x), then dried over sodium sulfate and concentrated in vacuo to give white solids; yield 17 mg (58%); <sup>1</sup>H NMR (400 MHz, Chloroform-d) δ 13.13 (s, 1H), 8.06 (d, J = 8.1 Hz, 1H), 7.28 (d, J = 8.1 Hz, 1H), 7.09 (s, 2H), 4.18 (s, 2H), 2.55 (s, 3H), 2.43 (s, 3H). MS m/z [M+H]<sup>+</sup> for C<sub>14</sub>H<sub>14</sub>N<sub>4</sub>OS: 287.09, found 287.0.



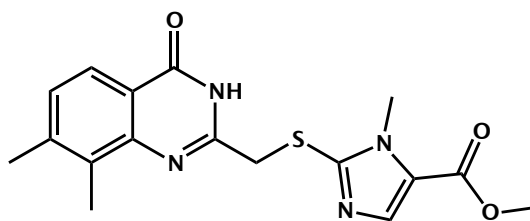
*7,8-Dimethyl-2-((thiazol-2-ylthio)methyl)quinazolin-4(3H)-one (novel compound), ITK-A11:* from 2-(chloromethyl)-7,8-dimethylquinazolin-4(3H)-one (25 mg, 0.11 mmol) and 2-mercaptothiazol; product precipitated as a white solid in water; yield 31 mg (94%); <sup>1</sup>H NMR (400 MHz, DMSO-d<sub>6</sub>) δ 12.35 (s, 1H), 7.84 (d, J = 8.1 Hz, 1H), 7.76 (d, J = 3.3 Hz, 1H), 7.70 (d, J = 3.4 Hz, 1H), 7.31 (d, J = 8.1 Hz, 1H), 4.43 (s, 2H), 2.40 (s, 6H). MS m/z [M+H]<sup>+</sup> for C<sub>14</sub>H<sub>13</sub>N<sub>3</sub>OS<sub>2</sub>: 304.05, found 303.9.



*2-(((5-Amino-1,3,4-thiadiazol-2-yl)thio)methyl)-7,8-dimethylquinazolin-4(3H)-one (novel compound), ITK-A12:* from 2-(chloromethyl)-7,8-dimethylquinazolin-4(3H)-one (25 mg, 0.11 mmol) and 2-Amino-5-mercapto-1,3,4-thiadiazole; product precipitated as a white solid in water; yield 22 mg (63%); <sup>1</sup>H NMR (400 MHz, DMSO-d<sub>6</sub>) δ 12.28 (s, 1H), 7.84 (d, J = 8.1 Hz, 1H), 7.36 (s, 2H), 7.32 (d, J = 8.1 Hz, 1H), 4.19 (s, 2H), 2.41 (s, 3H), 2.38 (s, 3H). MS m/z [M+H]<sup>+</sup> for C<sub>14</sub>H<sub>14</sub>N<sub>4</sub>OS<sub>2</sub>: 319.06, found 319.9.

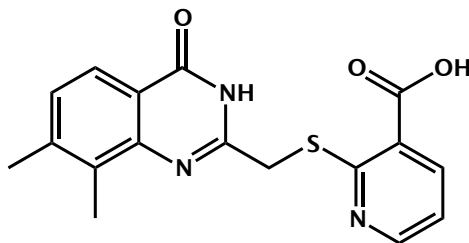


*2-(((5-Amino-1,3,4-thiadiazol-2-yl)thio)methyl)-7,8-dimethylquinazolin-4(3H)-one (novel compound), ITK-A13:* from 2-(chloromethyl)-7,8-dimethylquinazolin-4(3H)-one (30 mg, 0.13 mmol) and 2-Amino-5-mercapto-1,3,4-thiadiazole; fluffy yellow solids precipitated in EtOAc were collected by filtration and stirred in MeOH 10 min. The product was collected by filtration as white solids; yield 4 mg (10%);  $^1\text{H}$  NMR (400 MHz, DMSO- $d_6$ )  $\delta$  12.36 (s, 2H), 7.85 (d,  $J$  = 8.1 Hz, 1H), 7.32 (d,  $J$  = 8.1 Hz, 1H), 4.25 (s, 2H), 2.42 (s, 3H), 2.38 (s, 3H). MS  $m/z$   $[\text{M}+\text{H}]^+$  for  $\text{C}_{13}\text{H}_{14}\text{N}_6\text{OS}$ : 303.09, found 302.7.



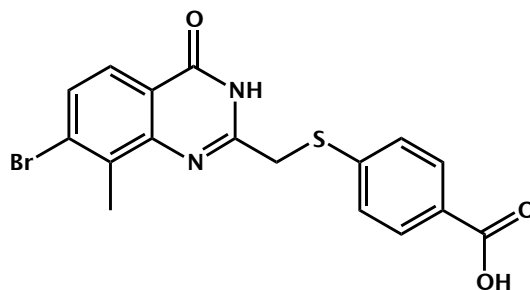
*Methyl 2-(((7,8-dimethyl-4-oxo-3,4-dihydroquinazolin-2-yl)methyl)thio)-1-methyl-1H-imidazole-5-carboxylate (novel compound), ITK-A14:* from 2-(chloromethyl)-7,8-dimethylquinazolin-4(3H)-one (50 mg, 0.22 mmol) and methyl 2-mercapto-1-methyl-1H-imidazole-5-carboxylate; product precipitated as a white solid in water; yield 27

mg (28%); <sup>1</sup>H NMR (400 MHz, DMSO-d<sub>6</sub>) δ 12.36 (s, 1H), 7.83 (d, J = 7.6 Hz, 1H), 7.71 (s, 1H), 7.31 (d, J = 8.1 Hz, 1H), 4.32 (s, 2H), 3.76 (d, J = 9.0 Hz, 6H), 2.35 (d, J = 7.8 Hz, 6H). MS m/z [M+H]<sup>+</sup> for C<sub>17</sub>H<sub>18</sub>N<sub>4</sub>O<sub>3</sub>S: 359.11, found 359.0.

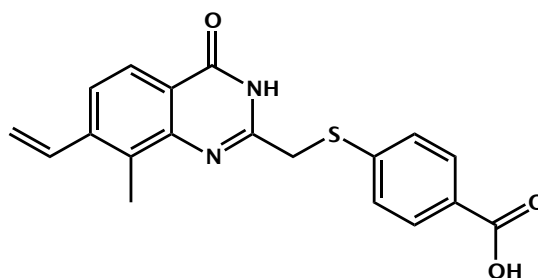


*2-(((7,8-Dimethyl-4-oxo-3,4-dihydroquinazolin-2-yl)methyl)thio)nicotinic acid (novel compound), ITK-A15:* from 2-(chloromethyl)-7,8-dimethylquinazolin-4(3H)-one (50 mg, 0.22 mmol) and 2-mercaptonicotinic acid; reaction poured over water and extracted with EtOAc (3x), combined organic layers were washed with sat. aqueous sodium bicarbonate (2x), and brine (2x), then dried over sodium sulfate and concentrated in vacuo to give yellow solids; yield 70 mg (93%); <sup>1</sup>H NMR (400 MHz, DMSO-d<sub>6</sub>) δ 12.26 (s, 1H), 8.63 (s, 1H), 8.25 (dd, J = 7.8, 1.8 Hz, 1H), 7.83 (d, J = 8.1 Hz, 1H), 7.35 – 7.19 (m, 2H), 4.36 (s, 2H), 2.43 (d, J = 19.7 Hz, 3H), 2.36 (s, 3H). MS m/z [M+H]<sup>+</sup> for C<sub>17</sub>H<sub>15</sub>N<sub>3</sub>O<sub>3</sub>S: 342.08, found 341.7.





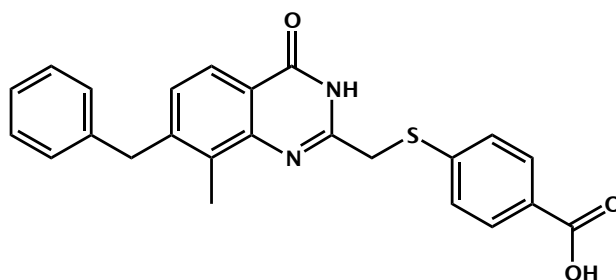
4-(((7-Bromo-8-methyl-4-oxo-3,4-dihydroquinazolin-2-yl)methyl)thio)benzoic acid (novel compound), **ITK-A16**: from 7-bromo-2-(chloromethyl)-8-methylquinazolin-4(3H)-one (10 mg, 0.03 mmol) and 4-mercaptobenzoic acid; product precipitated as white solids in water; yield 1.5 mg (12%). <sup>1</sup>H NMR (400 MHz, DMSO-d<sub>6</sub>) δ 12.62 (s, 1H), 7.84 (ddd, J = 9.0, 4.6, 2.1 Hz, 3H), 7.68 (dd, J = 8.5, 2.0 Hz, 1H), 7.64 – 7.57 (m, 2H), 4.28 (s, 2H), 2.54 (s, 3H).



4-(((8-Methyl-4-oxo-7-vinyl-3,4-dihydroquinazolin-2-yl)methyl)thio)benzoic acid (novel compound), **ITK-A17**: 4-(((7-Bromo-8-methyl-4-oxo-3,4-dihydroquinazolin-2-yl)methyl)thio)benzoic acid (50 mg, 0.11 mmol) was dissolved in anhydrous toluene and concentrated (3x 4 mL) then dried under vacuum for 1 hr. The flask was evacuated and

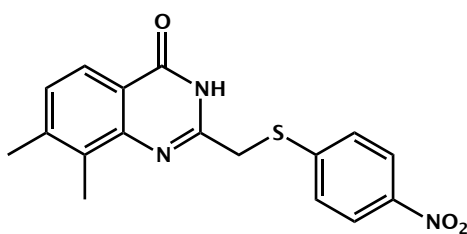
refilled with argon gas (3x), then anhydrous toluene (8 mL) added via syringe and the solution degassed with argon 10 minutes.

Tributyl(vinyl)tin (0.04 mL, 0.14 mmol) was added via syringe and the solution degassed 5 minutes. Palladium tetrakis (13 mg, 0.011 mmol) was added quickly and the solution degassed with argon for 3 minutes. The reaction mixture was refluxed at 115°C for 1 hr. TLC analysis (10% EtOAc in hexanes) showed consumption of starting benzoate. The reaction was cooled to RT and concentrated in vacuo. The crude residue was purified via a Combiflash Companion system (4 g Redisep silica column; 0-30% EtOAc in hexanes). Yield: 10 mg (10%) white solids. <sup>1</sup>H NMR (400 MHz, DMSO-d<sub>6</sub>) δ 12.43 (s, 1H), 7.91 (dd, J = 12.6, 8.3 Hz, 2H), 7.84 (d, J = 8.4 Hz, 1H), 7.64 (dd, J = 8.1, 5.8 Hz, 3H), 7.12 (dd, J = 17.4, 11.0 Hz, 1H), 5.88 (d, J = 17.9 Hz, 1H), 5.50 (d, J = 11.4 Hz, 1H), 4.27 (s, 2H). MS m/z [M+H]<sup>+</sup> for C<sub>19</sub>H<sub>16</sub>N<sub>2</sub>O<sub>3</sub>S: 353.09, found 352.7.

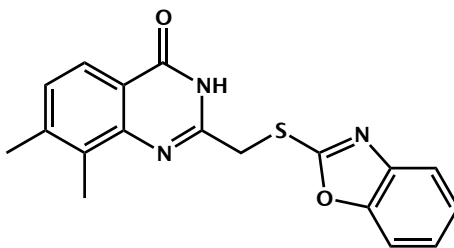


*4-(((7-Benzyl-8-methyl-4-oxo-3,4-dihydroquinazolin-2-yl)methyl)thio)benzoic acid (novel compound), ITK-A18:* from 7-benzyl-2-

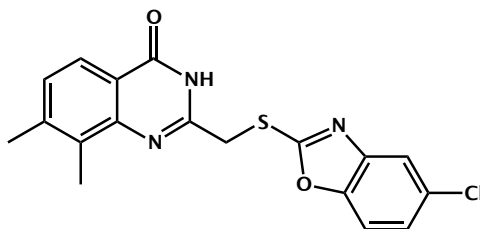
(chloromethyl)-8-methylquinazolin-4(3H)-one (50 mg, 0.17 mmol) and 4-mercaptobenzoic acid; product precipitated as white solids in water; yield 8 mg (11%). <sup>1</sup>H NMR (400 MHz, DMSO-d<sub>6</sub>) δ 12.38 (s, 1H), 7.88 (d, J = 8.2 Hz, 1H), 7.82 (d, J = 8.3 Hz, 2H), 7.61 (d, J = 8.3 Hz, 2H), 7.28 (t, J = 7.8 Hz, 3H), 7.16 (dd, J = 21.9, 7.3 Hz, 3H), 4.25 (s, 2H), 4.11 (s, 2H), 2.42 (s, 3H). MS m/z [M-H]<sup>-</sup> for C<sub>24</sub>H<sub>20</sub>N<sub>2</sub>O<sub>3</sub>S: 415.12, found 414.8.



*7,8-Dimethyl-2-(((4-nitrophenyl)thio)methyl)quinazolin-4(3H)-one (novel compound), ITK-A19*: from 2-(chloromethyl)-7,8-dimethylquinazolin-4(3H)-one (20 mg, 0.09 mmol) and 4-nitrobenzenethiol; product precipitated as white solids in water; yield: 24 mg (80%). <sup>1</sup>H NMR (400 MHz, DMSO-d<sub>6</sub>) δ 12.38 (s, 1H), 8.15 (d, J = 9.0 Hz, 2H), 7.83 (d, J = 7.6 Hz, 2H), 7.78 (d, J = 9.0 Hz, 2H), 7.31 (d, J = 8.1 Hz, 2H), 4.36 (s, 2H), 2.41 (s, 3H), 2.36 (s, 3H). MS m/z [M-H]<sup>-</sup> for C<sub>17</sub>H<sub>15</sub>N<sub>3</sub>O<sub>3</sub>S: 342.08, found 341.7.

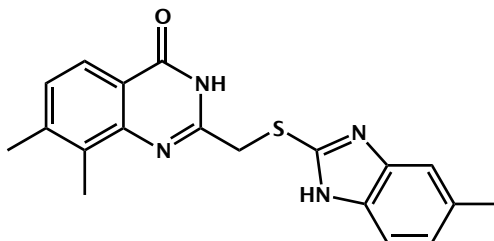


2-((Benzo[d]oxazol-2-ylthio)methyl)-7,8-dimethylquinazolin-4(3H)-one (novel compound), **ITK-A20**: from 2-(chloromethyl)-7,8-dimethylquinazolin-4(3H)-one (20 mg, 0.09 mmol) and benzo[d]oxazole-2-thiol; product precipitated as white solids in water; yield: 10 mg (33%). <sup>1</sup>H NMR (400 MHz, DMSO-d<sub>6</sub>) δ 12.46 (s, 1H), 7.85 (d, J = 8.1 Hz, 1H), 7.69 – 7.63 (m, 2H), 7.34 (ddd, J = 8.0, 3.1, 1.9 Hz, 2H), 4.67 (s, 2H), 2.36 (s, 4H). MS m/z [M+H]<sup>+</sup> for C<sub>18</sub>H<sub>15</sub>N<sub>3</sub>O<sub>2</sub>S: 338.09, found 337.7.

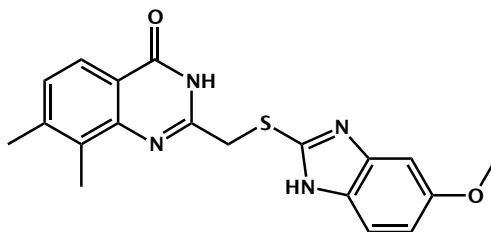


2-(((6-Chlorobenzo[d]oxazol-2-yl)thio)methyl)-7,8-dimethylquinazolin-4(3H)-one (novel compound), **ITK-A21**: from 2-(chloromethyl)-7,8-dimethylquinazolin-4(3H)-one (20 mg, 0.09 mmol) and 6-chlorobenzo[d]oxazole-2-thiol; product precipitated as white solids in water; yield: 10 mg (30%). <sup>1</sup>H NMR (400 MHz, DMSO-d<sub>6</sub>)

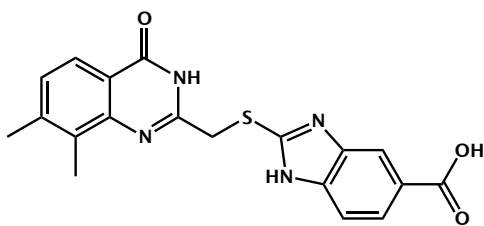
$\delta$  12.47 (s, 1H), 7.90 (d,  $J$  = 1.9 Hz, 1H), 7.85 (d,  $J$  = 8.0 Hz, 2H), 7.67 (d,  $J$  = 8.5 Hz, 1H), 7.44 – 7.39 (m, 2H), 7.32 (d,  $J$  = 8.2 Hz, 1H), 4.67 (s, 2H), 2.35 (s, 6H). MS  $m/z$   $[M+H]^+$  for  $C_{18}H_{14}ClN_3O_2S$ : 372.05, found 371.6.



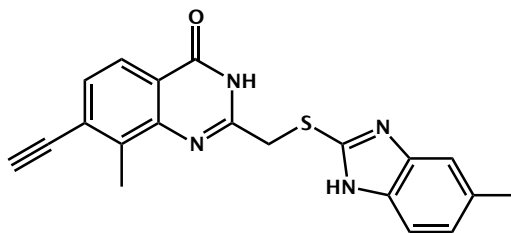
7,8-Dimethyl-2-(((5-methyl-1H-benzo[d]imidazol-2-yl)thio)methyl)quinazolin-4(3H)-one (*novel compound*), **ITK-A22**: from 2-(chloromethyl)-7,8-dimethylquinazolin-4(3H)-one (25 mg, 0.11 mmol) and 2-Mercapto-5-methylbenzimidazole; product precipitated as white solids in water; yield 33 mg (85%);  $^1H$  NMR (400 MHz, DMSO- $d_6$ )  $\delta$  12.60 (s, 1H), 12.42 (s, 1H), 7.84 (d,  $J$  = 8.1 Hz, 1H), 7.31 (d,  $J$  = 8.1 Hz, 1H), 6.97 (dt,  $J$  = 25.0, 8.4 Hz, 4H), 4.51 (s, 2H), 2.40 – 2.33 (m, 9H). MS  $m/z$   $[M+H]^+$  for  $C_{19}H_{18}N_4OS$ : 351.12, found 351.0.



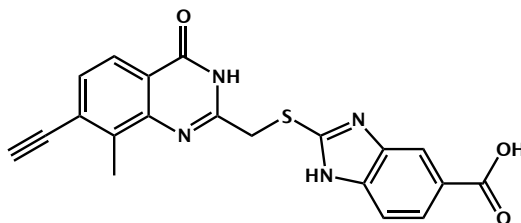
2-(((6-Chlorobenzo[d]oxazol-2-yl)thio)methyl)-7,8-dimethylquinazolin-4(3H)-one, **ITK-A23**: from 2-(chloromethyl)-7,8-dimethylquinazolin-4(3H)-one (20 mg, 0.09 mmol) and 6-methoxy-1H-benzo[d]imidazole-2-thiol; product precipitated as white solids in water; yield: 10 mg (30%). <sup>1</sup>H NMR (400 MHz, DMSO-d<sub>6</sub>) δ 7.85 (d, J = 8.1 Hz, 1H), 7.36 (s, 1H), 7.31 (d, J = 8.1 Hz, 1H), 6.97 (s, 1H), 6.78 (dd, J = 8.8, 2.4 Hz, 1H), 4.48 (s, 2H), 3.77 (s, 3H), 2.37 (d, J = 6.4 Hz, 6H). MS m/z [M+H]<sup>+</sup> for C<sub>19</sub>H<sub>18</sub>N<sub>4</sub>O<sub>2</sub>S: 367.12, found 367.0.



2-(((7,8-Dimethyl-4-oxo-3,4-dihydroquinazolin-2-yl)methyl)thio)-1H-benzo[d]imidazole-6-carboxylic acid (novel compound), **ITK-A24**: from 2-(chloromethyl)-7,8-dimethylquinazolin-4(3H)-one (20 mg, 0.09 mmol) 2-mercapto-1H-benzo[d]imidazole-6-carboxylic acid; product precipitated as white solids in water; yield: 15 mg (44%). <sup>1</sup>H NMR (400 MHz, DMSO-d<sub>6</sub>) δ 8.02 (s, 1H), 7.95 (s, 1H), 7.85 (d, J = 8.1 Hz, 1H), 7.77 (d, J = 8.4 Hz, 1H), 7.51 (d, J = 8.6 Hz, 1H), 7.31 (d, J = 8.2 Hz, 1H), 4.57 (s, 2H), 2.37 (d, J = 9.1 Hz, 6H). MS m/z [M+H]<sup>+</sup> for C<sub>19</sub>H<sub>16</sub>N<sub>4</sub>O<sub>3</sub>S: 381.09, found 380.9.

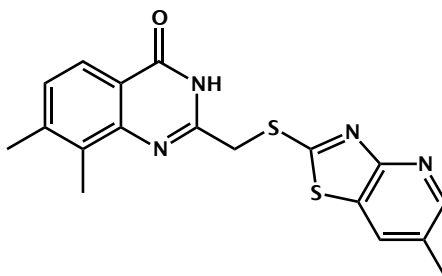


*7,8-Dimethyl-2-(((6-methyl-1H-benzo[d]imidazol-2-yl)thio)methyl)quinazolin-4(3H)-one (novel compound), ITK-A25:* from 2-(chloromethyl)-7-ethynyl-8-methylquinazolin-4(3H)-one (10 mg, 0.04 mmol) and 6-methyl-1H-benzo[d]imidazole-2-thiol; product precipitated as fine white solids in water; yield 10 mg (66%). <sup>1</sup>H NMR (400 MHz, DMSO-d<sub>6</sub>) δ 7.91 (d, J = 8.2 Hz, 1H), 7.49 (d, J = 8.2 Hz, 1H), 7.34 (s, 1H), 7.25 (s, 1H), 6.98 (d, J = 8.3 Hz, 1H), 4.70 (s, 1H), 4.50 (s, 2H), 2.39 (s, 3H). MS m/z [M+H]<sup>+</sup> for C<sub>20</sub>H<sub>16</sub>N<sub>4</sub>OS: 361.10, found 361.0.



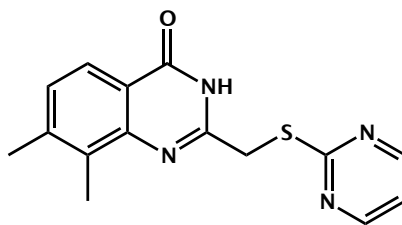
*2-(((7-Ethynyl-8-methyl-4-oxo-3,4-dihydroquinazolin-2-yl)methyl)thio)-1H-benzo[d]imidazole-6-carboxylic acid (novel compound), ITK-A26:* from 2-(chloromethyl)-7-ethynyl-8-methylquinazolin-4(3H)-one (15 mg, 0.07 mmol) and 2-mercapto-1H-

benzo[d]imidazole-6-carboxylic acid; product precipitated as white solids in water; yield: 5 mg (20%). <sup>1</sup>H NMR (400 MHz, DMSO-d<sub>6</sub>) δ 8.03 (s, 1H), 7.91 (d, J = 8.3 Hz, 1H), 7.78 (dd, J = 8.5, 1.6 Hz, 1H), 7.51 (t, J = 7.4 Hz, 2H), 4.70 (s, 1H), 4.59 (s, 2H), 2.52 (s, 3H). MS m/z [M+H]<sup>+</sup> for C<sub>20</sub>H<sub>14</sub>N<sub>4</sub>O<sub>3</sub>S: 391.08, found 390.0.

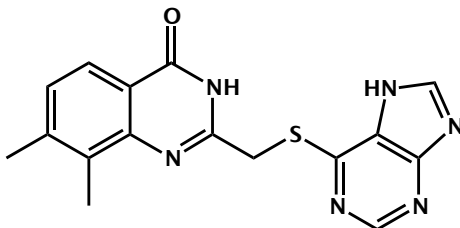


*7,8-Dimethyl-2-(((6-methylthiazolo[4,5-b]pyridin-2-yl)thio)methyl)quinazolin-4(3H)-one (novel compound), ITK-A27*: from 2-(chloromethyl)-7,8-dimethylquinazolin-4(3H)-one (25 mg, 0.11 mmol) and 2-Mercapto-6-methylthiazolo[4,5-b]pyridine; product precipitated as fine white solids in water; yield 20 mg (49%); <sup>1</sup>H NMR (400 MHz, DMSO-d<sub>6</sub>) δ 12.44 (s, 1H), 8.38 (s, 1H), 8.06 (s, 1H), 7.85 (d, J = 8.3 Hz, 1H), 7.32 (d, J = 8.0 Hz, 1H), 4.68 (s, 2H), 2.43 (s, 3H), 2.42 (s, 3H), 2.36 (s, 3H). MS m/z [M+H]<sup>+</sup> for C<sub>19</sub>H<sub>17</sub>N<sub>3</sub>OS<sub>2</sub>: 368.08, found 368.9.



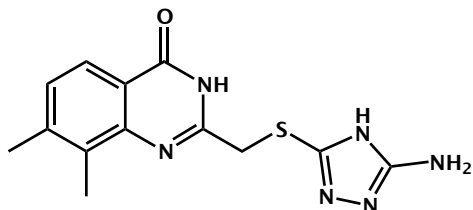


*7,8-Dimethyl-2-((pyrimidin-2-ylthio)methyl)quinazolin-4(3H)-one* (novel compound), **ITK1**: from 2-(chloromethyl)-7-methylquinazolin-4(3H)-one (18 mg, 0.08 mmol) and 2-mercaptopyrimidine; product precipitated as fine white solids in water; yield 15 mg (63%); <sup>1</sup>H NMR (400 MHz, Chloroform-d) δ 10.96 (s, 1H), 8.68 (d, J = 4.9 Hz, 2H), 8.01 (d, J = 8.0 Hz, 1H), 7.17 (t, J = 4.9 Hz, 1H), 4.33 (s, 2H), 2.56 (s, 3H), 2.43 (s, 3H); Rt: 7.58 min. HRMS m/z [M+H]<sup>+</sup> for C<sub>15</sub>H<sub>16</sub>N<sub>4</sub>OS: 299.09611, found 299.09727.

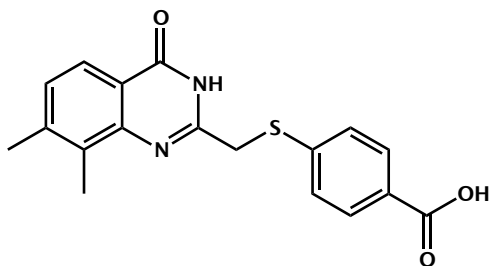


*2-(((7H-Purin-6-yl)thio)methyl)-7,8-dimethylquinazolin-4(3H)-one* (novel compound), **ITK2**: from 2-(chloromethyl)-7,8-dimethylquinazolin-4(3H)-one (25 mg, 0.11 mmol) and mercaptopurine; product precipitated as a white solid partitioned between water and EtOAc; yield 9.9 mg (27%); <sup>1</sup>H NMR (400 MHz,

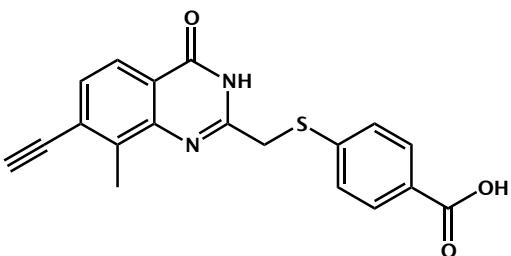
DMSO-d6)  $\delta$  8.73 (s, 1H), 8.54 (s, 1H), 7.84 (d,  $J$  = 8.0 Hz, 1H), 7.30 (d,  $J$  = 7.7 Hz, 1H), 4.68 (s, 2H), 3.57 (d,  $J$  = 1.8 Hz, 2H), 2.39 (s, 6H); Rt: 5.84 min. HRMS  $m/z$   $[M-H]^+$  for  $C_{16}H_{15}N_6OS$ : 337.08661, found 337.08676.



2-(((5-Amino-4H-1,2,4-triazol-3-yl)thio)methyl)-7,8-dimethylquinazolin-4(3H)-one (novel compound), **ITK3**: from 2-(chloromethyl)-7,8-dimethylquinazolin-4(3H)-one (25 mg, 0.11 mmol) and 3-Amino-5-mercapto-1,2,4-triazole; product precipitated as fine white solids in water; yield 25 mg (76%);  $^1H$  NMR (400 MHz, DMSO-d6)  $\delta$  12.28 (s, 1H), 12.09 (s, 1H), 7.84 (d,  $J$  = 8.1 Hz, 1H), 7.31 (d,  $J$  = 8.1 Hz, 1H), 6.20 (s, 2H), 4.19 (s, 2H), 2.44 (s, 3H), 2.38 (s, 3H); Rt: 4.76 min. HRMS  $m/z$   $[M-H]^+$  for  $C_{13}H_{15}N_6OS$ : 301.08661, found 301.08712.

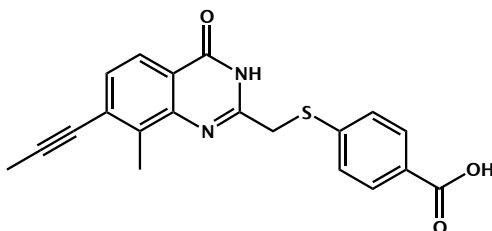


4-(((7,8-Dimethyl-4-oxo-3,4-dihydroquinazolin-2-yl)methyl)thio)benzoic acid (novel compound), **ITK4**: from 2-(chloromethyl)-7,8-dimethylquinazolin-4(3H)-one (25 mg, 0.11 mmol) and 4-mercaptobenzoic acid; product precipitated as pale yellow solids in water; yield 27 mg (73%); <sup>1</sup>H NMR (400 MHz, DMSO-d<sub>6</sub>) δ 12.95 (s, 1H), 12.33 (s, 1H), 7.93 (d, J = 8.3 Hz, 1H), 7.83 (t, J = 7.2 Hz, 2H), 7.63 (d, J = 8.1 Hz, 2H), 7.29 (d, J = 8.1 Hz, 1H), 4.26 (s, 2H), 2.41 (s, 3H), 2.36 (s, 3H); Rt: 6.70 min. HRMS m/z [M-H]<sup>+</sup> for C<sub>18</sub>H<sub>16</sub>N<sub>2</sub>O<sub>3</sub>S: 339.07979, found 339.08030.

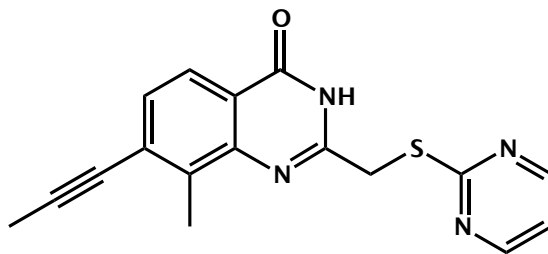


4-(((7-Ethynyl-8-methyl-4-oxo-3,4-dihydroquinazolin-2-yl)methyl)thio)benzoic acid (novel compound), **ITK5**: from 2-(chloromethyl)-7-ethynyl-8-methylquinazolin-4(3H)-one (10 mg, 0.043 mmol); crude product precipitated as fine white solids in water then purified by HPLC (mobile phase A: water; mobile phase B: methanol; flow rate: 20 mL/min; conditions: pre-run A = 5% B = 95%, 7 min: A = 5% B = 95%, 10 min: A = 5% B = 95%, 11 min: A = 35% B = 65%, 15 min: A = 35% B = 95; Retention time: 4.29 min; UV-Vis

detection:  $\lambda_1$  254 nm,  $\lambda_2$  = 220 nm. Yield 6.1 mg (42%);  $^1\text{H}$  NMR (400 MHz, DMSO- $d_6$ )  $\delta$  12.55 (s, 1H), 7.89 (d,  $J$  = 8.2 Hz, 1H), 7.85 (d,  $J$  = 8.1 Hz, 2H), 7.62 (d,  $J$  = 8.0 Hz, 2H), 7.49 (d,  $J$  = 8.2 Hz, 1H), 4.70 (s, 1H), 4.26 (s, 2H), 2.56 (s, 3H); Rt: 8.21 min. HRMS  $m/z$   $[\text{M}-\text{H}]^+$  for  $\text{C}_{19}\text{H}_{14}\text{N}_2\text{O}_3\text{S}$ : 349.06414, found 349.06489.



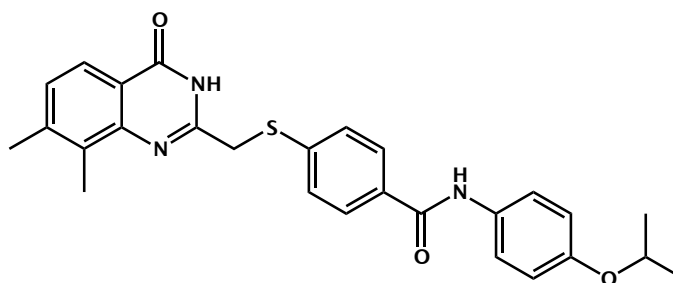
4-(((8-Methyl-4-oxo-7-(prop-1-yn-1-yl)-3,4-dihydroquinazolin-2-yl)methyl)thio)benzoic acid (novel compound), **ITK6**: from 2-(chloromethyl)-8-methyl-7-(prop-1-yn-1-yl)quinazolin-4(3H)-one (90 mg, 0.39 mmol); product precipitated as a white solid in water; yield 80.2 mg (56%);  $^1\text{H}$  NMR (400 MHz, DMSO- $d_6$ )  $\delta$  12.96 (s, 1H), 12.50 (s, 1H), 7.88 – 7.82 (m, 3H), 7.62 (d,  $J$  = 8.3 Hz, 2H), 7.40 (d,  $J$  = 8.2 Hz, 1H), 4.25 (s, 3H), 2.14 (s, 3H); Rt: 8.85 min. HRMS  $m/z$   $[\text{M}+\text{H}]^+$  for  $\text{C}_{20}\text{H}_{17}\text{N}_2\text{O}_3\text{S}$ : 365.09544, found 365.09574.



*8-Methyl-7-(prop-1-yn-1-yl)-2-((pyrimidin-2-ylthio)methyl)quinazolin-4(3H)-one (novel compound), ITK7*: from 2-(chloromethyl)-8-methyl-7-(prop-1-yn-1-yl)quinazolin-4(3H)-one one (15 mg, 0.06 mmol); reaction poured over water and extracted with EtOAc (3x), combined organic layers were washed with sat. aqueous sodium bicarbonate (2x), and brine (2x), then dried over sodium sulfate and concentrated in vacuo to give tan solids; yield 15.1 mg (76%); <sup>1</sup>H NMR (400 MHz, DMSO-d<sub>6</sub>) δ 12.49 (s, 1H), 8.66 (d, J = 4.9 Hz, 2H), 7.87 (d, J = 8.0 Hz, 1H), 7.41 (d, J = 8.2 Hz, 1H), 7.25 (t, J = 4.9 Hz, 1H), 4.44 (s, 2H), 2.53 (s, 3H), 2.14 (s, 3H). Rt: 8.90 min. HRMS m/z [M+H]<sup>+</sup> for C<sub>17</sub>H<sub>15</sub>N<sub>4</sub>O<sub>1</sub>S: 323.09611, found 323.09656.

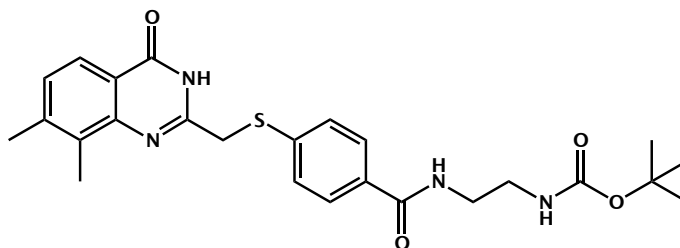
**General procedure for EDC coupling of amines to 4-(((7,8-dimethyl-4-oxo-3,4-dihydroquinazolin-2-yl)methyl)thio)benzoic acid:** 4-(((7,8-dimethyl-4-oxo-3,4-dihydroquinazolin-2-yl)methyl)thio)benzoic acid, EDC (1.5 eqv), DIPEA (2.0 eqv), and

DMAP (0.5 eqv) were dissolved in anhydrous DMF/DCM (1:1) and stirred at RT for 3 hrs. The appropriate amine was added and the reaction mixture stirred at RT for 24 hrs. Once complete by LC analysis reaction was poured over water and separated with EtOAc. The aqueous layer was extracted with EtOAc (3x), combined organic layers were washed with citrate buffer (pH 4.5) (1x), water (1x), and brine (1x), then dried over sodium sulfate and concentrated in vacuo to yield desired amide.

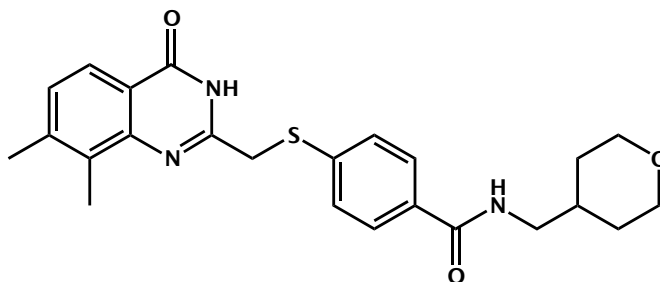


4-(((7,8-Dimethyl-4-oxo-3,4-dihydroquinazolin-2-yl)methyl)thio)-N-(4-isopropoxyphenyl)benzamide (*novel compound*), **ITK-A28**: from 4-(((7,8-dimethyl-4-oxo-3,4-dihydroquinazolin-2-yl)methyl)thio)benzoic acid (40 mg, 0.12 mmol) and 4-isopropoxyaniline (0.023 mL, 0.159 mmol); yield 3 mg (5%) brown solids;  $^1\text{H}$  NMR (400 MHz, DMSO- $d_6$ )  $\delta$  12.33 (s, 1H), 10.05 (s, 1H), 7.88 (d,  $J$  = 8.5 Hz, 2H), 7.83 (d,  $J$  = 8.0 Hz, 1H), 7.63 (dd,  $J$  = 13.6, 8.7 Hz, 4H), 7.30 (d,  $J$  = 8.2 Hz, 1H), 6.89 (d,  $J$  = 9.0 Hz, 2H),

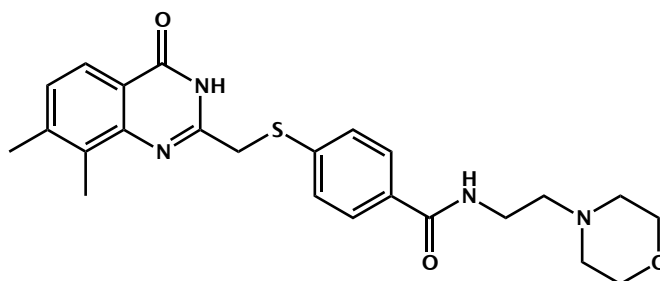
4.26 (s, 2H), 2.44 (s, 3H), 2.37 (s, 3H), 1.26 (s, 3H), 1.24 (s, 3H). MS m/z [M-H]<sup>-</sup> for C<sub>27</sub>H<sub>27</sub>N<sub>3</sub>O<sub>3</sub>S: 472.18, found 471.9.



*Tert-butyl (2-(4-(((7,8-dimethyl-4-oxo-3,4-dihydroquinazolin-2-yl)methyl)thio)benzamido)ethyl)carbamate (novel compound), ITK-A29:* from 4-(((7,8-dimethyl-4-oxo-3,4-dihydroquinazolin-2-yl)methyl)thio)benzoic acid (25 mg, 0.07 mmol) and tert-butyl (2-aminoethyl)carbamate (0.02 mL, 0.14 mmol); yield 5 mg (15%) brown solids; <sup>1</sup>H NMR (400 MHz, DMSO-d<sub>6</sub>) δ 12.32 (s, 1H), 8.42 (s, 1H), 7.82 (d, J = 8.1 Hz, 1H), 7.76 (d, J = 8.3 Hz, 1H), 7.60 (d, J = 8.4 Hz, 1H), 7.30 (d, J = 8.1 Hz, 1H), 6.91 (s, 1H), 4.23 (s, 2H), 2.43 (s, 3H), 2.37 (s, 3H), 1.36 (d, J = 6.5 Hz, 9H).



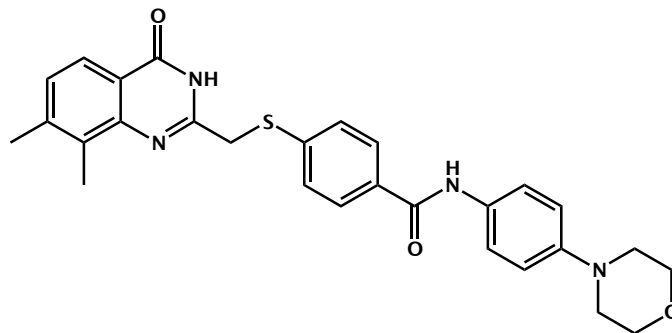
4-(((7,8-Dimethyl-4-oxo-3,4-dihydroquinazolin-2-yl)methyl)thio)-N-((tetrahydro-2H-pyran-4-yl)methyl)benzamide (novel compound), **ITK-A30**: from 4-(((7,8-dimethyl-4-oxo-3,4-dihydroquinazolin-2-yl)methyl)thio)benzoic acid (25 mg, 0.07 mmol) and (tetrahydro-2H-pyran-4-yl)methanamine; yield 12 mg (41%) white solids; <sup>1</sup>H NMR (400 MHz, DMSO-d<sub>6</sub>) δ 12.32 (s, 1H), 7.82 (d, J = 7.9 Hz, 1H), 7.77 (d, J = 8.4 Hz, 2H), 7.59 (d, J = 8.5 Hz, 2H), 7.29 (d, J = 8.0 Hz, 1H), 4.22 (s, 2H), 3.12 (t, J = 6.3 Hz, 2H), 2.71 – 2.63 (m, 3H), 2.41 (s, 3H), 2.36 (s, 3H). MS m/z [M-H]<sup>-</sup> for C<sub>24</sub>H<sub>27</sub>N<sub>3</sub>O<sub>3</sub>S: 436.18, found 435.9.



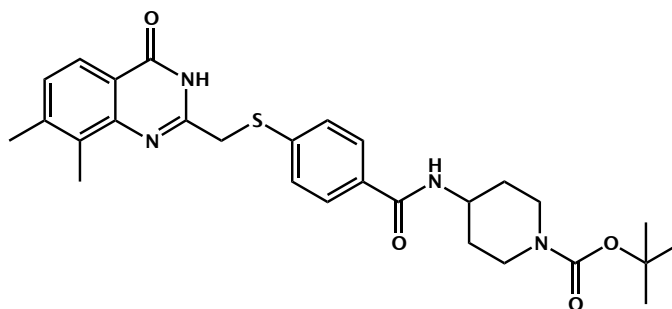
4-(((7,8-Dimethyl-4-oxo-3,4-dihydroquinazolin-2-yl)methyl)thio)-N-(2-morpholinoethyl)benzamide (novel compound), **ITK-A31**: from 4-(((7,8-dimethyl-4-oxo-3,4-dihydroquinazolin-2-yl)methyl)thio)benzoic acid (20 mg, 0.06 mmol) and 2-(tetrahydro-2H-pyran-4-yl)ethanamine; yield 21 mg (78%) tan solids; <sup>1</sup>H NMR (400 MHz, DMSO-d<sub>6</sub>) δ 12.32 (s, 1H), 7.82 (d, J = 8.0 Hz, 1H), 7.76 (d, J = 8.3 Hz, 2H), 7.60 (d, J = 8.4 Hz,



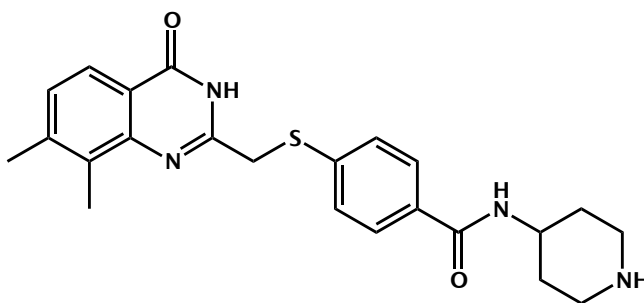
2H), 7.30 (d, J = 8.1 Hz, 1H), 4.23 (s, 2H), 3.56 (t, J = 4.6 Hz, 4H), 2.42 (s, 3H), 2.37 (s, 3H). MS m/z [M-H]<sup>-</sup> for C<sub>24</sub>H<sub>28</sub>N<sub>4</sub>O<sub>3</sub>S: 451.19, found 450.9.



*4-(((7,8-Dimethyl-4-oxo-3,4-dihydroquinazolin-2-yl)methyl)thio)-N-(4-morpholinophenyl)benzamide (novel compound), ITK-A32*: from 4-(((7,8-dimethyl-4-oxo-3,4-dihydroquinazolin-2-yl)methyl)thio)benzoic acid (20 mg, 0.06 mmol) and 4-morpholinoaniline; yield 9.7 mg (32%) white solids; <sup>1</sup>H NMR (400 MHz, DMSO-d<sub>6</sub>) δ 12.34 (s, 1H), 10.01 (s, 1H), 7.86 (dd, J = 21.6, 8.0 Hz, 3H), 7.62 (dd, J = 17.9, 8.5 Hz, 3H), 7.30 (d, J = 8.0 Hz, 1H), 6.93 (d, J = 9.0 Hz, 1H), 6.68 (d, J = 8.6 Hz, 1H), 6.49 (d, J = 8.5 Hz, 1H), 4.26 (s, 2H), 3.07 (d, J = 5.2 Hz, 2H), 2.87 (d, J = 4.5 Hz, 2H), 2.44 (s, 3H). MS m/z [M-H]<sup>-</sup> for C<sub>28</sub>H<sub>28</sub>N<sub>4</sub>O<sub>3</sub>S: 499.19, found 498.9.

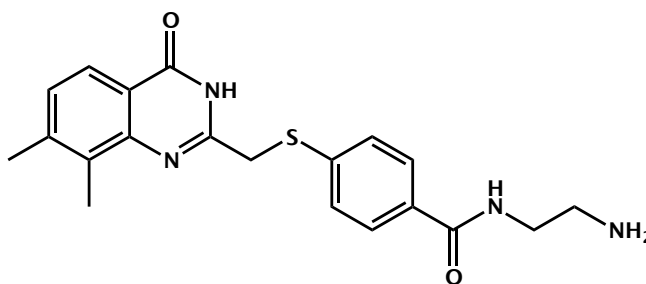


*Tert-butyl 4-(4-(((7,8-dimethyl-4-oxo-3,4-dihydroquinazolin-2-yl)methyl)thio)benzamido)piperidine-1-carboxylate (novel compound), ITK-A33:* from 4-(((7,8-dimethyl-4-oxo-3,4-dihydroquinazolin-2-yl)methyl)thio)benzoic acid (20 mg, 0.06 mmol) and tert-butyl 4-aminopiperidine-1-carboxylate; yield 21 mg (67%) tan solids;  $^1\text{H}$  NMR (400 MHz, DMSO- $d_6$ )  $\delta$  12.32 (s, 1H), 8.38 (s, 1H), 7.82 (d,  $J$  = 8.1 Hz, 2H), 7.76 (d,  $J$  = 8.4 Hz, 2H), 7.60 (d,  $J$  = 8.3 Hz, 1H), 7.30 (d,  $J$  = 8.1 Hz, 1H), 4.23 (s, 2H), 3.55 (d,  $J$  = 4.8 Hz, 3H), 2.67 (s, 1H), 2.42 (s, 3H), 2.36 (s, 3H). MS  $m/z$   $[\text{M}-\text{H}]^-$  for  $\text{C}_{28}\text{H}_{34}\text{N}_4\text{O}_4\text{S}$ : 521.23, found 520.9.



*4-(((7,8-Dimethyl-4-oxo-3,4-dihydroquinazolin-2-yl)methyl)thio)-N-(piperidin-4-yl)benzamide (novel compound), ITK-A34:* tert-butyl 4-(4-

((((7,8-dimethyl-4-oxo-3,4-dihydroquinazolin-2-yl)methyl)thio)benzamido)piperidine-1-carboxylate (15 mg, 0.03 mmol) was stirred in 4 M HCl (1,4-dioxane) and MeOH (1:1) at RT for 24 hrs. The reaction mixture was concentrated in vacuo to afford the product as a brown oil: 17.7 mg (130%); <sup>1</sup>H NMR (400 MHz, DMSO-d<sub>6</sub>) δ 12.33 (s, 1H), 8.42 (d, J = 7.3 Hz, 1H), 7.81 (dd, J = 12.2, 8.2 Hz, 2H), 7.60 (d, J = 8.4 Hz, 2H), 7.30 (d, J = 8.1 Hz, 1H), 4.24 (s, 2H), 3.30 (d, J = 12.5 Hz, 2H), 3.06 – 2.97 (m, 2H), 2.42 (s, 3H), 2.37 (s, 3H).



*N*-(2-aminoethyl)-4-(((7,8-dimethyl-4-oxo-3,4-dihydroquinazolin-2-yl)methyl)thio)benzamide (novel compound), **ITK-A37**: from tert-butyl (2-(4-(((7,8-dimethyl-4-oxo-3,4-dihydroquinazolin-2-yl)methyl)thio)benzamido)ethyl)carbamate (20 mg, 0.041 mmol) was stirred in 4 M HCl (1,4-dioxane) and MeOH (1:1) at RT for 24 hrs. The reaction mixture was concentrated in vacuo to afford the product as an amber oil: 21 mg (124%); <sup>1</sup>H NMR (400 MHz, DMSO-d<sub>6</sub>) δ 12.36 (s, 1H), 8.68 (s, 1H), 7.94 (s, 2H), 7.83 (d, J = 7.9 Hz, 2H), 7.62 (d, J = 8.5 Hz, 2H), 7.30 (d,

$J = 8.1$  Hz, 2H), 3.83 (s, 2H), 3.50 – 3.49 (m, 2H), 3.47 – 3.46 (m, 2H), 2.43 (s, 3H), 2.37 (s, 3H).

### **Crystallography studies**

Molecular cloning, protein expression, and purification. A synthetic cDNA fragment encoding a C-terminal segment of human PARP14 (Q460N5-6), codon optimized for expression in *Escherichia coli*, was obtained from Genscript. The fragment encoding Asp1611 – Lys1801 was inserted into pNIC-NHD (GenBank: FN677494.1). The expression construct included an N-terminus affinity tag consisting of a hexahistidine sequence separated from the protein sequence by a TEV (tobacco etch virus) protease cleavage site (sequence: MHHHHHHSSGVDLG TENLYFQSM). *Escherichia coli* BL21 (DE3) R3 pRARE cells transformed with the expression construct were used to inoculate 3 l Terrific Broth medium supplemented with 8 g/L glycerol, 50 µg/mL kanamycin and Antifoam 204 (Sigma). Cultures were grown in Tune Air shake flasks at 37 °C. When OD600 of approximately 1.5 was reached the temperature was lowered to 18°C and protein expression was induced by addition of 0.5 mM isopropyl β-D-thiogalactopyranoside and continued for approximately 20 h. Cells were harvested by centrifugation at 4430 g for 10 min in a Sorvall SLC-6000 rotor. The resulting pellet was suspended in 80 mL lysis buffer

(100 mM Hepes, 500 mM NaCl, 10% glycerol, 10 mM Imidazole, 0.5 mM TCEP, pH 8.0) supplemented with 1 tablet of Complete EDTA-free Protease Inhibitor (Roche Biosciences) and 8  $\mu$ L benzonase (2000 U). Suspended cells were stored at  $-80^{\circ}\text{C}$ . The cells were thawed and sonicated on ice (Sonics VibraCell) at 80% amplitude, pulse: 4" on and 4" off, for a total time of 3 mins, followed by centrifugation at 49000 x g in a Sorvall SA-800 rotor, 20 mins at  $4^{\circ}\text{C}$ . The soluble fraction was decanted and filtered through a 0.45  $\mu\text{m}$  filter. Protein purification using immobilized metal affinity chromatography followed by size exclusion chromatography were carried out as previously described<sup>3</sup>. Target protein mass was verified by mass spectrometry.

### **Protein Crystallization**

Crystals of the PARP14-ITK1 complex were obtained by the sitting-drop vapor-diffusion method in a 96-well plate (Corning) by mixing 0.2  $\mu\text{L}$  of protein at a concentration of 28 mg/ml including ITK1 dissolved in dimethyl sulfoxide (DMSO) and 0.2  $\mu\text{L}$  of reservoir solution containing 20% poly(ethylene glycol) 3350, 0.2M sodium nitrate. The plate was incubated at  $20^{\circ}\text{C}$ . After three weeks without any signs of crystal growth the plate was moved to  $4^{\circ}\text{C}$  and small rod crystals appeared within five days. Crystals were quickly soaked in cryo

solution supplemented with 20 % glycerol, 300mM sodium chloride and 0.2mM ITK1 and then stored under liquid nitrogen.

Crystals of PARP14-ITK6 complex were obtained by mixing 0.1  $\mu$ l of protein at a concentration of 30 mg/ml including ITK6 dissolved in dimethyl sulfoxide (DMSO) and 0.2  $\mu$ l of reservoir solution containing 20% Poly(ethylene glycol) 3350, 0.2 M sodium nitrate and 0.1 M Bis-Tris-Propane pH 6.5. The plate was incubated at 4 °C. Plate-shaped crystals appeared within seven weeks. Crystals were briefly soaked in cryo solution supplemented with 20 % Glycerol, 200 mM sodium chloride and 4 mM ITK6 and then stored under liquid nitrogen.

*Crystallographic data collection, phasing, and refinement.* A data set extending to 2.15 Å resolution was collected on a PARP14-ITK1 crystal at 0.92819 Å wavelength on a Dectris Pilatus 6M detector at beamline i04-1 at the Diamond Light Source (Oxfordshire, UK). The data were integrated and scaled using xia2. The crystal belonged to space group P1, and the Matthew's coefficient suggested the presence of four monomers in the asymmetric unit. The structure was solved using molecular replacement using Phaser and a previous structure of human PARP14 (PDB entry: 4F1L) as search model. Density for the ligand was observed in all chains and manual model building was done

using COOT. Structure refinement was done using data in the interval 30.92 - 2.15Å resolution with Buster and the progress of refinement was followed by decreasing R and Rfree values. Grade was used to obtain ligand restraints.

A data set extending to 2.67 Å resolution was collected on the best PARP14-ITK6 crystal at 0.96858 Å wavelength on a Dectris Pilatus3 6M detector at beamline i24 at Diamond Light Source (Oxfordshire, UK). The data were integrated and scaled using XDSAPP. The crystal belonged to space group P6122, and the Matthew's coefficient suggested the presence of two monomers in the asymmetric unit. The structure was solved using molecular replacement using Phaser and the PARP14•ITK1 structure as search model. Density for the ligand was observed in both chains and manual model building was done using COOT. Structure refinement was done using Buster. In the refinement, data in the interval 49.76 - 2.67Å resolution was used and the progress of refinement was followed by decreasing R and Rfree values. Grade was used to obtain ligand restraints.

*Summary of crystallographic data collection and refinement statistics for*

*PARP14•ITK1 (6FYM) Data collection:* Beam line: Diamond i04-1;

wavelength (Å): 0.92819; space group: P1; unit cell dimensions

(Å,Å,Å,°,°,°): 40.37, 84.04, 84.44, 119.77, 100.01, 91.44; resolution (Å):

36.7-2.15 (2.21-2.15); unique reflections: 47400 (3487); R(merge): 0.093 (0.94); completeness (%): 92.6 (91.8); redundancy: 3.6 (3.6);  $\langle I \rangle / \langle \text{SIGMAI} \rangle$ : 9.5 (1.2); CC(1/2): 0.996 (0.513). Refinement: resolution (Å): 30.9-2.15 (2.21-2.15); R-factor (%): 19.06 (22.60); reflections used for R-factor: 36637; R-free (%): 22.39 (26.50); reflections used for R-free: 1932; r.m.s.d. bond length (Å): 0.010; r.m.s.d. bond angle (°): 1.0; Wilson B-factor (Å<sup>2</sup>): 41.49; Mean B-factor (Å<sup>2</sup>): 46.74; most favoured (%): 98.1; disallowed (%): 0.

*Summary of crystallographic data collection and refinement statistics for*

*PARP14•ITK6 (6FZM)* Data collection: Beam line: Diamond i24; wavelength (Å): 0.96858; space group: P6122; unit cell dimensions (Å, Å, Å, °, °, °): 83.88, 83.88, 204.91, 90, 90, 120; resolution (Å): 49.76-2.67 (2.83 -2.67); unique reflections: 12549 (1739); R(merge): 0.453 (1.95); completeness (%): 97.8 (86.9); redundancy: 34.8 (30.5);  $\langle I \rangle / \langle \text{SIGMAI} \rangle$ : 10.6 (2.0); CC(1/2): 0.994 (0.769). Refinement: resolution (Å): 49.76-2.67 (2.92-2.67); R-factor (%): 23.46 (27.30); reflections used for R-factor: 12505; R-free (%): 28.88 (35.80); reflections used for R-free: 626; r.m.s.d. bond length (Å): 0.010; r.m.s.d. bond angle (°): 1.1; Wilson B-factor (Å<sup>2</sup>): 66.30; Mean B-factor (Å<sup>2</sup>): 51.93; most favoured (%): 90.6; disallowed (%): 0.3.



*Crystallographic data deposition.* Coordinates and structure factors for the crystal structures have been deposited in the RCSB Protein Data Bank under accession codes 6FYM and 6FZM.

## Chapter 4: Structure Guided Design of a Selective PARP4 Inhibitor

Ilsa T. Kirby, Ashley Person, and Michael S. Cohen

This work was in collaboration with Ashley Person who performed *in vitro* screening against PARP4 and synthesized AEP08.

## Abstract

Poly-ADP-ribose polymerases (PARPs1-16) are key regulators of diverse cellular functions and have been implicated in a wide range of pathologies. The majority of PARP enzymes are poorly characterized, due in large part to the lack of tools available to study them. Herein we focus on PARP4, a member of the MARylating PARP subfamily that is involved in host-viral interactions, neurodegeneration, and cancer, but little is known about the biological mechanism of PARP4. Herein we describe the structure-guided design of the first selective small molecule inhibitor of PARP4. This compound (AEP08) has a sub-micromolar *in vitro* IC<sub>50</sub> and will be a useful tool in future explorations of the biological role and mechanism of PARP4.

## Introduction

PARPs are a family of 17 post-translationally modifying enzymes known to catalyze the transfer of ADP-ribose from their endogenous substrate  $\text{NAD}^+$  to targets. This process of ADP-ribosylation can occur either as the addition of single monomers of ADP-ribose (MARylation), catalyzed by the majority of PARP enzymes (PARP3, 4, 6-8, 10-12, 14-16), or the addition of ADP-ribose polymers (PARylation) catalyzed by a few well-studied PARPs (PARP1, 2, 5a, 5b) (Hottiger et al. 2010). All active PARPs contain an H-Y-X triad motif in the  $\text{NAD}^+$  binding pocket that has been linked to their ADP-ribosylating activity: the HYE-PARPs (PARP1, 2, 3, 4, 5a and 5b) and the HY $\Phi$ -PARPs (PARP 6-8, 10-12, 14-16) (Hottiger et al. 2010). All HY $\Phi$ -PARPs have been shown to exclusively catalyze MARylation (Vyas et al. 2014), while the glutamate in the HYE motif is necessary for the poly-ADP-ribosylation (PARylation) activity of several HYE-PARPs (Marsischky et al. 1995; Rolli et al. 1997). Intriguingly, PARP3 and PARP4 confound these categories as HYE-PARPs that are only known to catalyze MARylation. A respectable body of work has explored the role of PARP3 primarily in cancer and DNA damage repair (Beck et al. 2014; Day et al. 2017; Beck et al. 2018), but relatively little work has been done to understand the biological role of PARP4.

PARP4 was originally identified in mammalian cells as a protein component of Vaults— massive ribonucleoprotein (RNP) complexes, sometimes considered organelles with a still undetermined biological function (Kickhoefer et al. 1999; Kedersha & Rome 1990; Kedersha 1986; Zheng et al. 2005). Since then PARP4 has been implicated in host-viral interactions (Daugherty et al. 2014), Parkinson’s disease (Mata et al. 2017), cancer (Ikeda et al. 2016; Y.-S. Ma et al. 2018), and actin polymerization in *Octopus Vulgaris* brains (De Maio et al. 2013). However, there has been little to no published follow-up work exploring the role of PARP4 in these pathologies, or its underlying biological function. Although PARP4 is potently inhibited by several PARP inhibitors, including those used as therapeutics in BRCA-/- cancers, there are no selective inhibitors that target PARP4 (Kirby & Cohen 2018). Indeed, this is part of a general shortage of selective inhibitors for PARPs, particularly the MARYlating members of the family (Kirby & Cohen 2018). A current survey of the literature reveals inhibitors for PARP10 (Venkannagari et al. 2016; Morgan et al. 2018), PARP11 (Kirby, Kojic, et al. 2018), and PARP14 (Peng et al. 2016; Yoneyama-Hirozane et al. 2017; Upton et al. 2017). With the exception of our PARP11 inhibitor (Chapter 3) these compounds have yet to be fully validated in terms of selectivity across the PARP family.

Building on the ongoing efforts in our laboratory and across the PARP field to address this paucity of PARP inhibitors we sought to develop a selective PARP4 inhibitor in the hopes of adding it to the emerging set of chemical tools for investigating PARP activity in cells.

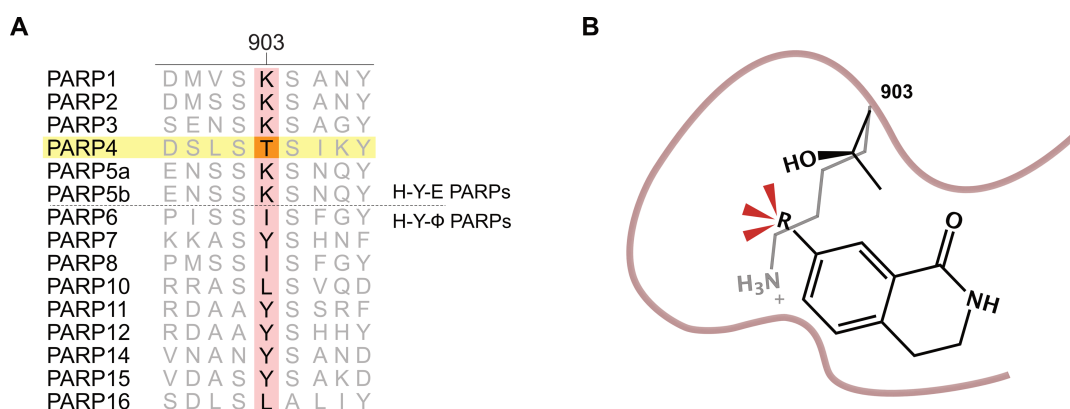
## Results and Discussion

### Sequence Guided Design

The PARP family is defined by a shared catalytic domain, a conserved structural feature that makes selective inhibition difficult. Guided by work in the kinase field (Bishop et al. 2000) we have previously employed chemical-genetic strategies to create orthogonal mutant-inhibitor pairs (the ‘bump-hole’ strategy) (Morgan et al. 2015; Carter-OConnell et al. 2014). To extrapolate this strategy to wild-type enzymes we inspected the highly-conserved catalytic domains of PARPs for any sequence variation that would suggest a unique sub-pocket (an endogenous ‘hole’) to target. This strategy led us to the discovery of a hydrophobic sub pocket in HY $\Phi$ -PARPs that we focused on to design a pan-HY $\Phi$ -PARP inhibitor (ITK6, Chapter 3) and from there a selective and potent PARP11 inhibitor (ITK7, Chapter 3) (Kirby, Kojic, et al. 2018).

In our efforts to design a selective PARP4 inhibitor we again leveraged this strategy by inspecting the catalytic domain sequences of

the active PARPs. We found that PARP4 contains a unique active site threonine at position 903 (human PARP1 numbering) (Figure 4-1A). Intriguingly, at this position in the other PARPs there are the significantly larger residues, for example lysine and tyrosine, or the slightly larger non-polar residues leucine and isoleucine. This led us to hypothesize that there may be a small ‘hole’ in the PARP4 active site at this position that is not present in any other PARPs that could be targeted by some chemical groups (Figure 4-1B). Unfortunately, there are no available crystal structures of PARP4 to confirm this hypothesis by direct inspection.



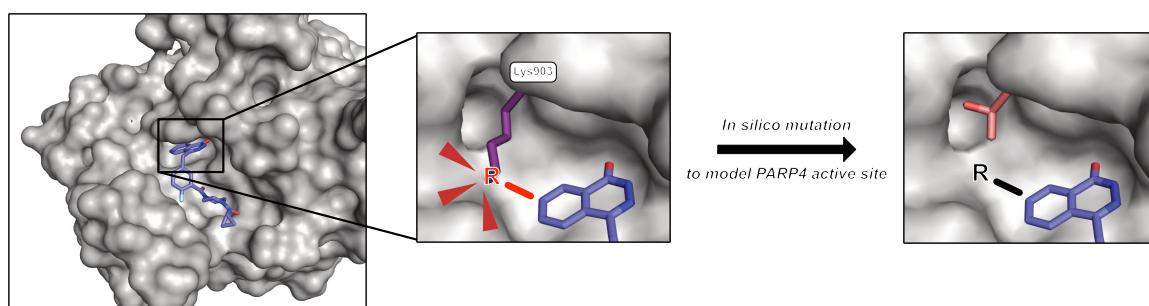
**Figure 4-1** A unique threonine in the PARP4 active site may leave space for an inhibitor

(A) Structure-based sequence alignment of the PARPs, with position 903 (human PARP1 numbering) highlighted in pink and PARP4 sequence highlighted in yellow. While all other PARPs have a bulky amino acid such as lysine or tyrosine at position 903, PARP4 has a comparatively small threonine residue at this position (highlighted in orange).

(B) Hypothetical model showing how an inhibitor bound to PARP4 could project into this space, but would clash with the larger residues present in other PARPs and lead to selective binding only to PARP4.

### Structural Extrapolation Suggests Space for a Unique Inhibitor Interaction with PARP4

To compensate for the lack of structure to guide our inhibitor design, we modeled the presumptive configuration of the PARP4 active site by “mutating” a crystal structure of PARP1 (PDB: 5DS3) bound to the PARP inhibitor olaparib *in silico* (Figure 4-2).

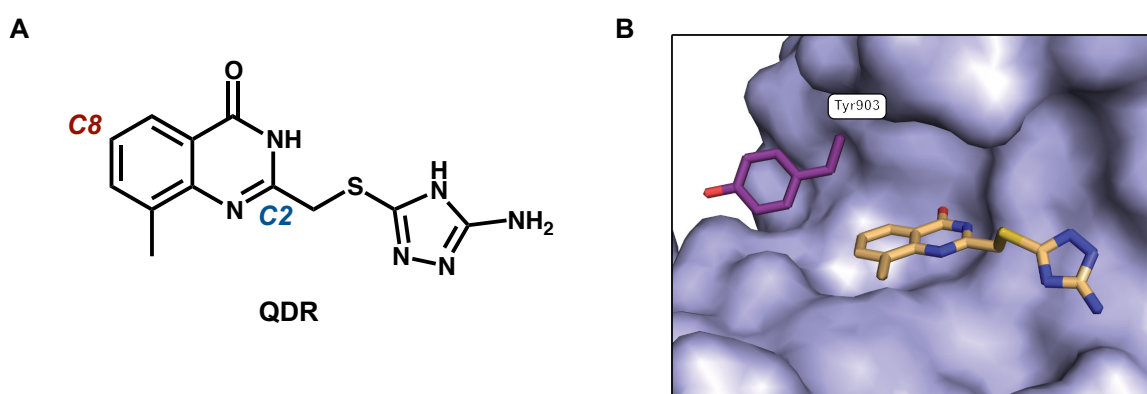


**Figure 4-2** Comparison of a PARP1 crystal structure (PDB: 5DS3) with a model of the PARP4 active site shows how a substituted inhibitor would clash with bulkier residues, such as Lys903 in PARP1, but fill the space created by the smaller Thr903 in PARP4.

We choose to base our inhibitors off of a quinazolin-4(3H)-one scaffold previously described as a non-selective PARP inhibitor, QDR (Figure 4-3A) (Wahlberg et al. 2012). A crystal structure of QDR in complex with PARP14 (PDB: 3SMI) shows the C8 position of QDR most closely



abuts the 903 position (a tyrosine in PARP14) (Figure 4-3B), leading us to target that position on the scaffold for modification. For synthetic ease we substituted a pyrimidine ring for the triazole at the C2 position of QDR. The pyrimidine substituted compound, here termed AEP01 (Figure 4-4A), was described in the same study as QDR and the two compounds were reported to have comparable activity (Wahlberg et al. 2012).

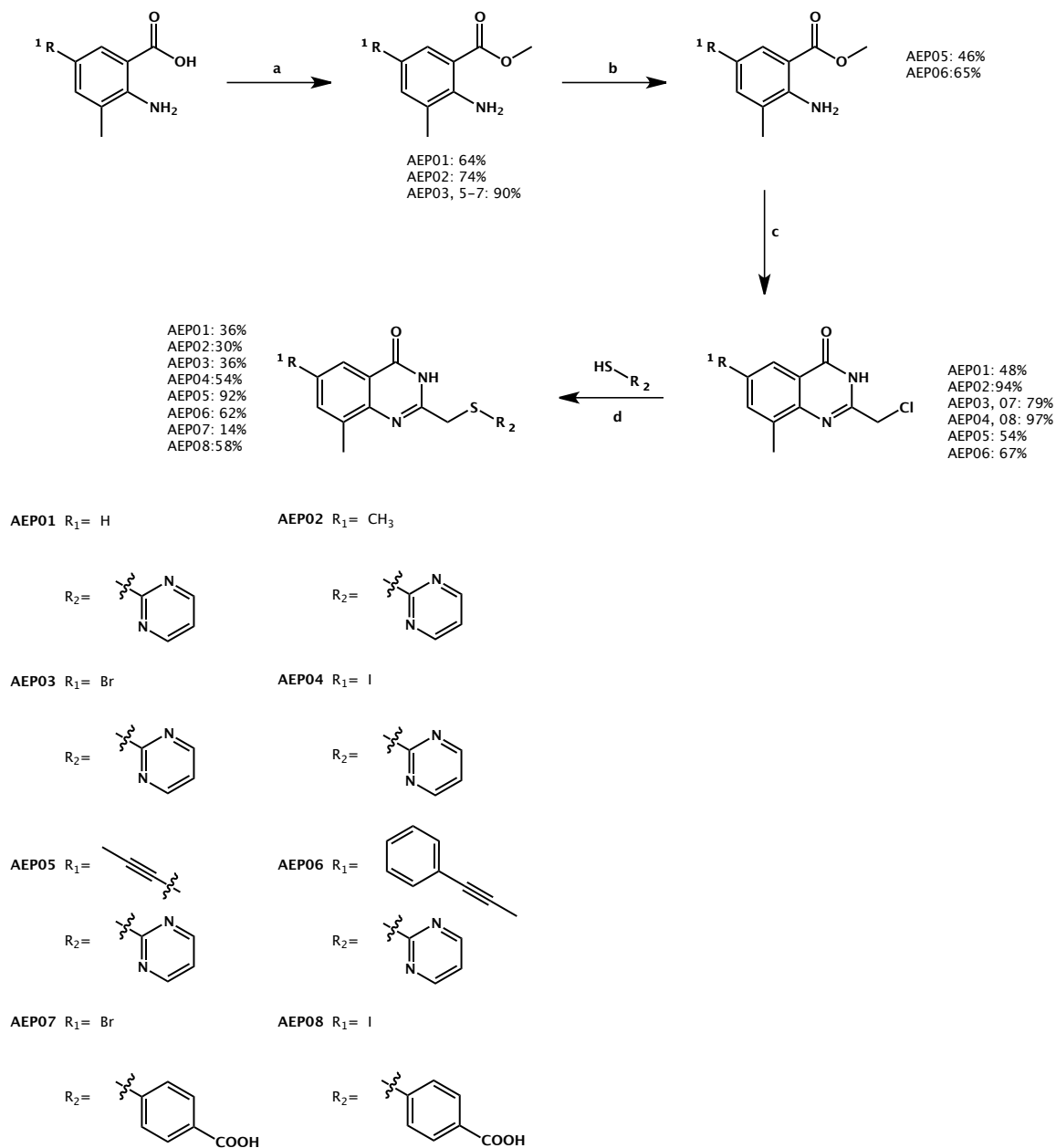


**Figure 4-3** A non-selective PARP inhibitor provides a starting point for PARP4 inhibitor design

- (A) Structure of QDR, a non-selective PARP inhibitor previously identified in a small molecule screen.
- (B) A crystal structure of QDR in complex with the catalytic domain of PARP14 (PDB: 3SMI)

### ***In Vitro* Testing Confirms PARP4 Specificity**

Initially, we synthesized a brief series of compounds with progressively bulkier groups at the C8 position of QDR (**Scheme 4-1 and Scheme 4-2**, Figure 4-4A). We then screened these compounds against the majority of the PARP family using our previously described 96-well PARP Inhibitor Screening Assay (PISA) (Chapter 2, Kirby, Morgan, et al. 2018; Kirby, Kojic, et al. 2018). Because PARP1 is the most highly expressed and active of the PARPs, much of our SAR was aimed at generating selectivity for PARP4 over PARP1.



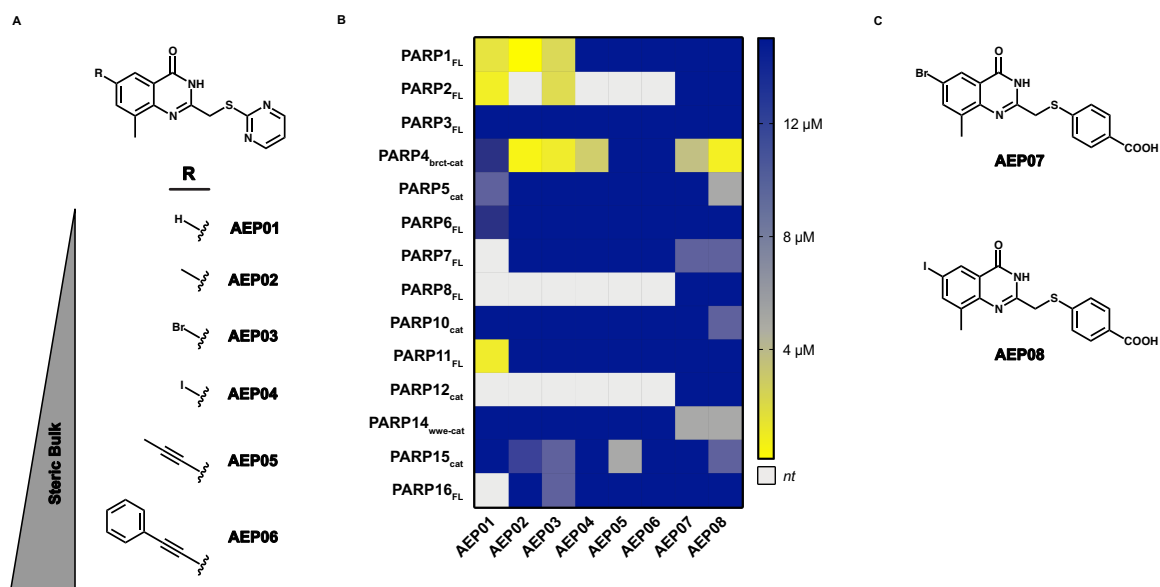
**Scheme 4-1** Synthesis of C8 substituted QDR analogues

a)  $\text{H}_2\text{SO}_4$ , MeOH,  $90^\circ\text{C}$ , 18 h; b) *Stille coupling*; c) chloroacetonitrile, 4 M HCl (1,4-dioxane),  $110^\circ\text{C}$ , 8 h;; d) NaH, DMF, RT, 1 h.

We found that the compound without C8 substituent, AEP01, potently inhibited PARP1 and PARP11 ( $\text{IC}_{50} = 1.5 \mu\text{M}$  and  $1 \mu\text{M}$

respectively) (Figure 4-4, Appendix B). Surprisingly, a methyl substituent at the C8 position (AEP02) increased potency for PARP1 beyond that of PARP4 ( $IC_{50}$  0.15  $\mu$ M and 0.5  $\mu$ M respectively). Meanwhile, halogen substitutions of a similar size to the methyl group (a bromo- on AEP03 and an iodo- on AEP04) reduced potency for PARP1 slightly while maintaining reasonable potency for PARP4 (Figure 4-4, Appendix B). This suggested an intriguing stereo-electronic component to PARP4 vs PARP1 binding for future exploration. Neither the propynyl nor propynyl-benzyl modifications at C8 showed potency for PARP4, but the benzyl substitution (AEP05) was found to be equipotent for PARP4 and PARP15 ( $IC_{50}$  = 5  $\mu$ M). We found that all substituents larger than a hydrogen at the C8 position decreased inhibition of any other PARPs tested up to at least 10  $\mu$ M, with the exception of the C8 benzyl substituent on AEP05.

Based on these results we can conclude that small halogenated or hydrophobic modifications at C8 yield selective inhibition of PARP4 over other PARPs including PARP1.



**Figure 4-4** Inhibitor series exploring modifications at the C8 position of the QDR scaffold

(A) AEP compounds with C8 substituents from least to greatest steric bulk

(B) Heat map showing *in vitro* AEP01-AEP08 screening results against PARP enzymes.

To improve the potency of our lead compounds we exchanged the pyrimidine ring at the C2 position of the QDR scaffold (Figure 4-3A) for a *para*-benzoic acid that we have previously found to improve potency for QDR-based inhibitors against some MARYlating PARPs. This modification reduce potency for PARP1/2 in some instances (Kirby, et al. 2018). We selected AEP03 and AEP04 for this modification to test if changing the group at C2 would affect the 1) selectivity of AEP03 for PARP1/2 vs PARP4, and 2) improve the potency of AEP04 for PARP4. These compounds were synthesized and screened across

the family (Figure 4-4B,C, Appendix B). The *para*-benzoic acid did lead to selectivity over PARP1/2 for the bromo- substituted analogue (AEP03  $IC_{50}$ =2.7  $\mu$ M for PARP1, 2.0  $\mu$ M for PARP2; AEP07 no inhibition of PARP1 up to 30  $\mu$ M, no inhibition of PARP2 up to 10  $\mu$ M). Unfortunately, the *para*-benzoic acid also decreased the potency for PARP4 slightly (AEP03  $IC_{50}$ =0.75  $\mu$ M, AEP07  $IC_{50}$ =1.9  $\mu$ M). However, in the case of the C8 iodo- substitution the *para*-benzoic acid increased potency for PARP4 from 2.8  $\mu$ M (AEP04) to 0.8  $\mu$ M (AEP08). Moreover, AEP08 did not inhibit PARP1 at concentrations up to 30  $\mu$ M or PARP2 at concentrations up to 10  $\mu$ M. These results bear out our hypothesis that substituents at the C8 position of the QDR scaffold could confer specificity towards PARP4, and that the *para*-benzoic acid would further modulate potency and selectivity, particularly with respect to PARP1/2. Indeed, AEP08 does not inhibit any of the other active PARPs up to concentrations of 5  $\mu$ M (Appendix B).

Using structure guided design and *in silico* modeling we have designed a selective PARP4 inhibitor with sub-micromolar potency. Structure based sequence alignment of the active PARP family led us to infer that the unique threonine in the PARP4 active site may create a space that could be exploited to design a selective PARP4 inhibitor. Based on our *in silico* model we identified the C8 position on a non-

selective quinazolinone for substitutions of increasing size. *In vitro* screening confirmed that specific substitutions at that position lead to selectivity across the PARP family, and minor modifications to the overall structure quickly led to AEP08, the first selective PARP4 inhibitor with sub-micromolar potency. Future studies will use this inhibitor to investigate the function of PARP4 in cells.

PARP4 has been implicated in a range of biological functions and pathologies, including host-viral interactions (Daugherty et al. 2014), neurodegenerative diseases (Mata et al. 2017), cancer (Ikeda et al. 2016; Y.-S. Ma et al. 2018), and actin regulation in the brain (De Maio et al. 2013). A selective PARP4 inhibitor will be indispensable for unraveling the role of this enzyme.

## Methods

### Cloning

cDNA encoding full length human PARP1, full length human PARP2, full length human, human brct-catalytic domain PARP4, human PARP5 catalytic domain, human PARP10 catalytic domain, full length human PARP11, human PARP12 catalytic domain, human PARP14 wwe-catalytic domain, human PARP15 catalytic domain, full length human

PARP16, and SRPK2 were obtained as previously described (Carter-OConnell et al. 2014; Morgan & Cohen 2015; Kirby, Kojic, et al. 2018).

Individual cDNA constructs encoding full length human PARP6, full length human PARP7, and full length human PARP8 were obtained using gBlock gene fragments containing the PARP11 gene as template (IDT) and the following primers (IDT) for subsequent Gibson assembly cloning:

PARP6<sub>FL</sub>:

- *Forward*: TACTTCCAATCCAATGCAGACATCAAAGGCC  
AGTTCTGGA
- *Reverse*: TTATCCACTTCCAATGTTATTAGTTTGT  
GTAAACCTGAGTTCCGATCA

PARP7<sub>FL</sub>:

- *Forward*: TACTTCCAATCCAATGCAGAAACCACCG  
CCGAACCTGAG
- *Reverse*: TTATCCACTTCCAATGTTATTAAATGGAAA  
CAGTGTTACTGACTTC

PARP8<sub>FL</sub>:

- *Forward*: TACTTCCAATCCAATGCAGGGATGTGTTCAA  
GGCAAGAGAG
- *Reverse*: TTATCCACTTCCAATGTTATTAAACCAGTCGCA  
GTCTGATTACCAATC



The amplified fragments were gel purified and cloned into a pET-His-SUMO-TEV LIC cloning vector (1B), a gift from Scott Gradia (Addgene plasmid #29653) by an isothermal assembly protocol using the Gibson assembly mix (NEB). The human PARP3 plasmid was obtained from DNAsu.

### **Expression and Purification of Proteins**

The following protein were expressed and purified as previously described: N-terminus hexahistidine (His6) human PARP1, PARP2, PARP3, PARP5<sub>bcat</sub>, PARP10<sub>cat</sub>, PARP14<sub>wwe-cat</sub>, PARP15<sub>cat</sub>, SRPK2; pET-His-SUMO-TEV human PARP4, PARP6, PARP11, and PARP16 (Carter-OConnell et al. 2014; Morgan & Cohen 2015; Kirby, Kojic, et al. 2018).

pET-His6-SUMO-TEV-PARP6<sub>FL</sub>, pET-His6-SUMO-TEV-PARP7<sub>FL</sub>, or pET-His6-SUMO-TEV-PARP8<sub>FL</sub> plasmids was transformed into Escherichia coli BL21 (DE3) competent cells (Millipore) and grown on an LB agar plate with kanamycin (50 mg/mL) and chloramphenicol (34 mg/mL) overnight at 37°C. A swath of cells was inoculated into a 50 mL starter culture of LB media with kanamycin (50 mg/mL) and chloramphenicol (34 mg/mL) at 225 rpm, 37°C overnight. For each protein of interest 1-2 liters of terrific broth (TB) media (12 g bacto tryptone, 24 g yeast extract, 0.4% glycerol, 17 mM KH<sub>2</sub>PO<sub>4</sub>, 72 mM K<sub>2</sub>HPO<sub>4</sub>, 1% glucose, 50 µg/mL kanamycin, 34 µg/mL

chloramphenicol) was inoculated with the starter culture and grown to an OD = 0.8-1.0 at 37°C, 225 rpm. Isopropyl- $\beta$ -thiogalactoside, IPTG (Sigma-Aldrich) was added to 0.4 mM to induce protein expression for 18-24 hrs at 16°C, 225 rpm. Cells were harvested by centrifuging, resuspended in lysis buffer (20 mM HEPES, pH 7.5, 1 mM  $\beta$ -mercaptoethanol, 1 mM benzamidine, 0.2% NP-40, 0.2% TWEEN-20, 500 mM NaCl, 1 mM phenylmethylsulfonyl fluoride (PMSF), 8.3 mg/L DNase I (Roche)) and lysed by sonication at 0°C (Branson sonifier 450). Lysates were incubated with pre-washed Ni-NTA agarose resin (50% slurry, Qiagen) with end-over-end rotation at 4°C for 1 h. Following extensive washing with buffer B1+20 (20 mM HEPES, pH 7.5, 1 mM  $\beta$ -Me, 1 mM PMSF, 1 mM benzamidine, 500 mM NaCl, 20 mM imidazole). protein was eluted in four fractions of B1 containing 100-400 mM imidazole. Fractions were analyzed by SDS page gel stained with coomassie blue, or western blot visualized with ponceau stain. Fractions found to contain the desired protein as judged by molecular weight were dialyzed to 50 mM Tris-HCl, pH 7.5, 0.1 mM EDTA, 1 mM  $\beta$ -Me, 0.4 M NaCl at 4°C. Protein concentration was determined from a standard curve of His6-PARP1<sub>FL</sub> of a known concentration on western blot visualized with a monoclonal anti-His antibody (Proteintech). Proteins were obtained in >90% purity.

### SRPK2 Plate Assays

96-well nickel coated plate (Pierce) was incubated with 350 ng His6-tagged SRPK2 in hB (50 mM HEPES pH 7.5, 100 mM NaCl, 4 mM MgCl<sub>2</sub>, 0.2 mM TCEP) for 60 min at RT. After extensively washing the plate, 4-400 ng (2x) of recombinant PARP enzyme in hB were added to individual wells of the 96-well plate. PARP<sub>3FL</sub> was activated by Dnick 5'P as described previously (Langelier et al. 2014). Varying concentrations of each inhibitor (0-200  $\mu$ M) were pre-incubated with 200  $\mu$ M 6-a-NAD<sup>+</sup> (2x) in hB at room temperature for 5-10 min, then added to the plate. This reaction proceeded for 60 min at 30°C, the plate was then washed three times with 1X PBST (1X PBS, 0.01% Tween-20), once with 1X PBS, then click conjugation was performed in CB (100  $\mu$ M biotin-PEG3-azide, 100  $\mu$ M Tris[(1-benzyl-1H-1,2,3-triazol-4-yl)methyl]amine (TBTA, Sigma), 1 mM CuSO<sub>4</sub>, 1 mM TCEP, 1X PBS) for 30 min at RT. The plate was then washed three times with 1X PBST, once with 1X PBS, and then blocked with 1% milk (Carnation) in 1X PBST for 30 min at RT. The plate was then washed three times with 1X PBST, once with 1X PBS, and then incubated with Strep-HRP (300 ng/ $\mu$ L BSA, 0.05 ng/ $\mu$ L Strep-HRP, 1X PBS) for 30 min at RT. The plate was then washed three times with 1X PBST, once with 1X PBS, and then developed

with QuantaRed™ Enhanced Chemifluorescent HRP Substrate (Thermo) for 30-45 s before quenching with Quanta Red Stop Solution. Fluorescence for each sample and control was read at excitation 570 nM and emission 600 nM with a Spectra Max i3 (Molecular Devices) within five min of development. Inhibitor dose response curves were fit using linear regression in Prism 7 (GraphPad™ Software). The mean IC<sub>50</sub> for each compound was calculated from at least three independent assays.

## Chemistry

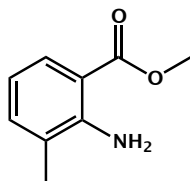
**General:** <sup>1</sup>H NMR spectra were recorded on a Bruker DPX spectrometer at 400 MHz. Chemical shifts are reported as parts per million (ppm) downfield from an internal tetramethylsilane standard or solvent references. For air- and water-sensitive reactions, glassware was flame- or oven-dried prior to use and reactions were performed under argon. Dimethylformamide was dried using the solvent purification system manufactured by Glass Contour, Inc. (Laguna Beach, CA). All other solvents were of ACS chemical grade (Fisher Scientific) and used without further purification unless otherwise indicated. Commercially available starting reagents were used without further purification. Analytical thin-layer chromatography was performed with silica gel 60 F254 glass plates (SiliCycle). Flash column

chromatography was conducted self-packed columns containing 200-400 mesh silica gel (SiliCycle) on a Combiflash Companion purification system (Teledyne ISCO). High performance liquid chromatography (HPLC) was performed on a Varian Prostar 210 (Agilent) using Polaris 5 C18-A columns (Analytical: 150 x 4.6 mm, 3  $\mu$ m; Preparative: 150 x 21.2 mm, 5  $\mu$ m) (Agilent). All final products were  $\geq 95\%$  pure as assessed by analytical HPLC (mobile phase A: 0.1% formic acid (aq), mobile phase B: 0.1% formic acid in acetonitrile; flow rate = 1.0 mL/min; conditions: pre-run A = 50% B = 50%, 7 min A = 5% B = 95%, 12 min A = 5% B = 95%, 13 min A = 70% B = 30%; UV-Vis detection:  $\lambda_1$  = 254 nm,  $\lambda_2$  = 220 nm. Retention times (Rt) refer to UV = 254 nm. Novel compounds indicated, for literature reports of synthesized compounds see Appendix F.

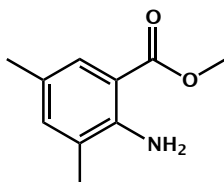
#### **General procedure for synthesis of benzoates:**

To a solution of the appropriate benzoic acid in methanol was added concentrated sulfuric acid (1% v/v) at RT. The reaction mixture was refluxed at 90°C for 18 h, monitored by TLC analysis (20% EtOAc in hexanes). Once complete the reaction mixture was poured over saturated aqueous sodium bicarbonate and separated with EtOAc. The aqueous layer was extracted with EtOAc (3x). The combined organic

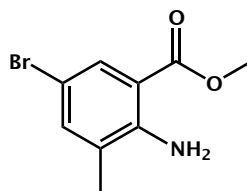
layers were washed with sat. aqueous sodium bicarbonate (1x), water (1x), and brine (1x), then dried over sodium sulfate and concentrated in vacuo to yield desired benzoate.



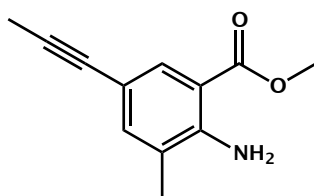
*Methyl 2-amino-3-methylbenzoate*: from 2-amino-3-methylbenzoic acid (500 mg, 3.3 mmol); yield 348 mg (64%) white solids. <sup>1</sup>H NMR (400 MHz, Chloroform-d)  $\delta$  7.77 (ddd,  $J$  = 8.1, 1.6, 0.6 Hz, 1H), 7.19 (ddq,  $J$  = 7.2, 1.7, 0.8 Hz, 1H), 6.59 (dd,  $J$  = 8.1, 7.2 Hz, 1H), 5.83 (s, 2H), 3.87 (s, 3H), 2.17 (d,  $J$  = 0.7 Hz, 3H).



*Methyl 2-amino-3,5-dimethylbenzoate*: from 2-amino-3,5-dimethylbenzoic acid (250 mg, 1.52 mmol); yield 200 mg (74%) white solids. <sup>1</sup>H NMR (400 MHz, DMSO-d<sub>6</sub>)  $\delta$  7.43 (d,  $J$  = 2.2 Hz, 1H), 7.04 (d,  $J$  = 2.2 Hz, 1H), 6.31 (s, 2H), 3.77 (s, 3H), 2.11 (dt,  $J$  = 20.3, 0.7 Hz, 6H).

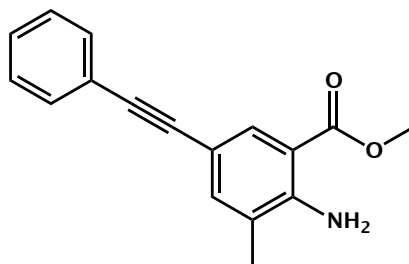


*Methyl 2-amino-5-bromo-3-methylbenzoate*: from 2-amino-5-bromo-3-methylbenzoic acid (50 mg, 0.22 mmol); yield 42.8 mg (90%) white solids. <sup>1</sup>H NMR (400 MHz, DMSO-d<sub>6</sub>) δ 7.87 (d, J = 2.2 Hz, 1H), 7.48 (dd, J = 2.1, 1.0 Hz, 1H), 6.70 – 6.62 (m, 2H), 3.79 (s, 3H), 2.09 (s, 3H).



*Methyl 2-amino-3-methyl-5-(prop-1-yn-1-yl)benzoate (novel compound)*: methyl 2-amino-5-bromo-3-methylbenzoate (200 mg, 0.8 mmol) was dissolved in anhydrous toluene and concentrated (3x 4 mL) then dried under vacuum for 1 h. The flask was evacuated and refilled with argon gas (3x), then anhydrous toluene (8 mL) was added via syringe and the solution degassed with argon 10 min. Tributyl(1-propynyl)tin (0.3 mL, 0.88 mmol) was added via syringe and the solution degassed 5 min. Palladium tetrakis (95 mg, 0.08 mmol) was added quickly and the solution degassed with argon for 3 min. The reaction mixture was refluxed at 115°C for 2.5 h. TLC analysis (10% EtOAc in hexanes)

showed consumption of starting benzoate. The reaction was cooled to RT and concentrated in vacuo. The crude residue was purified via a Combiflash Companion system (4 g Redisep silica column; 0-20% EtOAc in hexanes). Product was isolated as a crude yellow oil and taken on without further purification: 75 mg (46%). <sup>1</sup>H NMR (400 MHz, Chloroform-*d*)  $\delta$  7.86 (s, 1H), 7.22 (s, 1H), 5.93 (s, 3H), 3.86 (s, 3H), 2.13 (s, 3H), 2.02 (s, 3H).



*Methyl 2-amino-3-methyl-5-(phenylethynyl)benzoate (novel compound):*

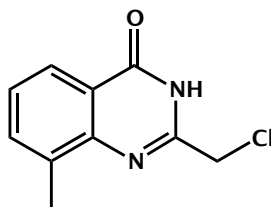
methyl 2-amino-5-bromo-3-methylbenzoate (150 mg, 0.6 mmol) was dissolved in anhydrous toluene and concentrated (3x 4 mL) then dried under vacuum for 1 h. The flask was evacuated and refilled with argon gas (3x), then anhydrous toluene (8 mL) was added via syringe and the solution degassed with argon 10 min.

tributyl(phenylethynyl)stannane (0.23 mL, 0.66 mmol) was added via syringe and the solution degassed 5 min. Palladium tetrakis (70 mg, 0.06 mmol) was added quickly and the solution degassed with argon for 3 min. The reaction mixture was refluxed at 115°C for 3 h. TLC

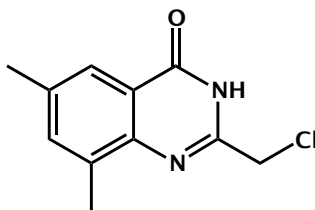


analysis (10% EtOAc in hexanes) showed consumption of starting benzoate. The reaction was cooled to RT and concentrated in vacuo. The crude residue was purified via a Combiflash Companion system (4 g Redisep silica column; 0-20% EtOAc in hexanes). Product was isolated as an orange oil: 100 mg (65%). <sup>1</sup>H NMR (400 MHz, Chloroform-d)  $\delta$  8.02 (d,  $J$  = 2.0 Hz, 1H), 7.49 (dd,  $J$  = 8.0, 1.7 Hz, 2H), 7.37 (s, 1H), 7.34 – 7.31 (m, 3H), 6.05 (s, 2H), 3.89 (s, 3H), 2.18 (d,  $J$  = 0.7 Hz, 3H).

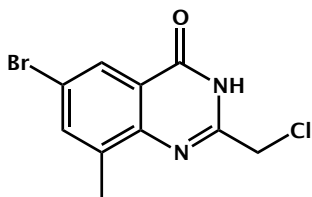
**General procedure for synthesis of quinazolin-4(3H)-ones:** The appropriate benzoate was added to a flame-dried flask and dissolved in 4 M HCl (1,4-dioxane) under argon. To this solution was added chloroacetonitrile (3 eqv.), and the reaction mixture was refluxed under argon at 125°C overnight. Once TLC analysis revealed consumption of the starting benzoate the reaction was cooled to RT and poured over cold sat. Aqueous sodium bicarbonate and left to stand at 4°C. The desired quinazolin-4(3H)-one readily precipitated and was collected by vacuum filtration.



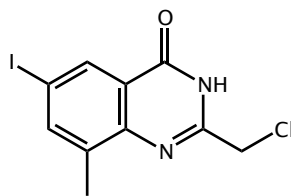
*2-(Chloromethyl)-8-methylquinazolin-4(3H)-one*: from methyl 2-amino-3-methylbenzoate (250 mg, 1.52 mmol); yield 210 mg (48%) tan solids; <sup>1</sup>H NMR (400 MHz, DMSO-d<sub>6</sub>) δ 12.57 (s, 1H), 7.97 (d, J = 7.9 Hz, 1H), 7.70 (d, J = 7.5 Hz, 1H), 7.44 (t, J = 7.6 Hz, 1H), 4.56 (d, J = 1.3 Hz, 2H), 2.53 (d, J = 9.2 Hz, 3H).



*2-(Chloromethyl)-6,8-dimethylquinazolin-4(3H)-one*: from methyl 2-amino-3,5-dimethylbenzoate (100 mg, 0.6 mmol); yield 125 mg (94%) tan solid. <sup>1</sup>H NMR (400 MHz, DMSO-d<sub>6</sub>) δ 12.49 (s, 1H), 7.76 (d, J = 2.1 Hz, 1H), 7.54 (d, J = 2.1 Hz, 1H), 4.55 (s, 2H), 2.40 (s, 3H).

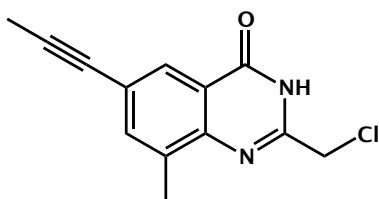


*6-Bromo-2-(chloromethyl)-8-methylquinazolin-4(3H)-one*: from methyl 2-amino-5-bromo-3-methylbenzoate (50 mg, 0.22 mmol); yield 50 mg (79%) tan solid; <sup>1</sup>H NMR (400 MHz, Chloroform-d) δ 9.80 (s, 1H), 8.26 (d, J = 2.3 Hz, 1H), 7.75 – 7.72 (m, 1H), 4.58 (s, 2H), 2.57 (s, 3H).



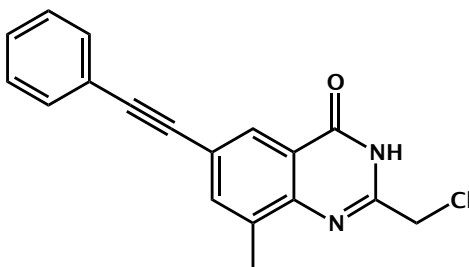
*2-(Chloromethyl)-6-iodo-8-methylquinazolin-4(3H)-one (novel compound):*

from methyl 2-amino-5-iodo-3-methylbenzoate (250 mg, 0.85 mmol); yield 275 mg (97%) tan solids. <sup>1</sup>H NMR (400 MHz, DMSO-d<sub>6</sub>) δ 12.75 (s, 1H), 8.23 (d, J = 2.1 Hz, 1H), 8.05 (d, J = 2.1 Hz, 1H), 4.55 (s, 2H), 2.46 (s, 3H).



*2-(Chloromethyl)-8-methyl-6-(prop-1-yn-1-yl)quinazolin-4(3H)-one (novel*

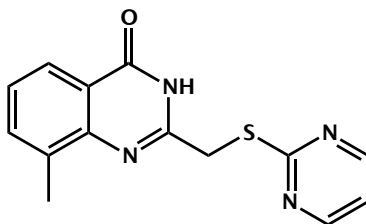
*compound):* from methyl 2-amino-3-methyl-5-(prop-1-yn-1-yl)benzoate (30 mg, 0.15 mmol); yield 20 mg (54%) tan solids. Taken on crude.



*2-(Chloromethyl)-8-methyl-6-(phenylethynyl)quinazolin-4(3H)-one (novel compound)*: from methyl 2-amino-3-methyl-5-(phenylethynyl)benzoate (100 mg, 0.4 mmol) yellow oil; yield 80 mg (67%). Taken on crude.

**General procedure for synthesis of ((pyrimidin-2-ylthio)methyl)quinazolin-4(3H)-ones:**

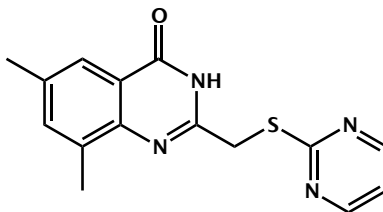
The appropriate thiol (2 eqv.) and sodium hydride (2 eqv.) were dissolved in anhydrous DMF and stirred at RT for 20 min. The appropriate quinazolin-4(3H)-one was added as a solid and the reaction mixture stirred at RT for 20 min. Once complete by TLC analysis (100% EtOAc) the reaction was poured over water, isolated, and purified as indicated.



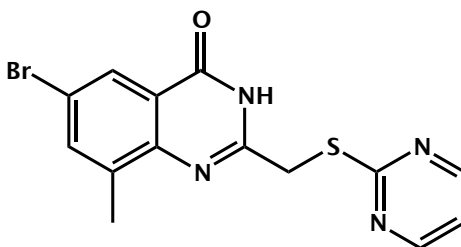
***8-Methyl-2-((pyrimidin-2-ylthio)methyl)quinazolin-4(3H)-one, AEPOI:***

From 2-(chloromethyl)-8-methylquinazolin-4(3H)-one (112 mg, 0.54 mmol); reaction was concentrated in vacuo and product recovered as a white solid; yield 55.3 mg (36%); <sup>1</sup>H NMR (400 MHz,

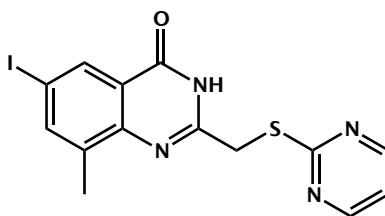
DMSO-d<sub>6</sub>)  $\delta$  12.46 (s, 1H), 8.70 (d,  $J$  = 4.9 Hz, 2H), 7.98 – 7.94 (m, 1H), 7.70 – 7.64 (m, 1H), 7.40 (t,  $J$  = 7.6 Hz, 1H), 7.29 (t,  $J$  = 4.9 Hz, 1H), 4.48 (s, 2H), 2.48 (s, 3H); Rt: 5.81 min. HRMS  $m/z$  [M+H]<sup>+</sup> for C<sub>14</sub>H<sub>13</sub>N<sub>4</sub>OS: 285.08046, found 285.08128.



*6,8-Dimethyl-2-((pyrimidin-2-ylthio)methyl)quinazolin-4(3H)-one* (novel compound), **AEPO2**: from 2-(chloromethyl)-6,8-dimethylquinazolin-4(3H)-one (25 mg, 0.11 mmol); product precipitated as fine white solids in water; yield 10 mg (30%). <sup>1</sup>H NMR (400 MHz, DMSO-d<sub>6</sub>)  $\delta$  12.33 (s, 1H), 8.74 – 8.60 (m, 2H), 7.72 (s, 1H), 7.47 (s, 1H), 7.26 (d,  $J$  = 5.1 Hz, 1H), 4.42 (s, 2H), 2.39 (d,  $J$  = 14.1 Hz, 6H). MS  $m/z$  [M+H]<sup>+</sup> for C<sub>14</sub>H<sub>13</sub>N<sub>4</sub>OS: 299.0, found 299.0. Rt = 4.94 min. HRMS  $m/z$  [M+H]<sup>+</sup> for C<sub>15</sub>H<sub>14</sub>N<sub>4</sub>OS: 299.09611, found 299.09897..



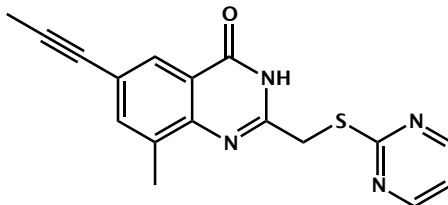
*6-Bromo-8-methyl-2-((pyrimidin-2-ylthio)methyl)quinazolin-4(3H)-one* (novel compound), **AEPO3**: from 6-bromo-2-(chloromethyl)-8-methylquinazolin-4(3H)-one (25 mg, 0.09 mmol); product precipitated as fine white solids in water; yield 12 mg (36%). <sup>1</sup>H NMR (400 MHz, DMSO-d<sub>6</sub>) δ 12.61 (s, 1H), 8.66 (d, J = 4.8 Hz, 2H), 8.19 (d, J = 2.1 Hz, 1H), 7.98 (s, 1H), 7.25 (t, J = 4.9 Hz, 1H), 4.42 (s, 2H), 2.40 (s, 3H). MS m/z [M+H]<sup>+</sup> for C<sub>14</sub>H<sub>11</sub>BrN<sub>4</sub>OS: 362.9, 364.9, found 362.8, 364.8. Rt = 5.37 min. HRMS m/z [M+H]<sup>+</sup> for C<sub>14</sub>H<sub>11</sub>BrN<sub>4</sub>OS: 364.98895, found 364.9917.



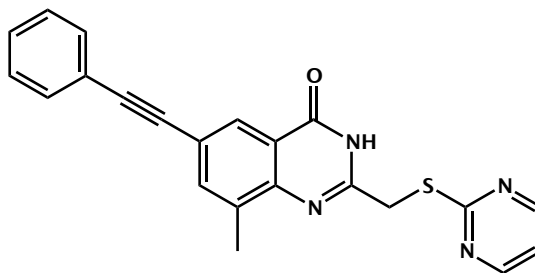
*6-Iodo-8-methyl-2-((pyrimidin-2-ylthio)methyl)quinazolin-4(3H)-one* (novel compound), **AEPO4**: from 2-(chloromethyl)-6-iodo-8-methylquinazolin-4(3H)-one (25 mg, 0.07 mmol) product precipitated as fine white solids in water; yield 15 mg (54%). <sup>1</sup>H NMR (400 MHz, DMSO-d<sub>6</sub>) δ 12.60 (s, 1H), 8.65 (d, J = 4.9 Hz, 2H), 8.19 (d, J = 2.1 Hz, 1H), 7.98 (s, 1H), 7.25 (t, J = 4.9 Hz, 1H), 4.42 (s, 2H), 2.39 (s, 3H). MS m/z [M-H]<sup>-</sup> for C<sub>14</sub>H<sub>11</sub>IIN<sub>4</sub>OS: 408.9, found

408.5. Rt = 5.57 min. HRMS m/z [M+H]<sup>+</sup> for C<sub>14</sub>H<sub>11</sub>N<sub>4</sub>OS:

410.97710, found 410.97996.

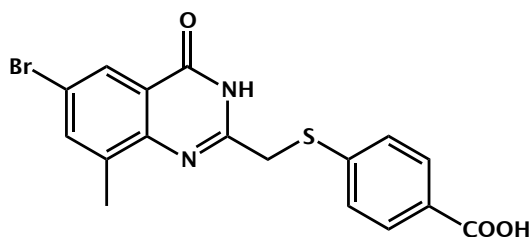


*8-Methyl-6-(prop-1-yn-1-yl)-2-((pyrimidin-2-ylthio)methyl)quinazolin-4(3H)-one (novel compound), AEPO5:* from 2-(chloromethyl)-8-methyl-6-(prop-1-yn-1-yl)quinazolin-4(3H)-one (30 mg, 0.08 mmol) ); product precipitated as fine white solids in water; yield 23 mg (92%). <sup>1</sup>H NMR (400 MHz, DMSO-d<sub>6</sub>) δ 8.70 – 8.63 (m, 2H), 7.84 (s, 1H), 7.61 (s, 1H), 7.25 (t, J = 4.8 Hz, 1H), 4.43 (d, J = 5.4 Hz, 2H), 2.40 (s, 3H), 2.07 (s, 3H). MS m/z [M-H]<sup>-</sup> for C<sub>17</sub>H<sub>14</sub>N<sub>4</sub>OS: 322.09, found 320.6. Rt = 5.17 min. HRMS m/z [M+H]<sup>+</sup> for C<sub>17</sub>H<sub>14</sub>N<sub>4</sub>OS: 323.09611, found 323.09896.



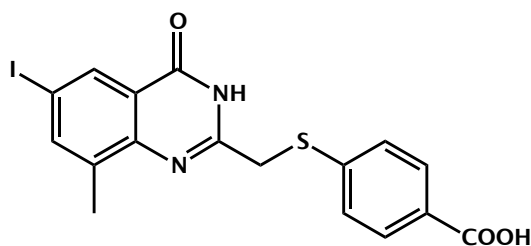
*8-Methyl-6-(phenylethynyl)-2-((pyrimidin-2-ylthio)methyl)quinazolin-4(3H)-one (novel compound), AEPO6:* from 2-(chloromethyl)-8-

methyl-6-(phenylethynyl)quinazolin-4(3H)-one (20 mg, 0.07 mmol); product precipitated as white solids in water; yield 18 mg (62%). <sup>1</sup>H NMR (400 MHz, DMSO-d<sub>6</sub>) δ 12.61 (s, 1H), 8.67 (d, *J* = 4.9 Hz, 2H), 8.05 (s, 1H), 7.80 (s, 1H), 7.62 – 7.58 (m, 2H), 7.48 – 7.43 (m, 3H), 7.26 (t, *J* = 4.9 Hz, 1H), 4.46 (s, 2H), 2.45 (s, 3H). MS *m/z* [M+H]<sup>+</sup> for C<sub>22</sub>H<sub>16</sub>N<sub>4</sub>OS: 384.1, found 384.8. Rt = 7.41 min. HRMS *m/z* [M+H]<sup>+</sup> for C<sub>22</sub>H<sub>16</sub>N<sub>4</sub>OS: 385.11176, found 385.11469.



*4-(((6-Bromo-8-methyl-4-oxo-3,4-dihydroquinazolin-2-yl)methyl)thio)benzoic acid (novel compound), AEPO7*: from 6-bromo-2-(chloromethyl)-8-methylquinazolin-4(3H)-one (20 mg, 0.07 mmol); product precipitated as tan solids in water; yield 5 mg (14%). <sup>1</sup>H NMR (400 MHz, DMSO-*d*<sub>6</sub>) δ 12.94 (s, 1H), 8.18 (d, *J* = 2.1 Hz, 1H), 7.98 (d, *J* = 2.7 Hz, 1H), 7.88 – 7.81 (m, 2H), 7.62 (d, *J* = 8.5 Hz, 2H), 4.24 (s, 2H), 2.40 (s, 3H). Rt = 5.02 min. HRMS *m/z* [M+H]<sup>+</sup> for C<sub>17</sub>H<sub>13</sub>BrN<sub>2</sub>O<sub>3</sub>S: 406.98895, found 406.99078.





4-(((6-Iodo-8-methyl-4-oxo-3,4-dihydroquinazolin-2-yl)methyl)thio)benzoic acid (novel compound), **AEPO8**: from 2-(chloromethyl)-6-iodo-8-methylquinazolin-4(3H)-one (25 mg, 0.08 mmol) product precipitated as fine white solids in water; yield 15 mg (58%). <sup>1</sup>H NMR (400 MHz, DMSO-d<sub>6</sub>) δ 12.93 (s, 1H), 12.60 (s, 1H), 8.18 (d, J = 2.1 Hz, 1H), 7.98 (t, J = 1.4 Hz, 1H), 7.87 – 7.82 (m, 2H), 7.62 (d, J = 8.5 Hz, 2H), 4.24 (s, 2H), 2.40 (s, 3H). MS m/z [M-H]<sup>-</sup> for C<sub>17</sub>H<sub>13</sub>IN<sub>2</sub>O<sub>3</sub>S: 450.9, found 450.5. Rt = 4.79 min. HRMS m/z [M+H]<sup>+</sup> for C<sub>17</sub>H<sub>13</sub>IN<sub>2</sub>O<sub>3</sub>S: 452.97643, found 452.97873.

## Chapter 5: Covalent Inhibition of PARP16

Ilsa T. Kirby, Haihong Jin, Rory K. Morgan, Anke Vermehren-Schmaedick, Tangpo Yang, Jack Taunton, and Michael S. Cohen

This work was in collaboration with Dr. Haihong Jin who synthesized HJ-52, Dr. Rory K. Morgan who performed the *in vitro* validation of HJ-52, Dr. Anke Vermehren-Schmaedick who cloned GFP-PARP16 mutants, and Drs. Tangpo Yang and Jack Taunton of UCSF who developed and kindly provided the PARP16 occupancy probes ADC-4 and ADC-5. I performed all cellular studies using ADC-4.

## Abstract

Poly-ADP-ribose polymerases (PARPs1-16) are key regulators of diverse cellular functions and are implicated in a wide range of disease states. However, little is known about the function of the majority of PARP family members, particularly those that catalyze MARylation. PARP16 is a MARylating enzyme that has been reported to play a role in the unfolded protein response, but whether catalytic activity is required is unclear. Therefore we sought to develop a PARP16 inhibitor to more precisely study the role of PARP16 mediated ADP-ribosylation in the UPR. The UPR is a well-established signaling cascade activated in response to the accumulation of unfolded or misfolded proteins in the endoplasmic reticulum (ER) lumen.

Here we describe the development and cellular validation of an inhibitor that covalently binds to a non-conserved cysteine in the PARP16 active site through an acrylamide moiety. This compound (HJ-52) covalently binds to PARP16 in cells, but elicits no effect on the UPR as measured by PRKR-like endoplasmic reticulum kinase (PERK) phosphorylation or ATF-4 levels. These results suggest that PARP16 catalytic activity does not play a role in the UPR. Further studies will be required to understand if PARP16 effects the UPR.

## Introduction

Poly-ADP-ribose-polymerases (PARPs) are a family of post translationally modifying proteins that catalyze the transfer of ADP-ribose from Nicotinamide Adenine Dinucleotide (NAD<sup>+</sup>) onto their targets. There are 17 PARPs ubiquitously expressed in humans, defined by a shared NAD<sup>+</sup> binding domain (Pinto & Schöler 2015). ADP-ribosylation can occur as either the addition of ADP-ribose polymers (PARylation) catalyzed by a few well-studied PARPs (PARP1, 2, 5a, 5b), or as the addition of single monomers of ADP-ribose (MARylation), catalyzed by the majority of PARP enzymes (PARP3, 4, 6-8, 10-12, 14-16) (Hottiger et al. 2010). PARylating PARPs have been the subject of thorough investigation, while the MARylating PARPs remain largely uncharacterized, despite a growing body of evidence suggesting their biological importance.

PARP16 is a MARylating PARP that has been shown to regulate the unfolded protein response (UPR) by affecting the activity of key endoplasmic reticulum (ER) sensors (Jwa & Chang 2012). During the UPR expression of ER chaperone proteins increases to aid in protein folding and reduce protein aggregation, protein translation is temporarily inhibited to reduce protein transit through the ER, and membrane lipid synthesis is stimulated leading to an increase in ER

volume. Degradation of unfolded proteins is increased by activation of the endoplasmic reticulum-associated protein degradation (ERAD) pathway (Qi et al. 2011, Menear et al. 2008). The mammalian UPR is controlled primarily through three signaling pathways mediated by activation of the ER-resident transmembrane proteins: activation of the inositol-requiring enzyme-1 (IRE1) pathway increases expression of genes involved in the UPR; activation of the PKR-like ER kinase (PERK) pathway inhibits global mRNA translation, leading to a decrease in total protein synthesis and thus reducing the protein load at the ER; activating transcription factor-6 (ATF6) regulates several genes associated with the UPR and contributes to initiation of cytoprotective mechanisms to restore normal ER function (Qi et al. 2011, Menear et al. 2008). Previous work has reported that PARP16 is required for activation of PERK and IRE1 $\alpha$  during the UPR by ADP-ribosylation of these targets, leading to an increase in their kinase activities and the endonuclease activity of IRE1 $\alpha$  (Jwa & Chang 2012). ADP-ribosylation by PARP16 is sufficient to activate PERK and IRE1 $\alpha$  even in the absence of ER stress (Jwa & Chang 2012). PARP16 enzymatic activity is also upregulated during ER stress, and PARP16 knockdown has been shown to sensitize cells to ER stress and leads to an increase in cell death under ER stress (Jwa & Chang 2012).

PARP16 has also been shown to regulate be necessary and sufficient for the formation of Sec bodies and cell survival upon amino-acid starvation in *Drosophila* cells (Aguilera-Gomez et al. 2016; Aguilera-Gomez & Rabouille 2017). Under normal conditions, after proteins are synthesized in the ER they are packaged in vesicles that bud at ER exit sites (ERES). These vesicles are then transported to the Golgi apparatus where they are processed, sorted, and released. Inhibition of protein transport through the secretory pathway due to amino-acid starvation triggers remodeling of ERES and the formation of Sec bodies, a pro-survival stress assembly that sequesters proteins required for normal protein packaging and transport from the ER to the Golgi (Aguilera-Gomez & Rabouille 2017). One such protein, Sec16—a large hydrophilic scaffold protein—is ADP-ribosylated by PARP16 in *Drosophila* cells. It has been shown that PARP16 mediated ADP-ribosylation of Sec16 initiates the formation of Sec bodies under stress conditions, linking PARP16 enzymatic activity to stress assembly formation at the ER during metabolic stress (Aguilera-Gomez & Rabouille 2017).

The studies conducted by Chang et al. and Aguilera-Gomez et al. assessed the role of catalytic activity by mutating residues in the NAD<sup>+</sup> binding domain, H152Q and Y182A in human PARP16 (Jwa &

Chang 2012) and Y2221A in *Drosophila* PARP16 (Aguilera-Gomez & Rabouille 2017). These mutations most likely stop PARP16 enzymatic activity by changing the structure of the active site such that it precludes NAD<sup>+</sup> binding. This does not preclude the possibility that results from these mutants may be due to a loss of NAD<sup>+</sup> binding rather than a loss of ADP-ribosylation. The importance of NAD<sup>+</sup> to PARPs independent from enzymatic activity has not been well characterized in the field. Speculatively, the NAD<sup>+</sup> binding event may lead to structural shifts that influence availability of modifiable residues, activation or inhibition of functional domains outside the catalytic site, target recognition through shifts in the flexible D-loop (Chapter 1), all of which may have profound and unexplored impacts on activity, localization, and protein-protein interaction. Use of a small molecule inhibitor that mimics NAD<sup>+</sup> binding in the active site but does not allow for ADP-ribosylation by PARP16 would provide a more precise understanding of the role of PARP16 in the cell.

Herein I describe an ongoing effort in the Cohen laboratory to develop and leverage a selective covalent PARP16 inhibitor to parse the underlying biological mechanism of PARP16, specifically in the context of the UPR. There are currently no reported covalent PARP inhibitors, and the development of the compound described in this chapter

represent the first success in a broader effort to covalently drug PARP enzymes.

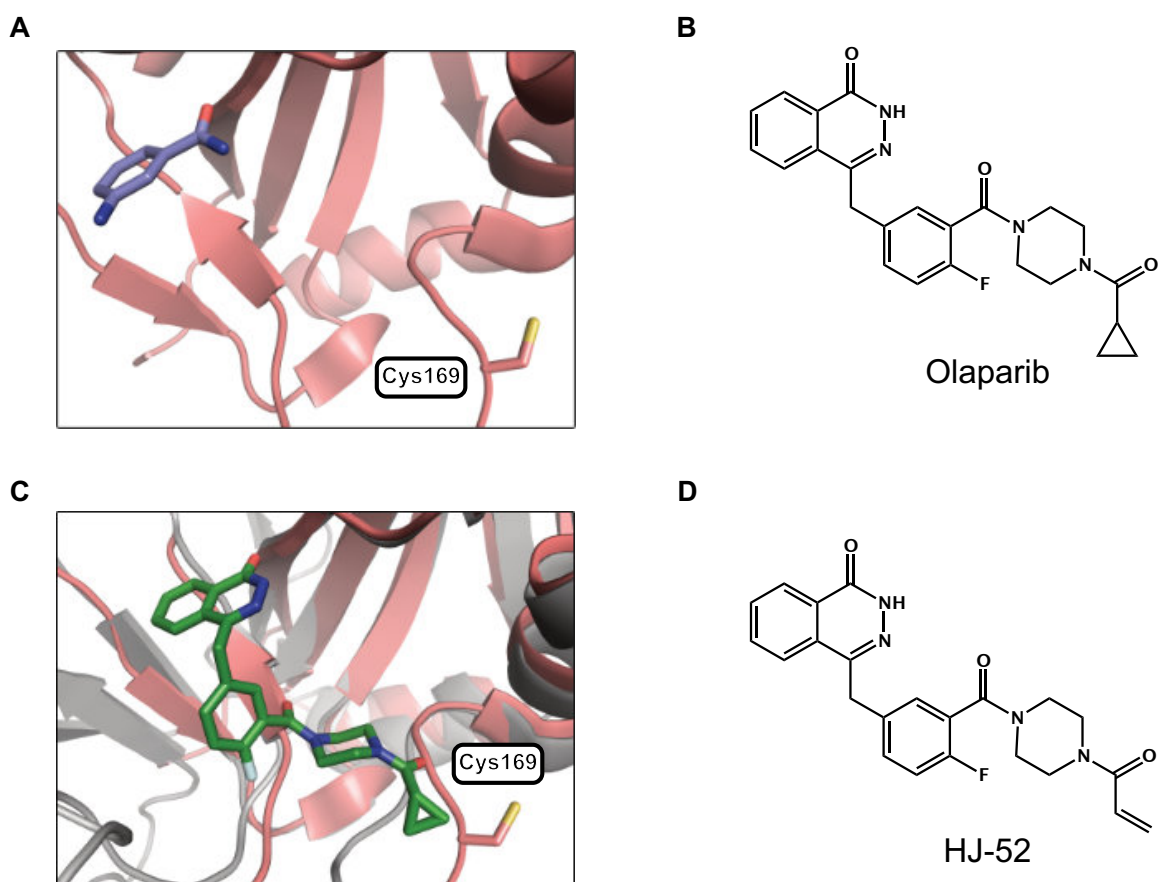
## Results

### Structure-guided Design Leads to a Covalent PARP16 Inhibitor

PARPs share a highly conserved active site, and selective inhibition requires identification and targeting of small unique features in sequence and structure. To address this issue, we set out to identify non-conserved cysteines in the PARP16 active site for potential covalent inhibitor binding. By inspecting the active-site of PARP16 we identified an unique cysteine residue (Cys169, Figure 5-1A). There are numerous examples of covalent kinase inhibitors that target non-conserved cysteines with various electrophiles, including acrylamides (Lui et al. 2013). To target this cysteine, we needed to identify a scaffold that could present an electrophile toward Cys169. Previous studies have reported that the clinical PARP1/2 inhibitor olaparib also inhibits PARP16 (Thorsell et al. 2016). Based on *in silico* modeling we found that the cyclopropyl amide group of olaparib is near Cys169 of PARP16 (Figure 5-1C). Based on this we reasoned that a nucleophile at this position on the olaparib scaffold would likely react to form a covalent bond with Cys169. To test this hypothesis, Dr. Haihong Jin synthesized

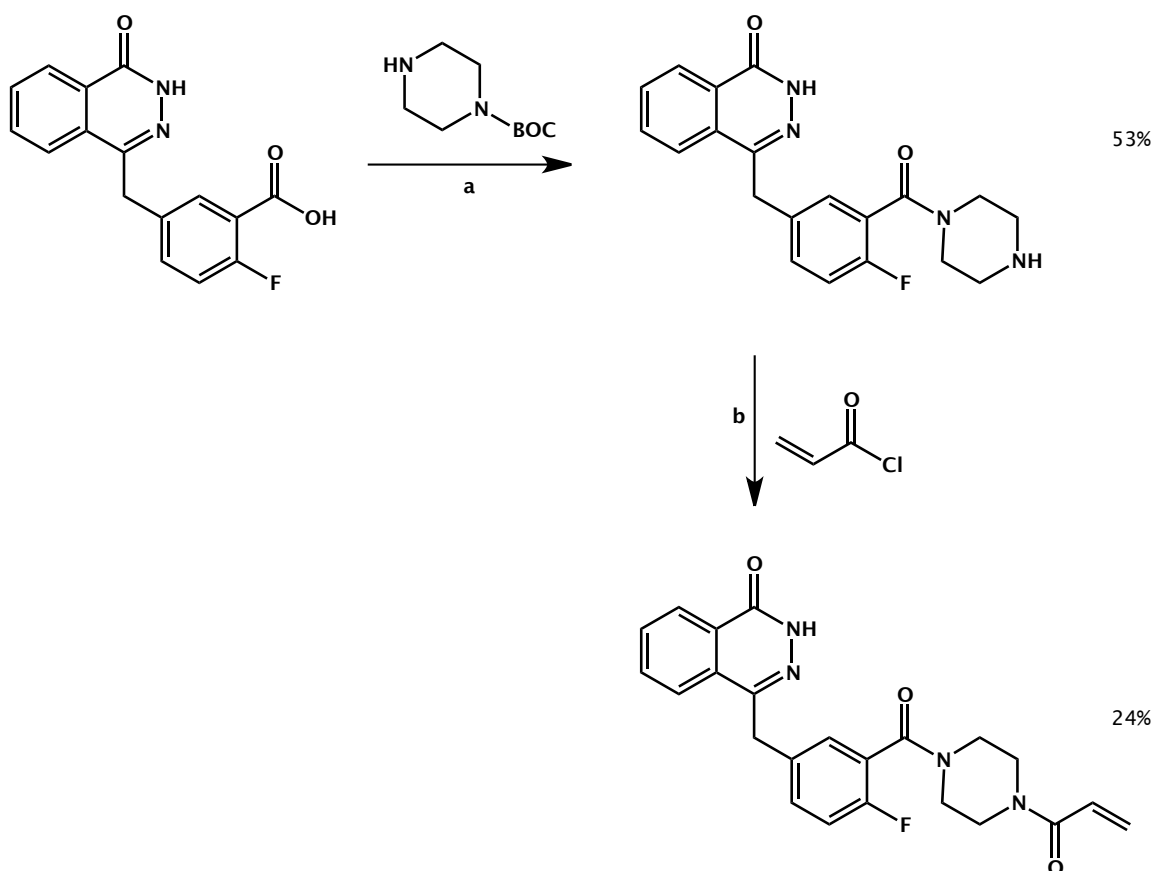


an olaparib analogue that replaced the cyclopropyl amide group of olaparib with an acrylamide (**HJ-52**, Figure 5-1D, Scheme 5-1), an electrophilic group that reacts selectively with cysteines in proteins. This strategy has been used to great effect in the kinase field, where there are many covalent kinase inhibitors that contain an acrylamide electrophile that targets a non-conserved cysteine (Lui et al. 2013). We hypothesized that the acrylamide on HJ-52 would form a covalent bond with Cys169 of PARP16.



**Figure 5-1** Olaparib accesses a cysteine residue in the active site of PARP16

- (A) Crystal structure of PARP16 bound to pan-PARP inhibitor 3-aminobenzamide shows Cys169 sits approximately 5 Å away from the cyclopropyl group of olaparib (PDB: 4F0D)
- (B) Structure of PARP1/2 inhibitor olaparib
- (C) Overlay of PARP1 bound to olaparib (Grey, PDB: 5DS3) and PARP16 (Pink, PDB: 4F0D) show the cyclopropyl group of olaparib directly adjacent to Cys169 of PARP16.



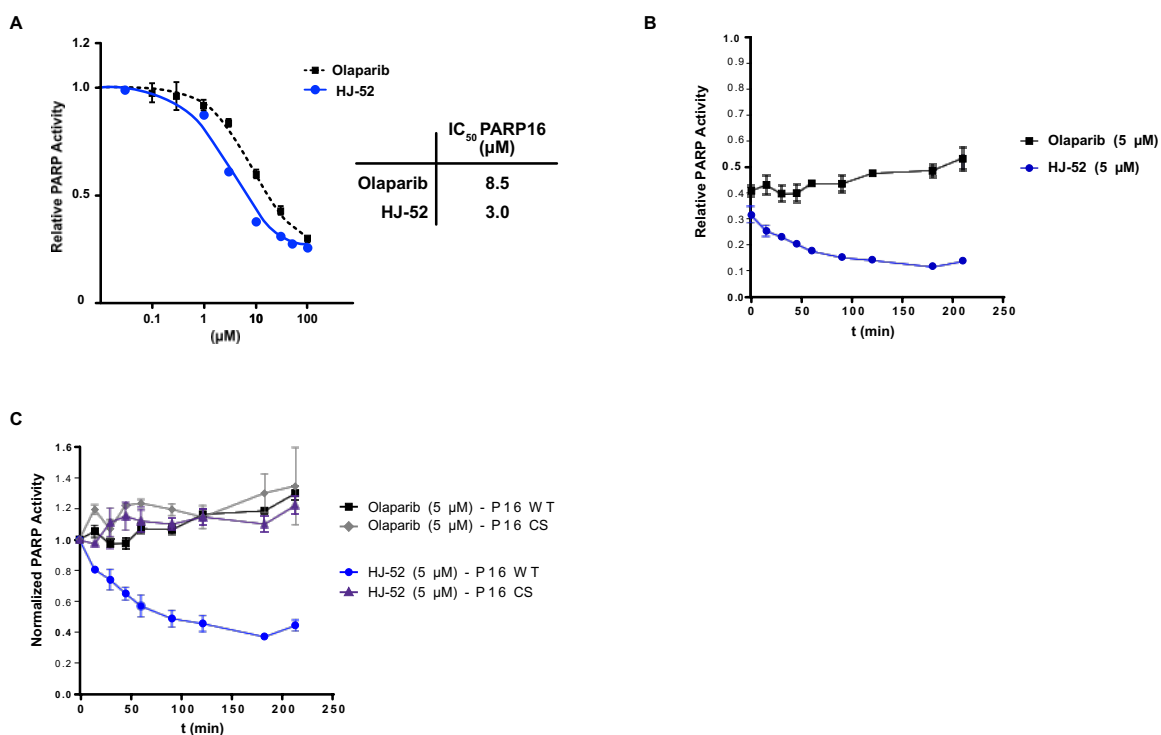
**Scheme 5-1** Synthesis of HJ-52. *Synthesis performed by Dr. Haihong Jin.*

a) TBTU, DIPEA, DMF, RT; b) N,N-Diisopropylethylamine, DCM, RT

### ***In vitro* validation of PARP16 covalent inhibitor mutant validation of target**

To assess the efficacy of HJ-52 against PARP16 Dr. Rory Morgan determined the *in vitro* IC<sub>50</sub> using our previously reported PARP inhibitor screening assay using native NAD<sup>+</sup> (Chapter 2, Kirby, Morgan, et al. 2018). Dr. Morgan found that HJ-52 is slightly more potent than olaparib for PARP16 (3  $\mu$ M and 8.5  $\mu$ M, respectively) (Figure 5-2A). To determine if HJ-52 inhibits PARP16 via a covalent mechanism Dr. Rory Morgan went on to examine if HJ-52 exhibits time-dependent inhibition of PARP16. He found that HJ-52 mediated inhibition of PARP16 increases over time while inhibition of PARP16 by olaparib does not (Figure 5-2B). These results suggest that HJ-52 is a covalent inhibitor of PARP16. To determine if this time-dependent inhibition is due to a covalent reaction at Cys169, Dr. Morgan generated the Cys169 to serine mutant of PARP16 (PARP16<sup>CS</sup>). If HJ-52 covalently inhibits PARP16 by reacting with Cys169, then HJ-52 should not exhibit time-dependent inhibition of PARP16<sup>CS</sup> as PARP16<sup>WT</sup>. Dr. Morgan found that HJ-52 inhibition of PARP16<sup>CS</sup> did not increase over time and closely matched the inhibition of the non-covalent inhibitor olaparib against PARP16<sup>WT</sup> (Figure 5-2C). To directly determine if HJ-52 forms a covalent bond with PARP16, Dr. Morgan performed whole-protein

mass spectrometry analysis. He found that HJ-52 forms a 1:1 covalent complex with PARP16, confirming that it covalently binds to PARP16 (Appendix C). Together these *in vitro* data demonstrate that HJ-52 covalently targets Cys169 in PARP16.



**Figure 5-2** HJ-52 inhibits PARP16 *in vitro* by covalently labeling Cys169 *Data acquired and figure provided by Dr. Rory Morgan.*

(A) *In vitro* IC<sub>50</sub> curves of olaparib and HJ-52 against PARP16.

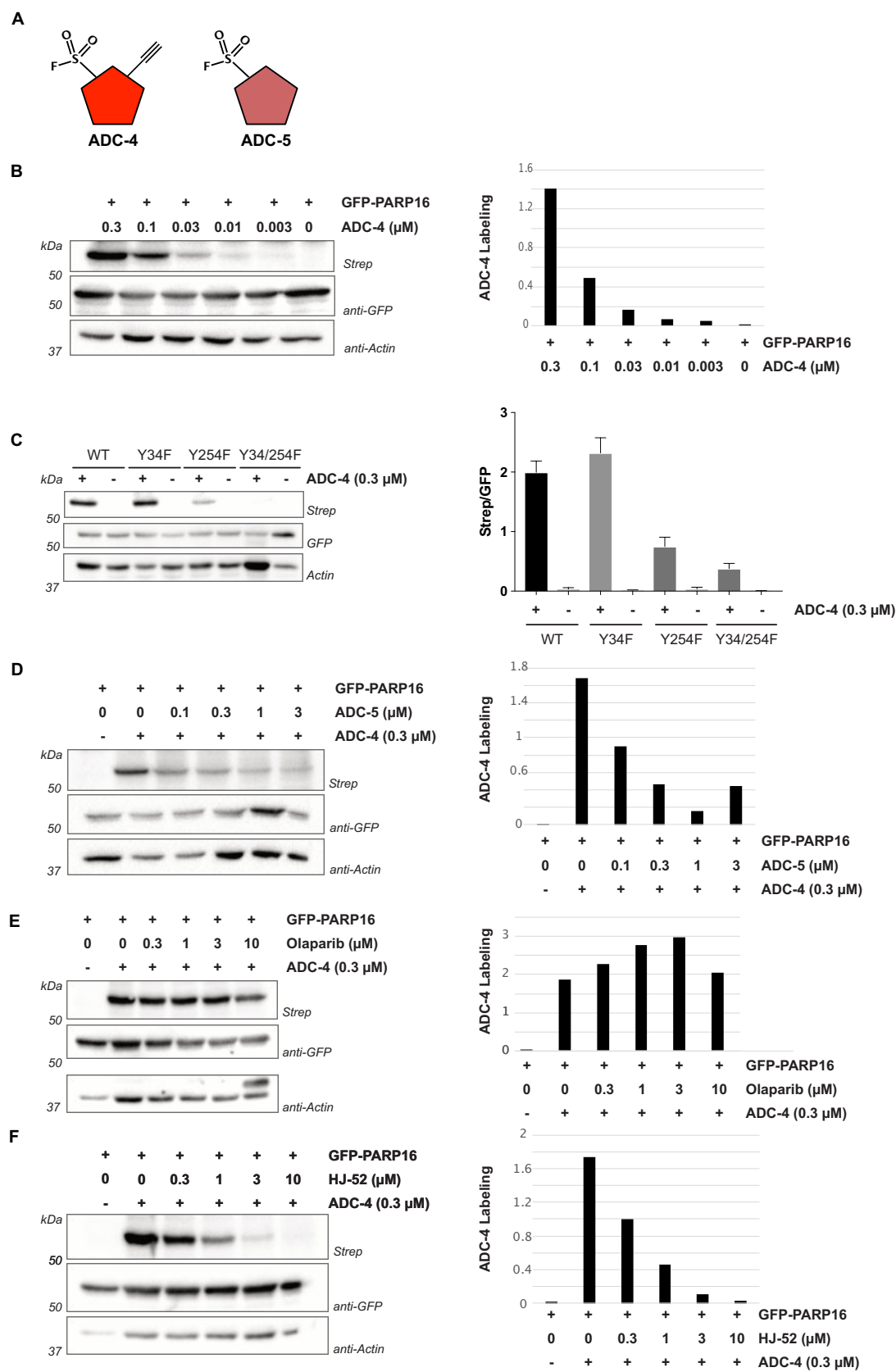
(B) Time course comparing olaparib and HJ-52 inhibition of PARP16 over 200 min show HJ-52 inhibition increases with time while olaparib decreases.

(C) Time course comparing olaparib and HJ-52 inhibition of PARP16<sup>WT</sup> and PARP16<sup>CS</sup> over 200 min show HJ-52 selectively inhibits PARP16<sup>WT</sup>. Error bars represent SEM from at least two replicates.

## HJ-52 binds to PARP16 in cells

Building on the work of Drs. Jin and Morgan, I next sought to validate HJ-52 as a covalent inhibitor of PARP16 in cells. My efforts were initially stymied by our inability to detect auto-MARylation of over-expressed GFP-PARP16 in cells, despite robust GFP expression (Figure 5-3) (many other active MARylating PARPs auto-modify). Fortunately, Dr. Taunton at UCSF has recently discovered a covalent PARP16 binder in a chemoproteomic mass spectrometry-based screen aimed at identifying covalent kinase inhibitors targeting tyrosines and lysines. Dr. Taunton generously shared this compound (ADC-4, Figure 5-3A, structure concealed until publication), which contains a sulfonyl fluoride for covalent attachment to tyrosine or lysine and an alkyne tag for click-chemistry-based visualization. I first confirmed that ADC-4 covalently targets PARP16. For these experiments I treated wild-type GFP-PARP16 (GPF-PARP16<sup>WT</sup>) expressing cells with increasing doses of ADC-4, followed by click chemistry mediated labeling of the lysates with biotin azide. I found that ADC4 exhibits dose-dependent labeling of GFP-PARP16<sup>WT</sup> (Figure 5-3B). Based on preliminary mass-spectrometry data from the Taunton lab (personal communication) we suspected that ADC-4 labeled one of two tyrosines in the PARP16 active site: Tyr34 and/or Tyr254. To confirm that ADC-4 labels one of these

active site residues I tested ADC-4 in cells expressing the individual and double tyrosine to phenylalanine mutants of these residues (GFP-PARP16<sup>Y34F</sup>, GFP-PARP16<sup>Y254F</sup>, GFP-PARP16<sup>Y34/254F</sup>, constructs produced by Dr. Vermehren-Schmaedic). I found that ADC-4 robustly labels GFP-PARP16<sup>WT</sup> and GFP-PARP16<sup>Y34F</sup> had greatly reduced labeling of GFP-PARP16<sup>Y254F</sup>, and no detectible labeling of GFP-PARP16<sup>Y34/254F</sup> (Figure 5-3C). These results suggest that ADC-4 preferentially labels Tyr254 with some background labeling of Tyr34. Based on these results I concluded that ADC-4 labels PARP16 in the active site and can therefore be used as an active-site occupancy probe to assess binding of other compounds. Next, using a non-alkyne tagged version of ADC-4 (ADC-5, Figure 5-3A), also provided by the Taunton lab, I demonstrated that ADC-4 could be competed away from the PARP16 binding site and used as a read out for PARP16 binding (Figure 5-3D). With this occupancy probe strategy in hand, I then tested if olaparib and HJ-52 bind to PARP16 in cells. I found that olaparib—a non-covalent inhibitor—did not compete away ADC-4 at doses up to 10  $\mu$ M (Figure 5-3E). However, HJ-52—our cysteine targeted covalent inhibitor— competed away ADC-4 with an IC<sub>50</sub> of approximately 0.5  $\mu$ M (Figure 5-3F). These results support the hypothesis that HJ-52 binds to Cys169 in the GFP-PARP16 active site in cells.

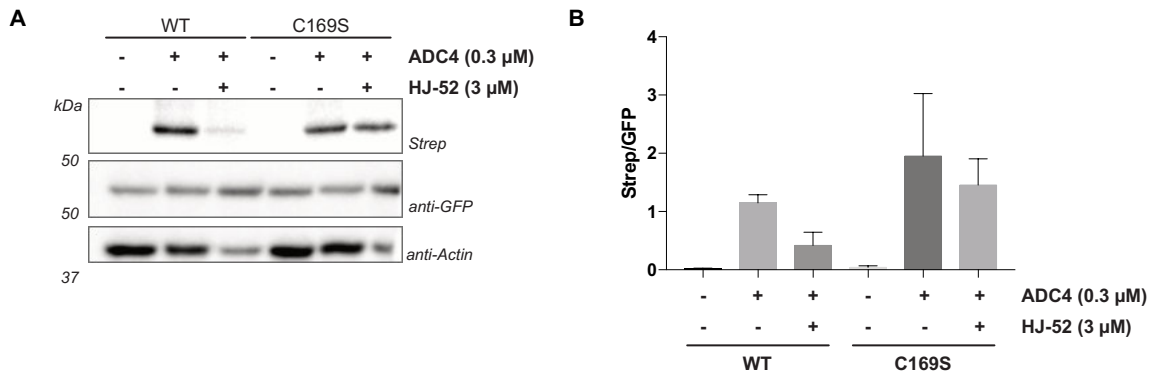


**Figure 5-3** Competition with a PARP16 occupancy probe show covalent labeling of GFP-PARP16 in cells by HJ-52, Strep stands for HRP-Strep visualized with a chemiluminescent substrate. HRP-Strep was normalized to GFP levels for analysis.

- (A) Representations of PARP16 occupancy probe ADC-4 and its non-alkyne labeled analogue ADC-5.
- (B) ADC-4 robustly labels GFP-PARP16 in cells at 0.1  $\mu$ M.
- (C) ADC-4 preferentially labels Tyr254 (representative western blot, quantification from three replicates)
- (D) ADC-5 competes with ADC-4 for GFP-PARP16 active site occupancy, demonstrating the efficacy of ADC-4 as an occupancy probe for GFP-PARP16.
- (E) Olaparib, a non-covalent inhibitor, does not compete with ADC-4 for binding to GFP-PARP16.
- (F) HJ-51 competes with ADC-4 for GFP-PARP16 binding.

I next used a GFP-PARP16 cysteine to serine mutant (GFP-PARP16<sup>CS</sup>) to confirm our *in vitro* findings that HJ-52 labels Cys169 of PARP16 in cells. I performed a single dose competition experiment with HJ-52 and ADC-4 using GFP-PARP16<sup>WT</sup> and GFP-PARP16<sup>CS</sup>. As expected, HJ-52 competes for GFP-PARP16<sup>WT</sup> labeling but not for GFP-PARP16<sup>CS</sup> labeling (Figure 5-4). Taken together these results confirm that HJ-52 binds to Cys169 in GFP-PARP16 in cells.





**Figure 5-4** HJ-52 robustly labels wild-type GFP-PARP16 in cells but does not label C169S GFP-PARP16 mutant at statistically significant levels.

(A) Representative western blot showing that HJ-52 competes with ADC-4 for GFP-PARP16<sup>WT</sup> but not GFP-PARP16<sup>CS</sup> binding.

(B) Quantification of (A), two replicates

### Preliminary work suggesting catalytic activity may not be required for PARP16 involvement in ER Stress response

Previous work has reported that PARP16 regulates the unfolded protein response (UPR) in the ER by activating PERK and IRE1 $\alpha$  (Jwa & Chang 2012). This study concluded that MARYlation of PERK and IRE1 $\alpha$  by PARP16 increases their kinase activity. In this study Jwa et. al first performed preliminary characterization of PARP16 confirming that it is an ER localized C terminus anchored transmembrane protein with a cytoplasmic N terminal that performs ADP-ribosylation at the ER microsomal lumen. To characterize the involvement of PARP16 in the UPR Jwa et. al conducted a thorough series of experiments using whole cell and *in vitro* assays to look at the effects of PARP16

overexpression and short interfering RNA (shRNA) mediated PARP16 knockdown (KD) under UPR activation induced with tunicamycin, brefeldin A, or thapsigargin. PARP16 KD led to increased rates of cell death as measured by trypan blue staining, a result consistent with inhibition of the UPR (Jwa & Chang 2012).

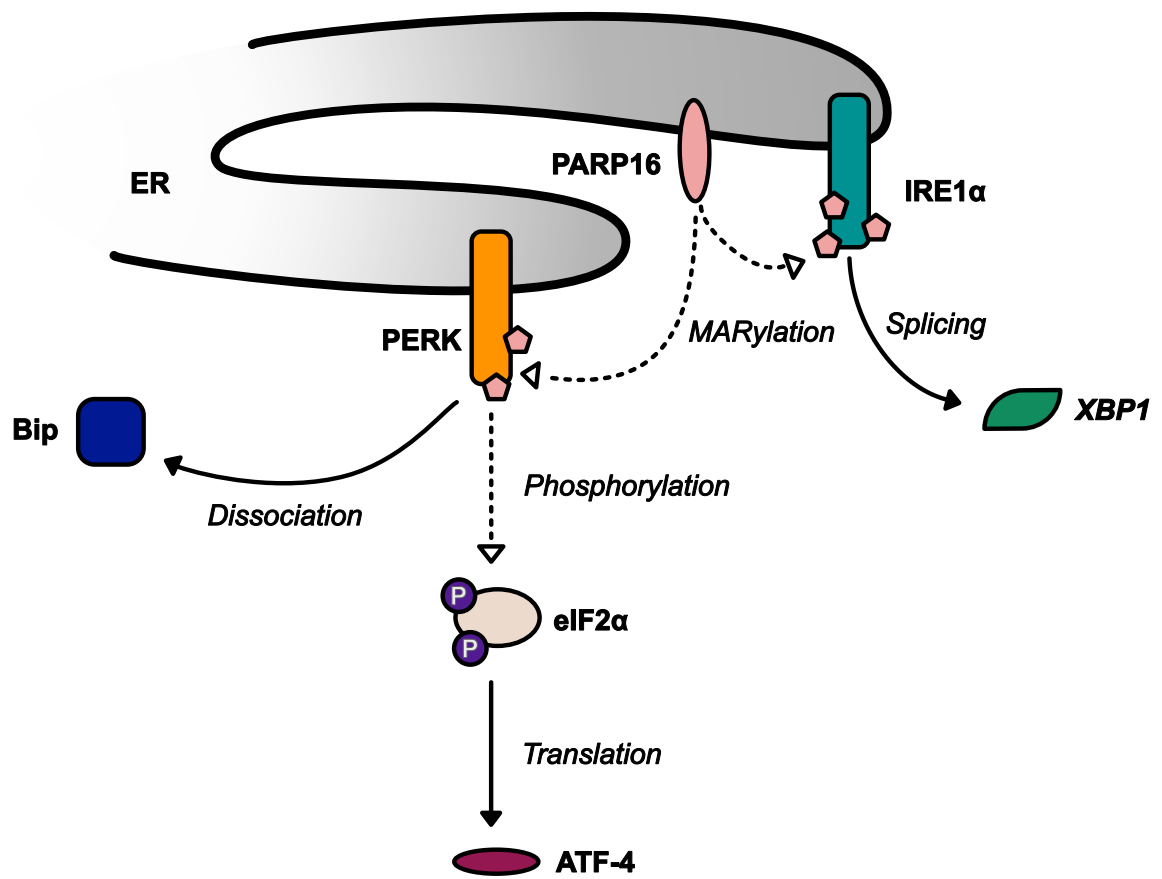
Using these techniques Jwa et. al demonstrated that PARP16 KD sensitizes cells to ER stress and leads to an increase in cell death. Importantly, non-UPR related cellular stress responses such a DNA damage repair remained intact in PARP16 KD cells and PARP16 KD or GFP-PARP16 overexpression did not result in significant changes in ERAD.

Cells expressing GFP-PARP16<sup>WT</sup> with or without ER stress inducing treatments showed an increase in GFP-PARP16<sup>WT</sup> auto-modification. In these studies, PERK and RE1 $\alpha$  were found to precipitate with GFP-PARP16<sup>WT</sup> under 450 mM NaCl conditions demonstrating association between these proteins. PERK and IRE1 $\alpha$  were also found to be ADP-ribosylated. To assess binding between PARP16 and these UPR-related proteins, GFP fusions of PARP16<sup>WT</sup>, PERK, IRE1 $\alpha$ , ATF6, or SEC6 (a non-UPR-related ER transmembrane protein) were expressed and co-immunoprecipitated. Only PERK and IRE1 $\alpha$  were identified as likely binders to PARP16 (Jwa & Chang 2012).

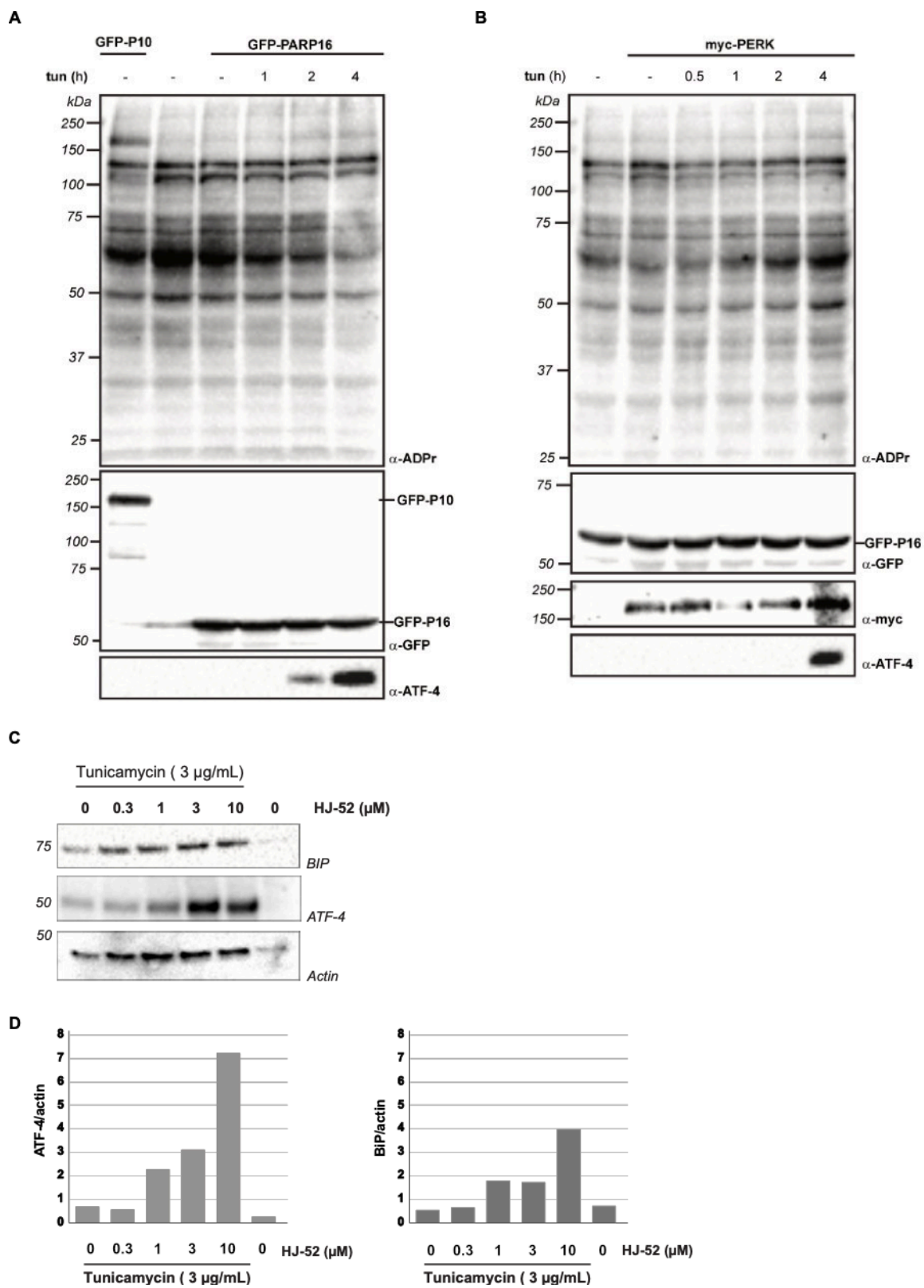
GFP-PARP16<sup>WT</sup> mediated ribosylation of PERK and IRE1 $\alpha$  was found to increase with ER stress induction as measured by [<sup>32</sup>P]NAD<sup>+</sup> in radiograph analysis. Over expression of GFP-PARP16<sup>WT</sup>, but not the catalytically incompetent PARP16<sup>H152Q/Y182A</sup> mutant, was found to increase PERK kinase activity, as measured by auto-phosphorylation at Thr918 by PERK, phosphorylation of its substrate eIF2 $\alpha$  at Ser51, and increased ATF-4 production. IRE1 $\alpha$  activation was measured through splicing of XBP1 messenger RNA. Further *in vitro* autoradiography studies show that PARP16 ADP-ribosylates PERK and IRE1 $\alpha$  and that this leads to an increase in their kinase activity. BiP, an ER specific chaperone that is bound to PERK, IRE1 $\alpha$ , and ATF6 normally but released under ER-stress activation of these enzymes, also increased with GFP-PARP16 over expression but not with PARP16 KD. These results were not seen in PARP16 KD cells, suggesting that ADP-ribosylation by PARP16<sup>WT</sup> is responsible for PERK and IRE1 $\alpha$  activation under ER stress conditions (Jwa & Chang 2012).

This study did not include any small molecule inhibitor of PARP16 and instead used active site point mutations to prevent NAD<sup>+</sup> binding and ADP-ribosylation. To substantiate these findings and in the hopes of further elucidating the role of PARP16 in the UPR and ER stress in general we attempted to recapitulate these findings using HJ-52. The

model presented by Jwa et al. suggests that under stress conditions PARP16 ADP-ribosylation leads to activation PERK and IRE1 $\alpha$  leading to increased flux through these pathways measured through several downstream effectors (Figure 5-5). In our preliminary work Dr. Morgan and I have attempted to measure changes in PARP16 activity under tunicamycin (3  $\mu$ g/mL) treatment by assessing levels of ATF-4. Dr. Morgan observed ATF-4 production after 4 h in HEK 293T cells over-expressing GFP-PARP16<sup>WT</sup> alone or in combination with overexpression of Myc-PERK, but saw no significant changes in ADP-ribosylation under these conditions as measured using an ADP-ribose binding reagent (Millipore) (Figure 5-6A,B). I treated HeLa cells with increasing doses of HJ-52 and tunicamycin (3  $\mu$ g/mL) for three hours and measured ATF-4 and BiP levels (Figure 5-6C,D). Intriguingly, I saw a dose dependent increase of ATF-4 and BiP under HJ-52 treatment. However, these results could not be replicated in two subsequent tests. Time constraints prevented me from exploring this pathway further, but future work in the Cohen lab will seek to clarify the role of PARP16 effect of HJ-52 treatment in the UPR.



**Figure 5-5** PARP16 has been reported to activate PERK and RE1α through MARylation leading to an increase in their downstream effects.



**Figure 5-6** Preliminary cellular studies of PARP16 in the UPR. *Panels A and B provided by Dr. Rory Morgan.*

- (A) Over expression of GFP-PARP16 or GFP-PARP10 with tunicamycin (3  $\mu\text{g/mL}$ ) in HeLa cells leads to increased levels of ATF-4 after 2 h, but no observable change in global ADP-ribosylation.
- (B) Over expression of GFP-PARP16 and Myc-PERK in HeLa cells with tunicamycin (3  $\mu\text{g/mL}$ ) leads to increased levels of ATF-4 after 4 h, but no observable change in global ADP-ribosylation.
- (C) HeLa cells treated with tunicamycin (3  $\mu\text{g/mL}$ ) show a dose dependent increase in ATF-4 and BiP levels.
- (D) Quantification of results shown in (C).

## Discussion

We developed a covalent PARP16 inhibitor (HJ-52) based on the structure of olaparib. HJ-52 was designed to label PARP16 at Cys169 in the D-loop. We confirmed this target through *in vitro* and cellular models comparing the wild type protein with a cysteine to serine mutant, as well as mass spectrometry. To date, there are no reported covalent PARP inhibitors, making HJ-52 an exciting advance and demonstrating that this targeted strategy is applicable to PARPs. Within the active site of PARPs there are many conserved and unique residues that are ripe for covalent targeting. We hope that our work with HJ-52 will lay the foundation for future covalent PARP inhibitor development.

Regarding the biological role of PARP16, it is unclear based on our preliminary work what effect HJ-52 has on the PARP16 pathway. Initial tests show that HJ-52 treatment in HeLa cells under tunicamycin induced stress lead to a dose dependent increase in ATF-4 and BiP levels, however this results could not be replicated in subsequent experiments. Future work with HJ-52 will explore how catalytic inhibition of PARP16 effects the UPR. In their study, Jwa et al. used autoradiography amutated two residues in a key triad motif within the PARP16 active site, these mutations ablate catalytic activity and radiolabeled NAD<sup>+</sup> to assess PARP16 ADP-ribooslyation activity. Our studies used a pan-ADP-ribose binding reagents or pan-ADP-ribose antibody. It is likely that autoradiography is more sensitive than these antibodies and we may be unable to detect PARP16 activity, limiting our ability to validate the experiments Jwa et. al performed using a catalytically incompetent PARP16 mutant with our small molecule inhibitor HJ-52. The mutant used by Jwa et. al is also likely to prevent or greatly reduce NAD<sup>+</sup> binding. It is possible that the binding of NAD<sup>+</sup> is key to the mechanisms by which PARP16 affects the ER stress response by causing a structural change within PARP16. Futureu studies with HJ-52 will seek to clarify the details of the role and mechanism of PARP16 in the UPR.



# Methods

## Cloning

cDNA encoding full length human PARP16 was obtained as previously described (Kirby, Kojic, et al. 2018).

## Expression and Purification of Proteins

PARP16 was expressed and purified as previously described (Kirby, Kojic, et al. 2018).

## SRPK2 Plate Assays

96-well nickel coated plate (Pierce) was incubated with 350 ng His6-tagged SRPK2 in hB (50 mM HEPES pH 7.5, 100 mM NaCl, 4 mM MgCl<sub>2</sub>, 0.2 mM TCEP) for 60 min at RT. After extensively washing the plate, 4-400 ng (2x) of recombinant PARP enzyme in hB were added to individual wells of the 96-well plate. PARP<sub>3FL</sub> was activated by Dnick 5'P as described previously (Langelier et al. 2014). Varying concentrations of each inhibitor (0-200  $\mu$ M) were pre-incubated with 200  $\mu$ M NAD<sup>+</sup> (2x) in hB at room temperature for 5-10 min, then added to the plate. This reaction proceeded for 60 min at 30°C, the plate was then washed three times with 1X PBST (1X PBS, 0.01% Tween-20), once with 1X PBS, then blocked with 5%

milk (Carnation) in 1X PBST for for 30 min at RT. The plate was then washed three times with 1X PBST, once with 1X PBS, and then incubated with pan-ADPr binding reagent (Milipore) and incubate for 60 min at RT. The plate was then washed three times with 1X PBST, once with 1X PBS, and then incubated with anti-rabbit IgG HRP linked secondary antibody (Santa Cruz Biotechnology) and incubate for 30 min at RT. The plate was then washed three times with 1X PBST, once with 1X PBS, and then developed with QuantaRed™ Enhanced Chemifluorescent HRP Substrate (Thermo) for 30-45 s before quenching with Quanta Red Stop Solution. Fluorescence for each sample and control was read at excitation 570 nM and emission 600 nM with a Spectra Max i3 (Molecular Devices) within five min of development. Inhibitor dose response curves were fit using linear regression in Prism 7 (GraphPad™ Software). The mean IC<sub>50</sub> for each compound was calculated from at least three independent assays.

### **GFP-PARP16 labeling with ADC-4 in cells**

HEK293T cells expressing GFP-tagged PARP16 WT were treated with increasing concentrations of ADC-4 in serum-free media and incubated at 37°C for 60 min. The medium was removed and cells were washed with cold (4°C) PBS and lysed by freezing in liquid nitrogen and

thawing in buffer containing 25 mM HEPES at pH 7.5, 50 mM NaCl, 10% glycerol, 1% Nonidet P-40 (NP-40), 3  $\mu$ M rucaparib, and 1X complete EDTA-free protease inhibitor cocktail (Roche) and clarified by centrifugation at 14,000g for 5 min at 4°C. Lysates were subjected to click conjugation with 3X CB (300  $\mu$ M of TBTA, 3 mM CuSO<sub>4</sub>, 300  $\mu$ M biotin-azide (BiotinPEG3-Azide, Click Chemistry Tools), 3 mM TCEP·HCl in 1X PBS with 1% SDS) and incubated at room temperature for 30 min. A 4X Laemmli sample buffer with 5% BME was added prior to SDS-PAGE. Immunblot detection with Streptavidin-HRP was used to quantify levels of ADC-4 labeled GFP-PARP16. GFP-PARP16 and actin levels were assessed using a polyclonal anti-GFP produced primary antibody in rabbit (ChromoTek) or a monoclonal anti-beta-Actin primary antibody produced in mouse (Santa Cruz Biotechnology) followed by incubation with HRP-conjugated secondary antibodies. Proteins were detected by chemiluminescence and imaged on a ChemiDoc MP system (Bio-Rad).

### **GFP-PARP16 labeling with ADC-4 occupancy probe in cells**

HEK293T cells expressing GFP-tagged PARP16 WT or PARP16 C169S were treated with an inhibitor (ADC-5, olaparib, or HJ-52) in serum-free media and incubated at 37°C for 30 min, followed by treatment with ADC-4 in serum-free media and incubated at 37°C for 60 min.

The medium was removed and cells were washed with cold (4°C) PBS and lysed by freezing in liquid nitrogen and thawing in buffer containing 25 mM HEPES at pH 7.5, 50 mM NaCl, 10% glycerol, 1% Nonidet P-40 (NP-40), 3  $\mu$ M rucaparib, and 1X complete EDTA-free protease inhibitor cocktail (Roche) and clarified by centrifugation at 14,000g for 5 min at 4°C. Lysates were subjected to click conjugation with 3X CB (300  $\mu$ M of TBTA, 3 mM CuSO<sub>4</sub>, 300  $\mu$ M biotin-azide (BiotinPEG3-Azide, Click Chemistry Tools), 3 mM TCEP·HCl in 1X PBS with 1% SDS) and incubated at room temperature for 30 min. A 4X Laemmli sample buffer with 5% BME was added prior to SDS-PAGE. Immunoblot detection with Streptavidin-HRP was used to quantify levels of ADC-4 labeled GFP-PARP16. GFP-PARP16 and actin levels were assessed using a polyclonal anti-GFP primary antibody produced in rabbit (ChromoTek) or a monoclonal anti-beta-Actin primary antibody produced in mouse (Santa Cruz Biotechnology) followed by incubation with HRP-conjugated secondary antibodies. Proteins were detected by chemiluminescence and imaged on a ChemiDoc MP system (Bio-Rad).

### **GFP-PARP16 inhibition under ER stress response stimulation in HeLa cells**

HeLa cells expressing GFP-PARP-10, GFP-PARP16, Myc-PERK or a combination there-of were treated with tunicamycin (3  $\mu$ g/mL) at 0, 1,

2, and 4 h and incubated at 37°C. At 4 h the medium was removed and cells were washed with cold (4°C) PBS and lysed by freezing in liquid nitrogen and thawing in buffer containing 25 mM HEPES at pH 7.5, 50 mM NaCl, 10% glycerol, 1% Nonidet P-40 (NP-40), 3 µM rucaparib, and 1X complete EDTA-free protease inhibitor cocktail (Roche) and subjected to centrifugation at 14,000g for 5 min at 4°C. A 4X Laemmli sample buffer with 5% BME was added prior to SDS-PAGE. BiP, ATF-4, Myc, GFP, ADP-ribosylation, and beta-actin levels were assessed using a monoclonal anti-BiP produced in rabbit (Cell Signaling Technology), a monoclonal anti-ATF-4 primary antibody produced in rabbit, a monoclonal anti-Myc primary antibody produced in mice (Cell Signaling Technology), a polyclonal anti-GFP primary antibody produced in rabbit (ChromoTek), a pan-ADP-ribose binding reagent (Millipore), or a monoclonal anti-beta-Actin primary antibody produced in mouse (Santa Cruz Biotechnology) followed by incubation with HRP-conjugated secondary antibodies. Proteins were detected by chemiluminescence and imaged on a ChemiDoc MP system (Bio-Rad).

#### **GFP-PARP16 inhibition under ER stress response stimulation in HeLa cells**

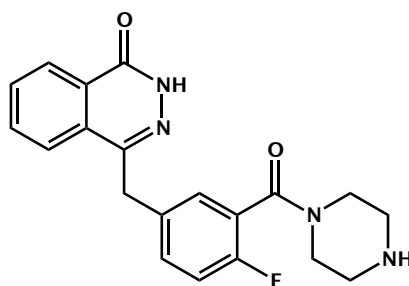
HeLa cells expressing endogenous PARP-16 were treated with tunicamycin (3 µg/mL) and increasing concentrations of HJ-52 in

serum-free media and incubated at 37°C for 180 min. The medium was removed and cells were washed with cold (4°C) PBS and lysed by freezing in liquid nitrogen and thawing in buffer containing 25 mM HEPES at pH 7.5, 50 mM NaCl, 10% glycerol, 1% Nonidet P-40 (NP-40), 3  $\mu$ M rucaparib, and 1X complete EDTA-free protease inhibitor cocktail (Roche) and subjected to centrifugation at 14,000g for 5 min at 4°C. A 4X Laemmli sample buffer with 5% BME was added prior to SDS-PAGE. BiP, ATF-4 and beta-actin levels were assessed using a monoclonal anti-BiP produced in rabbit (Cell Signaling Technology), a monoclonal anti-ATF-4 primary antibody produced in rabbit, or a monoclonal anti-beta-Actin primary antibody produced in mouse (Santa Cruz Biotechnology) followed by incubation with HRP-conjugated secondary antibodies. Proteins were detected by chemiluminescence and imaged on a ChemiDoc MP system (Bio-Rad).

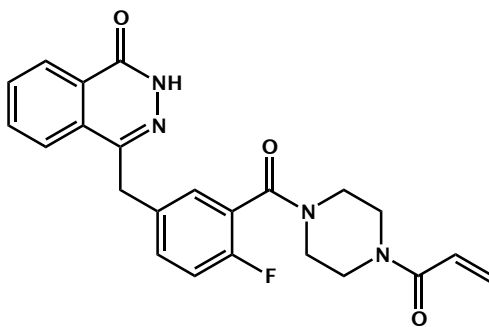
## Chemistry

**General:** <sup>1</sup>H NMR spectra were recorded on a Bruker DPX spectrometer at 400 MHz. Chemical shifts are reported as parts per million (ppm) downfield from an internal tetramethylsilane standard or solvent references. For air- and water-sensitive reactions, glassware was flame- or oven-dried prior to use and reactions were performed

under argon. Dimethylformamide was dried using the solvent purification system manufactured by Glass Contour, Inc. (Laguna Beach, CA). All other solvents were of ACS chemical grade (Fisher Scientific) and used without further purification unless otherwise indicated. Commercially available starting reagents were used without further purification. Analytical thin-layer chromatography was performed with silica gel 60 F254 glass plates (SiliCycle). Flash column chromatography was conducted self-packed columns containing 200-400 mesh silica gel (SiliCycle) on a Combiflash Companion purification system (Teledyne ISCO). All final products were  $\geq 95\%$  pure as assessed by analytical HPLC (mobile phase A: 0.1% formic acid (aq), mobile phase B: 0.1% formic acid in acetonitrile; flow rate = 1.0 mL/min; conditions: pre-run A = 90 % B = 10%, 10 min A = 5% B = 95%, 11 min A = 5% B = 95%, 13 min A = 90% B = 10%; UV-Vis detection:  $\lambda_1$  = 254 nm,  $\lambda_2$  = 220 nm. Retention times (Rt) refer to UV = 254 nm. Novel compounds indicated, for literature reports of synthesized compounds see Appendix F.



*4-(4-Fluoro-3-(piperazine-1-carbonyl)benzyl)phthalazin-1(2H)-one*: 2-fluoro-5-((4-oxo-3,4-dihydrophthalazin-1-yl)methyl)benzoic acid (50 mg, 0.17 mmol), TBTU (60 mg, 0.19 mmol) and tert-butyl piperazine-1-carboxylate (35 mg, 0.19 mmol) were added to a flame dried flask and dissolved in anhydrous DMF/DCM (1:10) (5 mL). DIPEA (0.06 mL, 0.34 mmol) was added under argon and the reaction stirred at RT for 18 h. The product was then precipitated in water (100 mL) and collected by vacuum filtration. The BOC-protected product was then stirred with acetyl chloride (0.074 mL, 0.95 mmol) in methanol for 72 h at RT. Product was precipitated in water as a white solid. Yield: 50 mg (63%). <sup>1</sup>H NMR (400 MHz, DMSO-d<sub>6</sub>) δ 12.59 (s, 1H), 8.29 – 8.23 (m, 1H), 7.97 (d, J = 7.9 Hz, 1H), 7.93 – 7.87 (m, 1H), 7.83 (t, J = 7.3 Hz, 1H), 7.45 – 7.37 (m, 1H), 7.32 (dd, J = 6.6, 2.3 Hz, 1H), 7.25 – 7.15 (m, 1H), 4.32 (s, 2H), 2.97 (s, 3H), 2.79 (d, J = 1.2 Hz, 3H).



*4-(3-(4-Acryloylpiperazine-1-carbonyl)-4-fluorobenzyl)phthalazin-1(2H)-one*, **HJ-52**: 4-(4-fluoro-3-(piperazine-1-



carbonyl)benzyl)phthalazin-1(2H)-one (72 mg, 0.2 mmol) was added to a flame dried flask and dissolved in anhydrous DCM (5 mL) followed by addition of N,N-Diisopropylethylamine (48.8 mg, 0.38 mmol) and acryloyl chloride (0.025 mL, 0.3 mmol). Once the starting material was consumed by TLC (10% DCM in MeOH) the reaction was purified via ISCO Combiflash chromatography (silica, 1 g, 0-15% MeOH in DCM: 20 mg (24%) white solids. <sup>1</sup>H NMR (400 MHz, DMSO-d<sub>6</sub>) δ 8.26 (d, J = 7.8 Hz, 1H), 7.97 (d, J = 8.0 Hz, 1H), 7.90 (t, J = 7.5 Hz, 1H), 7.84 (t, J = 7.6 Hz, 1H), 7.45 (s, 1H), 7.37 (s, 1H), 7.24 (t, J = 9.0 Hz, 1H), 6.74 (s, 1H), 6.13 (dd, J = 16.7, 2.3 Hz, 1H), 5.75 – 5.68 (m, 1H), 4.33 (s, 2H), 3.63 (s, 4H), 3.47 (s, 2H), 3.20 (s, 2H). MS m/z [M+H]<sup>+</sup> for C<sub>23</sub>H<sub>21</sub>N<sub>4</sub>O<sub>3</sub>: 418.7. R<sub>t</sub> = 7.34 min.

## Chapter 6: Elaborations on the Olaparib Scaffold

Ilsa T. Kirby, Moriah R. Arnold, Anke Vermehren-Schmaedick, and Michael S. Cohen

This work was in collaboration with Moriah R. Arnold and Dr. Anke Vermehren-Schmaedick who performed cellular studies that have guided the design of the reported compounds.

## Abstract

Much of our understanding of Poly-ADP-ribose-polymerases (PARPs) is based on PARP1 and its role in DNA damage repair. Small molecule inhibitors have played a key role in studying the mechanism of PARP1, and have been more recently developed into frontline therapeutics for BRCA-/- cancers. The first PARP inhibitor advanced to clinic was olaparib, a phthalazinone based compound that is a broad spectrum PARP inhibitor. Recently, the pharmaceutical company AstraZeneca published a series of olaparib analogues that culminated in a non-specific PARP6 and PARP8 inhibitor (AZ0108). Based on these findings we have synthesized a series of olaparib analogues as part of an ongoing study examining the role of PARP6 and PARP8 in DNA damage repair and cell survival.

## Introduction

Poly-ADP-ribose-polymerases (PARPs) are a family of post translationally modifying proteins that catalyze the transfer of ADP-ribose from Nicotinamide Adenine Dinucleotide (NAD<sup>+</sup>) onto their targets. The PARP family consists of 17 ubiquitously expressed enzymes (in humans) defined by a shared NAD<sup>+</sup> binding site (Pinto & Schöler 2015). The family is further delineated by their enzymatic activity: the true ADP-ribose-polymerases (PARP1, 2, 5a and 5b), the mono-ADP-ribose transferases (PARP3, 4, 6-8, 10-12, and 14-16), and two inactive family members (PARP9 and 13) (Hottiger et al. 2010). PARP1 was the first discovered PARP and has remained at the forefront of the field as a key player in DNA damage repair and therapeutic target in BRCA<sup>-/-</sup> cancers (Farmer et al. 2005; Bryant et al. 2005; Ferraris 2010). Much of our understanding of PARP1 has been based on studies conducted using small molecule inhibitors of PARP1 (Feng et al. 2015). The inhibitor olaparib was first disclosed in 2008 (Menear et al. 2008) before quickly advancing through clinical trials and becoming the first FDA approved PARP inhibitor in 2014. Olaparib was long considered by many the gold standard of PARP1 inhibitors. In recent years further studies revealed that olaparib is a broad spectrum PARP inhibitor (Chapter 1, Thorsell et al. 2017). This led us to consider olaparib as a

lead compound for developing more selective PARP inhibitors. This same strategy has been explored by researchers at the pharmaceutical company AstraZeneca to identify AZ0108, a reported PARP1, 2, and 6 inhibitor (Johannes, Almeida, Daly, et al. 2015).

Based on these findings and our previous success advancing lead compounds to selective and potent PARP inhibitors (Kirby, Kojic, et al. 2018), we explored possible variations on the olaparib scaffold and screened these compounds against the PARP family before advancing promising compounds to cellular studies. We targeted two sites for modification. First, the C7 position, which we have previously substituted on a similar scaffold to ablate binding to PARPs containing an active site glutamate at position 988 (HYE-PARPs) while improving potency for the bulk of the PARP family which contain a smaller hydrophobic residue at this position (HY $\Phi$ -PARPs). Second, the C1 amide linked substituent of the pendant ring was exchanged for various piperazine and pyrazine-based substituents to explore differential interactions with the ADP-ribose sub-site of the active site (see Chapter 1 for full discussion of the PARP active site sections).

A previously described compound with cyano substituted piperazine at this position is a potent but non-selective PARP7 inhibitor, with promising strategies outlined to produce a selective analogue (Mikule

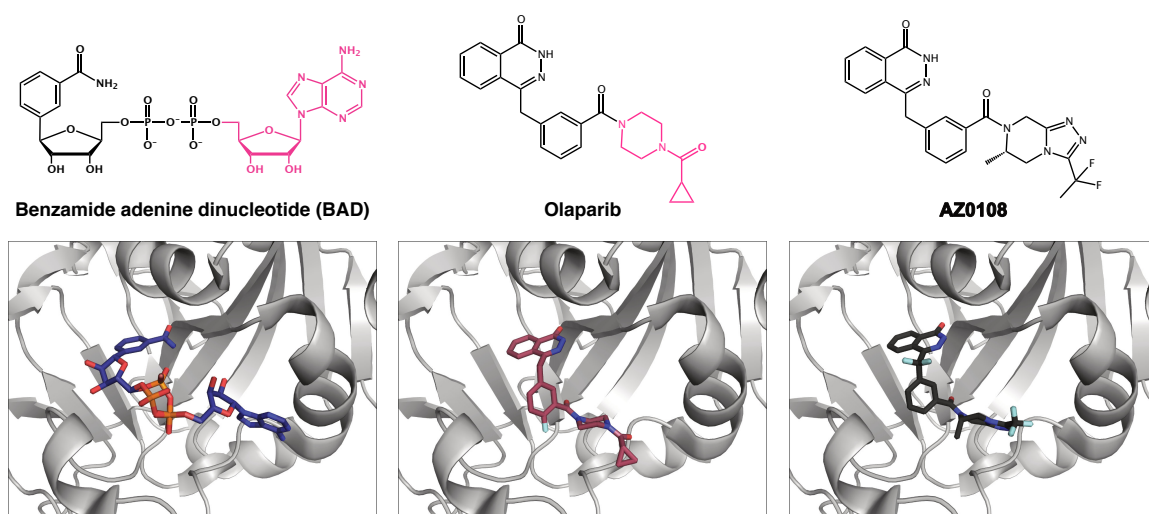
et al. 2016). PARP7, also known as 2,3,7,8-tetrachlorodibenzo-p-dioxin (TCDD)-inducible poly(ADP-ribose) polymerase (TiPARP), was first described as a negative regulator of aryl hydrocarbon receptor (AHR) (Q. Ma et al. 2001). It has since been found to play a role in innate immunity, stem cell pluripotency, and co-activator of liver X receptors (Hutin et al. 2018, Bindesbøll et al. 2016). There have been no reported inhibitors for PARP7 (Kirby & Cohen 2018), and we hope that this compound will help to further our understanding of this enzyme and its role in biology and pathology.

We have also developed a series of AZ0108 analogues that are part of ongoing cellular studies looking at PARP1, PARP6, and PARP8 in DNA damage repair and cell survival, the biological results of which will not be discussed here.

## Results

To identify opportune points of modification on the olaparib scaffold we compared crystal structures of olaparib bound to PARP1 (PDB: 5DS3), AZ0108 bound to PARP5a (PDB:5EBT), and a non-hydrolyzable NAD<sup>+</sup> analogue (BAD) bound to PARP1 (PDB: 6BHV) (Figure 6-1). Based on these comparisons we found that these compounds occupy the same binding space with the piperazine or pyrazine moieties of

olaparib and AZ0108 occupying in the ADP-ribose pocket of the PARP1 active site (see Chapter 1 for a full discussion of the NAD<sup>+</sup> binding pocket and its subsections). Because this is also where olaparib and AZ0108 differ structurally we hypothesized that the different selectivity profiles of olaparib and AZ0108 may be due to unique interactions in that region of the binding pocket. Based on this we targeted this part of the scaffold for modification. Happily, we found this to be synthetically tractable as the benzoic acid precursor to olaparib was commercially available (ArkPharm). We were thus able to rapidly produce a series of olaparib and AZ0108 analogues using peptide-like coupling with a range of piperazines and pyrazines (Scheme 6-1, 2), including some previously described in publications from AstraZeneca (Johannes, Almeida, Daly, et al. 2015).

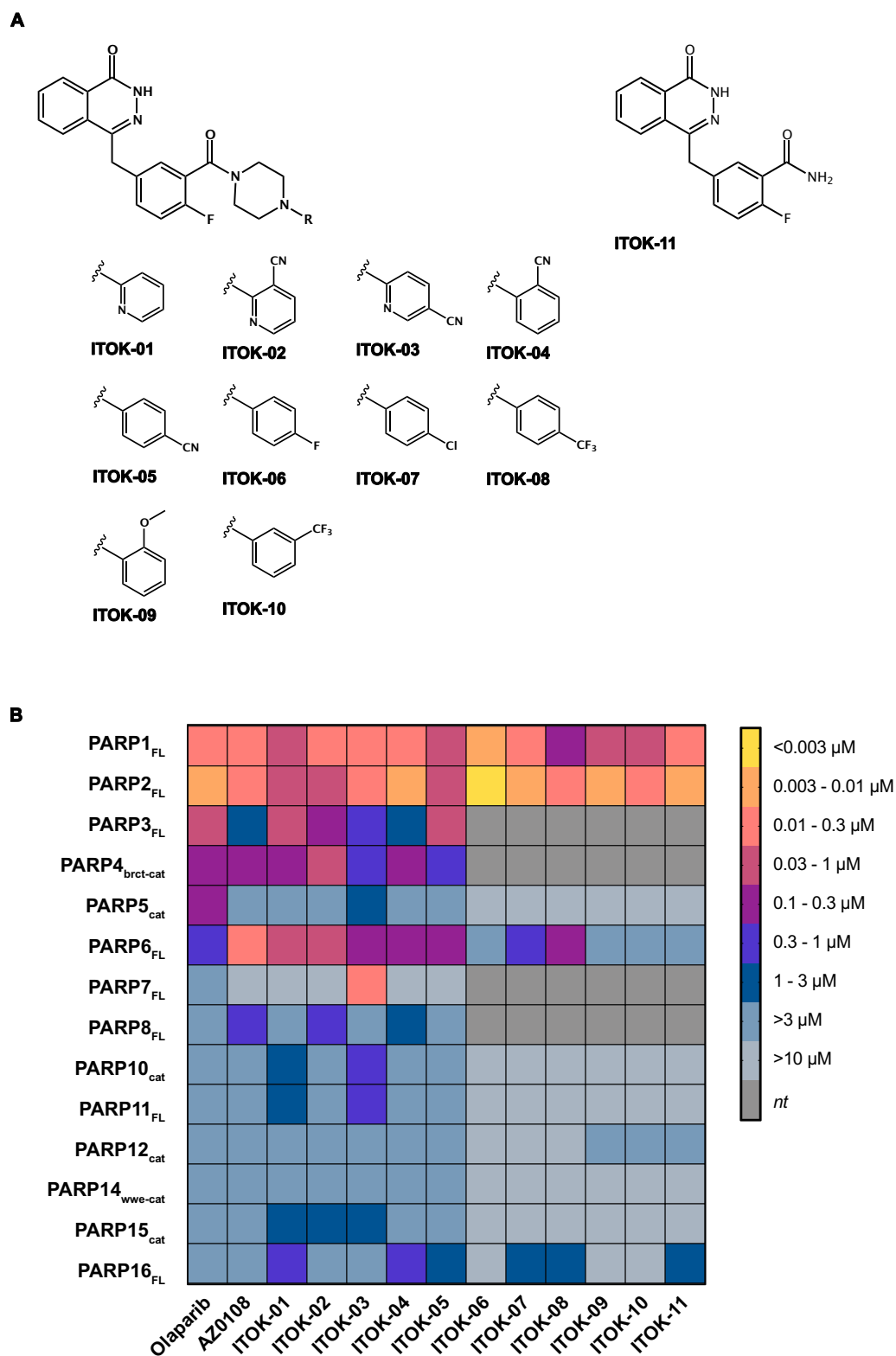


**Figure 6-1** Olaparib and AZ0108 occupy the same steric space as a non-hydrolyzable NAD<sup>+</sup> analogue (BAD) within the PARP1 active site. The most divergent aspect of these inhibitors (pink) sits in the same position as the ADP-ribose moiety of BAD (pink), suggesting that their different selectivity profiles may be dictated primarily by interactions with this part of the binding pocket.

### **A Series of Elaborated Olaparib Analogues Lead to a Potent PARP7 Inhibitor**

We first synthesized a series of olaparib analogues with various piperazine modifications (Scheme 6-1). We then screened these compounds against the PARP family and identified three major points of interest from this series of compounds (Figure 6-2, Appendix D). First, that the essential scaffold of olaparib appears sufficient to potently inhibit PARP1/2 (ITOK-11); second, that PARP3 and PARP8 appears to be the most sensitive to the modifications within this series; third, ITOK-03 is a low nano-molar inhibitor of PARP1, PARP2, and PARP7 and the potency for PARP7 strictly requires both the para-cyano group and the nitrogen in the pyridine ring. This final point most captured our attention, and we focused on designing a selective PARP7 inhibitor.

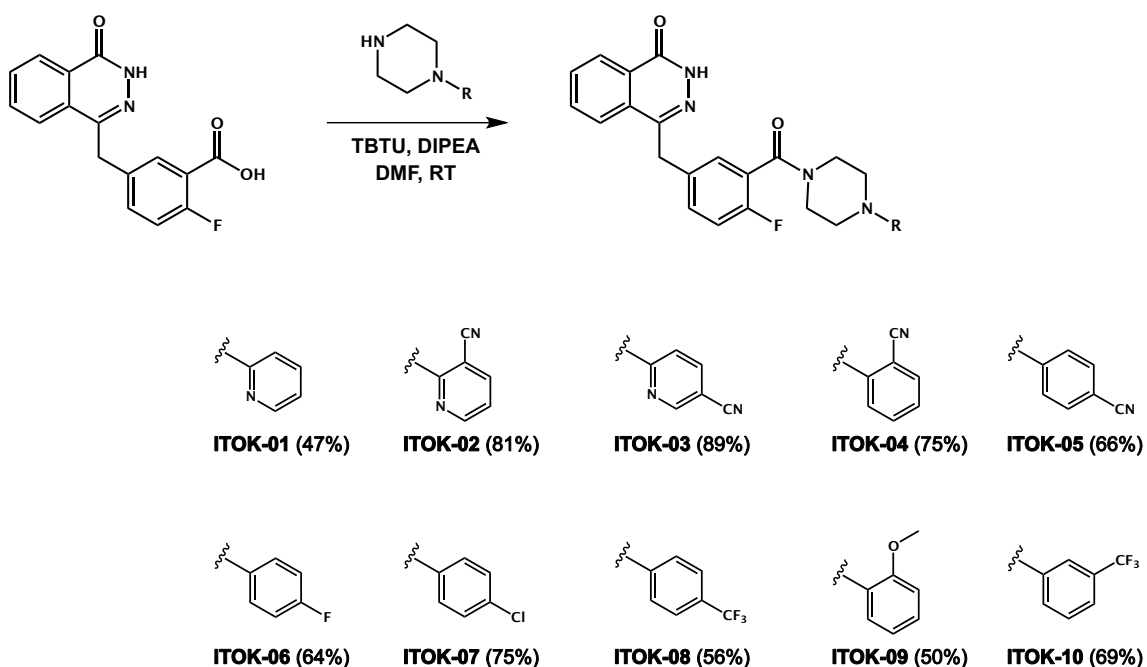




**Figure 6-2** Olaparib analogues reveal minimalist compound necessary for PARP1 inhibition, clues to PARP3 inhibition, and a highly potent PARP7 inhibitor

(A) Structures of ITOK-01 - 11

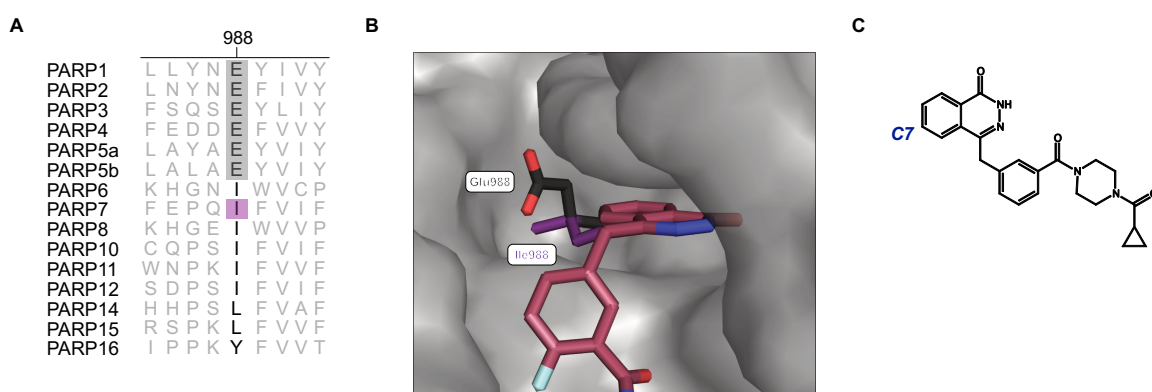
(B) Heat map showing *in vitro* IC<sub>50</sub> values (μM) of ITOK-01 through ITOK-11 against the active PARP family. Values represent averages from at least three replicates.



**Scheme 6-1** Synthesis of olaparib analogues

With a potent but non-selective PARP7 inhibitor in hand, we choose to apply our previously successful strategy of adding a small substituent to the central scaffold of an inhibitor that would clash with the active site glutamate of the HYE-PARPs (Chapter 3, (Kirby, Kojic, et al. 2018)). PARP7 contains an isoleucine at this position (Figure 6-3A). There are no crystal structures of PARP7 available, so an *in silico* model based on a PARP1 crystal structure was used to assess the structure of

the active site. This model suggests that Ile998 in PARP7 would leave a small space in the PARP7 binding pocket that would be occluded by the glutamate in HYE-PARPs (Figure 6-3B). This structure also indicates that the C7 position on the olaparib scaffold most closely abuts this part of the active site and thus was targeted for modification.



**Figure 6-3** A structure-based approach to improve ITOK-03 selectivity for PARP7

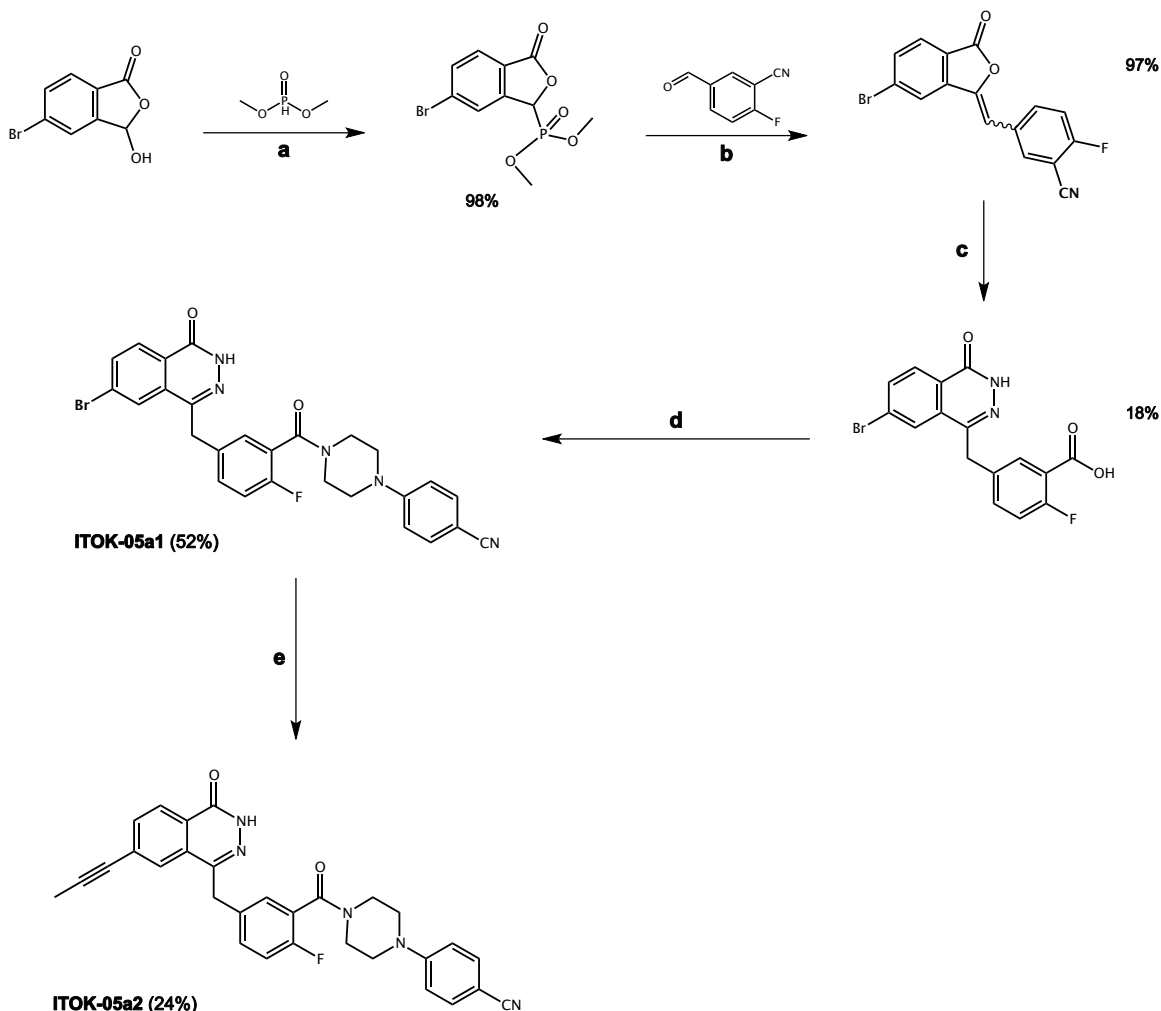
- (A) Structure based sequence alignment of the active PARP family shows PARP1-5a,b contain a glutamate at position 988 (human PARP1 numbering) while PARP7 contains an isoleucine.
- (B) A structure of olaparib bound to PARP1 (PDB: 5DS3) with a modeled isoleucine overlay shows a potential space in the PARP7 active site occluded by Glu988 in PARP1. This space can be accessed through substitutions at the C7 position of the olaparib scaffold (C).

We synthesized a C7-bromo-substituted olaparib precursor based on a published protocol for the non-brominated compound (Scheme 6-3) (Zmuda et al. 2015). Synthetic work to couple this compound with 6-(piperazin-1-yl)nicotinonitrile to produce a C7-

brominated ITOK-03 analogue is ongoing (Scheme 6-2). Surprisingly, while initial attempts at this reaction have proved synthetically intractable, coupling to the 4-(piperazin-1-yl)benzonitrile of ITOK-05 has not. As a preliminary test this compound (ITOK-05a1) was made and then functionalized with a propynyl group through a Stille coupling (Scheme 6-2) to produce a second analogue (ITOK-05a2). Functionalization with vinyl and benzyl groups through a Molander reaction at both the final reaction and the benzoic acid intermediate were attempted, but the desired product was not obtained. The Stille coupling of a propynyl also failed when conducted on the benzoic acid intermediate. Based on these results once the brominated analogue of ITOK-03 has been completed we will favor a Stille coupling as the primary method of functionalization at this position.

A preliminary screening against PARP1 and PAPR7 demonstrate that, as expected, both the bromo- and the propynyl- substituted analogues (ITOK-5a1 and ITOK-5a2 respectively, Scheme 6-2) had greatly reduced potency for PARP1, showing no *in vitro* inhibition at 10  $\mu$ M, compared to an  $IC_{50}$  of 30 nM for the unsubstituted ITOK-05 (Figure 6-2, Appendix D). These preliminary findings suggest that C7 substitution of the olaparib scaffold can effectively reduce inhibition of PARP1. This work is ongoing and will next seek to finish synthesizing a

brief series of substituted ITOK-03 analogues and screen these against the PARP family *in vitro* to determine potency and selectivity. If these compounds are found to more selectively inhibit PARP7 *in vitro* we will proceed to testing our lead compound in cells.



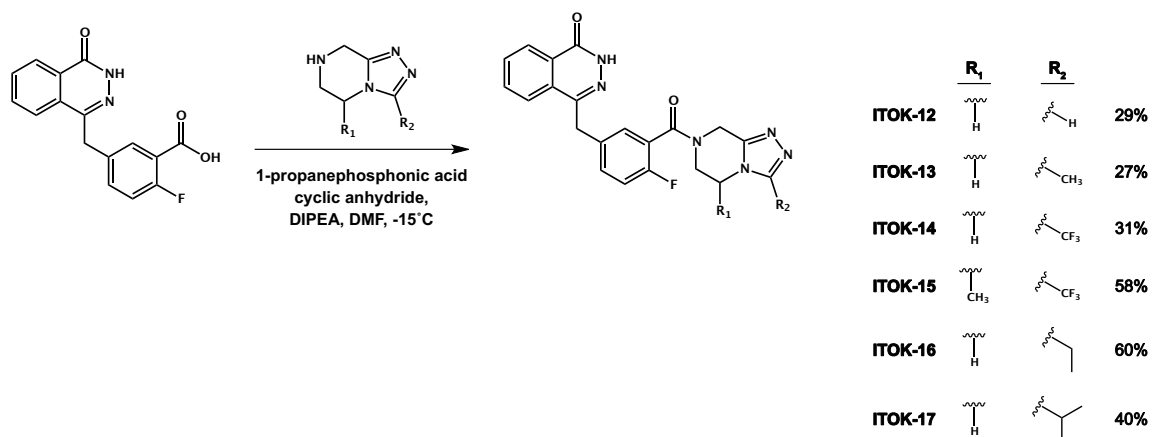
**Scheme 6-2** Synthesis of C7 substituted ITOK-05 analogues

- a) i. NaOMe, MeOH, 0°C to RT 18 h, ii. MeSO<sub>3</sub>H RT, 30 min; b) Et<sub>3</sub>N, THF, 0°C to RT, 48 h; c) i. 8 M NaOH, EtOH, 75°C, 24 h, ii. NH<sub>2</sub>NH<sub>2</sub>•H<sub>2</sub>O, 50°C, 72 h; d) 6-(piperazin-1-yl)nicotinonitrile, TBTU, DIPEA, RT 18 h; e) Pd(PPh<sub>3</sub>)<sub>4</sub>, tributyl(1-propynyl)tin, reflux 2 h.

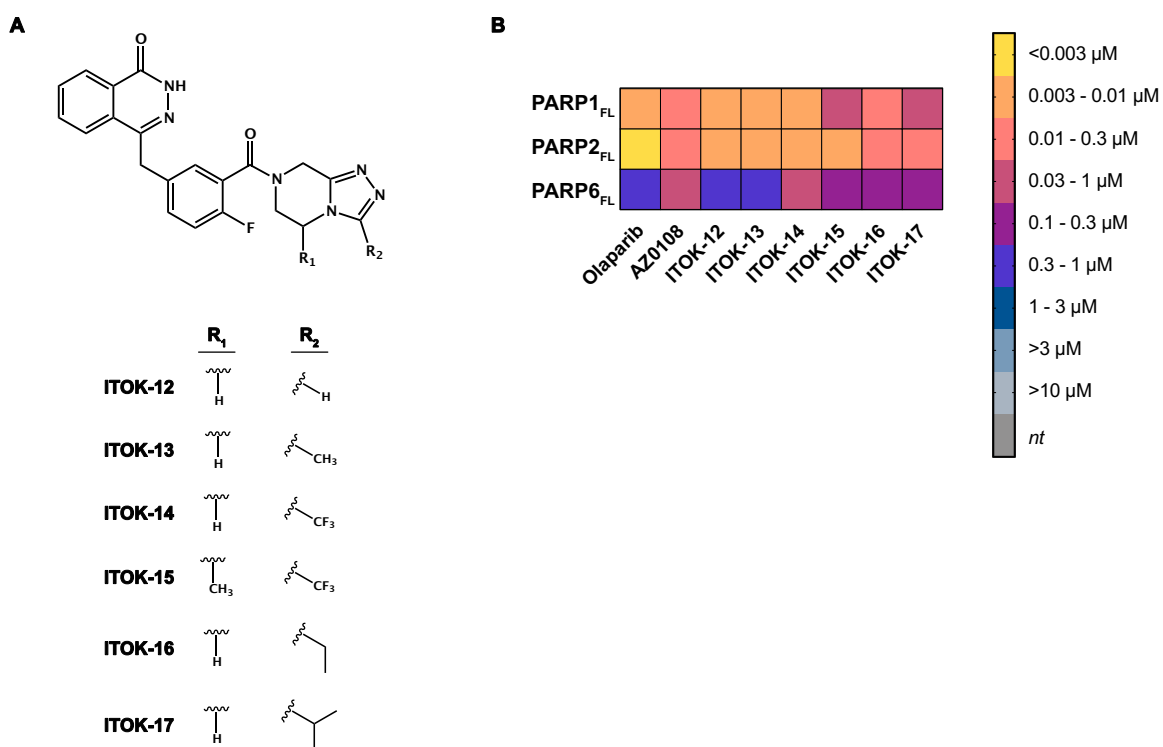
### A Brief Exploration of AZ0108 Analogues

In parallel to the olaparib analogue project, we developed a series of AZ0108 analogues with various pyrazine modifications (Scheme 6-3). We screened these compounds against a limited subset of the PARP family based on our interest in inhibition of PARP1, PARP2, and PARP6 (Figure 6-4, Appendix D). From this series of compounds we found that the  $-\text{CF}_3$  of ITOK-14, similar to the  $-\text{CF}_2\text{-CH}_3$  group of AZ0108 confer potency towards PARP6. Future work exploring halogenated substituents at this point may reveal additional opportunities to increase potency and specificity of these inhibitors. In the case of ITOK-14 and ITOK-15 substitution of a hydrogen vs. a methyl group at the 5 position of the pyrazine ( $\text{R}_1$  in Figure 6-4) had a small effect on compound activity.

The work regarding AZ0108 presented here was done for an ongoing study conducted by Moriah Arnold of the Cohen lab investigating the mechanisms of PARP1 trapping to DNA and the possible role of PARP6 and PARP8 in DNA damage repair and cell survival. Because my role in this project has been strictly limited to synthesis and *in vitro* screening the data obtained by Ms. Arnold data will not be shown here.



**Scheme 6-3** Synthesis of AZ0108 analogues



**Figure 6-4** AZ0108 series reveals structural features to target PARP6

(A) Structures of ITOK-12 - 17

(B) Heat map showing *in vitro* IC<sub>50</sub> values (μM) of ITOK-12 - 17 against PARP1, PARP2, and PARP6. Values represent averages from at least three replicates.

## Discussion

Based on the success of olaparib as a clinical PARP1/2 inhibitor, and the promising work done by AstraZeneca, we explored modifications at two positions on the olaparib scaffold. We found that a preliminary set of small substituents at the C7 position ablate potency for PARP1. Based on the structural logic of this modification born out in our work with PARP11 (Chapter 3) we expected that a similar trend would be seen across the other PARPs with active site glutamates (the HYE-PARPs, PARP1, 2, 3, 4, 5a and 5b). Synthesis and screening of C7 substituted ITOK-03 analogues is ongoing, and we expect that these modifications will yield a potent and selective PARP7 inhibitor. If such a compound is successfully produced, we will move forward to cellular studies to explore the role of PARP7 catalytic activity in innate immunity, stem cell pluripotency, and co-activator of liver X receptors (Hutin et al. 2018, Bindesbøll et al. 2016).

We produced a series of AZ0108 analogues to explore inhibition of PARP6 and PARP8 as part of an ongoing study looking at the role of these enzymes in DNA damage repair and cell survival. Based on this series we found that the -CF<sub>3</sub> group of ITOK-14 confers particular



potency towards PARP6. Future work on this project will explore other halogenated modification at this position, and the possibility of using a C7 substituted analogue to selectively inhibit PARP6.

Moriah Arnold of the Cohen lab is performing ongoing cellular studies using these compounds, with a primary focus on PARP1, PARP6, and PARP8. Preliminary results indicate that the compounds most potent for PARP6 and PARP8, ITOK-02 and ITOK-14, are most effective in inhibiting proliferation in a 4-Succinate dehydrogenase activity (MTT) cell proliferation assay. At doses below 100 nM these compounds are more effective at reducing cell proliferation than AZ0108, and more effective than olaparib at concentrations up to 3  $\mu$ M (Figure??). Though no definite conclusions have yet been reached, Ms. Arnold's work so far hints at a heretofore unknown role of PARP6 and PARP8 in cell survival and DNA damage repair. We expect that this work will lead to exciting and potentially paradigm shifting discoveries within the PARP field.

## Methods

### Cloning

cDNA encoding full length human PARP1, full length human PARP2, full length human, human brct-catalytic domain PARP4, humanPARP5

catalytic domain, human PARP10 catalytic domain, full length human PARP11, human PARP12 catalytic domain, human PARP14 wwe-catalytic domain, human PARP15 catalytic domain, full length human PARP16, and SRPK2 were obtained as previously described (Carter-OConnell et al. 2014; Morgan & Cohen 2015; Kirby, Kojic, et al. 2018).

Individual cDNA constructs encoding full length human PARP6, full length human PARP7, and full length human PARP8 were obtained using gBlock gene fragments containing the PARP11 gene as template (IDT) and the following primers (IDT) for subsequent Gibson assembly cloning:

PARP6<sub>FL</sub>:

- *Forward*: TACTTCCAATCCAATGCAGACATCAAAGGCC  
AGTTCTGGA
- *Reverse*: TTATCCACTTCCAATGTTATTAGTTTGT  
GTAAACCTGAGTTCCGATCA

PARP7<sub>FL</sub>:

- *Forward*: TACTTCCAATCCAATGCAGAAACCACCG  
CCGAACCTGAG
- *Reverse*: TTATCCACTTCCAATGTTATTAAATGGAAA  
CAGTGTTACTGACTTC

PARP8<sub>FL</sub>:

- *Forward*: TACTTCCAATCCAATGCAGGGATGTGTTCAA  
GGCAAGAGAG
- *Reverse*: TTATCCACTTCCAATGTTATTAAACCAGTCGCA

## GTCTGATTACCAATC

The amplified fragments were gel purified and cloned into a pET-His-SUMO-TEV LIC cloning vector (1B), a gift from Scott Gradia (Addgene plasmid #29653) by an isothermal assembly protocol using the Gibson assembly mix (NEB). The human PARP3 plasmid was obtained from DNAsu.

### Expression and Purification of Proteins

The following protein were expressed and purified as previously described: N-terminus hexahistidine (His6) human PARP1, PARP2, PARP3 PARP5<sub>bcat</sub>, PARP10<sub>cat</sub>, PARP14<sub>fwwe-cat</sub>, PARP15<sub>cat</sub>, SRPK2; pET-His-SUMO-TEV human PARP4, PARP6, PARP11, and PARP16 (Carter-OConnell et al. 2014; Morgan & Cohen 2015; Kirby, Kojic, et al. 2018).

pET-His6-SUMO-TEV-PARP6<sub>FL</sub>, pET-His6-SUMO-TEV-PARP7<sub>FL</sub>, or pET-His6-SUMO-TEV-PARP8<sub>FL</sub> plasmids was transformed into Escherichia coli BL21 (DE3) competent cells (Millipore) and grown on an LB agar plate with kanamycin (50 mg/mL) and chloramphenicol (34 mg/mL) overnight at 37°C. A swath of cells was inoculated into a 50 mL starter culture of LB media with kanamycin (50 mg/mL) and chloramphenicol (34 mg/mL) at 225 rpm, 37°C overnight. For each protein of interest 1-2 liters of terrific broth

(TB) media (12 g bacto tryptone, 24 g yeast extract, 0.4% glycerol, 17 mM  $\text{KH}_2\text{PO}_4$ , 72 mM  $\text{K}_2\text{HPO}_4$ , 1% glucose, 50  $\mu\text{g/mL}$  kanamycin, 34  $\mu\text{g/mL}$  chloramphenicol) was inoculated with the starter culture and grown to an OD = 0.8-1.0 at 37°C, 225 rpm. Isopropyl- $\beta$ -thiogalactoside, IPTG (Sigma-Aldrich) was added to 0.4 mM to induce protein expression for 18-24 hrs at 16°C, 225 rpm. Cells were harvested by centrifuging, resuspended in lysis buffer (20 mM HEPES, pH 7.5, 1 mM  $\beta$ -mercaptoethanol, 1 mM benzamidine, 0.2% NP-40, 0.2% TWEEN-20, 500 mM NaCl, 1 mM phenylmethylsulfonyl fluoride (PMSF), 8.3 mg/L DNase I (Roche)) and lysed by sonication at 0°C (Branson sonifier 450). Lysates were incubated with pre-washed Ni-NTA agarose resin (50% slurry, Qiagen) with end-over-end rotation at 4°C for 1 h. Following extensive washing with buffer B1+20 (20 mM HEPES, pH 7.5, 1 mM  $\beta$ -Me, 1 mM PMSF, 1 mM benzamidine, 500 mM NaCl, 20 mM imidazole). protein was eluted in four fractions of B1 containing 100-400 mM imidazole. Fractions were analyzed by SDS page gel stained with coomassie blue, or western blot visualized with ponceau stain. Fractions found to contain the desired protein as judged by molecular weight were dialyzed to 50 mM Tris-HCl, pH 7.5, 0.1 mM EDTA, 1 mM  $\beta$ -Me, 0.4 M NaCl at 4°C. Protein concentration was determined from a standard curve of His6-PARP1<sub>FL</sub> of a known concentration on western

blot visualized with a monoclonal anti-His antibody (Proteintech). Proteins were obtained in >90% purity.

### **SRPK2 Plate Assays**

96-well nickel coated plate (Pierce) was incubated with 350 ng His6-tagged SRPK2 in hB (50 mM HEPES pH 7.5, 100 mM NaCl, 4 mM MgCl<sub>2</sub>, 0.2 mM TCEP) for 60 min at RT. After extensively washing the plate, 4-400 ng (2x) of recombinant PARP enzyme in hB were added to individual wells of the 96-well plate. PARP3<sub>FL</sub> was activated by Dnick 5'P as described previously (Langelier et al. 2014) Varying concentrations of each inhibitor (0-200  $\mu$ M) were pre-incubated with 200  $\mu$ M 6-a-NAD<sup>+</sup> (2x) in hB at room temperature for 5-10 min, then added to the plate. This reaction proceeded for 60 min at 30°C, the plate was then washed three times with 1X PBST (1X PBS, 0.01% Tween-20), once with 1X PBS, then click conjugation was performed in CB (100  $\mu$ M biotin-PEG3-azide, 100  $\mu$ M Tris[(1-benzyl-1H-1,2,3-triazol-4-yl)methyl]amine (TBTA, Sigma), 1 mM CuSO<sub>4</sub>, 1 mM TCEP, 1X PBS) for 30 min at RT. The plate was then washed three times with 1X PBST, once with 1X PBS, and then blocked with 1% milk (Carnation) in 1X PBST for 30 min at RT. The plate was then washed three times with 1X PBST, once with 1X PBS, and then

incubated with Strep-HRP (300 ng/ $\mu$ L BSA, 0.05 ng/ $\mu$ L Strep-HRP, 1X PBS) for 30 min at RT. The plate was then washed three times with 1X PBST, once with 1X PBS, and then developed with QuantaRed™ Enhanced Chemifluorescent HRP Substrate (Thermo) for 30-45 s before quenching with Quanta Red Stop Solution. Fluorescence for each sample and control was read at excitation 570 nM and emission 600 nM with a Spectra Max i3 (Molecular Devices) within five min of development. Inhibitor dose response curves were fit using linear regression in Prism 7 (GraphPad™ Software). The mean IC<sub>50</sub> for each compound was calculated from at least three independent assays.

## Chemistry

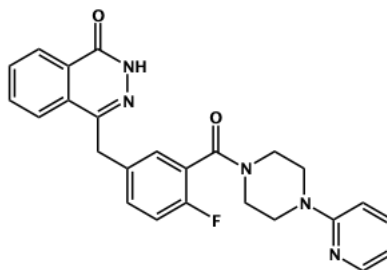
**General:** <sup>1</sup>H NMR spectra were recorded on a Bruker DPX spectrometer at 400 MHz. Chemical shifts are reported as parts per million (ppm) downfield from an internal tetramethylsilane standard or solvent references. For air- and water-sensitive reactions, glassware was flame- or oven-dried prior to use and reactions were performed under argon. Dimethylformamide was dried using the solvent purification system manufactured by Glass Contour, Inc. (Laguna Beach, CA). All other solvents were of ACS chemical grade (Fisher

Scientific) and used without further purification unless otherwise indicated. Commercially available starting reagents were used without further purification. Analytical thin-layer chromatography was performed with silica gel 60 F254 glass plates (SiliCycle). Flash column chromatography was conducted self-packed columns containing 200-400 mesh silica gel (SiliCycle) on a Combiflash Companion purification system (Teledyne ISCO). High performance liquid chromatography (HPLC) was performed on a Varian Prostar 210 (Agilent) using Polaris 5 C18-A columns (Analytical: 150 x 4.6 mm, 3  $\mu$ m; Preparative: 150 x 21.2 mm, 5  $\mu$ m) (Agilent). All final products were  $\geq 95\%$  pure as assessed by analytical HPLC (mobile phase A: 0.1% formic acid (aq), mobile phase B: 0.1% formic acid in acetonitrile; flow rate = 1.0 mL/min; conditions: pre-run A = 90 % B = 10%, 10 min A = 5% B = 95%, 11 min A = 5% B = 95%, 13 min A = 90% B = 10%; UV-Vis detection:  $\lambda_1$  = 254 nm,  $\lambda_2$  = 220 nm. Retention times (Rt) refer to UV = 254 nm. Novel compounds indicated, for literature reports of synthesized compounds see Appendix F.

**General procedure for synthesis of ITOK-01 through ITK-10:**

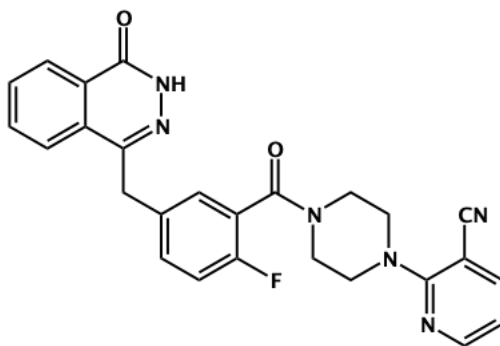
2-fluoro-5-((4-oxo-3,4-dihydrophthalazin-1-yl)methyl)benzoic acid (50 mg, 0.17 mmol), TBTU (60 mg, 0.19 mmol) and the indicated piperazine were added to a flame dried flask and dissolved in

anhydrous DMF/DCM (1:10) (5 mL). DIPEA (0.06 mL, 0.34 mmol) was added under argon and the reaction stirred at RT for 18 h. The product was then precipitated in water (100 mL) and collected by vacuum filtration.

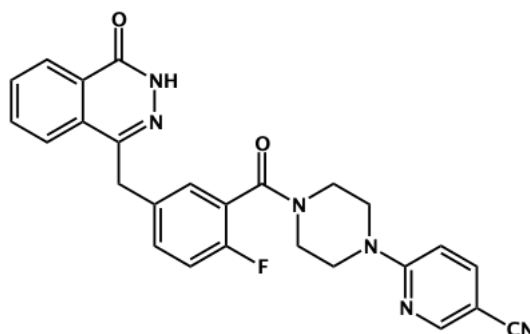


*4-(4-Fluoro-3-(4-(pyridin-2-yl)piperazine-1-carbonyl)benzyl)phthalazin-1(2H)-one, ITOK-10, ITOK-01*: from 1-(pyridin-2-yl)piperazine (31 mg, 0.19 mmol). Yield: 35 mg (47%) white solids. <sup>1</sup>H NMR (400 MHz, DMSO-d<sub>6</sub>) δ 12.60 (s, 1H), 8.26 (dd, J = 7.7, 1.4 Hz, 1H), 8.13 (dt, J = 5.0, 1.3 Hz, 1H), 7.98 (d, J = 7.9 Hz, 1H), 7.91 (td, J = 8.1, 7.6, 1.5 Hz, 1H), 7.88 – 7.80 (m, 1H), 7.56 (ddd, J = 8.9, 7.1, 2.1 Hz, 1H), 7.44 (ddd, J = 8.1, 5.1, 2.3 Hz, 1H), 7.39 (dd, J = 6.5, 2.3 Hz, 1H), 7.29 – 7.20 (m, 1H), 6.83 (d, J = 8.7 Hz, 1H), 6.72 – 6.64 (m, 1H), 4.34 (s, 2H), 3.72 (s, 2H), 3.58 (d, J = 5.4 Hz, 2H), 3.42 (s, 2H), 3.28 (s, 2H). MS m/z [M-H]<sup>-</sup> for C<sub>25</sub>H<sub>22</sub>FN<sub>5</sub>O<sub>2</sub>: 441.7. Rt = 6.28 min.

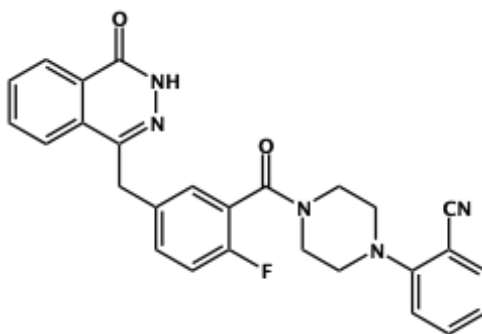




*2-(4-(2-Fluoro-5-((4-oxo-3,4-dihydrophthalazin-1-yl)methyl)benzoyl)piperazin-1-yl)nicotinonitrile (novel compound), ITOK-02*: from 2-(piperazin-1-yl)nicotinonitrile (36 mg, 0.19 mmol). Yield: 65 mg (81%) white solids. <sup>1</sup>H NMR (400 MHz, DMSO-d<sub>6</sub>) δ 12.60 (s, 1H), 8.44 (dd, J = 4.8, 1.9 Hz, 1H), 8.26 (d, J = 7.8 Hz, 1H), 8.11 (dd, J = 7.7, 1.9 Hz, 1H), 7.98 (d, J = 8.0 Hz, 1H), 7.90 (td, J = 8.2, 7.6, 1.5 Hz, 1H), 7.87 – 7.79 (m, 1H), 7.48 – 7.38 (m, 2H), 7.25 (t, J = 9.0 Hz, 1H), 6.98 (dd, J = 7.7, 4.8 Hz, 1H), 4.34 (s, 2H), 3.77 (s, 2H), 3.68 (d, J = 5.4 Hz, 2H), 3.53 (s, 2H). MS m/z [M-H]<sup>-</sup> for C<sub>26</sub>H<sub>21</sub>FN<sub>6</sub>O<sub>2</sub>: 466.7. Rt = 9.56 min.

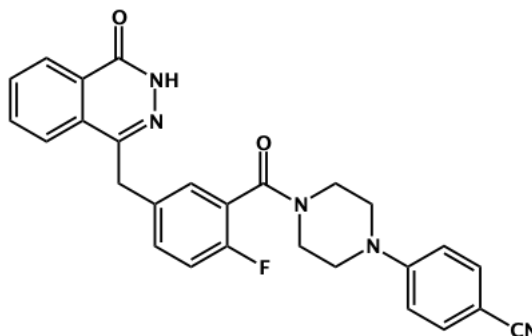


6-(4-(2-Fluoro-5-((4-oxo-3,4-dihydrophthalazin-1-yl)methyl)benzoyl)piperazin-1-yl)nicotinonitrile (*novel compound*), **ITOK-03**: from 6-(piperazin-1-yl)nicotinonitrile (36 mg, 0.19 mmol). Yield: 70 mg (89%) white solids. <sup>1</sup>H NMR (400 MHz, DMSO-d<sub>6</sub>) δ 12.60 (s, 1H), 8.51 (d, J = 2.3 Hz, 1H), 8.27 (dd, J = 7.7, 1.5 Hz, 1H), 8.01 – 7.95 (m, 1H), 7.95 – 7.87 (m, 2H), 7.87 – 7.80 (m, 1H), 7.45 (td, J = 5.5, 5.0, 2.7 Hz, 1H), 7.39 (dd, J = 6.5, 2.3 Hz, 1H), 7.25 (t, J = 9.0 Hz, 1H), 6.93 (d, J = 9.1 Hz, 1H), 4.34 (s, 2H), 3.79 – 3.69 (m, 4H), 3.61 (s, 2H). MS m/z [M-H]<sup>-</sup> for C<sub>26</sub>H<sub>21</sub>FN<sub>6</sub>O<sub>2</sub>: 466.7. Rt = 8.95 min.

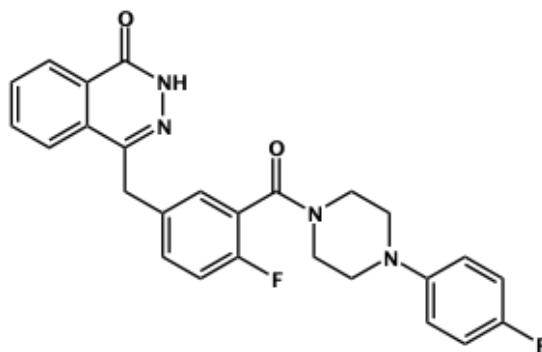


2-(4-(2-Fluoro-5-((4-oxo-3,4-dihydrophthalazin-1-yl)methyl)benzoyl)piperazin-1-yl)benzonitrile (*novel compound*), **ITOK-04**: from 2-(piperazin-1-yl)benzonitrile (35 mg, 0.19 mmol). Yield: 60 mg (75%) white solids. <sup>1</sup>H NMR (400 MHz, DMSO-d<sub>6</sub>) δ 12.61 (s, 1H), 8.30 – 8.23 (m, 1H), 7.98 (d, J = 8.0 Hz, 1H), 7.90 (td, J = 7.6, 1.5 Hz, 1H), 7.83 (t, J = 7.5 Hz, 1H), 7.74 (dd, J = 7.7, 1.7 Hz, 1H), 7.67 – 7.58

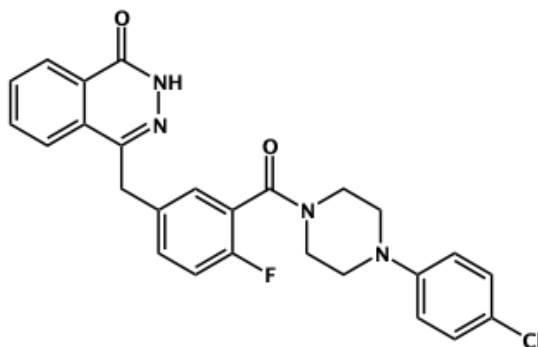
(m, 1H), 7.42 (ddd, J = 16.3, 6.1, 2.7 Hz, 2H), 7.25 (t, J = 9.0 Hz, 1H), 7.20 – 7.12 (m, 2H), 4.35 (s, 2H), 3.80 (d, J = 5.5 Hz, 2H), 3.19 (d, J = 12.6 Hz, 3H), 3.05 (d, J = 6.4 Hz, 2H), 2.66 (s, 1H). MS m/z [M-H]<sup>-</sup> for C<sub>27</sub>H<sub>22</sub>FN<sub>5</sub>O<sub>2</sub>: 465.7. Rt = 9.27 min.



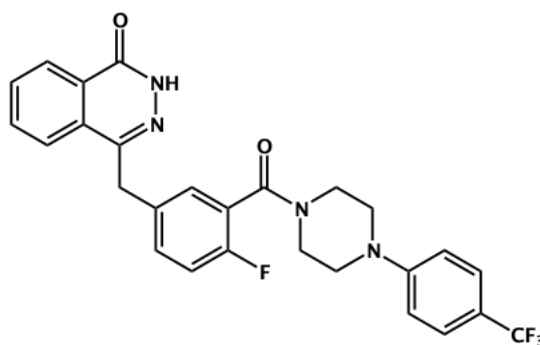
*4-(4-(2-Fluoro-5-((4-oxo-3,4-dihydrophthalazin-1-yl)methyl)benzoyl)piperazin-1-yl)benzonitrile (novel compound), ITOK-05*: from 4-(piperazin-1-yl)benzonitrile (35 mg, 0.19 mmol). Yield: 53 mg (66%) white solids. <sup>1</sup>H NMR (400 MHz, DMSO-d<sub>6</sub>) δ 12.59 (s, 1H), 8.27 (d, J = 7.7 Hz, 1H), 7.97 (d, J = 7.9 Hz, 1H), 7.90 (t, J = 7.4 Hz, 1H), 7.84 (t, J = 7.4 Hz, 1H), 7.61 (d, J = 8.9 Hz, 2H), 7.46 (d, J = 5.7 Hz, 1H), 7.39 (d, J = 6.6 Hz, 1H), 7.25 (t, J = 9.0 Hz, 1H), 7.01 (d, J = 9.0 Hz, 2H), 4.34 (s, 2H), 3.74 (s, 2H), 3.44 (d, J = 8.1 Hz, 2H), 3.28 (s, 2H). MS m/z [M-H]<sup>-</sup> for C<sub>27</sub>H<sub>22</sub>FN<sub>5</sub>O<sub>2</sub>: 465.7. Rt = 9.22 min.



*4-(4-Fluoro-3-(4-(4-fluorophenyl)piperazine-1-carbonyl)benzyl)phthalazin-1(2H)-one, ITOK-06:* from 1-(4-fluorophenyl)piperazine (34 mg, 0.19 mmol). Yield: 50 mg (64%) white solids. <sup>1</sup>H NMR (400 MHz, DMSO-d<sub>6</sub>)  $\delta$  12.59 (s, 1H), 8.27 (d, J = 7.7 Hz, 1H), 7.97 (d, J = 8.1 Hz, 1H), 7.90 (t, J = 6.8 Hz, 1H), 7.84 (t, J = 7.5 Hz, 1H), 7.44 (s, 1H), 7.37 (d, J = 6.6 Hz, 1H), 7.24 (t, J = 9.0 Hz, 1H), 7.07 (t, J = 8.9 Hz, 2H), 6.96 (dd, J = 9.2, 4.6 Hz, 2H), 4.34 (s, 2H), 3.76 (s, 2H), 3.13 (s, 2H), 2.96 (s, 2H). MS m/z [M-H]<sup>-</sup> for C<sub>26</sub>H<sub>22</sub>F<sub>2</sub>N<sub>4</sub>O<sub>2</sub>: 458.7. Rt = 9.56 min.

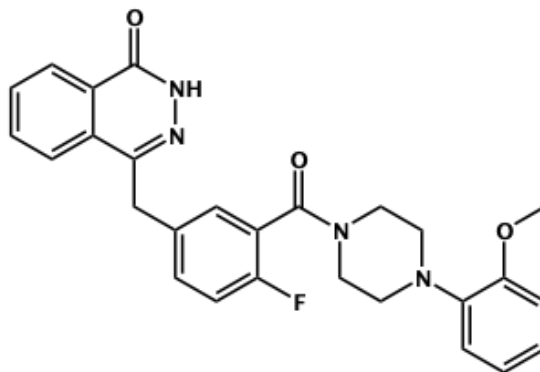


4-(3-(4-(4-Chlorophenyl)piperazine-1-carbonyl)-4-fluorobenzyl)phthalazin-1(2H)-one (novel compound), **ITOK-07**: from 1-(4-chlorophenyl)piperazine (38 mg, 0.19 mmol). Yield 60 mg (75%) white solids. <sup>1</sup>H NMR (400 MHz, DMSO-d<sub>6</sub>) δ 12.60 (s, 1H), 8.27 (dd, J = 7.8, 1.5 Hz, 1H), 7.97 (d, J = 7.9 Hz, 1H), 7.94 – 7.88 (m, 1H), 7.88 – 7.80 (m, 1H), 7.44 (td, J = 5.8, 5.0, 3.0 Hz, 1H), 7.38 (dd, J = 6.6, 2.3 Hz, 1H), 7.25 (t, J = 8.8 Hz, 3H), 6.99 – 6.92 (m, 2H), 4.34 (s, 2H), 3.75 (s, 2H), 3.20 (s, 2H), 3.03 (s, 2H). MS m/z [M-H]<sup>-</sup> for C<sub>26</sub>H<sub>22</sub>ClFN<sub>4</sub>O<sub>2</sub>: 474.7. R<sub>t</sub> = 10.31 min.

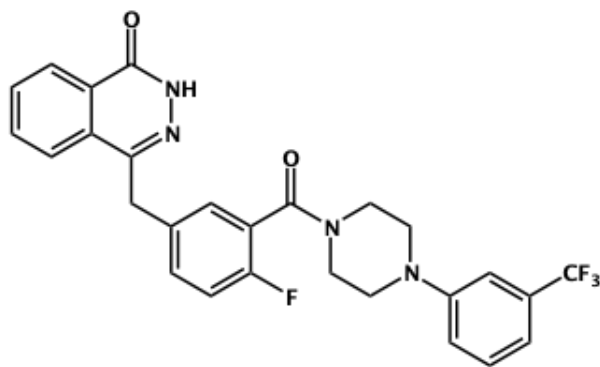


4-(4-Fluoro-3-(4-(4-(trifluoromethyl)phenyl)piperazine-1-carbonyl)benzyl)phthalazin-1(2H)-one (novel compound), **ITOK-08**: from 1-(4-(trifluoromethyl)phenyl)piperazine (44 mg, 0.19 mmol). Yield 48 mg (56%) white solids. <sup>1</sup>H NMR (400 MHz, DMSO-d<sub>6</sub>) δ 12.60 (s, 1H), 8.27 (d, J = 8.2 Hz, 1H), 7.97 (d, J = 8.0 Hz, 1H), 7.90 (td, J = 8.2, 7.6, 1.5 Hz, 1H), 7.87 – 7.80 (m, 1H), 7.53 (d, J = 8.7 Hz, 2H), 7.49 – 7.41 (m, 1H), 7.39 (dd, J = 6.6, 2.3 Hz, 1H), 7.25 (t, J = 9.0 Hz,

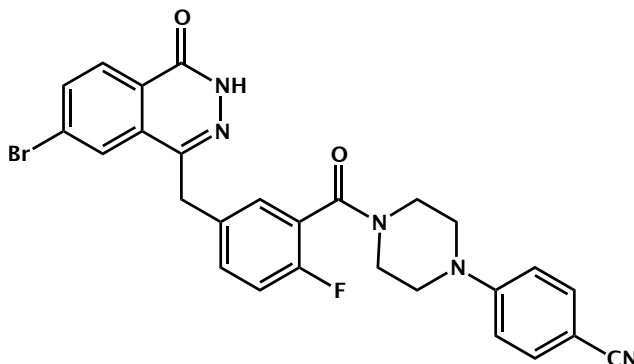
1H), 7.06 (d, J = 8.7 Hz, 2H), 4.34 (s, 2H), 3.76 (s, 2H), 3.20 (s, 2H). MS  
m/z [M-H]<sup>-</sup> for C<sub>27</sub>H<sub>22</sub>F<sub>4</sub>N<sub>4</sub>O<sub>2</sub>: 508.7. Rt = 10.60 min.



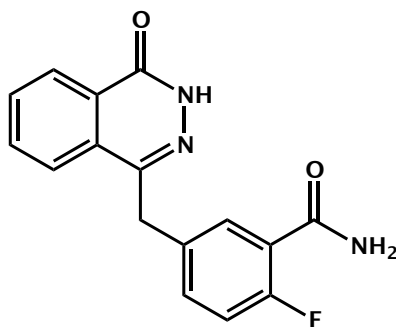
*4-(4-Fluoro-3-(4-(2-methoxyphenyl)piperazine-1-carbonyl)benzyl)phthalazin-1(2H)-one, ITOK-09*: from 1-(2-methoxyphenyl)piperazine (36 mg, 0.19 mmol). Yield: 40 mg (50%) white solids. <sup>1</sup>H NMR (400 MHz, DMSO-d<sub>6</sub>) δ 12.61 (s, 1H), 8.30 – 8.23 (m, 1H), 7.98 (d, J = 8.0 Hz, 1H), 7.90 (td, J = 8.1, 7.7, 1.6 Hz, 1H), 7.87 – 7.80 (m, 1H), 7.44 (dd, J = 7.1, 4.5 Hz, 1H), 7.37 (d, J = 6.5 Hz, 1H), 7.24 (t, J = 9.0 Hz, 1H), 7.03 – 6.95 (m, 2H), 6.90 – 6.84 (m, 2H), 4.35 (s, 2H), 3.78 (s, 3H), 3.75 (s, 2H), 2.99 (s, 2H), 2.83 (s, 2H). MS  
m/z [M-H]<sup>-</sup> for C<sub>27</sub>H<sub>25</sub>FN<sub>4</sub>O<sub>3</sub>: 470.7. Rt = 9.02 min.



4-(4-Fluoro-3-(4-(3-(trifluoromethyl)phenyl)piperazine-1-carbonyl)benzyl)phthalazin-1(2H)-one, **ITOK-10**: from 1-(3-(trifluoromethyl)phenyl)piperazine (43 mg, 0.19 mmol). Yield: 60 mg (69%) white solids.  $^1\text{H}$  NMR (400 MHz, DMSO- $d_6$ )  $\delta$  12.60 (d,  $J$  = 2.1 Hz, 1H), 8.30 – 8.23 (m, 1H), 7.98 (d,  $J$  = 8.0 Hz, 1H), 7.95 – 7.79 (m, 2H), 7.48 – 7.42 (m, 1H), 7.38 (dt,  $J$  = 6.3, 3.0 Hz, 1H), 7.24 (td,  $J$  = 8.4, 7.7, 4.9 Hz, 2H), 7.15 – 7.10 (m, 2H), 7.08 – 7.02 (m, 1H), 4.35 (s, 2H), 3.78 (s, 2H), 3.24 (t,  $J$  = 5.1 Hz, 1H), 3.16 – 3.10 (m, 1H), 3.08 – 2.98 (m, 2H), 2.90 (d,  $J$  = 5.1 Hz, 1H), 2.61 (t,  $J$  = 5.1 Hz, 1H). MS  $m/z$  [M-H] $^-$  for  $\text{C}_{27}\text{H}_{22}\text{F}_4\text{N}_4\text{O}_2$ : 508.5.  $R_t$  = 9.65 min.



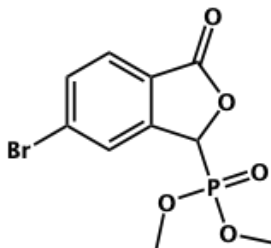
*4-(4-(5-((7-Bromo-4-oxo-3,4-dihydrophthalazin-1-yl)methyl)-2-fluorobenzoyl)piperazin-1-yl)benzonitrile (novel compound), ITOK-05a1:* from 5-((7-bromo-4-oxo-3,4-dihydrophthalazin-1-yl)methyl)-2-fluorobenzoic acid (100 mg, 0.27 mmol) and 4-(piperazin-1-yl)benzonitrile (50 mg, 0.27 mol); yield: 75 mg (52%) white solids. <sup>1</sup>H NMR (400 MHz, DMSO-d<sub>6</sub>) δ 12.73 (d, J = 21.0 Hz, 1H), 8.35 (s, 1H), 8.16 (d, J = 6.9 Hz, 1H), 8.12 – 7.86 (m, 2H), 7.61 (d, J = 8.4 Hz, 2H), 7.39 (d, J = 27.5 Hz, 2H), 7.26 (s, 1H), 7.01 (d, J = 8.7 Hz, 2H), 4.34 (d, J = 4.8 Hz, 2H), 3.74 (s, 2H), 3.45 (s, 3H). MS m/z [M-H](#)- for C<sub>27</sub>H<sub>21</sub>BrFN<sub>5</sub>O<sub>2</sub>: 544, 546. Rt = 9.90



*4-(4-Fluoro-3-(piperazine-1-carbonyl)benzyl)phthalazin-1(2H)-one, ITOK-II:* from tert-butyl piperazine-1-carboxylate (35 mg, 0.19 mmol), followed by removal of BOC group by stirring with acetyl chloride (0.074 mL, 0.95 mmol) in methanol for 3 days at RT. Product was precipitated in water as a white solid. Yield: 50 mg (63%). <sup>1</sup>H NMR (400 MHz, DMSO-d<sub>6</sub>) δ 12.59 (s, 1H), 8.29 – 8.23



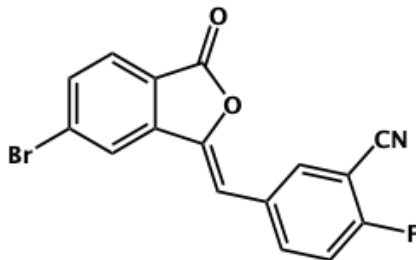
(m, 1H), 7.97 (d, J = 7.9 Hz, 1H), 7.93 – 7.87 (m, 1H), 7.83 (t, J = 7.3 Hz, 1H), 7.45 – 7.37 (m, 1H), 7.32 (dd, J = 6.6, 2.3 Hz, 1H), 7.25 – 7.15 (m, 1H), 4.32 (s, 2H), 2.97 (s, 3H), 2.79 (d, J = 1.2 Hz, 3H). MS m/z [M+H]<sup>+</sup> for C<sub>16</sub>H<sub>12</sub>FN<sub>3</sub>O<sub>2</sub>: 298.0. R<sub>t</sub> = 7.17 min.



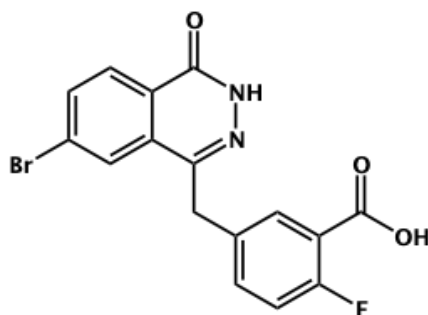
*Dimethyl (6-bromo-3-oxo-1,3-dihydroisobenzofuran-1-yl)phosphonate:*

Sodium methoxide (3 g, 56 mmol) was added to a flame dried flask and dissolved in anhydrous methanol (25 mL) then cooled to 0°C. Dimethyl phosphonate (4.8 mL, 52.5 mmol) was added dropwise and the reaction mixture stirred under argon for 10 min. 5-bromo-3-hydroxyisobenzofuran-1(3H)-one (4 g, 17.5 mmol) was added in three portions the reaction was allowed to slowly warm to room temperature. The reaction was stirred under argon for 18 h at RT. When TLC analysis (10% MeoH in DCM) showed complete consumption of the starting furan methane sulfonic acid (4.3 mL, 63 mmol) was added causing precipitation of ample white solids. The reaction was stirred for an additional 1 h then diluted in water (100 mL) and the white solids collected by vacuum filtration: 5.5 g (98%). 1H

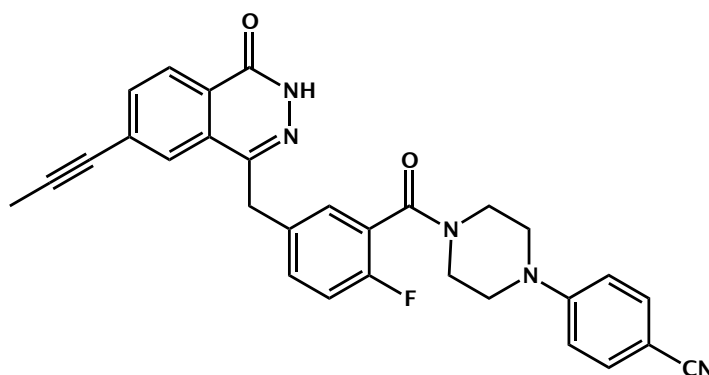
NMR (400 MHz, Methanol-d<sub>4</sub>)  $\delta$  7.94 (dt,  $J$  = 1.9, 0.9 Hz, 1H), 7.87 (dd,  $J$  = 1.5, 0.9 Hz, 2H), 3.94 (d,  $J$  = 11.0 Hz, 3H), 3.78 (d,  $J$  = 10.8 Hz, 3H).



*(Z)*-5-((6-bromo-3-oxoisobenzofuran-1(3H)-ylidene)methyl)-2-fluorobenzonitrile (*novel compound*): dimethyl (6-bromo-3-oxo-1,3-dihydroisobenzofuran-1-yl)phosphonate (5.5 g, 17.13 mmol) and 2-fluoro-5-formylbenzonitrile (2.6 g, 17.13 mmol) were added to a flame dried flask and dissolved in anhydrous THF (100 mL). Triethylamine (4.7 mL) added and the reaction stirred at RT under argon for 72 h. Once the starting materials were consumed by TLC (10% MeOH in DCM) the reaction was poured over water (1000 mL) and the product obtained as a white solid by vacuum filtration: 5.8 g (97%). <sup>1</sup>H NMR (400 MHz, DMSO-d<sub>6</sub>)  $\delta$  8.43 (d,  $J$  = 1.6 Hz, 1H), 8.14 (ddt,  $J$  = 16.5, 5.3, 2.3 Hz, 2H), 7.96 – 7.86 (m, 2H), 7.67 (t,  $J$  = 9.1 Hz, 1H), 7.10 (s, 1H).



*5-((7-Bromo-4-oxo-3,4-dihydrophthalazin-1-yl)methyl)-2-fluorobenzoic acid: (Z)-5-((6-bromo-3-oxoisobenzofuran-1(3H)-ylidene)methyl)-2-fluorobenzonitrile* (1g, 2.9 mmol) was added to a bomb flask and dissolved in ethanol (30 mL). Freshly prepared aqueous sodium hydroxide was added to a final concentration of 8 M and stirred for 30 min at RT. Hydrazine monohydrate (1.25 mL, 40 mmol) was added and the reaction was sealed and stirred at 80°C for 80 h. Once no starting material could be detected by MS (ESI-) the reaction was poured over water (500 mL) and acidulated with HCl to pH 4. The product was collected by vacuum filtration as a red solid at 90% purity and taken on crude without characterization: 178 mg (17%).

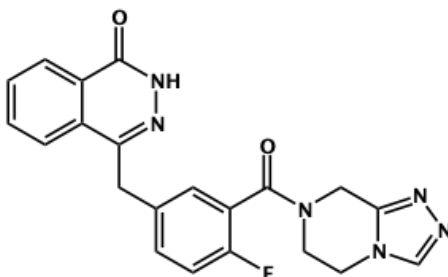


4-(4-(2-Fluoro-5-((4-oxo-7-(prop-1-yn-1-yl)-3,4-dihydrophthalazin-1-yl)methyl)benzoyl)piperazin-1-yl)benzonitrile (*novel compound*), **ITOK-05a2**: 4-(4-(5-((7-bromo-4-oxo-3,4-dihydrophthalazin-1-yl)methyl)-2-fluorobenzoyl)piperazin-1-yl)benzonitrile (50 mg, 0.09 mmol) was concentrated from anhydrous toluene (3x, 10 mL) then dissolved in anhydrous toluene under argon. Tributyl(1-propynyl)tin (0.3 mL, 0.1 mmol) and palladium tetrakis (11mg, 0.009 mmol) were quickly added and the reaction refluxed under argon for 2 h. The crude reaction was concentrated in vacuo followed by purification via ISCO Combiflash chromatography (silica, 4g, 0-10% MeOH in DCM): 11 mg (24%) white solids. <sup>1</sup>H NMR (400 MHz, Methanol-d<sub>4</sub>) δ 8.31 – 8.26 (m, 1H), 7.91 – 7.85 (m, 1H), 7.76 (ddd, J = 11.0, 8.4, 1.7 Hz, 1H), 7.58 – 7.53 (m, 2H), 7.50 (ddd, J = 8.1, 5.0, 2.3 Hz, 1H), 7.38 (ddd, J = 14.5, 6.4, 2.3 Hz, 1H), 7.19 (td, J = 9.0, 5.2 Hz, 1H), 7.04 – 6.98 (m, 2H), 4.37 (s, 2H), 3.90 (q, J = 5.3 Hz, 2H), 3.46 (dq, J = 11.4, 4.9 Hz, 4H), 3.28 (dd, J = 11.2, 5.7 Hz, 2H), 2.08 (d, J = 22.4 Hz, 3H). MS m/z [M-H](#)<sup>-</sup> for C<sub>30</sub>H<sub>24</sub>FN<sub>5</sub>O<sub>2</sub>: 504.

#### General procedure for ITOK-12 through 17:

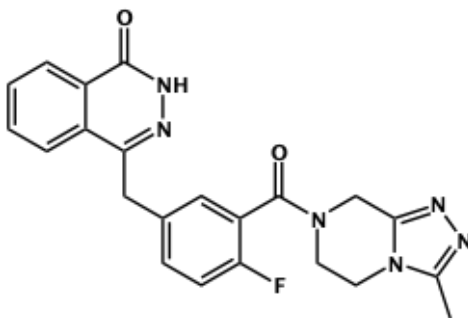
2-fluoro-5-((4-oxo-3,4-dihydrophthalazin-1-yl)methyl)benzoic acid (100 mg, 0.34 mmol) and the indicated pyrazine (1.0 eqv) were added

to a flame dried flask and dissolved in anhydrous DMF (3 mL). DIPEA (0.3 mL, 1.7 mmol) was added under argon and the reaction cooled to -15°C and stirred for 10 min. 1-propanephosphonic acid cyclic anhydride (50% in DMF, Acros Organics) (0.4 mL, 0.68 mmol) was added dropwise to the reaction mixture under argon and the reaction stirred for 10 min at -15°C, then slowly warmed to RT and stirred for 18 h. The reaction mixture was then poured over water (100 mL) and extracted with DCM (3x 40 mL). The combined organic layers were washed with water (1x 100 mL) and brine (1x 100 mL) and concentrated in vacuo followed by purification via ISCO Combiflash chromatography (silica, 4g, 0-10% MeOH in DCM).

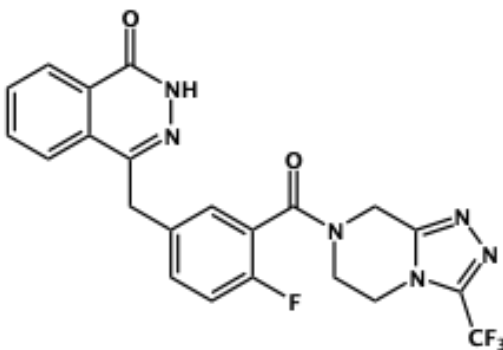


*4-(4-Fluoro-3-(5,6,7,8-tetrahydro-[1,2,4]triazolo[4,3-a]pyrazine-7-carbonyl)benzyl)phthalazin-1(2H)-one, ITOK-12*: from 5,6,7,8-tetrahydro-[1,2,4]triazolo[4,3-a]pyrazine hydrochloride (54 mg, 0.34 mmol). Yield: 40 mg (29%) white solids. <sup>1</sup>H NMR (400 MHz, DMSO-d<sub>6</sub>) δ 12.58 (s, 1H), 8.51 (s, 1H), 8.27 (d, J = 7.8 Hz, 1H), 7.97 (d, J = 8.4 Hz, 1H), 7.94 – 7.87 (m, 1H), 7.87 – 7.80 (m, 1H), 7.53 – 7.41 (m,

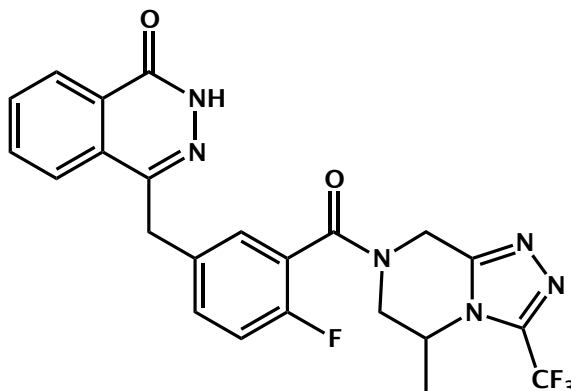
2H), 7.33 – 7.24 (m, 1H), 4.94 (s, 1H), 4.60 (s, 1H), 4.14 (d, J = 5.4 Hz, 1H), 4.08 (d, J = 4.1 Hz, 1H), 4.00 (t, J = 5.5 Hz, 1H), 3.63 (s, 1H). MS m/z [M+H]<sup>+</sup> for C<sub>21</sub>H<sub>17</sub>N<sub>6</sub>O<sub>2</sub>: 405.2. Rt = 6.62 min.



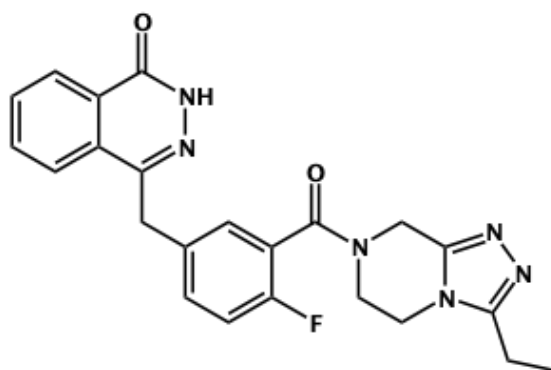
4-(4-Fluoro-3-(3-methyl-5,6,7,8-tetrahydro-[1,2,4]triazolo[4,3-a]pyrazine-7-carbonyl)benzyl)phthalazin-1(2H)-one, **ITOK-13**: from 3-methyl-5,6,7,8-tetrahydro-[1,2,4]triazolo[4,3-a]pyrazine (46 mg, 0.34 mmol). Yield: 38 mg (27%) white solids. <sup>1</sup>H NMR (400 MHz, DMSO-d<sub>6</sub>) δ 12.58 (s, 1H), 8.27 (d, J = 7.6 Hz, 1H), 7.99 – 7.80 (m, 3H), 7.49 (s, 1H), 7.43 (d, J = 6.7 Hz, 1H), 7.29 (t, J = 8.9 Hz, 1H), 4.87 (s, 1H), 4.54 (s, 1H), 4.34 (s, 2H), 4.08 (s, 1H), 3.98 (s, 1H), 3.70 (s, 1H), 3.59 (s, 1H), 2.29 (d, J = 15.9 Hz, 3H). MS m/z [M-H]<sup>-</sup> for C<sub>22</sub>H<sub>19</sub>N<sub>6</sub>O<sub>2</sub>: 416.7. Rt = 6.71 min.



4-(4-Fluoro-3-(3-(trifluoromethyl)-5,6,7,8-tetrahydro-[1,2,4]triazolo[4,3-a]pyrazine-7-carbonyl)benzyl)phthalazin-1(2H)-one, **ITOK-14**: from 3-(trifluoromethyl)-5,6,7,8-tetrahydro-[1,2,4]triazolo[4,3-a]pyrazine (65 mg, 0.34 mmol). Yield: 50 mg (31%) white solids. <sup>1</sup>H NMR (400 MHz, DMSO-d<sub>6</sub>) δ 12.58 (s, 1H), 8.26 (dd, J = 7.3, 1.6 Hz, 1H), 7.97 – 7.79 (m, 3H), 7.52 (d, J = 8.4 Hz, 1H), 7.44 (d, J = 6.3 Hz, 1H), 7.30 (t, J = 8.8 Hz, 1H), 5.02 (s, 1H), 4.70 (s, 1H), 4.34 (s, 2H), 4.23 (s, 1H), 4.14 (s, 1H), 3.97 (s, 1H), 3.67 (s, 1H). MS m/z [M-H]<sup>-</sup> for C<sub>22</sub>H<sub>16</sub>F<sub>4</sub>N<sub>6</sub>O<sub>2</sub>: 471.0. Rt = 8.00 min.



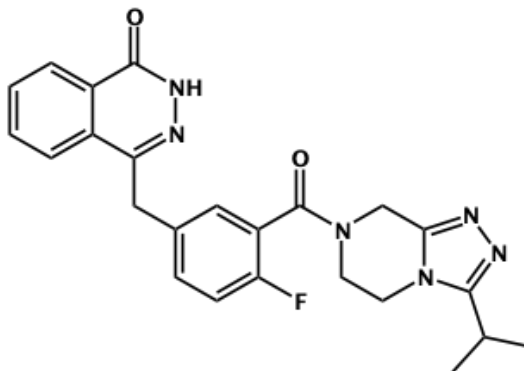
*4-(4-Fluoro-3-(5-methyl-3-(trifluoromethyl)-5,6,7,8-tetrahydro-[1,2,4]triazolo[4,3-a]pyrazine-7-carbonyl)benzyl)phthalazin-1(2H)-one*, **ITOK-15**: from 3,5-dimethyl-5,6,7,8-tetrahydro-[1,2,4]triazolo[4,3-a]pyrazine (70 mg, 0.34 mmol). Yield: 57 mg (58%) white solids. <sup>1</sup>H NMR (400 MHz, DMSO-d<sub>6</sub>) δ 12.60 (s, 1H), 8.26 (dd, J = 7.9, 1.5 Hz, 1H), 8.02 – 7.79 (m, 3H), 7.52 (d, J = 6.6 Hz, 1H), 7.40 (d, J = 6.4 Hz, 1H), 7.30 (q, J = 9.2 Hz, 1H), 4.86 – 4.50 (m, 3H), 4.36 (s, 2H), 3.79 (d, J = 14.2 Hz, 1H), 3.55 (t, J = 13.2 Hz, 1H), 1.14 (s, 3H). MS m/z [M-H]<sup>-</sup> for C<sub>23</sub>H<sub>18</sub>F<sub>4</sub>N<sub>6</sub>O<sub>2</sub>: 485.0. Rt = 8.32.



*4-(3-(3-Ethyl-5,6,7,8-tetrahydro-[1,2,4]triazolo[4,3-a]pyrazine-7-carbonyl)-4-fluorobenzyl)phthalazin-1(2H)-one* (novel compound), **ITOK-16**: from 3-ethyl-5,6,7,8-tetrahydro-[1,2,4]triazolo[4,3-a]pyrazine (52 mg, 0.34 mmol). Yield: 90 mg (60%) white solids. <sup>1</sup>H NMR (400 MHz, DMSO-d<sub>6</sub>) δ 12.58 (s, 1H), 8.27 (d, J = 7.6 Hz, 1H), 7.95 (s, 1H), 7.90 (d, J = 12.0 Hz, 1H), 7.84 (t, J = 7.4 Hz, 1H), 7.49 (s,



1H), 7.44 (s, 1H), 7.29 (t, J = 8.8 Hz, 1H), 4.88 (s, 1H), 4.55 (s, 1H), 4.34 (s, 2H), 4.07 (s, 1H), 4.00 (s, 1H), 3.72 (s, 1H), 3.58 (s, 1H), 2.64 (dq, J = 14.8, 7.4 Hz, 2H), 1.23 (t, J = 7.4 Hz, 3H). MS m/z [M-H]<sup>-</sup> for C<sub>23</sub>H<sub>21</sub>FN<sub>6</sub>O<sub>2</sub>: 430.7. Rt = 6.98 min



4-(4-Fluoro-3-(3-isopropyl-5,6,7,8-tetrahydro-[1,2,4]triazolo[4,3-a]pyrazine-7-carbonyl)benzyl)phthalazine-1(2H)-one, **ITOK-17**: from 3-isopropyl-5,6,7,8-tetrahydro-[1,2,4]triazolo[4,3-a]pyrazine (56 mg, 0.34 mmol). Yield: 60 mg (40%) white solids. <sup>1</sup>H NMR (400 MHz, DMSO-d<sub>6</sub>) δ 12.58 (s, 1H), 8.26 (d, J = 7.6 Hz, 1H), 7.98 – 7.79 (m, 3H), 7.52 – 7.42 (m, 2H), 7.30 (t, J = 8.9 Hz, 1H), 4.88 (s, 1H), 4.55 (d, J = 3.4 Hz, 1H), 4.34 (s, 2H), 4.09 (q, J = 5.2 Hz, 1H), 3.75 (s, 1H), 3.58 (s, 1H), 3.17 (dd, J = 5.3, 0.9 Hz, 2H), 2.14 – 2.06 (m, 1H), 1.24 (d, J = 6.8 Hz, 6H). MS m/z [M-H]<sup>-</sup> for C<sub>24</sub>H<sub>23</sub>FN<sub>6</sub>O<sub>2</sub>: 444.9. Rt = 6.98 min.

## Chapter 7: Concluding remarks

Poly-ADP-ribose-polymerases (PARPs) have emerged as important regulators of cellular function with implications for disease. Though termed “polymerases” only four of the seventeen human PARP enzymes have been substantiated as polymerases: PARP1, PARP2, and PARP5a/b (also known as the Tankyrase). The majority of the PARP family have been characterized as mono-ADP-ribose-transferases, hydrolyzing and transferring a single ADP-ribose moiety from nicotinamide adenine dinucleotide (NAD<sup>+</sup>) onto their targets. The true polymerases, or PARylating PARPs, were discovered and studied much earlier and more thoroughly than the mono-transferases, MARylating PARPs, which were only completely described in the ~~the~~ last decade. The PARylating PARPs have been primarily studied in the context of cancer, a precedent set by the discovery of PARP1’s involvement in DNA damage repair and its success as a therapeutic target in BRCA-/- cancers {Farmer:2005bf, Bryant:2005ba}. MARylating PARPs have also been connected to cancer, as well as inflammation, neurodevelopment, and host-viral interactions (Iansante et al. 2015; Barbarulo et al. 2013; Mehrotra et al. 2013; J. Y. Huang et al. 2016; Daugherty et al. 2014). But these enzymes remain poorly understood and have not been targeted in clinic.

A key factor in building our understanding of PARylating PARPs has been the availability of potent inhibitors to drug these enzymes, while conversely there are very few inhibitors available to target MARYlating PARPs. Currently, the only published inhibitors for MARYlating PARPs target PARP10 (Venkannagari et al. 2016; Morgan et al. 2018), PARP11 (Kirby, Kojic, et al. 2018), and PARP14 (Peng et al. 2016; Yoneyama-Hirozane et al. 2017; Upton et al. 2017). In Chapter 1, I dove into the history of PARP inhibitor development, structural features of PARP inhibitors, PARP inhibitor screening assays, and the current challenges and opportunities for PARP inhibitor development. In the following chapters I described my efforts over the course of my dissertation to address the dearth of tools and methodologies for PARP inhibitor development, and the development of several novel PARP inhibitors.

A major shortcoming in the field has been the lack of effective, standardized reagents or assays to assess PARP activity and thus inhibitor efficacy and selectivity. It is standard practice within the field to screen novel inhibitors against two to five PARP family members and disregard the rest of the family, despite the highly conserved binding domain and ample evidence that many PARP inhibitors—including FDA approved drugs such as olaparib—exhibit broad

spectrum inhibition across the family. Though there is a useful therapeutic window for these compounds, use of a non-selective inhibitor to study biological mechanisms can quickly lead to confusion and misinterpretation. In Chapter 2 I described an assay I designed to address this issue. Briefly, in this assay a promiscuous PARP substrate or the PARP itself was chelated to a 96-well nickel coated plate (Pierce) through a His6 tag. A recombinant PARP purified from *E. coli* and an inhibitor of interest at increasing concentration are added with NAD<sup>+</sup> or a clickable NAD<sup>+</sup> analogue (6-alkyne-NAD<sup>+</sup>) (Jiang et al. 2010) to the plate. The extent of ADP-ribosylation at each inhibitor concentration was measured using either a NAD<sup>+</sup> binding reagent (Millipore) or a chemifluorescent HRP-substrate (Thermo) reacting with a click conjugated biotin azide tag. This assay proved to be sensitive, reproducible, and generalizable to the entire PARP family.

In Chapter 3, I used this assay to inform the design of a PARP11 inhibitor that exploits a small hydrophobic sub-pocket in the active site of most MARYlating PARPs, and a uniquely favorable interaction with a flexible loop (the donor-loop or D-loop) abutting the active site of PARP11. This inhibitor (ITK7) was potent in cells and in live-cell imaging caused quick and persistent dissociation of GFP-PARP11 from the nuclear pore. This finding revealed a possible connection between

catalytic activity—or potentially substrate binding—and PARP localization. Though little is known about the biological role of PARP11, it has been shown to modify proteins at the nuclear pore (Carter-OConnell et al. 2016) and regulate nuclear envelope morphology in spermatids (Meyer-Ficca et al. 2015). This inhibitor will be useful in establishing the role of PARP11 in nuclear envelope morphology and stability, nuclear pore biology, and male fertility.

In Chapter 4 I applied the same strategies as in Chapter 3 to target another unique sub-pocket of the active site, this time in PARP4. This work quickly led to a selective PARP4 inhibitor (AEP08). In future work this compound could be used to evaluate the importance of PARP4 in cancers, where it has been found to be highly up-regulated particularly in some pediatric glioblastomas (Personal communication, Dr. Cho, Oregon Health and Science University). Because of the free benzoic acid on AEP08, this compound could easily be adapted to a pro-drug strategy {Placzek:2016jo, Meinig:2017fc, Ferrara:2017gz, Meinig:2018im} for effective delivery across the blood brain barrier. It could also be functionalized into a proteomics probe to identify PARP4 targets and interacting proteins.

In Chapter 5 I built on previous work by Dr. Haihong Jin and Dr. Rory Morgan to validate the potency and mechanism of action of a

covalent PARP16 inhibitor (HJ-52) in cells. This work would not have been possible without the generous assistance of the Taunton lab at UCSF which provided an occupancy probe for PARP16 that could be labeled through click conjugation. This compound was indispensable for our studies because PARP16 does not have detectable ADP-ribosylation activity in cells, though it demonstrates robust MARYlating activity *in vitro*. The lack of detectible ADP-ribosylation activity in cells may be due to limitations of the available reagents, or it may indicate that PARP16 is only active in cells under certain conditions. Previous studies have reported that PARP16 MARYlates PERK and IRE1 $\alpha$  as part of the unfolded protein response in the endoplasmic reticulum. Further work will be required to determine whether the previously reported effects of PARP16 are in fact due to MARYlation activity, or to the presence of PARP16 independent of catalytic activity, and whether substrate binding impacts the localization, activity, or mechanistic effects of PARP16.

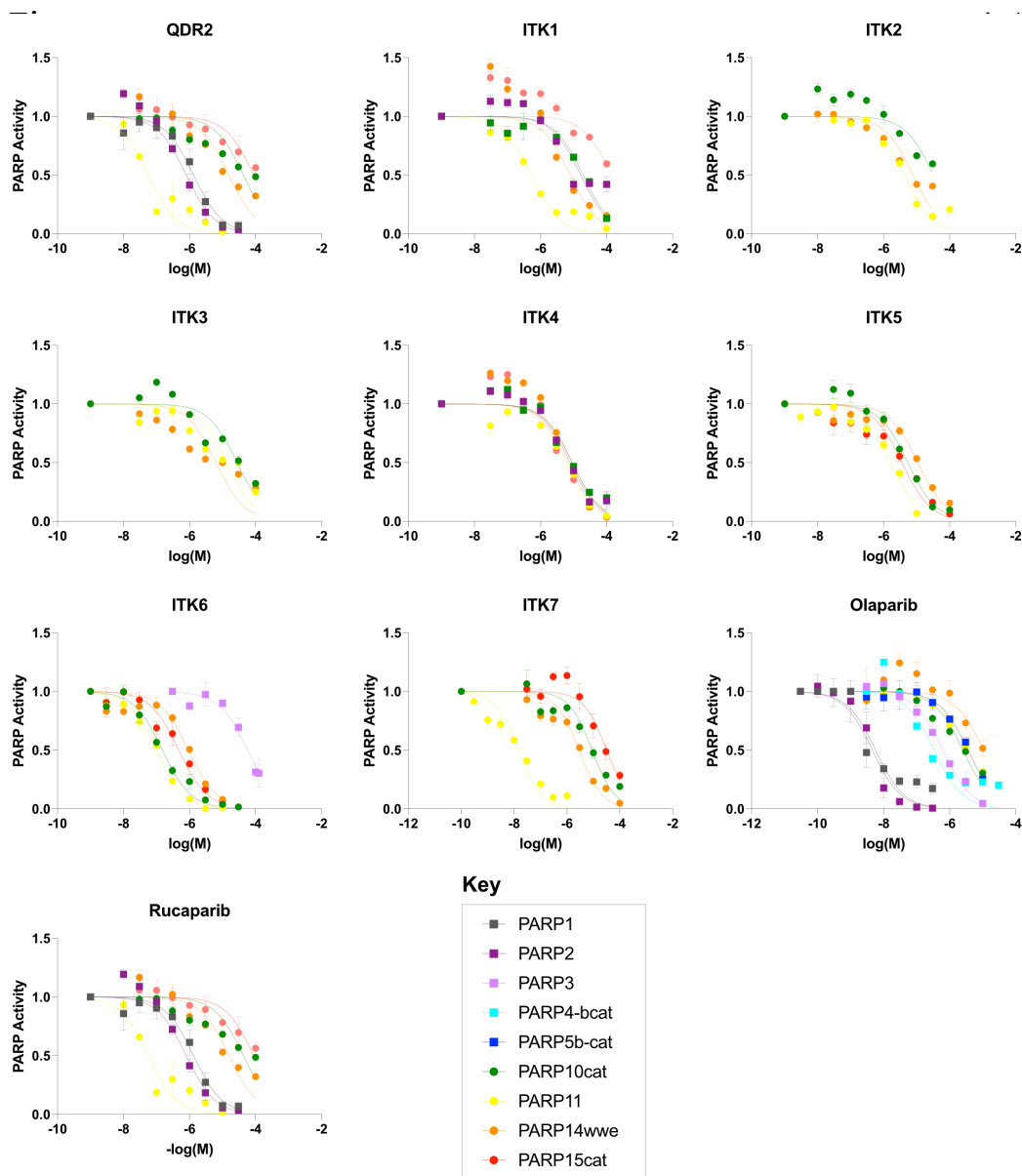
In Chapter 6 I briefly described ongoing work exploring modifications to the olaparib scaffold. This series of inhibitors is part of a study being conducted by Ms. Moriah Arnold in the Cohen Lab investigating the role of PARP6 and PARP8 in DNA damage repair and cell survival. Within this series of compounds we stumbled upon a

potent inhibitor of PARP1, PARP2, and PARP7. I applied the same strategy used in Chapter 3 to reduce binding affinity towards PARP1 and PARP2. This strategy proved successful with a preliminary analogue, ITOK-03. The synthesis of optimized analogues and biological testing to determine whether this is in fact the first potent and selective PARP7 inhibitor is currently underway.

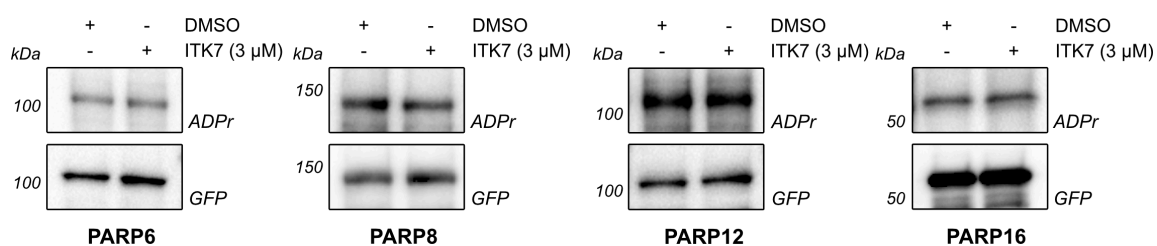
I anticipate that the inhibitors I have produced will be useful in expanding our understanding of MARYlating PARPs in biology and disease. The methods for PARP inhibitor development I have developed can be used as a platform for future PARP inhibitor design. Together they lay the groundwork for eventually having selective and potent inhibitors of each PARP that can be used individually or in combination to understand the fundamental role, interplay, and importance of PARPs in biology and disease.



## **Appendix A: Full IC<sub>50</sub> Data for Compounds in Chapter 3**

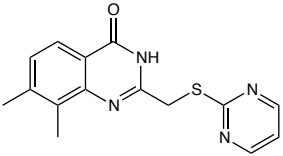
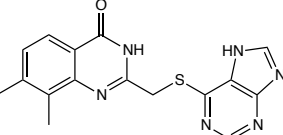


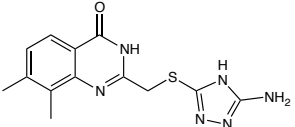
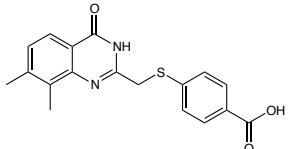
**Figure A-1** Dose response curves for QDR2 and ITK1-7, olaparib, and rucaparib against PARP1<sub>FL</sub>, PARP2<sub>FL</sub>, PARP3<sub>FL</sub>, PARP4<sub>brct-cat</sub>, PARP5b<sub>cat</sub>, PARP7<sub>FL</sub>, PARP10<sub>cat</sub>, PARP11<sub>FL</sub>, PARP14<sub>cat-wwe</sub>, and PARP15<sub>cat</sub> determined with *in vitro* plate assays using either SRPK2 or the PARP itself as a substrate and 6-a-NAD<sup>+</sup> followed by click chemistry. Curves generated using Prism 7 (Graph Pad); error bars indicate  $\pm$ SEM from at least three replicates.

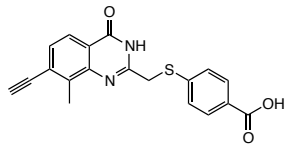


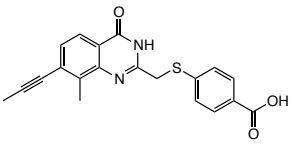
**Figure A-2** HEK 293T cells transfected with GFP-PARP6, GFP-PARP8, GFP-PARP12, or GFP-PARP16 were lysed after 24 h and GFP-PARPs immunoprecipitated on magnetic beads. Immunoprecipitated PARPs were incubated with either DMSO or ITK7 (3 μM) for 1.5 h at 25°C with 100 μM (GFP-PARP6-12) or 400 μM (GFP-PARP16) 6-a-NAD<sup>+</sup> based on the literature *K<sub>m</sub>* of NAD<sup>+</sup> (Thorsell et al., 2017). Auto-MARylation was analyzed by Western blot with an ADP-ribose (ADPr) binding reagent (Millipore)

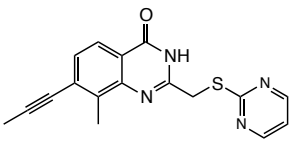
**Table A-1** In vitro IC<sub>50</sub> (μM) values for ITK1-7, olaparib and rucaparib; SEM from a minimum of three dose-response experiments.

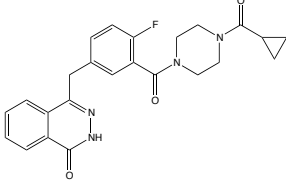
ITK1	PARP1	PARP2	PARP3
	>30	17.4±3.3	>30
	<b>PARP4<sub>brct-cat</sub></b>	<b>PARP5b<sub>cat</sub></b>	<b>PARP6</b>
	nt	>10	nt
	<b>PARP5b<sub>cat</sub></b>	<b>PARP8</b>	<b>PARP10<sub>cat</sub></b>
	>10	nt	19.7±0.95
	<b>PARP11</b>	<b>PARP12<sub>cat</sub></b>	<b>PARP14<sub>cat-wwe</sub></b>
	0.55±0.11	nt	8.55±0.80
	<b>PARP15<sub>cat</sub></b>	<b>PARP16</b>	
	>30	nt	
ITK2	PARP1	PARP2	PARP3
	>30	>30	>30
	<b>PARP4<sub>brct-cat</sub></b>	<b>PARP5b<sub>cat</sub></b>	<b>PARP6</b>
	nt	>10	nt
	<b>PARP7</b>	<b>PARP8</b>	<b>PARP10<sub>cat</sub></b>
	nt	nt	32.8±3.6
	<b>PARP11</b>	<b>PARP12<sub>cat</sub></b>	<b>PARP14<sub>cat-wwe</sub></b>
	4.52±1.4	nt	7.87±0.20
	<b>PARP15<sub>cat</sub></b>	<b>PARP16</b>	
	>30	nt	
ITK3	PARP1	PARP2	PARP3

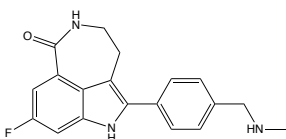
	>30	>30	>30
	<b>PARP4<sub>brct-cat</sub></b>	<b>PARP5b<sub>cat</sub></b>	<b>PARP6</b>
	nt	>10	nt
	<b>PARP7</b>	<b>PARP8</b>	<b>PARP10<sub>cat</sub></b>
	nt	nt	27.9±3.9
	<b>PARP11</b>	<b>PARP12<sub>cat</sub></b>	<b>PARP14<sub>cat-wwe</sub></b>
	13.6±1.4	nt	6.73±1.8
	<b>PARP15<sub>cat</sub></b>	<b>PARP16</b>	
<b>ITK4</b> 	<b>PARP1</b>	<b>PARP2</b>	<b>PARP3</b>
	>30	8.46±1.40	>30
	<b>PARP4<sub>brct-cat</sub></b>	<b>PARP5b<sub>cat</sub></b>	<b>PARP6</b>
	nt	>10	nt
	<b>PARP7</b>	<b>PARP8</b>	<b>PARP10<sub>cat</sub></b>
	nt	nt	9.29±0.20
	<b>PARP11</b>	<b>PARP12<sub>cat</sub></b>	<b>PARP14<sub>cat-wwe</sub></b>
	5.50±0.80	nt	8.71±0.80
	<b>PARP15<sub>cat</sub></b>	<b>PARP16</b>	
	6.85±0.99	nt	

<b>ITK5</b>	<b>PARP1</b>	<b>PARP2</b>	<b>PARP3</b>
	>30	>30	>30
	<b>PARP4<sub>brct-cat</sub></b>	<b>PARP5b<sub>cat</sub></b>	<b>PARP6</b>
	nt	>10	nt

	<b>PARP7</b>	<b>PARP8</b>	<b>PARP10<sub>cat</sub></b>
	nt	nt	5.40±0.17
	<b>PARP11</b>	<b>PARP12<sub>cat</sub></b>	<b>PARP14<sub>cat-wwe</sub></b>
	1.62±0.33	nt	10.8±0.75
	<b>PARP15<sub>cat</sub></b>	<b>PARP16</b>	
	4.03±0.77	nt	
<b>ITK6</b>	<b>PARP1</b>	<b>PARP2</b>	<b>PARP3</b>
	>30	>30	>30
	<b>PARP4<sub>brct-cat</sub></b>	<b>PARP5b<sub>cat</sub></b>	<b>PARP6</b>
	>30	>30	>3
	<b>PARP7</b>	<b>PARP8</b>	<b>PARP10<sub>cat</sub></b>
	>30	>3	0.156±0.018
	<b>PARP11</b>	<b>PARP12<sub>cat</sub></b>	<b>PARP14<sub>cat-wwe</sub></b>
	0.099±0.016	nt	0.917±0.086
	<b>PARP15<sub>cat</sub></b>	<b>PARP16</b>	
	0.496±0.19	nt	

<b>ITK7</b>	<b>PARP1</b>	<b>PARP2</b>	<b>PARP3</b>
	>30	>30	>30
	<b>PARP4<sub>brct-cat</sub></b>	<b>PARP5b<sub>cat</sub></b>	<b>PARP6</b>
	>30	>30	>3
	<b>PARP7</b>	<b>PARP8</b>	<b>PARP10<sub>cat</sub></b>
	24.6±0.5	>3	9.28±1.57
	<b>PARP11</b>	<b>PARP12<sub>cat</sub></b>	<b>PARP14<sub>cat-wwe</sub></b>

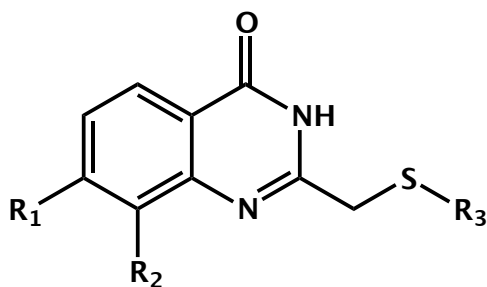
	0.014±0.003	>3	2.86±0.35
	<b>PARP15<sub>cat</sub></b>	<b>PARP16</b>	
	>30	>3	
<b>Olaparib</b>	<b>PARP1</b>	<b>PARP2</b>	<b>PARP3</b>
	0.025±0.002	0.007±0.0003	0.083±0.037
	<b>PARP4<sub>brct-cat</sub></b>	<b>PARP5b<sub>cat</sub></b>	<b>PARP6</b>
	0.241±0.015	0.211±0.081	<i>nt</i>
	<b>PARP7</b>	<b>PARP8</b>	<b>PARP10<sub>cat</sub></b>
	<i>nt</i>	>3	4.5±0.3
	<b>PARP11</b>	<b>PARP12<sub>cat</sub></b>	<b>PARP14<sub>cat-wwe</sub></b>
	>10	~10	>10
	<b>PARP15<sub>cat</sub></b>	<b>PARP16</b>	
	>10	~5	

<b>Rucaparib</b>	<b>PARP1</b>	<b>PARP2</b>	<b>PARP3</b>
	0.008±0.002	0.005±0.001	0.72±0.37
	<b>PARP4<sub>brct-cat</sub></b>	<b>PARP5b<sub>cat</sub></b>	<b>PARP6</b>
	0.450±0.101	3.6±0.3	<i>nt</i>
	<b>PARP7</b>	<b>PARP8</b>	<b>PARP10<sub>cat</sub></b>
	<i>nt</i>	<i>nt</i>	2.5±0.2
	<b>PARP11</b>	<b>PARP12<sub>cat</sub></b>	<b>PARP14<sub>cat-wwe</sub></b>
	3.4±0.5	~7	>10
	<b>PARP15<sub>cat</sub></b>	<b>PARP16</b>	
	>10	<i>n.i.</i>	

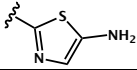
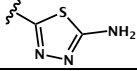
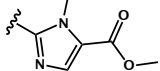
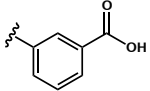
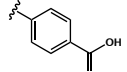
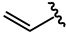
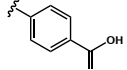
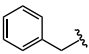
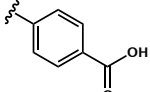
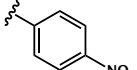
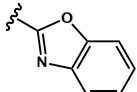
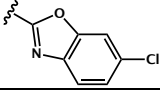
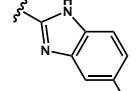
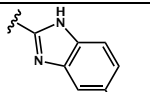
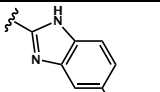

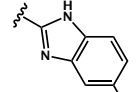

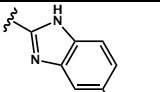
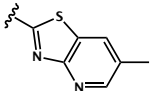




**Table A-2** Approximate IC<sub>50</sub> values of compounds not appearing in Chapter 3

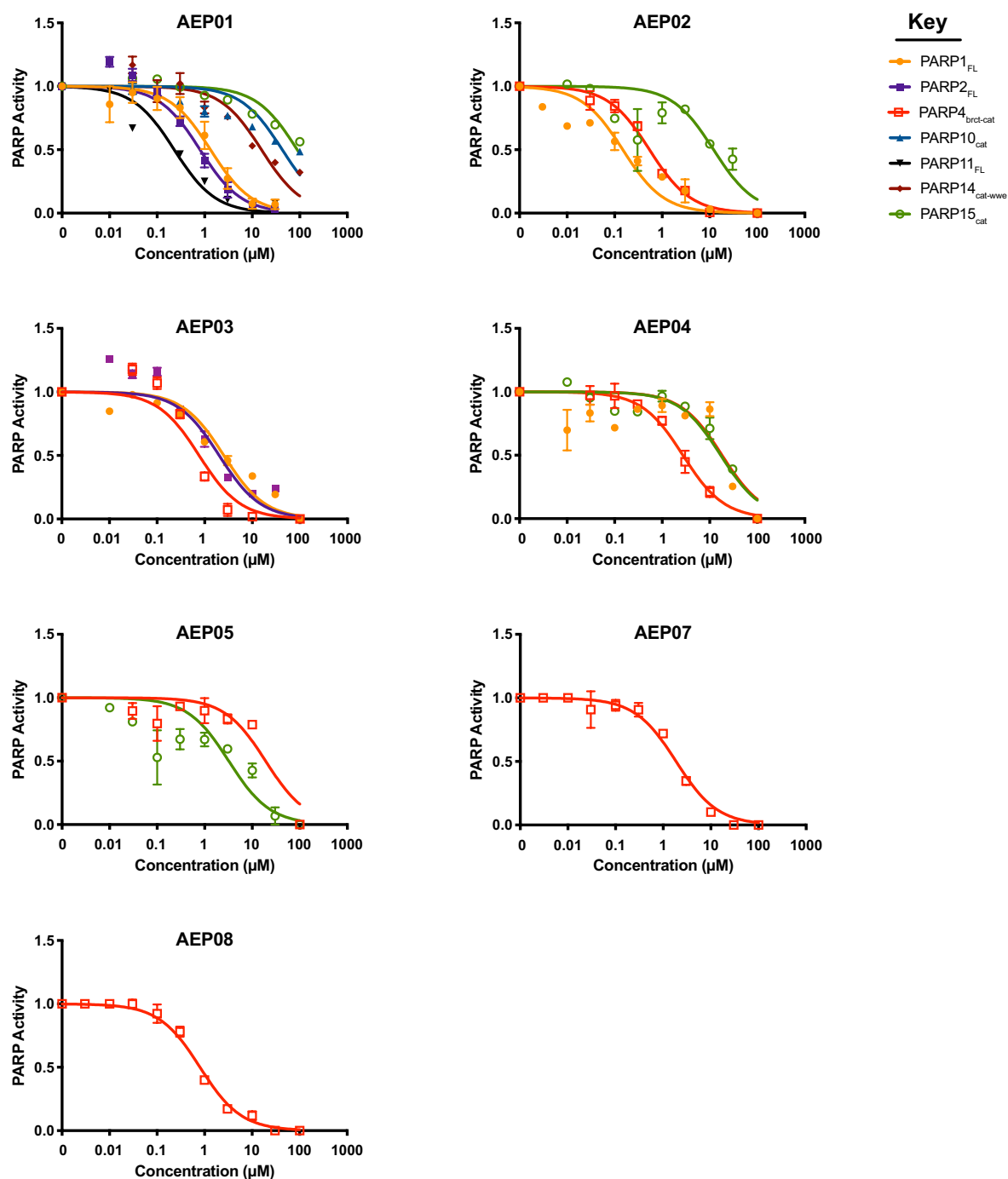


ID	-R1	-R2	-R3	IC <sub>50</sub>		
				PARP14 <sub>cat</sub>	PARP10 <sub>cat</sub>	PARP1 <sub>FL</sub>
ITK-A1	H	H		>10	>10	-
ITK-A2	CH <sub>3</sub>	H		>10	>10	-
ITK-A3	Br	H		>10	>10	-
ITK-A4	CF <sub>3</sub>	H		>10	>10	-
ITK-A5	OMe	H		~10	>10	-
ITK-A6	NO <sub>2</sub>	H		>10	>10	-
ITK-A7	H	Br		>10	>10	-
ITK-A8	H	OCF <sub>3</sub>		>10	>10	-
ITK-A9	CH <sub>3</sub>	CH <sub>3</sub>		>10	>10	-
ITK-A10	CH <sub>3</sub>	CH <sub>3</sub>		~10	<10	<10
ITK-A11	CH <sub>3</sub>	CH <sub>3</sub>		~10	>10	>10

ITK-A12	CH <sub>3</sub>	CH <sub>3</sub>		>10	>10	-
ITK-A13	CH <sub>3</sub>	CH <sub>3</sub>		>30	~5	>30
ITK-A14	CH <sub>3</sub>	CH <sub>3</sub>		>10	<10	-
ITK-A15	CH <sub>3</sub>	CH <sub>3</sub>		>10	>10	-
ITK-A16	Br	CH <sub>3</sub>		>10	<10	-
ITK-A17		CH <sub>3</sub>		5	2	>10
ITK-A18		CH <sub>3</sub>		>10	7.15	-
ITK-A19	CH <sub>3</sub>	CH <sub>3</sub>		>10	>10	>10
ITK-A20	CH <sub>3</sub>	CH <sub>3</sub>		>10	>10	>10
ITK-A21	CH <sub>3</sub>	CH <sub>3</sub>		>10	>10	>10
ITK-A22	CH <sub>3</sub>	CH <sub>3</sub>		>10	2.5	~10
ITK-A23	CH <sub>3</sub>	CH <sub>3</sub>		>10	>10	>10
ITK-A24	CH <sub>3</sub>	CH <sub>3</sub>		5	6	<10
ITK-A25		CH <sub>3</sub>		>50	>50	> 10
ITK-A26		CH <sub>3</sub>		10	1	>10
ITK-A27	CH <sub>3</sub>	CH <sub>3</sub>		>10	8	>10

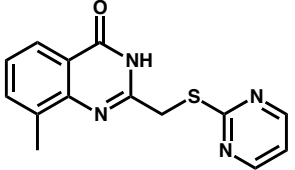
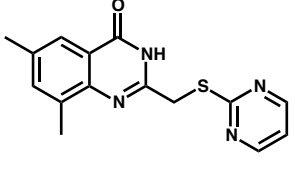


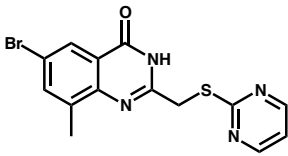
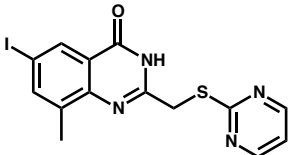
## Appendix B: Full IC<sub>50</sub> Data for Compounds in Chapter 4

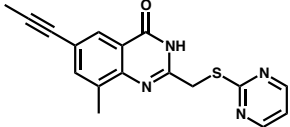


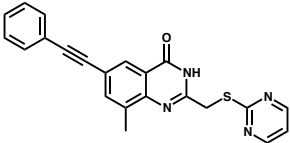
**Figure B-1** Dose response curves for AEP series against active PARP family determined with *in vitro* plate assays using either SRPK2 or the PARP itself as a substrate and 6-a-NAD<sup>+</sup> followed by click chemistry. Curves generated using Prism 7 (Graph Pad); error bars indicate  $\pm$ SEM from at least three replicates.

**Table B-1** *In vitro* IC<sub>50</sub> (μM) values for full AEP series; SEM from a minimum of three dose-response experiments.

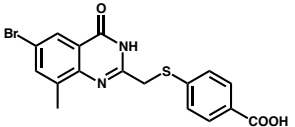
AEP01	PARP1	PARP2	PARP3
	1.5±0.6	0.85±0.1	>10
	PARP4 <sub>brct-cat</sub>	PARP5b <sub>cat</sub>	PARP6
	>10	>10	>10
	PARP7	PARP8	PARP10 <sub>cat</sub>
	<i>nt</i>	<i>nt</i>	43±2
	PARP11	PARP12 <sub>cat</sub>	PARP14 <sub>cat-wwe</sub>
	~0.5	<i>nt</i>	16±0.5
	PARP15 <sub>cat</sub>	PARP16	
	>10	<i>nt</i>	
AEP02	PARP1	PARP2	PARP3
	0.15±0.05	>10	>10
	PARP4 <sub>brct-cat</sub>	PARP5b <sub>cat</sub>	PARP6
	2.8±0.3	>10	>10
	PARP7	PARP8	PARP10 <sub>cat</sub>
	<i>nt</i>	<i>nt</i>	>10
	PARP11	PARP12 <sub>cat</sub>	PARP14 <sub>cat-wwe</sub>
	>10	<i>nt</i>	>10
	PARP15 <sub>cat</sub>	PARP16	
	12±1	>10	

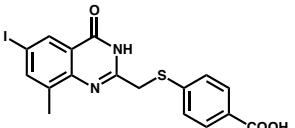
AEP03	PARP1	PARP2	PARP3
	2.7±0.4	2.0±0.1	>10
	PARP4 <sub>brct-cat</sub>	PARP5b <sub>cat</sub>	PARP6
	0.75±0.1	>10	>10
	PARP7	PARP8	PARP10 <sub>cat</sub>
	>10	<i>nt</i>	>10
	PARP11	PARP12 <sub>cat</sub>	PARP14 <sub>cat-wwe</sub>
	>10	<i>nt</i>	>10
	PARP15 <sub>cat</sub>	PARP16	
	~10	~10	
AEP04	PARP1	PARP2	PARP3
	>10	<i>nt</i>	>10
	PARP4 <sub>brct-cat</sub>	PARP5b <sub>cat</sub>	PARP6
	2.8±0.3	>10	>10
	PARP7	PARP8	PARP10 <sub>cat</sub>
	>10	<i>nt</i>	>10
	PARP11	PARP12 <sub>cat</sub>	PARP14 <sub>cat-wwe</sub>
	>10	<i>nt</i>	>10
	PARP15 <sub>cat</sub>	PARP16	
	>10	>10	

AEP05	PARP1	PARP2	PARP3
	>10	<i>nt</i>	>10
	<b>PARP4<sub>brct-cat</sub></b>	<b>PARP5b<sub>cat</sub></b>	<b>PARP6</b>
	19±0.05	>10	>10
	<b>PARP7</b>	<b>PARP8</b>	<b>PARP10<sub>cat</sub></b>
	>10	<i>nt</i>	>10
	<b>PARP11</b>	<b>PARP12<sub>cat</sub></b>	<b>PARP14<sub>cat-wwc</sub></b>
	>10	<i>nt</i>	>10
	<b>PARP15<sub>cat</sub></b>	<b>PARP16</b>	
	3.3±0.7	>10	

AEP06	PARP1	PARP2	PARP3
	>10	<i>nt</i>	>10
	<b>PARP4<sub>brct-cat</sub></b>	<b>PARP5b<sub>cat</sub></b>	<b>PARP6</b>
	>10	>10	>10
	<b>PARP7</b>	<b>PARP8</b>	<b>PARP10<sub>cat</sub></b>
	>10	<i>nt</i>	>10
	<b>PARP11</b>	<b>PARP12<sub>cat</sub></b>	<b>PARP14<sub>cat-wwc</sub></b>
	>10	<i>nt</i>	>10
	<b>PARP15<sub>cat</sub></b>	<b>PARP16</b>	
	>10	>10	

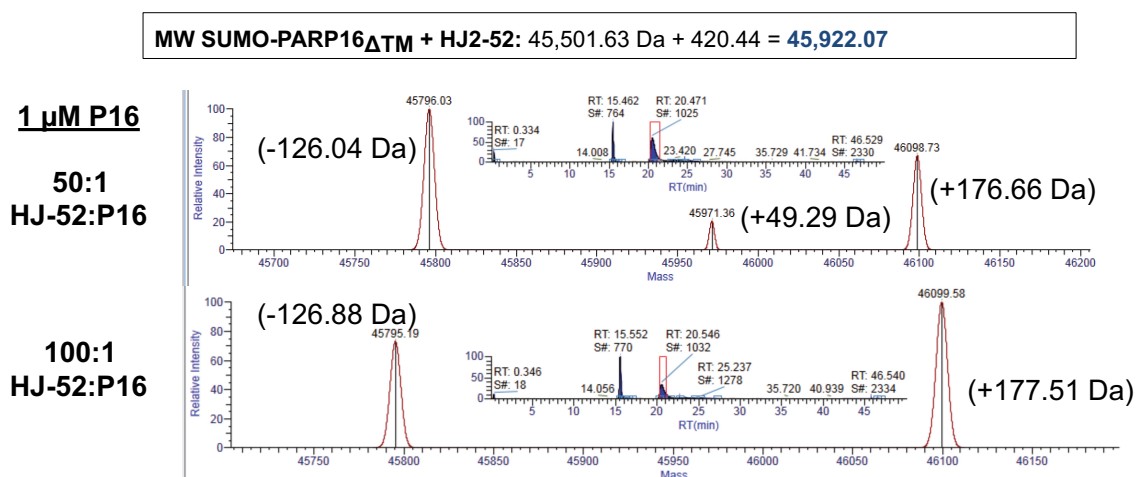
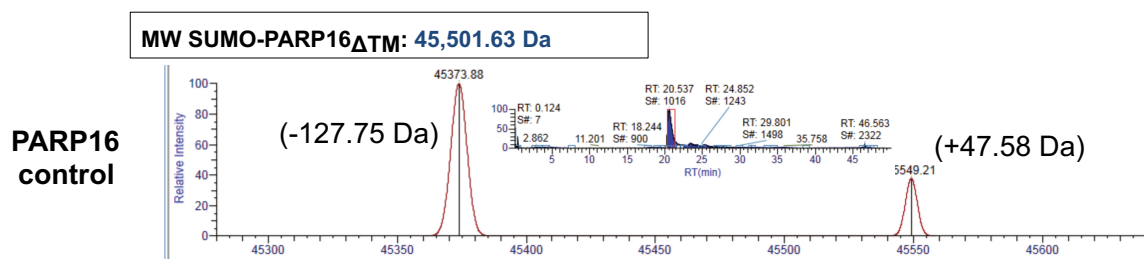


AEP07	PARP1	PARP2	PARP3
	>30	>10	>10
	PARP4 <sub>brct-cat</sub>	PARP5 <sub>b<sub>cat</sub></sub>	PARP6
	1.9±0.2	>30	>10
	PARP7	PARP8	PARP10 <sub>cat</sub>
	~10	>10	>10
	PARP11	PARP12 <sub>cat</sub>	PARP14 <sub>cat-wwc</sub>
	>10	>10	~5
	PARP15 <sub>cat</sub>	PARP16	
	>10	>10	

AEP08	PARP1	PARP2	PARP3
	>30	>10	>10
	PARP4 <sub>brct-cat</sub>	PARP5 <sub>b<sub>cat</sub></sub>	PARP6
	0.80±0.1	>5	>10
	PARP7	PARP8	PARP10 <sub>cat</sub>
	~10	>10	~10
	PARP11	PARP12 <sub>cat</sub>	PARP14 <sub>cat-wwc</sub>
	>10	>10	>5
	PARP15 <sub>cat</sub>	PARP16	
	~10	>10	

## **Appendix C: Mass Spectrometry Analysis of PARP16 and HJ-52**

## Covalent labeling of PAR16 with electrophilic HJ02-52



## Appendix D: Full IC<sub>50</sub> data for Compounds in Chapter 6

A

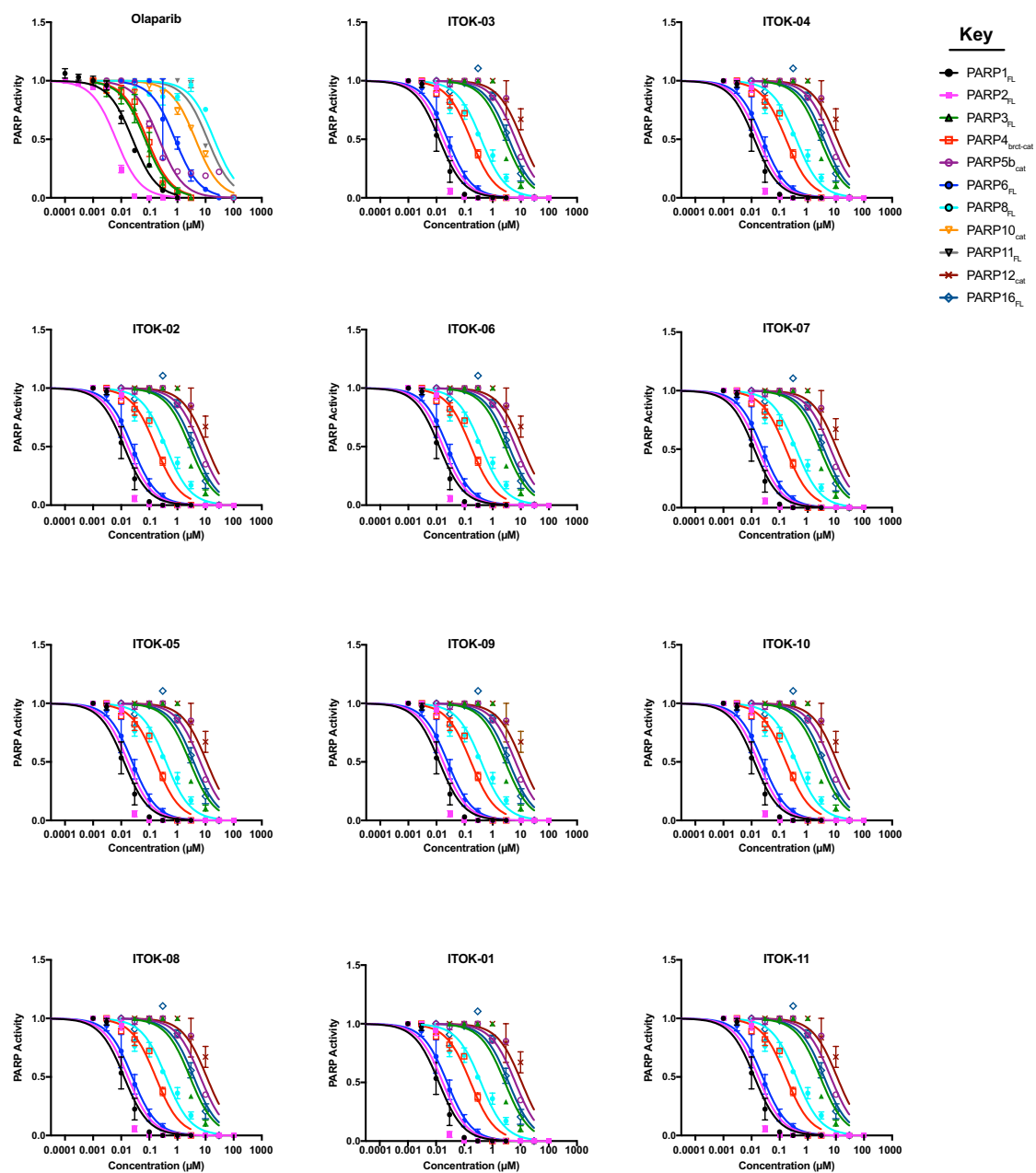
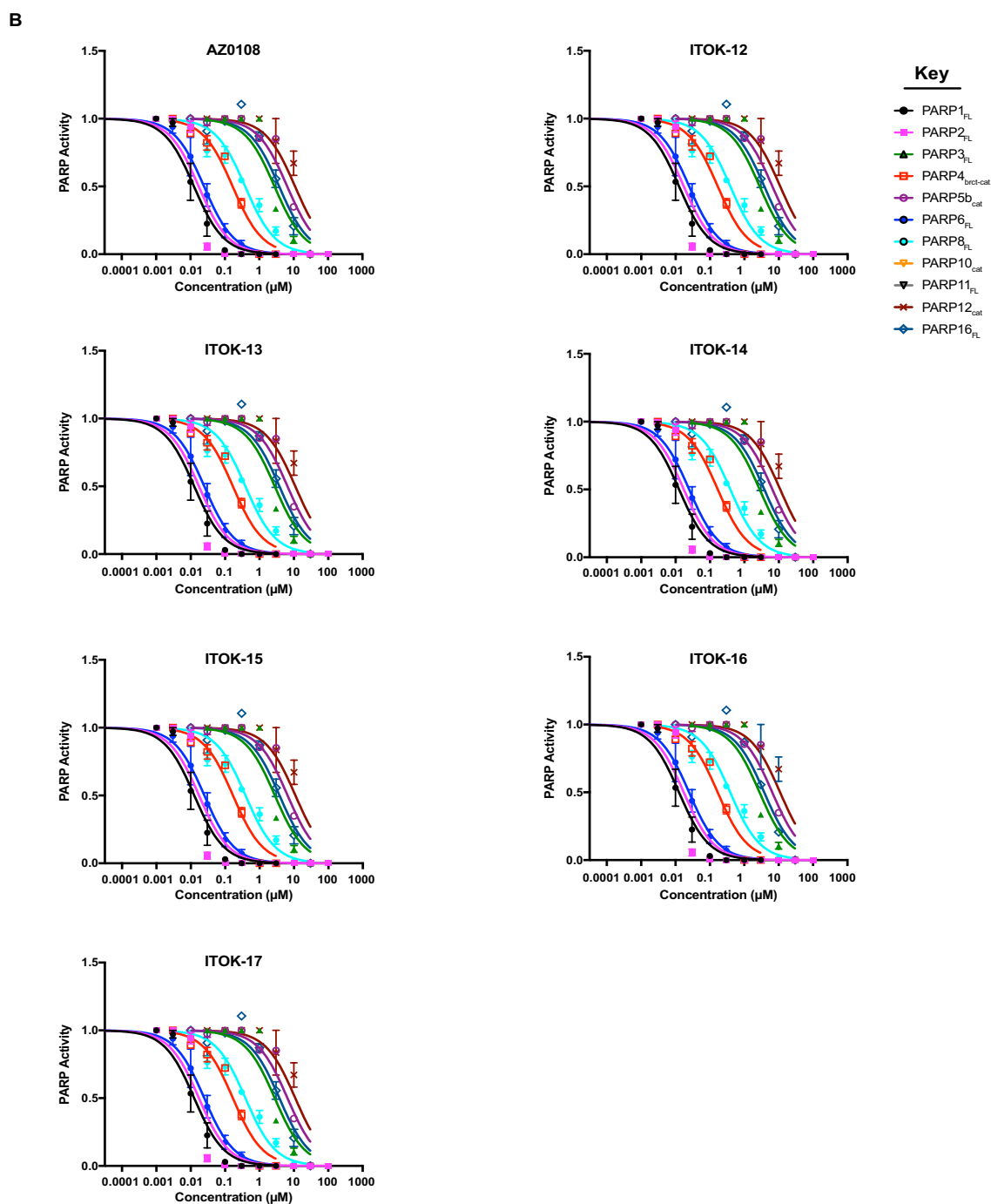


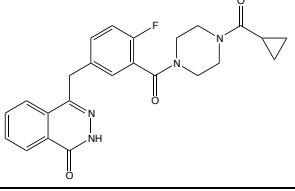
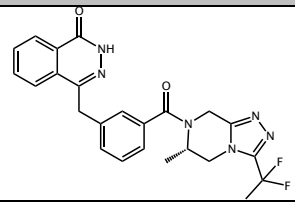
Figure D-1 A (caption below)



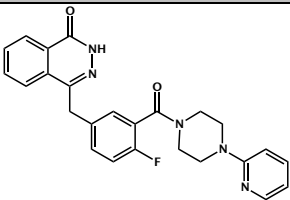
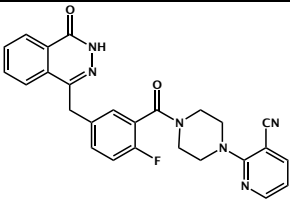
**Figure D-1** *In vitro* dose response curves for (A) olaparib and ITOK-01 - 11, and (B) AZ0108 and ITOK-12 - 17 against PARP1<sub>FL</sub>, PARP2<sub>FL</sub>, PARP3<sub>FL</sub>, PARP4<sub>brct-cat</sub>, PARP5b<sub>cat</sub>, PARP6<sub>FL</sub>, PARP10<sub>cat</sub>, PARP11<sub>FL</sub>, PARP12<sub>cat</sub>, and PARP16<sub>FL</sub>

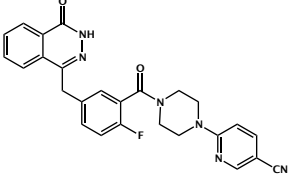
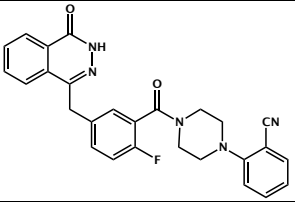
determined with *in vitro* plate assays using either SRPK2 or the PARP itself as a substrate and 6-a-NAD<sup>+</sup> followed by click chemistry. Curves generated using Prism 7 (Graph Pad); error bars indicate  $\pm$ SEM from at least two replicates.

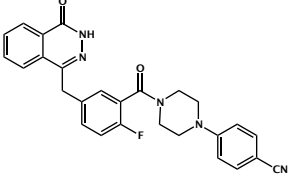
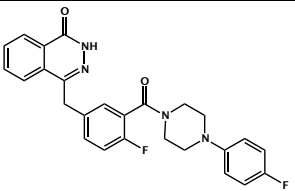
**Table D-1** In vitro IC<sub>50</sub> (μM) values for (A) ITOK-01 - 11, and (B) ITOK-12 - 17; SEM from a minimum of two dose-response experiments.

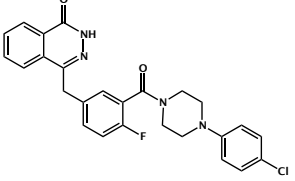
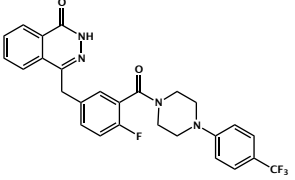
<b>Olaparib</b>	<b>PARP1</b>	<b>PARP2</b>	<b>PARP3</b>
	0.025±0.002	0.0070±0.0003	0.083±0.04
	<b>PARP4<sub>brct-cat</sub></b>	<b>PARP5<sub>bcat</sub></b>	<b>PARP6</b>
	0.24±0.02	0.21±0.08	>10
	<b>PARP7</b>	<b>PARP8</b>	<b>PARP10<sub>cat</sub></b>
	>3	>10	4.5±0.3
	<b>PARP11</b>	<b>PARP12<sub>cat</sub></b>	<b>PARP14<sub>cat-wwe</sub></b>
	>10	>10	>10
	<b>PARP15<sub>cat</sub></b>	<b>PARP16</b>	
	~10	>10	
<b>AZ0108</b>	<b>PARP1</b>	<b>PARP2</b>	<b>PARP3</b>
	0.017±0.001	0.017±0.001	2.8±0.1
	<b>PARP4<sub>brct-cat</sub></b>	<b>PARP5<sub>bcat</sub></b>	<b>PARP6</b>
	0.17±0.006	6.5±0.2	0.028±0.006
	<b>PARP7</b>	<b>PARP8</b>	<b>PARP10<sub>cat</sub></b>
	~10	0.46±0.1	>10
	<b>PARP11</b>	<b>PARP12<sub>cat</sub></b>	<b>PARP14<sub>cat-wwe</sub></b>
	>10	>10	>10
	<b>PARP15<sub>cat</sub></b>	<b>PARP16</b>	
	>3	>3	

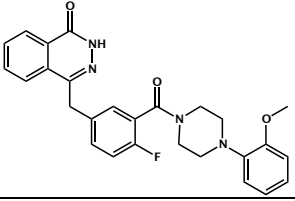
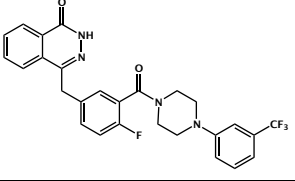


ITOK-01	PARP1	PARP2	PARP3
	0.035±0.002	0.033±0.002	0.061±0.003
	<b>PARP4<sub>brct-cat</sub></b>	<b>PARP5<sub>bcat</sub></b>	<b>PARP6</b>
	0.21±0.07	>3	0.059±0.03
	<b>PARP7</b>	<b>PARP8</b>	<b>PARP10<sub>cat</sub></b>
	>3	>3	1.7±0.2
	<b>PARP11</b>	<b>PARP12<sub>cat</sub></b>	<b>PARP14<sub>cat-wwe</sub></b>
	2.6±0.07	>3	>3
	<b>PARP15<sub>cat</sub></b>	<b>PARP16</b>	
	2.3±0.08	0.83±0.001	
ITOK-02	PARP1	PARP2	PARP3
	0.015±0.001	0.051±0.01	0.12±0.0002
	<b>PARP4<sub>brct-cat</sub></b>	<b>PARP5<sub>bcat</sub></b>	<b>PARP6</b>
	0.060±0.002	5.0±0.09	0.053±0.02
	<b>PARP7</b>	<b>PARP8</b>	<b>PARP10<sub>cat</sub></b>
	>10	0.79±0.2	>3
	<b>PARP11</b>	<b>PARP12<sub>cat</sub></b>	<b>PARP14<sub>cat-wwe</sub></b>
	>3	>3	>10
	<b>PARP15<sub>cat</sub></b>	<b>PARP16</b>	
	1.8±0.6	>3	

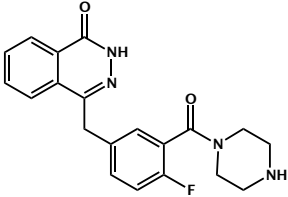
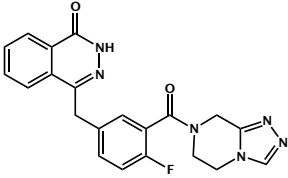
ITOK-03	PARP1	PARP2	PARP3
	0.021±0.004	0.028±0.005	0.32±0.002
	<b>PARP4<sub>brct-cat</sub></b>	<b>PARP5b<sub>cat</sub></b>	<b>PARP6</b>
	0.35±0.002	2.52±0.2	0.18±0.05
	<b>PARP7</b>	<b>PARP8</b>	<b>PARP10<sub>cat</sub></b>
	0.014±0.002	4.7±1	0.86±0.3
	<b>PARP11</b>	<b>PARP12<sub>cat</sub></b>	<b>PARP14<sub>cat-wwe</sub></b>
	0.46±0.02	>3	>10
	<b>PARP15<sub>cat</sub></b>	<b>PARP16</b>	
	2.0±0.3	4.3±1	
ITOK-04	PARP1	PARP2	PARP3
	0.018±0.01	0.0047±0.0002	1.3±0.4
	<b>PARP4<sub>brct-cat</sub></b>	<b>PARP5b<sub>cat</sub></b>	<b>PARP6</b>
	0.21±0.07	8.78±0.0	0.19±0.07
	<b>PARP7</b>	<b>PARP8</b>	<b>PARP10<sub>cat</sub></b>
	>10	2.16±0.2	>10
	<b>PARP11</b>	<b>PARP12<sub>cat</sub></b>	<b>PARP14<sub>cat-wwe</sub></b>
	>10	>10	>10
	<b>PARP15<sub>cat</sub></b>	<b>PARP16</b>	
	5.9±0.1	0.50±0.02	

ITOK-05	PARP1	PARP2	PARP3
	0.031±0.003	0.034±0.01	0.073±0.03
	<b>PARP4<sub>brct-cat</sub></b>	<b>PARP5<sub>bcat</sub></b>	<b>PARP6</b>
	0.43±0.01	>3	0.2±0.04
	<b>PARP7</b>	<b>PARP8</b>	<b>PARP10<sub>cat</sub></b>
	>10	>3	2.92±0.08
	<b>PARP11</b>	<b>PARP12<sub>cat</sub></b>	<b>PARP14<sub>cat-wwe</sub></b>
	3.92±0.7	>3	>3
	<b>PARP15<sub>cat</sub></b>	<b>PARP16</b>	
	8.1±0.7	1.1±0.1	
ITOK-06	PARP1	PARP2	PARP3
	0.0068±0.003	0.0021±0.0001	<i>nt</i>
	<b>PARP4<sub>brct-cat</sub></b>	<b>PARP5<sub>bcat</sub></b>	<b>PARP6</b>
	<i>nt</i>	>10	3.65±0.3
	<b>PARP7</b>	<b>PARP8</b>	<b>PARP10<sub>cat</sub></b>
	<i>nt</i>	<i>nt</i>	>10
	<b>PARP11</b>	<b>PARP12<sub>cat</sub></b>	<b>PARP14<sub>cat-wwe</sub></b>
	>10	>10	>10
	<b>PARP15<sub>cat</sub></b>	<b>PARP16</b>	
	>10	>10	

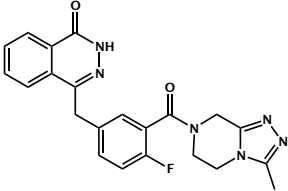
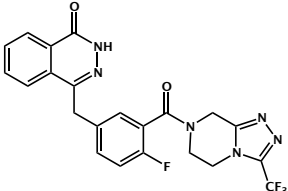
ITOK-07	PARP1	PARP2	PARP3
	0.015±0.001	0.0082±0.003	<i>nt</i>
	<b>PARP4<sub>brct-cat</sub></b>	<b>PARP5b<sub>cat</sub></b>	<b>PARP6</b>
	<i>nt</i>	>10	0.41±0.1
	<b>PARP7</b>	<b>PARP8</b>	<b>PARP10<sub>cat</sub></b>
	<i>nt</i>	<i>nt</i>	>10
	<b>PARP11</b>	<b>PARP12<sub>cat</sub></b>	<b>PARP14<sub>cat-wwe</sub></b>
	>10	>10	>10
	<b>PARP15<sub>cat</sub></b>	<b>PARP16</b>	
	>10	>10	
ITOK-08	PARP1	PARP2	PARP3
	0.010±0.004	0.02±0.008	<i>nt</i>
	<b>PARP4<sub>brct-cat</sub></b>	<b>PARP5b<sub>cat</sub></b>	<b>PARP6</b>
	<i>nt</i>	>10	0.96±0.09
	<b>PARP7</b>	<b>PARP8</b>	<b>PARP10<sub>cat</sub></b>
	<i>nt</i>	<i>nt</i>	>10
	<b>PARP11</b>	<b>PARP12<sub>cat</sub></b>	<b>PARP14<sub>cat-wwe</sub></b>
	>10	>10	>10
	<b>PARP15<sub>cat</sub></b>	<b>PARP16</b>	
	>10	>10	

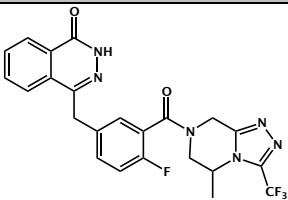
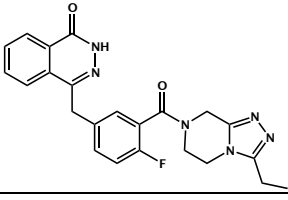
ITOK-09	PARP1	PARP2	PARP3
	0.035±0.003	0.0067±0.00008	<i>nt</i>
	PARP4 <sub>brct-cat</sub>	PARP5b <sub>cat</sub>	PARP6
	<i>nt</i>	>10	6.6±0.3
	PARP7	PARP8	PARP10 <sub>cat</sub>
	<i>nt</i>	<i>nt</i>	>10
	PARP11	PARP12 <sub>cat</sub>	PARP14 <sub>cat-wwe</sub>
	>10	>5	>10
	PARP15 <sub>cat</sub>	PARP16	
	>10	>10	
ITOK-10	PARP1	PARP2	PARP3
	0.039±0.004	0.011±0.002	<i>nt</i>
	PARP4 <sub>brct-cat</sub>	PARP5b <sub>cat</sub>	PARP6
	<i>nt</i>	>10	3.1±0.2
	PARP7	PARP8	PARP10 <sub>cat</sub>
	<i>nt</i>	<i>nt</i>	>10
	PARP11	PARP12 <sub>cat</sub>	PARP14 <sub>cat-wwe</sub>
	>10	>5	>10
	PARP15 <sub>cat</sub>	PARP16	
	>10	>10	

ITOK-11	PARP1	PARP2	PARP3
---------	-------	-------	-------

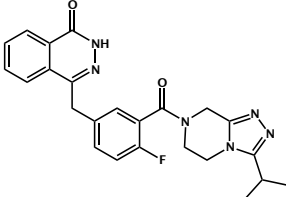
	0.019±0.007	0.0039±0.001	<i>nt</i>
	<b>PARP4<sub>brct-cat</sub></b>	<b>PARP5b<sub>cat</sub></b>	<b>PARP6</b>
	<i>nt</i>	>10	2.9±1
	<b>PARP7</b>	<b>PARP8</b>	<b>PARP10<sub>cat</sub></b>
	<i>nt</i>	<i>nt</i>	>10
	<b>PARP11</b>	<b>PARP12<sub>cat</sub></b>	<b>PARP14<sub>cat-wwe</sub></b>
	>10	>5	>10
	<b>PARP15<sub>cat</sub></b>	<b>PARP16</b>	
	>10	>10	
<b>ITOK-12</b>	<b>PARP1</b>	<b>PARP2</b>	<b>PARP3</b>
	0.0040±0.001	0.004±0.001	<i>nt</i>
	<b>PARP4<sub>brct-cat</sub></b>	<b>PARP5b<sub>cat</sub></b>	<b>PARP6</b>
	<i>nt</i>	>10	2.9±1
	<b>PARP7</b>	<b>PARP8</b>	<b>PARP10<sub>cat</sub></b>
	<i>nt</i>	<i>nt</i>	>10
	<b>PARP11</b>	<b>PARP12<sub>cat</sub></b>	<b>PARP14<sub>cat-wwe</sub></b>
	>10	>5	>10
	<b>PARP15<sub>cat</sub></b>	<b>PARP16</b>	
	>10	>10	

<b>ITOK-13</b>	<b>PARP1</b>	<b>PARP2</b>	<b>PARP3</b>
	0.0047±0.002	0.014±0.007	<i>nt</i>

	<b>PARP4<sub>brct-cat</sub></b>	<b>PARP5b<sub>cat</sub></b>	<b>PARP6</b>
	<i>nt</i>	<i>nt</i>	0.24±0.1
	<b>PARP7</b>	<b>PARP8</b>	<b>PARP10<sub>cat</sub></b>
	<i>nt</i>	<i>nt</i>	<i>nt</i>
	<b>PARP11</b>	<b>PARP12<sub>cat</sub></b>	<b>PARP14<sub>cat-wwe</sub></b>
	<i>nt</i>	<i>nt</i>	<i>nt</i>
	<b>PARP15<sub>cat</sub></b>	<b>PARP16</b>	
	<b>PARP1</b>	<b>PARP2</b>	<b>PARP3</b>
	0.0048±0.002	0.0048±0.005	<i>nt</i>
	<b>PARP4<sub>brct-cat</sub></b>	<b>PARP5b<sub>cat</sub></b>	<b>PARP6</b>
	<i>nt</i>	<i>nt</i>	0.031±0.007
	<b>PARP7</b>	<b>PARP8</b>	<b>PARP10<sub>cat</sub></b>
	<i>nt</i>	<i>nt</i>	<i>nt</i>
	<b>PARP11</b>	<b>PARP12<sub>cat</sub></b>	<b>PARP14<sub>cat-wwe</sub></b>
	<i>nt</i>	<i>nt</i>	<i>nt</i>
	<b>PARP15<sub>cat</sub></b>	<b>PARP16</b>	
	<i>nt</i>	<i>nt</i>	

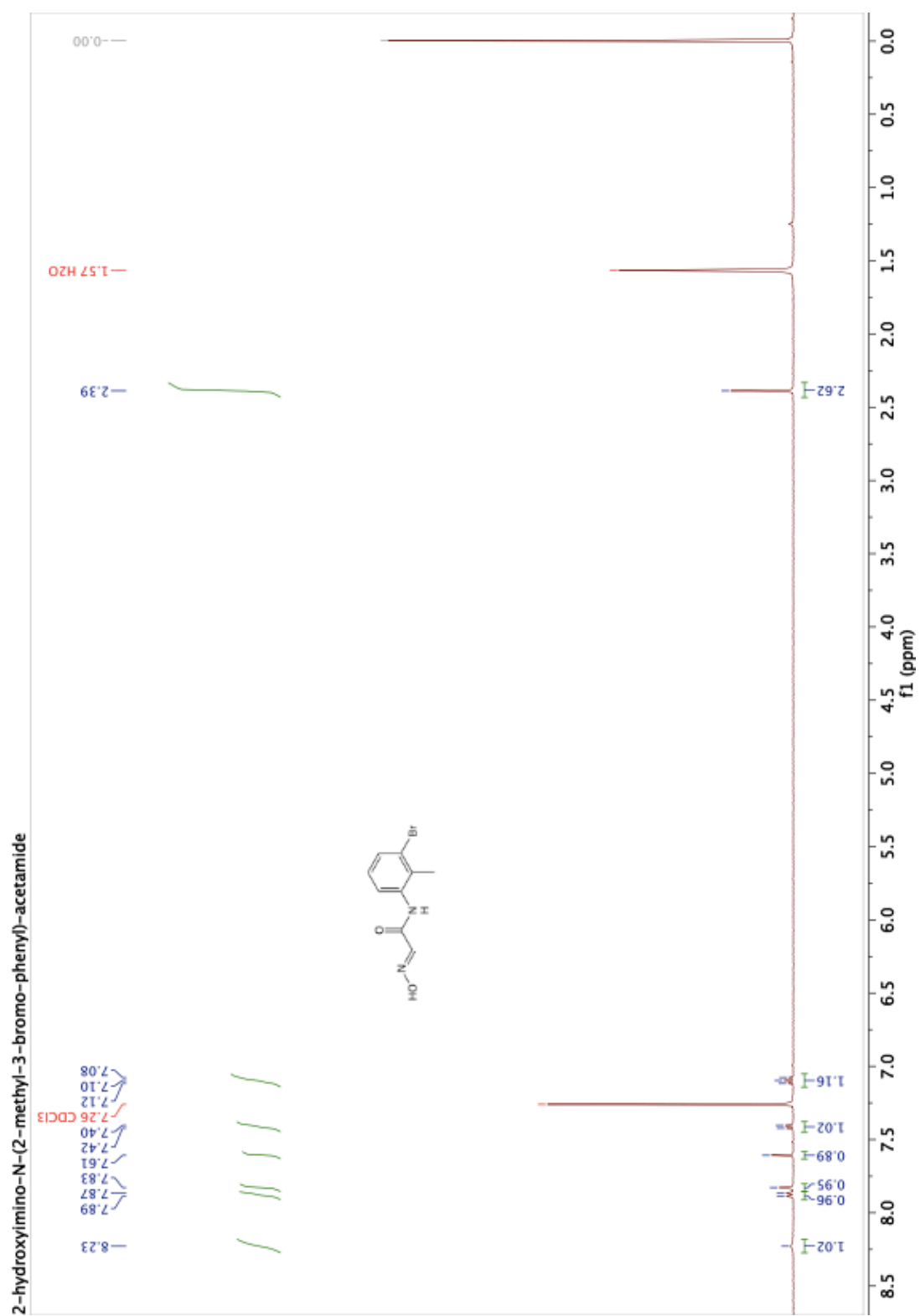
ITOK-15	PARP1	PARP2	PARP3
	$0.11 \pm 0.08$	$0.0039 \pm 0.001$	<i>nt</i>
	<b>PARP4<sub>brct-cat</sub></b>	<b>PARP5b<sub>cat</sub></b>	<b>PARP6</b>
	<i>nt</i>	<i>nt</i>	$0.77 \pm 0.4$
	<b>PARP7</b>	<b>PARP8</b>	<b>PARP10<sub>cat</sub></b>
	<i>nt</i>	<i>nt</i>	<i>nt</i>
	<b>PARP11</b>	<b>PARP12<sub>cat</sub></b>	<b>PARP14<sub>cat-wwe</sub></b>
	<i>nt</i>	<i>nt</i>	<i>nt</i>
	<b>PARP15<sub>cat</sub></b>	<b>PARP16</b>	
	<i>nt</i>	<i>nt</i>	
ITOK-16	PARP1	PARP2	PARP3
	$0.026 \pm 0.003$	$0.011 \pm 0.002$	<i>nt</i>
	<b>PARP4<sub>brct-cat</sub></b>	<b>PARP5b<sub>cat</sub></b>	<b>PARP6</b>
	<i>nt</i>	<i>nt</i>	$0.17 \pm 0.06$
	<b>PARP7</b>	<b>PARP8</b>	<b>PARP10<sub>cat</sub></b>
	<i>nt</i>	<i>nt</i>	<i>nt</i>
	<b>PARP11</b>	<b>PARP12<sub>cat</sub></b>	<b>PARP14<sub>cat-wwe</sub></b>
	<i>nt</i>	<i>nt</i>	<i>nt</i>
	<b>PARP15<sub>cat</sub></b>	<b>PARP16</b>	
	<i>nt</i>	<i>nt</i>	

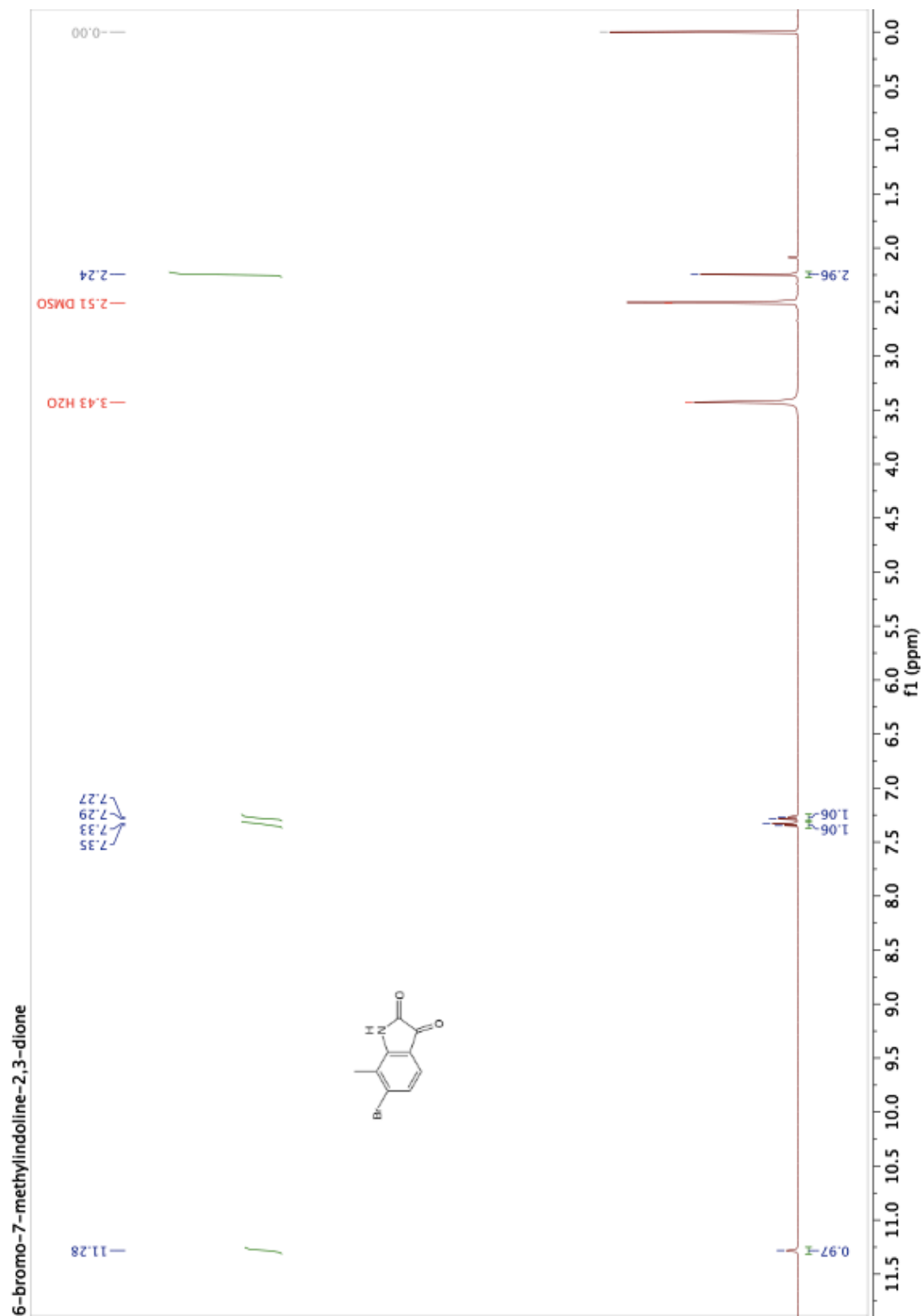


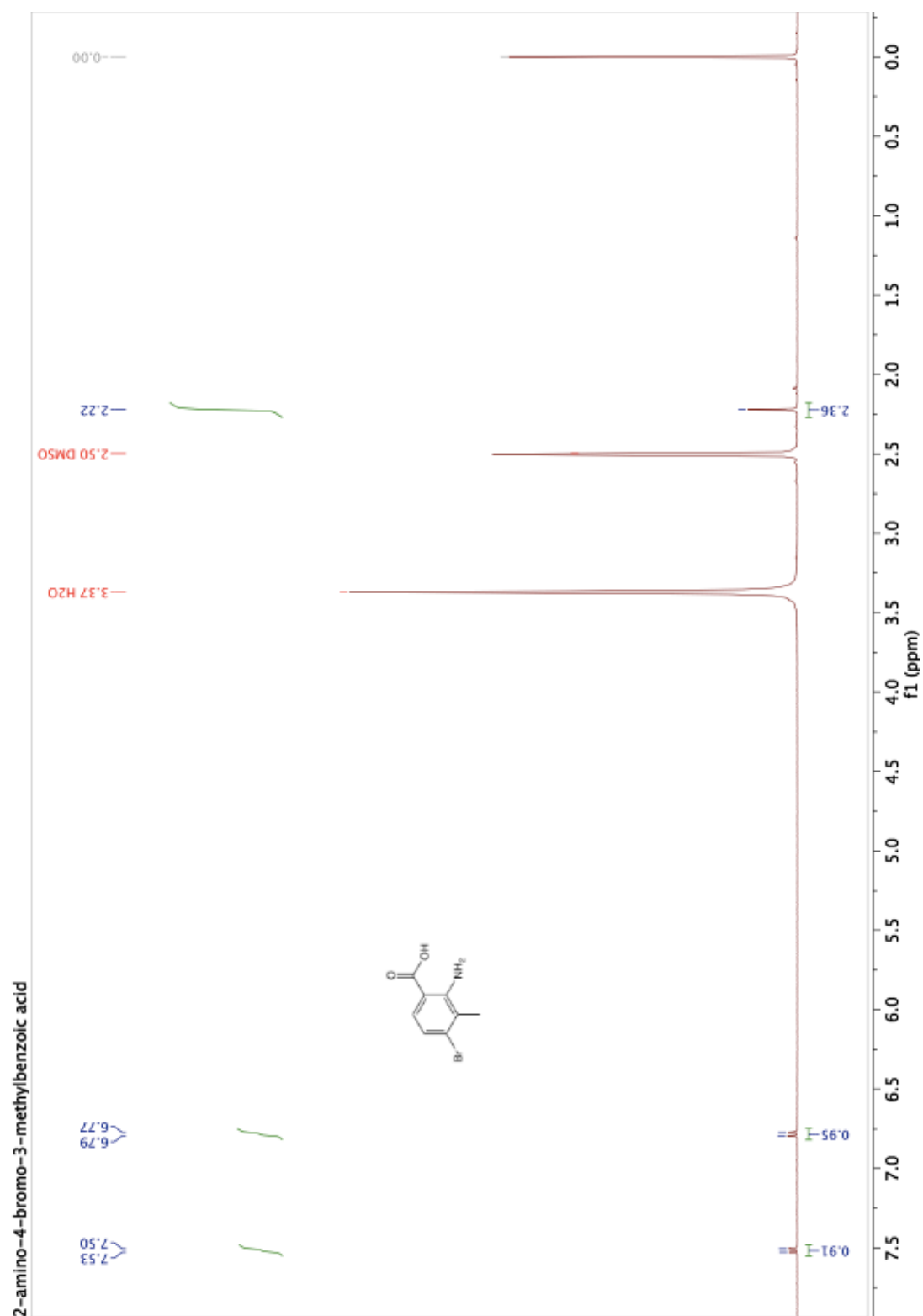
ITOK-17	PARP1	PARP2	PARP3
	0.032±0.004	0.018±0.005	<i>nt</i>
	PARP4 <sub>brct-cat</sub>	PARP5b <sub>cat</sub>	PARP6
	<i>nt</i>	<i>nt</i>	0.13±0.02
	PARP7	PARP8	PARP10 <sub>cat</sub>
	<i>nt</i>	<i>nt</i>	<i>nt</i>
	PARP11	PARP12 <sub>cat</sub>	PARP14 <sub>cat-wwc</sub>
	<i>nt</i>	<i>nt</i>	<i>nt</i>
	PARP15 <sub>cat</sub>	PARP16	
	<i>nt</i>	<i>nt</i>	

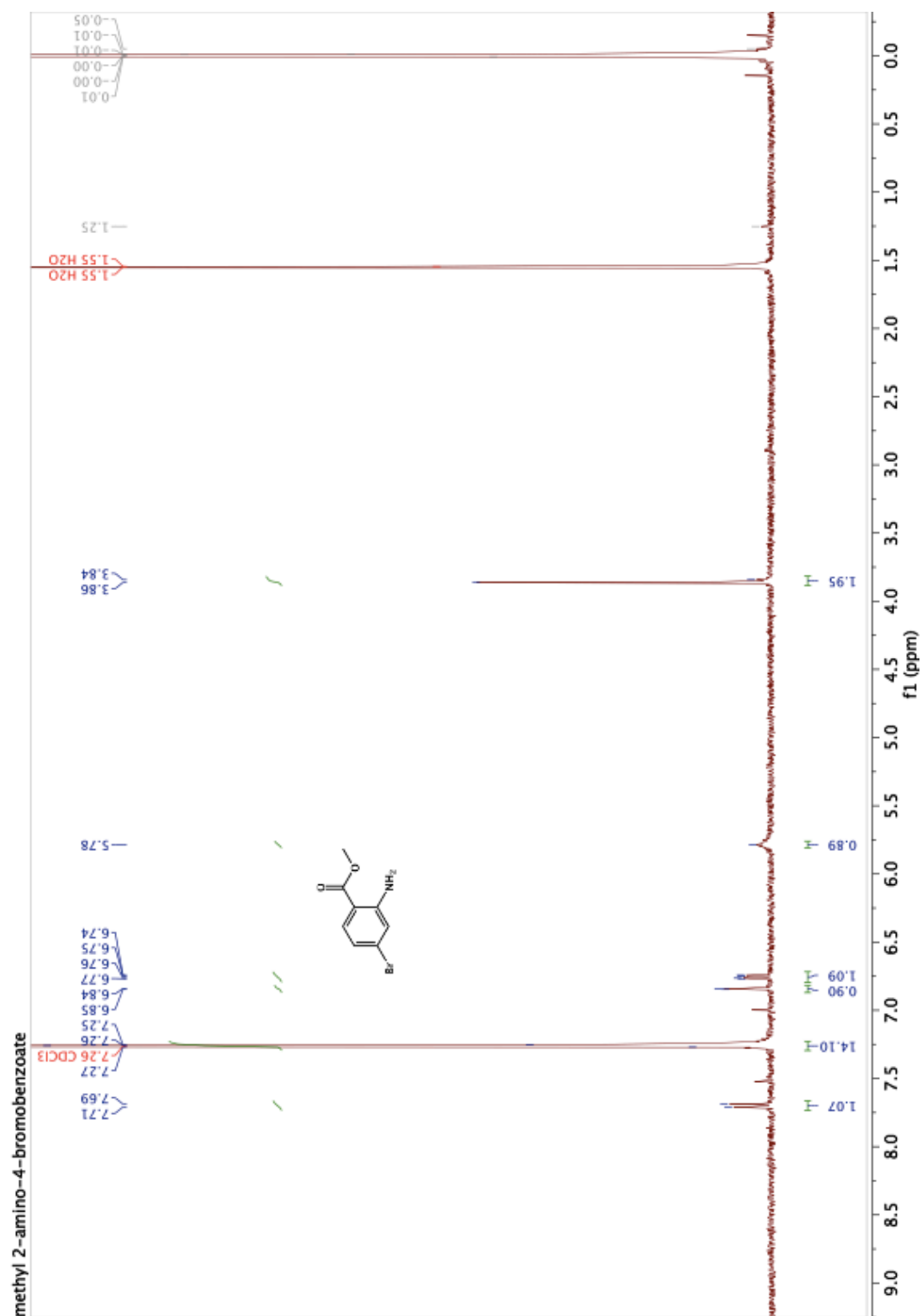
## Appendix E: H1 NMR Spectra

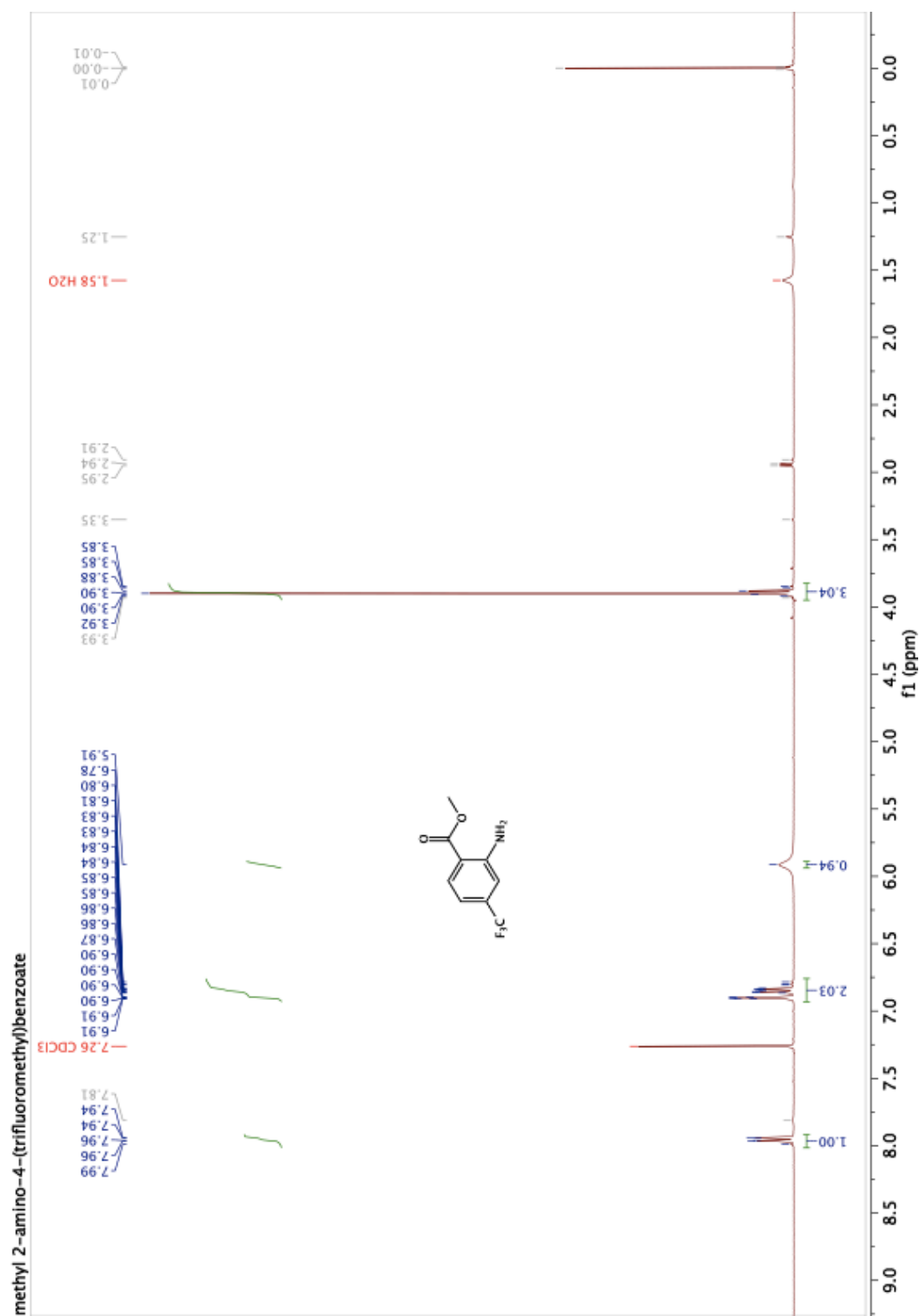
## Chapter 3

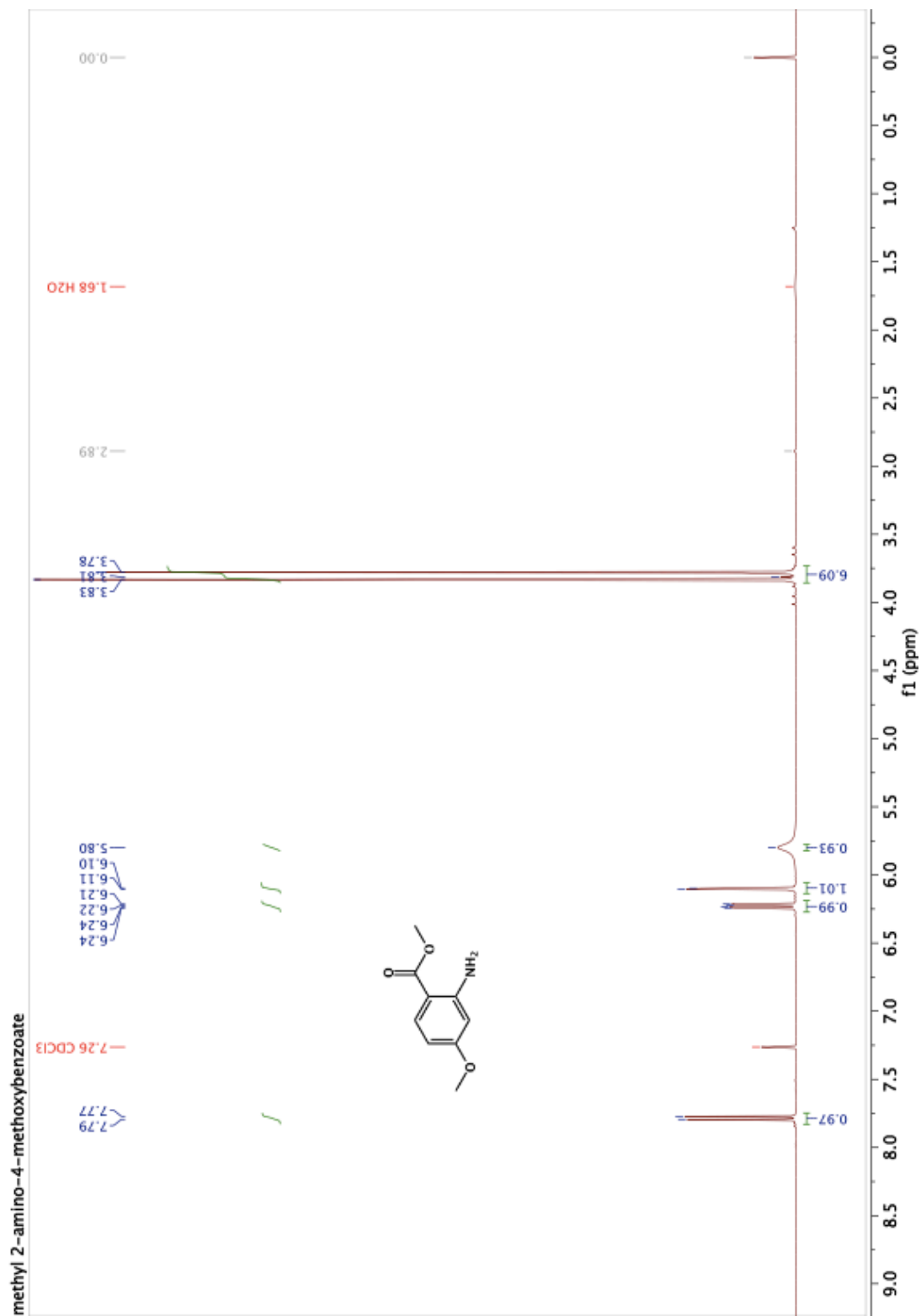




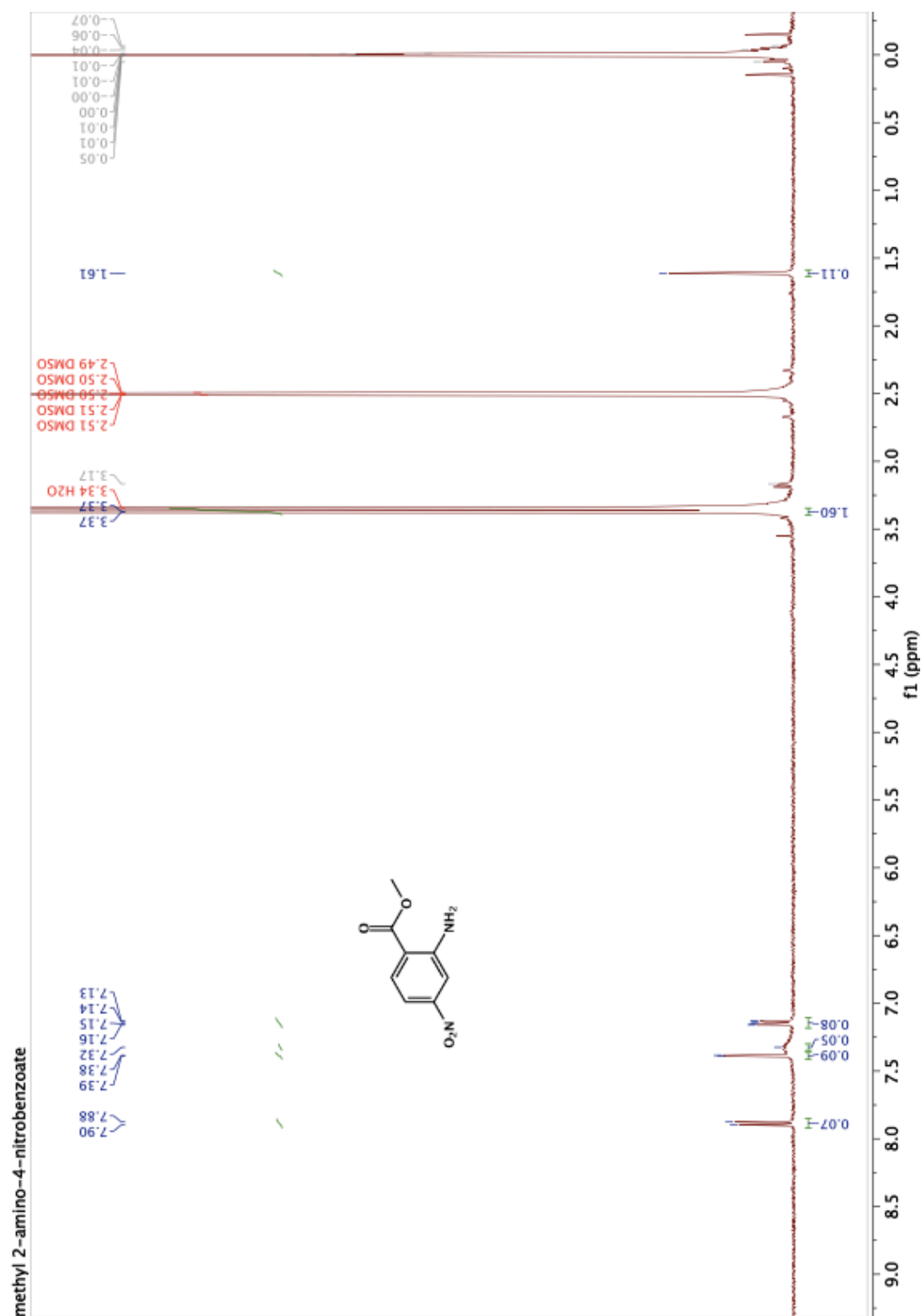




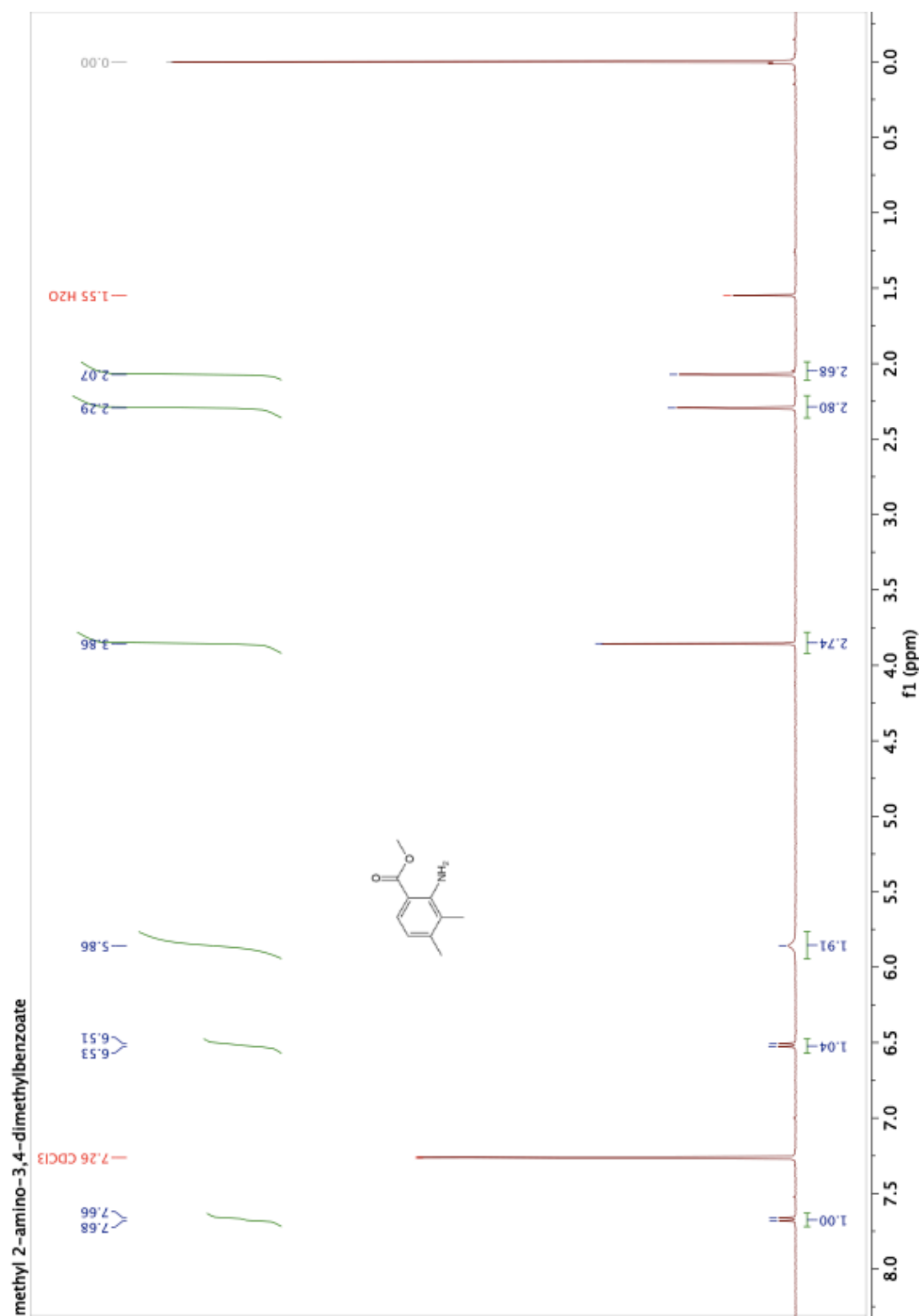


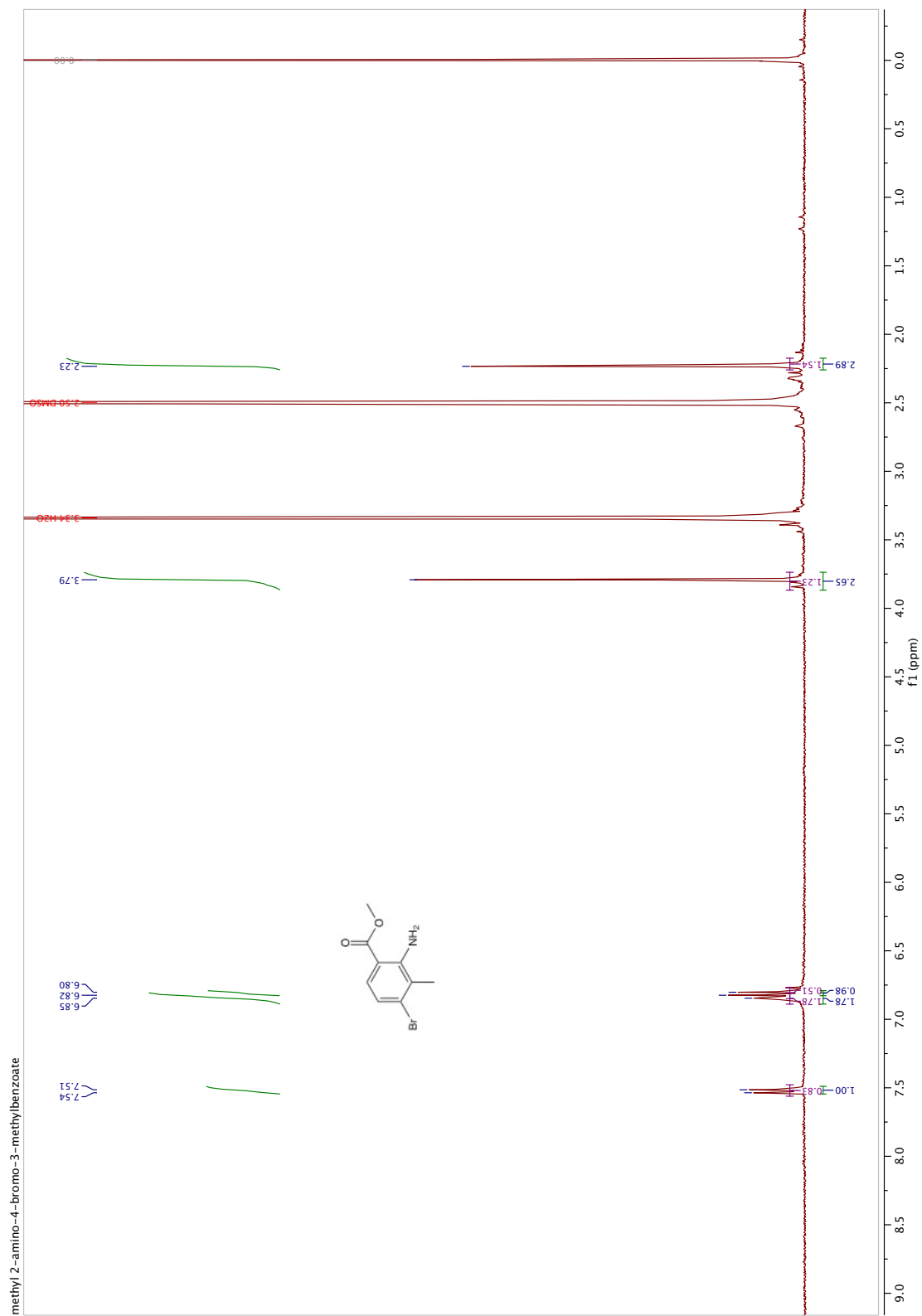


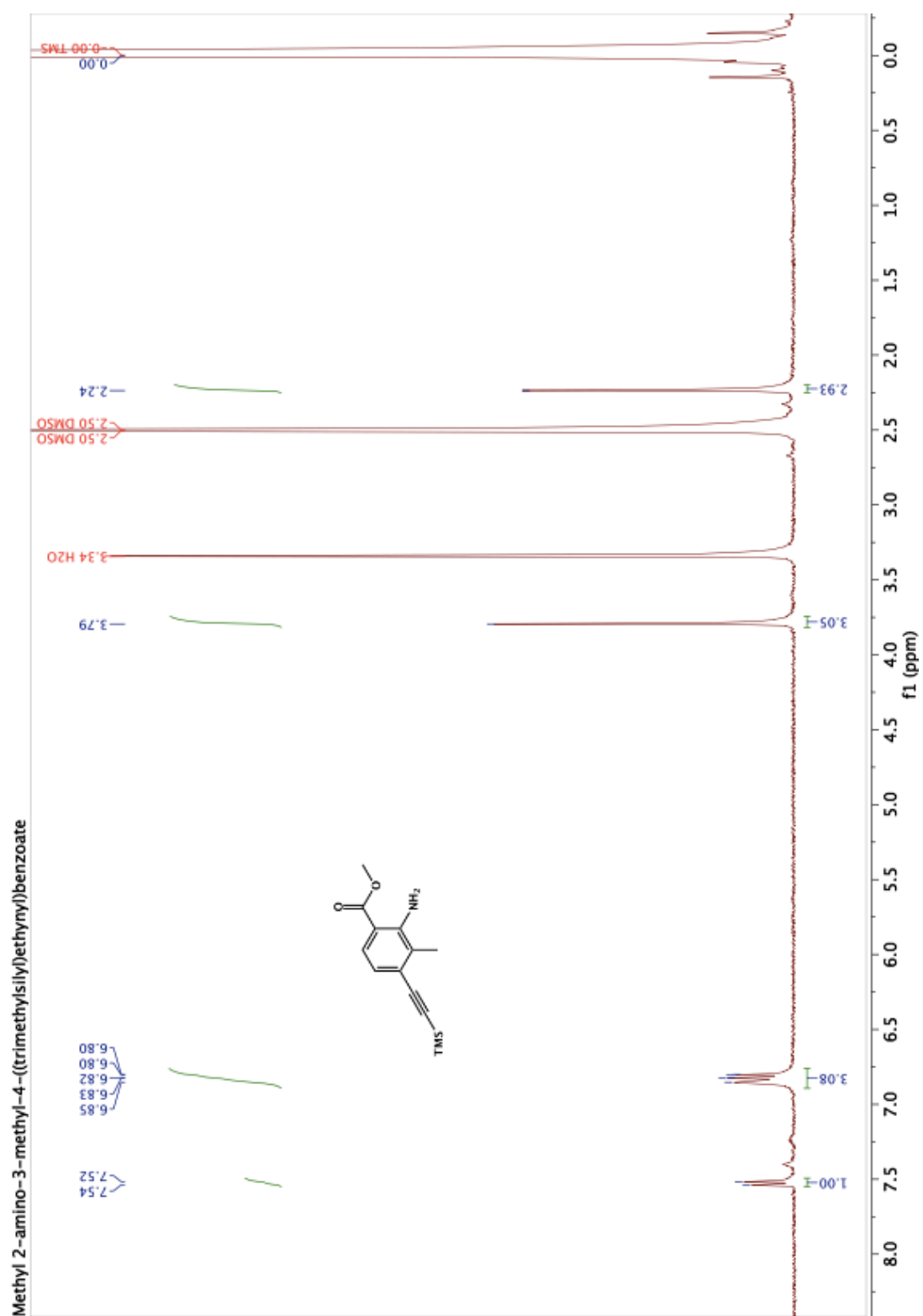


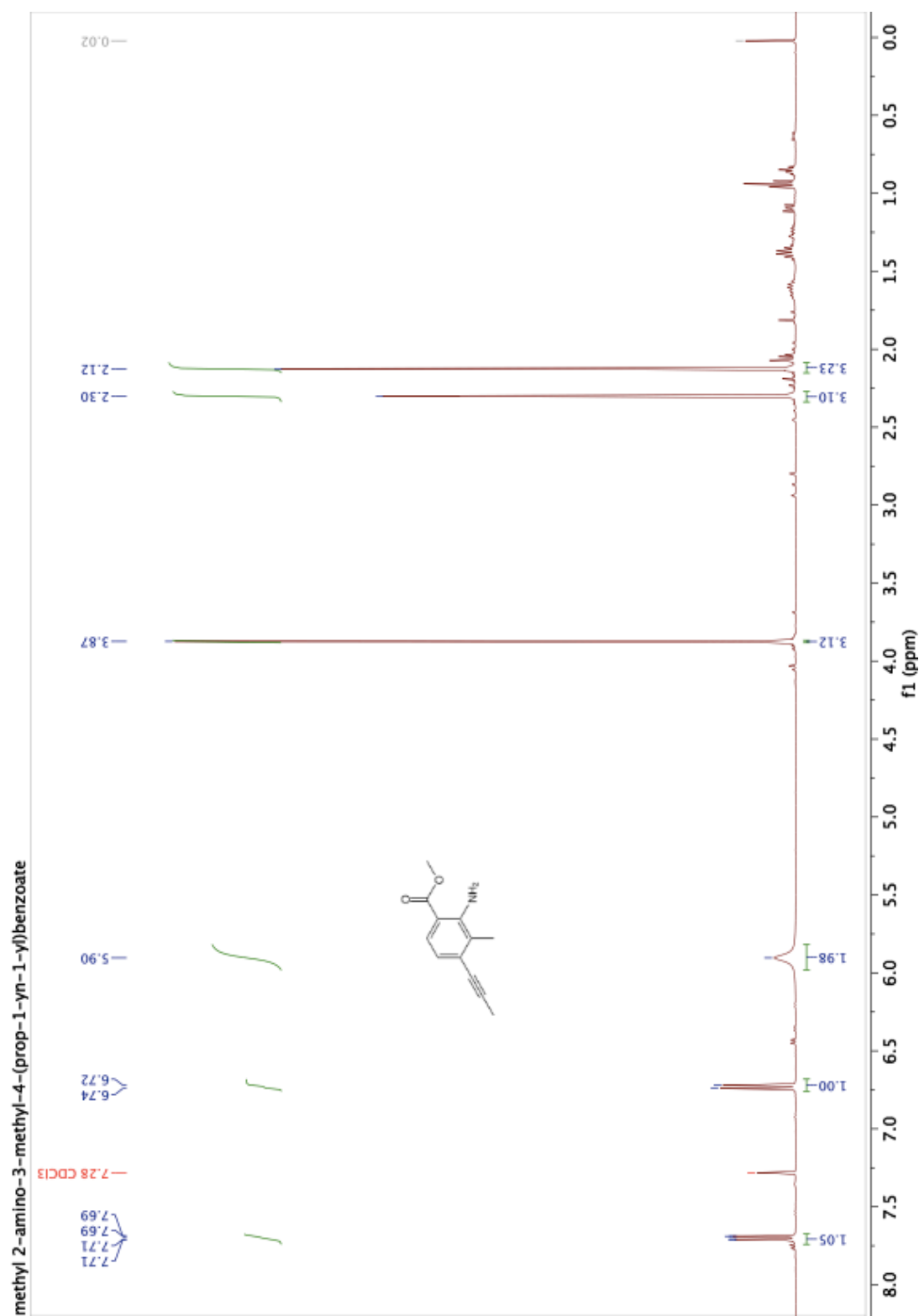


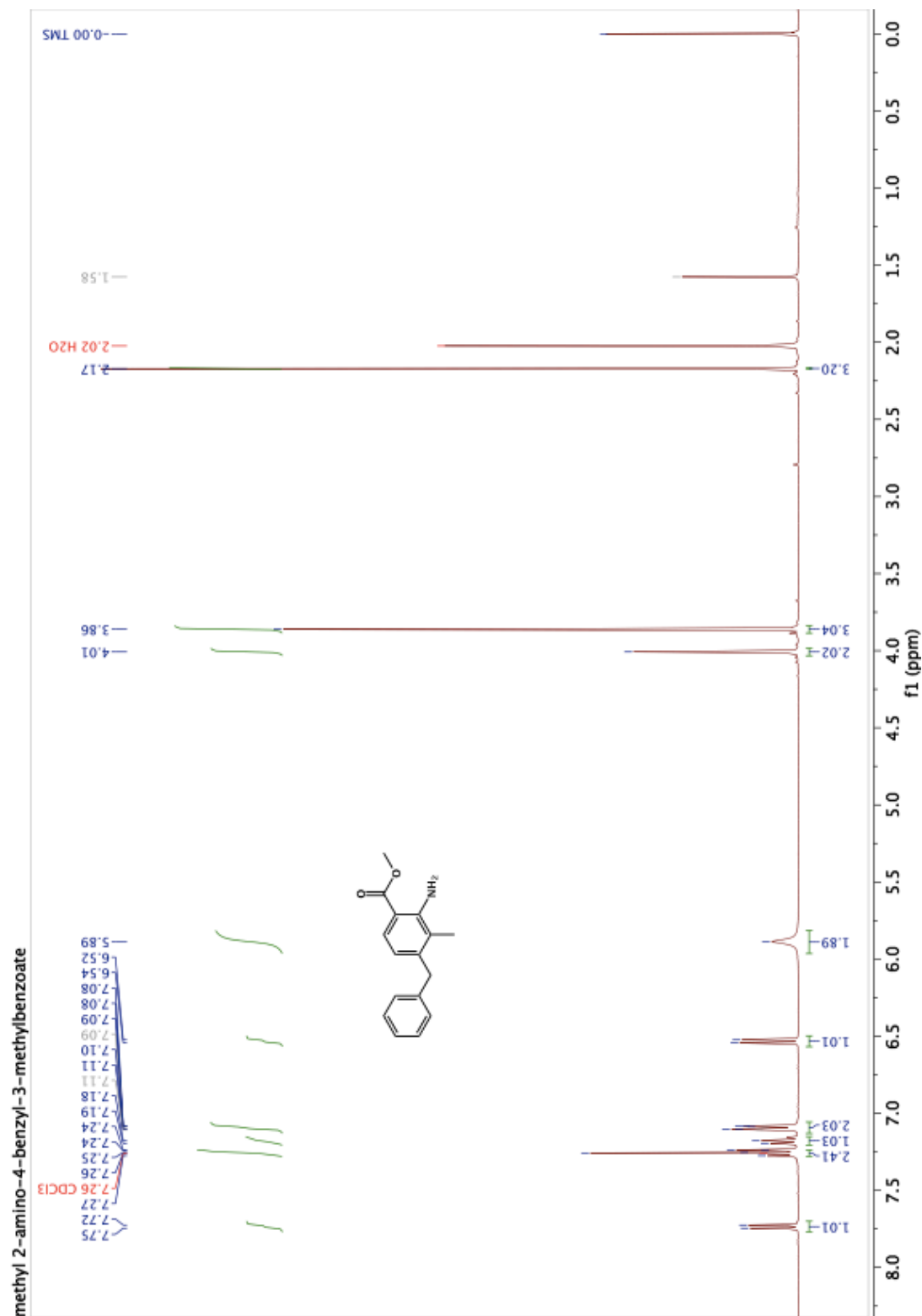


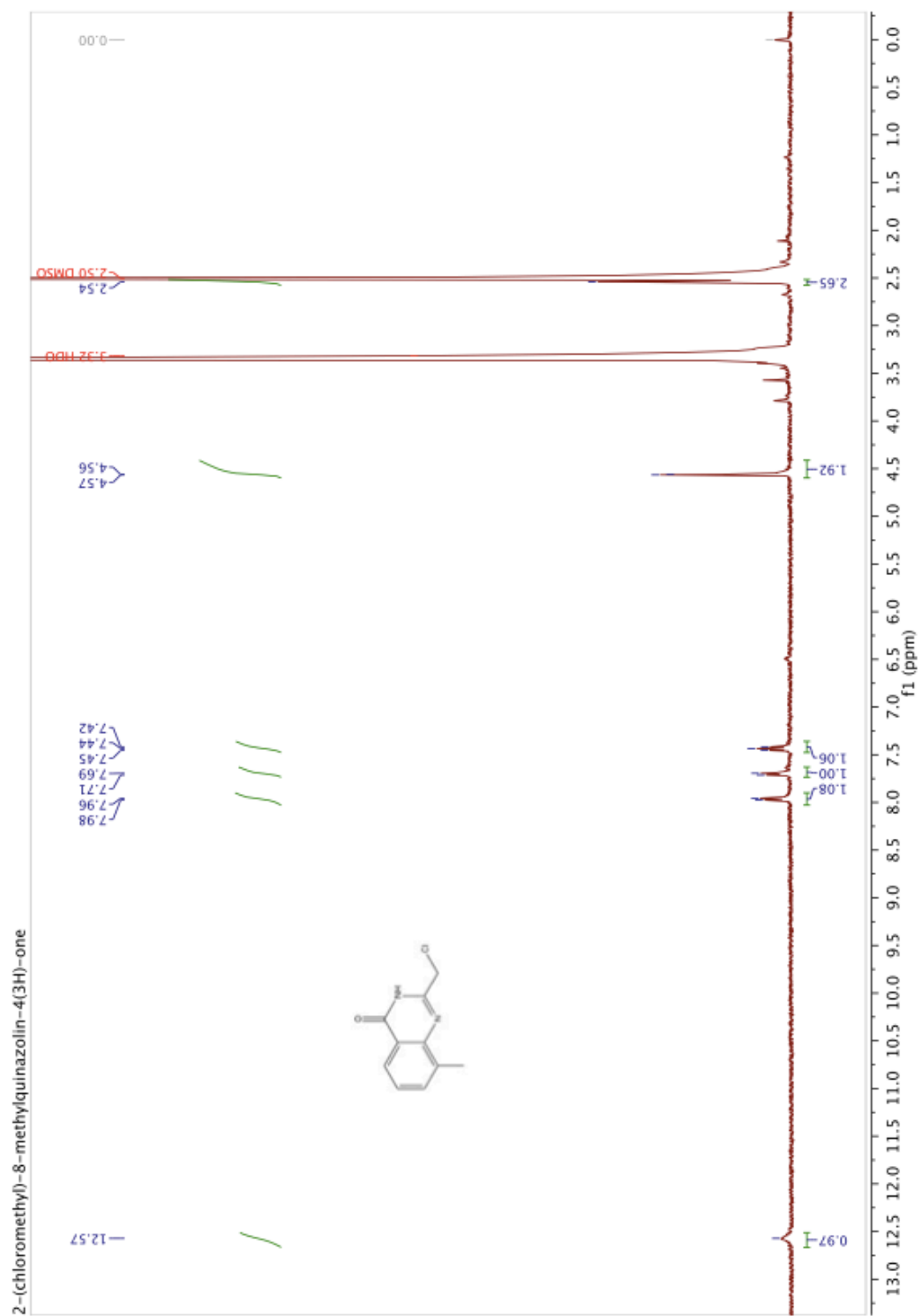




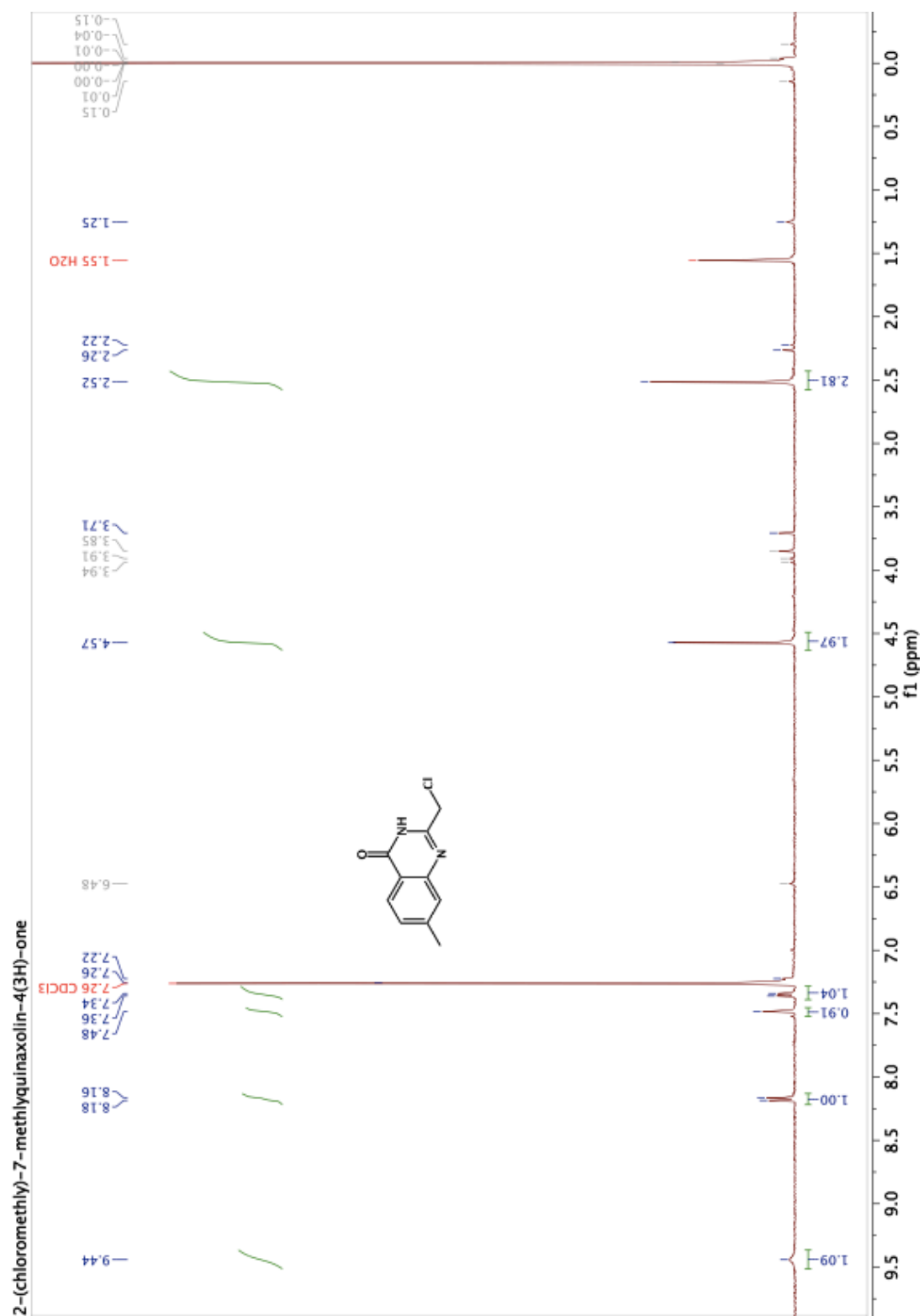


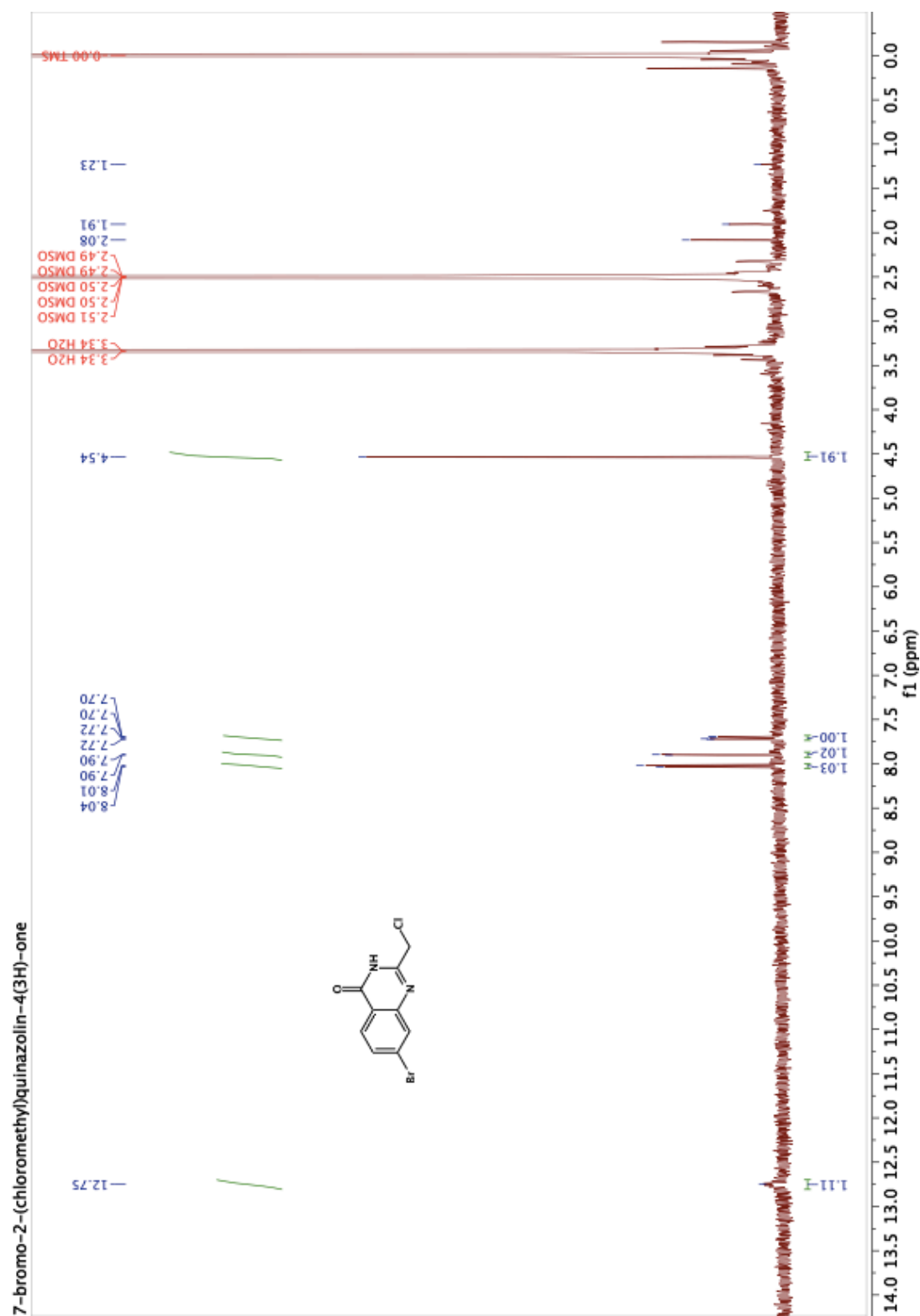


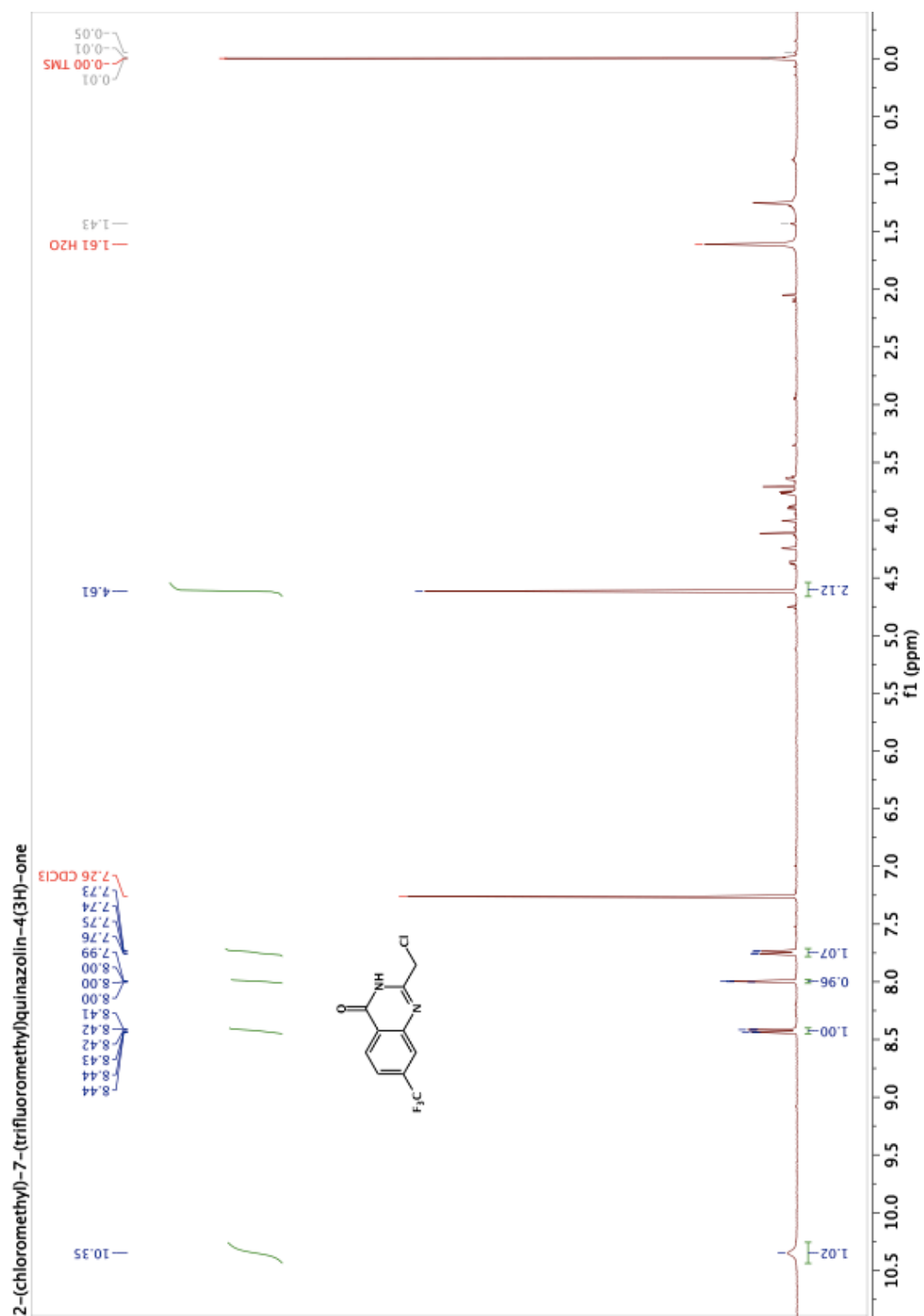




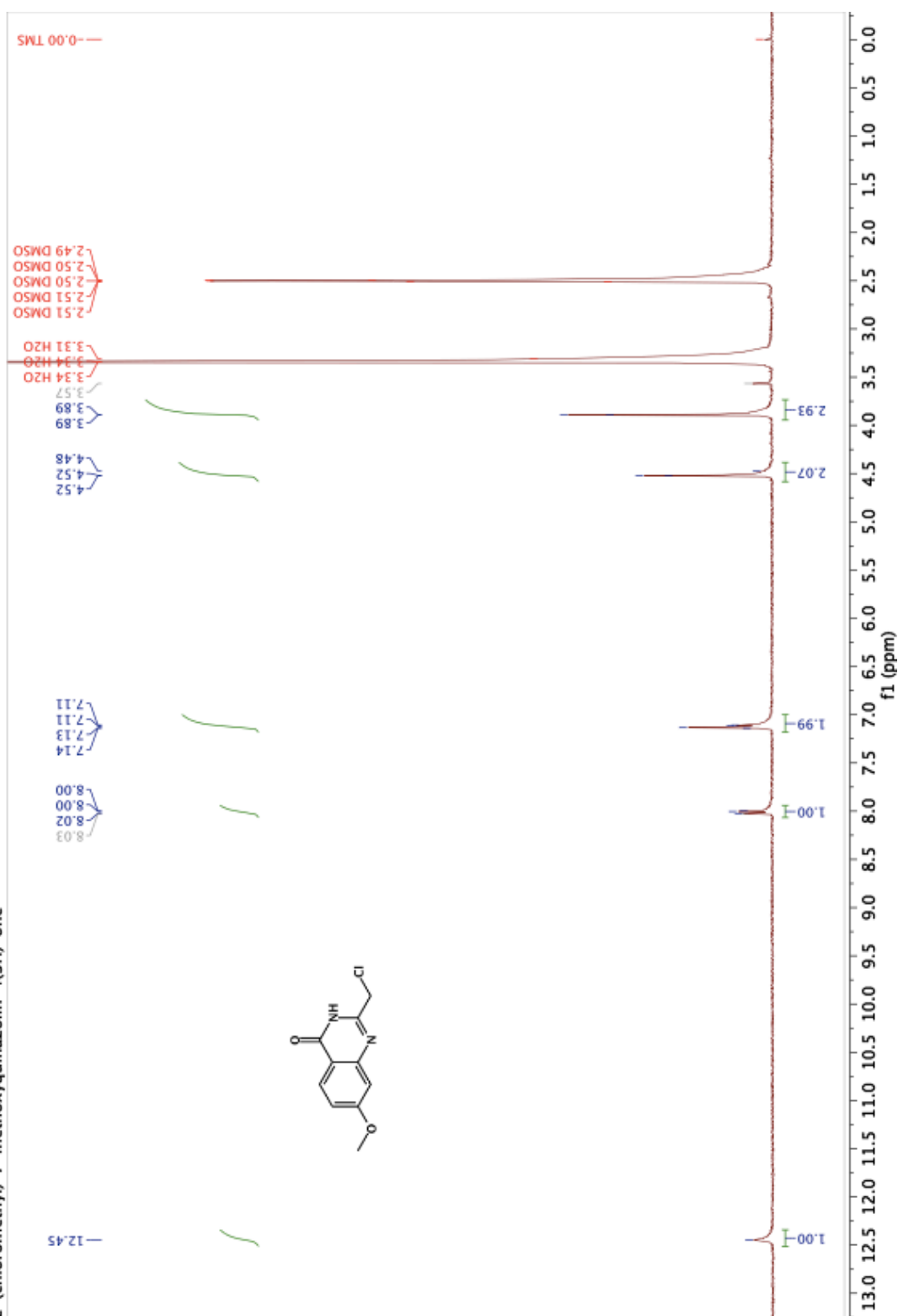




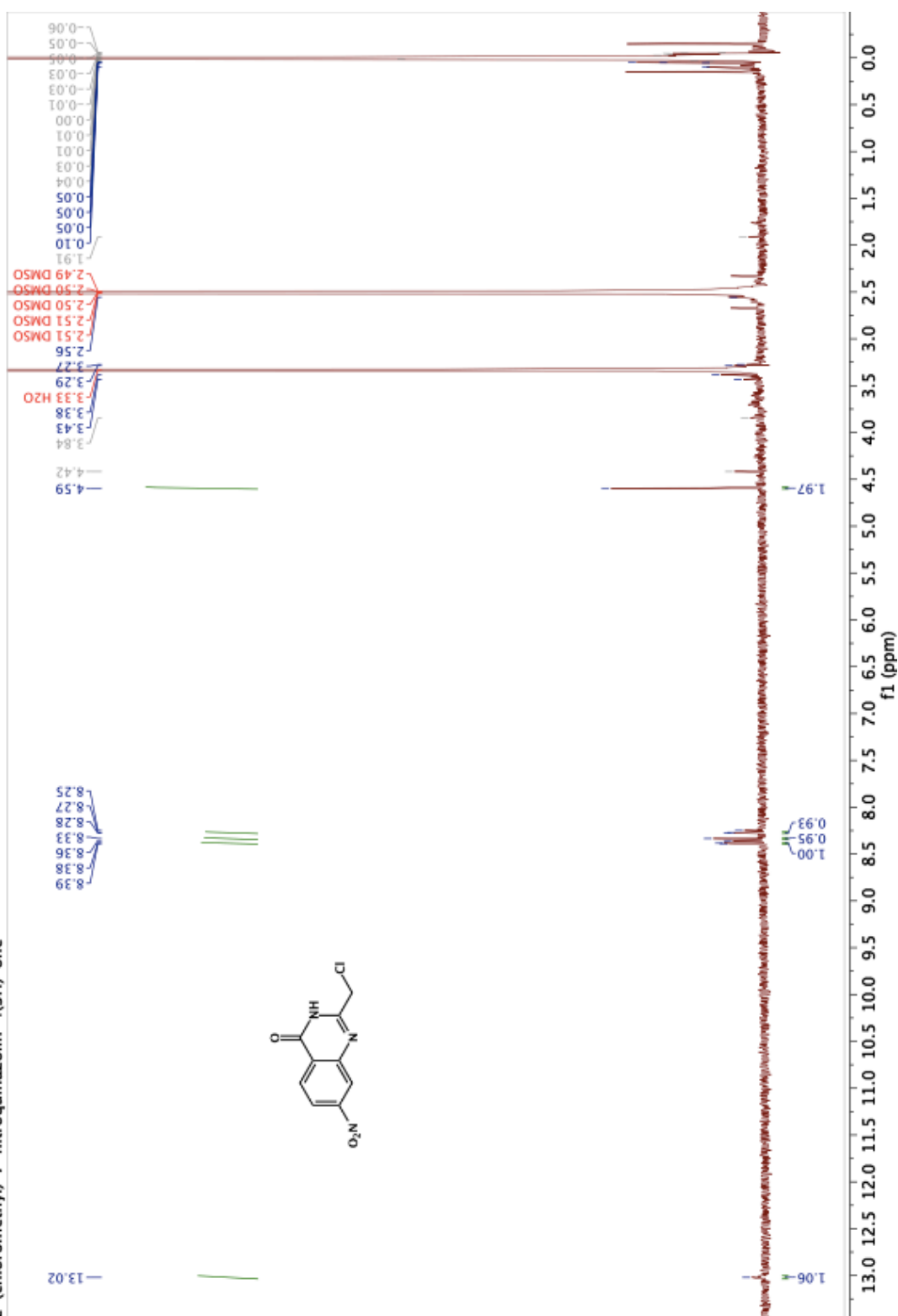


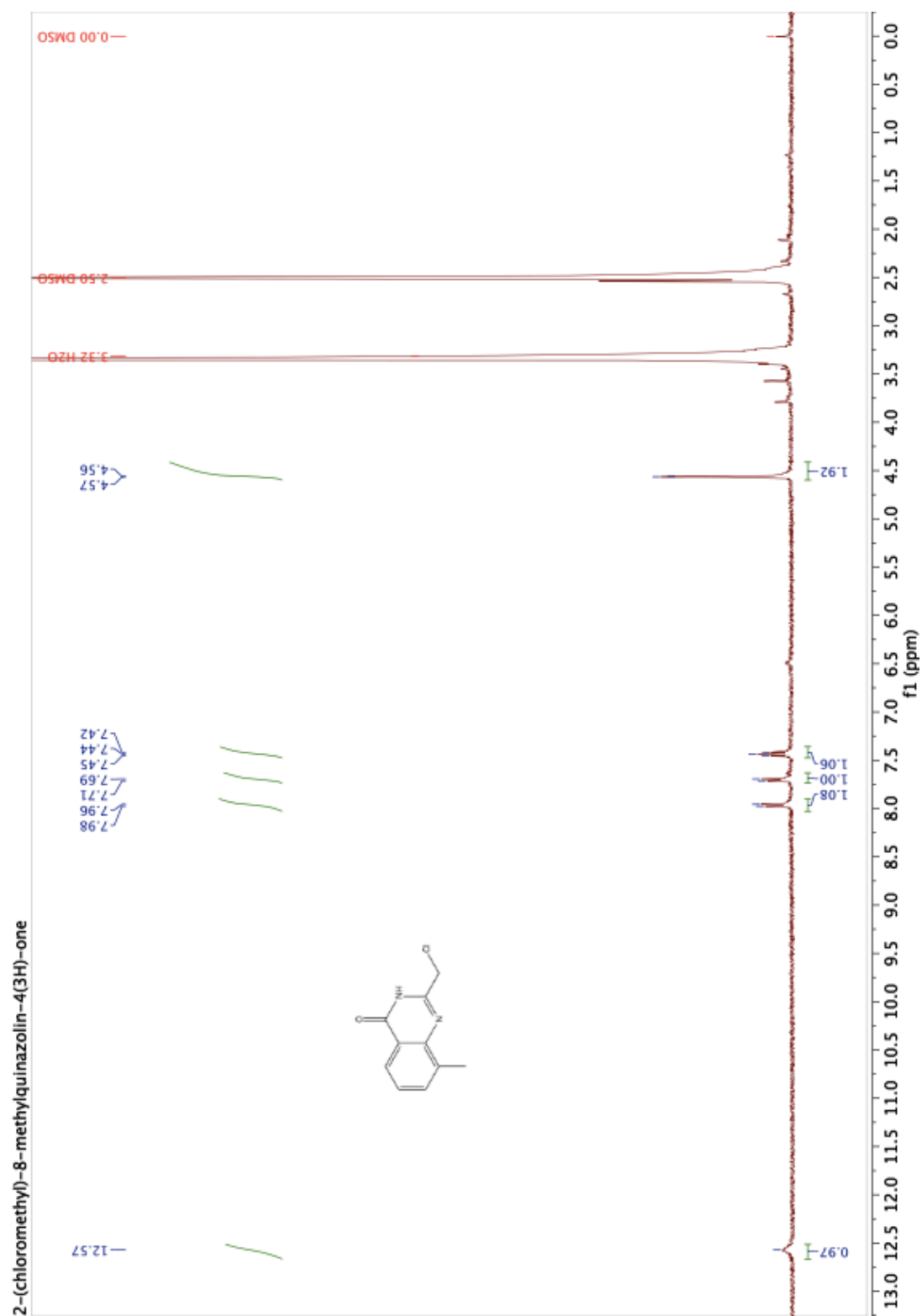


2-(chloromethyl)-7-methoxyquinazolin-4(3H)-one

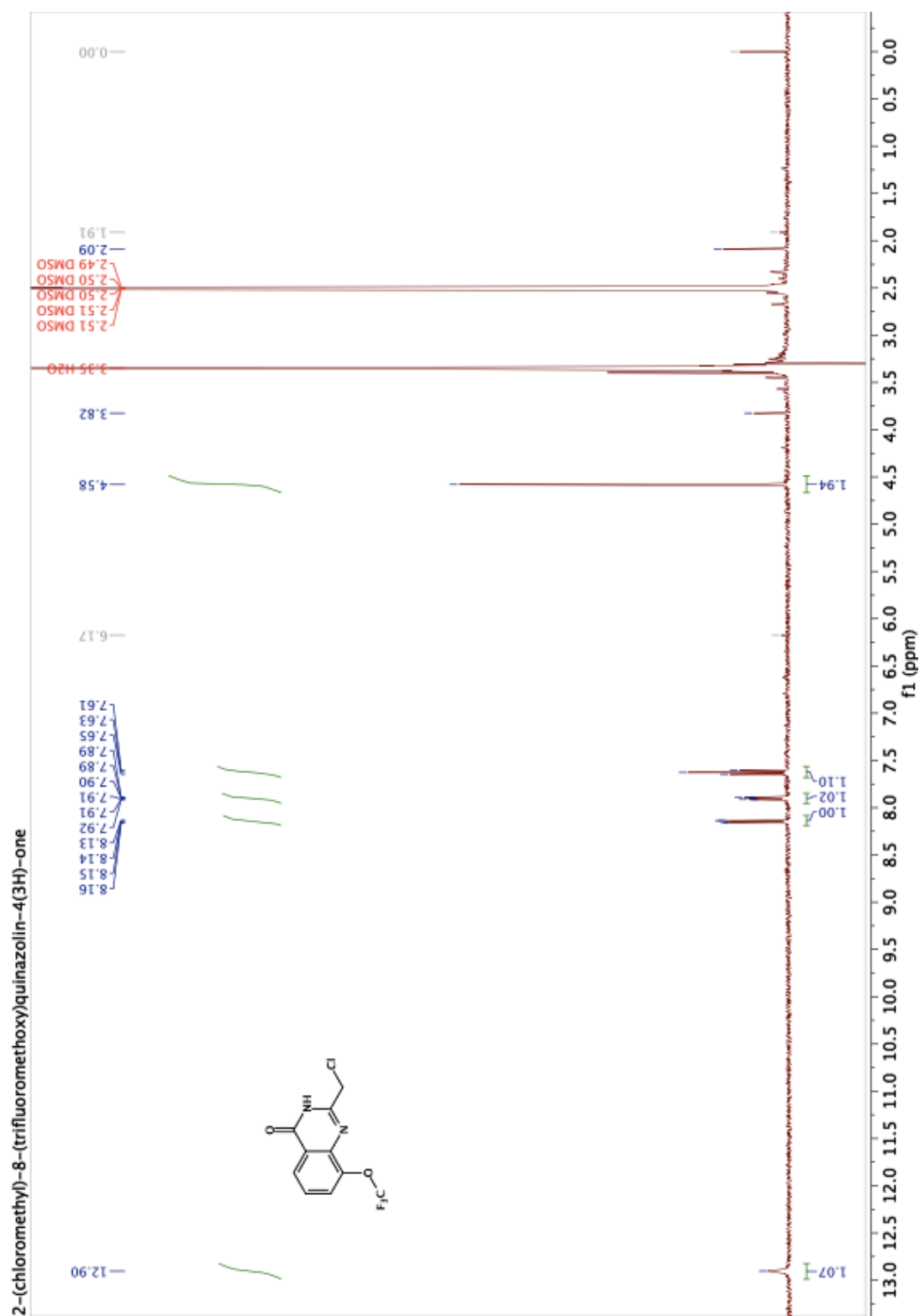


2-(chloromethyl)-7-nitroquinazolin-4(3H)-one

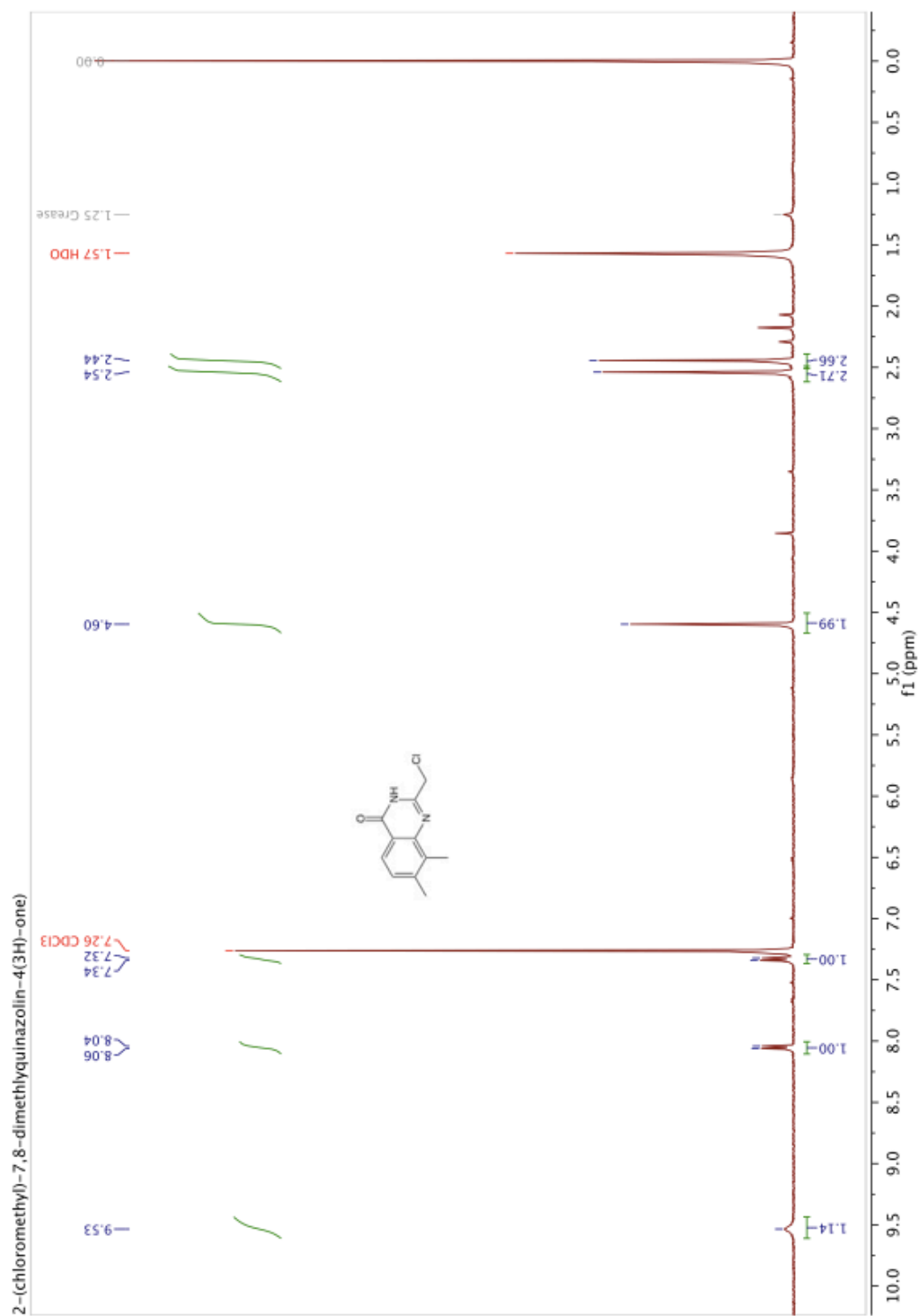


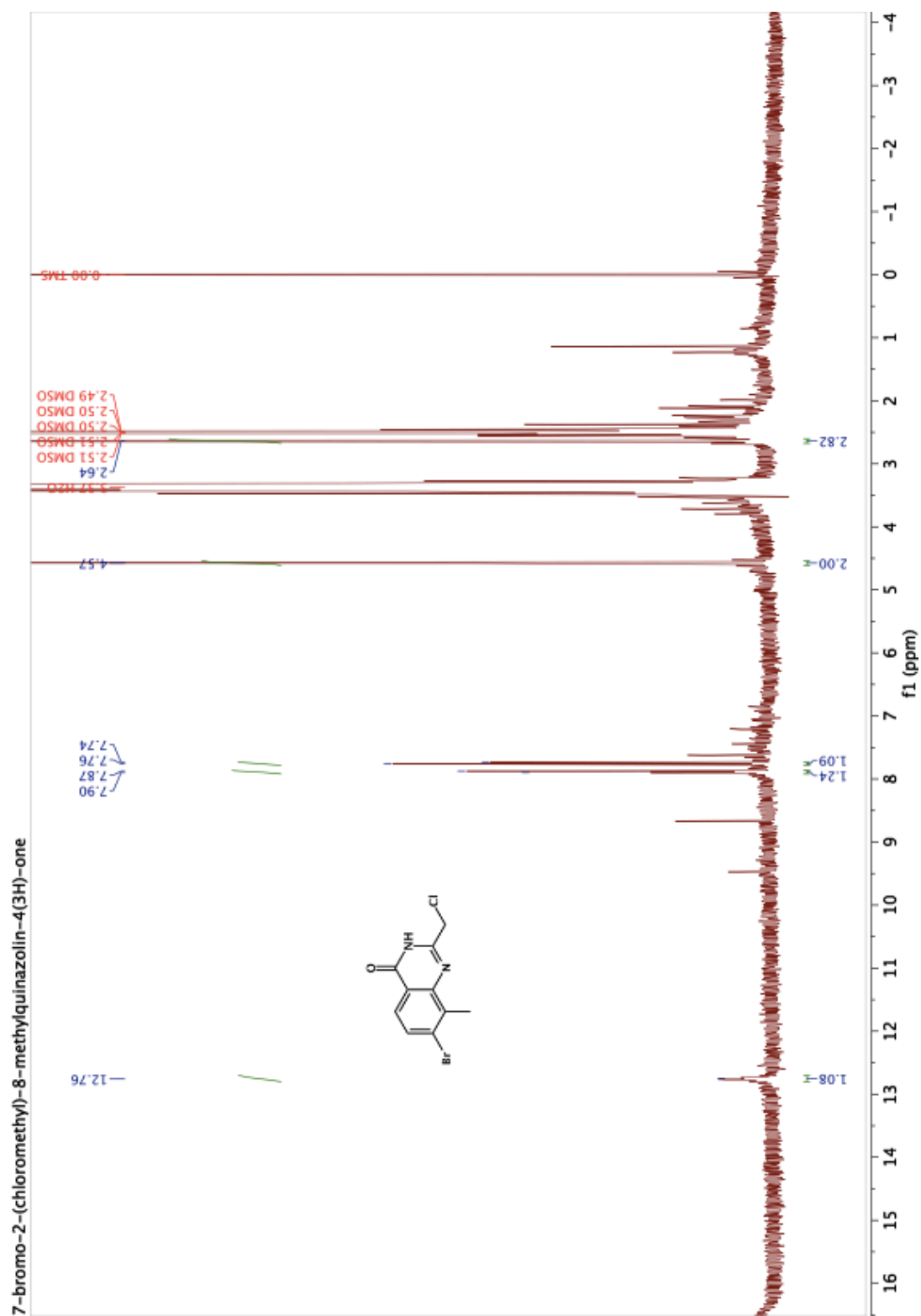


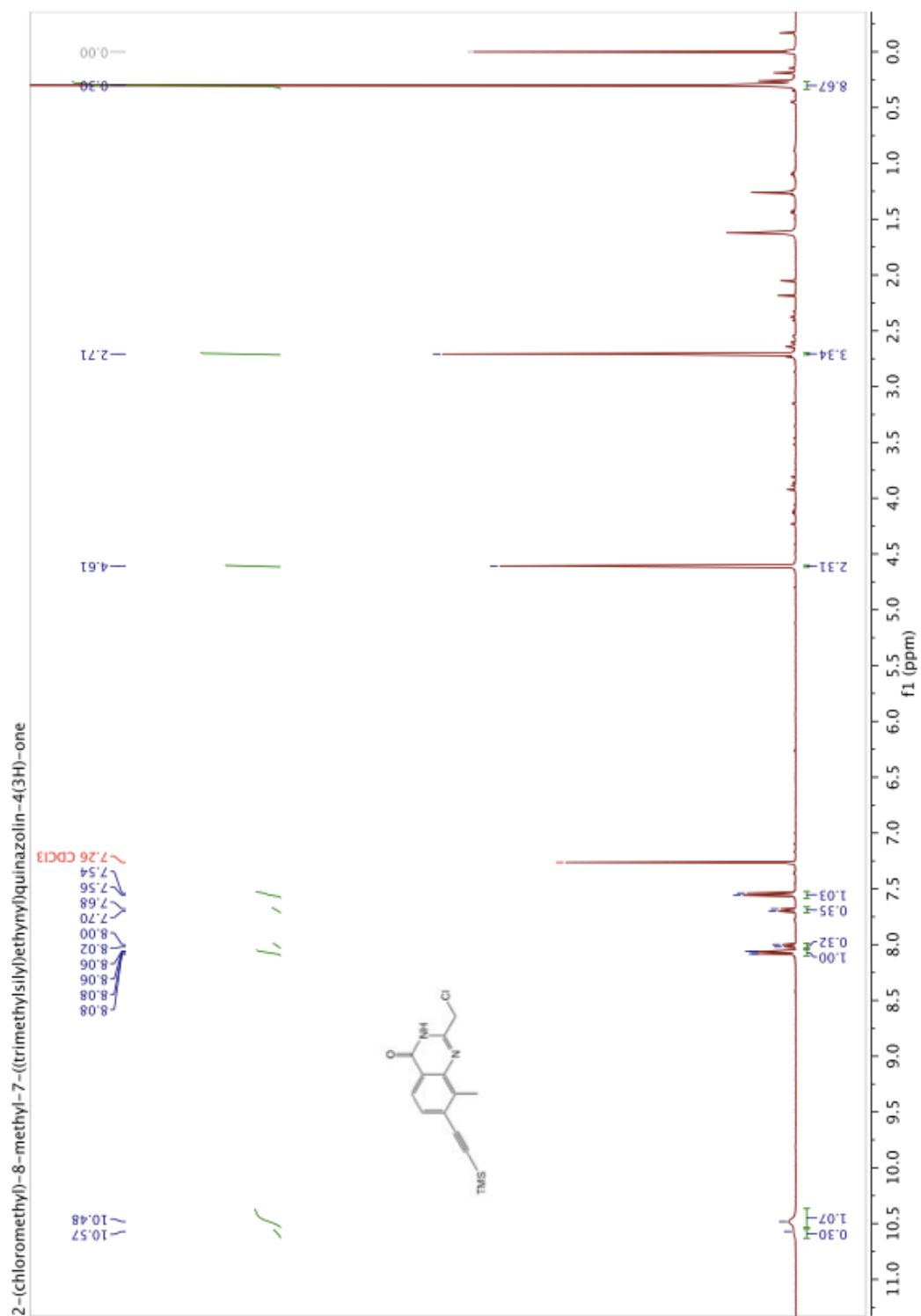


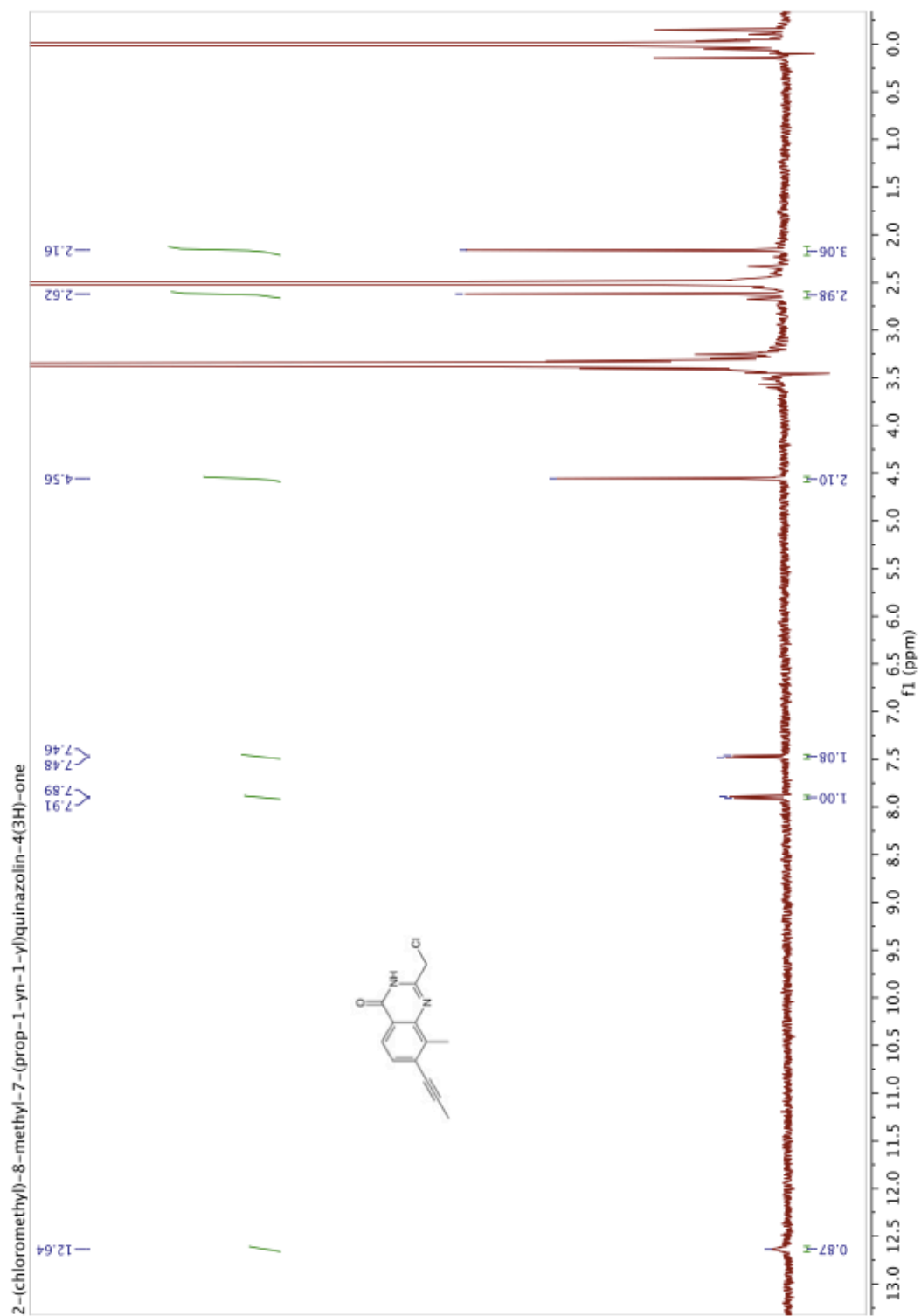


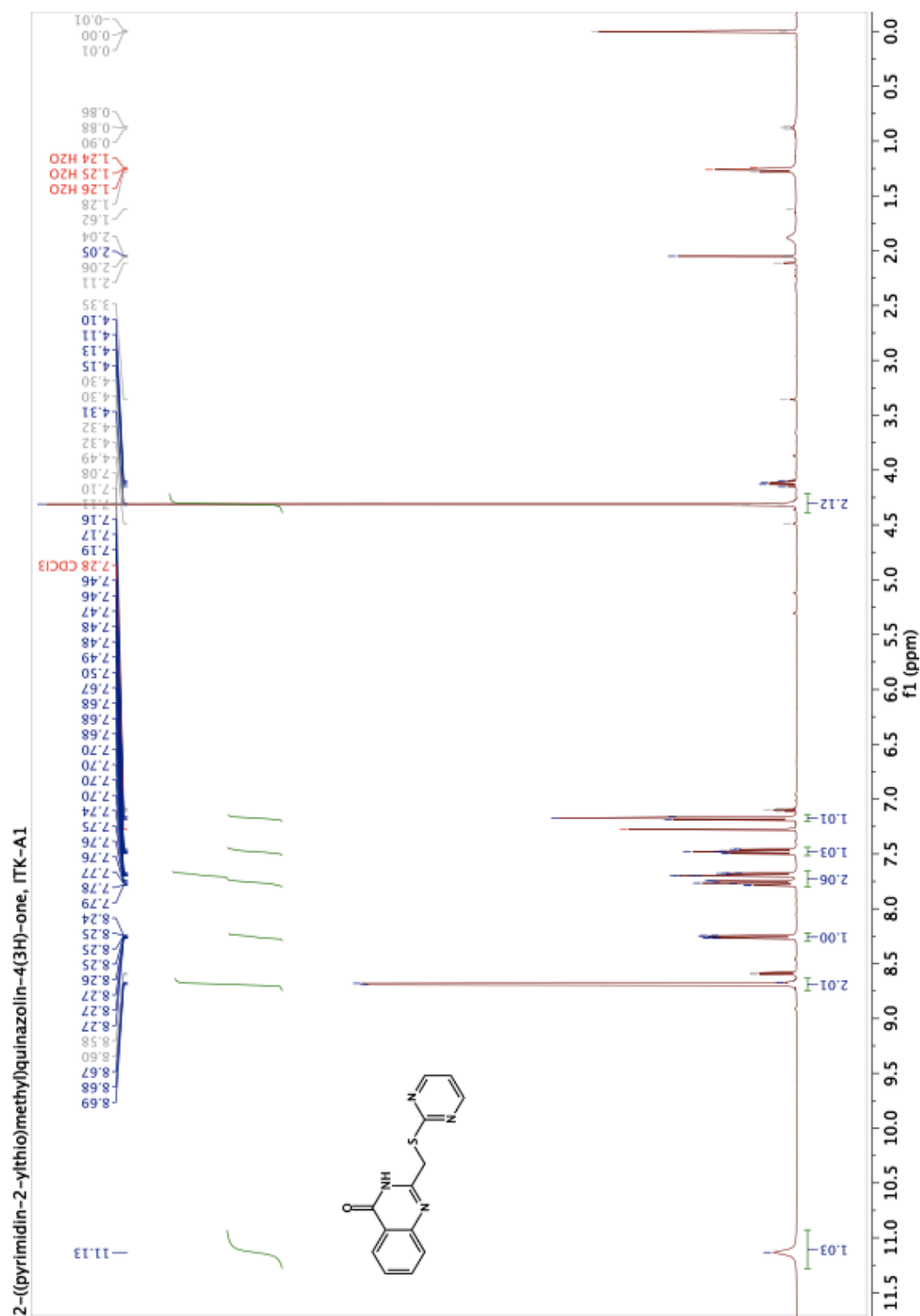




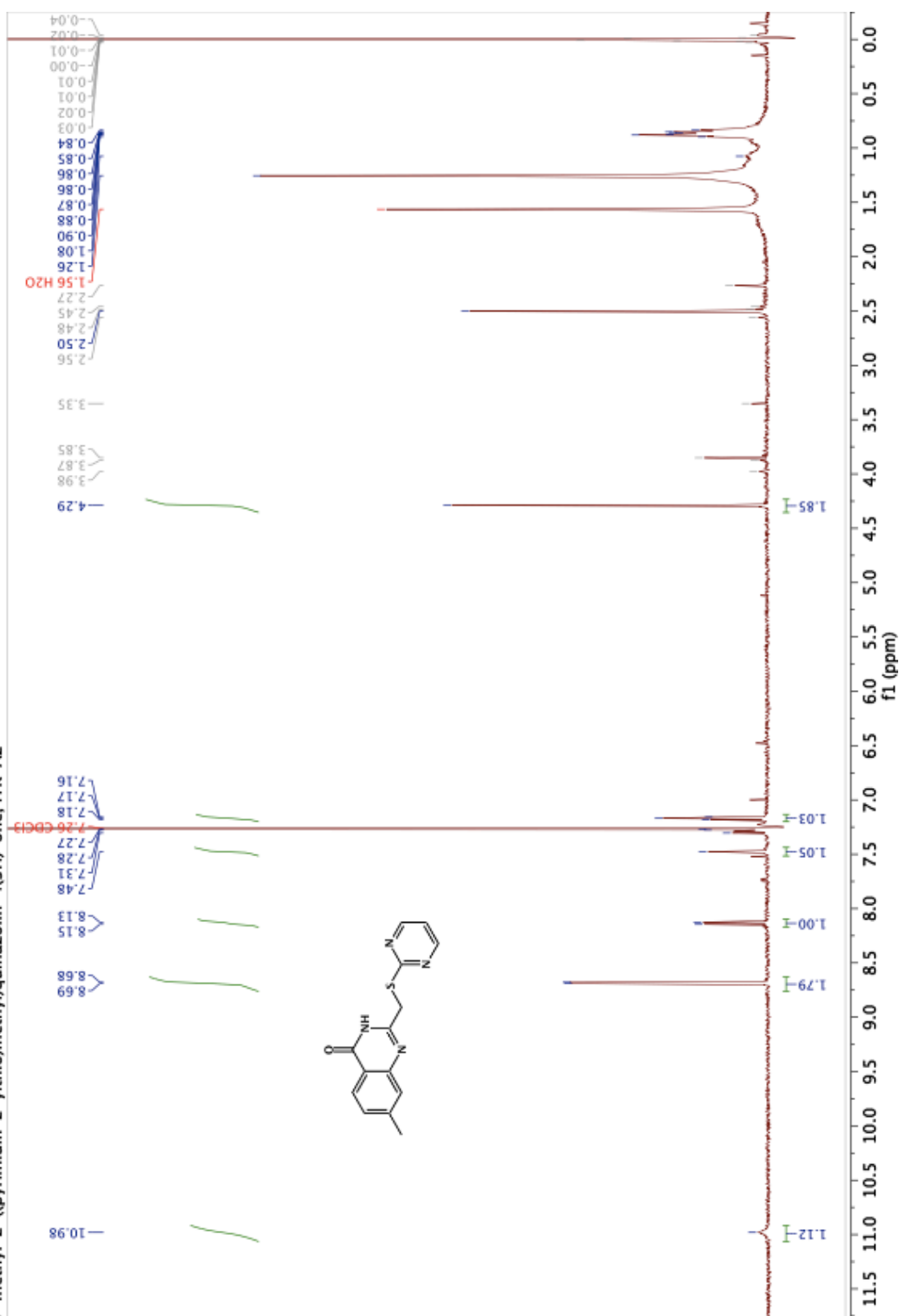


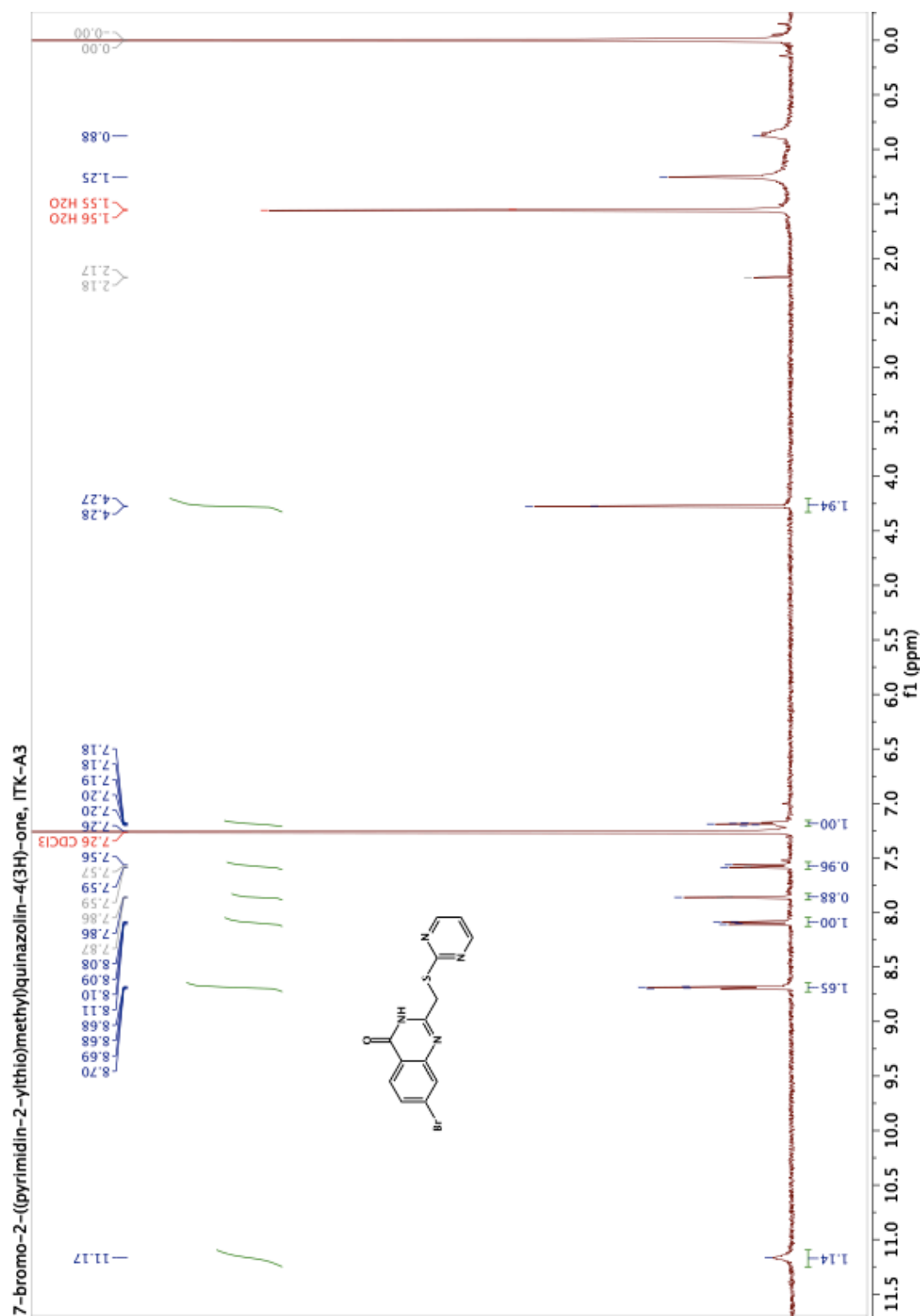




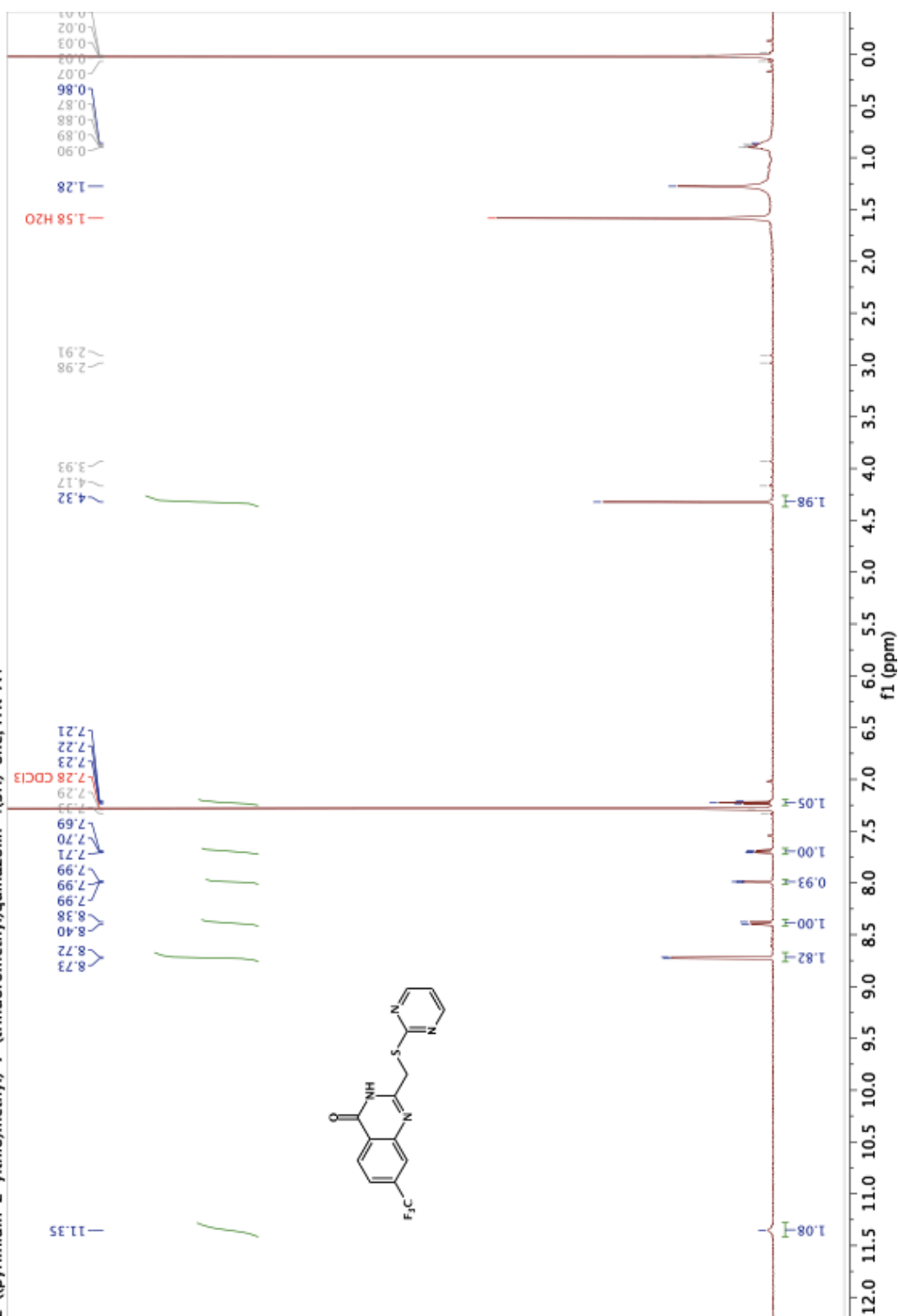


7-methyl-2-((pyrimidin-2-ylthio)methyl)quinazolin-4(3H)-one, ITK-A2



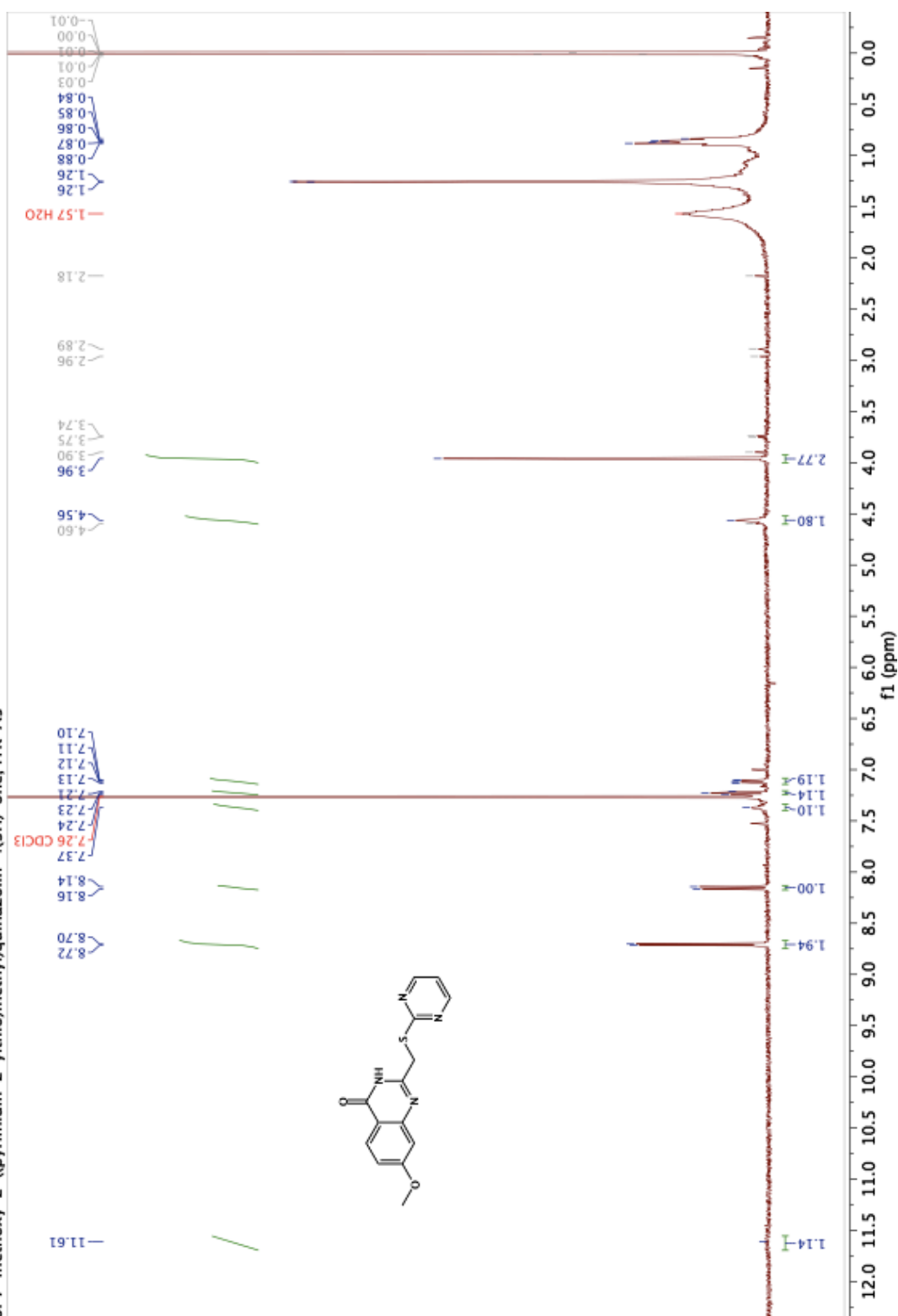


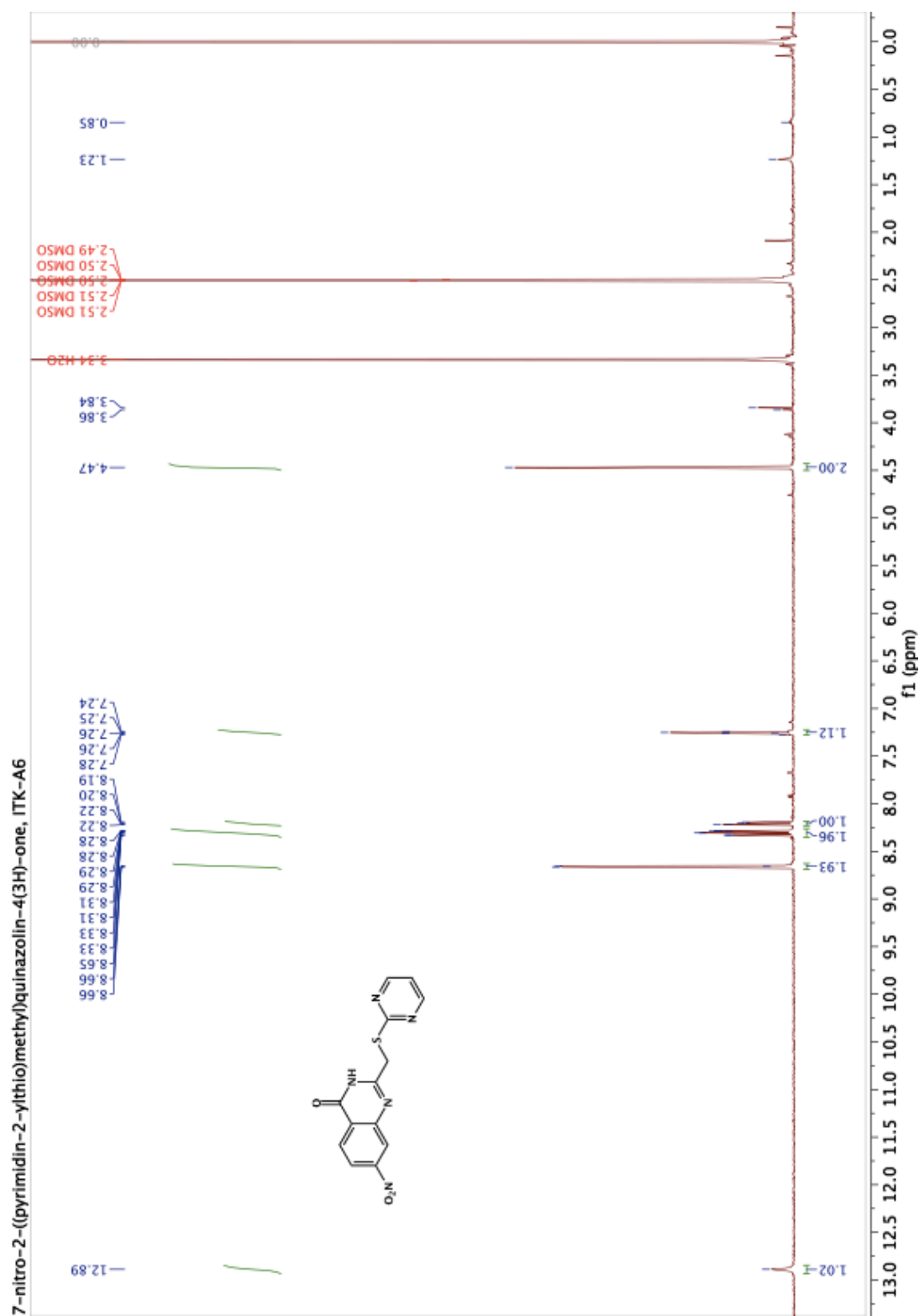
2-((pyrimidin-2-ylthio)methyl)-7-(trifluoromethyl)quinazolin-4(3H)-one, ITK-A4

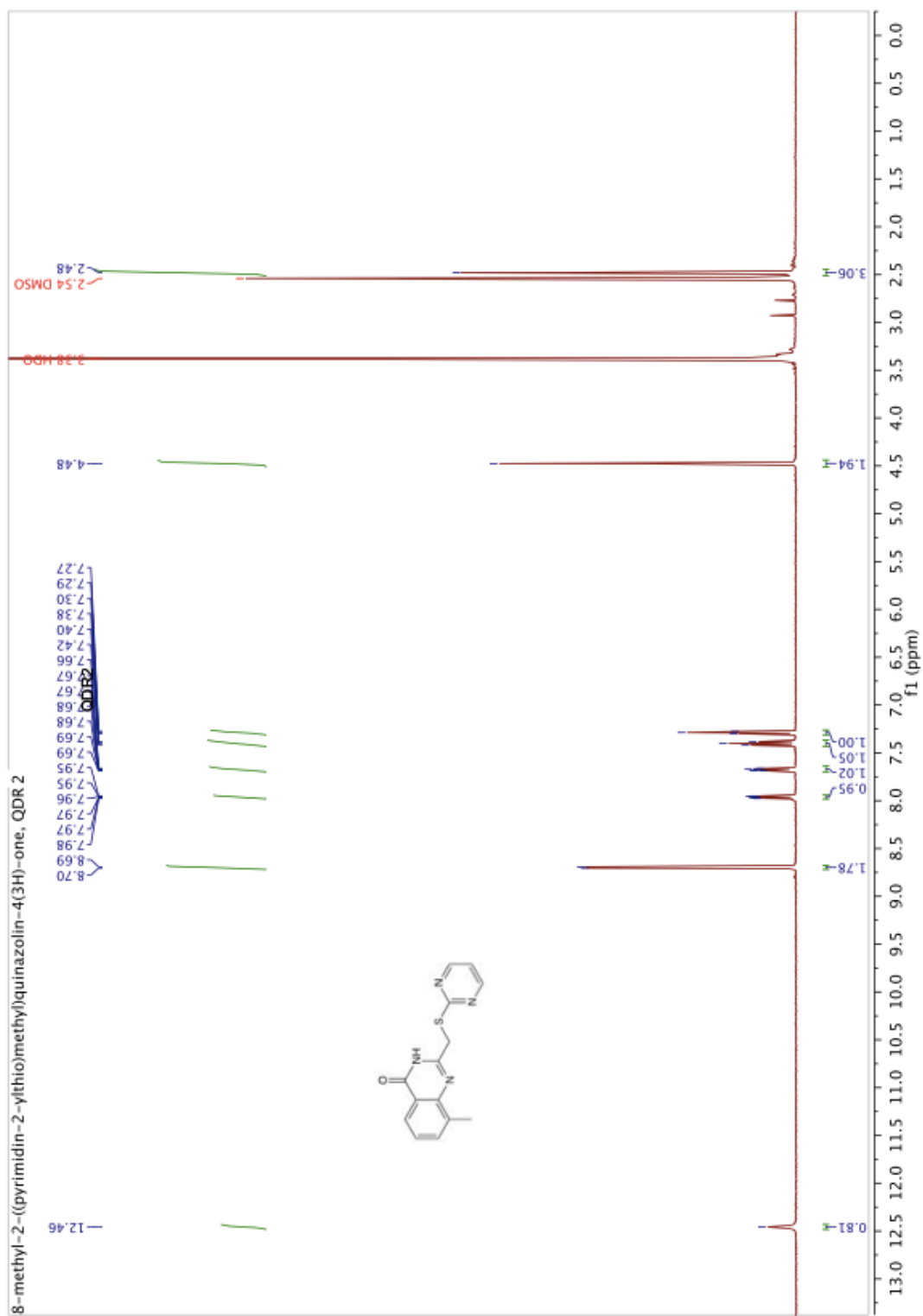


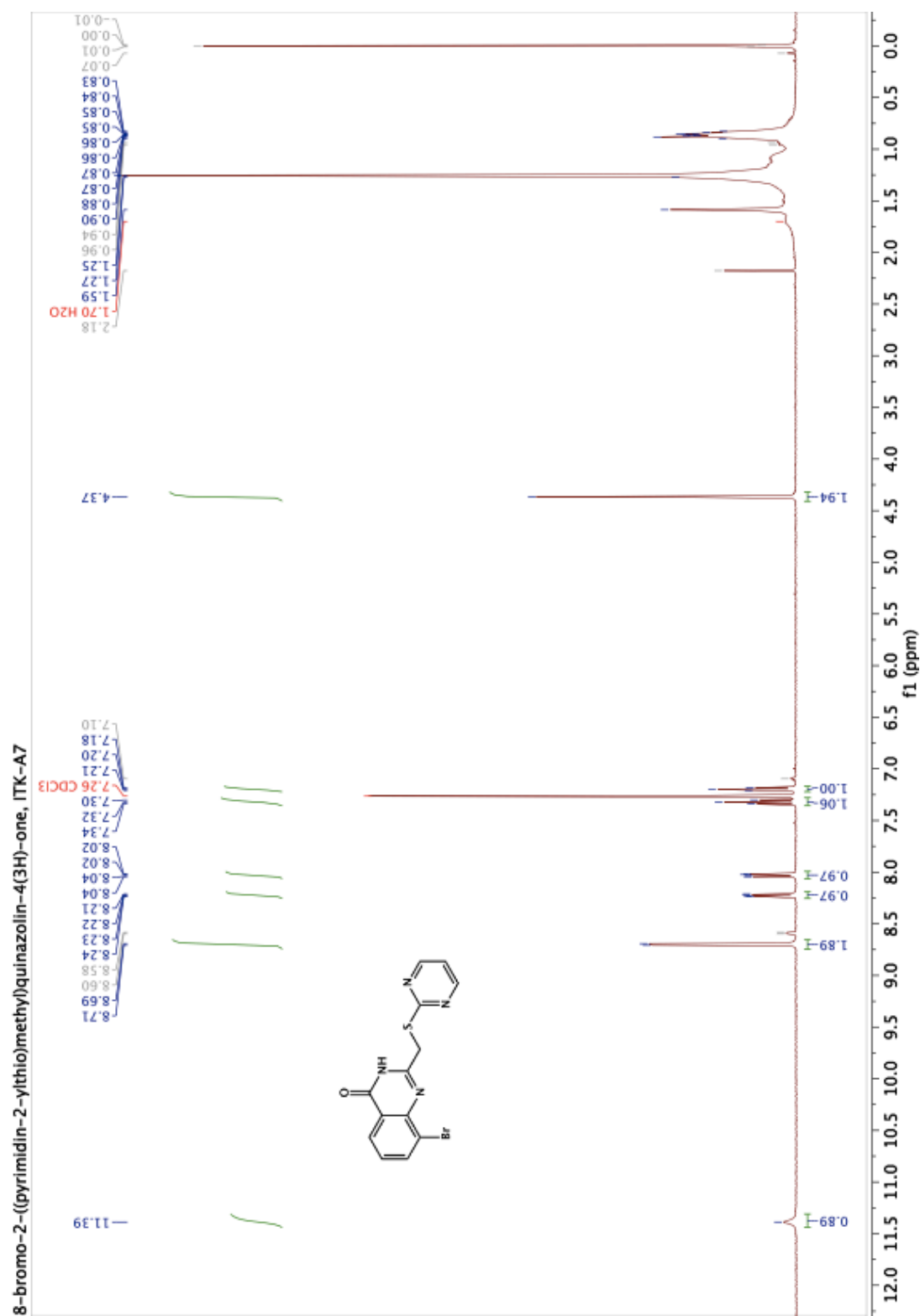


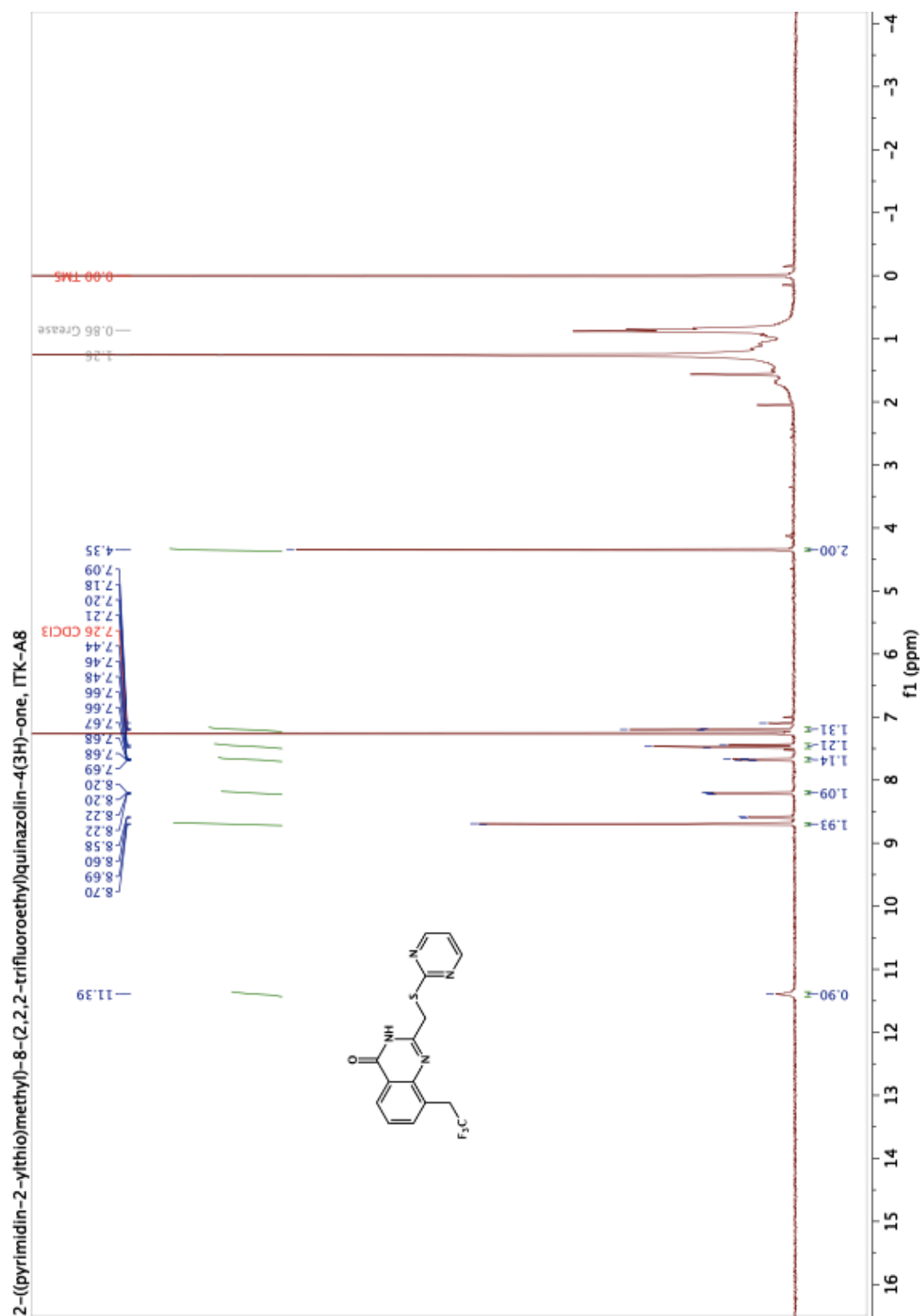
of 7-methoxy-2-((pyrimidin-2-ylthio)methyl)quinazolin-4(3H)-one, ITK-A5

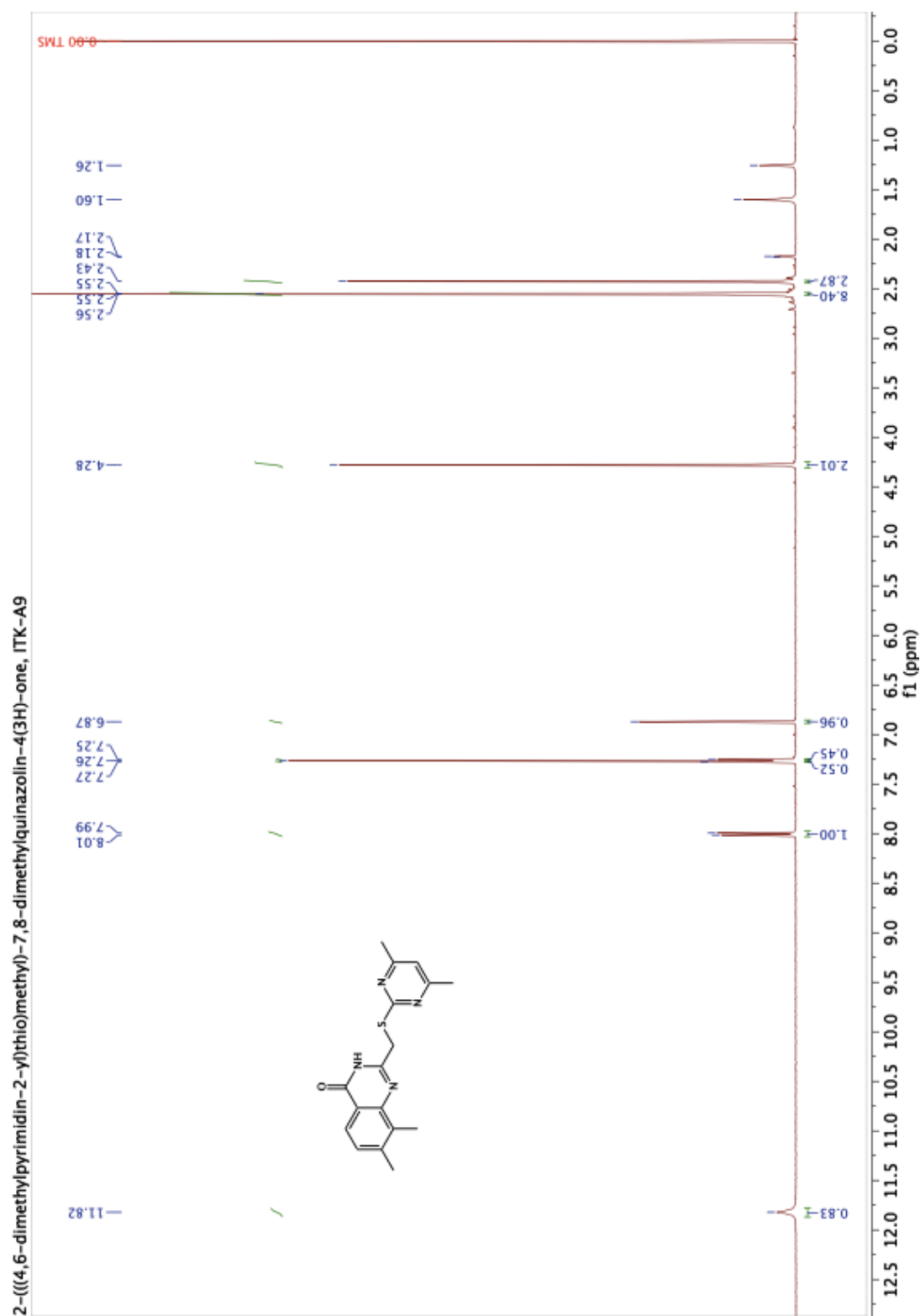


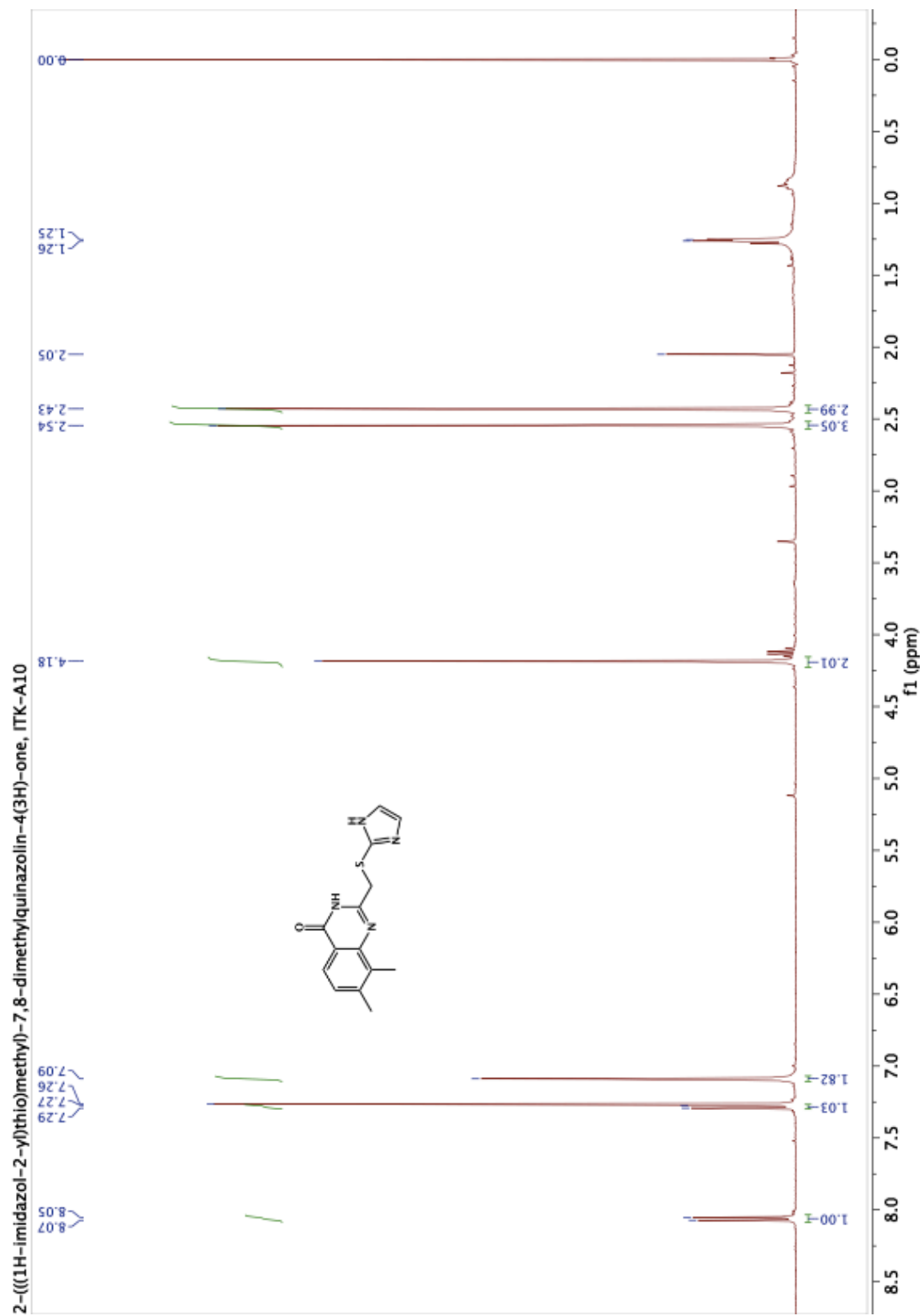


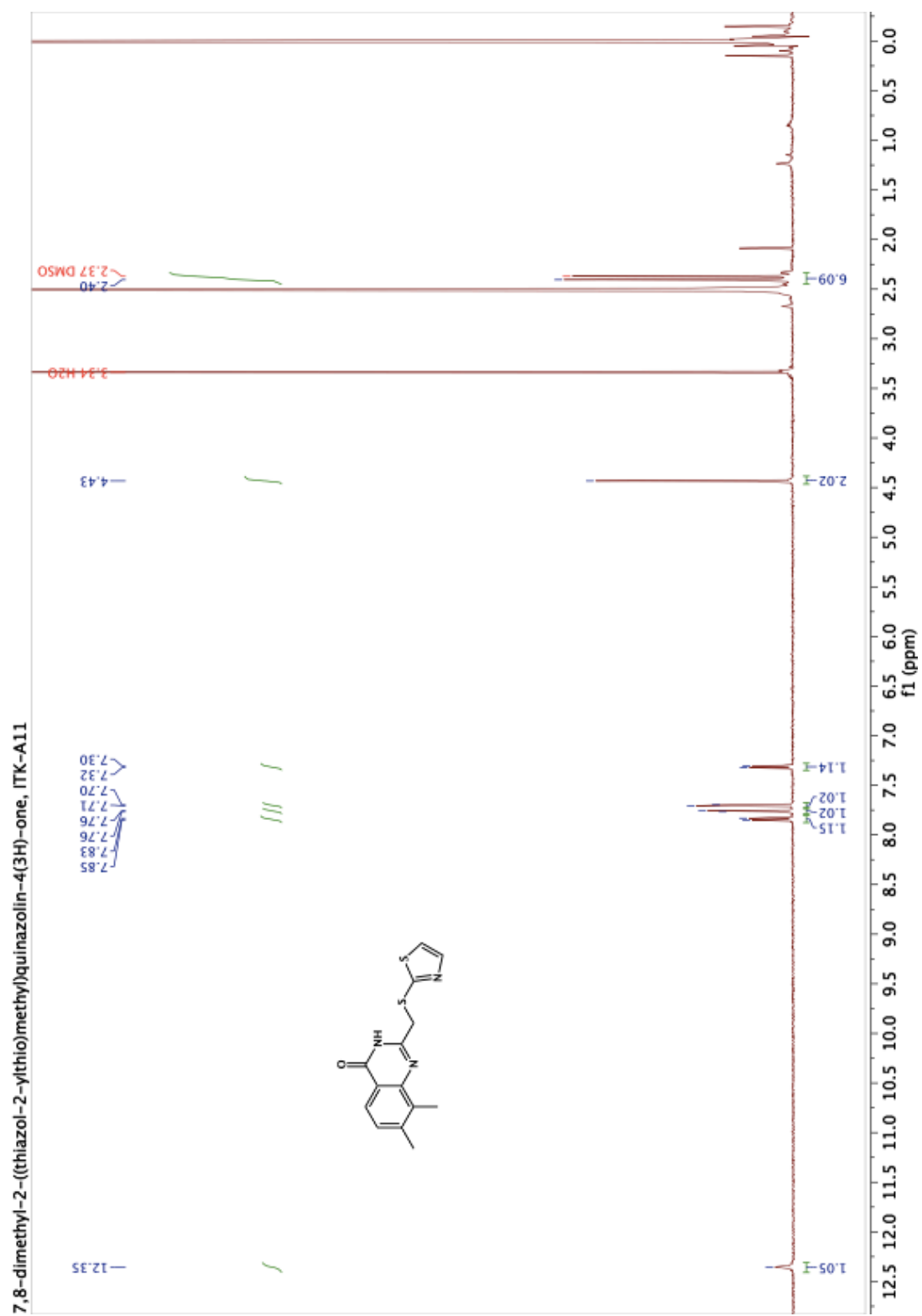




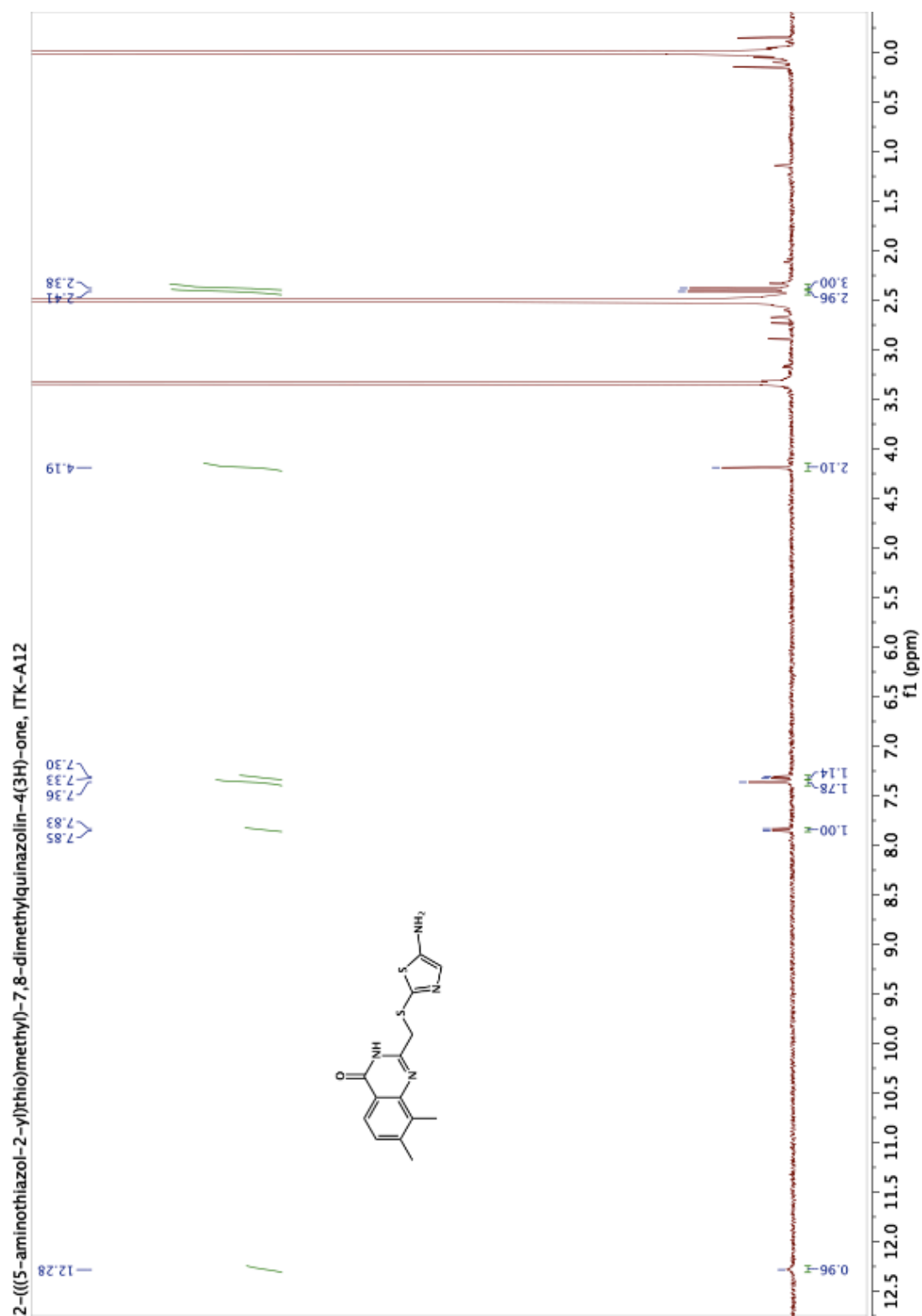




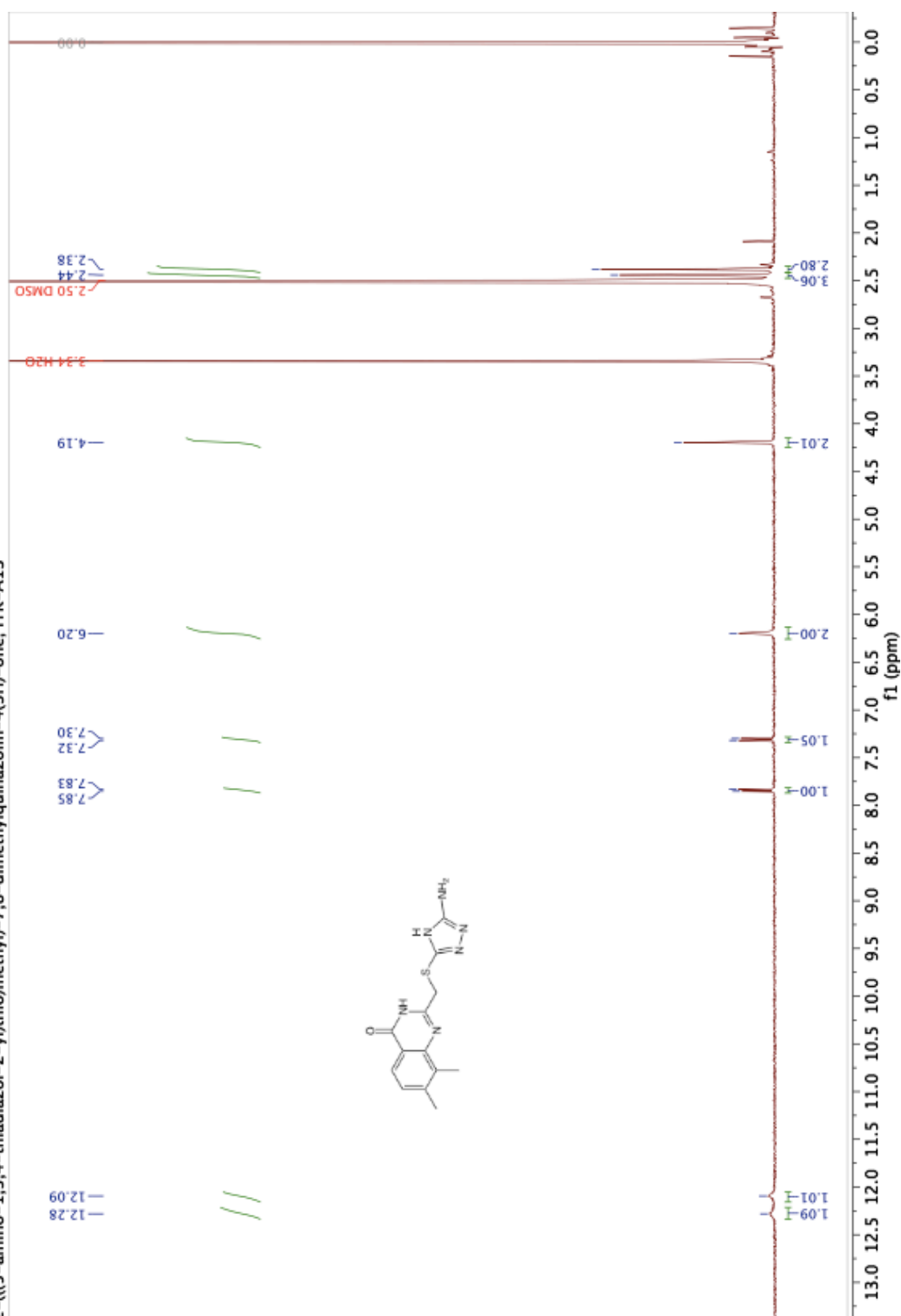


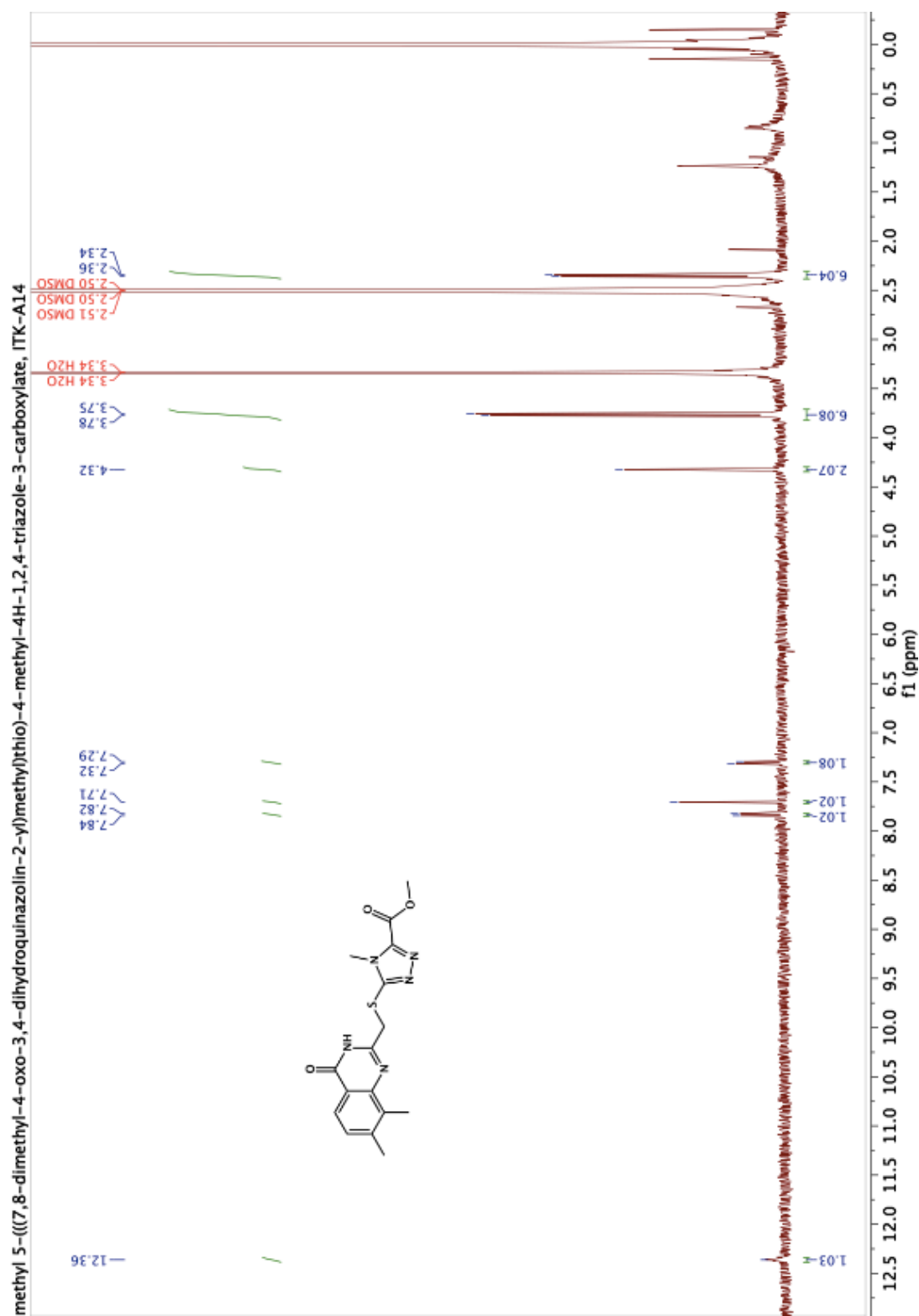


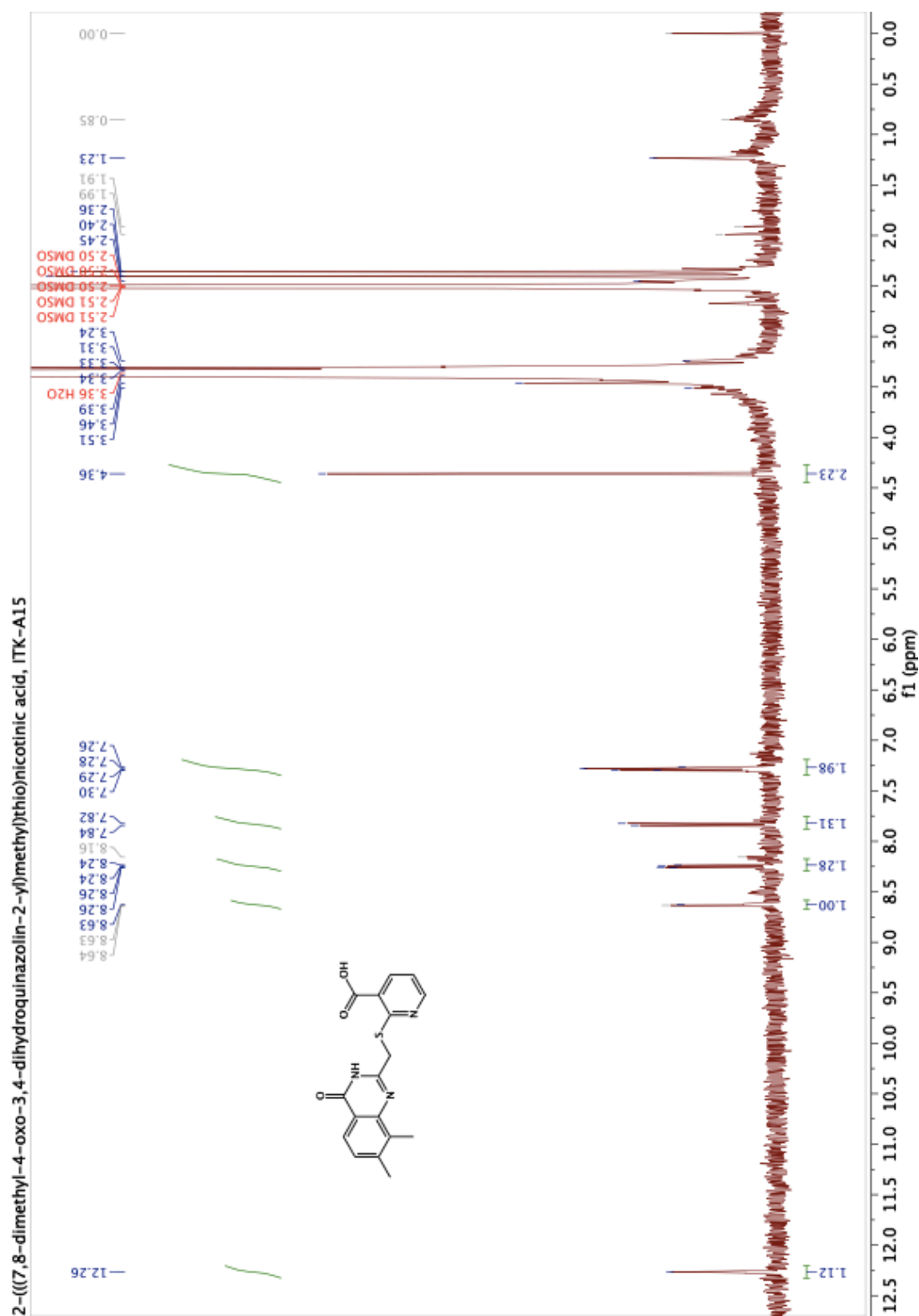


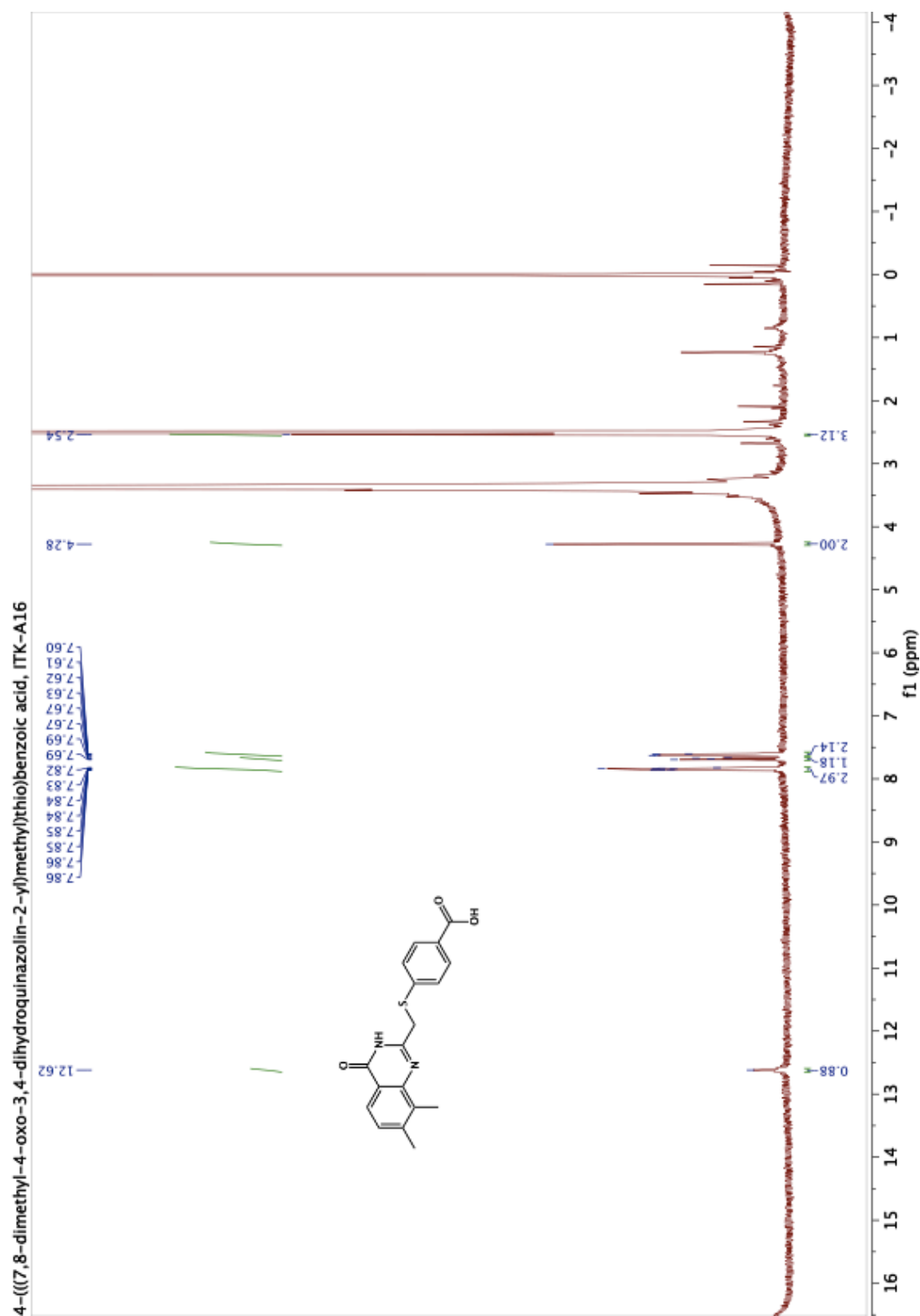


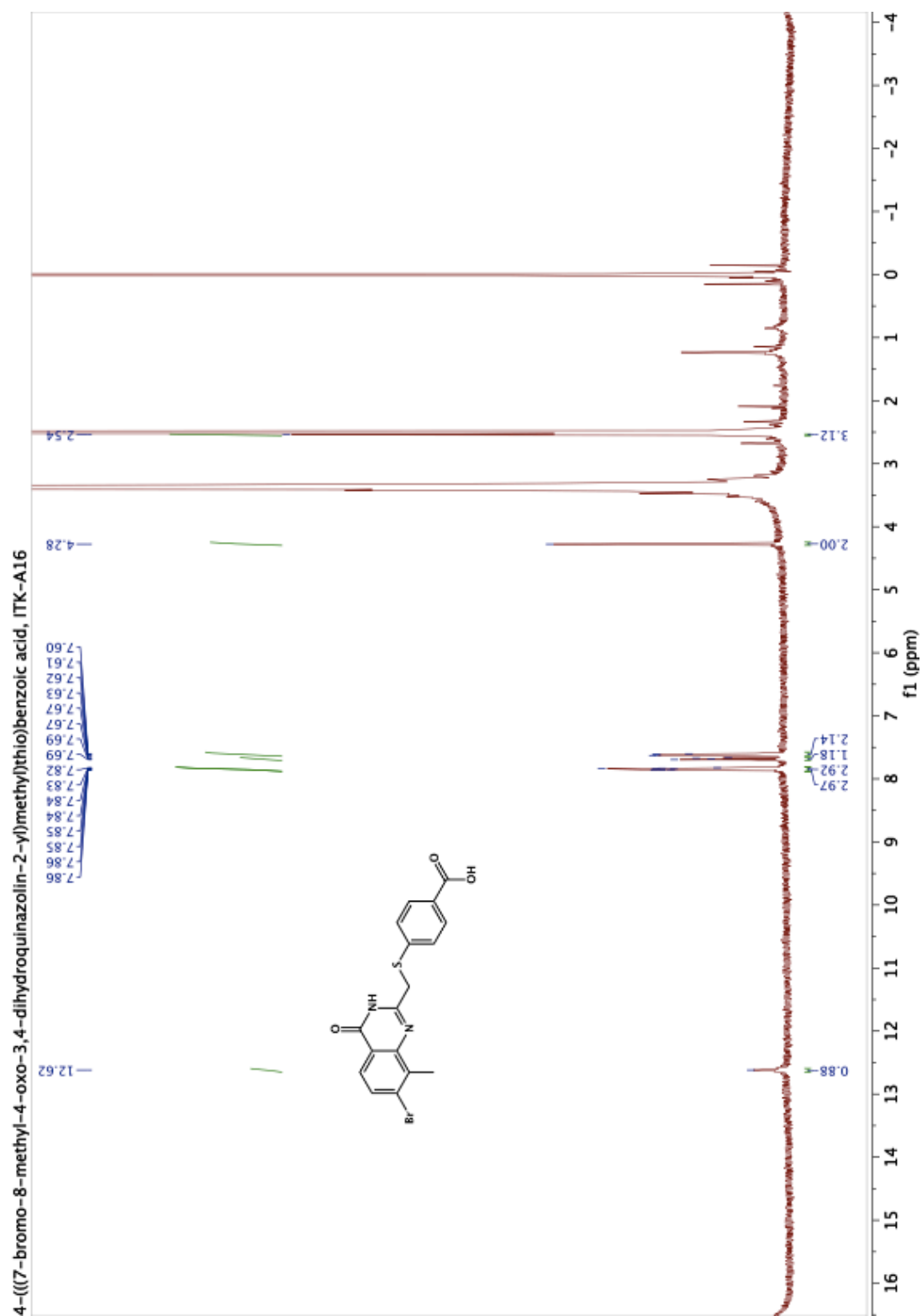
2-(((5-amino-1,3,4-thiadiazol-2-yl)thio)methyl)-7,8-dimethylquinazolin-4(3H)-one, ITK-A13

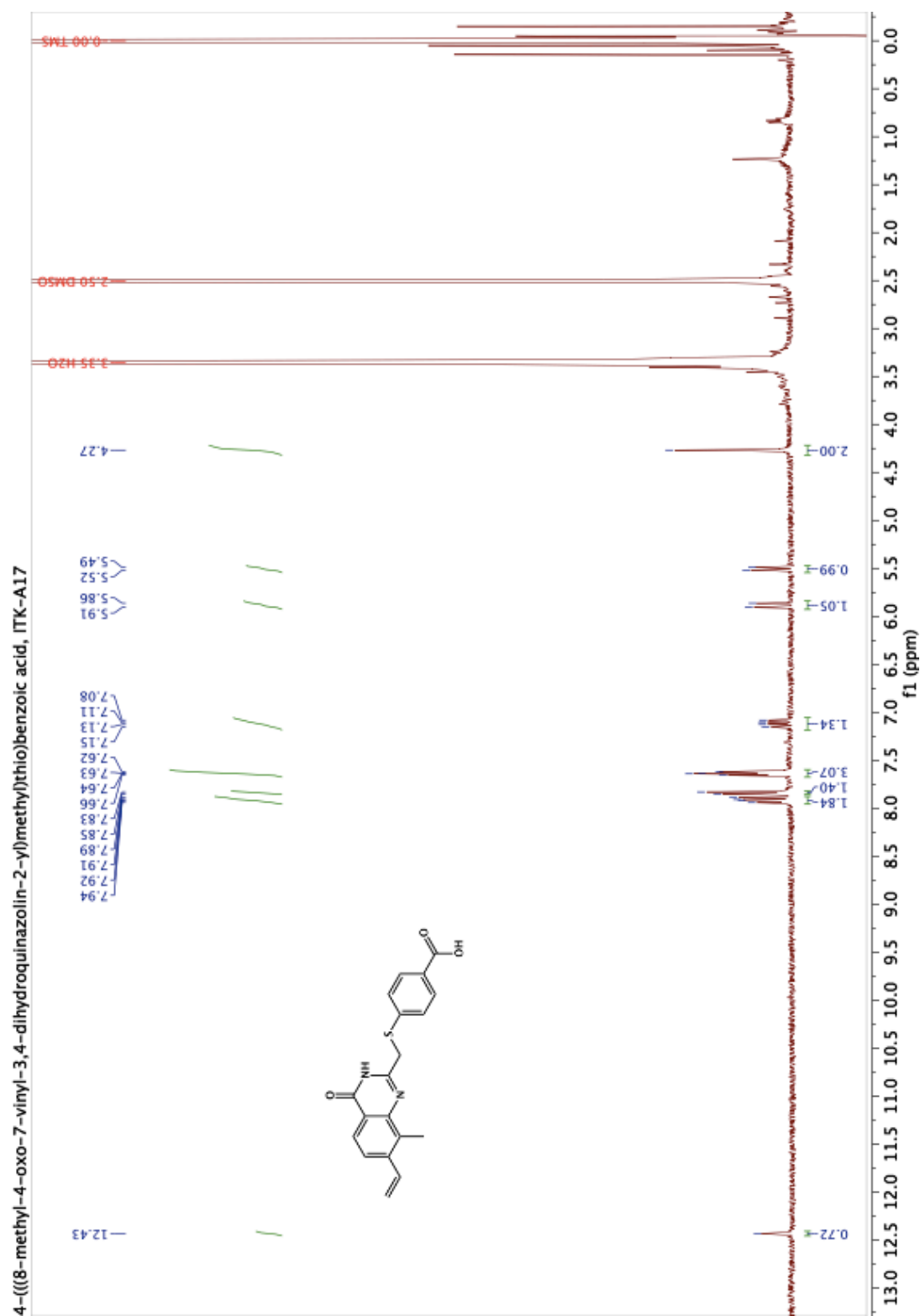




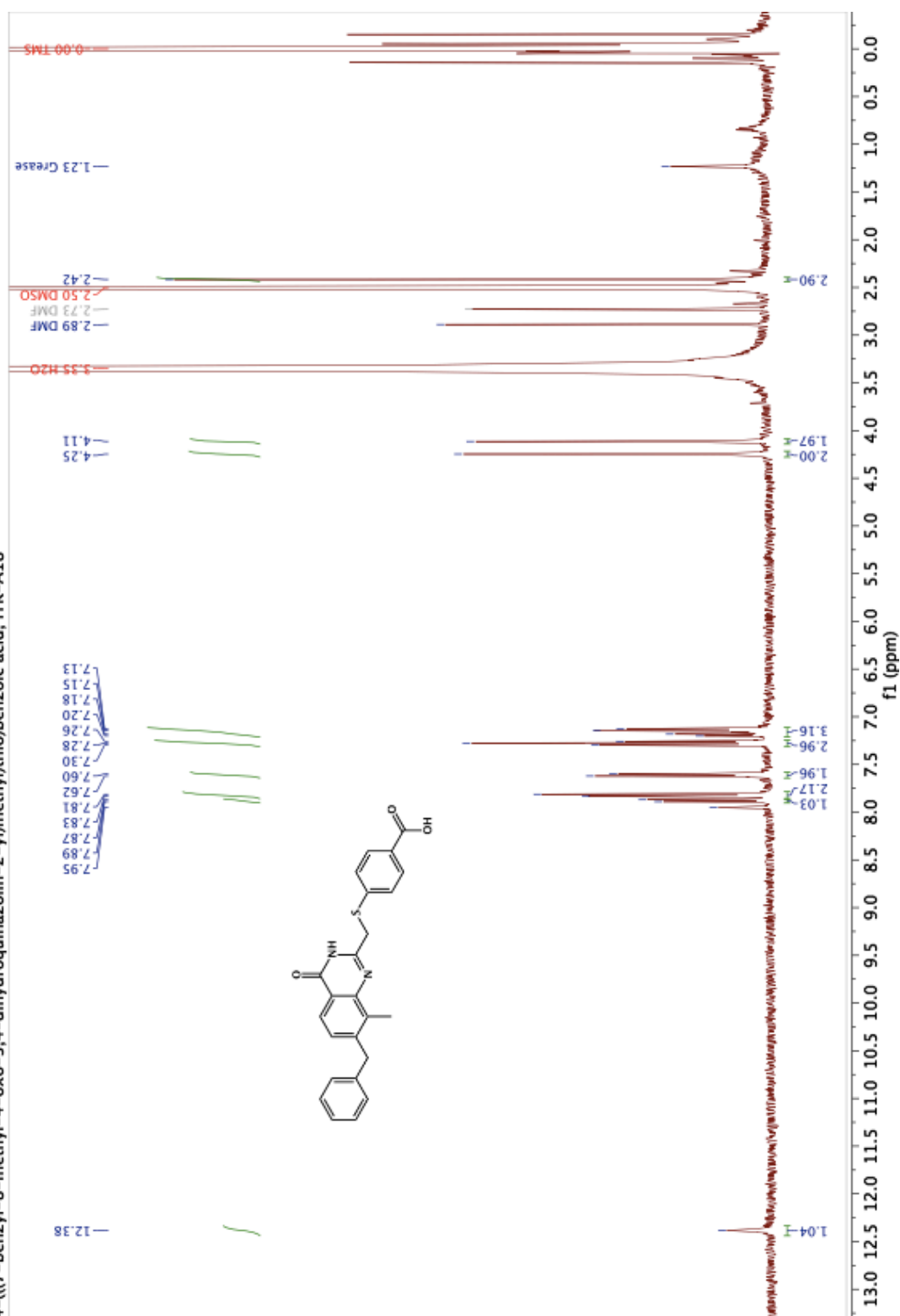






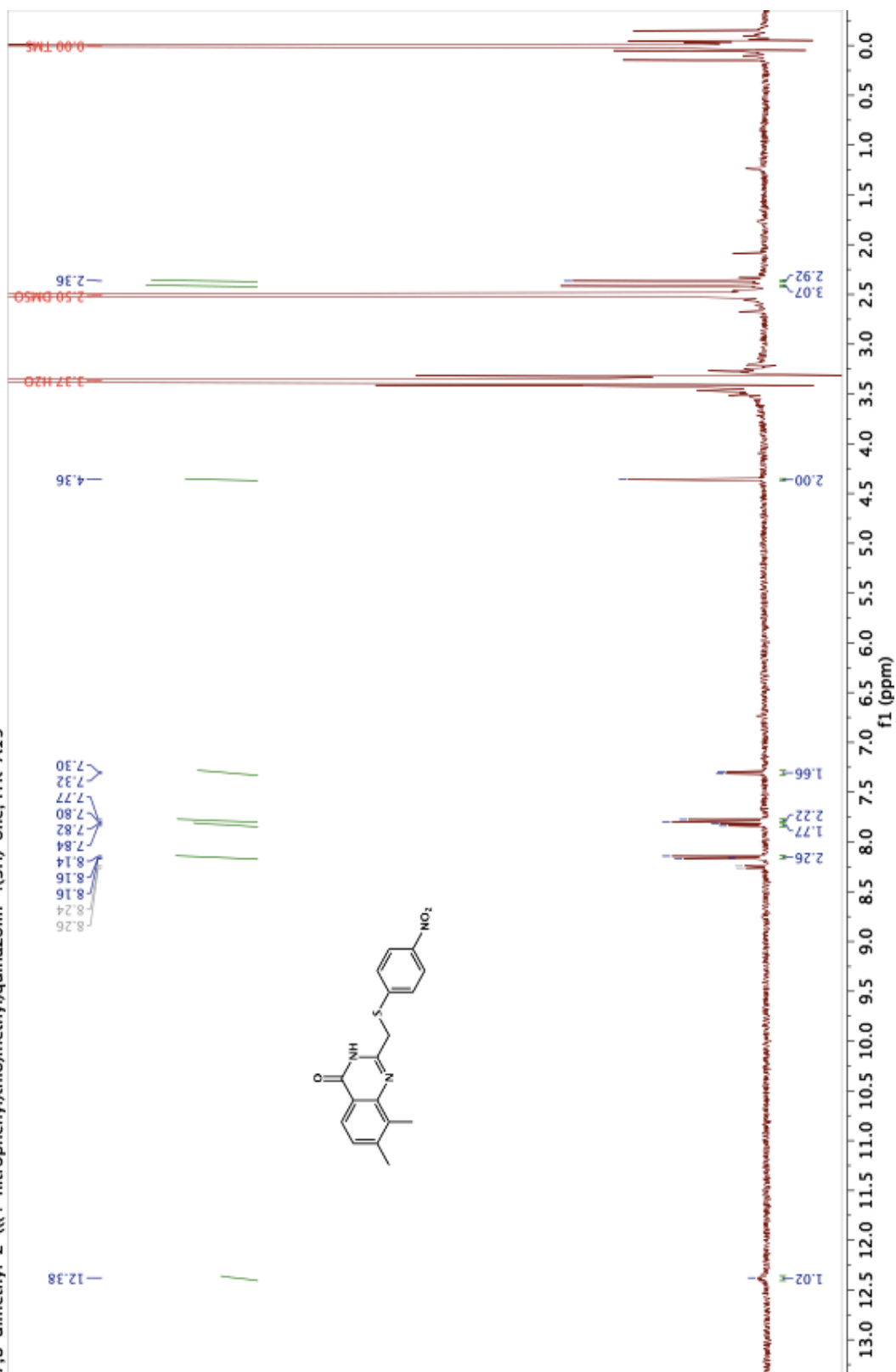


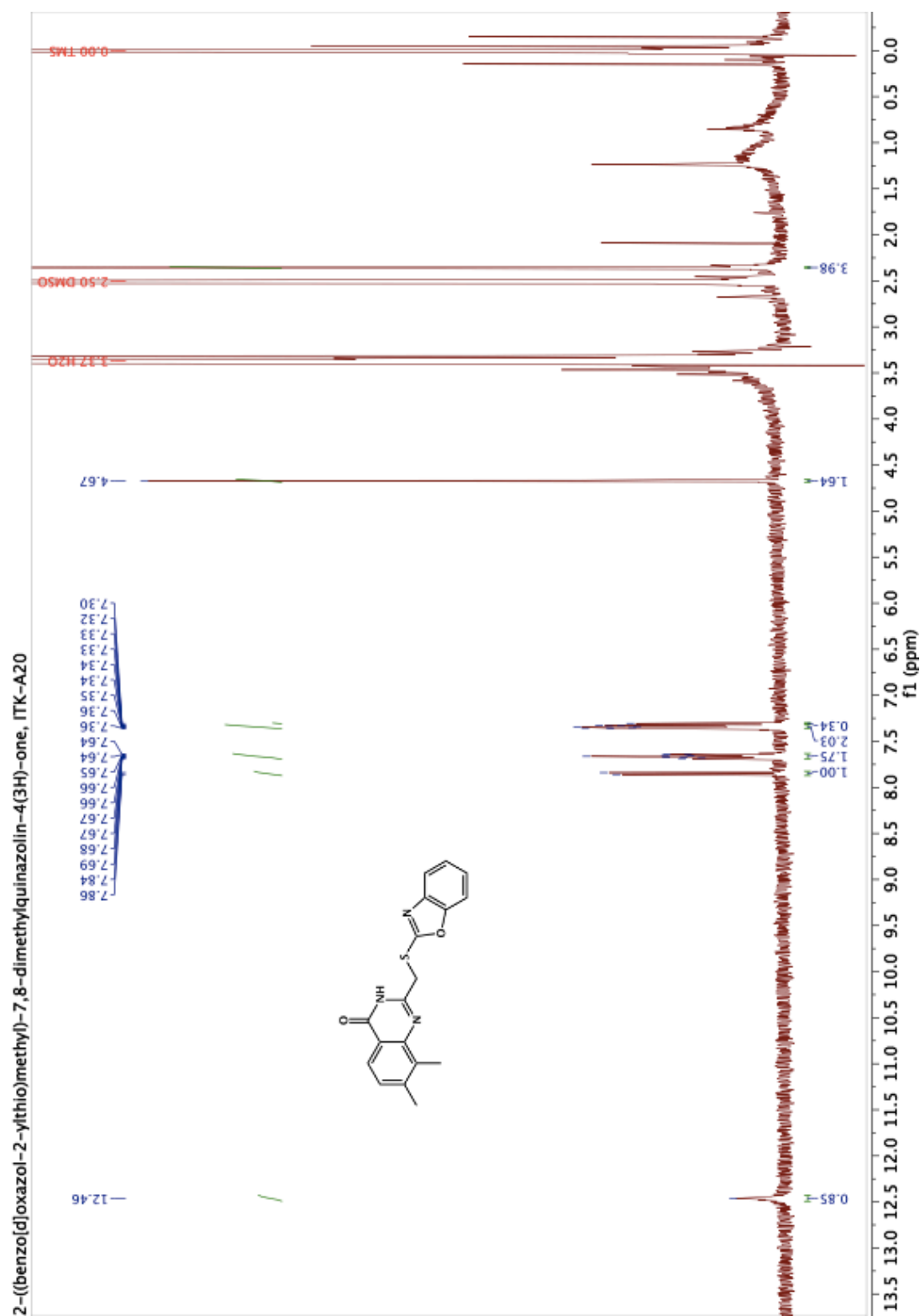
4-(((7-benzyl-8-methyl-4-oxo-3,4-dihydroquinazolin-2-yl)methyl)thio)benzoic acid, ITK-A18

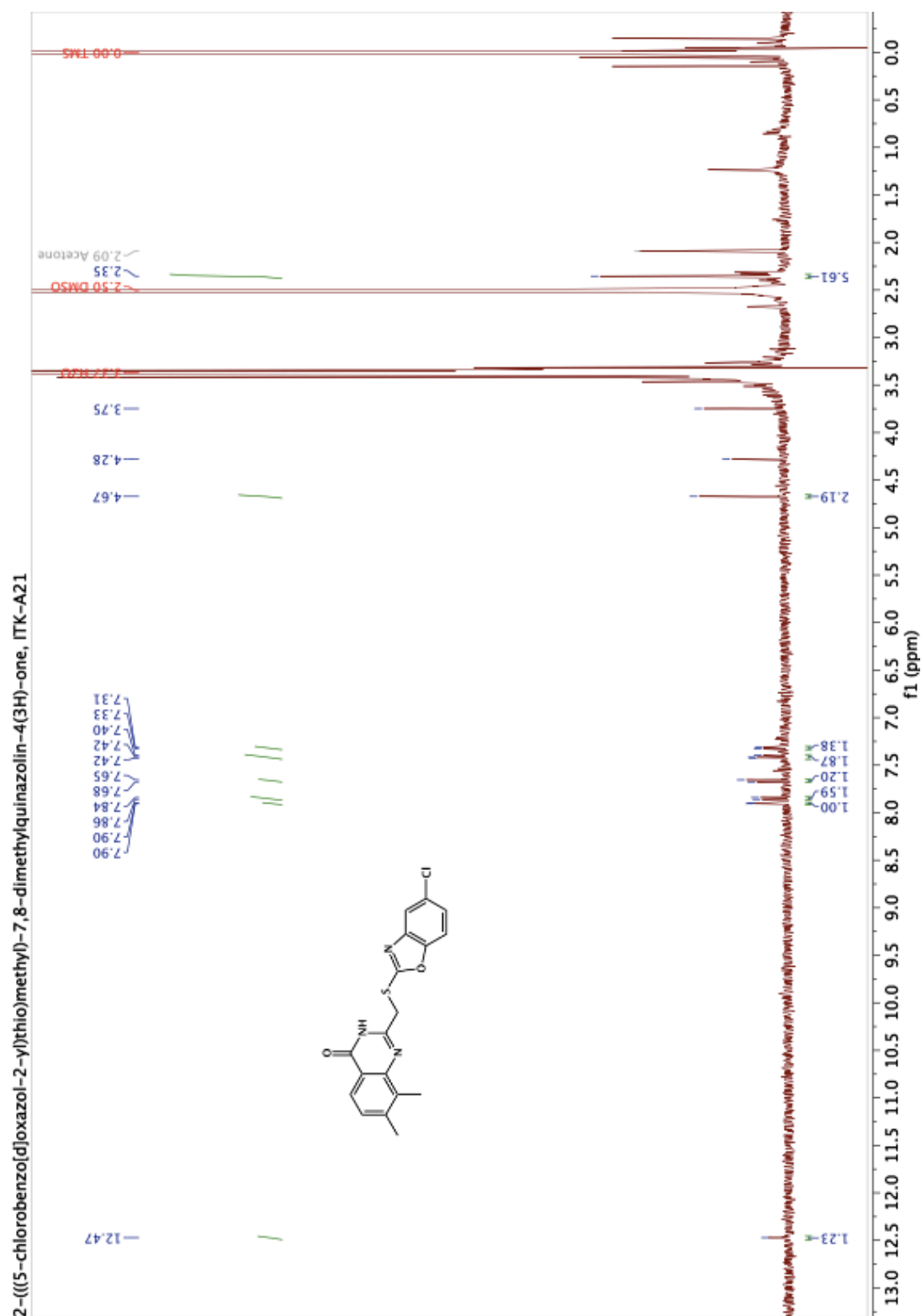




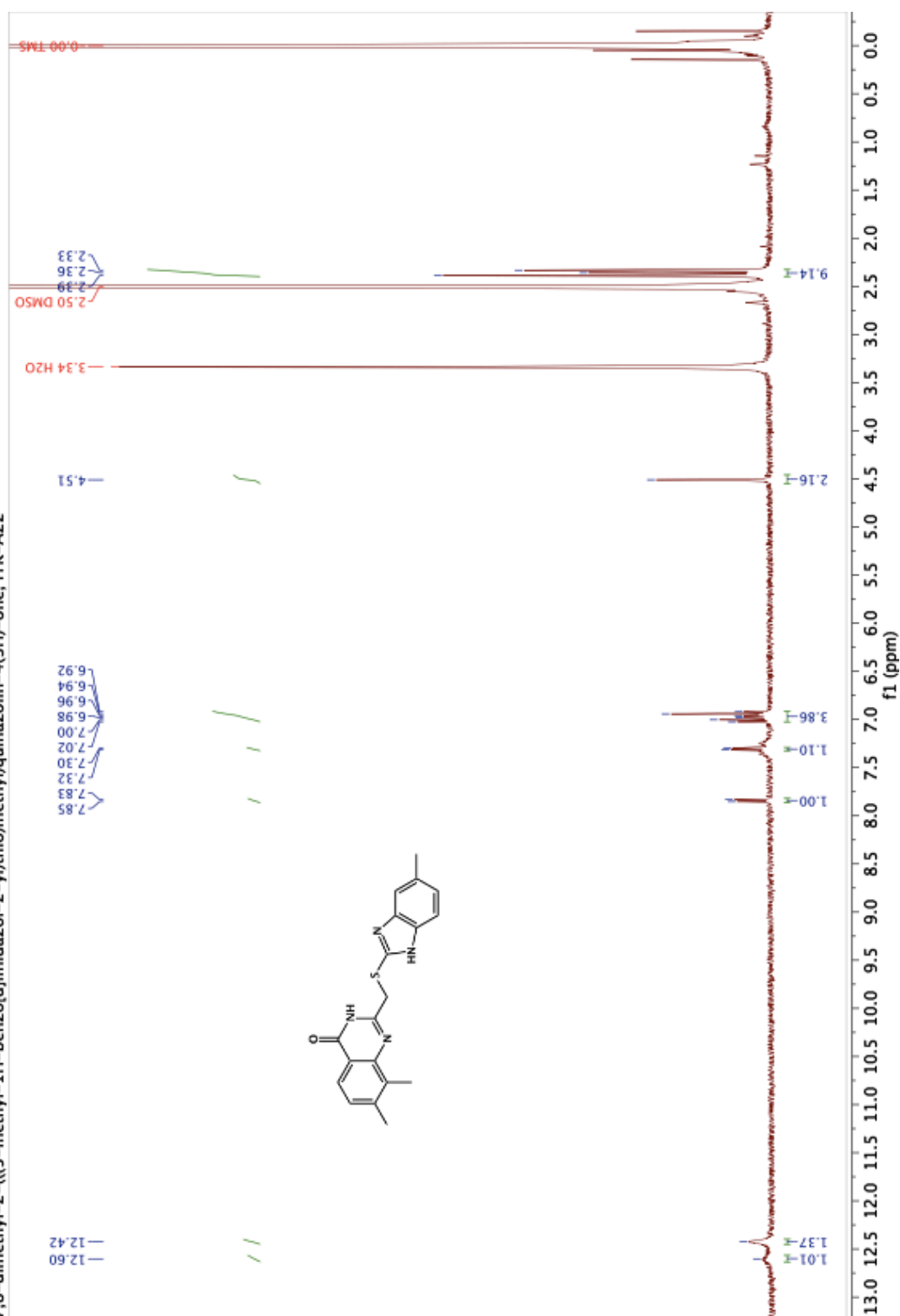
7,8-dimethyl-2-(((4-nitrophenyl)thio)methyl)quinazolin-4(3H)-one, ITK-A19

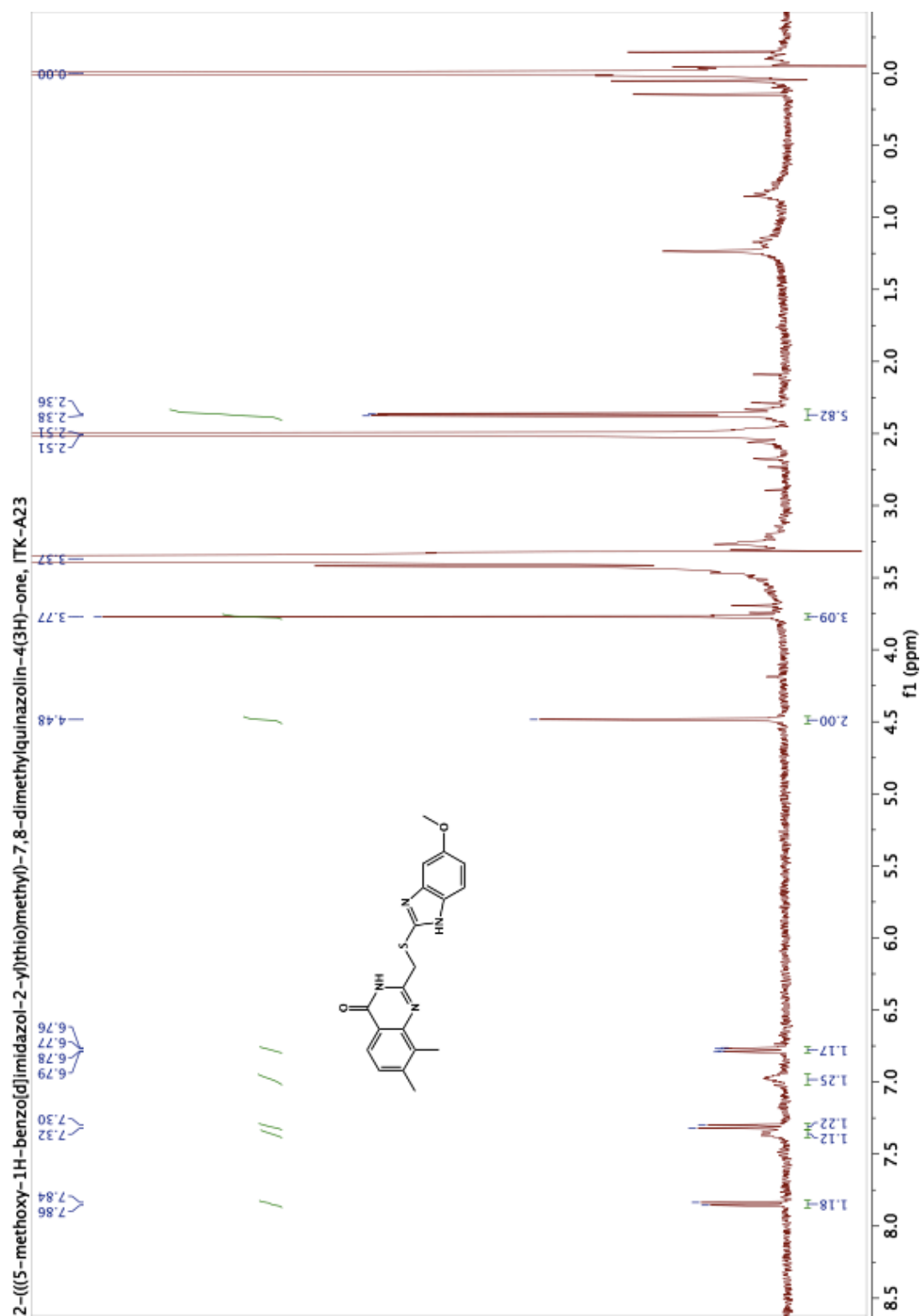


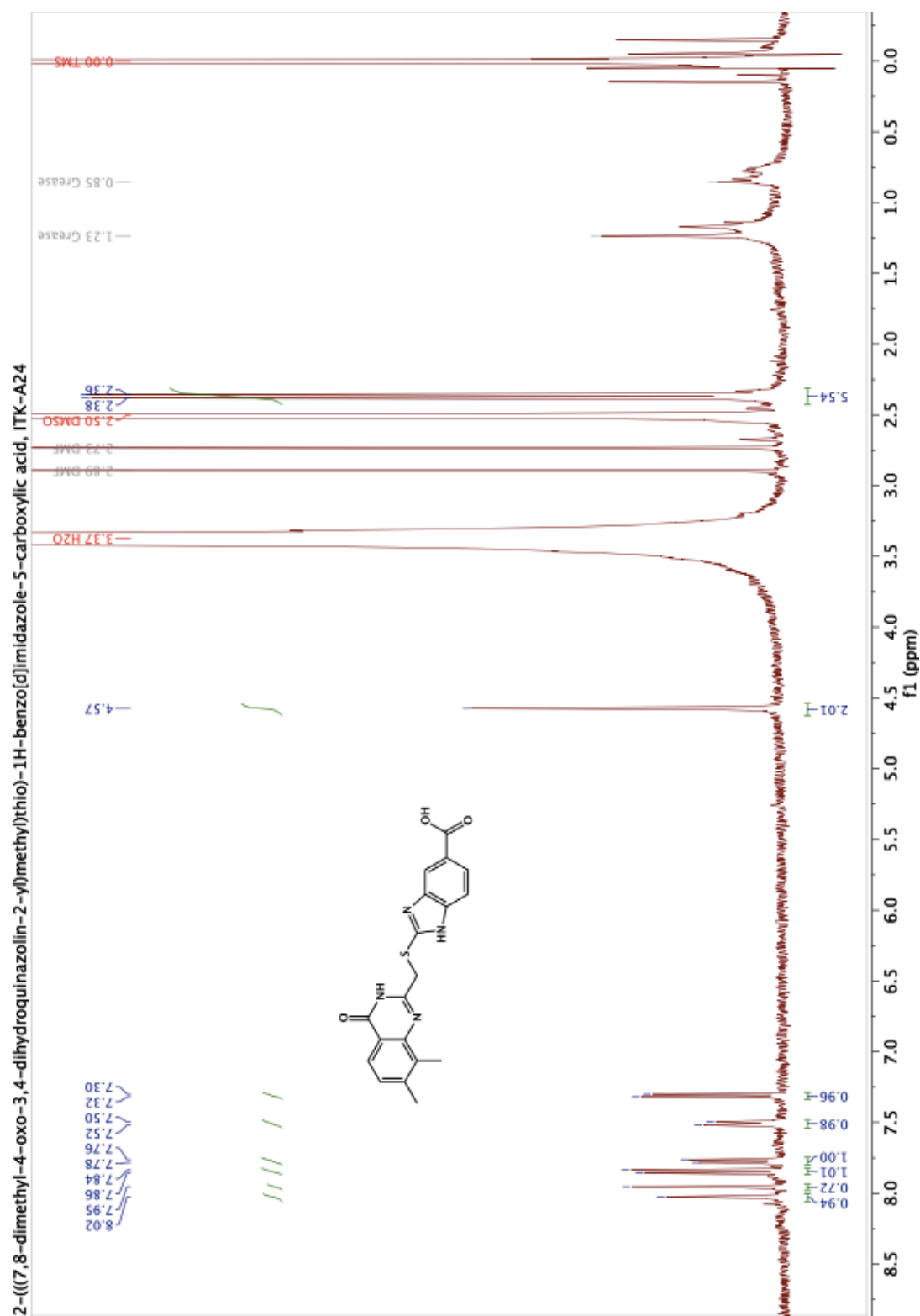


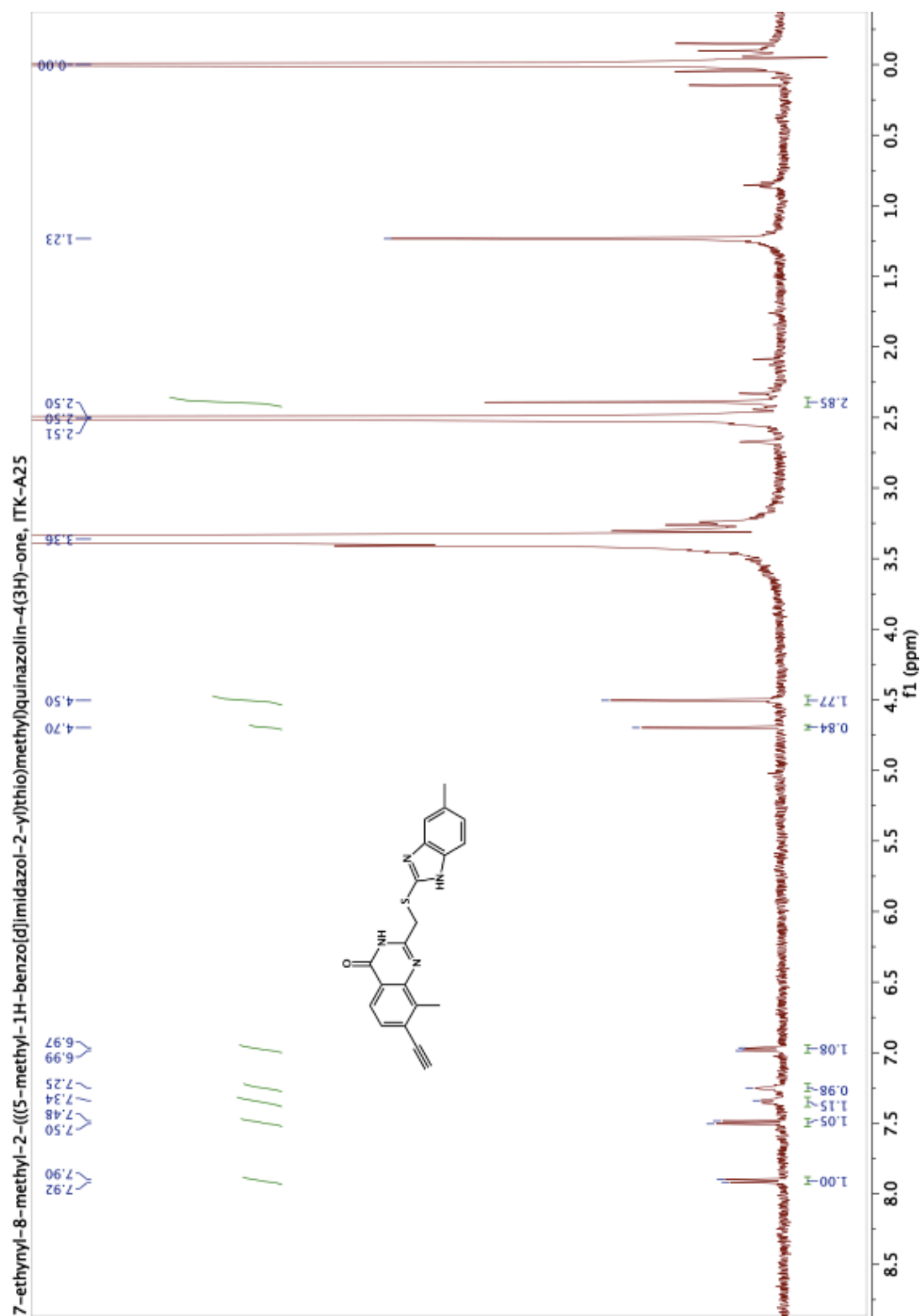


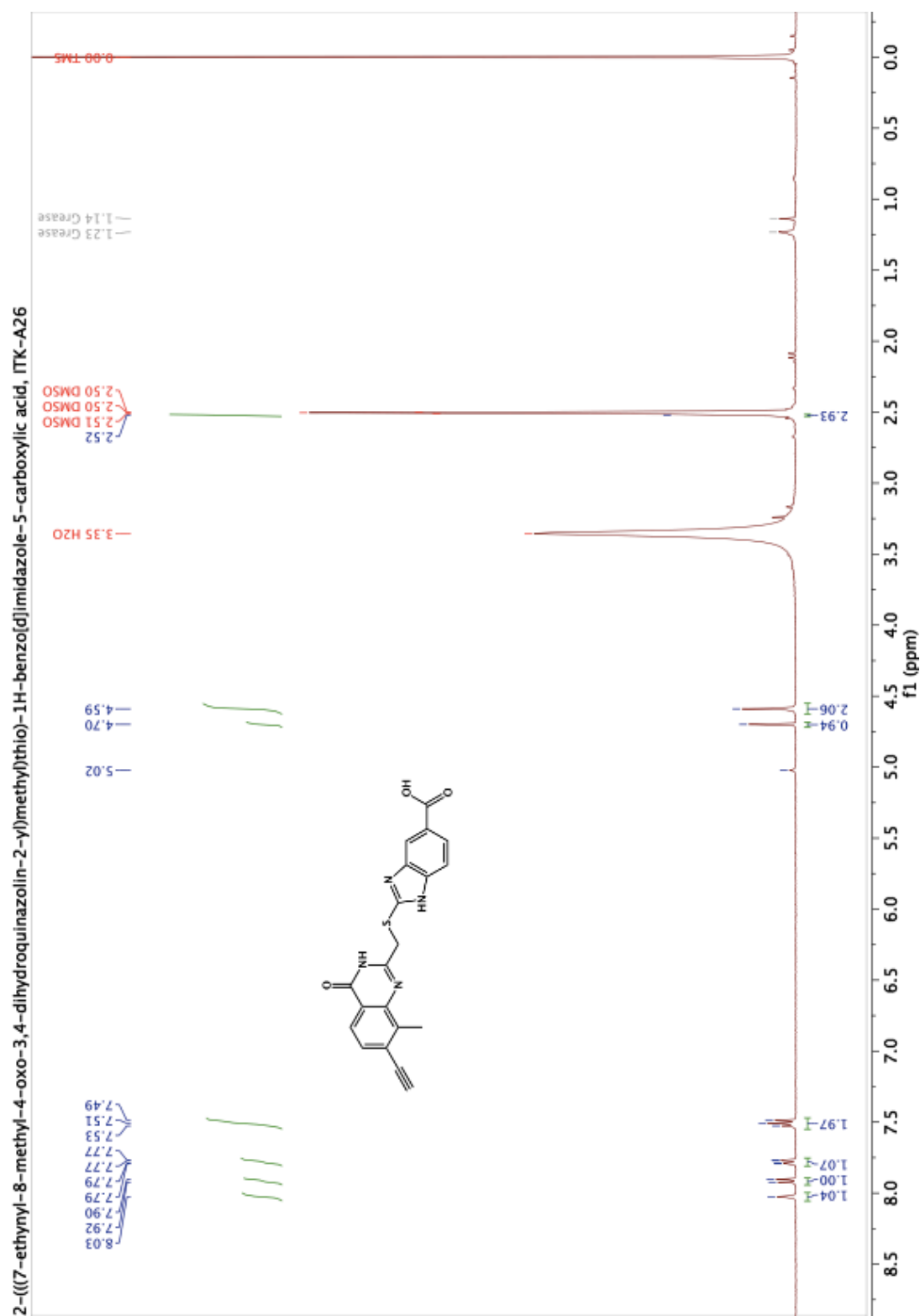
7,8-dimethyl-2-(((5-methyl-1H-benzof[d]imidazol-2-yl)thio)methyl)quinazolin-4(3H)-one, ITK-A22





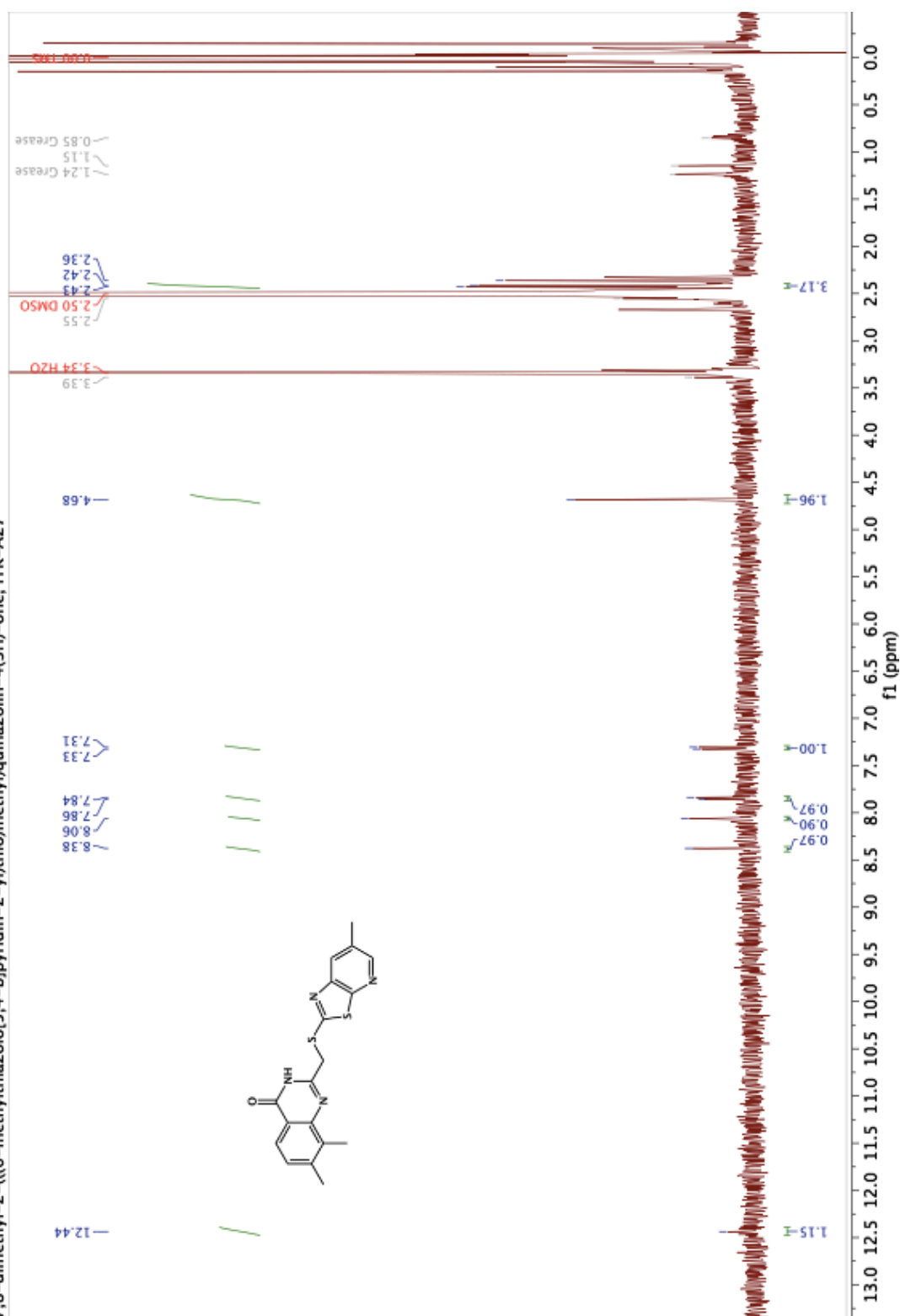


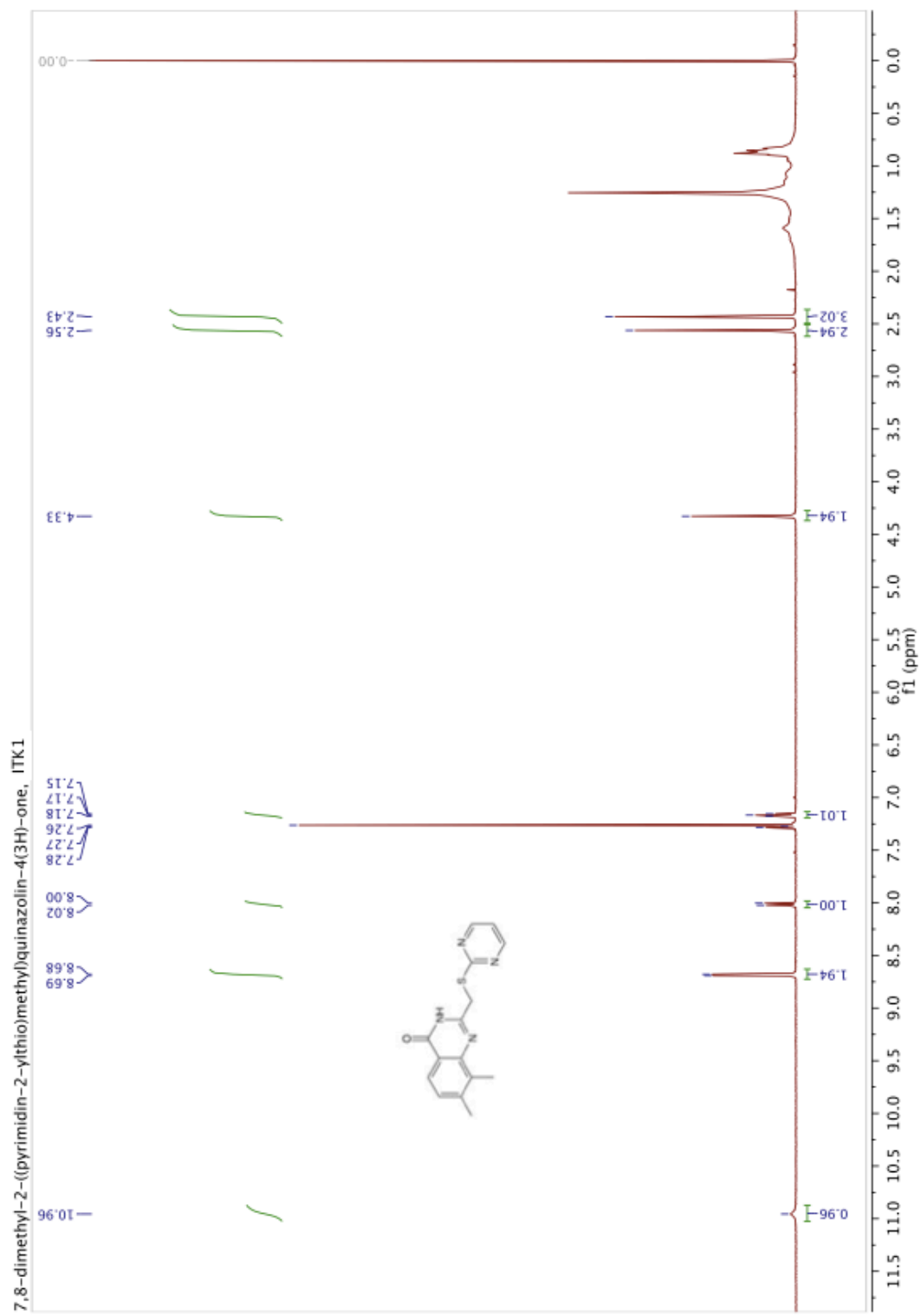


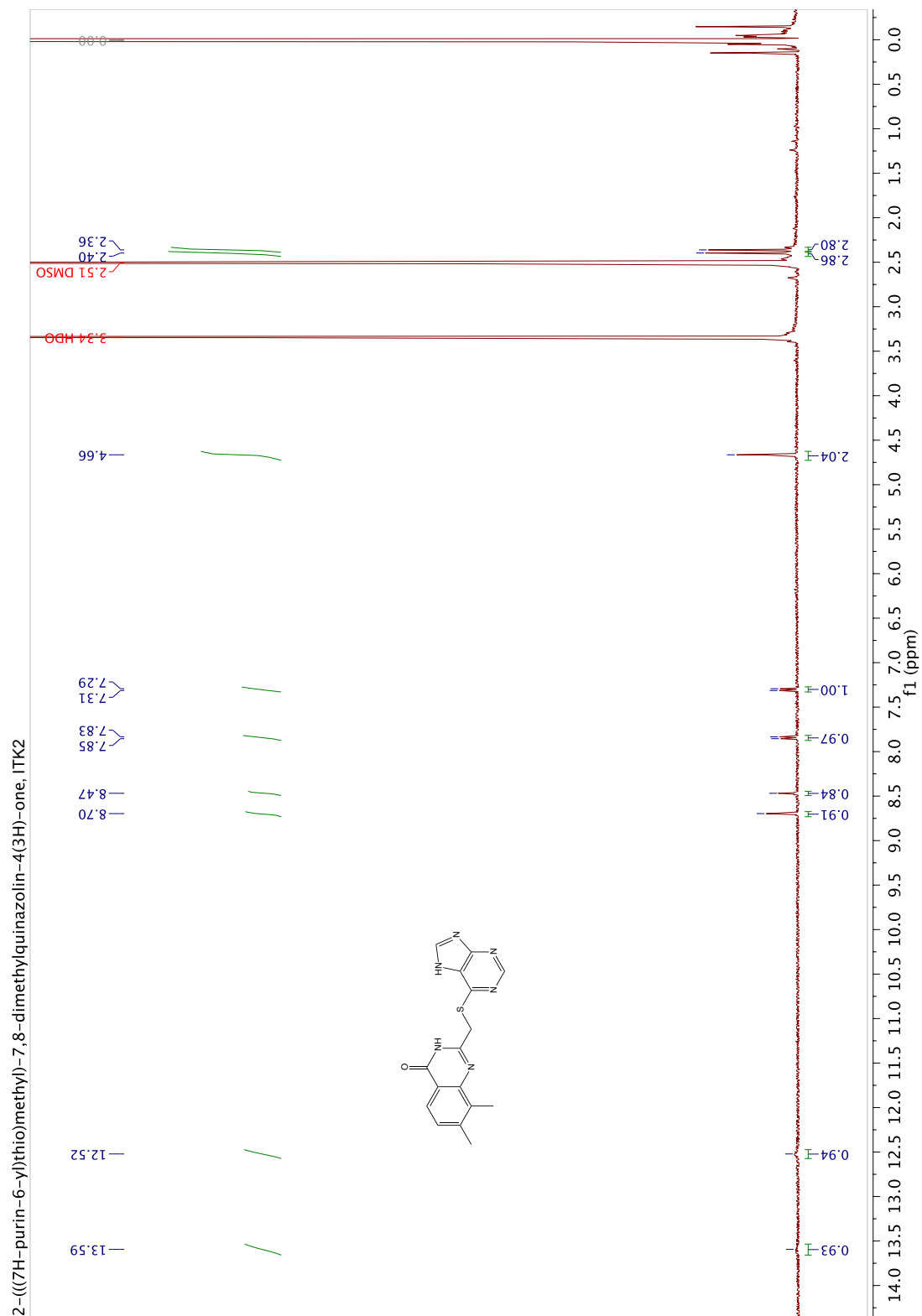




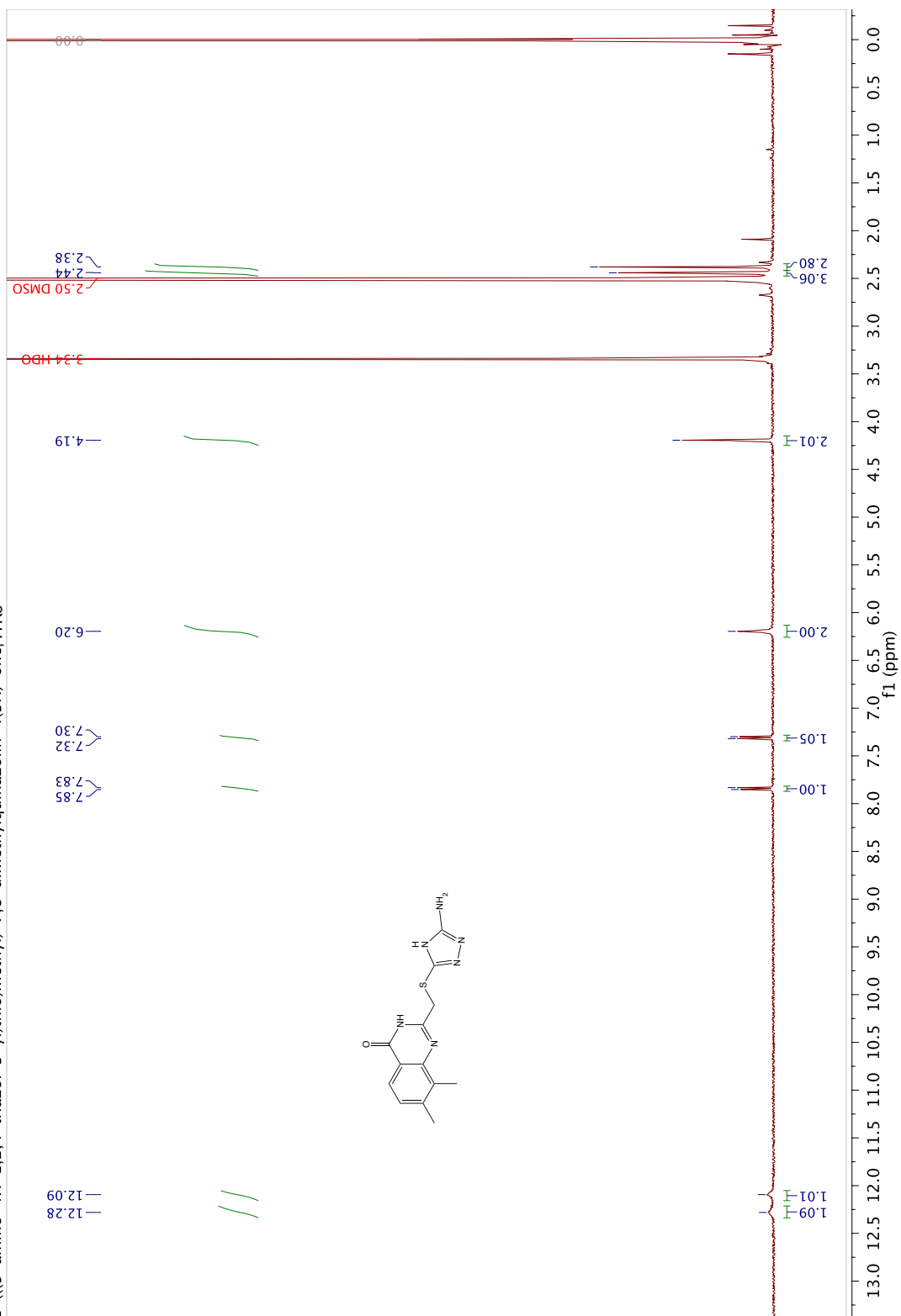
7,8-dimethyl-2-(((6-methylthiazolo[5,4-b]pyridin-2-yl)thio)methyl)quinazolin-4(3H)-one, ITK-A27

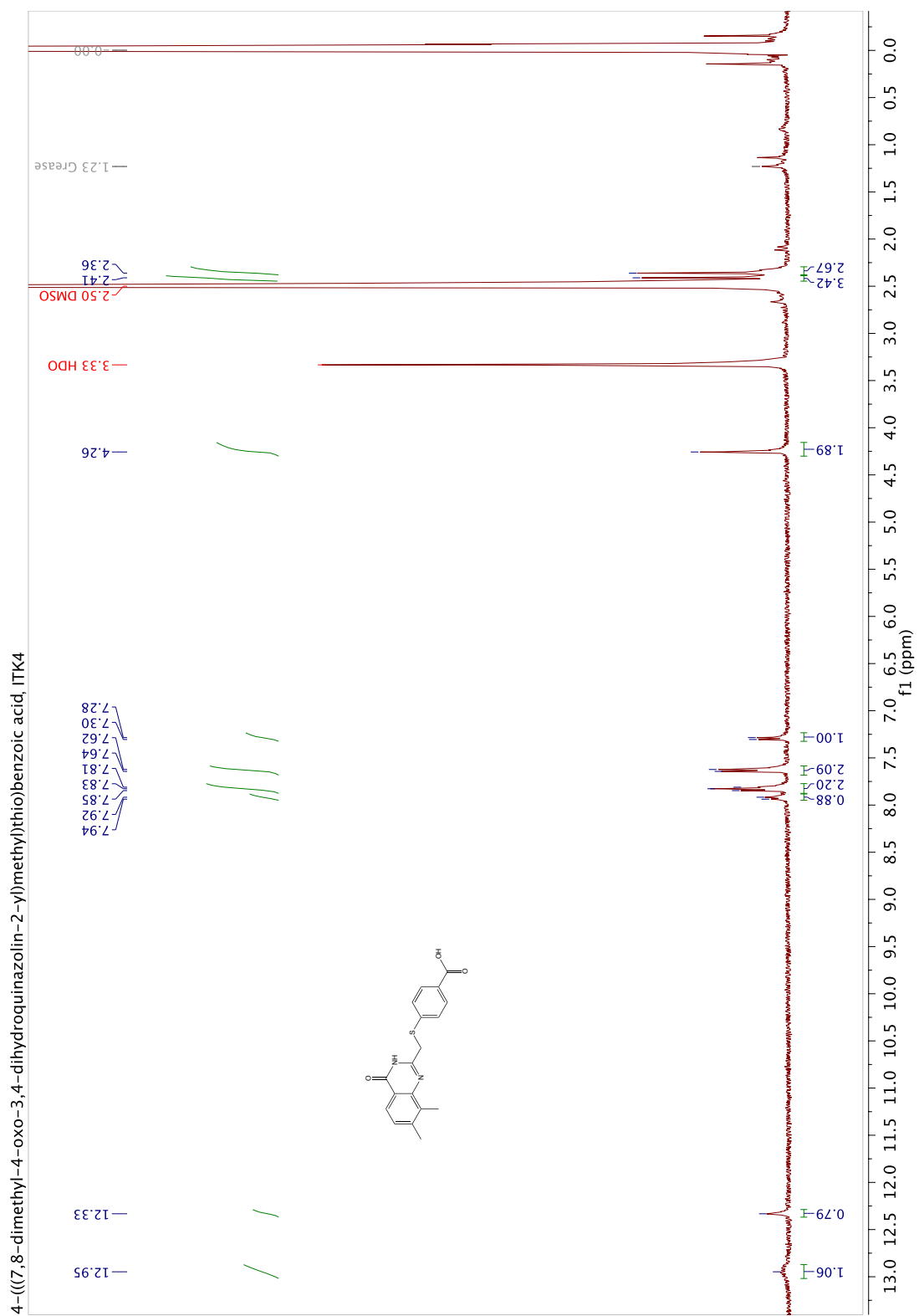




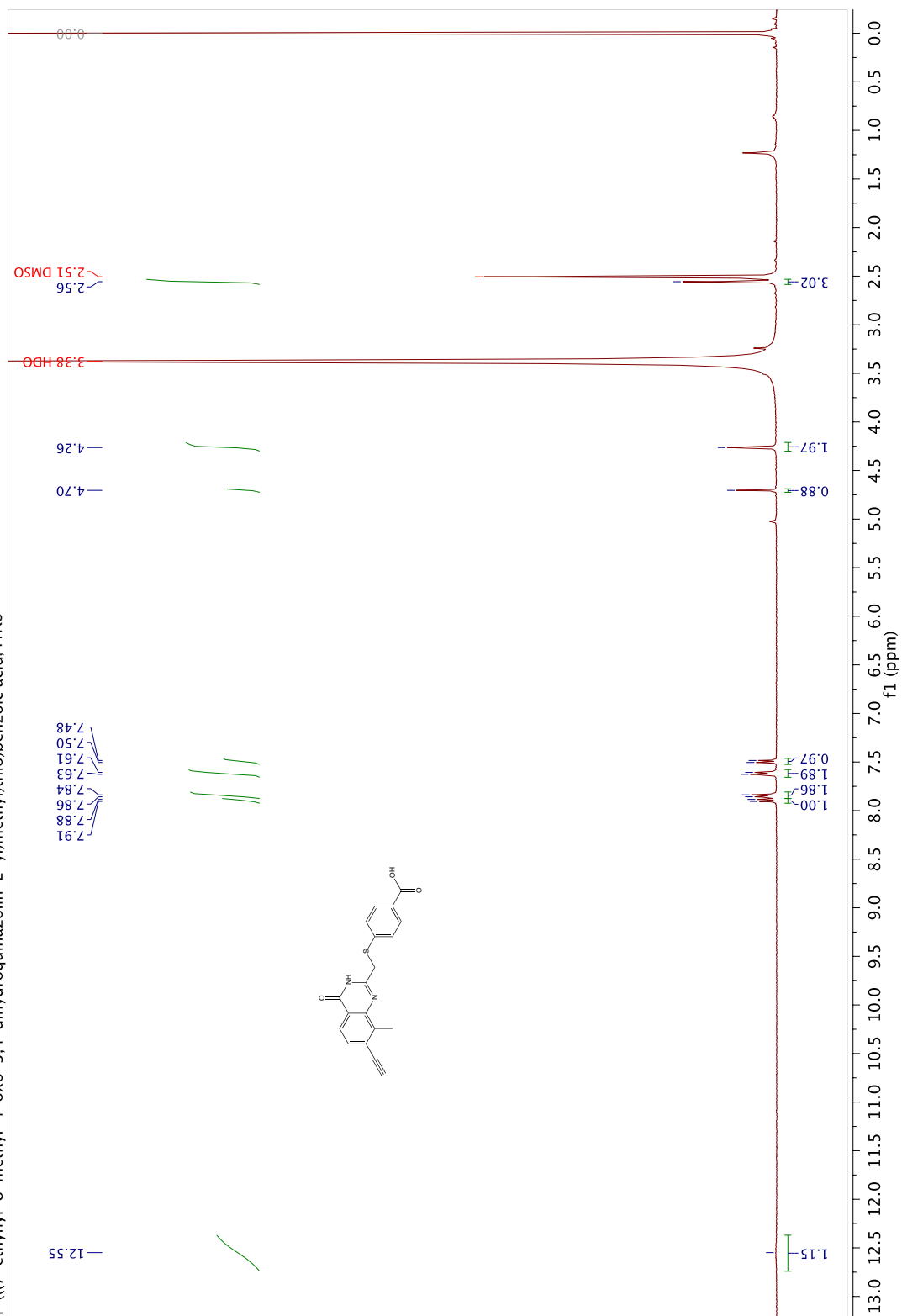


2-(((5-amino-4H-1,2,4-triazol-3-yl)thio)methyl)-7,8-dimethylquinazolin-4(3H)-one, ITK3

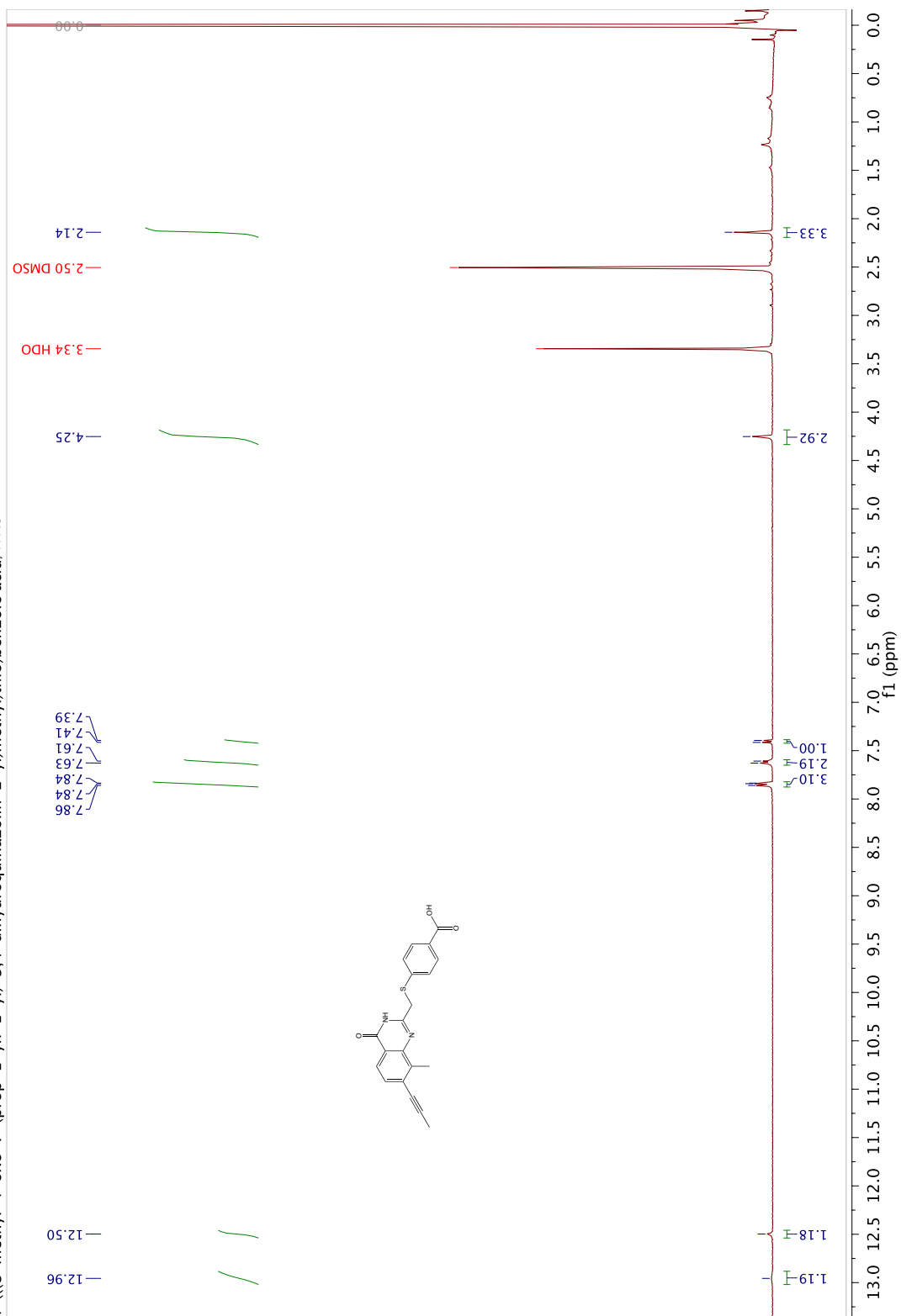




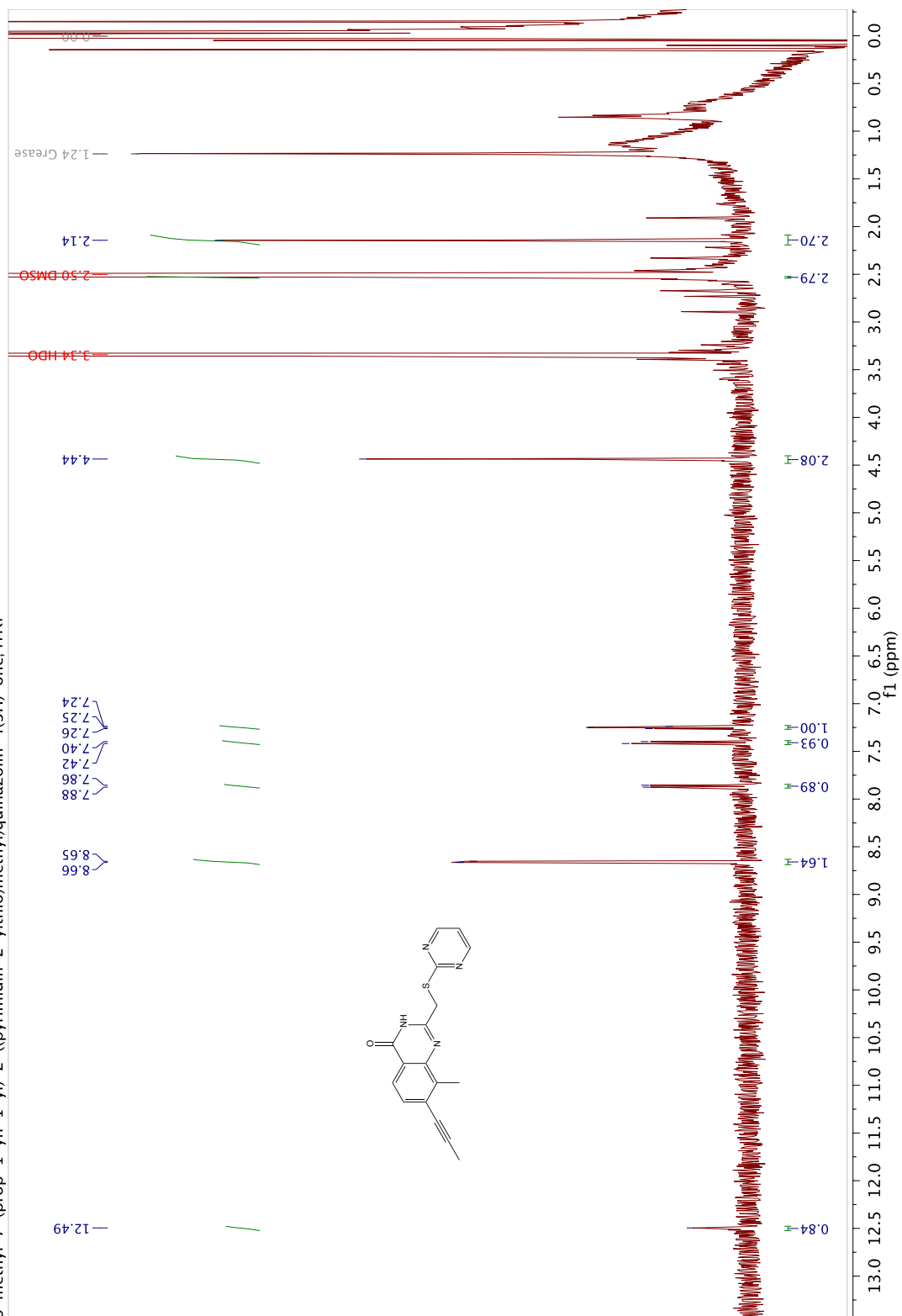
4-(((7-ethynyl-8-methyl-4-oxo-3,4-dihydroquinazolin-2-yl)methyl)thio)benzoic acid, ITK5



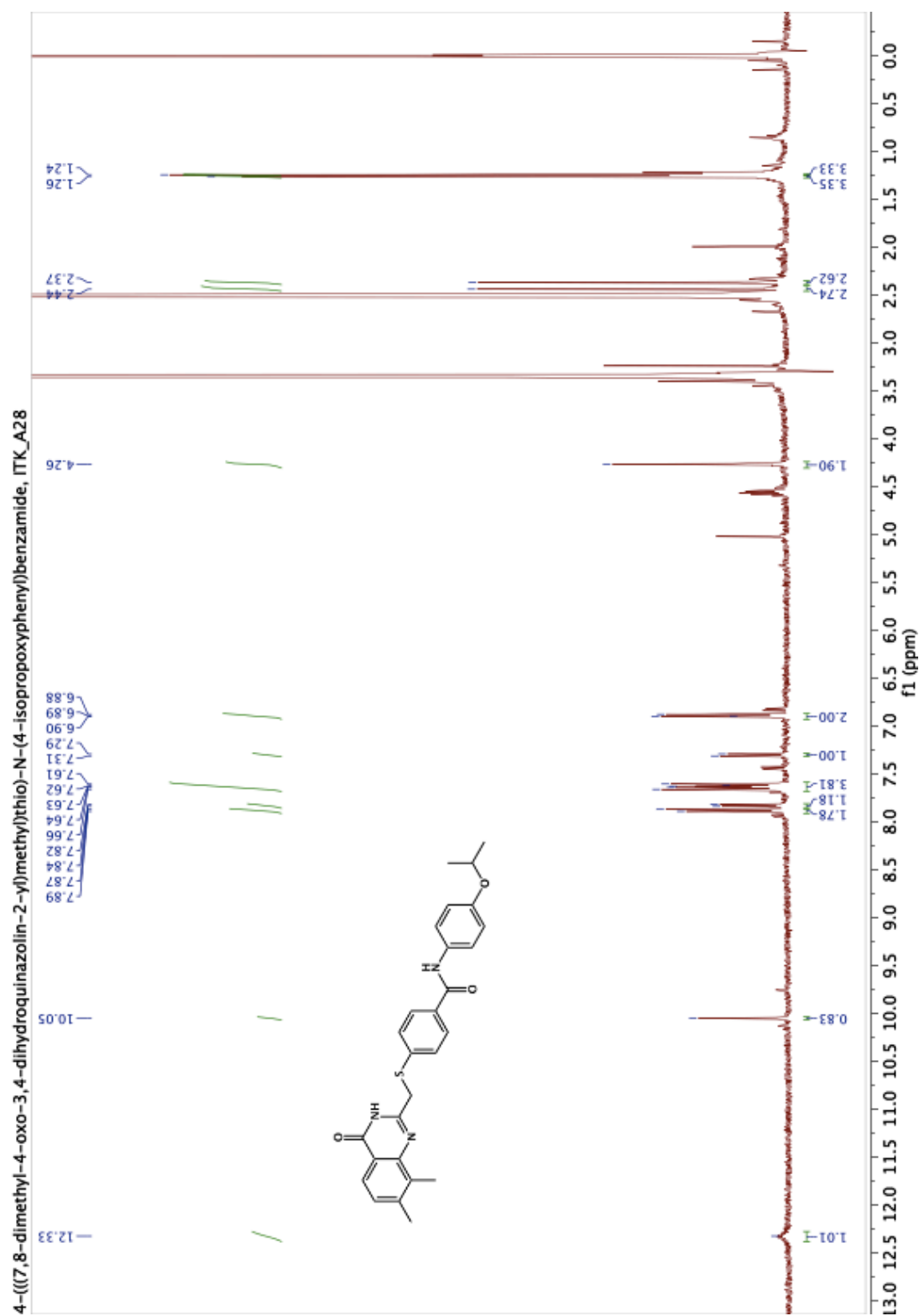
4-(((8-methyl-4-oxo-7-(prop-1-yn-1-yl)-3,4-dihydroquinazolin-2-yl)methyl)thio)benzoic acid, ITK6

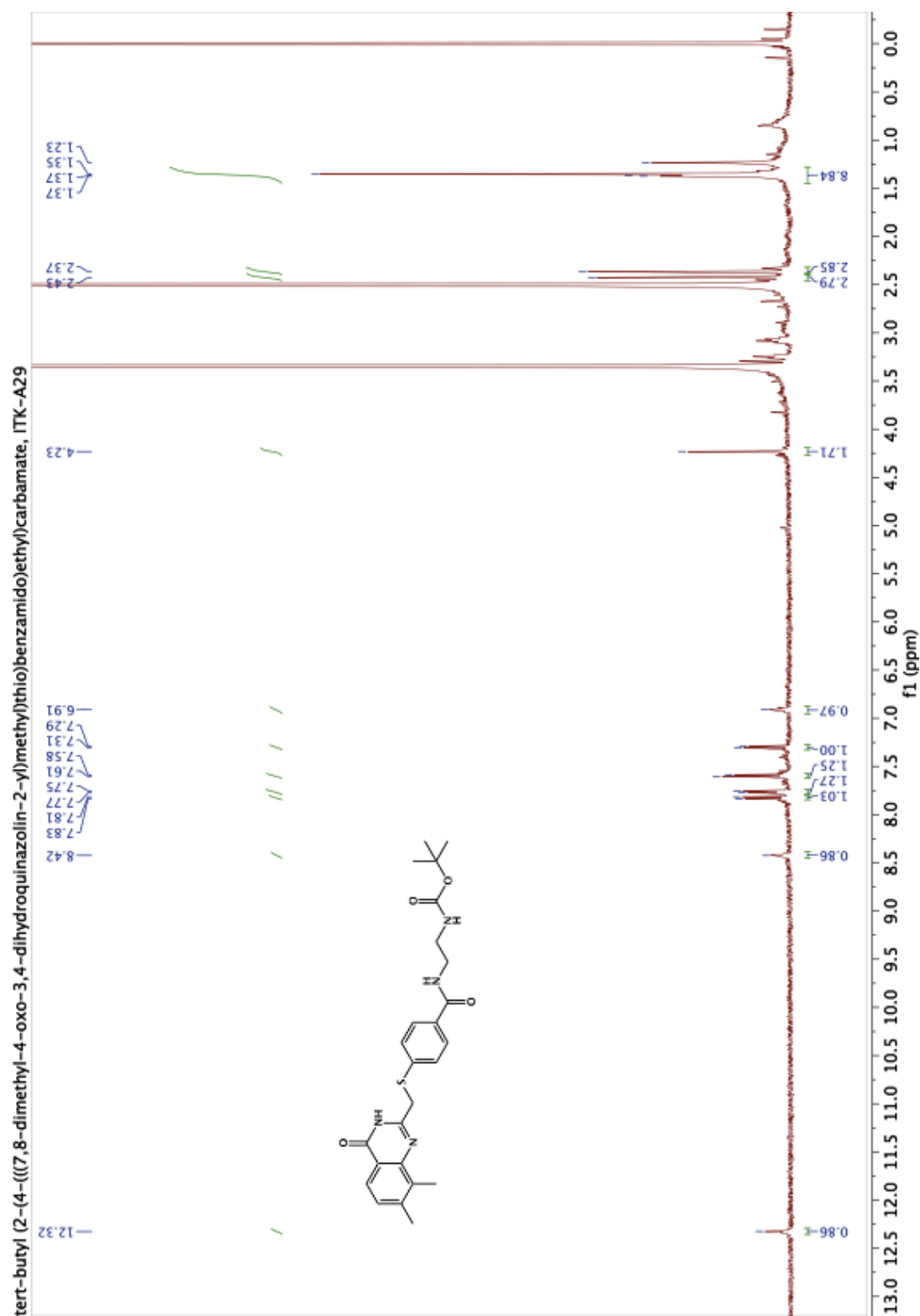


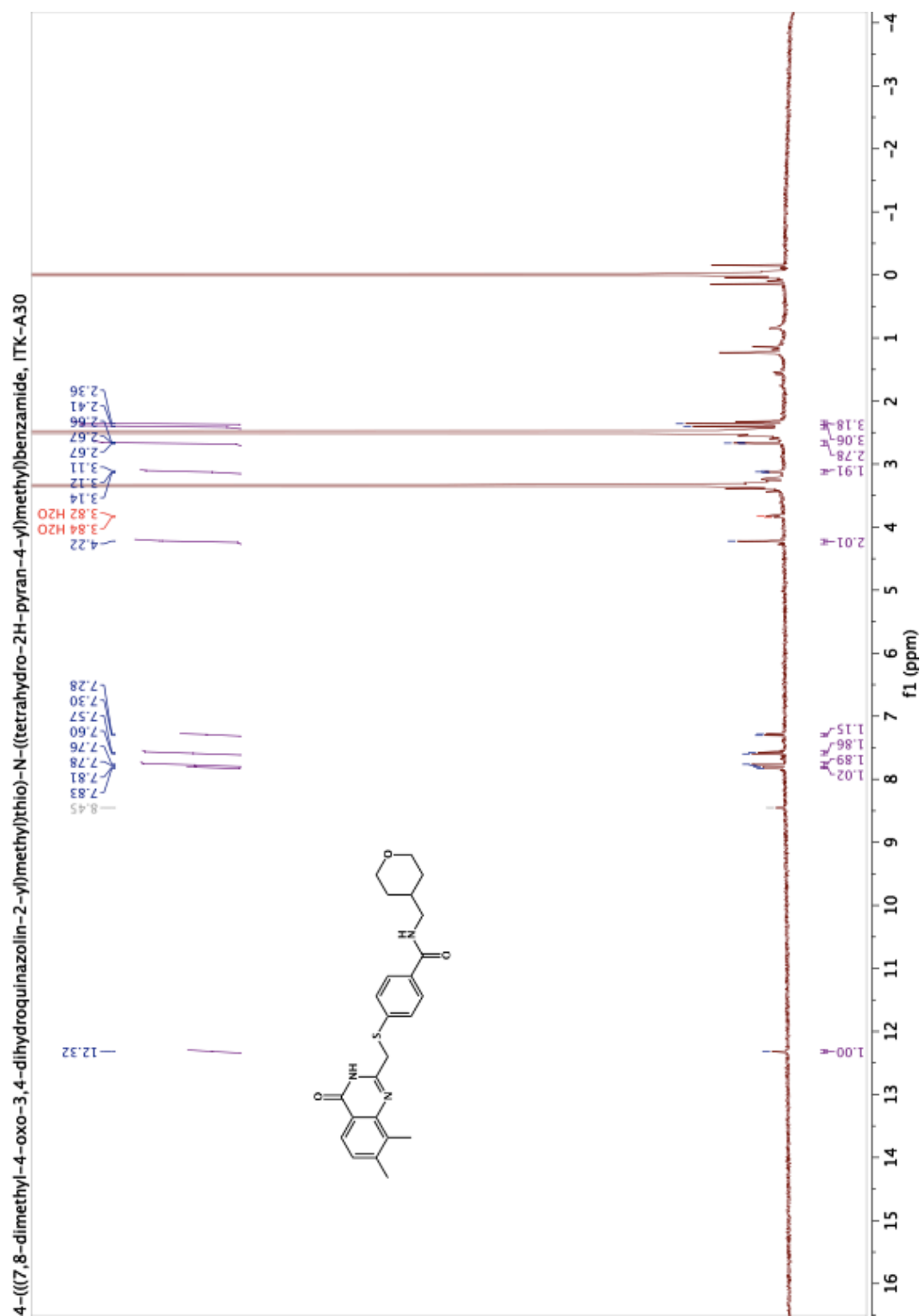
8-methyl-7-(prop-1-yn-1-yl)-2-((pyrimidin-2-ylthio)methyl)quinazolin-4(3H)-one, ITK7



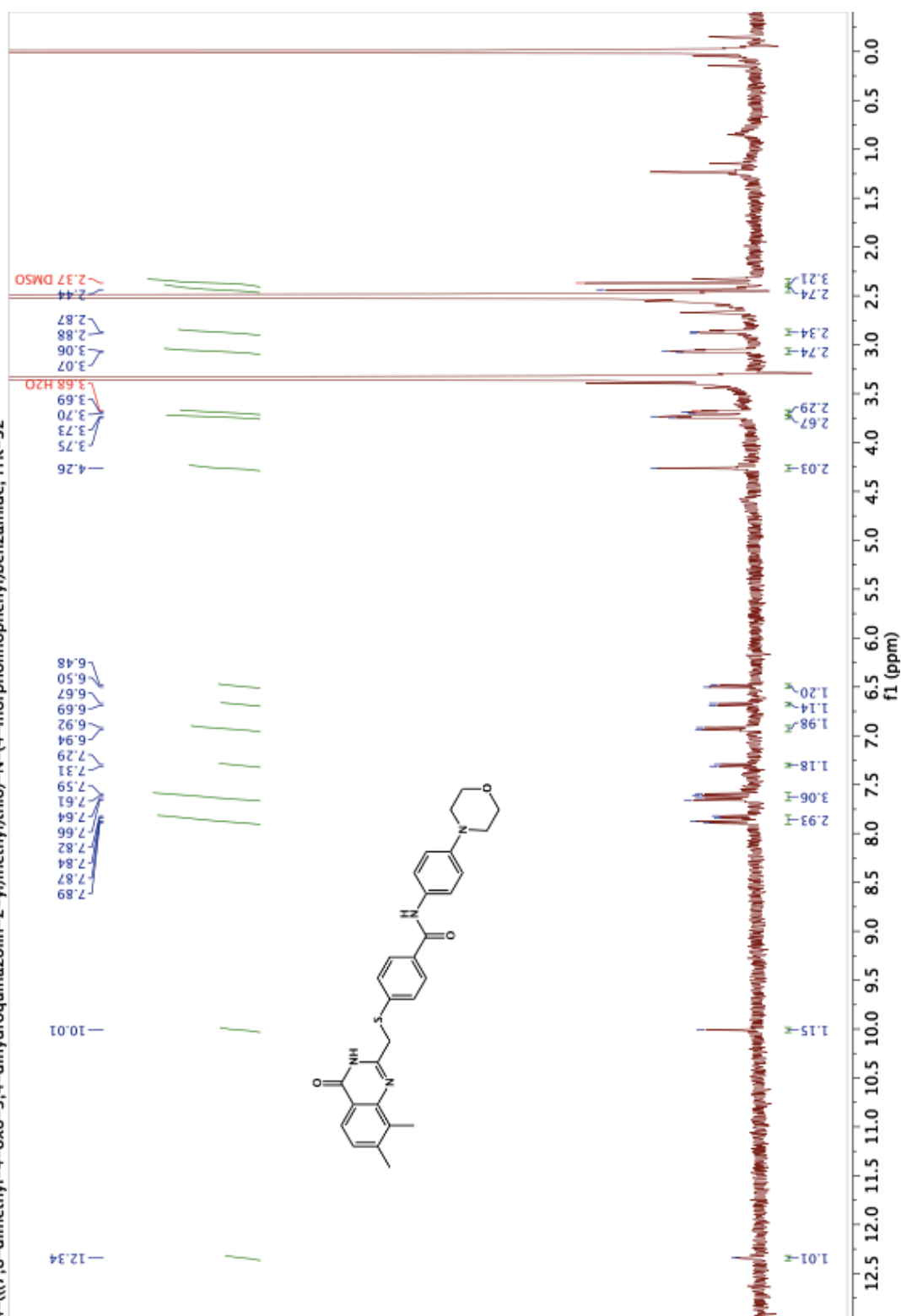


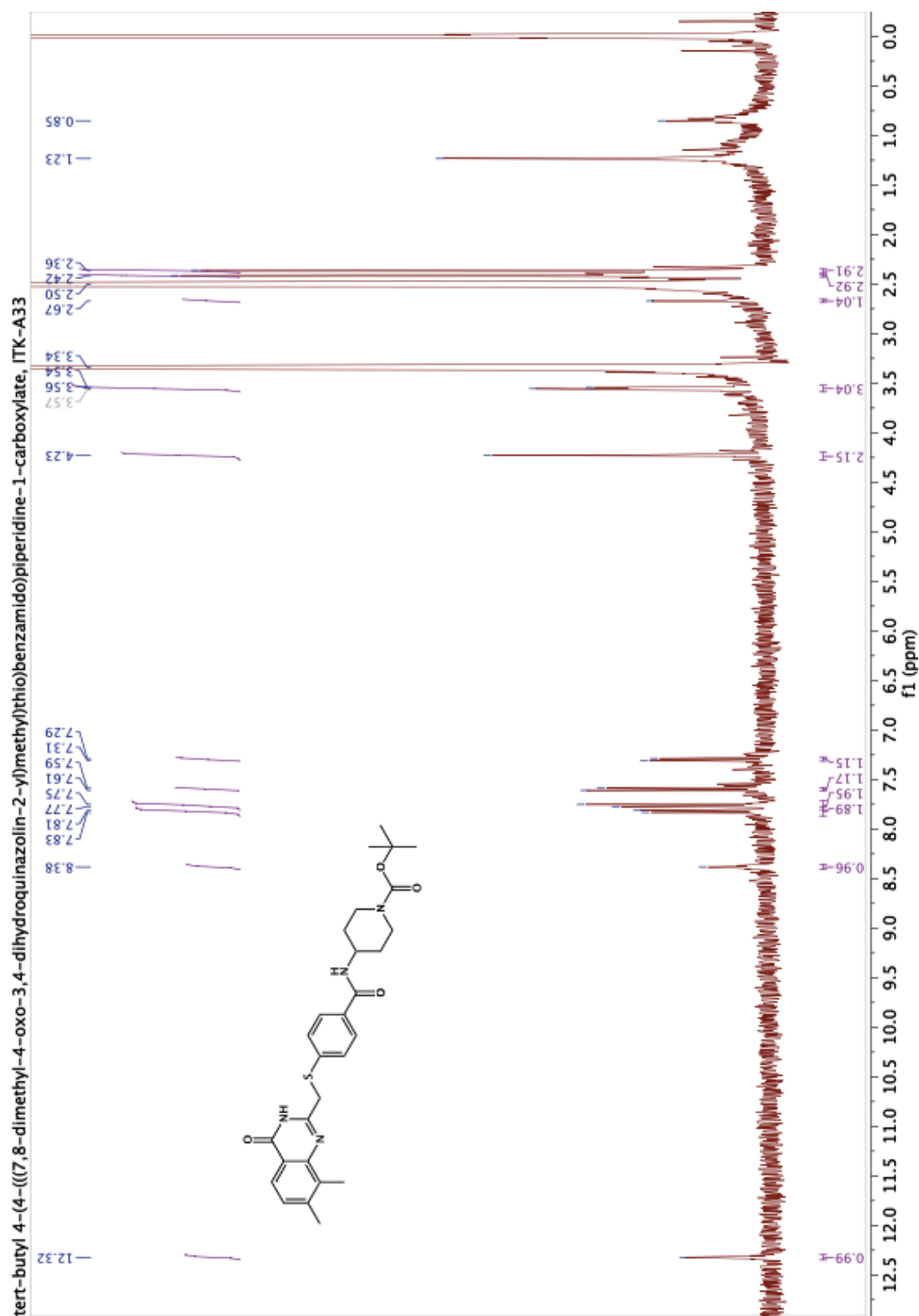


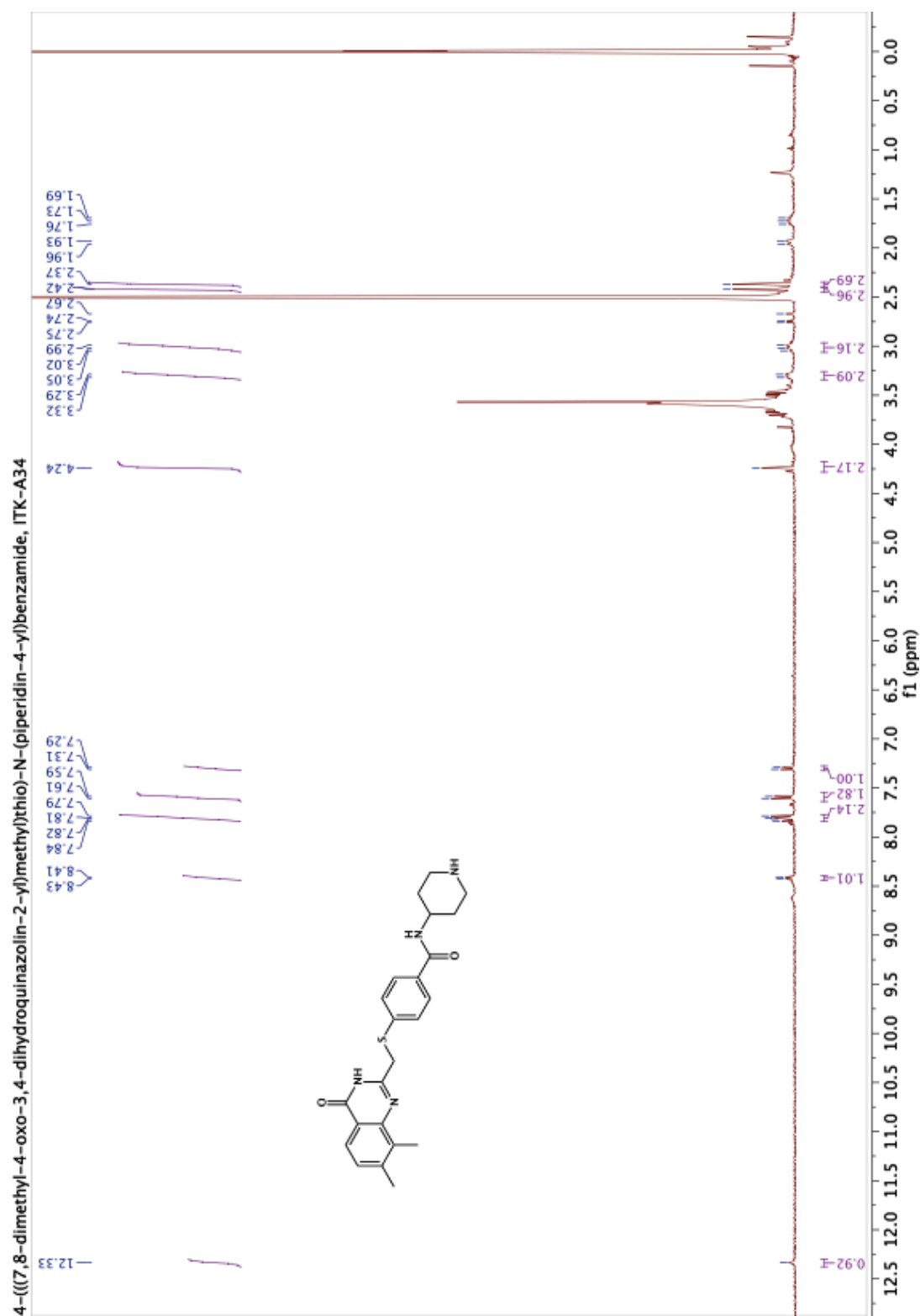




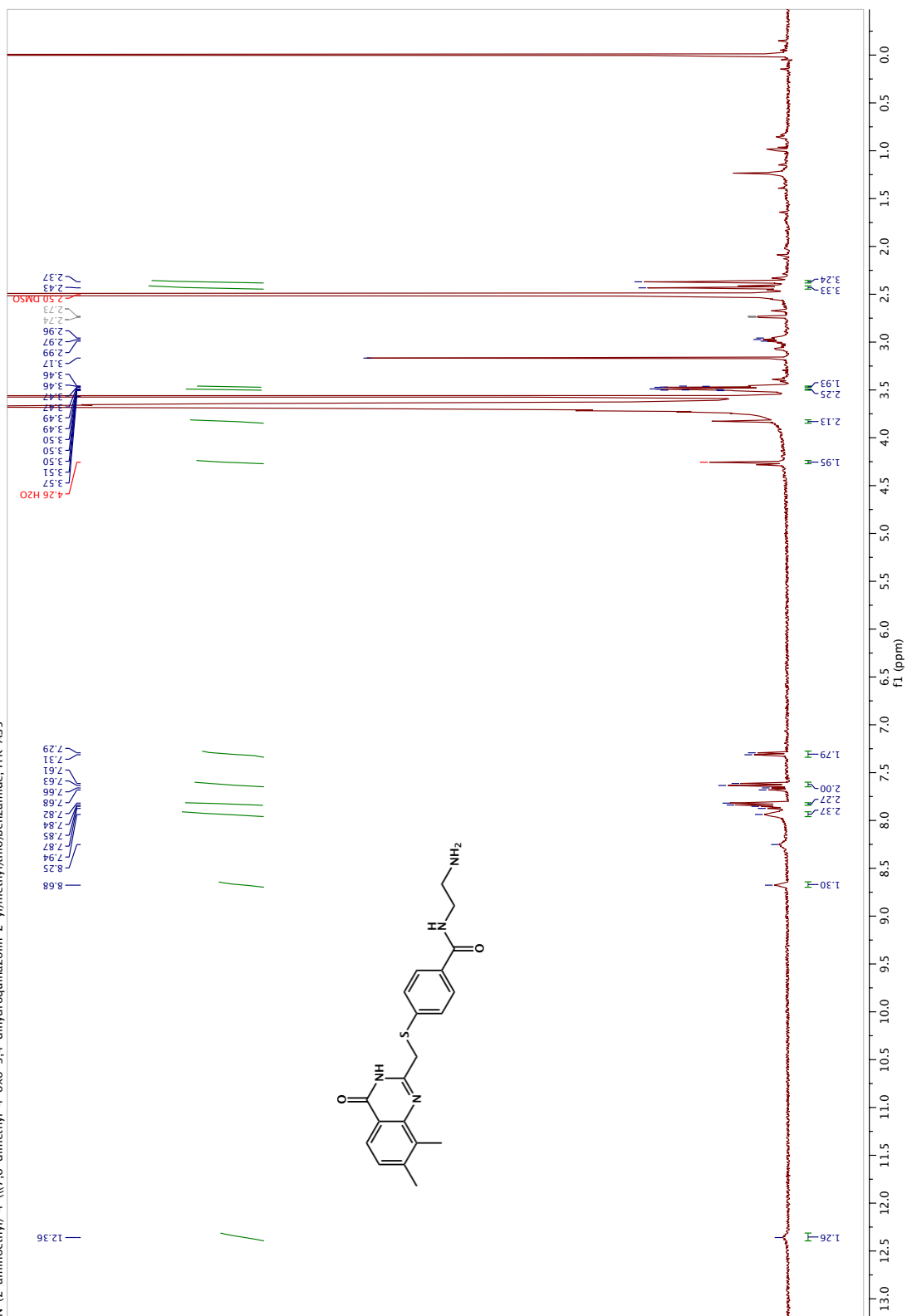
4-(((7,8-dimethyl-4-oxo-3,4-dihydroquinazolin-2-yl)methylthio)-N-(4-morpholinophenyl)benzamide, ITK-32



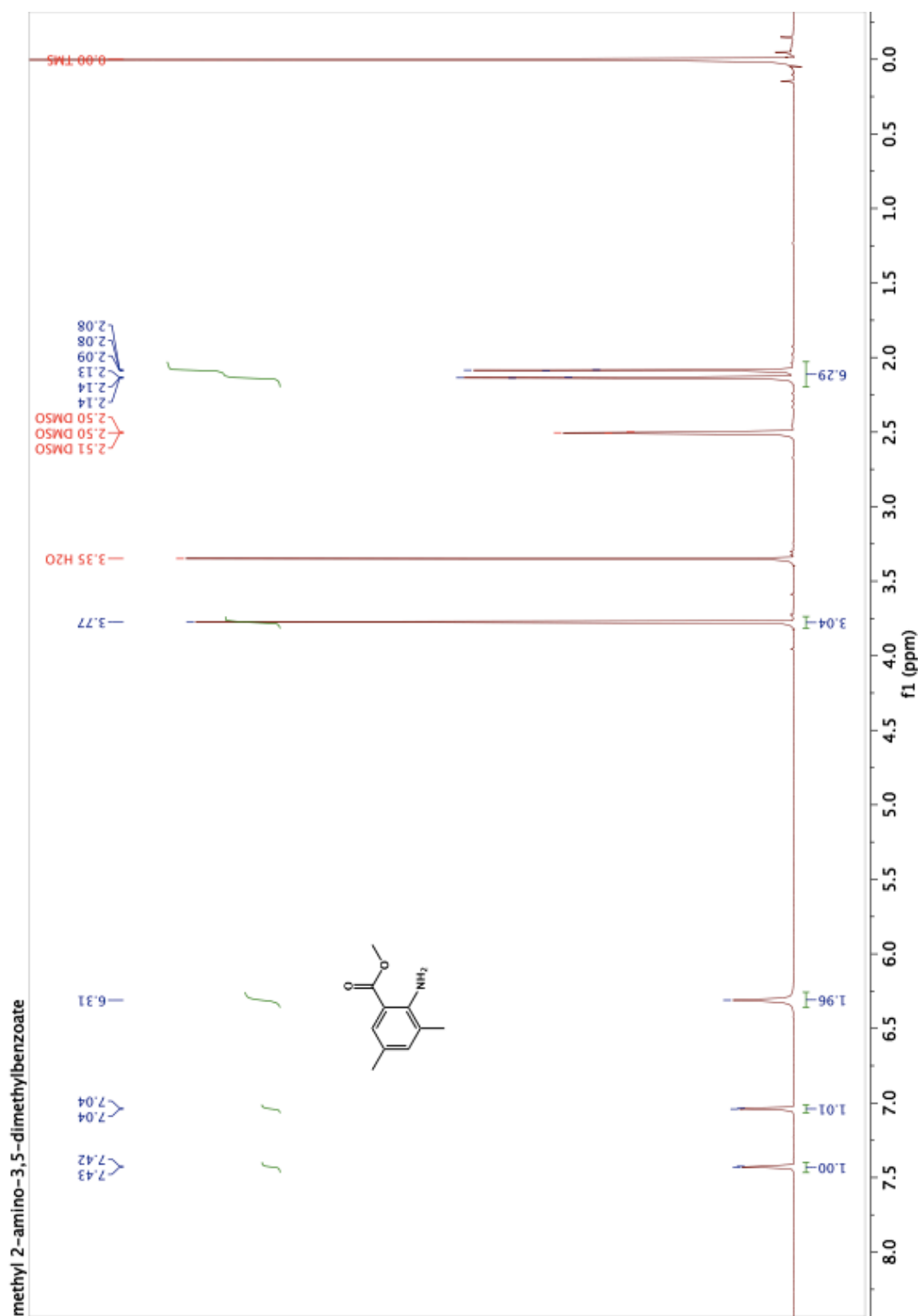




N-(2-aminoethyl)-4-(((7,8-dimethyl-4-oxo-3,4-dihydroquinazolin-2-yl)methyl)thio)benzamide, ITK-A35

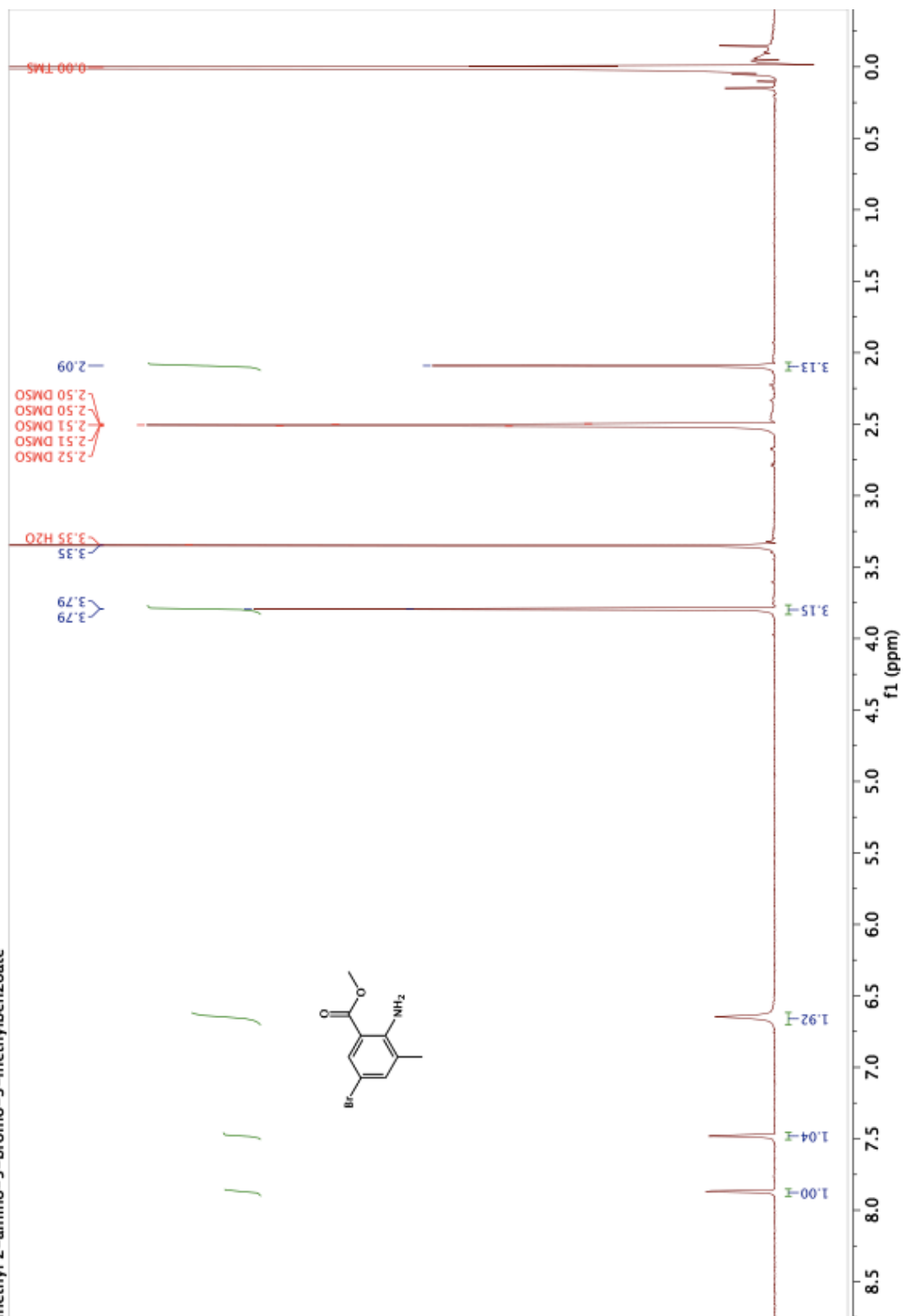


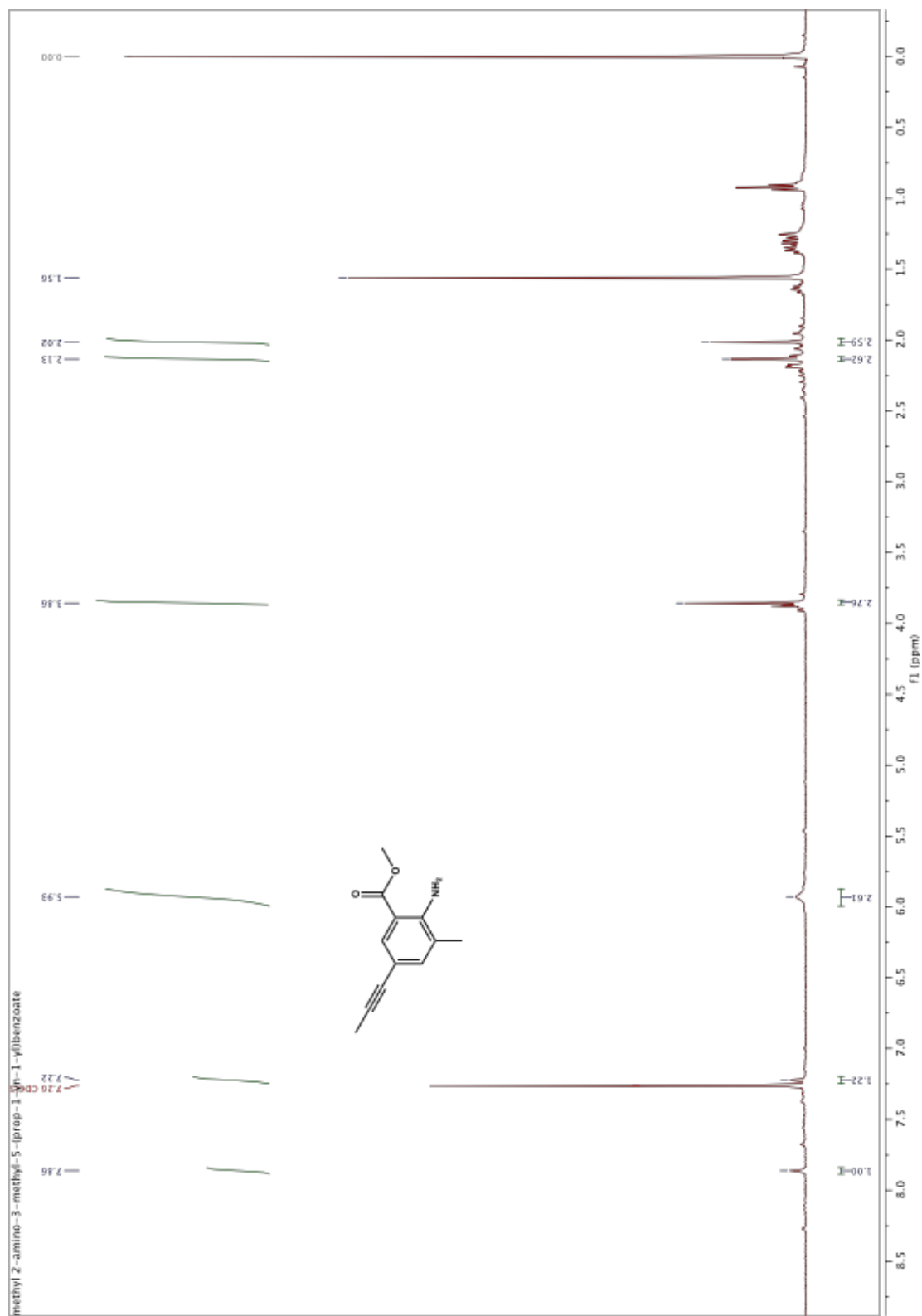
## Chapter 4

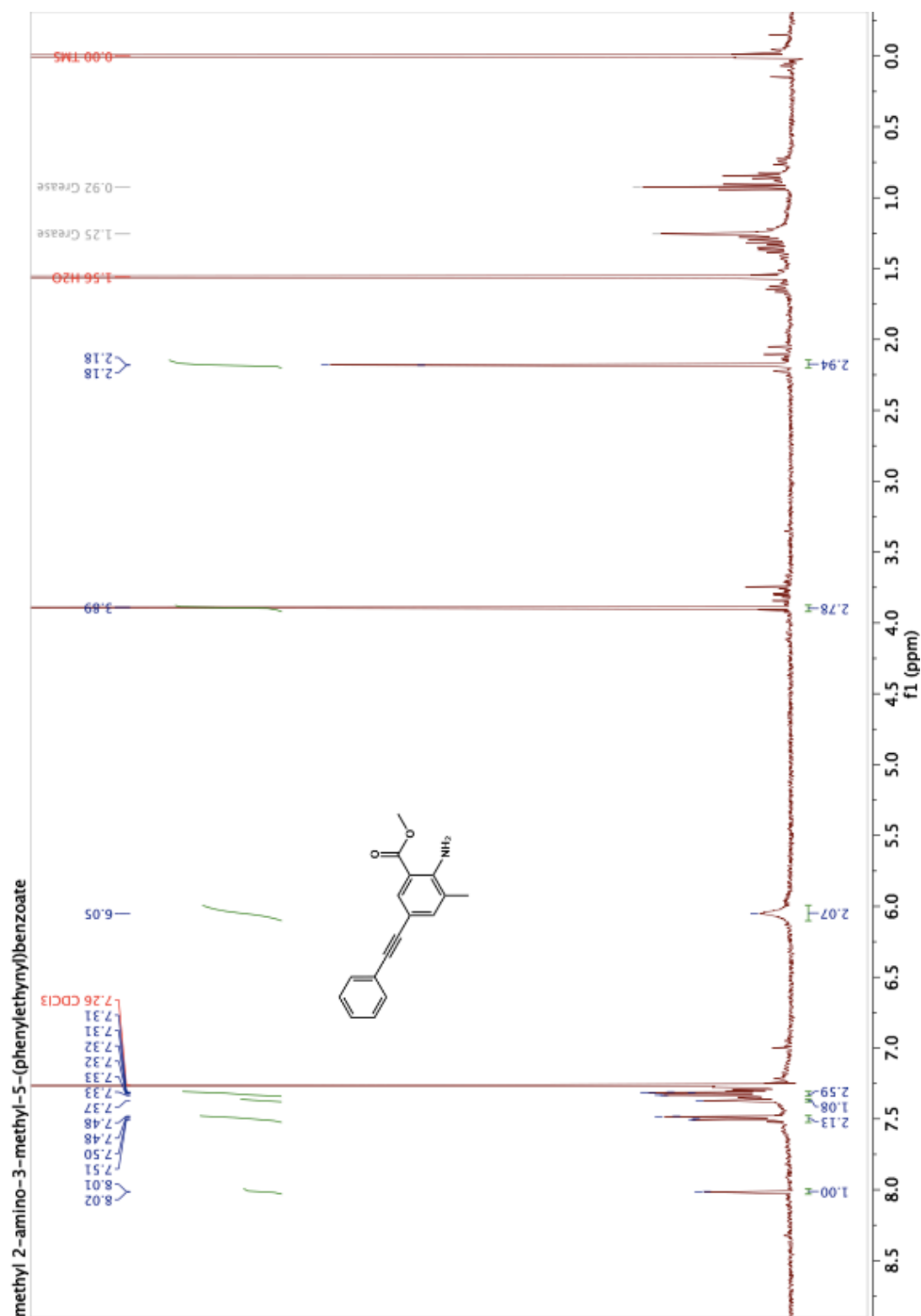


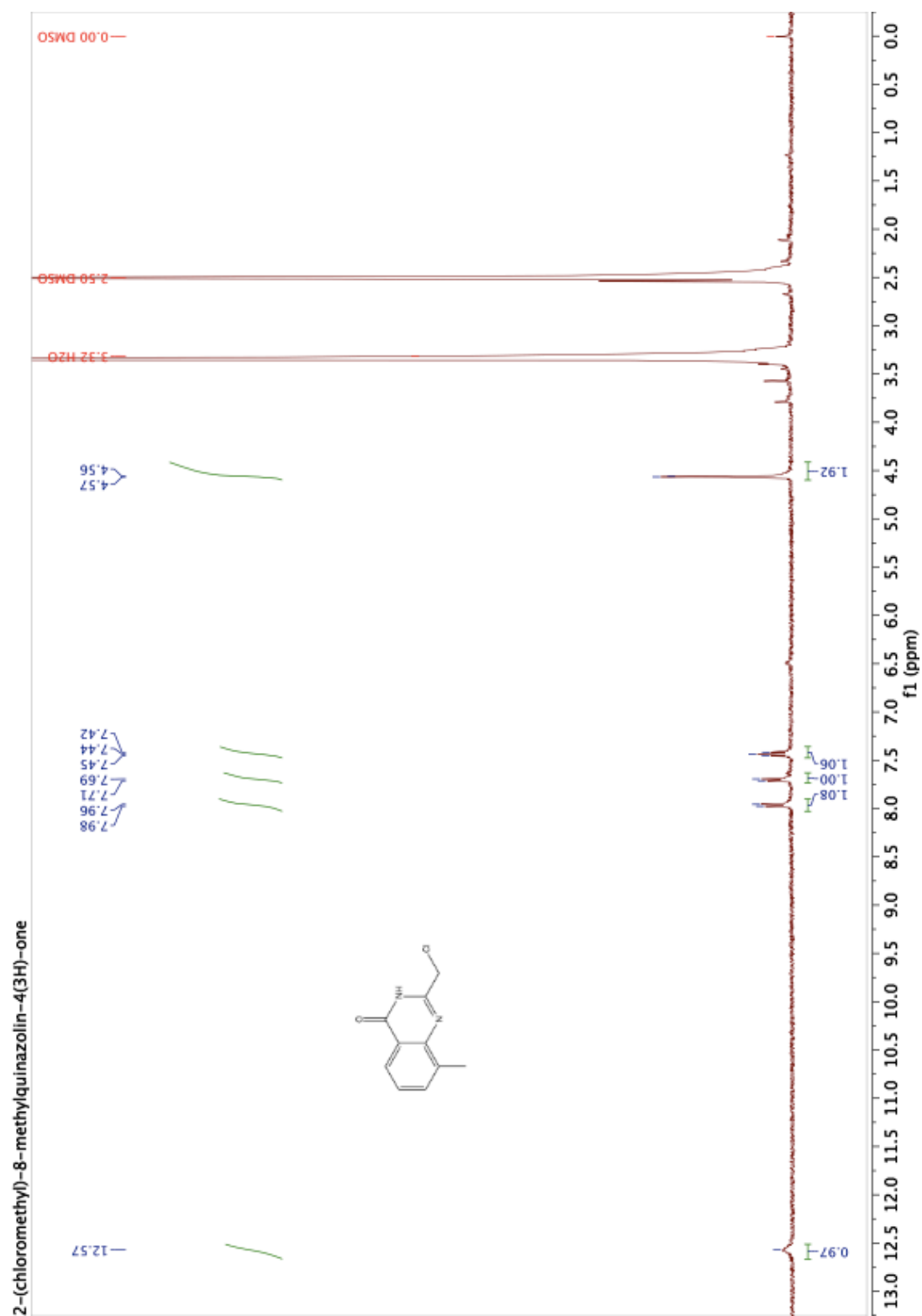


methyl 2-amino-5-bromo-3-methylbenzoate

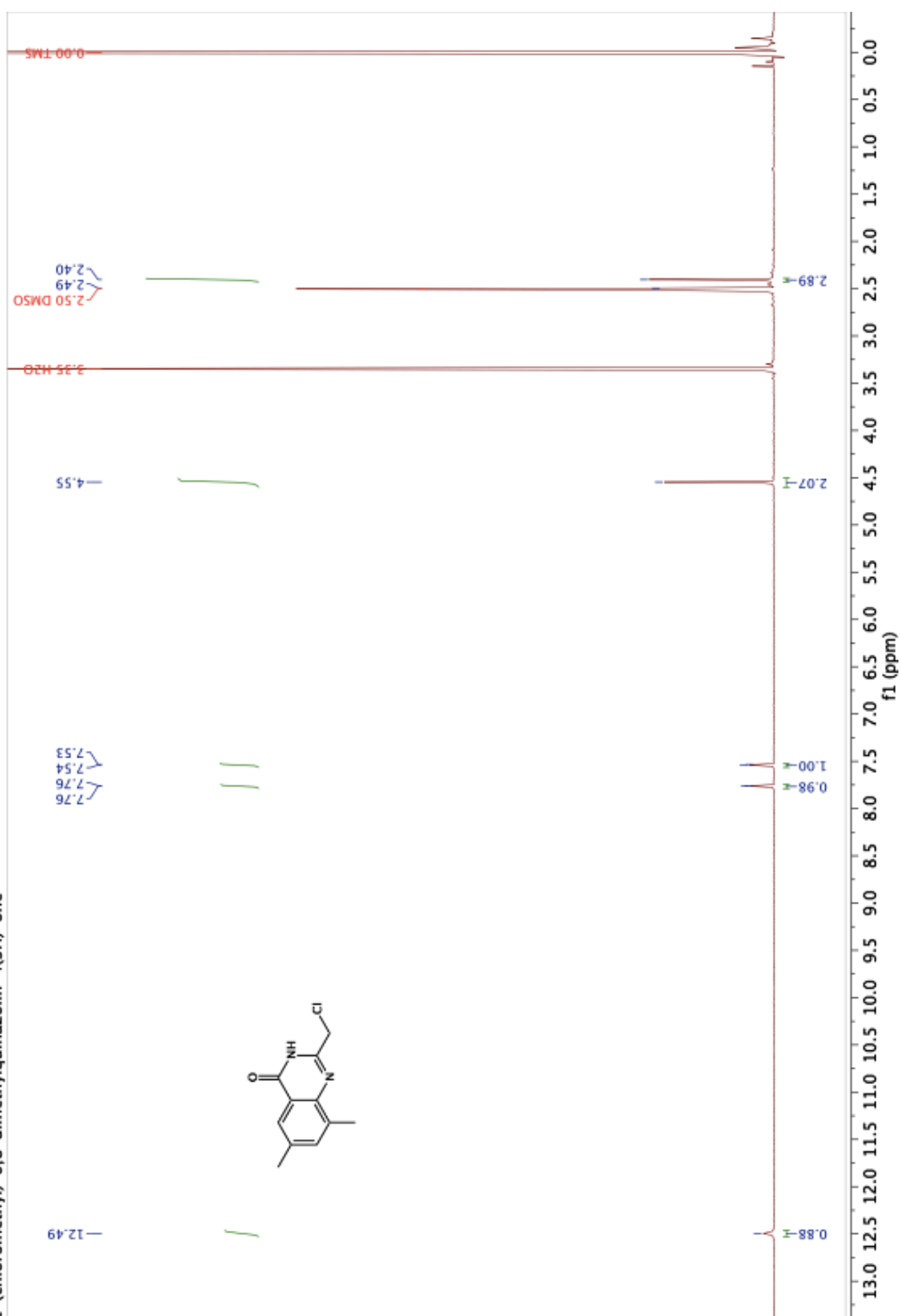


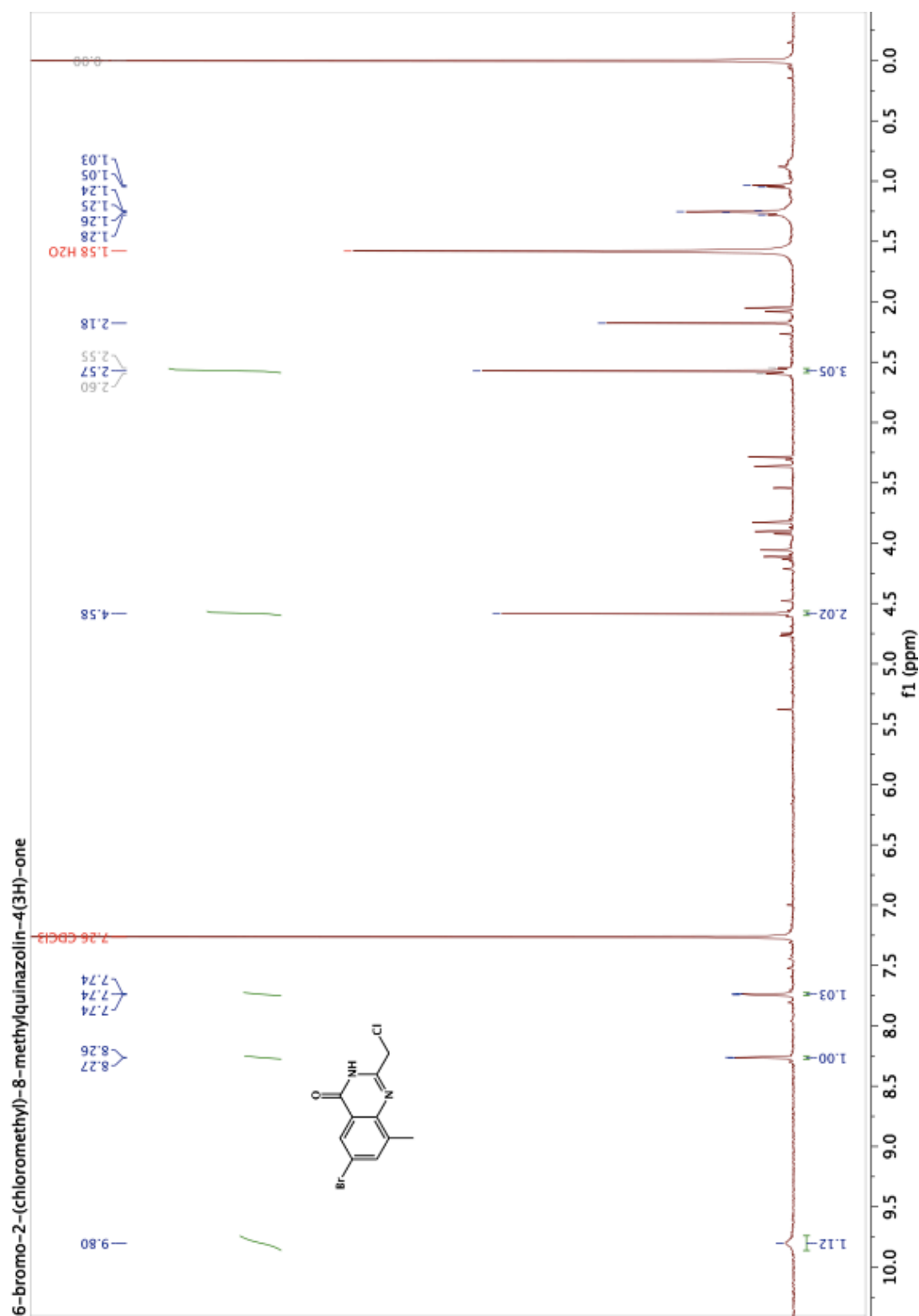


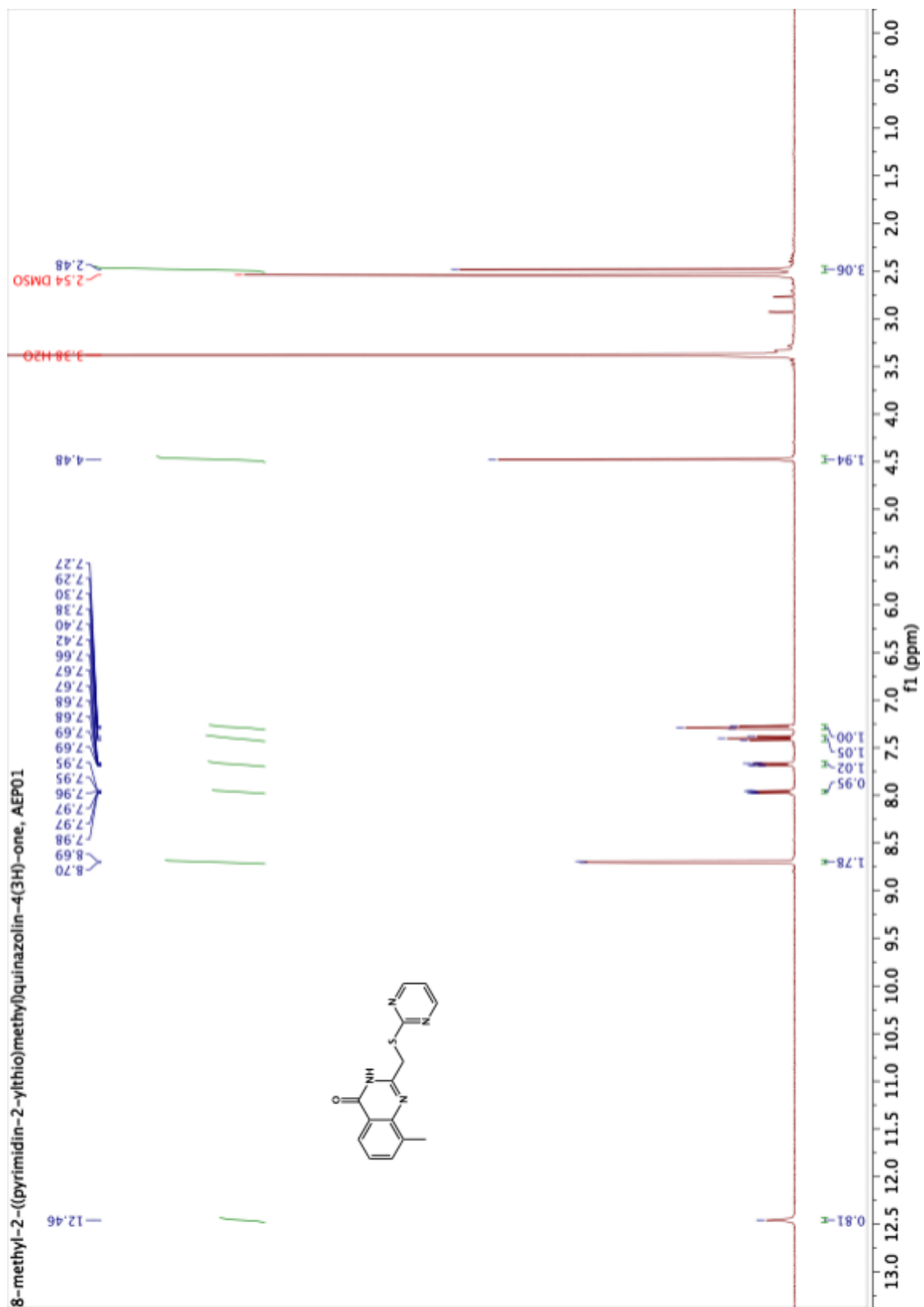




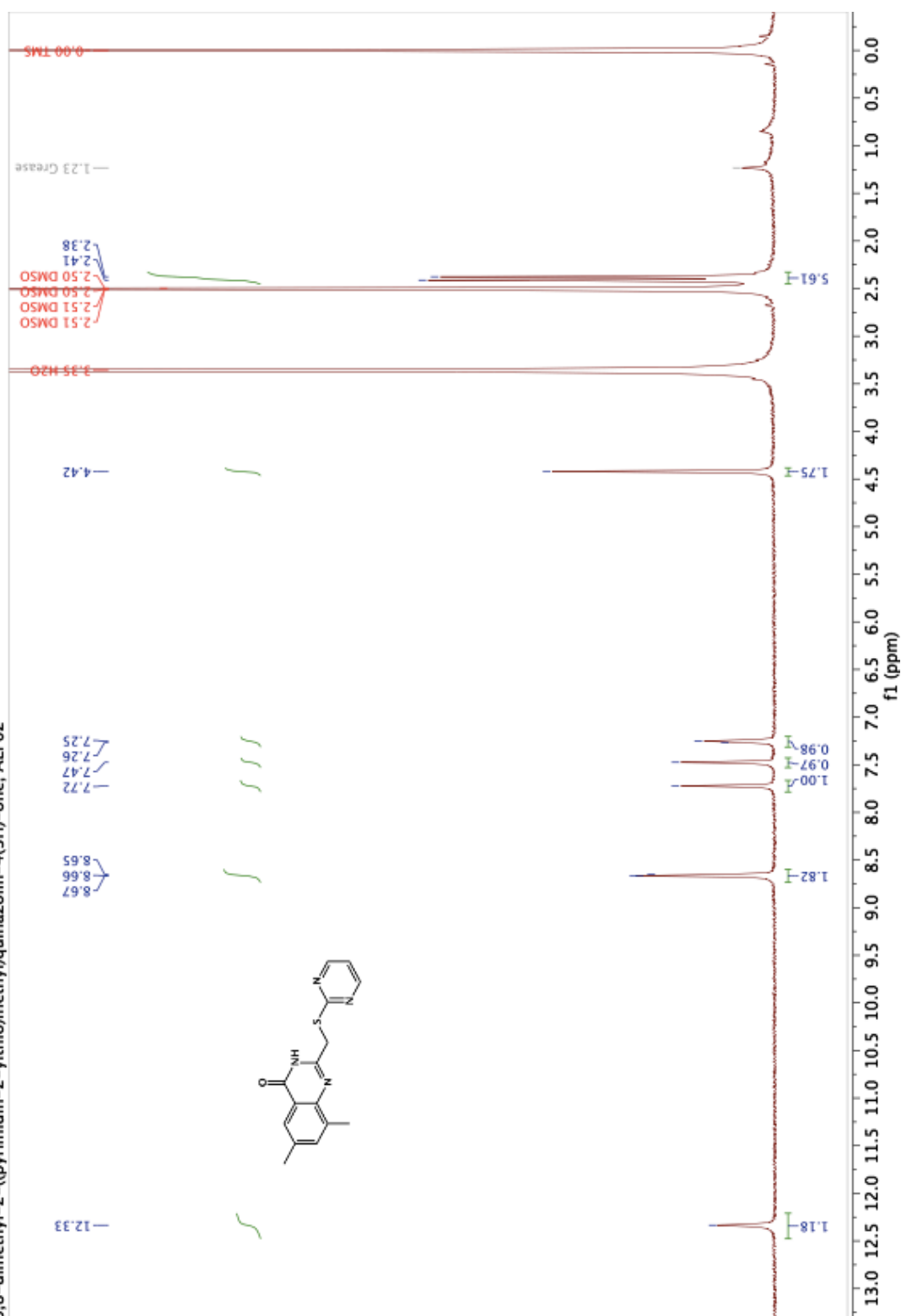
2-(chloromethyl)-6,8-dimethylquinazolin-4(3H)-one





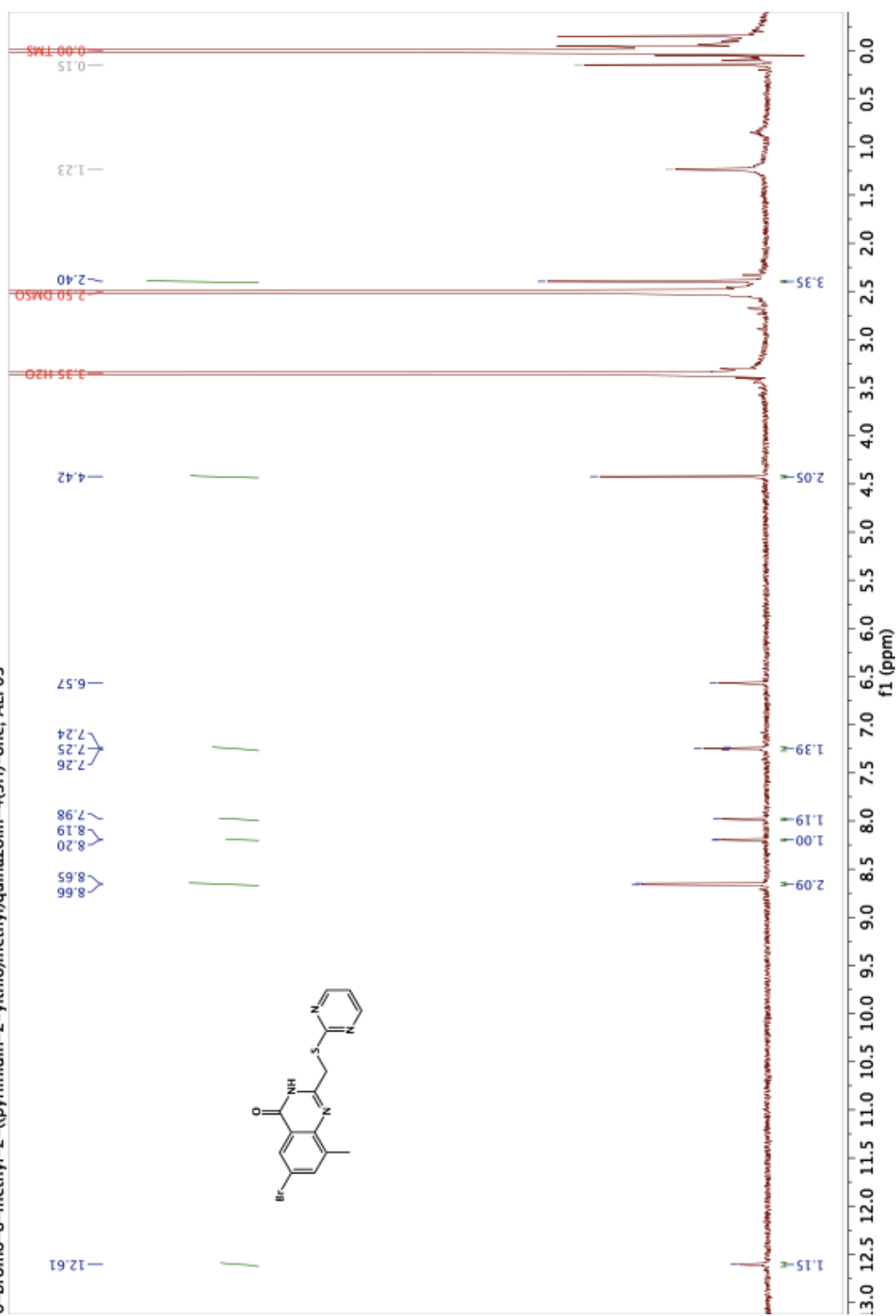


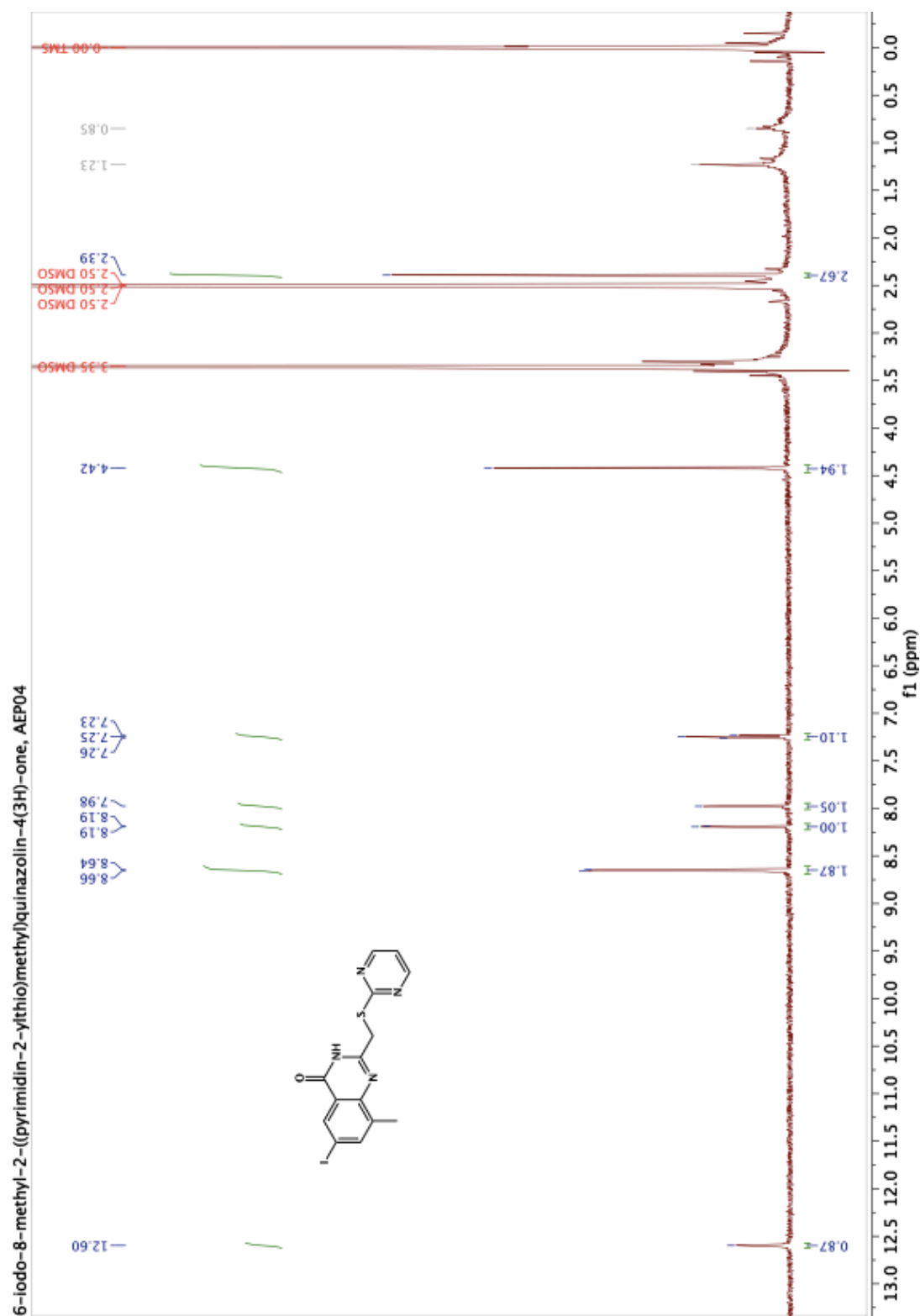
6,8-dimethyl-2-((pyrimidin-2-ylthio)methyl)quinazolin-4(3H)-one, AEP02



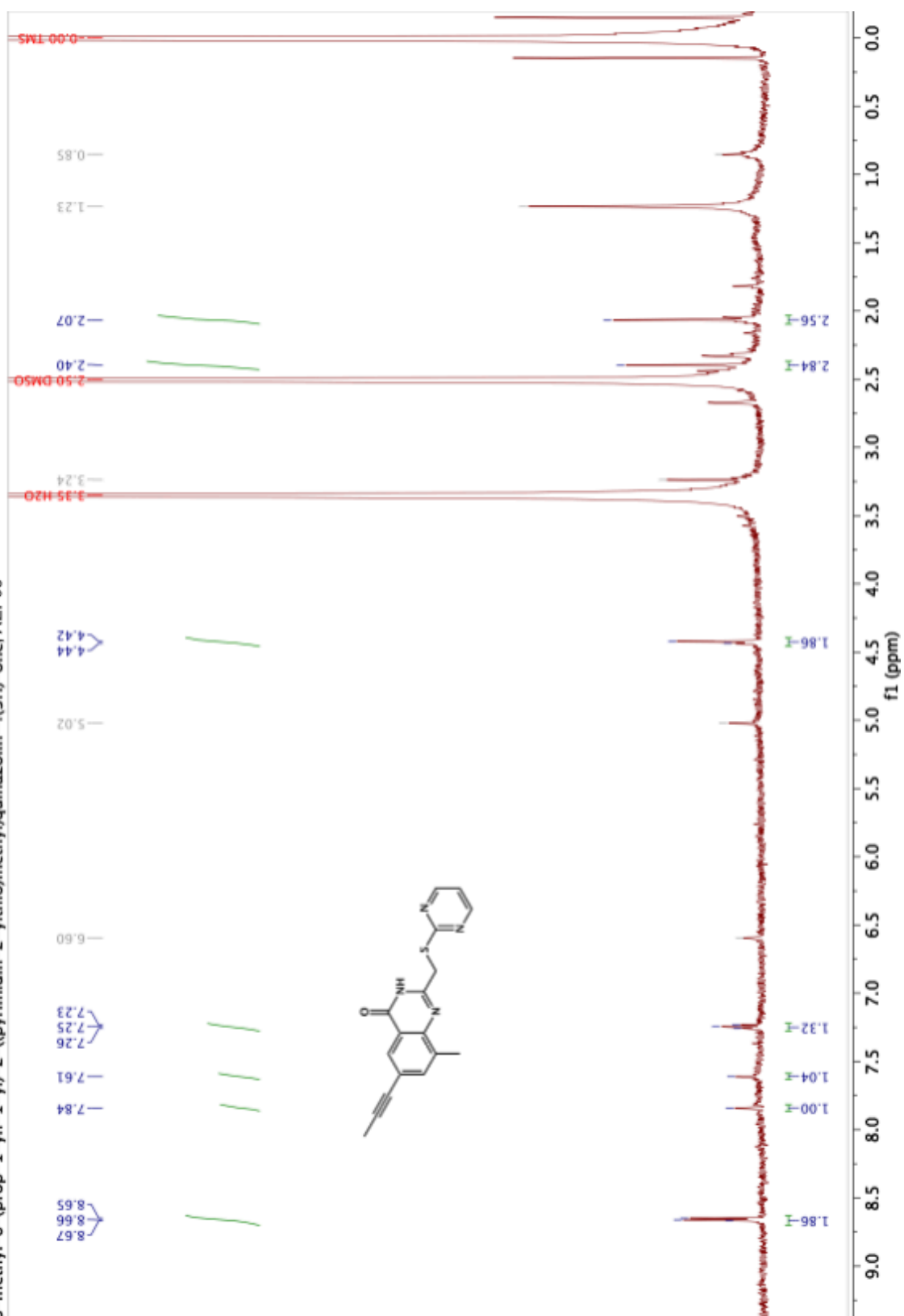


6-bromo-8-methyl-2-((pyrimidin-2-ylthio)methyl)quinazolin-4(3H)-one, AEP03

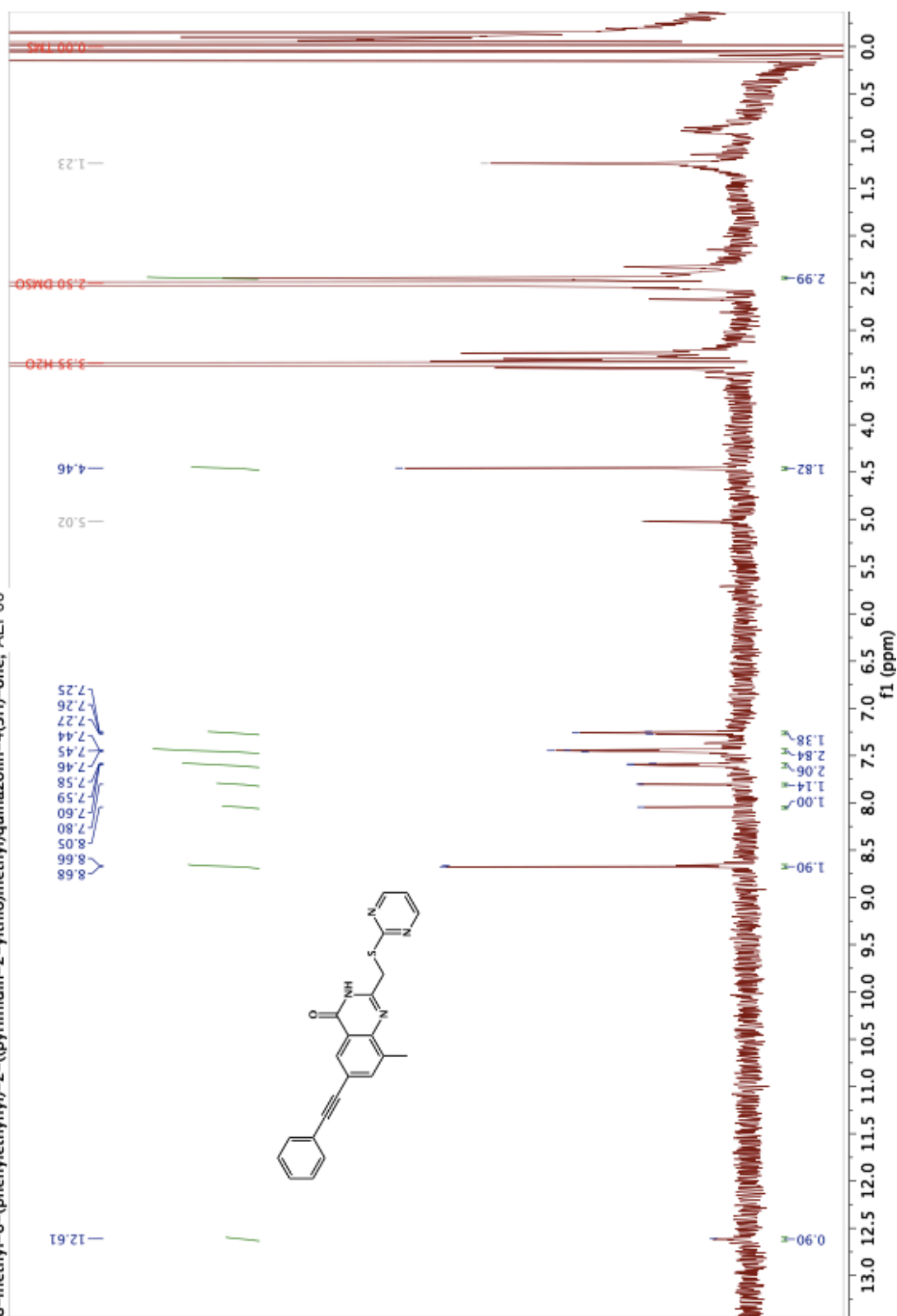


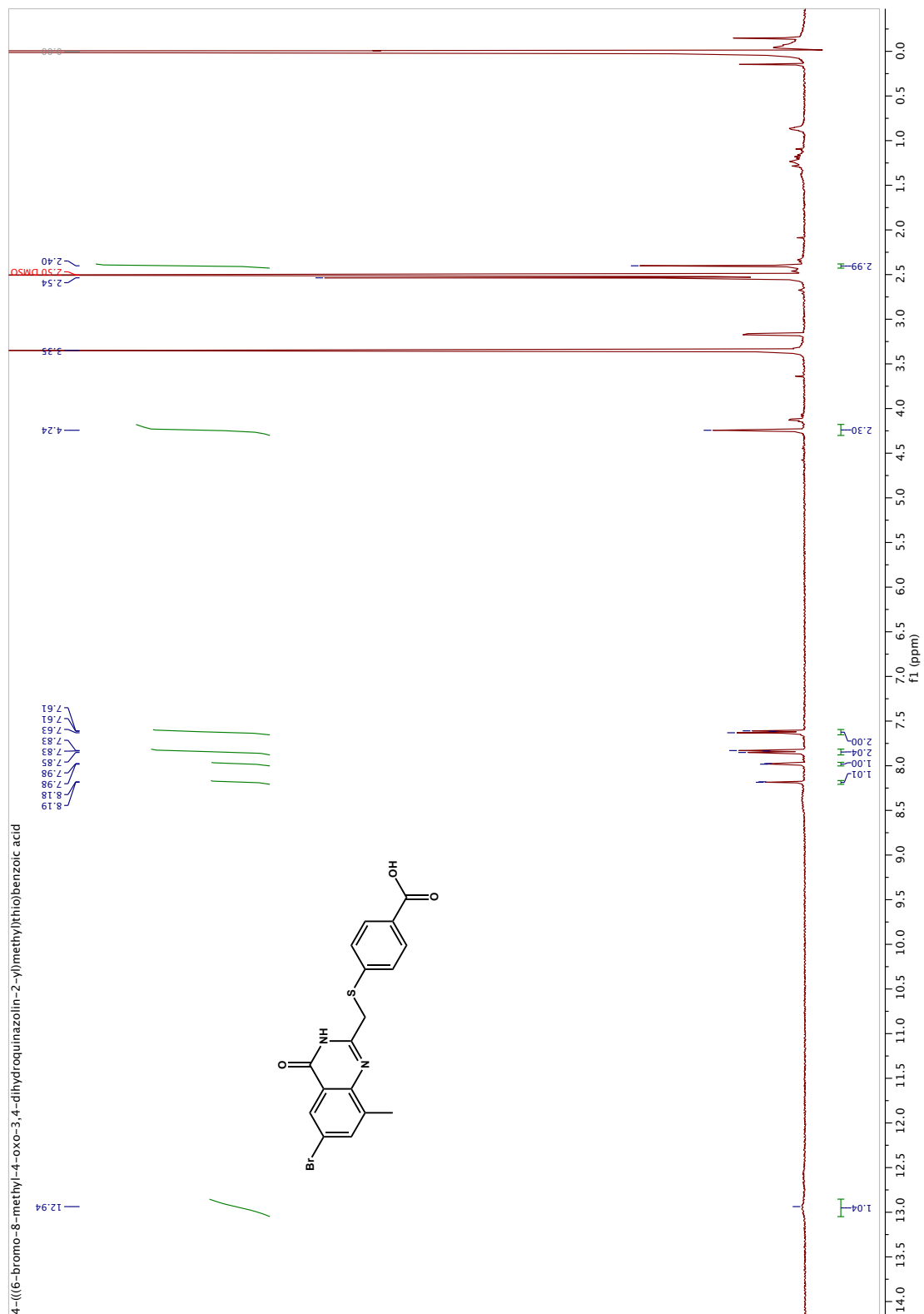


8-methyl-6-(prop-1-yn-1-yl)-2-((pyrimidin-2-ylthio)methyl)quinazolin-4(3H)-one, AEP05

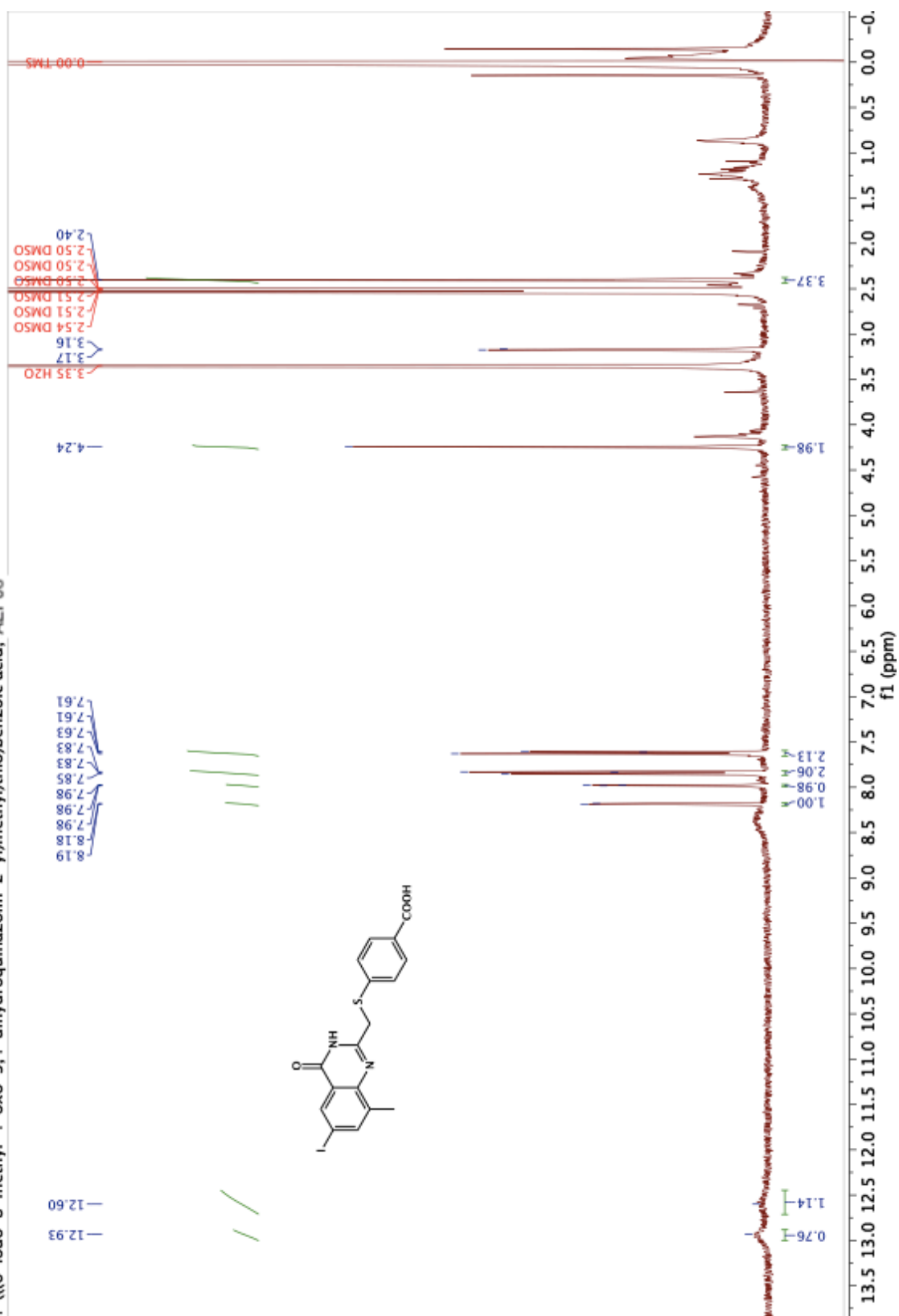


8-methyl-6-(phenylethynyl)-2-((pyrimidin-2-ylthio)methyl)quinazolin-4(3H)-one, AEP06

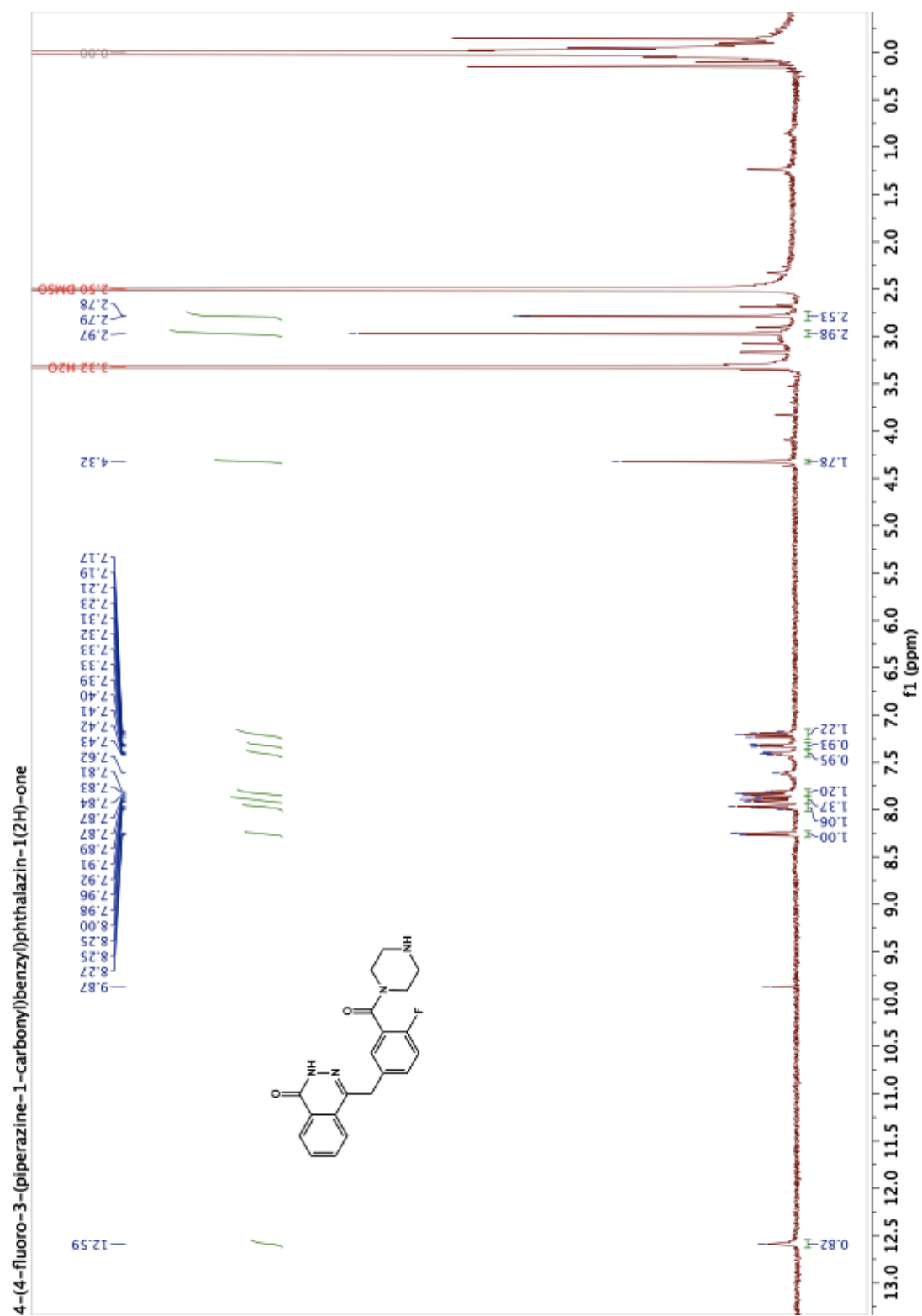


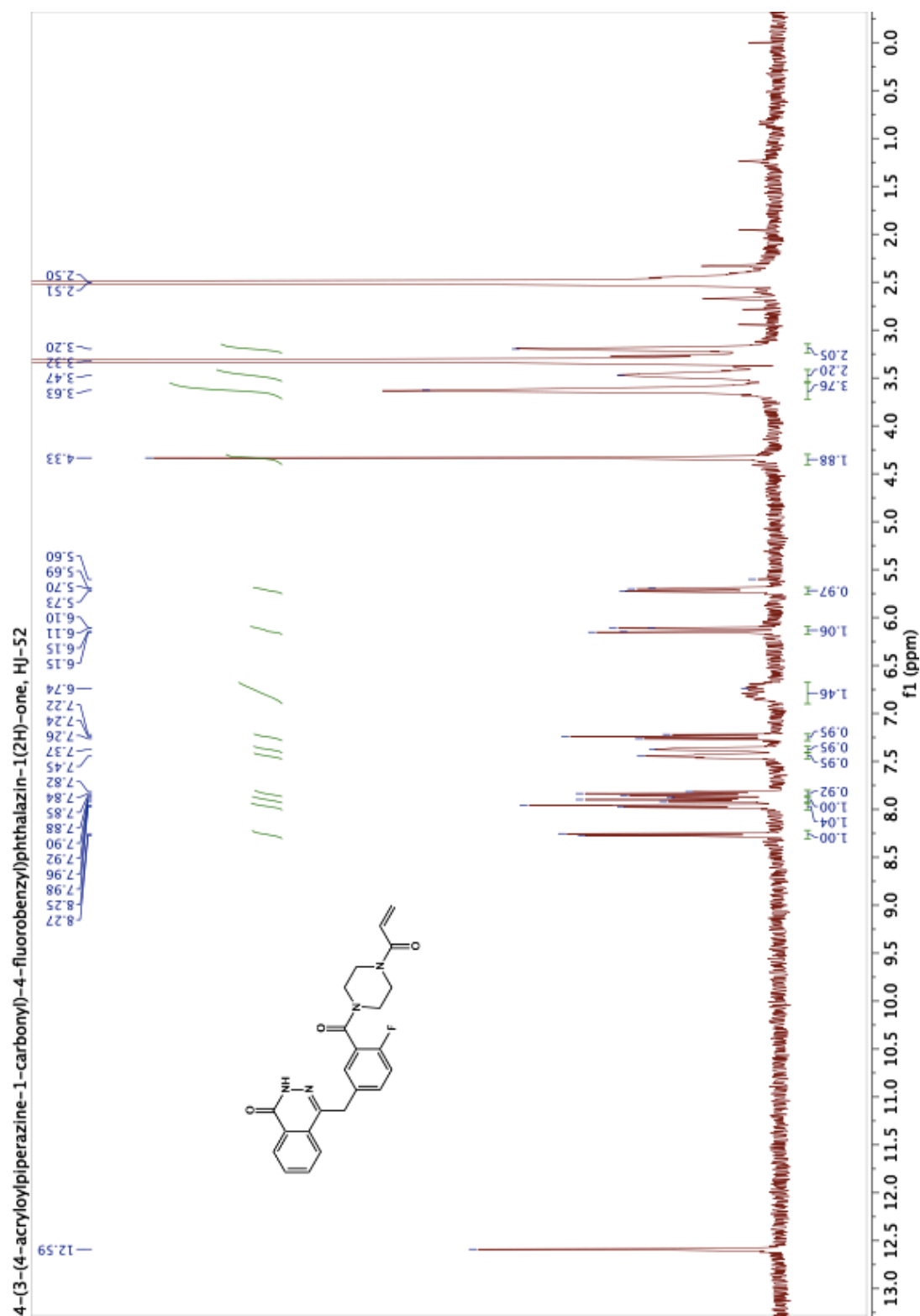


4-(((6-iodo-8-methyl-4-oxo-3,4-dihydroquinazolin-2-yl)methyl)thio)benzoic acid, AEP08



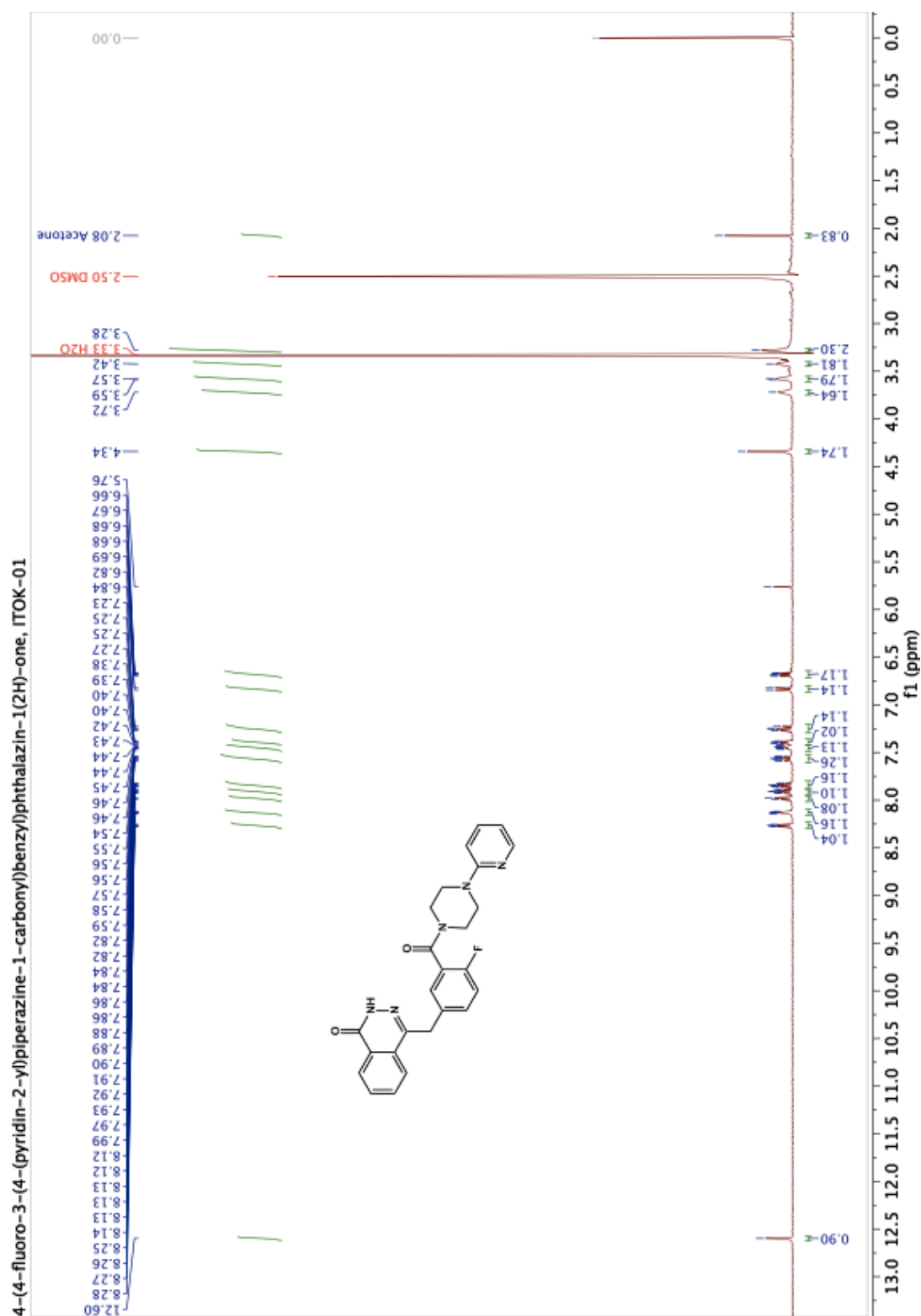
## Chapter 5



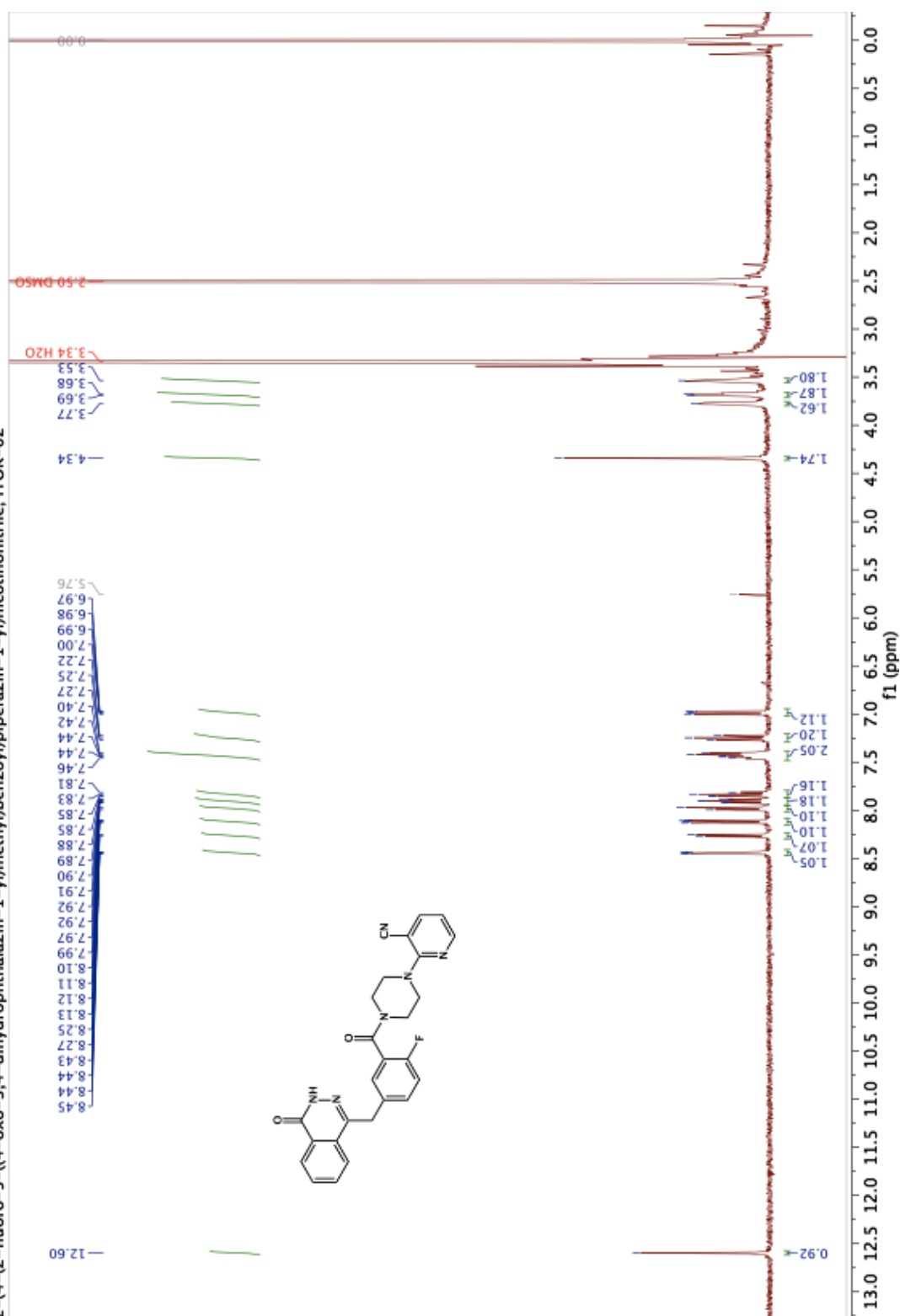


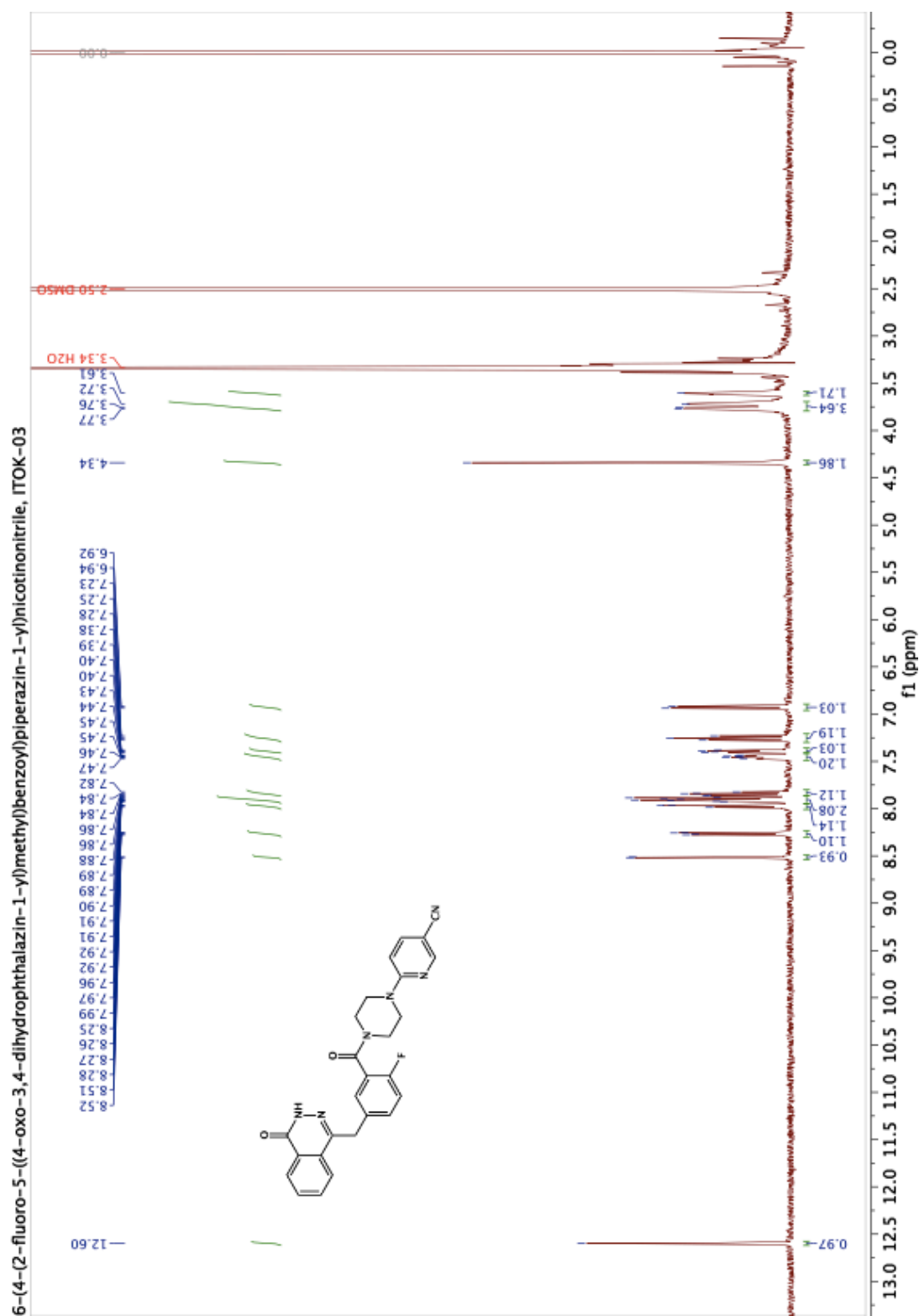


## Chapter 6

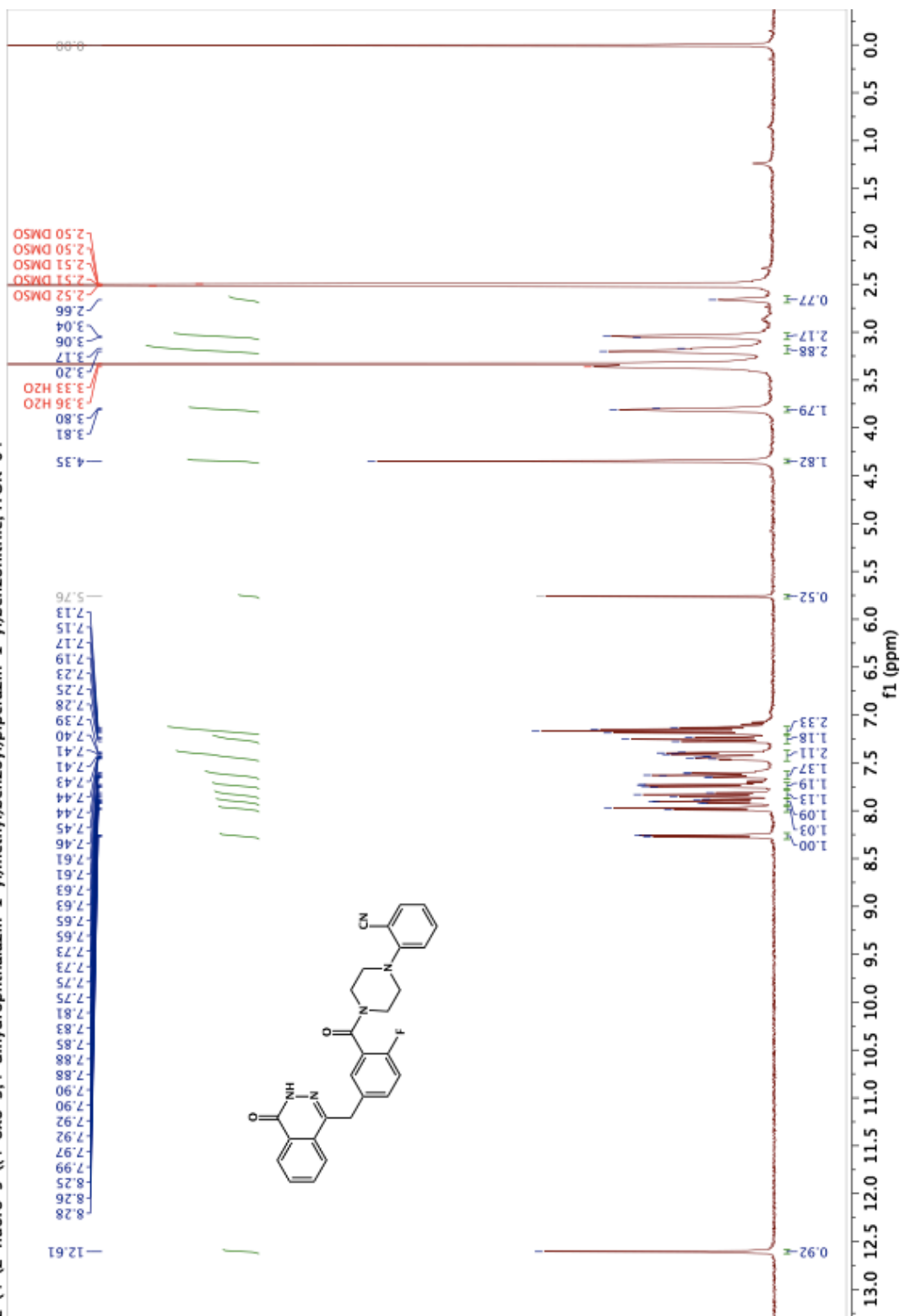


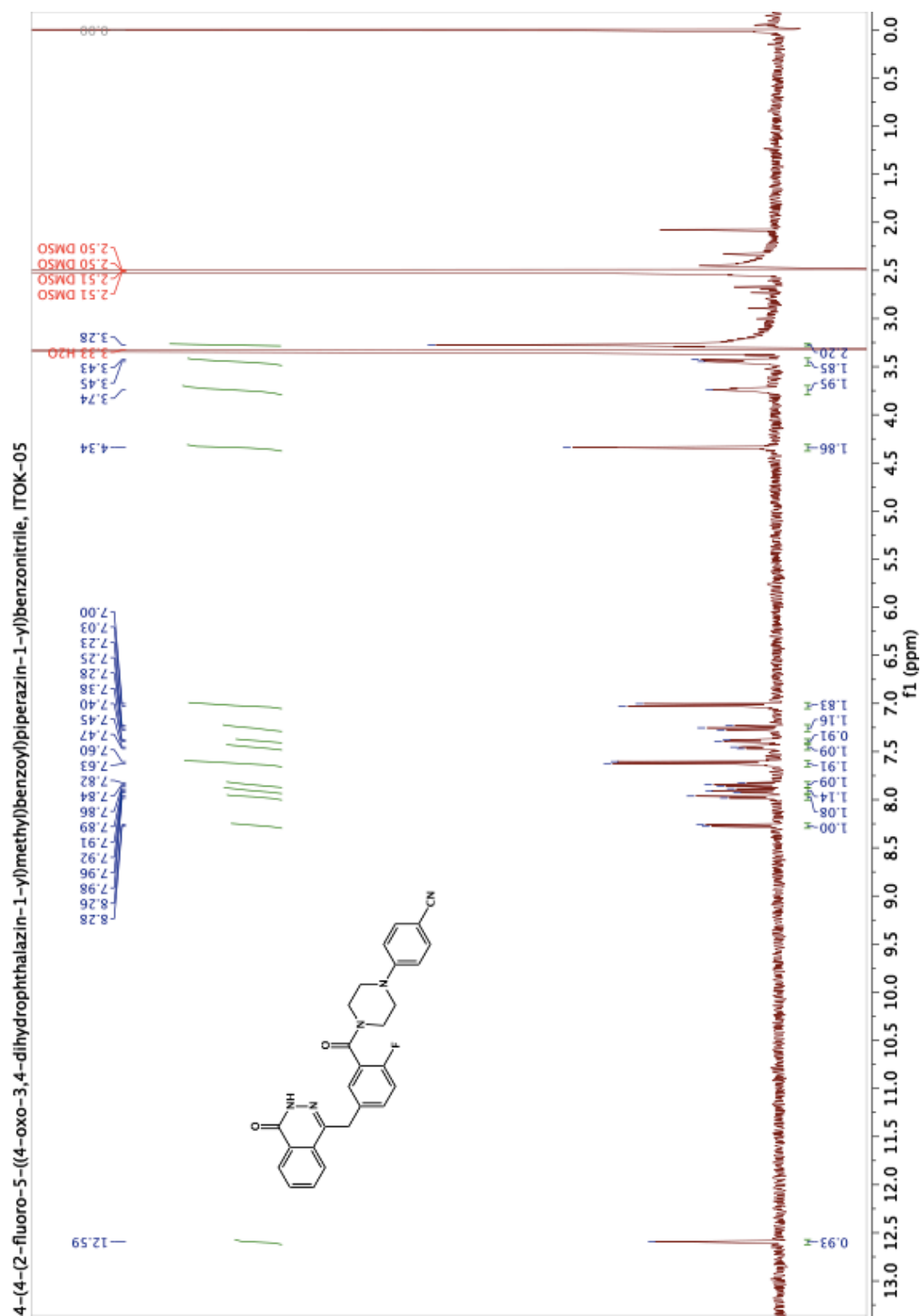
2-(4-(2-fluoro-5-((4-oxo-3,4-dihydrophthalazin-1-yl)methyl)benzoyl)piperazin-1-yl)methyl)benzoyl)piperazin-1-yl)nicotinonitrile, ITOK-02



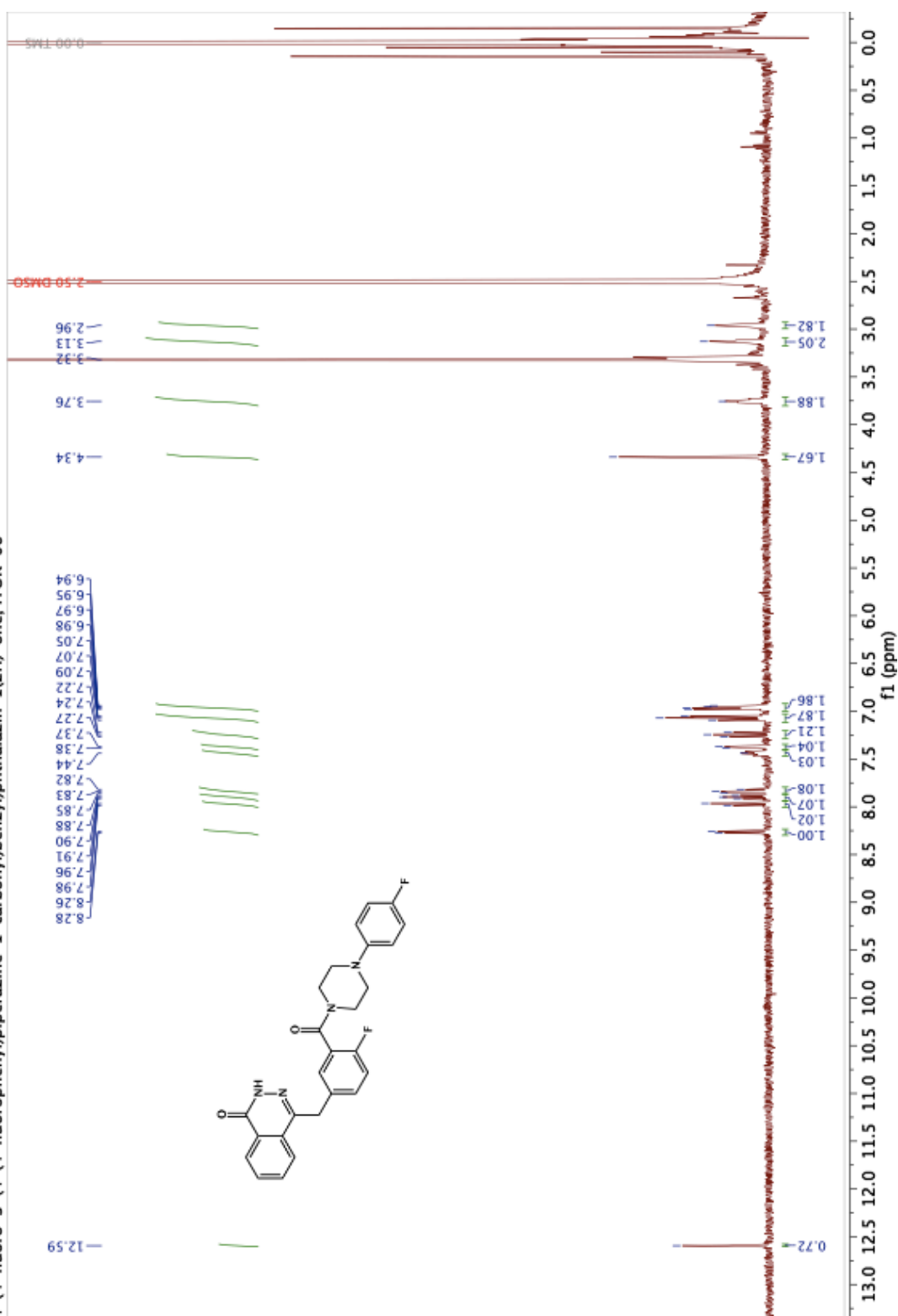


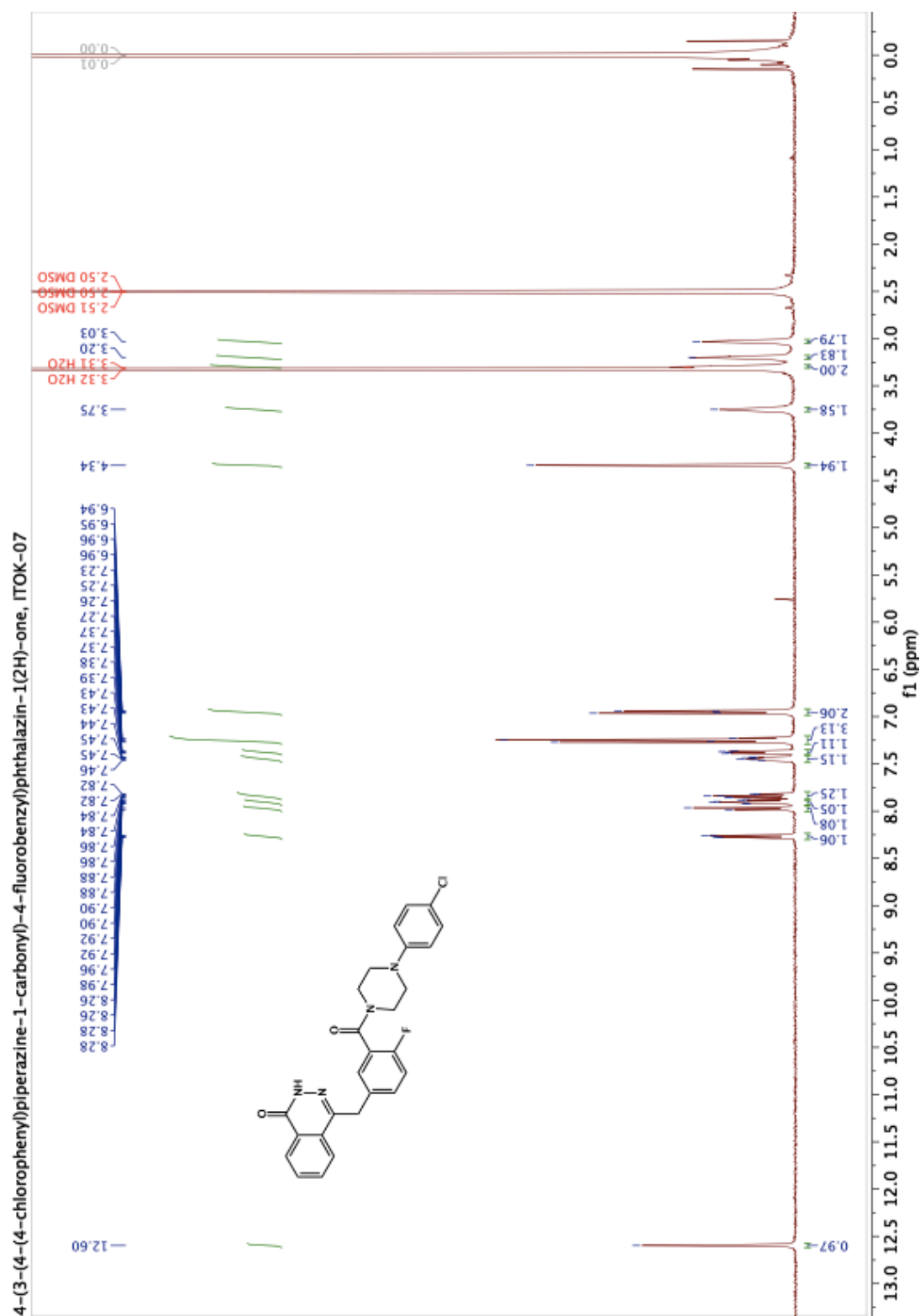
2-(4-(2-fluoro-5-((4-oxo-3,4-dihydrophthalazin-1-yl)methyl)benzoyl)piperazin-1-yl)methyl)benzonitrile, ITOK-04



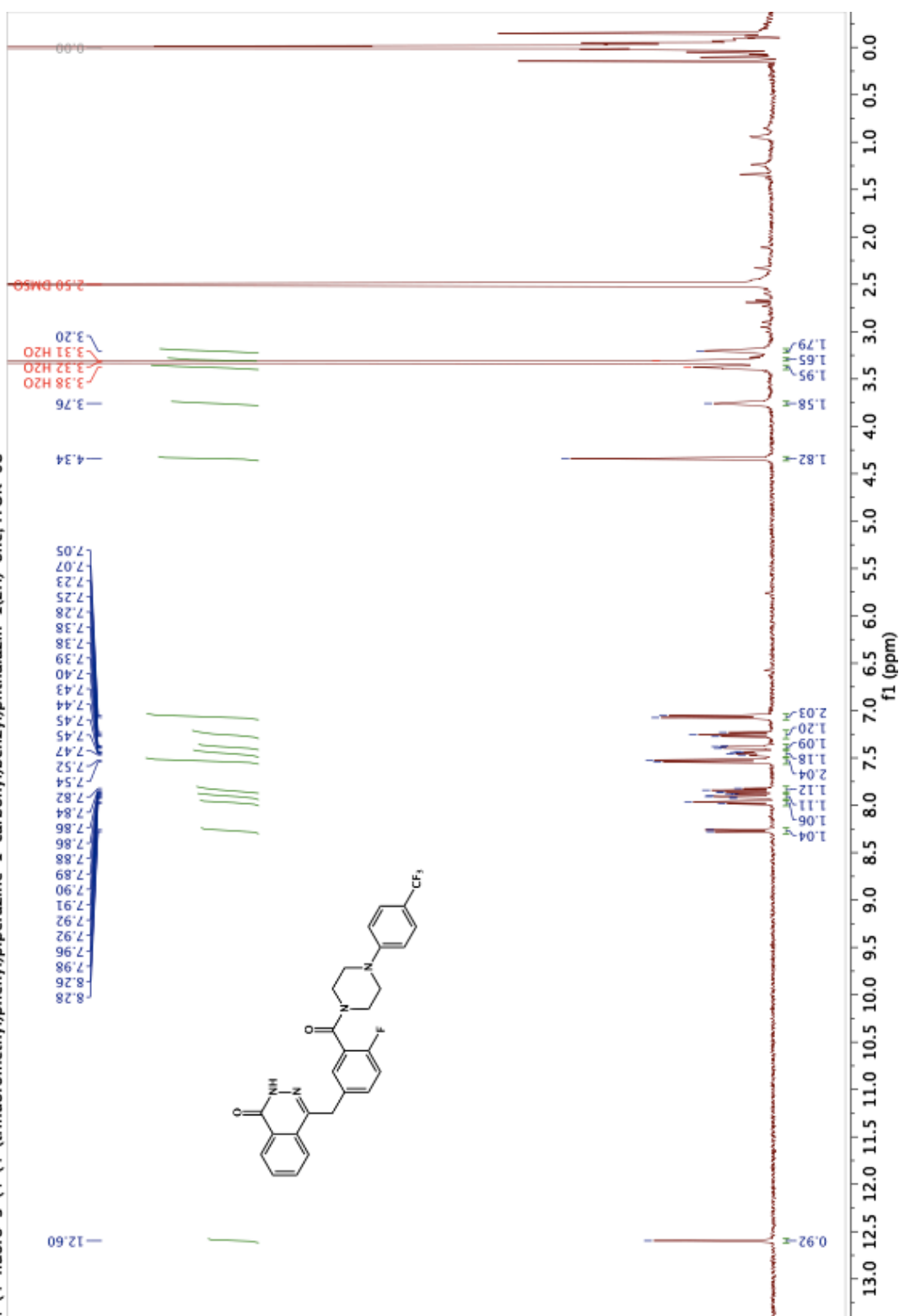


4-(4-fluoro-3-(4-(4-fluorophenyl)piperazine-1-carbonyl)benzyl)phthalazin-1(2H)-one, ITOK-06

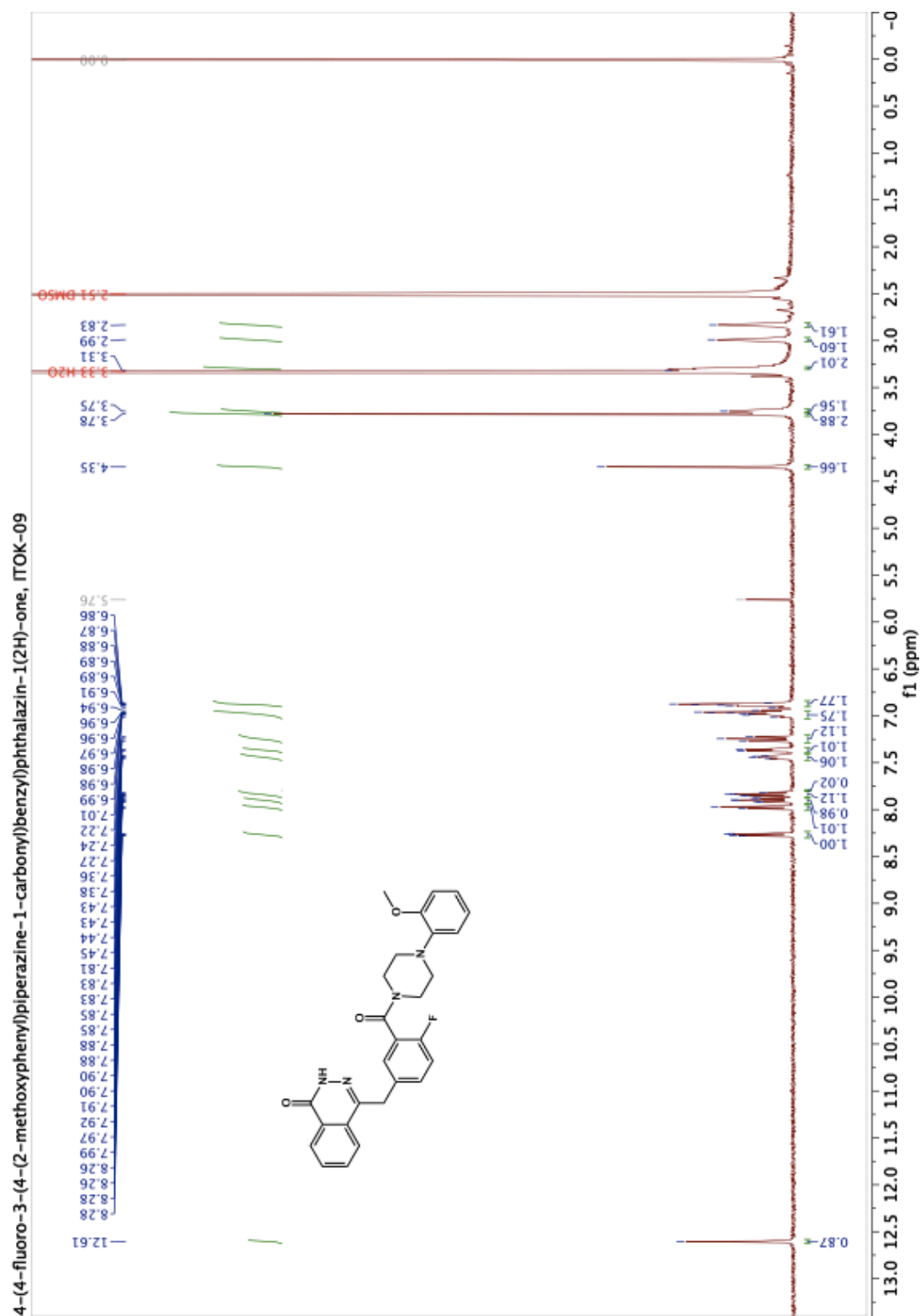




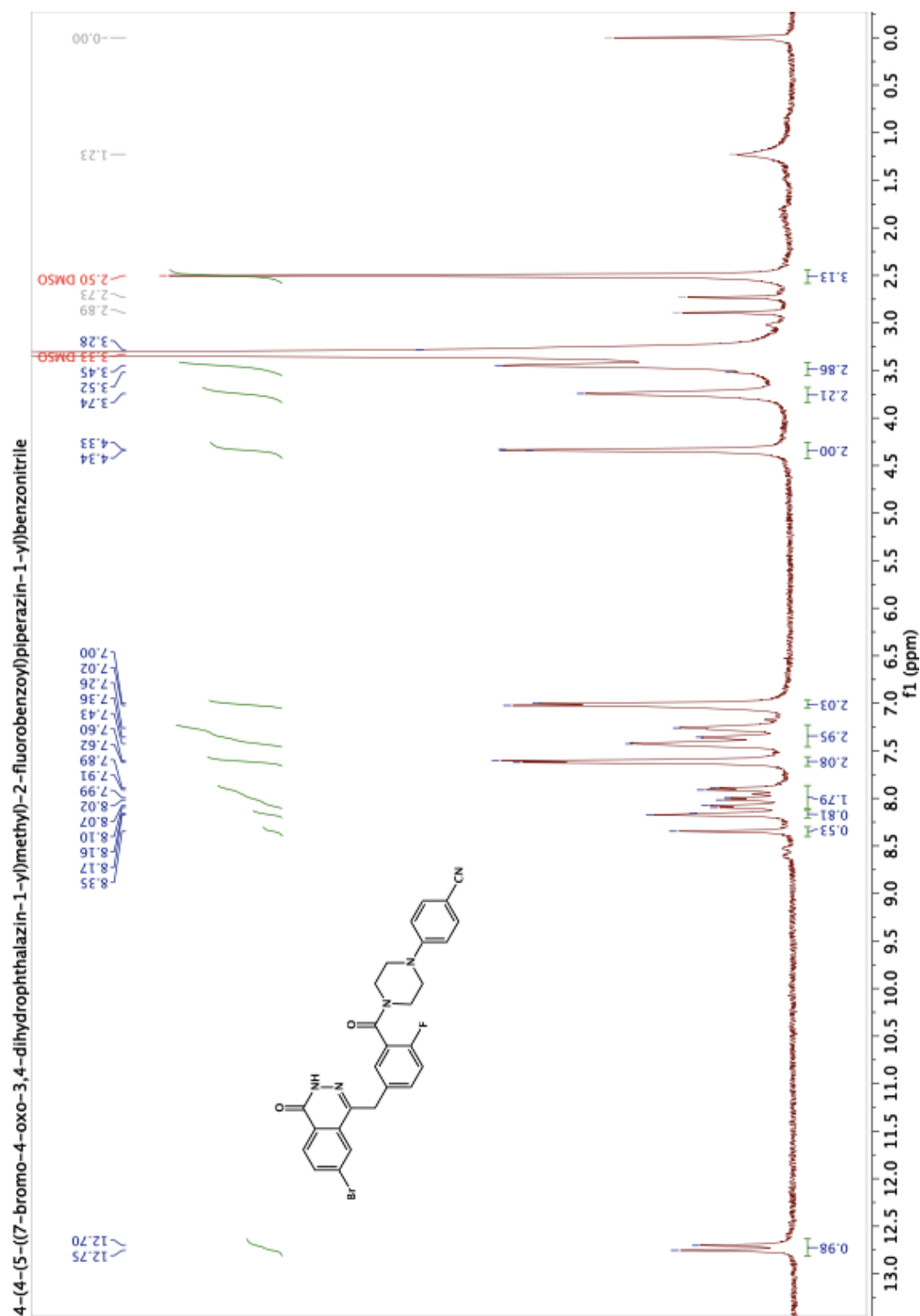
4-(4-fluoro-3-(4-(4-(trifluoromethyl)phenyl)piperazine-1-carbonyl)benzyl)phthalazin-1(2H)-one, ITOK-08



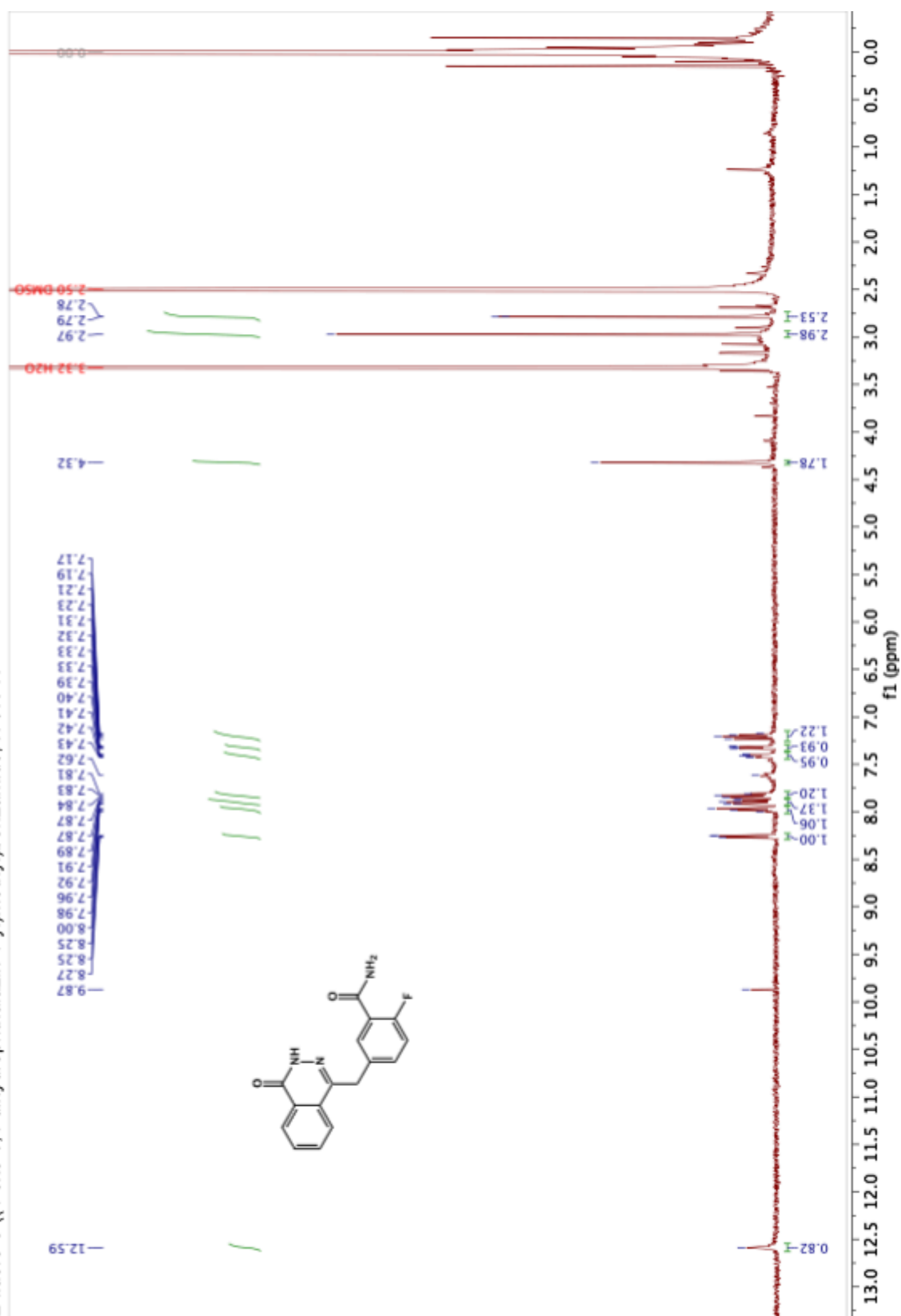




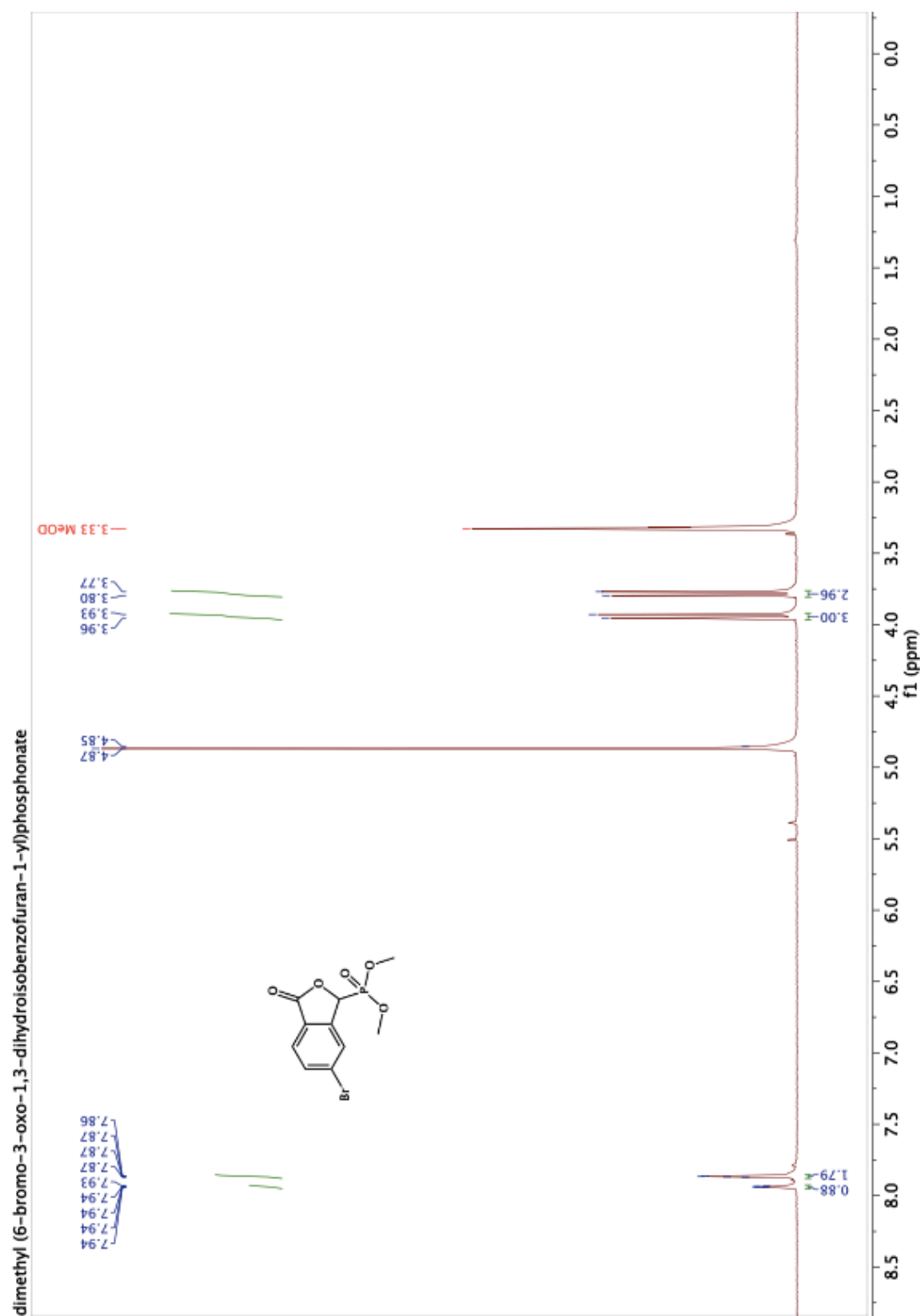


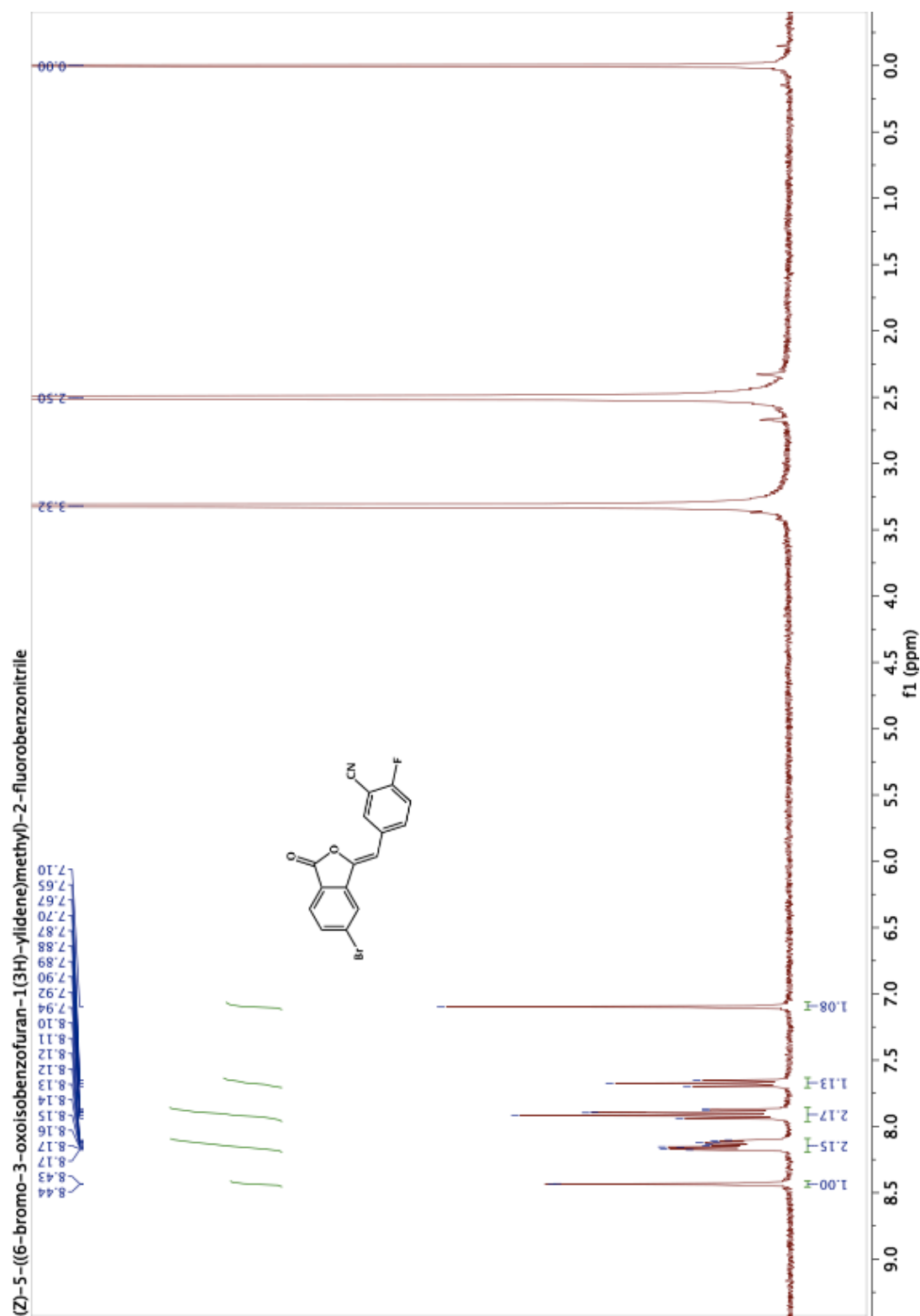


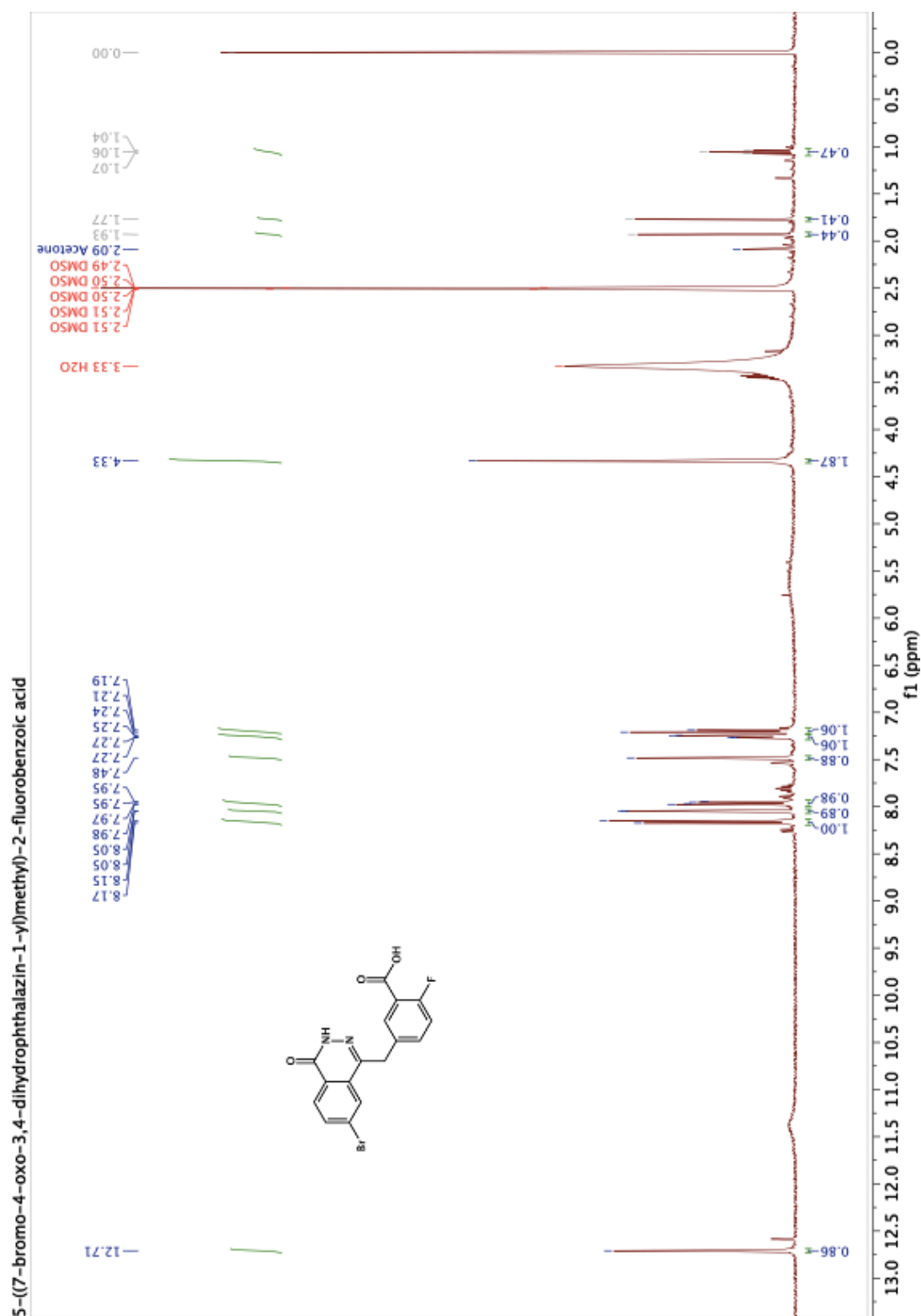
2-fluoro-5-((4-oxo-3,4-dihydrophthalazin-1-yl)methyl)benzamide, ITOK-11



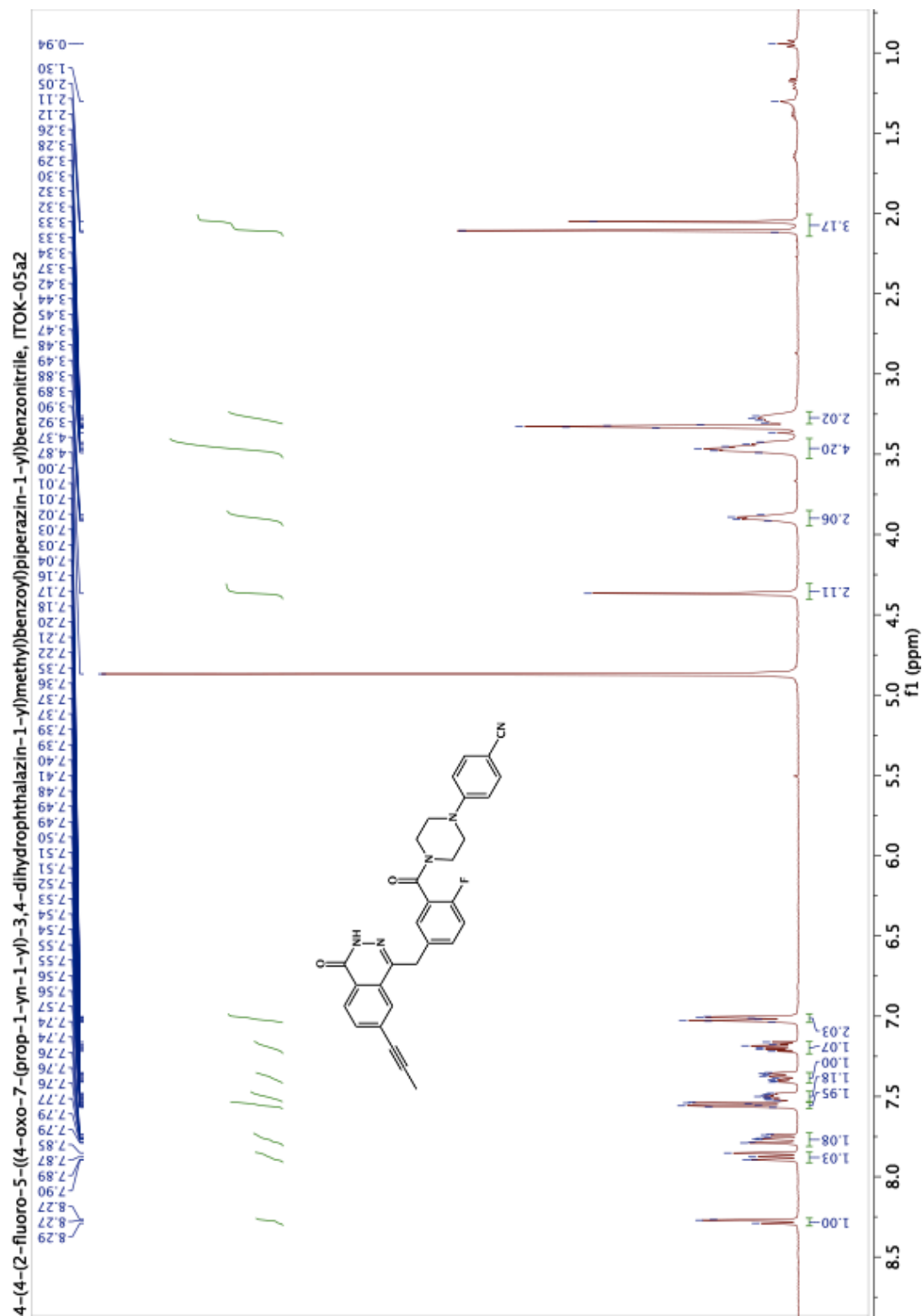


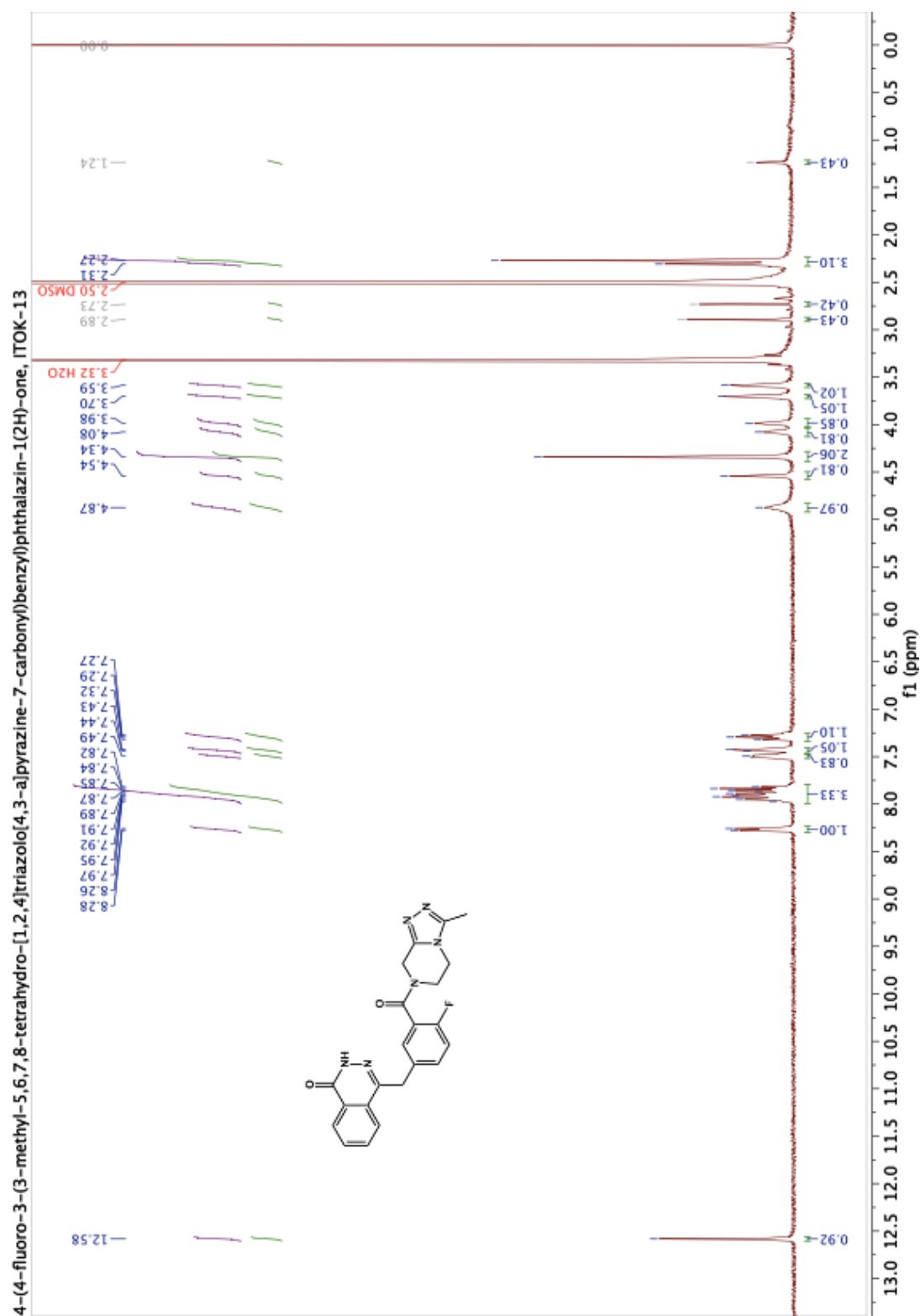


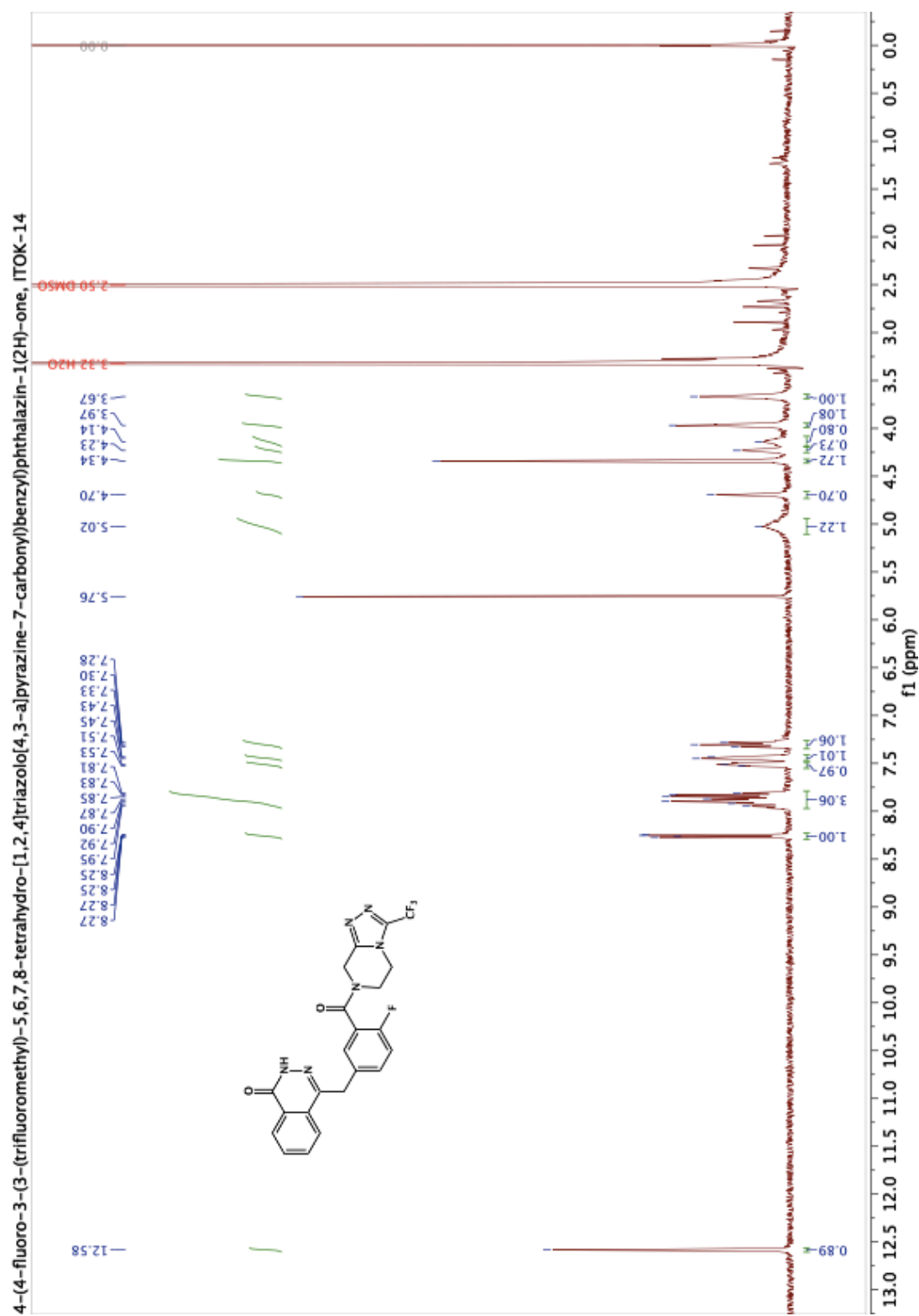


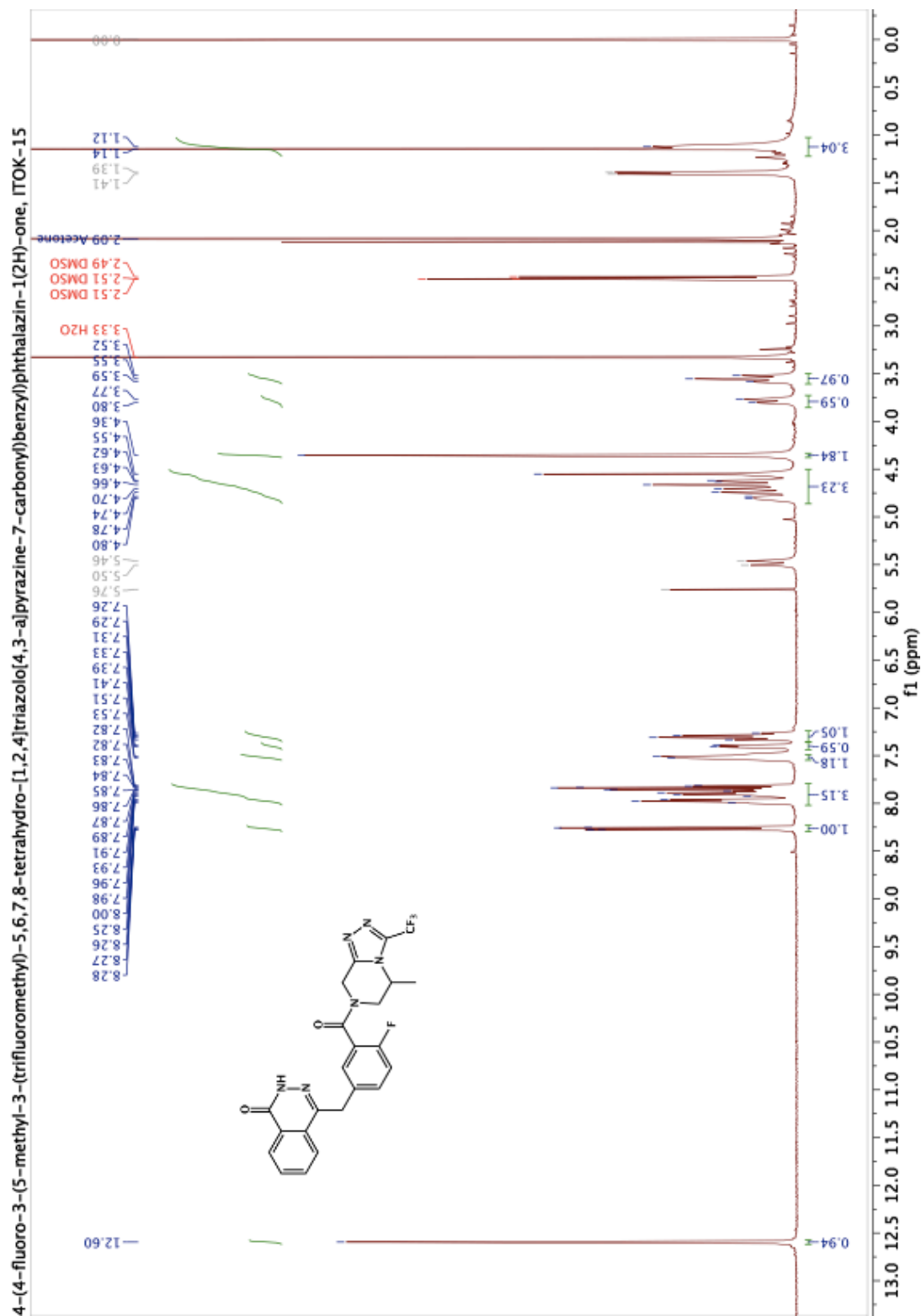


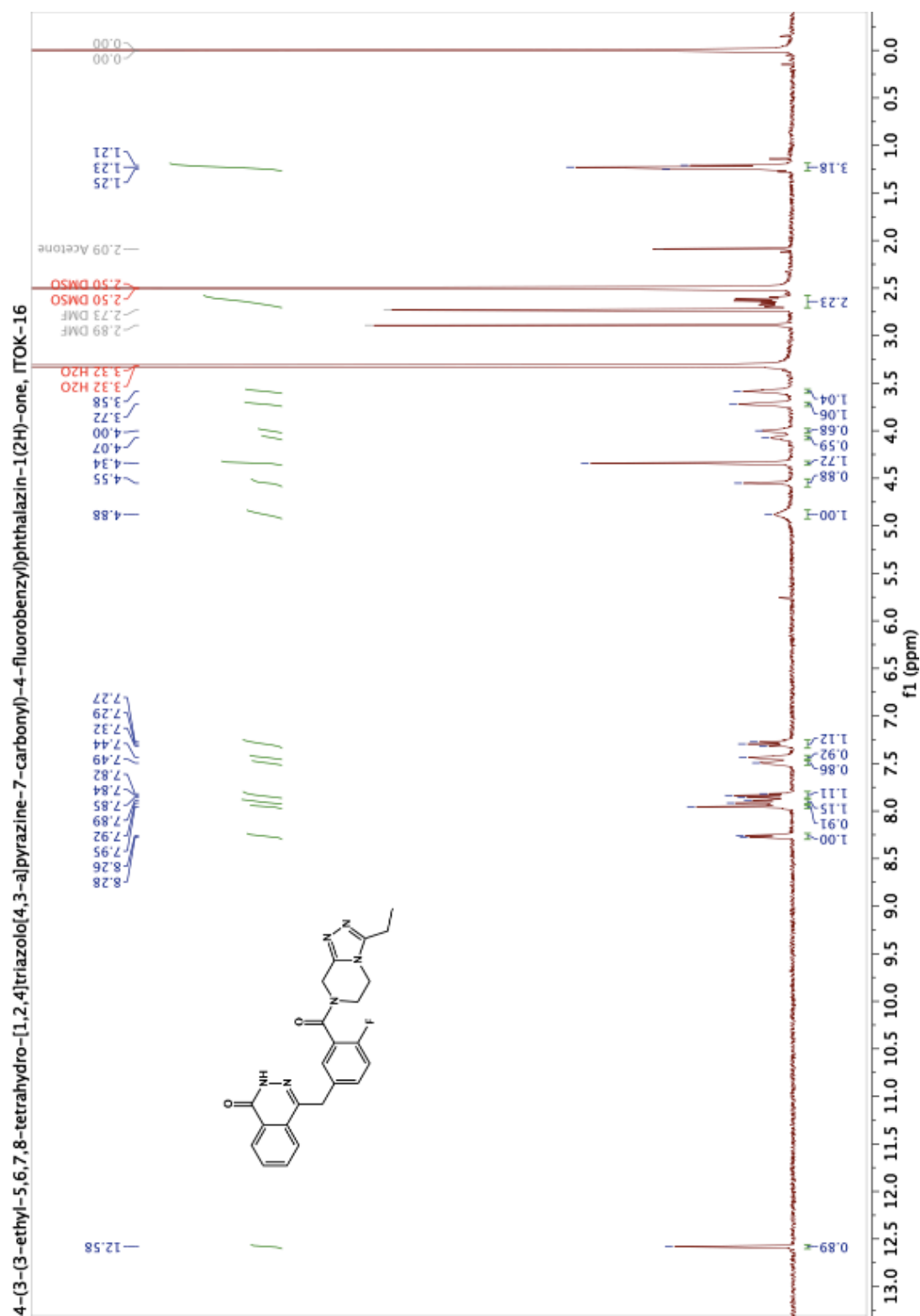


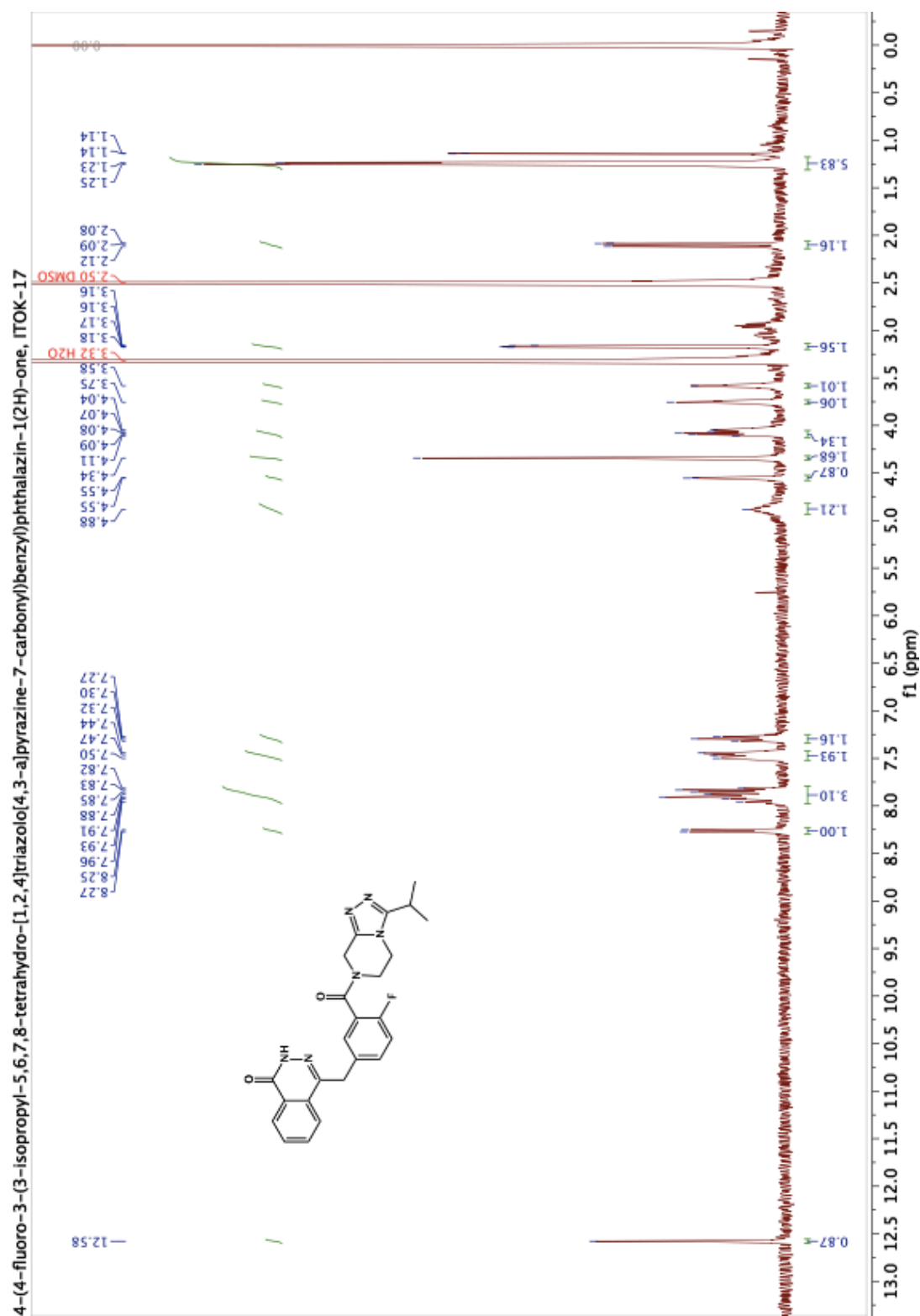






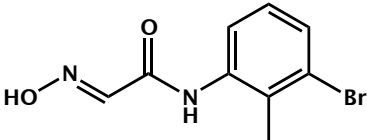
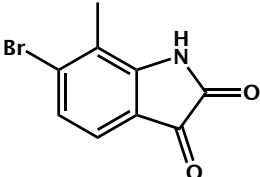
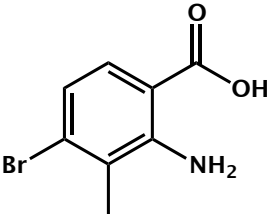
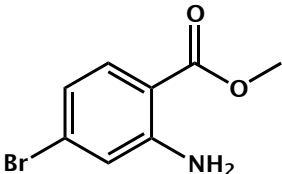




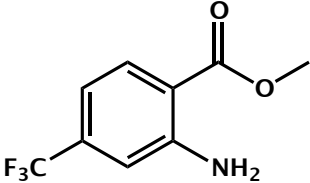
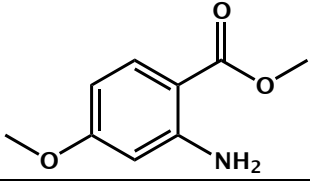
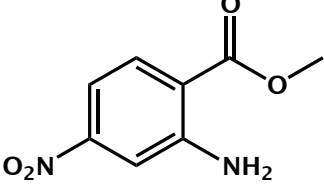
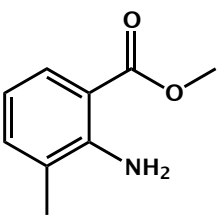
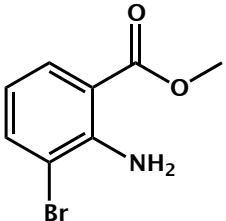


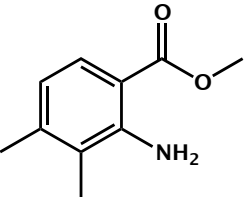
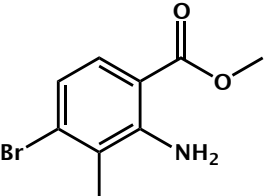
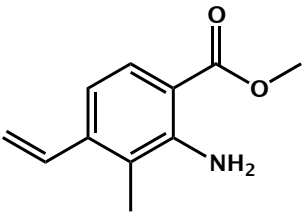
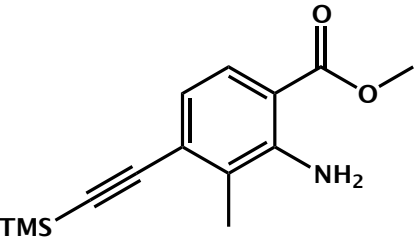
## Appendix F: Reported Compound Literature References

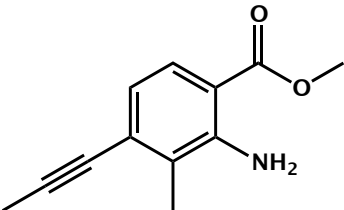
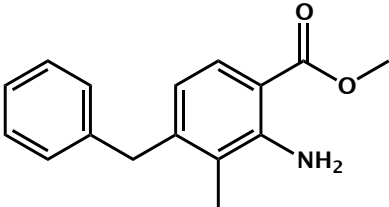
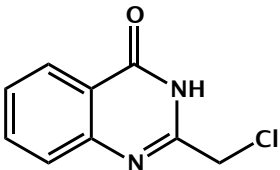
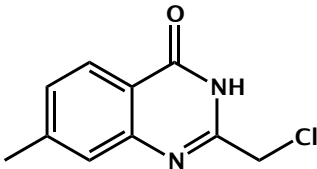
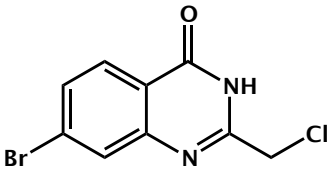
**Table F-1** First reported literature source and CAS numbers for synthesized compounds. Novel compounds, and compounds reported as commercially available but without literature reports, are indicated. The information reported here reflects SciFinder results as of 11 pm January 31st, 2019.

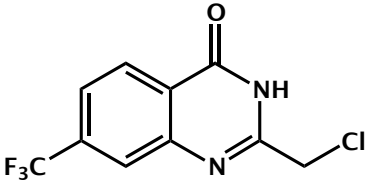
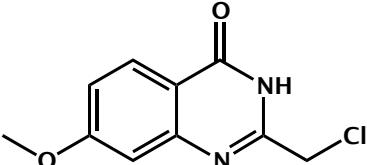
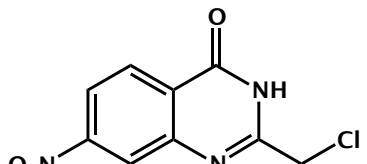
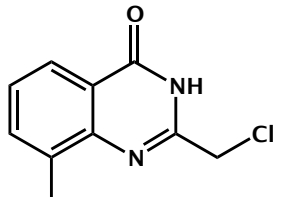
Structure	IUPAC Name	CAS	Literature
	<i>2-hydroxyimino-N-(2-methyl-3-bromo-phenyl)-acetamide</i>	129833-52-9	Engelhardt, H. et al. Indolinone analogues as BRD4 inhibitors. WO2014154760 A1, 2014
	<i>6-bromo-7-methylindoline-2,3-dione</i>	129833-54-1	Engelhardt, H. et al. Indolinone analogues as BRD4 inhibitors. WO2014154760 A1, 2014
	<i>2-amino-4-bromo-3-methylbenzoic acid</i>	129833-29-0	Engelhardt, H. et al. Indolinone analogues as BRD4 inhibitors. WO2014154760 A1, 2014
	<i>Methyl 2-amino-4-bromobenzoate</i>	135484-83-2	Robertson, A. & Waters, R. B. IX.—Syntheses of glucosides. Part VII. The synthesis of 6-bromoindican. <i>J. Chem. Soc.</i> <b>0</b> , 72–76 (1931).

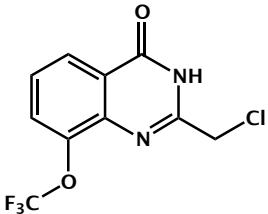
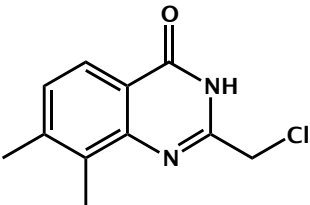
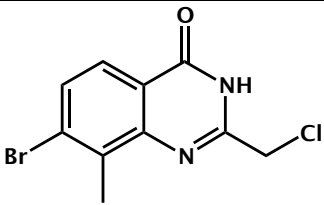
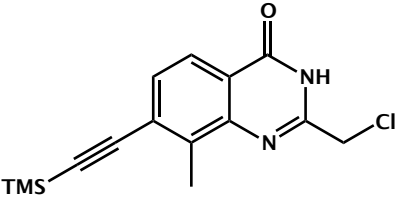
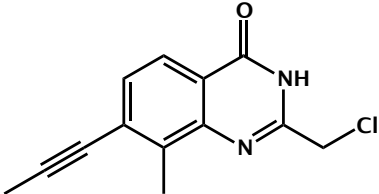


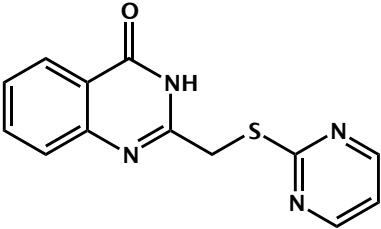
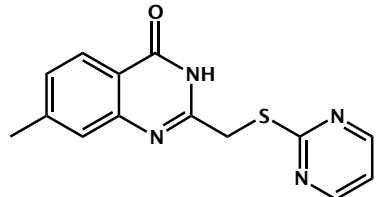
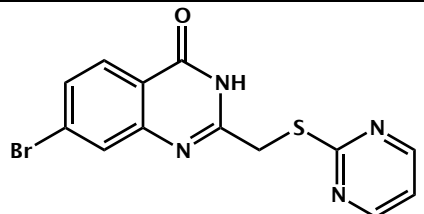
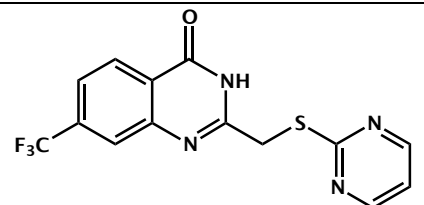
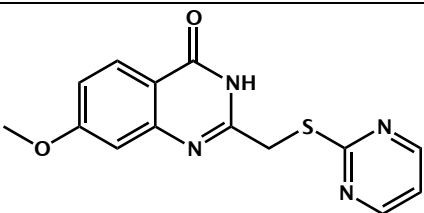
	<i>Methyl 2-amino-4-(trifluoromethyl)benzoate</i>	61500-87-6	Cotrel, C. et. Al; <u>Heterocyclic compounds for pharmaceutical use</u> , Ger. Offen. (1976), DE 2615067 A1 Oct 28, 1976.
	<i>Methyl 2-amino-4-methoxybenzoate</i>	50413-30-4	Friedlander, P., Bruckner, S. & Deutsch, G. Bromo- and Methoxy Derivatives of Indigo. <i>Justus Liebigs Annalen der Chemie</i> <b>388</b> ,
	<i>Methyl 2-amino-4-nitrobenzoate</i>	3558-19-8	Da Settimo, A. & Saettone, M. F. Nitration of methyl- substituted indole- 3- carboxaldehydes in sulfuric acid. <i>Tetrahedron</i> <b>21</b> , 1923–1929 (1965).
	<i>Methyl 2-amino-3-methylbenzoate</i>	22223-49-0	Overberger, C. G., Lombardino, J. G., Tashlick, I. & Hiskey, R. G. SEVEN- AND EIGHT-MEMBERED RING AZO COMPOUNDS. <i>J. Am. Chem. Soc.</i> <b>79</b> , 2662–2662 (1957).
	<i>Methyl 2-amino-3-bromobenzoate</i>	104670-74-8	Oba, H. et. al; Syntheses of aminobenzoic acids, Kokai Tokkyo Koho (1986), JP 61012653 A Jan 21, 1986.

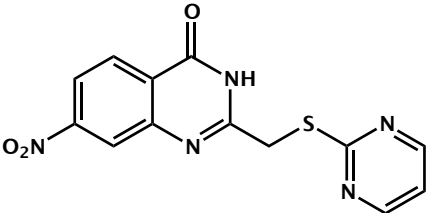
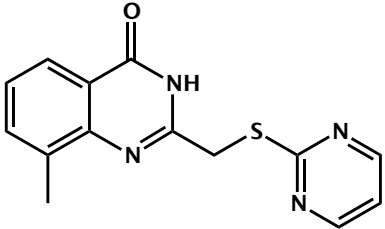
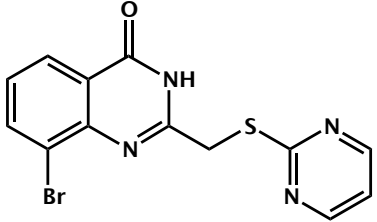
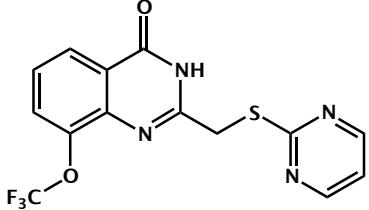
	<i>Methyl 2-amino-3,4-dimethylbenzoate</i>	31928-20-8	Gabel, L. P.; Simpson, W. Physiologically active 4-amino-quinazolines. Ger. Offen. (1970), DE 2009472 A Sep 17, 1970
	<i>Methyl 2-amino-4-bromo-3-methylbenzoate</i>	851045-38-0	Cao, G. et al. Preparation of benzazepines as inhibitors of cholesterol ester transfer protein for treating dyslipidemia, PCT Int. Appl. (2005), WO 2005037796 A1 Apr 28, 2005.
	<i>Methyl 2-amino-3-methyl-4-vinylbenzoate</i>		Novel compound
	<i>methyl 2-amino-3-methyl-4-((trimethylsilyl)ethynyl)benzoate</i>		Novel compound

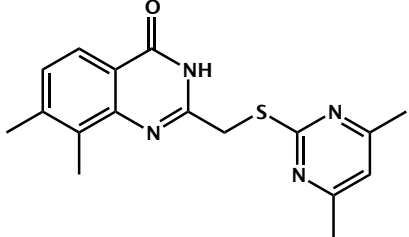
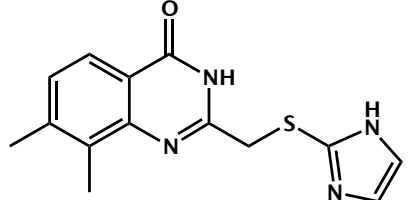
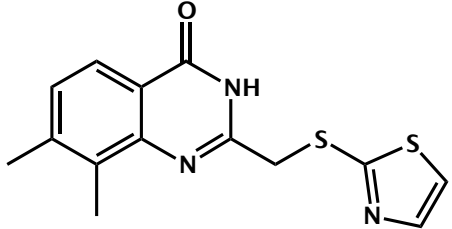
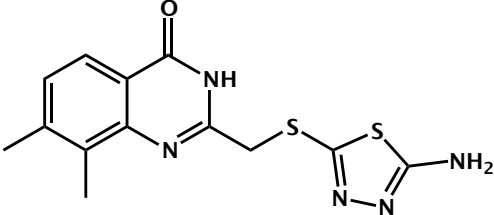
	<i>Methyl 2-amino-3-methyl-4-(prop-1-yn-1-yl)benzoate</i>		Novel compound
	<i>Methyl 2-amino-4-benzyl-3-methylbenzoate</i>		Novel compound
	<i>2-(chloromethyl)quinazolin-4(3H)-one</i>	3817-05-8	Dymek, W. & Lubimowski, B. Synthesis and transformations of 2- chloromethyl- 4- quinazolinone. <i>Dissertationes Pharmaceuticae</i> <b>16</b> , 247–253
	<i>2-(chloromethyl)-7-methylquinazolin-4(3H)-one</i>	1263413-62-2	Blunt, R et. al. <u>Preparation of benzoxazinone derivatives as GlyT1 inhibitors useful in the treatment of GlyT1 mediated disorders</u> , PCT Int. Appl. (2011), WO 2011012622 A1 Feb 03, 2011.
	<i>7-bromo-2-(chloromethyl)quinazolin-4(3H)-one</i>	573681-17-1	Bakthavatchatam, R. et. al, <u>Preparation of substituted quinazolin-4-ylamine analogs as VR1 capsaicin receptor antagonists for relieving pain</u> ,

			PCT Int. Appl. (2003), WO 2003062209 A2 Jul 31, 2003.
	2-(chloromethyl)-7-(trifluoromethyl)quinazolin-4(3H)-one	730976-60-0	Bakthavatchalam, R. et. al, <u>Preparation of quinazolinamines and analogs as capsaicin receptor agonists</u> , U.S. Pat. Appl. Publ. (2006), US 20060194805 A1 Aug 31, 2006.
	2-(chloromethyl)-7-methoxyquinazolin-4(3H)-one	1257043-54-1	Blunt, R. et. Al; <u>Preparation of benzoxazinone derivatives as GlyT1 inhibitors useful in the treatment of GlyT1 mediated disorders</u> , PCT Int. Appl. (2011), WO 2011012622 A1 Feb 03, 2011.
	2-(chloromethyl)-7-nitroquinazolin-4(3H)-one	1608460-41-8	Cao, S. et. Al; <u>Preparation of 4(3H)-quinazolinone derivatives as anticancer agents</u> , Faming Zhuanli Shenqing (2014), CN 103755647 A Apr 30, 2014.
	2-(chloromethyl)-8-methylquinazolin-4(3H)-one	848369-52-8	Cao, S. et. Al; <u>Preparation of 4(3H)-quinazolinone derivatives as anticancer agents</u> . Faming Zhuanli Shenqing (2014), CN 103755647 A Apr 30, 2014.

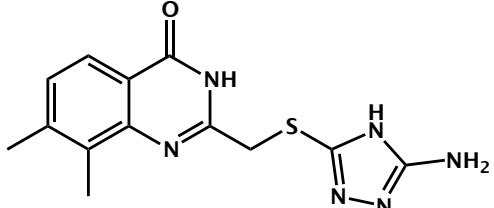
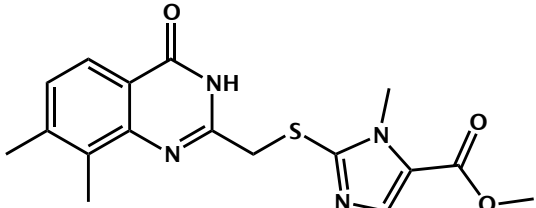
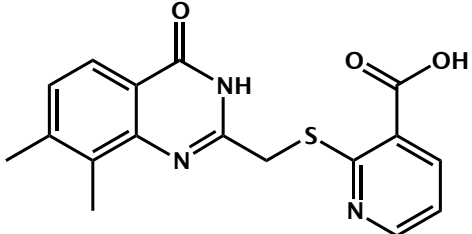
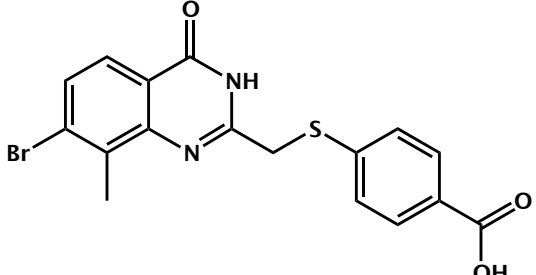
	2-(chloromethyl)-8-(trifluoromethoxy)quinazolin-4(3H)-one		Novel compound
	2-(chloromethyl)-7,8-dimethylquinazolin-4(3H)-one		Novel compound
	7-bromo-2-(chloromethyl)-8-methylquinazolin-4(3H)-one	169207 8-32-2	Reported commercially available, no literature references.
	2-(chloromethyl)-7-ethynyl-8-methylquinazolin-4(3H)-one		Novel compound
	2-(chloromethyl)-8-methyl-7-(prop-1-yn-1-yl)quinazolin-4(3H)-one		Novel compound

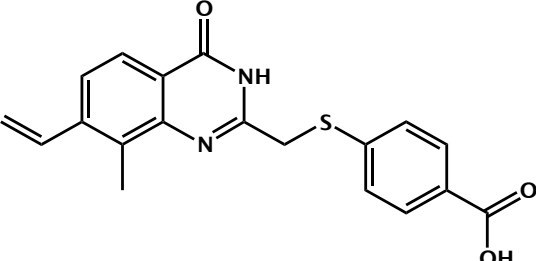
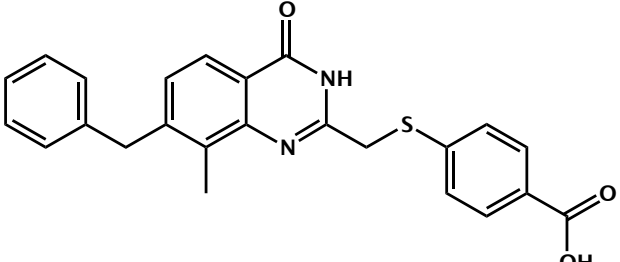
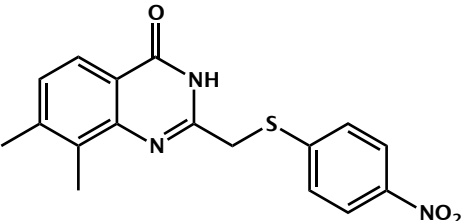
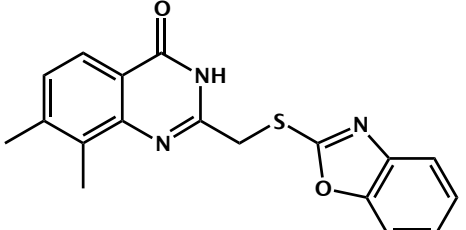
	<i>2-((pyrimidin-2-ylthio)methyl)quinazolin-4(3H)-one</i>	896024-56-9	Reported commercially available, no literature references.
	<i>7-methyl-2-((pyrimidin-2-ylthio)methyl)quinazolin-4(3H)-one</i>		Novel compound
	<i>7-bromo-2-((pyrimidin-2-ylthio)methyl)quinazolin-4(3H)-one</i>		Novel compound
	<i>2-((pyrimidin-2-ylthio)methyl)-7-(trifluoromethyl)quinazolin-4(3H)-one</i>		Novel compound
	<i>7-methoxy-2-((pyrimidin-2-ylthio)methyl)quinazolin-4(3H)-one</i>		Novel compound

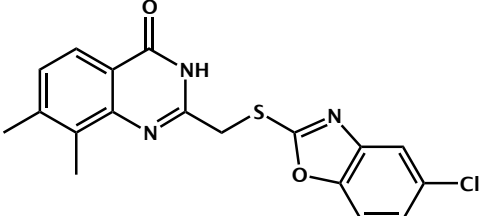
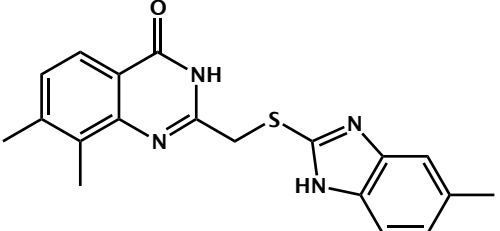
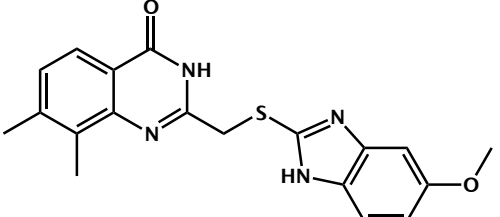
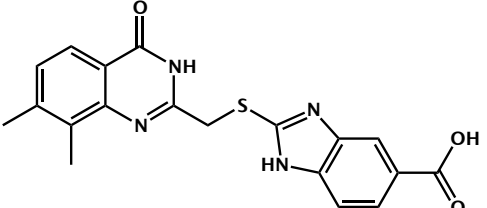
	7-nitro-2-((pyrimidin-2-ylthio)methyl)quinazolin-4(3H)-one		Novel compound
	8-methyl-2-((pyrimidin-2-ylthio)methyl)quinazolin-4(3H)-one	923807-40-3	Wahlberg, E. <i>et al.</i> Family-wide chemical profiling and structural analysis of PARP and tankyrase inhibitors. <i>Nat Biotechnol</i> <b>30</b> , 283–288 (2012).
	8-bromo-2-((pyrimidin-2-ylthio)methyl)quinazolin-4(3H)-one		Novel compound
	2-((pyrimidin-2-ylthio)methyl)-8-(trifluoromethoxy)quinazolin-4(3H)-one		Novel compound

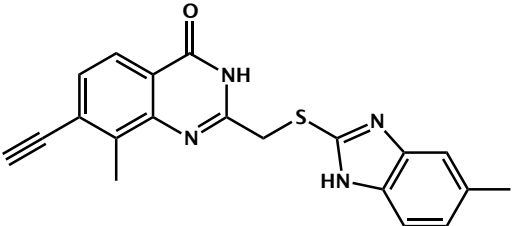
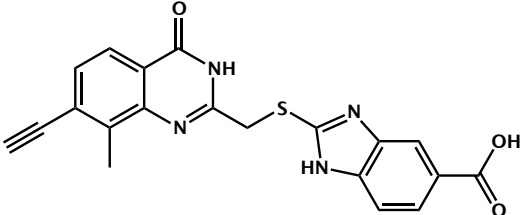
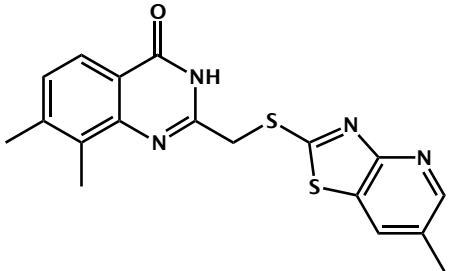
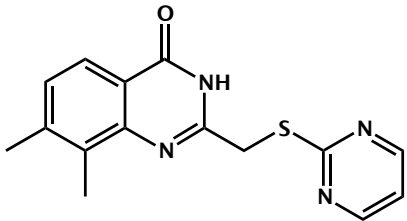
	<p>2-(((4,6-dimethylpyrimidin-2-yl)thio)methyl)-7,8-dimethylquinazolin-4(3H)-one</p>		<p>Novel compound</p>
	<p>2-(((1H-imidazol-2-yl)thio)methyl)-7,8-dimethylquinazolin-4(3H)-one</p>		<p>Novel compound</p>
	<p>7,8-dimethyl-2-((thiazol-2-ylthio)methyl)quinazolin-4(3H)-one</p>		<p>Novel compound</p>
	<p>2-(((5-amino-1,3,4-thiadiazol-2-yl)thio)methyl)-7,8-dimethylquinazolin-4(3H)-one</p>		<p>Novel compound</p>

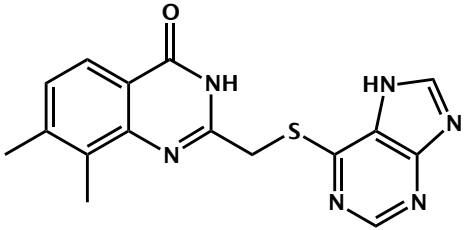
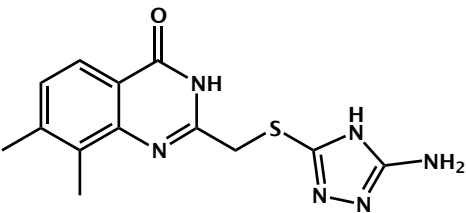
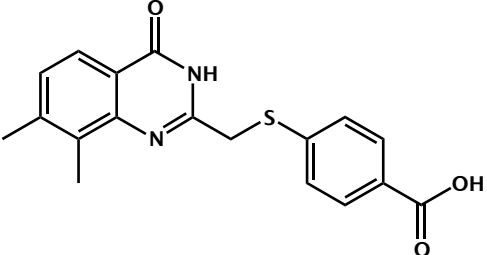
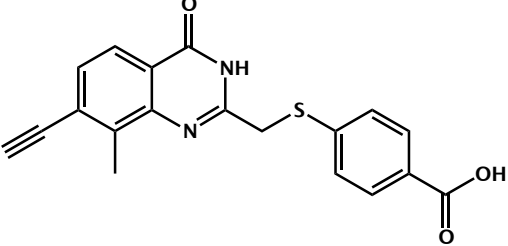


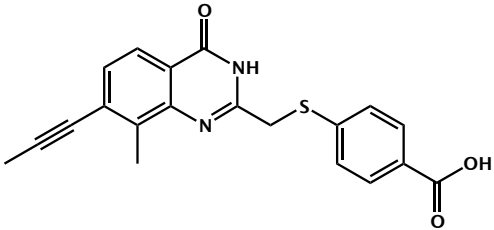
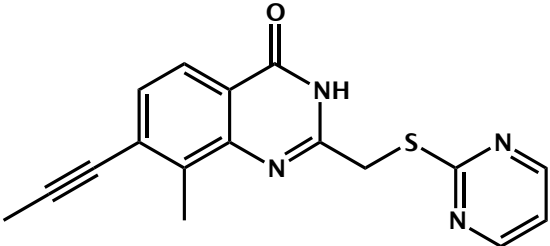
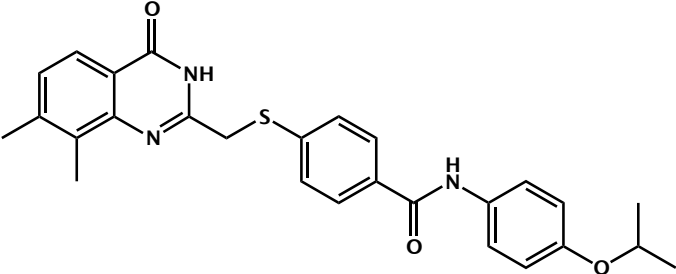
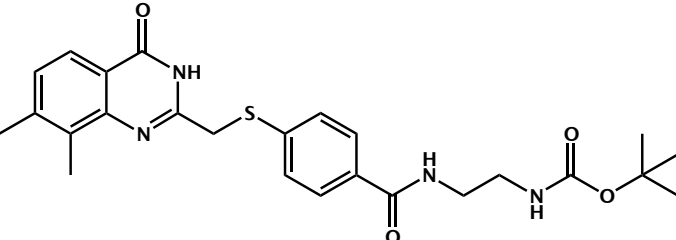
	<p>2-(((5-amino-1,3,4-thiadiazol-2-yl)thio)methyl)-7,8-dimethylquinazolin-4(3H)-one</p>		<p>Novel compound</p>
	<p>Methyl 2-(((7,8-dimethyl-4-oxo-3,4-dihydroquinazolin-2-yl)methyl)thio)-1-methyl-1H-imidazole-5-carboxylate</p>		<p>Novel compound</p>
	<p>2-(((7,8-dimethyl-4-oxo-3,4-dihydroquinazolin-2-yl)methyl)thio)nicotinic acid</p>		<p>Novel compound</p>
	<p>4-(((7-bromo-8-methyl-4-oxo-3,4-dihydroquinazolin-2-yl)methyl)thio)benzoic acid</p>		<p>Novel compound</p>

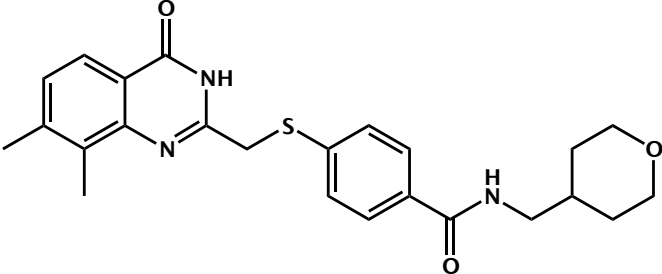
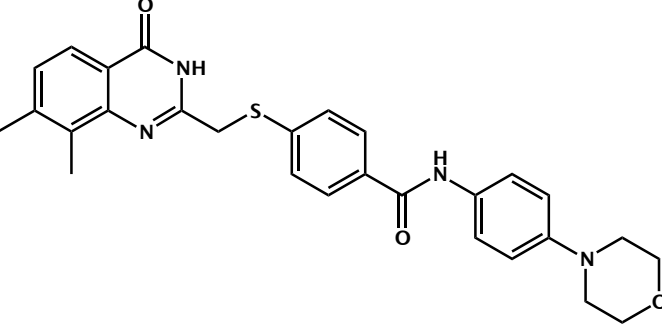
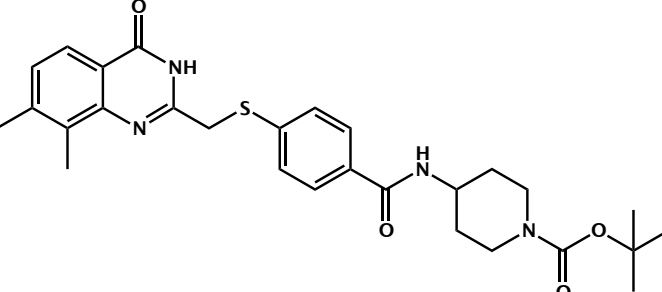
	<p>4-(((8-methyl-4-oxo-7-vinyl-3,4-dihydroquinazolin-2-yl)methyl)thio)benzoic acid</p>		<p>Novel compound</p>
	<p>4-(((7-benzyl-8-methyl-4-oxo-3,4-dihydroquinazolin-2-yl)methyl)thio)benzoic acid</p>		<p>Novel compound</p>
	<p>7,8-dimethyl-2-(((4-nitrophenyl)thio)methyl)quinazolin-4(3H)-one,</p>		<p>Novel compound</p>
	<p>2-((benzo[d]oxazol-2-ylthio)methyl)-7,8-dimethylquinazolin-4(3H)-one</p>		<p>Novel compound</p>

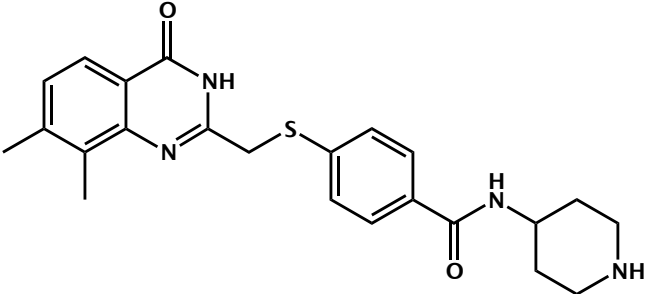
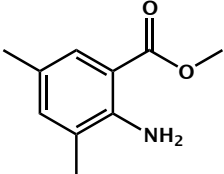
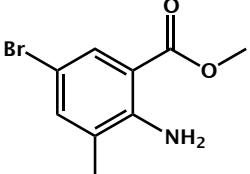
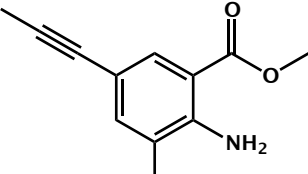
	<p>2-(((6-chlorobenzo[d]oxazol-2-yl)thio)methyl)-7,8-dimethylquinazolin-4(3H)-one</p>		<p>Novel compound</p>
	<p>7,8-dimethyl-2-(((5-methyl-1H-benzo[d]imidazol-2-yl)thio)methyl)quinazolin-4(3H)-one</p>		<p>Novel compound</p>
	<p>2-(((6-chlorobenzo[d]oxazol-2-yl)thio)methyl)-7,8-dimethylquinazolin-4(3H)-one</p>		<p>Novel compound</p>
	<p>2-(((7,8-dimethyl-4-oxo-3,4-dihydroquinazolin-2-yl)methyl)thio)-1H-benzo[d]imidazole-6-carboxylic acid</p>		<p>Novel compound</p>

	<p>7,8-dimethyl-2-(((6-methyl-1H-benzo[d]imidazol-2-yl)thio)methyl)quinazolin-4(3H)-one</p>		<p>Novel compound</p>
	<p>2-(((7-ethynyl-8-methyl-4-oxo-3,4-dihydroquinazolin-2-yl)methyl)thio)-1H-benzo[d]imidazole-6-carboxylic acid</p>		<p>Novel compound</p>
	<p>7,8-dimethyl-2-(((6-methylthiazolo[4,5-b]pyridin-2-yl)thio)methyl)quinazolin-4(3H)-one</p>		<p>Novel compound</p>
	<p>7,8-dimethyl-2-((pyrimidin-2-ylthio)methyl)quinazolin-4(3H)-one</p>		<p>Kirby, I. T. <i>et al.</i> A Potent and Selective PARP11 Inhibitor Suggests Coupling between Cellular Localization and Catalytic Activity. <i>Cell Chemical Biology</i> (2018). doi:10.1016/j.chembiol.2018.09.011</p>

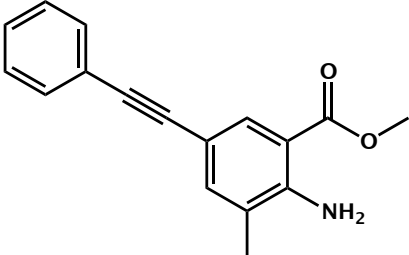
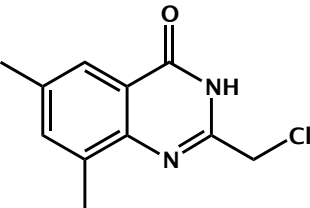
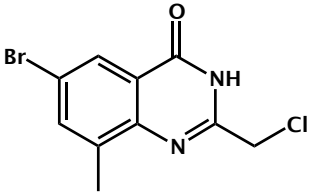
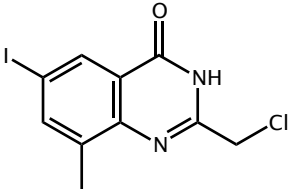
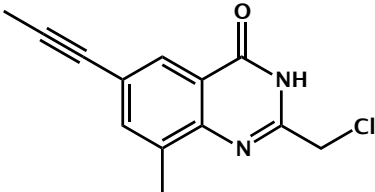
	<p>2-(((7H-purin-6-yl)thio)methyl)-7,8-dimethylquinazolin-4(3H)-one</p>	<p>Kirby, I. T. <i>et al.</i> A Potent and Selective PARP11 Inhibitor Suggests Coupling between Cellular Localization and Catalytic Activity. <i>Cell Chemical Biology</i> (2018). doi:10.1016/j.chembiol.2018.09.011</p>
	<p>2-(((5-amino-4H-1,2,4-triazol-3-yl)thio)methyl)-7,8-dimethylquinazolin-4(3H)-one</p>	<p>Kirby, I. T. <i>et al.</i> A Potent and Selective PARP11 Inhibitor Suggests Coupling between Cellular Localization and Catalytic Activity. <i>Cell Chemical Biology</i> (2018). doi:10.1016/j.chembiol.2018.09.011</p>
	<p>4-(((7,8-dimethyl-4-oxo-3,4-dihydroquinazolin-2-yl)methyl)thio)benzoic acid</p>	<p>Kirby, I. T. <i>et al.</i> A Potent and Selective PARP11 Inhibitor Suggests Coupling between Cellular Localization and Catalytic Activity. <i>Cell Chemical Biology</i> (2018). doi:10.1016/j.chembiol.2018.09.011</p>
	<p>4-(((7-ethynyl-8-methyl-4-oxo-3,4-dihydroquinazolin-2-yl)methyl)thio)benzoic acid</p>	<p>Kirby, I. T. <i>et al.</i> A Potent and Selective PARP11 Inhibitor Suggests Coupling between Cellular Localization and Catalytic Activity. <i>Cell Chemical Biology</i> (2018). doi:10.1016/j.chembiol.2018.09.011</p>

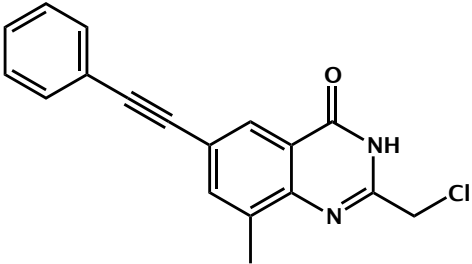
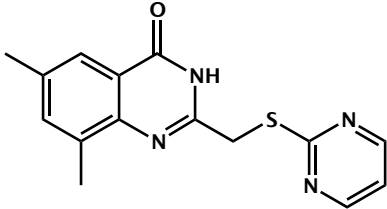
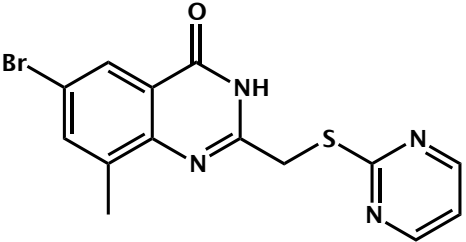
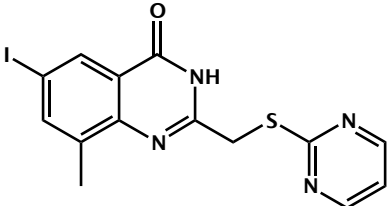
	<p>4-(((8-methyl-4-oxo-7-(prop-1-yn-1-yl)-3,4-dihydroquinazolin-2-yl)methyl)thio)benzoic acid</p>		<p>Kirby, I. T. <i>et al.</i> A Potent and Selective PARP11 Inhibitor Suggests Coupling between Cellular Localization and Catalytic Activity. <i>Cell Chemical Biology</i> (2018). doi:10.1016/j.chembiol.2018.09.011</p>
	<p>8-methyl-7-(prop-1-yn-1-yl)-2-((pyrimidin-2-ylthio)methyl)quinazolin-4(3H)-one</p>		<p>Kirby, I. T. <i>et al.</i> A Potent and Selective PARP11 Inhibitor Suggests Coupling between Cellular Localization and Catalytic Activity. <i>Cell Chemical Biology</i> (2018). doi:10.1016/j.chembiol.2018.09.011</p>
	<p>4-(((7,8-dimethyl-4-oxo-3,4-dihydroquinazolin-2-yl)methyl)thio)-N-(4-isopropoxyphenyl)benzamide</p>		<p>Novel compound</p>
	<p>Tert-butyl (2-(4-(((7,8-dimethyl-4-oxo-3,4-dihydroquinazolin-2-yl)methyl)thio)benzamido)ethyl)carbamate</p>		<p>Novel compound</p>

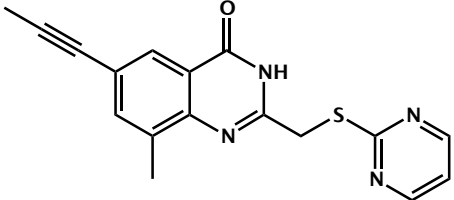
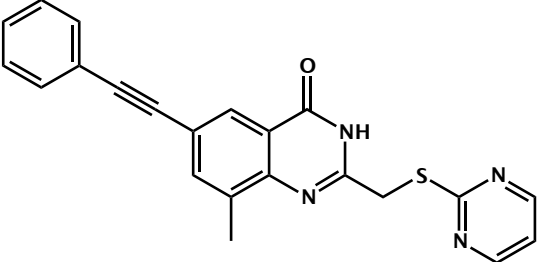
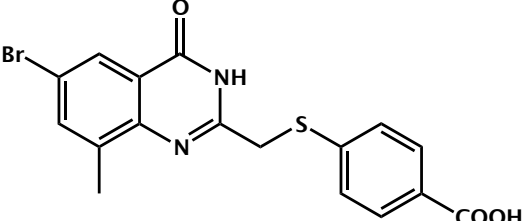
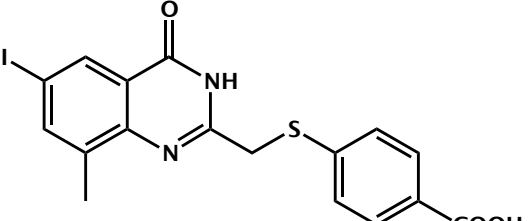
	<p>4-(((7,8-dimethyl-4-oxo-3,4-dihydroquinazolin-2-yl)methyl)thio)-N-((tetrahydro-2H-pyran-4-yl)methyl)benzamide</p>		<p>Novel compound</p>
	<p>4-(((7,8-dimethyl-4-oxo-3,4-dihydroquinazolin-2-yl)methyl)thio)-N-(4-morpholinophenyl)benzamide</p>		<p>Novel compound</p>
	<p>Tert-butyl 4-(4-(((7,8-dimethyl-4-oxo-3,4-dihydroquinazolin-2-yl)methyl)thio)benzamido)piperidine-1-carboxylate</p>		<p>Novel compound</p>

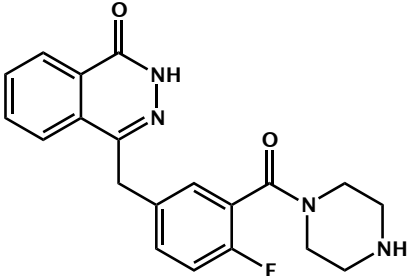
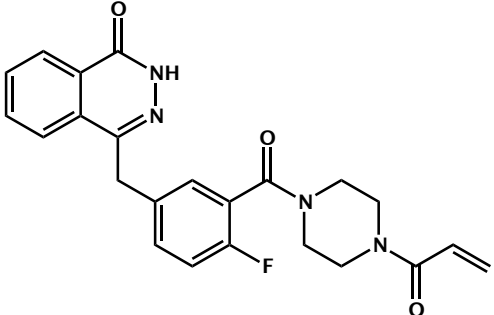
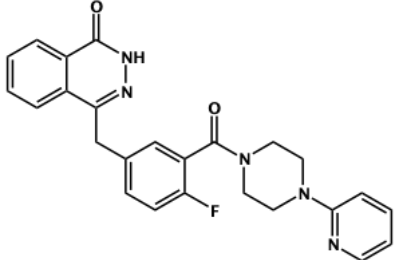
	<p>4-(((7,8-dimethyl-4-oxo-3,4-dihydroquinazolin-2-yl)methyl)thio)-N-(piperidin-4-yl)benzamide</p>		<p>Novel compound</p>
	<p>Methyl 2-amino-3,5-dimethylbenzoate</p>	<p>206551-23-7</p>	<p>Levin, J.; <u>The preparation and use of ortho-sulfonamido aryl hydroxamic acids as matrix metalloproteinase and TACE inhibitors</u>. PCT Int. Appl. (1998), WO 9816503 A2 Apr 23, 1998.</p>
	<p>Methyl 2-amino-5-bromo-3-methylbenzoate</p>	<p>206548-13-2</p>	<p>Levin, J. et. al, <b><u>The preparation and use of ortho-sulfonamido aryl hydroxamic acids as matrix metalloproteinase and TACE inhibitors</u></b>, PCT Int. Appl. (1998), WO 9816503 A2 Apr 23, 1998.</p>
	<p>Methyl 2-amino-3-methyl-5-(prop-1-yn-1-yl)benzoate</p>		<p>Novel compound</p>

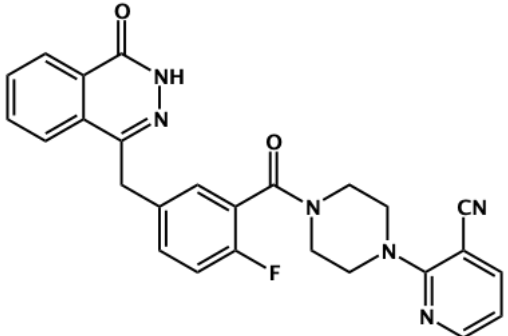
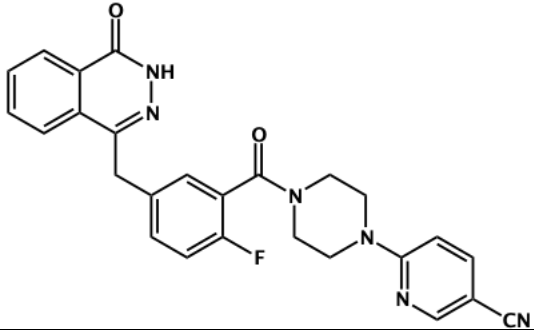
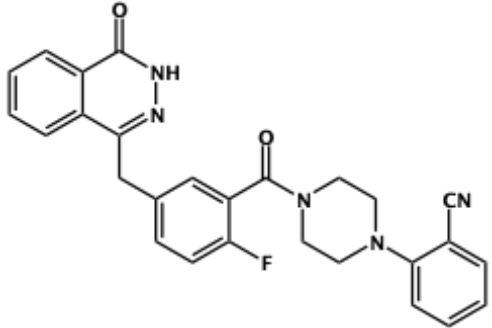


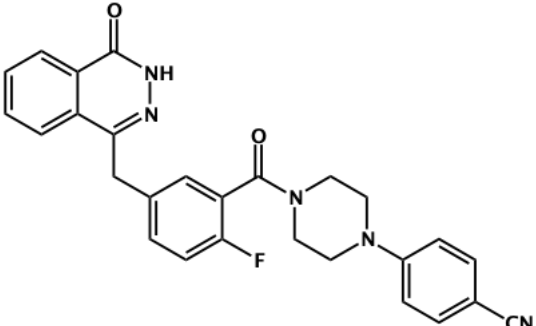
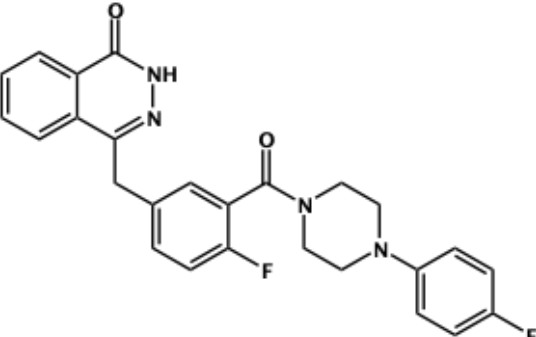
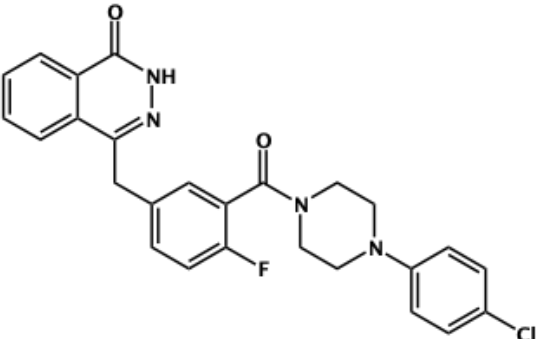
	<i>Methyl 2-amino-3-methyl-5-(phenylethynyl)benzoate</i>		Novel compound
	<i>2-(chloromethyl)-6,8-dimethylquinazolin-4(3H)-one</i>	694456-71-7	Reported commercially available, no literature references.
	<i>6-bromo-2-(chloromethyl)-8-methylquinazolin-4(3H)-one</i>	1695884-59-3	Reported commercially available, no literature references.
	<i>2-(chloromethyl)-6-iodo-8-methylquinazolin-4(3H)-one</i>		Novel compound
	<i>2-(chloromethyl)-8-methyl-6-(prop-1-yn-1-yl)quinazolin-4(3H)-one</i>		Novel compound

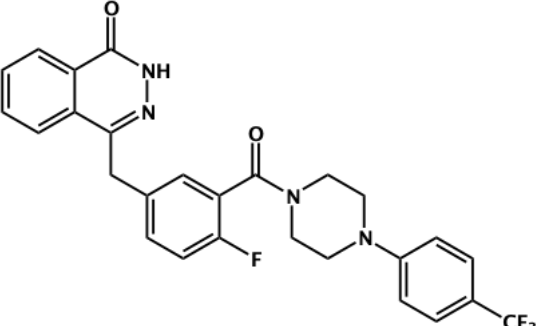
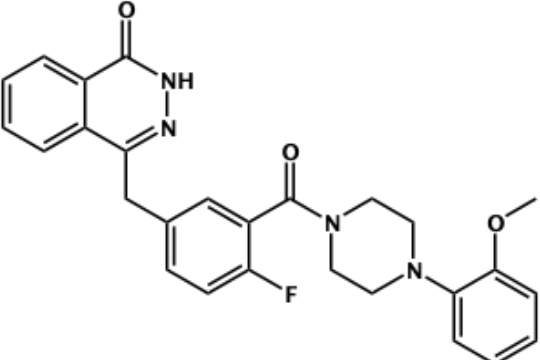
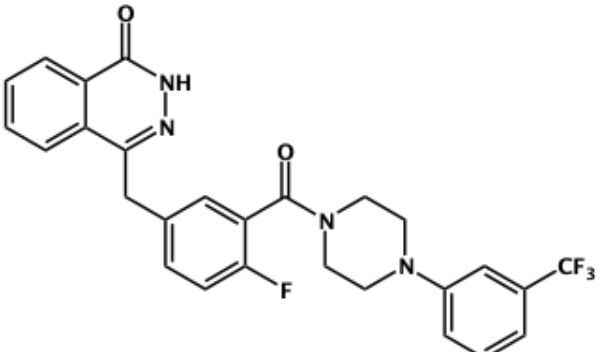
	<p><i>2-(chloromethyl)-8-methyl-6-(phenylethynyl)quinazolin-4(3H)-one</i></p>		<p>Novel compound</p>
	<p><i>6,8-dimethyl-2-((pyrimidin-2-ylthio)methyl)quinazolin-4(3H)-on</i></p>		<p>Novel compound</p>
	<p><i>6-bromo-8-methyl-2-((pyrimidin-2-ylthio)methyl)quinazolin-4(3H)-one</i></p>		<p>Novel compound</p>
	<p><i>6-iodo-8-methyl-2-((pyrimidin-2-ylthio)methyl)quinazolin-4(3H)-one</i></p>		<p>Novel compound</p>

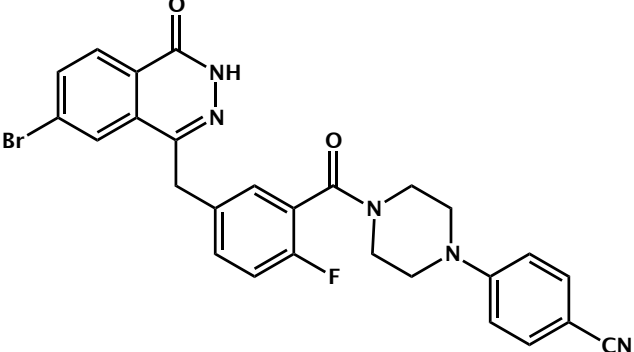
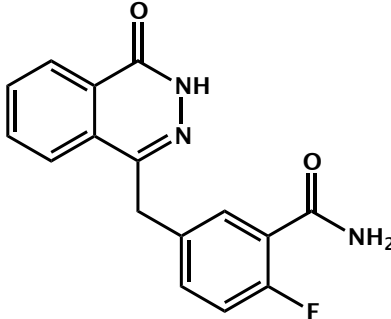
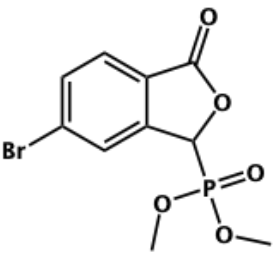
	<p><i>8-methyl-6-(prop-1-yn-1-yl)-2-((pyrimidin-2-ylthio)methyl)quinazolin-4(3H)-one</i></p>		<p>Novel compound</p>
	<p><i>8-methyl-6-(phenylethynyl)-2-((pyrimidin-2-ylthio)methyl)quinazolin-4(3H)-one</i></p>		<p>Novel compound</p>
	<p><i>4-(((6-bromo-8-methyl-4-oxo-3,4-dihydroquinazolin-2-yl)methyl)thio)benzoic acid</i></p>		<p>Novel compound</p>
	<p><i>4-(((6-iodo-8-methyl-4-oxo-3,4-dihydroquinazolin-2-yl)methyl)thio)benzoic acid</i></p>		<p>Novel compound</p>

	<p>4-(4-fluoro-3-(piperazine-1-carbonyl)benzyl)phthalazin-1(2H)-one</p>	<p>763111-47-3</p>	<p>Martin, N. et. al, <u>Preparation of phthalazinones as PARP inhibitors</u>, PCT Int. Appl. (2004), WO 2004080976 A1 Sep 23, 2004.</p>
	<p>4-(3-(4-acryloylpiperazine-1-carbonyl)-4-fluorobenzyl)phthalazin-1(2H)-one</p>		<p>Gao, H. et. al, <u>Phthalazone derivative prodrug or its pharmaceutically acceptable salt, and pharmaceutical composition and application thereof</u>, Faming Zhuanli Shenqing (2018), CN 108383798 A Aug 10, 2018.</p>
	<p>4-(4-fluoro-3-(4-(pyridin-2-yl)piperazine-1-carbonyl)benzyl)phthalazin-1(2H)-one</p>	<p>1070772-11-0</p>	<p>Menear, K. A. et al. 4-[3-(4-cyclopropanecarbonylpiperazine-1-carbonyl)-4-fluorobenzyl]-2H-phthalazin-1-one: a novel bioavailable inhibitor of poly(ADP-ribose) polymerase-1. <i>J. Med. Chem.</i> <b>51</b>, 6581–6591 (2008).</p>

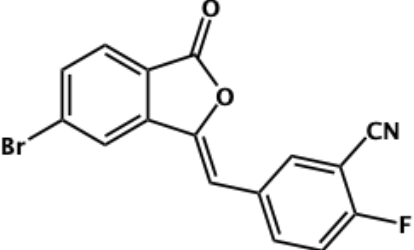
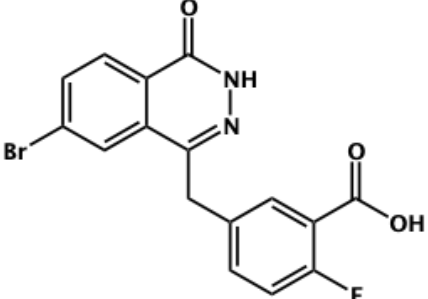
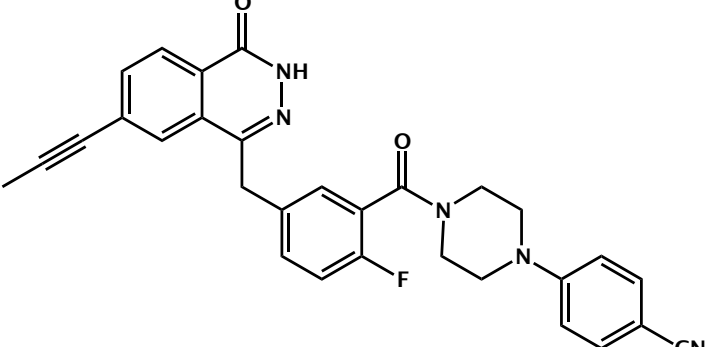
	<p>2-(4-(2-fluoro-5-((4-oxo-3,4-dihydrophthalazin-1-yl)methyl)benzoyl)piperazin-1-yl)nicotinonitrile</p>		<p>Novel compound</p>
	<p>6-(4-(2-fluoro-5-((4-oxo-3,4-dihydrophthalazin-1-yl)methyl)benzoyl)piperazin-1-yl)nicotinonitrile</p>		<p>Novel compound</p>
	<p>2-(4-(2-fluoro-5-((4-oxo-3,4-dihydrophthalazin-1-yl)methyl)benzoyl)piperazin-1-yl)benzonitrile</p>		<p>Novel compound</p>

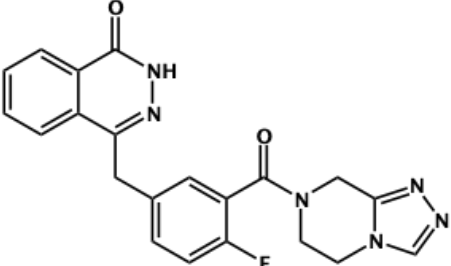
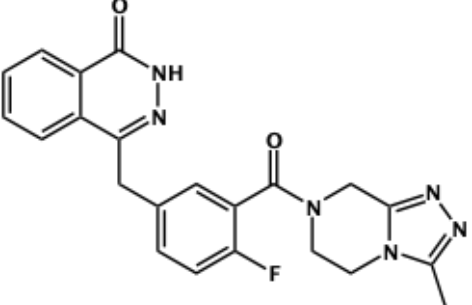
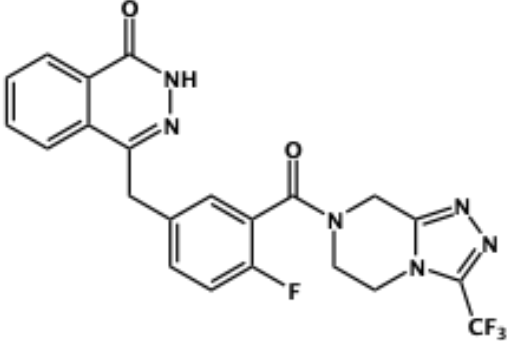
	<p>4-(4-(2-fluoro-5-((4-oxo-3,4-dihydrophthalazin-1-yl)methyl)benzoyl)piperazin-1-yl)benzonitrile</p>		<p>Novel compound</p>
	<p>4-(4-fluoro-3-(4-(4-fluorophenyl)piperazine-1-carbonyl)benzyl)phthalazin-1(2H)-one</p>	<p>848135-90-0</p>	<p>Martin, N. et. al, <u>Preparation of phthalazinones as PARP inhibitors</u>, PCT Int. Appl. (2004), WO 2004080976 A1 Sep 23, 2004.</p>
	<p>4-(3-(4-(4-chlorophenyl)piperazine-1-carbonyl)-4-fluorobenzyl)phthalazin-1(2H)-one</p>		<p>Novel compound</p>

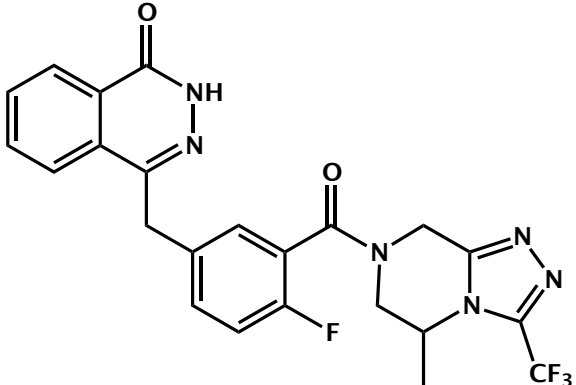
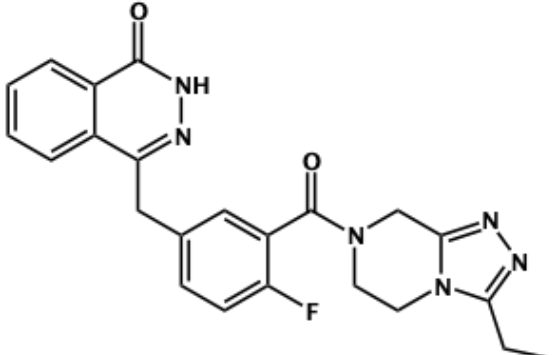
	<p>4-(4-fluoro-3-(4-(4-(trifluoromethyl)phenyl)piperazine-1-carbonyl)benzyl)phthalazin-1(2H)-one</p>		<p>Novel compound</p>
	<p>4-(4-fluoro-3-(4-(2-methoxyphenyl)piperazine-1-carbonyl)benzyl)phthalazin-1(2H)-one</p>	<p>848135-82-0</p>	<p>Martin, N. et. al, <u>Preparation of phthalazinones as PARP inhibitors</u>, PCT Int. Appl. (2004), WO 2004080976 A1 Sep 23, 2004.</p>
	<p>4-(4-fluoro-3-(4-(3-(trifluoromethyl)phenyl)piperazine-1-carbonyl)benzyl)phthalazin-1(2H)-one</p>	<p>848135-67-1</p>	<p>Martin, N. et. al, <u>Preparation of phthalazinones as PARP inhibitors</u>, PCT Int. Appl. (2004), WO 2004080976 A1 Sep 23, 2004.</p>

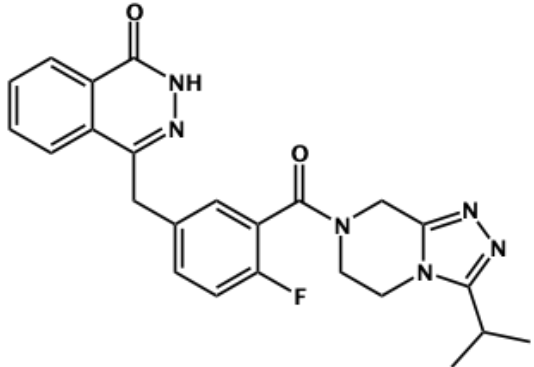
			Novel compound
	<p><i>4-(4-(5-((7-bromo-4-oxo-3,4-dihydrophthalazin-1-yl)methyl)-2-fluorobenzoyl)piperazin-1-yl)benzonitrile</i></p>	195634 0-97-8	Reported commercially available, no literature references
	<p><i>Dimethyl (6-bromo-3-oxo-1,3-dihydroisobenzofuran-1-yl)phosphonate</i></p>	133917 4-73-0	Zhu, G. et. al, <u>Phthalazin-1(2H)-one derivatives as Cdc7 inhibitors and their preparation and use for the treatment of cancer</u> , PCT Int. Appl. (2011), WO 2011130478 A1 Oct 20, 2011.



	<p><i>(Z)</i>-5-((6-bromo-3-oxoisobenzofuran-1(3H)-ylidene)methyl)-2-fluorobenzonitrile</p>		<p>Novel compound</p>
	<p>5-((7-bromo-4-oxo-3,4-dihydrophthalazin-1-yl)methyl)-2-fluorobenzoic acid</p>	<p>117404 4-56-4</p>	<p>Menear, K. et. al, <u>Phthalazine derivatives and their pharmaceutical compositions as PARP inhibitors useful for the treatment of diseases and preparation thereof</u>, PCT Int. Appl. (2009), WO 2009093032 A1 Jul 30, 2009.</p>
	<p>4-(4-(2-fluoro-5-((4-oxo-7-(prop-1-yn-1-yl)-3,4-dihydrophthalazin-1-yl)methyl)benzoyl)piperazin-1-yl)benzonitrile</p>		

	<p>4-(4-fluoro-3-(5,6,7,8-tetrahydro-[1,2,4]triazolo[4,3-a]pyrazine-7-carbonyl)benzyl)phthalazin-1(2H)-one</p>	<p>135871 5-14-6</p>	<p>Tang, P. et. al, Preparation of phthalazinone derivatives useful as antitumor agents, PCT Int. Appl. (2012), WO 2012019427 A1 Feb 16, 2012.</p>
	<p>4-(4-fluoro-3-(3-methyl-5,6,7,8-tetrahydro-[1,2,4]triazolo[4,3-a]pyrazine-7-carbonyl)benzyl)phthalazin-1(2H)-one</p>	<p>142225 4-11-2</p>	<p>Wang, Y. et. al, Phthalazinone derivatives as PARP inhibitors and their preparation, pharmaceutical compositions and use in the treatment of cancer, Faming Zhuanli Shenqing (2013), CN 102898377 A Jan 30, 2013.</p>
	<p>4-(4-fluoro-3-(3-(trifluoromethyl)-5,6,7,8-tetrahydro-[1,2,4]triazolo[4,3-a]pyrazine-7-carbonyl)benzyl)phthalazin-1(2H)-one</p>	<p>135871 4-82-5</p>	<p>Tang, P. et. al, Preparation of phthalazinone derivatives useful as antitumor agents, PCT Int. Appl. (2012), WO 2012019427 A1 Feb 16, 2012.</p>

	<p>4-(4-fluoro-3-(5-methyl-3-(trifluoromethyl)-5,6,7,8-tetrahydro-[1,2,4]triazolo[4,3-a]pyrazine-7-carbonyl)benzyl)phthalazin-1(2H)-one</p>	<p>155135 5-46-4</p>	<p>Zhang, A. et. al, <b><u>Preparation of piperazinotriazole compounds as highly selective PARP1 inhibitors</u></b>, PCT Int. Appl. (2014), WO 2014019468 A1 Feb 06, 2014.</p>
	<p>4-(3-(3-ethyl-5,6,7,8-tetrahydro-[1,2,4]triazolo[4,3-a]pyrazine-7-carbonyl)-4-fluorobenzyl)phthalazin-1(2H)-one</p>		<p>Novel compound</p>

	<p><i>4-(4-fluoro-3-(3-isopropyl-5,6,7,8-tetrahydro-[1,2,4]triazolo[4,3-a]pyrazine-7-carbonyl)benzyl)phthalazin-1(2H)-one</i></p>	<p>142225 4-08-7</p>	<p>Wang, Y. et. al, Phthalazinone derivatives as PARP inhibitors and their preparation, pharmaceutical compositions and use in the treatment of cancer, Faming Zhuanli Shenqing (2013), CN 102898377 A Jan 30, 2013.</p>
---	---	--------------------------	--

## References

- Aguilera-Gomez, A. & Rabouille, C., 2017. Membrane-bound organelles versus membrane-less compartments and their control of anabolic pathways in *Drosophila*. *Developmental biology*, 428(2), pp.310–317.
- Aguilera-Gomez, A. et al., 2016. In vivo visualization of mono-ADP-ribosylation by dPARP16 upon amino-acid starvation. *eLife*, 5.
- Andersson, C.D. et al., 2012. Discovery of ligands for ADP-ribosyltransferases via docking-based virtual screening. *Journal of medicinal chemistry*, 55(17), pp.7706–7718.
- Andreone, T.L. et al., 2003. Poly(ADP-Ribose) Polymerase-1 Regulates Activation of Activator Protein-1 in Murine Fibroblasts. *The Journal of Immunology*, 170(4), pp.2113–2120.
- Bai, P. & Virág, L., 2012. Role of poly(ADP-ribose) polymerases in the regulation of inflammatory processes. *FEBS Letters*, 586(21), pp.3771–3777.
- Barbarulo, A. et al., 2013. Poly(ADP-ribose) polymerase family member 14 (PARP14) is a novel effector of the JNK2-dependent pro-survival signal in multiple myeloma. *Oncogene*, 32(36), pp.4231–4242.
- Barrio, J.R., Secrist, J.A. & Leonard, N.J., 1972. A Fluorescent Analog of Nicotinamide Adenine Dinucleotide. *Proceedings of the National Academy of Sciences*, 69(8), pp.2039–2042.
- Beck, C. et al., 2014. PARP3 affects the relative contribution of homologous recombination and nonhomologous end-joining pathways. *Nucleic Acids Research*, 42(9), pp.5616–5632.
- Beck, C. et al., 2018. PARP3, a new therapeutic target to alter Rictor/mTORC2 signaling and tumor progression in BRCA1-associated cancers. *Cell Death & Differentiation*, 31(Pt 20), p.101.
- Belousova, E.A., Ishchenko, A.A. & Lavrik, O.I., 2018. Dna is a New Target of Parp3. *Scientific Reports*, 8(1), p.101.

- Bindesbøll, C. et al., 2016. TCDD-inducible poly-ADP-ribose polymerase (TIPARP/PARP7) mono-ADP-ribosylates and co-activates liver X receptors. *Biochemical Journal*, 473(7), pp.899–910.
- Bishop, A.C. et al., 2000. A chemical switch for inhibitor-sensitive alleles of any protein kinase. *Nature*, 407(6802), pp.395–401.
- Bitler, B.G., Gynecologic, Z.W.2017, 2017. PARP inhibitors: clinical utility and possibilities of overcoming resistance. *gynecologiconline.net*, 147(3), pp.695–704.
- Bock, F.J., Todorova, T.T. & Chang, P., 2015. RNA Regulation by Poly(ADP-Ribose) Polymerases. *Molecular cell*, 58(6), pp.959–969.
- Bryant, H.E. et al., 2005. Specific killing of BRCA2-deficient tumours with inhibitors of poly(ADP-ribose) polymerase. *Nature*, 434(7035), pp.913–917.
- Cambronne, X.A. et al., 2016. Biosensor reveals multiple sources for mitochondrial NAD. *Science*, 352(6292), pp.1474–1477.
- Carter-OConnell, I. et al., 2014. Engineering the substrate specificity of ADP-ribosyltransferases for identifying direct protein targets. *Journal of the American Chemical Society*, 136(14), pp.5201–5204.
- Carter-OConnell, I. et al., 2016. Identifying Family-Member-Specific Targets of Mono-ARTDs by Using a Chemical Genetics Approach. *Cell Reports*, 14(3), pp.621–631.
- Cravatt, B.F., Wright, A.T. & Kozarich, J.W., 2008. Activity-Based Protein Profiling: From Enzyme Chemistry to Proteomic Chemistry. *Annual Review of Biochemistry*, 77(1), pp.383–414.
- Dani, N. et al., 2009. Combining affinity purification by ADP-ribose-binding macro domains with mass spectrometry to define the mammalian ADP-ribosyl proteome. *Proceedings of the National Academy of Sciences of the United States of America*, 106(11), pp.4243–4248.
- Daugherty, M.D. et al., 2014. Rapid Evolution of PARP Genes Suggests a Broad Role for ADP-Ribosylation in Host-Virus Conflicts W. E. Johnson, ed. *PLoS Genetics*, 10(5), p.e1004403.

- Day, T.A. et al., 2017. PARP3 is a promoter of chromosomal rearrangements and limits G4 DNA. *Nature communications*, 8, p.15110.
- De Maio, A. et al., 2013. Vault-poly-ADP-ribose polymerase in the *Octopus vulgaris* brain: A regulatory factor of actin polymerization dynamic. *Comparative Biochemistry and Physiology Part B: Biochemistry and Molecular Biology*, 166(1), pp.40–47.
- Durrant, L.G. & Boyle, J.M., 1982. Potentiation of cell killing by inhibitors of poly (ADP-ribose) polymerase in four rodent cell lines exposed to N-methyl-N-nitrosourea or UV light. *Chemico-Biological Interactions*, 38(3), pp.325–338.
- Ekblad, T. et al., 2015. Towards small molecule inhibitors of mono-ADP-ribosyltransferases. *European Journal of Medicinal Chemistry*, 95, pp.546–551.
- Farmer, H. et al., 2005. Targeting the DNA repair defect in BRCA mutant cells as a therapeutic strategy. *Nature*, 434(7035), pp.917–921.
- Feng, F.Y. et al., 2015. Chromatin to Clinic: The Molecular Rationale for PARP1 Inhibitor Function. *Molecular cell*, 58(6), pp.925–934.
- Ferraris, D.V., 2010. Evolution of poly(ADP-ribose) polymerase-1 (PARP-1) inhibitors. From concept to clinic. *Journal of medicinal chemistry*, 53(12), pp.4561–4584.
- Fong, P.C. et al., 2009. Inhibition of Poly(ADP-Ribose) Polymerase in Tumors from BRCA Mutation Carriers. *New England Journal of Medicine*, 361(2), pp.123–134.
- Giansanti, V. et al., 2010. PARP inhibitors: New tools to protect from inflammation. *Biochemical Pharmacology*, 80(12), pp.1869–1877.
- Gibbs-Seymour, I. et al., 2016. HPF1/C4orf27 Is a PARP-1-Interacting Protein that Regulates PARP-1 ADP-Ribosylation Activity. *Molecular cell*, 62(3), pp.432–442.
- Gibson, B.A. et al., 2016. Chemical genetic discovery of PARP targets reveals a role for PARP-1 in transcription elongation. *Science*, 353(6294), pp.45–50.

- Gibson, B.A. et al., 2017. Generation and Characterization of Recombinant Antibody-like ADP-Ribose Binding Proteins. *Biochemistry*, 56(48), pp.6305–6316.
- Golkowski, M. et al., 2014. Rapid profiling of protein kinase inhibitors by quantitative proteomics. *Med. Chem. Commun.*, 5(3), pp.363–369.
- Gupte, R., Liu, Z. & Kraus, W.L., 2017. PARPs and ADP-ribosylation: recent advances linking molecular functions to biological outcomes. *Genes & Development*, 31(2), pp.101–126.
- Hottiger, M.O. et al., 2010. Toward a unified nomenclature for mammalian ADP-ribosyltransferases. *Trends in Biochemical Sciences*, 35(4), pp.208–219.
- Huang, J.Y. et al., 2016. PARP6 is a Regulator of Hippocampal Dendritic Morphogenesis. *Scientific Reports*, 6(1), p.208.
- Huang, S.-M.A. et al., 2009. Tankyrase inhibition stabilizes axin and antagonizes Wnt signalling. *Nature*, 461(7264), pp.614–620.
- Hutin, D., Grimaldi, G. & Matthews, J., 2018. Methods to Study TCDD-Inducible Poly-ADP-Ribose Polymerase (TIPARP) Mono-ADP-Ribosyltransferase Activity. *Methods in molecular biology (Clifton, N.J.)*, 1813, pp.109–124.
- Iansante, V. et al., 2015. PARP14 promotes the Warburg effect in hepatocellular carcinoma by inhibiting JNK1-dependent PKM2 phosphorylation and activation. *Nature communications*, 6, p.7882.
- Ikeda, Y. et al., 2016. Germline PARP4 mutations in patients with primary thyroid and breast cancers. *Endocrine-Related Cancer*, 23(3), pp.171–179.
- Ishida, J. et al., 2006. Discovery of potent and selective PARP-1 and PARP-2 inhibitors: SBDD analysis via a combination of X-ray structural study and homology modeling. *Bioorganic & Medicinal Chemistry*, 14(5), pp.1378–1390.
- Jiang, H. et al., 2010. Clickable NAD analogues for labeling substrate proteins of poly(ADP-ribose) polymerases. *Journal of the American Chemical Society*, 132(27), pp.9363–9372.



- Johannes, J.W., Almeida, L., Barlaam, B., et al., 2015. Pyrimidinone Nicotinamide Mimetics as Selective Tankyrase and Wnt Pathway Inhibitors Suitable for in Vivo Pharmacology. *ACS Medicinal Chemistry Letters*, 6(3), pp.254–259.
- Johannes, J.W., Almeida, L., Daly, K., et al., 2015. Discovery of AZ0108, an orally bioavailable phthalazinone PARP inhibitor that blocks centrosome clustering. *Bioorganic & medicinal chemistry letters*, 25(24), pp.5743–5747.
- Jwa, M. & Chang, P., 2012. PARP16 is a tail-anchored endoplasmic reticulum protein required for the PERK- and IRE1 $\alpha$ -mediated unfolded protein response. *Nature Cell Biology*, 14(11), pp.1223–1230.
- Jørgensen, R. et al., 2005. Exotoxin A–eEF2 complex structure indicates ADP ribosylation by ribosome mimicry. *Nature*, 436(7053), pp.979–984.
- Jørgensen, R. et al., 2008. The nature and character of the transition state for the ADP-ribosyltransferase reaction. *EMBO reports*, 9(8), pp.802–809.
- Kamal, A. et al., 2014. Tankyrase inhibitors as therapeutic targets for cancer. *Current topics in medicinal chemistry*, 14(17), pp.1967–1976.
- Karlberg, T. et al., 2010. Structural basis for the interaction between tankyrase-2 and a potent Wnt-signaling inhibitor. *Journal of medicinal chemistry*, 53(14), pp.5352–5355.
- Karras, G.I. et al., 2005. The macro domain is an ADP-ribose binding module. *The EMBO Journal*, 24(11), pp.1911–1920.
- Kawamitsu, H. et al., 1984. Monoclonal antibodies to poly(adenosine diphosphate ribose) recognize different structures. *Biochemistry*, 23(16), pp.3771–3777.
- Kedersha, N.L., 1986. Isolation and characterization of a novel ribonucleoprotein particle: large structures contain a single species of small RNA. *The Journal of Cell Biology*, 103(3), pp.699–709.
- Kedersha, N.L. & Rome, L.H., 1990. Vaults: Large cytoplasmic RNP's that associate with cytoskeletal elements. *Molecular Biology Reports*, 14(2-3), pp.121–122.

- Kickhoefer, V.A. et al., 1999. The 193-Kd Vault Protein, Vparp, Is a Novel Poly(Adp-Ribose) Polymerase. *The Journal of Cell Biology*, 146(5), pp.917–928.
- Kirby, I.T. & Cohen, M.S., 2018. Small-Molecule Inhibitors of PARPs: From Tools for Investigating ADP-Ribosylation to Therapeutics. In *Current Topics in Microbiology and Immunology*. Berlin, Heidelberg: Springer Berlin Heidelberg, pp. 7706–21.
- Kirby, I.T., Kojic, A., et al., 2018. A Potent and Selective PARP11 Inhibitor Suggests Coupling between Cellular Localization and Catalytic Activity. *Cell Chemical Biology*.
- Kirby, I.T., Morgan, R.K. & Cohen, M.S., 2018. A Simple, Sensitive, and Generalizable Plate Assay for Screening PARP Inhibitors. *Methods in molecular biology (Clifton, N.J.)*, 1813, pp.245–252.
- Knezevic, C.E. et al., 2016. Proteome-wide Profiling of Clinical PARP Inhibitors Reveals Compound-Specific Secondary Targets. *Cell Chemical Biology*, 23(12), pp.1490–1503.
- Krishnakumar, R. & Kraus, W.L., 2010. The PARP Side of the Nucleus: Molecular Actions, Physiological Outcomes, and Clinical Targets. *Molecular cell*, 39(1), pp.8–24.
- Küpper, J.-H. et al., 1996. Detection of poly(ADP-ribose) polymerase and its reaction product poly(ADP-ribose) by immunocytochemistry. *The Histochemical Journal*, 28(5), pp.391–395.
- Langelier, M.-F. et al., 2018. NAD<sup>+</sup> analog reveals PARP-1 substrate-blocking mechanism and allosteric communication from catalytic center to DNA-binding domains. *Nature communications*, 9(1), p.844.
- Langelier, M.-F., Riccio, A.A. & Pascal, J.M., 2014. PARP-2 and PARP-3 are selectively activated by 5' phosphorylated DNA breaks through an allosteric regulatory mechanism shared with PARP-1. *Nucleic Acids Research*, 42(12), pp.7762–7775.
- Liu, Q. et al., 2013. Developing Irreversible Inhibitors of the Protein Kinase Cysteine. *Chemistry & Biology*, 20(2), pp.146–159.
- Ma, Q. et al., 2001. TCDD-Inducible Poly(ADP-ribose) Polymerase: A Novel Response to 2,3,7,8-Tetrachlorodibenzo-p-dioxin. *Biochemical and Biophysical Research Communications*, 289(2), pp.499–506.

- Ma, Y.-S. et al., 2018. Proteogenomic characterization and comprehensive integrative genomic analysis of human colorectal cancer liver metastasis. *Molecular Cancer*, 17(1), p.87.
- Mah, R. et al., 2014. Drug discovery considerations in the development of covalent inhibitors. *Bioorganic & Medicinal Chemistry Letters*, 24, pp.33-39.
- Mariappan, L. et al., 2017. Emerging treatment options for ovarian cancer: focus on rucaparib. *International Journal of Women's Health*, Volume 9, pp.913–924.
- Marsischky, G.T., Wilson, B.A. & Collier, R.J., 1995. Role of glutamic acid 988 of human poly-ADP-ribose polymerase in polymer formation. Evidence for active site similarities to the ADP-ribosylating toxins. *Journal of Biological Chemistry*, 270(7), pp.3247–3254.
- Mata, I.F. et al., 2017. Large-scale exploratory genetic analysis of cognitive impairment in Parkinson's disease. *Neurobiology of aging*, 56, pp.211.e1–211.e7.
- Mehrotra, P. et al., 2013. Poly (ADP-ribose) polymerase 14 and its enzyme activity regulates TH2 differentiation and allergic airway disease. *Journal of Allergy and Clinical Immunology*, 131(2), pp.521–531.e12.
- Menear, K.A. et al., 2008. 4-[3-(4-cyclopropanecarbonylpiperazine-1-carbonyl)-4-fluorobenzyl]-2H-phthalazin-1-one: a novel bioavailable inhibitor of poly(ADP-ribose) polymerase-1. *Journal of medicinal chemistry*, 51(20), pp.6581–6591.
- Meyer, T. & Hilz, H., 1986. Production of anti-(ADP-ribose) antibodies with the aid of a dinucleotide-pyrophosphatase-resistant hapten and their application for the detection of mono(ADP-ribosyl)ated polypeptides. *European Journal of Biochemistry*, 155(1), pp.157–165.
- Meyer-Ficca, M.L. et al., 2015. Spermatid Head Elongation with Normal Nuclear Shaping Requires ADP-Ribosyltransferase PARP11 (ARTD11) in Mice. *Biology of Reproduction*, 92(3), p.33.
- Mikule, K. and Wang, Z. (2016). Treatment of Cancer.

- Morgan, R.K. & Cohen, M.S., 2015. A Clickable Aminooxy Probe for Monitoring Cellular ADP-Ribosylation. *ACS chemical biology*, 10(8), pp.1778–1784.
- Morgan, R.K. et al., 2018. Rational Design of Cell-active Inhibitors of PARP10. *ACS Publications*.
- Morgan, R.K., Carter-OConnell, I. & Cohen, M.S., 2015. Selective inhibition of PARP10 using a chemical genetics strategy. *Bioorganic & medicinal chemistry letters*, 25(21), pp.4770–4773.
- Munnur, D. & Ahel, I., 2017. Reversible mono-ADP-ribosylation of DNA breaks. *The FEBS journal*, 284(23), pp.4002–4016.
- Narendja, F.M. & Sauermann, G., 1994. The Use of Biotinylated Poly(ADP-Ribose) for Studies on Poly(ADP-Ribose)-Protein Interaction. *Analytical Biochemistry*, 220(2), pp.415–419.
- Narwal, M., Venkannagari, H. & Lehtiö, L., 2012. Structural basis of selective inhibition of human tankyrases. *Journal of medicinal chemistry*, 55(3), pp.1360–1367.
- NDUKA, N., Skidmore, C.J. & Shall, S., 1980. The Enhancement of Cytotoxicity of N-Methyl-N-nitrosourea and of  $\gamma$ -Radiation by Inhibitors of Poly(ADP-ribose) Polymerase. *European Journal of Biochemistry*, 105(3), pp.525–530.
- Oei, S.L. et al., 1999. NAD<sup>+</sup> analogs substituted in the purine base as substrates for poly(ADP-ribosyl) transferase. *FEBS Letters*, 397(1), pp.17–21.
- Ohmoto, A. & Yachida, S., 2017. Current status of poly(ADP-ribose) polymerase inhibitors and future directions. *OncoTargets and Therapy*, Volume 10, pp.5195–5208.
- Papeo, G. et al., 2014. Insights into PARP Inhibitors' Selectivity Using Fluorescence Polarization and Surface Plasmon Resonance Binding Assays. *Journal of Biomolecular Screening*, 19(8), pp.1212–1219.
- Peng, B. et al., 2016. Small Molecule Microarray Based Discovery of PARP14 Inhibitors. *Angewandte Chemie International Edition*, 56(1), pp.248–253.

- Pinto, A.F. & Schöler, H., 2015. Comparative structural analysis of the putative mono-ADP-ribosyltransferases of the ARTD/PARP family. *Current topics in microbiology and immunology*, 384(Chapter 417), pp.153–166.
- Placzek, A.T. et al., 2016. Sobetirome prodrug esters with enhanced blood–brain barrier permeability. *Bioorganic & Medicinal Chemistry*, 24(22), pp.5842–5854.
- Purnell, M.R. & Whish, W.J., 1980. Novel inhibitors of poly(ADP-ribose) synthetase. *Biochemical Journal*, 185(3), pp.775–777.
- Rolli, V. et al., 1997. Random Mutagenesis of the Poly(ADP-ribose) Polymerase Catalytic Domain Reveals Amino Acids Involved in Polymer Branching †. *Biochemistry*, 36(40), pp.12147–12154.
- Rosado, M.M. et al., 2013. Beyond DNA repair, the immunological role of PARP-1 and its siblings. *Immunology*, 139(4), pp.428–437.
- Surowy, C.S. & Berger, N.A., 1985. A 3-aminobenzamide-resistant labeled protein in [32P]NAD<sup>+</sup>-labeled cells. *Biochimica et Biophysica Acta (BBA) - Molecular Cell Research*, 847(3), pp.309–315.
- Thomas, H.D. et al., 2007. Preclinical selection of a novel poly(ADP-ribose) polymerase inhibitor for clinical trial. *Molecular Cancer Therapeutics*, 6(3), pp.945–956.
- Thorsell, A.-G. et al., 2017. Structural Basis for Potency and Promiscuity in Poly(ADP-ribose) Polymerase (PARP) and Tankyrase Inhibitors. *Journal of medicinal chemistry*, 60(4), pp.1262–1271.
- Tsurumura, T. et al., 2013. Arginine ADP-ribosylation mechanism based on structural snapshots of iota-toxin and actin complex. *Proceedings of the National Academy of Sciences*, 110(11), pp.4267–4272.
- Upton, K. et al., 2017. Design and synthesis of potent inhibitors of the mono(ADP-ribosyl)transferase, PARP14. *Bioorganic & medicinal chemistry letters*, 27(13), pp.2907–2911.
- Venkannagari, H. et al., 2013. Activity-based assay for human mono-ADP-ribosyltransferases ARTD7/PARP15 and ARTD10/PARP10 aimed at screening and profiling inhibitors. *European journal of pharmaceutical sciences : official journal of the European Federation for Pharmaceutical Sciences*, 49(2), pp.148–156.

- Venkannagari, H. et al., 2016. Small-Molecule Chemical Probe Rescues Cells from Mono-ADP-Ribosyltransferase ARTD10/PARP10-Induced Apoptosis and Sensitizes Cancer Cells to DNA Damage. *Cell Chemical Biology*, 23(10), pp.1251–1260.
- Voronkov, A. et al., 2013. Structural Basis and SAR for G007-LK, a Lead Stage 1,2,4-Triazole Based Specific Tankyrase 1/2 Inhibitor. *Journal of medicinal chemistry*, 56(7), pp.3012–3023.
- Vyas, S. et al., 2014. Family-wide analysis of poly(ADP-ribose) polymerase activity. *Nature communications*, 5(1), p.4426.
- Wahlberg, E. et al., 2012. Family-wide chemical profiling and structural analysis of PARP and tankyrase inhibitors. *Nature Biotechnology*, 30(3), pp.283–288.
- Wallrodt, S. et al., 2016. Bioorthogonally Functionalized NAD<sup>+</sup> Analogues for In-Cell Visualization of Poly(ADP-Ribose) Formation. *Angewandte Chemie International Edition*, 55(27), pp.7660–7664.
- Wang, Y. et al., 2014. Chain-Terminating and Clickable NAD<sup>+</sup> Analogues for Labeling the Target Proteins of ADP-Ribosyltransferases. *Angewandte Chemie International Edition*, 53(31), pp.8159–8162.
- Watson, C.Y., Whish, W.J.D. & Threadgill, M.D., 1998. Synthesis of 3-Substituted Benzamides and 5-Substituted Isoquinolin-1(2H)-ones and Preliminary Evaluation as Inhibitors of Poly(ADP-ribose)polymerase (PARP). *Bioorganic & Medicinal Chemistry*, 6(6), pp.721–734.
- Yoneyama-Hirozane, M. et al., 2017. Identification of PARP14 inhibitors using novel methods for detecting auto-ribosylation. *Biochemical and Biophysical Research Communications*, 486(3), pp.626–631.
- Zhan, P. et al., 2014. Recent advances in the structure-based rational design of TNKSI. *Mol. BioSyst.*, 10(11), pp.2783–2799.
- Zhang, J. & Snyder, S.H., 1992. Nitric oxide stimulates auto-ADP-ribosylation of glyceraldehyde-3-phosphate dehydrogenase. *Proceedings of the National Academy of Sciences*, 89(20), pp.9382–9385.
- Zheng, C.-L. et al., 2005. Characterization of MVP and VPARP assembly into vault ribonucleoprotein complexes. *Biochemical and Biophysical Research Communications*, 326(1), pp.100–107.

- Zingarelli, B., Salzman, A.L. & Szabó, C., 1998. Genetic Disruption of Poly (ADP-Ribose) Synthetase Inhibits the Expression of P-Selectin and Intercellular Adhesion Molecule-1 in Myocardial Ischemia/Reperfusion Injury. *Circulation Research*, 83(1), pp.85–94.
- Zmuda, F. et al., 2015. Synthesis and Evaluation of a Radioiodinated Tracer with Specificity for Poly(ADP-ribose) Polymerase-1 (PARP-1) in Vivo . *Journal of medicinal chemistry*, 58(21), pp.8683–8693.